DEVELOPMENT OF NOVEL MOLECULAR PROBES AND SYNCHROTRON IMAGING TECHNIQUES TO STUDY THE UPTAKE OF METALLO-CYLINDER DRUGS

UNIVERSITY OF BIRMINGHAM

Ashleigh Elizabeth Freer

A thesis submitted to the University of Birmingham for the degree of Doctor of Philosophy

School of Chemistry
University of Birmingham
September 2016

UNIVERSITY OF
BIRMINGHAM

University of Birmingham Research Archive

e-theses repository

This unpublished thesis/dissertation is copyright of the author and/or third parties. The intellectual property rights of the author or third parties in respect of this work are as defined by The Copyright Designs and Patents Act 1988 or as modified by any successor legislation.

Any use made of information contained in this thesis/dissertation must be in accordance with that legislation and must be properly acknowledged. Further distribution or reproduction in any format is prohibited without the permission of the copyright holder.

Table of Contents

Abstract i

Acknowledgements ii

Abbreviations iii

1 Introduction 2

1.1DNA 3

1.2 Molecular DNA recognition 9

1.2.1 Major and minor groove binding 9

1.2.2 Intercalation 11

1.2.3 Alkylating agents 12

1.2.4 Backbone binders 13

1.2.5 Targeting DNA quadruplex structures 14

1.2.6 Targeting DNA junctions 15

1.3Metallo anti-cancer drugs 17

1.3.1 Platinum based anti-cancer drugs 17

1.3.2 Non-platinum metal based drugs 19

1.3.3 Iron based anti-cancer drugs 19

1.3.4 Ruthenium based anti-cancer drugs 21

1.3.5 Nickel based anti-cancer drugs 23

1.3.6 Copper based anti-cancer drugs 25

1.4 Fluorescent probes. 26

1.4.1 Fluorescent dye-anticancer drug conjugates 27

1.5Supramolecular chemistry 28

1.5.1 Metallo supramolecular helicates 28

1.5.2 Supramolecular metallo cylinder. 30

1.6 Thesis aims 36

1.7 References 37

2 Pyridylimine cylinders 43

2.1Introduction and aims 43

2.2Molecular design 43

2.3Sonogashira reaction 44

2.4Click chemistry 46

2.5Synthesis of coumarin ligand and complexes. 47

2.5.1 Synthesis of 5-ethynyl-2-formylpyridine. 47

2.5.2 Synthesis of 3-azido-7-diethylaminocoumarin 49

2.5.3 Synthesis of 5-(1-(7-(diethylamino)-2-oxo-2H-chromen-3-yl)-1H-1,2,3-triazol-4-yl)picolinaldehyde 51

2.5.4 Synthesis of L^{C5} 54

2.5.5 Synthesis of $(L^{C5}{}_3Fe_2)[\ PF_6]_4$ 55

2.5.6 Attempted Synthesis if $(L^{C5}{}_3Ru_2)4PF_6$ 56

2.6Synthesis and design of dansyl ligands and complexes. 57

2.6.1 Synthesis of dansyl-PEG3-azide 57

2.6.2 Synthesis of 5-(dimethylamino)-N-(2-(2-(2-(2-(4-(6-formylpyridin-3-yl)-1H-1,2,3-triazol-1-yl)ethoxy)ethoxy)ethoxy)ethyl)naphthalene-1-sulfonamide 59

2.6.3 Synthesis of L^{D5} 61

2.6.4 Synthesis of $[L^{D5}{}_3Fe_2][\ PF_6]_4$ 62

2.7Functionalisation in the fourth position *63*
2.7.1 Synthesis of 4-ethynyl-2-formylpyridine 64
2.7.2 Synthesis of clicked courmarin product in fourth position. 65
2.7.3 Synthesis of L^{C4} 66
2.7.4 Synthesis of $[L^{C4}{}_3Fe_2][PF_6]_4$ 68
2.7.5 Synthesis of clicked dansyl in fourth position 69
2.7.6 Synthesis of L^{D4} 71
2.7.7 Synthesis of $[L^{D4}{}_3Fe_2][PF_6]$ 72
2.8Attempted synthesis of 5-azidopyridine-2-carbaldehyde. *73*
2.9Attempted synthesis of $[L^{TB5}{}_3Ru_2][PF_6]_4$ *74*
2.10 Attempted click reaction *75*
2.11 Stability studies *77*
2.12 Fluorimeter studies *79*
2.13 Imaging *80*
2.14 Conclusions and future work *84*
2.15 References *86*

3 Imidazolimine cylinders **89**
3.1 Introduction *89*
3.2 Molecular design *92*
3.3 Synthesis of azide functionalised ligands and complexes *92*
3.3.1 Synthesis of azide imidazole 93
3.3.2 Synthesis of azide functionalised imidazole ligand L^{imN} 95
3.3.3 Synthesis of $[L^{imN}{}_3Fe_2][PF_6]_4$ 96
3.3.4 Synthesis of $[L^{imN}{}_3Ni_2][PF_6]_4$ 97
3.4 Synthesis of alkyne functionalised ligands and complexes *98*
3.4.1 Synthesis of alkyne imidazole 98
3.4.2 Synthesis of alkyne functionalised imidazole ligand L^{imTB} 99
3.4.3 Synthesis of $[L^{imTB}{}_3Fe_2][PF_6]_4$ 101
3.4.4 Synthesis of $[L^{inTB}{}_3Ni_2][PF_6]_4$ 101
3.5 'Click' reactions with imidazole ligands *102*
3.6 Copper free click reactions *104*
3.7 Synthesis of $[L^{im}{}_3Ru_2][PF_6]_4$ *105*
3.7.1 Synthesis of L^{im} 106
3.7.2 Attempted synthesis of $[L^{im}{}_3Ru_2][PF_6]_4$ 107
3.8 Conclusions and future work *108*
3.9 References *110*

4 Synchrotron Imaging Techniques **112**
4.1 Introduction *112*
4.1.1 Synchrotron systems and radiation 112
4.1.2 XRF and XANES 113
4.1.3 Synchrotron XRF and XANES imaging applications 116
4.1.3 Aims 118
4.2Sample preparation *119*
4.2.1 Iron(II) metallo-cylinder complex preparation 119
4.2.2 Biological sample preparation 120
4.3XRF and XANES beam line Set up *121*
4.4XRF and XANES results *124*

4.5Bromine cylinders *138*
4.5.1 Synthesis of bromine cylinders 138
4.5.2 Stability of bromine cylinders 142
4.5.3 Synchrotron XRF imaging of bromine cylinders 145
4.6Cryo soft x-ray tomographic imaging *149*
4.6.1 Introduction 149
4.6.2 Literature examples of cryo soft X–ray tomographic imaging 150
4.6.3 Aims 153
4.6.4 Sample preparation for cryo soft X–ray tomographic imaging 153
4.6.5 Beamline set-up 155
4.6.6 Results of cryo soft X–ray tomographic imaging 156
4.7 Conclusion and future work *159*
4.8 References *161*

5 Experimental **163**
5.1 General experimental *163*
5.1.1 Preparation of 5-trimethylsilylethynyl-2-formyl pyridine 164
5.1.2 Preparation of 5-ethynyl-2-formylpyridine 165
5.1.3 Preparation of 4-trimethylsilylethynyl-2-formyl pyridine 165
5.1.4 Preparation of 4-ethynyl-2-formylpyridine 166
5.1.5 Preparation of 3-nitro-7-diethylamino coumarin 166
5.1.6 Preparation of 3-amino-7-diethylamino coumarin 167
5.1.7 Preparation of 3-azido-7-diethylaminocoumarin 168
5.1.8 Preparation of 4-(1-(7-(diethylamino)-2-oxo-2H-chromen-3-yl)-1H-1,2,3-triazol-4-yl)picolinaldehyde 168
5.1.9 Preparation of 5-(1-(7-(diethylamino)-2-oxo-2H-chromen-3-yl)-1H-1,2,3-triazol-4-yl)picolinaldehyde 169
5.1.10 Preparation of L^{C5} 170
5.1.11 Preparation of $[Fe_2L^{C5}{}_3][PF_6]_4$ 170
5.1.12 Preparation of L^{C4} 171
5.1.13 Preparation of $[Fe_2L^{C4}{}_3][PF_6]_4$ 172
5.1.14 Preparation of dansyl-PEG_3-azide 172
5.1.15 Preparation of 5-(dimethylamino)-N-(2-(2-(2-(2-(4-(6-formylpyridin-3-yl)-1H-1,2,3-triazol-1-yl)ethoxy)ethoxy)ethoxy)ethyl)naphthalene-1-sulfonamide 173
5.1.16 Preparation of 4-(dimethylamino)-N-(2-(2-(2-(2-(4-(2-formylpyridin-4-yl)-1H-1,2,3-triazol-1-yl)ethoxy)ethoxy)ethoxy)ethyl)naphthalene-1-sulfonamide 174
5.1.17 Preparation of L^{D5} 175
5.1.18 Preparation of $[Fe_2L^{D5}{}_3][PF_6]_4$ 176
5.1.19 Preparation of L^{D4} 176
5.1.20 Preparation of $[Fe_2L^{D4}{}_3][PF_6]_4$ 177
5.1.21 Preparation of L^{Br5} 178
5.1.22 Preparation of $[Fe_2L^{Br5}{}_3][PF_6]_4$ 178
5.1.23 Preparation of L^{Br4} 178
5.1.24 Preparation of $[Fe_2L^{Br4}{}_3][PF_6]_4$ 179
5.1.25 Preparation of 1-(prop-2-yn-1-yl)-1H-imidazole-2-carbaldehyde 179
5.1.26 Preparation of L^{TBim} 180
5.1.27 Preparation of $[Fe_2L^{TBim}{}_3][PF_6]_4$ 180
5.1.28 Preparation of $[Ni_2L^{TBim}{}_3][PF_6]_4$ 181
5.1.29 Preparation of 3-azidopropan-1-ol 181

5.1.30 Preparation of 3-azidopropyl methanesulfonate 181
5.1.31 Preparation of 1-(3-azidopropyl)-1H-imidazole-2-carbaldehyde 182
5.1.32 Preparation of L^{imN} 182
5.1.33 Preparation of $[Fe_2L^{imN}_3][PF_6]_4$ 183
5.1.34 Preparation of $[Ni_2L^{imN}_3][PF_6]_4$ 183
5.1.35 Preparation of L 184
5.1.36 Preparation of $[Fe_2L_3]Cl_4$ 184
5.1.37 Preparation of L^{im} 185
5.1.38 Preparation of 1-((1-(7-(diethylamino)-2-oxo-2H-chromen-3-yl)-1H-1,2,3-triazol-4-yl)methyl)-1H-imidazole-2-carbaldehyde 186
5.1.39 Preparation of L^{imC} 187
5.1.40 Preparation of $[Fe_2L^{imC}_3][PF_6]_4$ 187
5.1.41 Preparation of $[Ni_2L^{imC}_3][PF_6]_4$ 188
5.1.42 Preparation of dasnyl _C3_N3 188
5.1.43 Preparation of FITC_C3_N3 189
5.1.44 Preparation of FITC_PEG3_N3 189
5.1.45 Preparation of L^{TB5} 190
5.2 Cell culture experimental *191*
5.2.1 General cell culture 191
5.2.2 Cell lines 191
5.2.3 Cell media preparation 192
5.2.4 Cell culture passage 192
5.2.5 Cryopreservation of cells 192
5.2.6 Cell counting 193
5.2.7 Sapphire disc sample preparation 193
5.2.8 TEM grid sample preparation 194
5.2.9 MatTek dish preparation 194
6 Appendix **196**
6.1 NMR spectra of 5-trimethylsilylethynyl-2-formyl pyridine *196*
6.2 NMR spectra of 5-ethynyl-2-formylpyridine *197*
6.3 NMR spectra of 4-trimethylsilylethynyl-2-formyl pyridine *198*
6.4 NMR spectra of 4-ethynyl-2-formylpyridine *199*
6.5 NMR spectra of 3-nitro-7-diethylamino coumarin *200*
6.6 NMR spectra of 3-amino-7-diethylamino coumarin *202*
6.7 NMR spectra of 3-azido-7-diethylaminocoumarin *204*
6.8NMR spectra of 4-(1-(7-(diethylamino)-2-oxo-2H-chromen-3-yl)-1H-1,2,3-triazol-4-yl)picolinaldehyde *206*
6.9NMR spectra of 5-(1-(7-(diethylamino)-2-oxo-2H-chromen-3-yl)-1H-1,2,3-triazol-4-yl)picolinaldehyde *209*
6.10 NMR spectra of L^{C5} *211*
6.11 NMR spectra of $[Fe_2L^{C5}_3][PF_6]_4$ *212*
6.12 NMR spectra of L^{C4} *213*
6.13 NMR spectra of $[Fe_2L^{C4}_3][PF_6]_4$ *215*
6.14 NMR spectra of dansyl-PEG_3-azide *216*
6.15 NMR spectra of 5-(dimethylamino)-N-(2-(2-(2-(2-(4-(6-formylpyridin-3-yl)-1H-1,2,3-triazol-1-yl)ethoxy)ethoxy)ethoxy)ethyl)naphthalene-1-sulfonamide *219*
6.16 NMR spectra of 4-(dimethylamino)-N-(2-(2-(2-(2-(4-(2-formylpyridin-4-yl)-1H-1,2,3-triazol-1-yl)ethoxy)ethoxy)ethoxy)ethyl)naphthalene-1-sulfonamide *221*

6.17 NMR spectra of L^{D5} 222
6.18 NMR spectra of $[Fe_2L^{D5}{}_3][PF_6]_4$ 225
6.19 NMR spectra of L^{D4} 226
6.20 NMR spectrum of $[Fe_2L^{D4}{}_3][PF_6]_4$ 228
6.21 NMR spectra of L^{Br5} 229
6.22 NMR spectrum of $[Fe_2L^{Br5}{}_3][PF_6]_4$ 230
6.23 NMR spectra of L^{Br4} 231
6.24 NMR spectra of $[Fe_2L^{Br4}{}_3][PF_6]_4$ 232
6.25 NMR spectra of 1-(prop-2-yn-1-yl)-1H-imidazole-2-carbaldehyde 233
6.26 NMR spectra of L^{TBim} 234
6.27 NMR spectrum of 3-azidopropan-1-ol 235
6.28 NMR spectrum of 3-azidopropyl methanesulfonate 235
6.29 NMR spectra of 1-(3-azidopropyl)-1H-imidazole-2-carbaldehyde 236
6.30 NMR spectra of L^{Nim} 236
6.31 NMR spectrum of $[Fe_2L^{Nim}{}_3][PF_6]_4$ 238
6.32NMR spectra of 1-((1-(7-(diethylamino)-2-oxo-2H-chromen-3-yl)-1H-1,2,3-triazol-4-yl)methyl)-1H-imidazole-2-carbaldehyde 239
6.33 NMR spectra of L^{imC} 240
6.34 NMR spectrum of L 242
6.35 NMR spectrum of $[Fe_2L_3]Cl_4$ 242
6.36 NMR spectra of L^{im} 243
6.37 NMR spectra of dansyl _C3_N_3 244
6.38 NMR spectra of FITC_C3_N_3 245
6.39 NMR spectra of FITC_PEG3_N_3 247
6.40 NMR spectrum of L^{TB5} 250

Abstract

Work described in this thesis shows the design and synthesis of functionalised, triple stranded, dinuclear, supramolecular helicates. Click chemistry has been utilized to functionalise the parent ligand with dansyl and coumarin moiety's. These ligands have been used to successfully form four novel metal complexes upon reaction with iron(II) chloride. The stability and fluorescence of these complexes has been monitored. Imidazole ligands has been functionalised by the addition of alkyne and azide side chains to allow them to undergo click reactions. This modification has not been shown to impede complex formation, as the ligand have been utilized to form novel triple stranded iron(II) and nickel(II) complexes.

Synchrotron imaging has been used to produce elemental maps of cells treated with the parent metallo cylinder. This has allowed the uptake of the complex to be monitored. Two novel bromine functionalised cylinders has been developed to allow co-localisation experiments to be undertaken using XRF imaging. Cryo-SXT experiments have been undertaken to examine the morphology of HeK cells after treatment with parent metallo cylinder.

Acknowledgements

Firstly, I would like to thank my supervisor Professor Mike Hannon for the help, support and guidance he has given me throughout my PhD. I would like to convey my gratitude for allowing me to be a member of the Hannon research group which has enabled me to develop understanding in this area of science and has allowed me to develop my skills in a number of interdisciplinary areas.

I would also like to thank all members of the Hannon group for their support and the knowledge they have shared with me over the past four years. With special thanks to Lois, Jeni and Pete for all the help and cake they have given me throughout this experience.

I would also like to express my gratitude to all members of my PSIBS cohort for the help they have given me in this interdisciplinary project. I would particularly like to thank Lois, Chris, David, Vicky and Rachel for keeping me sane throughout this project.

I am grateful to Nik Hodges for his help and guidance throughout this project and for allowing me to use his cell culture facilities. I would also like to thank the Hodges group, specifically Zahra and Lorna for making me feel so welcome and for their help. I am thankful to all members of the analytical department within the School of Chemistry for their help and advice.

I would also like to thank the Diamond Light source for allowing me to conduct my research. With special thanks being paid to Tina for her late nights and help and guidance during my visits. I would also like to thank Liz for allowing me to use her beam line and for her help with my experiments.

I would like to thank the EPSRC for funding this research and allowing me to increase my knowledge of the area further by attending numerous conferences.

Finally, I would like to thank my family for the love and support they have shown me throughout my life.

Abbreviations

Δ	chemical shift relating to NMR
^{o}C	degrees Celsius
ε	molar absorption coefficient ($mol^{-1}dm^{-1}cm^{-1}$)
Φ	DNA unwinding angle
λ	wavelength
λ_{max}	wavelength maximum
^{13}C NMR	carbon nuclear magnetic resonance
^{1}H NMR	proton nuclear magnetic resonance
A	adenine
b	broad relating to IR
BF_4	tetrafluoroborate
bs	broad singlet relating to NMR
C	cytosine
CD	circular dichroism
CD_3CN	deuterated acetonitrile
$CDCl_3$	deuterated chloroform
$(CD_3)_2SO$	deuterated dimethylsulphoxide
CD_3OD	deuterated methanol
cm	centimeter
conc.	concentrated
COSY	correlation spectroscopy
ct-DNA	calf thymus deoxyribonucleic acid
d	doublet relating to NMR
D_2O	deuterated water
DCM	dichloromethane
dd	doublet of doublets relating to NMR
DMF	dimethylformide
DNA	deoxyribonucleic acid
EI-MS	electron impact mass spectrometry
em.	emission

eq.	equivalents
ESI-MS	electrospray mass spectrometry
ex.	excitation
G	guanine
g	gram
h	hours
Hz	hertz
H_2SO_4	sulphuric acid
HCl	hydrochloric acid
HRMS	high resolution mass spectrometry
IR	infra-red
J	coupling constant
LD	linear dichroism
m	multiplet relating to NMR
M	molar (mol dm^{-3})
min	minutes
m/z	mass to charge ratio
MeCN	acetonitrile
MeOH	methanol
mg	milligram
MHz	megahertz
mL	milliliters
mM	millimolar
mmol	millimole
MTT	3-(4,5-dimethylthiazol-2-yl)-2,5-diphenyltetrazolium bromide
NaOH	sodium hydroxide
nm	nanometer
NMR	nuclear magnetic resonance
PF_6	hexafluorophospahte
ppm	parts per million
q	quartet relating to NMR

qu	quintet relating to NMR
RNA	ribonucleic acid
RT	room temperature
s	singlet relating to NMR
T	thymine
t	triplet relating to NMR
THF	tetrahydrofuran
TLC	thin layer chromatography
UV	ultraviolet
µM	micromolar
µL	microliter

Chapter 1

1 Introduction

Deoxyribonucleic acid (DNA) carries the genetic information used in the growth, development and reproduction of all living organisms. The nuclear genome is comprised of approximately 3.2 billion bases in human DNA[1]. This information is stored in 23 pairs of chromosomes in diploid cells. The mitochondrial genome is a circular piece of DNA comprised of approximately 16.5 thousand bases, with approximately 10 copies of this DNA per mitochondria and 8000 copies per cell [1].

DNA mutations and damage can be caused by a number of factors including, copying errors during replication, mutagenic chemicals and certain types of radiation [2]. If these mutations and changes in DNA sequence are not repaired somatic cells may accumulate so many mutations that they can no longer function. Carcinogens and mutagens can cause tumors by changing the sequence of DNA and by the errors that are introduced into the cell during its efforts to repair this damage [2]. UV and ionizing radiation such as X-rays and atomic particles cause modifications in the DNA. This is evident from the rise in leukemia in survivors of World War II who were near atomic bomb drops, and also in the development of melanomas from the prolonged and repeated exposure to sunlight [2]. There are a number of DNA lesions that require repair including missing bases, altered bases, incorrect bases, bulges caused by insertion or deletion of a nucleotide and single or double stand breaks. Ineffective or error prone DNA repair mechanisms can perpetuate mutations, inducing tumour formation [2]. As such, DNA has long been viewed as a target for cancer therapeutics, either in its ability to detect these lesions or to induce them, such as the stand links caused by cisplatin. By causing these lesions in cancer cells it is hoped that the cell will induce DNA repair mechanisms. The DNA damage at the site of the lesion can be too great and the repair mechanisms fail, leading to the programmed cell death of

the cancer cell by a number of mechanisms including apoptosis. However these agents, such as cisplatin can be very genotoxic, leading to subsequent tumours, commonly leukemia later in life [3]. A move towards more specific DNA targets and DNA processes has been seen in recent years, hopefully lessening the toxicity to normal cells. An example of this would be the development of trastuzumab emtansine (Kadcyla), an antibody drug conjugate made up of the monoclonal antibody trastuzumab (Herceptin) linked to the cytotoxic drug emtansine (DM1) [4]. This has been used to treat HER2 positive breast cancers, where Herceptin binds to the HER2/neu receptor of the tumour and stops the growth of cancer cells and DM1 enters cell, binds to tubulin and destroys cells [5].

1.1 DNA

DNA was first isolated in 1869 by Friedrich Miescher [6]. Its molecular structure was later determined in 1953 by James Watson and Francis Crick [7], whose names describe the Watson Crick base pairing observed in duplex DNA (Figure 1.1). DNA is formed from repeating subunits of deoxyribonucleotides. These nucleotides are comprised of a phosphate group, a 2-deoxyribose sugar and a nucleobase. The nucleobases Adenine (A) and Guanine (G) are heterocyclic purines, whilst Thymine (T) and Cytosine (C) are pyrimidines [8]. Watson Crick base pairing denotes that adenine binds with thymine *via* two hydrogen bonds, and guanine binds with cytosine *via* three hydrogen bonds [9]. The sugar phosphate backbone is made of alternating phosphate and ribose groups. DNA is very rarely found as a single strand, and instead hybridises together to form a double helix with a hydrophobic core, formed by hydrogen bonding between the bases[9]. It is this hydrogen bonding combined with solvation of the external polyphosphate backbone that stabilize DNA.

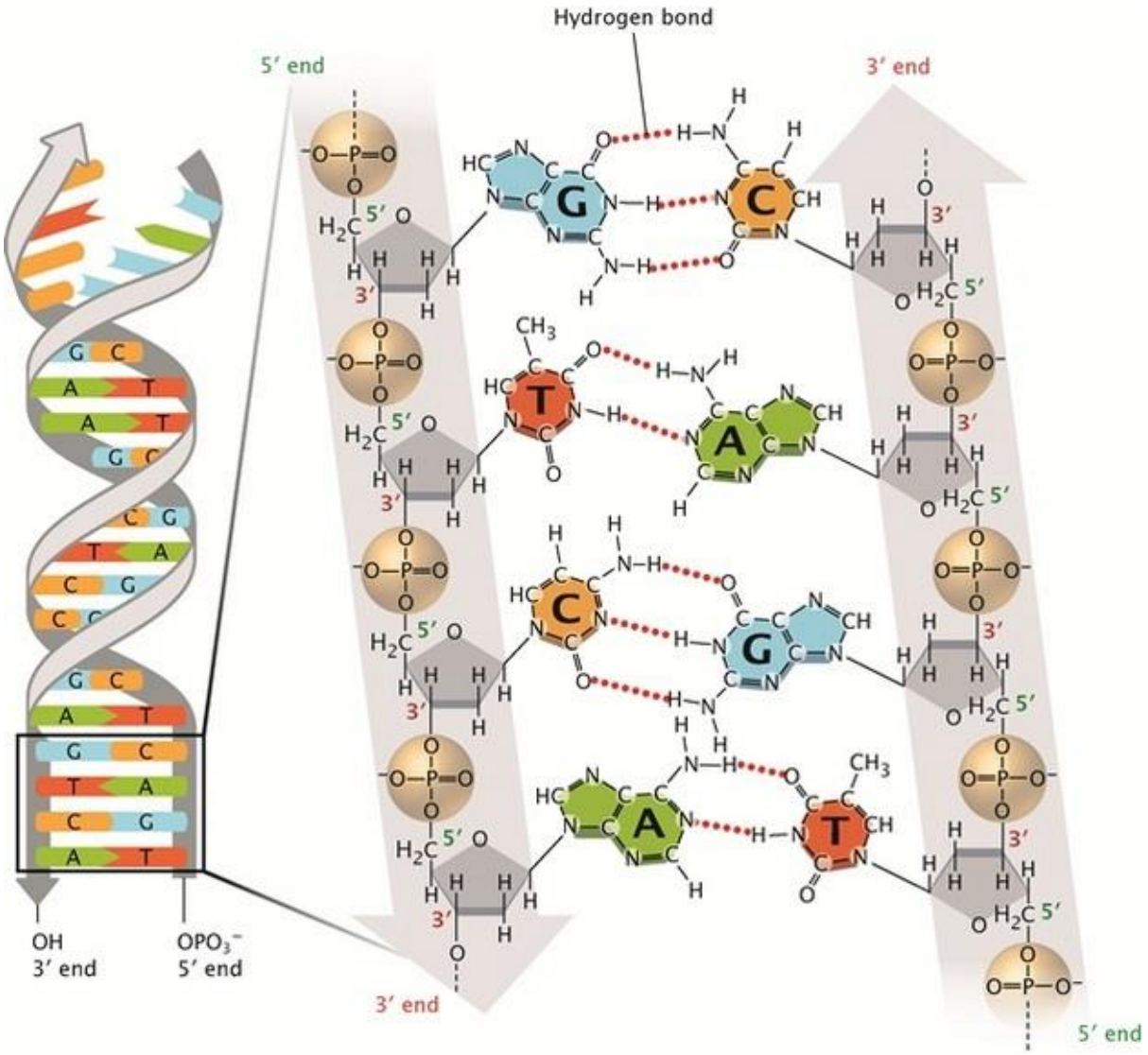

Figure 1.1 Shows the duplex structure of DNA, the alternating phosphate and deoxyribose sugar units forming the sugar phosphate backbone. The structures of the DNA bases adenine (A), thymine (T), cytosine (C) and guanine (G) are shown with the Watson-Crick base pairing and hydrogen bonds between the bases depicted as red dotted lines. (Taken from reference [7])

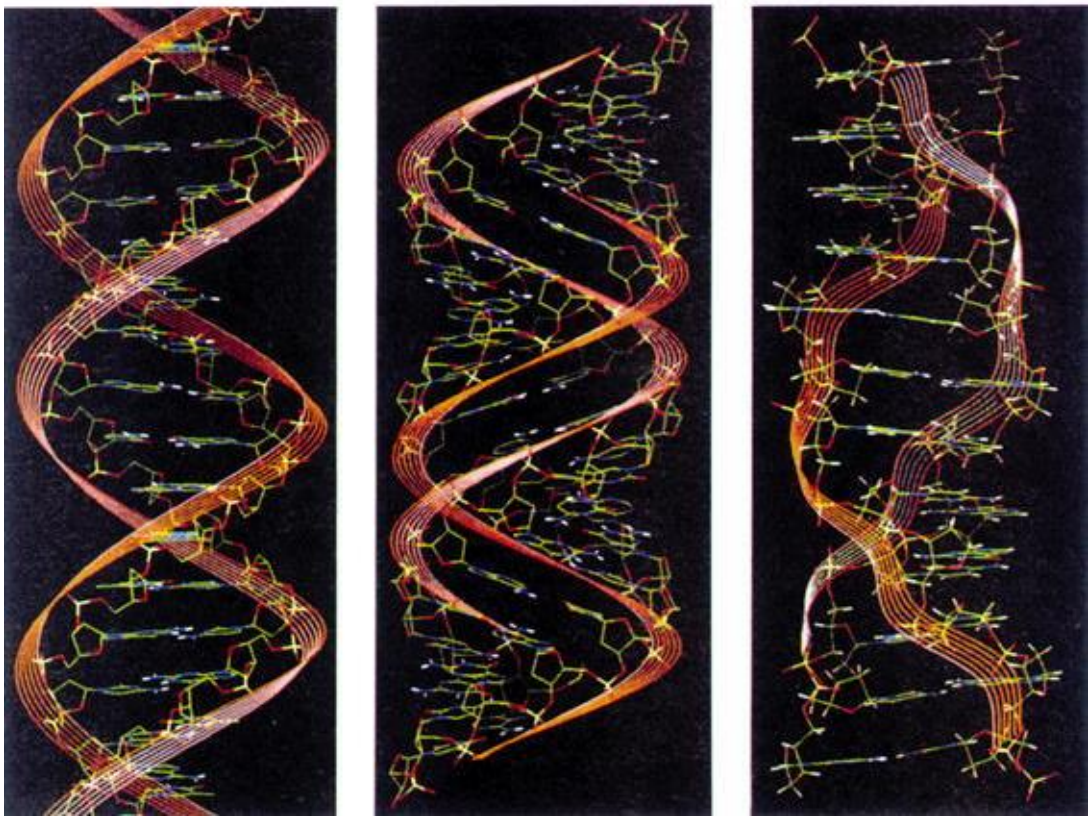

Figure 1.2 Conformational shape Of B-DNA, A-DNA and Z-DNA (from left to right) ((Taken from reference [1])

There are many possible confirmations of duplex DNA, with A, B and Z forms being the most common (Figure 1.2). B-DNA is the most prevalent form of DNA found in organisms. It is a right handed double helix and has 10.5 bases per rotation. The site of attachment for bases to the backbone leads to the formation of a deep, narrow minor and a shallow, wide major groove. These are both used as targets for therapeutic agents. A-DNA is also a right handed helix, but with a wider diameter that B-DNA and also more base pairs per rotation, leading to a shallower, wider minor groove and a deeper, narrower major grove. This A-form of DNA is also the conformational structure that RNA duplex and RNA-DNA hybrids take, as observed during transcription. Unlike A and B-DNA, Z-DNA is a left handed helix. It has a greater number of base pairs per rotation, 12, leading to little difference in its major and minor grooves, and a narrower helix diameter than B-DNA.

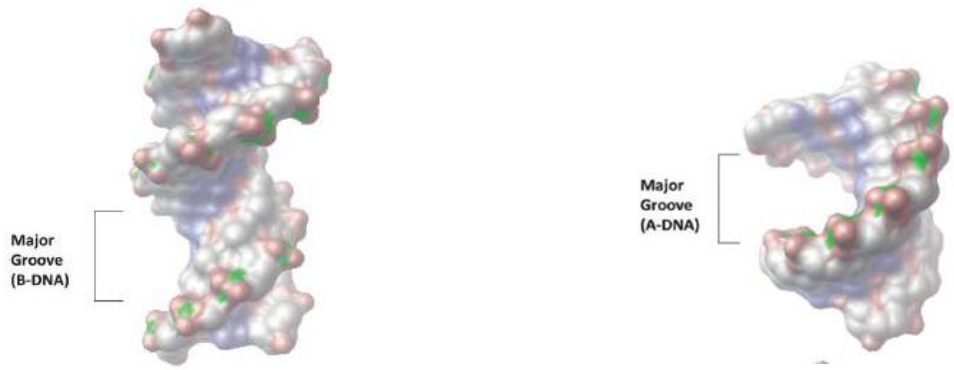

Figure 1.3 Model of the major groove in A-DNA which id deep and narrow and B-DNA that is wider. (Taken from reference [10])

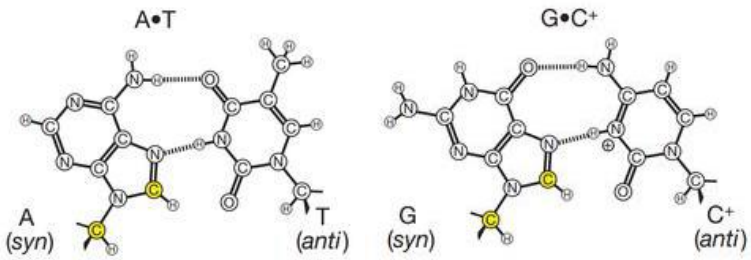

Figure 1.4 The Schematic diagram shows Hoogsteen base pairing with hydrogen bond formed between the purine bases (A and G) and the pyrimidine bases (C and T) (Taken from reference [11]).

As well as duplex DNA, other structures are possible, such as triplex DNA, junctions and quadruplex structures. The triplex conformation arises when a third strand of DNA wraps around a B-DNA structure, filling the major groove of the double helix. This third strands usually targets purine rich areas and is held in place by forming Hoogsteen pairs with the purine bases (Figure 1.5).

Many junction structures have been observed in DNA such as Y-shaped junctions, three way junctions (3-WJ), four ways or Holliday junctions (4-WJ) and B-Z transitions. Y-shaped junctions are formed whenever DNA is processed, commonly during transcription or replication, when the enzyme helicase unwinds and opens the DNA duplex leading to the formation of a transcription/replication fork/Y shaped junction. Since cancer cells have an increased replication rate, Y-shaped junctions can be an advantageous target for therapeutic agents. Three way junctions are formed when three strands of duplex DNA

converge towards a junction point (Figure 1.5). At this junction point, one strand from each duplex of DNA pairs with another strand from a different duplex with a complementary sequence, producing the three-way junction. Holliday or 4 way junctions are important in genetic recombination. They are formed when two duplex structures converge and one stand from each duplex, pairs with a complementary strand on the opposing duplex, forming a box like junction (Figure 1.5)

Quadruplex structures are commonly found in guanine rich areas of DNA, particularly in the telomeres and nuclease-hypersensitive promoter regions. Four guanine bases are held in a coplanar fashion by the formation of Hoogsteen bonds, forming a guanine tetrad (Figure 1.6). One strand of DNA folds up, stacking three or more tetrads, leading to the formation of a G-quadruplex (Figure 1.6). There can be loops of DNA above and below the face of the quadruplex. The quadruplex can also adopt a parallel or anti parallel conformation depending on the direction of the strand that forms the tetrads. The tetrads can be further stabilized by a sodium or potassium cation occupying the central channel. The small size of sodium allows it to sit between the middle of one tetrad; potassium's increased size means it has to occupy the space between two tetrads.

G-quadruplex structures are thought to be functionally important in transcription regulation and DNA replication. The extension of telomeres is inhibited by the formation of a quadruplex, as it stops the enzyme telomerase. The extension of telomeres is up regulated in cancer cell, making quadruple structures an important target for anti-cancer drug design.

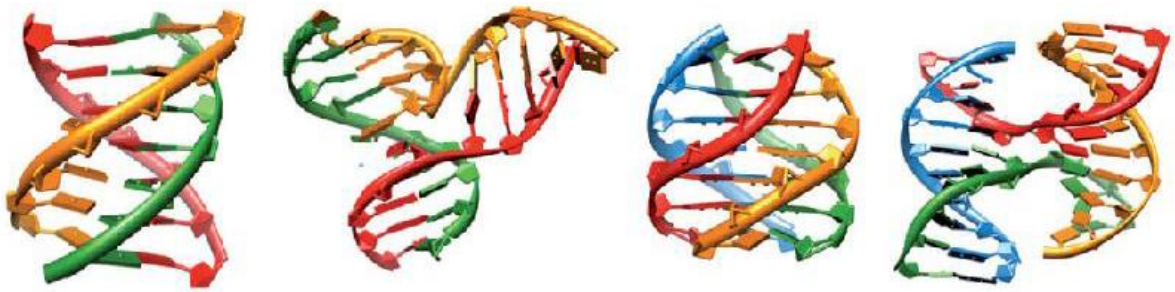

Figure 1.5 3D models that show the structure of triplex DNA, three way junction DNA, G-Quadraplex DNA and four-way/Holliday Junction DNA. (taken from reference [12])

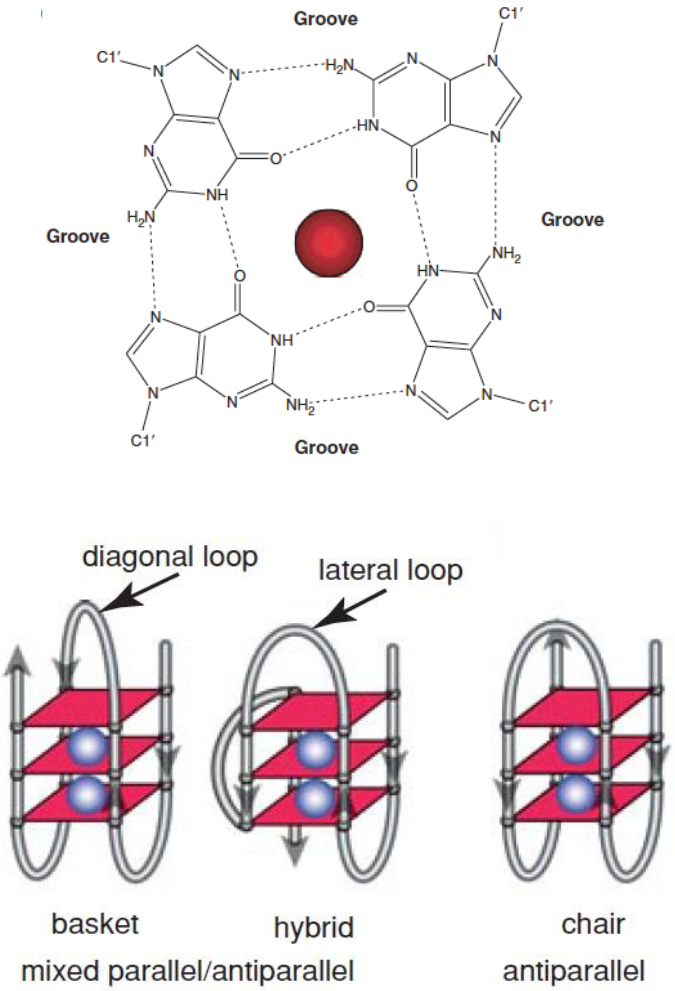

Figure 1.6 (Top) Schematic diagram showing a guanine tetrad stabilised by a metal ion in the central channel, with dashed lines depicting the Hoogsteen bonding between the guanine bases [13]. (bottom) Schematic diagrams depicting three guanine tetrads staked on top of each other, with a DNA strand forming loops around G-quadruplex, (left and centre mixed parallel/antiparallel qurdruplex, right antiparallel quadruplex) [14].

1.2 Molecular DNA recognition

Due to the variety of conformational forms DNA can adopt there are a number of structural targets for therapeutic agents to bind to and interact with. Such as the major and minor groove, junction points, replication forks, quadruplex structures, backbone and bulges. The components that make up DNA can also be targeted: alkylating agents bind to DNA bases, whereas backbone binders attach to the highly anionic DNA phosphate backbone.

1.2.1 Major and minor groove binding

The major groove of DNA is wider and deeper than the minor grove; this increase in size allows it to accommodate larger molecules. The major groove is a common binding site for protein molecules. They bind non-covalently using DNA sequence recognition, forming hydrogen bonds with the edges of base pairs [15]. Naturally occurring zinc finger proteins are relatively small protein motifs that bind in the major groove of DNA. Their alpha-helix regions form base specific interactions with DNA[16]. Oligonucleotides also reside in the major groove of DNA, forming a triplex. Their recognition can be used to regulate gene expression, as the strand can recognize a sequence specific target of the duplex [17]. The synthetic drug ditercalinium (Figure 1.7) interacts with DNA by a non-covalent interaction, resulting in the chain linker sitting in the major groove of B-DNA [10]. Neomycin is a non-aromatic aminosugar antibiotic. The lack of aromatic rings limits its binding to the major groove of DNA, with it preferentially preferring A-form over B-form DNA [10]. Synthetic supramolecular structures such as the metallo-cylinder developed by Hannon also bind in the major groove. The metallo-cylinder is a similar size to naturally occurring zinc finger proteins (~2nm by 1nm)[18]. (Discussed further in section 1.5.1 Metallo supramolecular helicates)

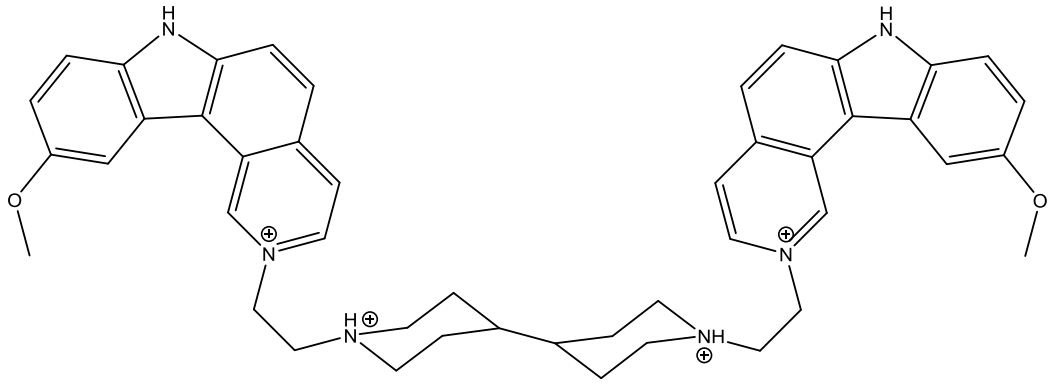

Figure 1.7 Structure of ditercalinium which interacts with the major groove of DNA. (reproduced from reference[10])

Due to their small size a large proportion of synthetic agents preferentially bind in the minor groove over the major groove. Diarylamidines compounds such as DAPI, berenil and pentamidine all bind to the minor groove of DNA and are effective at treating protozoal diseases [19]. DAPI has had limited clinical use due to its undesirables side effects, however due to its fluorescent nature it has been used as a chromosomal stain for fluorescence microscopy. DAPI has a high affinity for the ATT sequence in DNA. It binds in regions high in A-T base pairs as these form a narrower minor groove in the DNA, leading to a snug fit around the DAPI molecule[20].

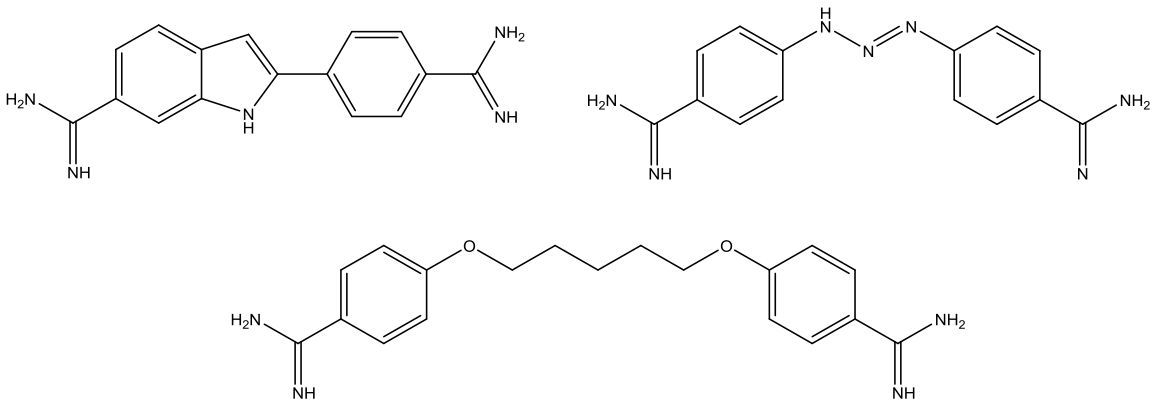

Figure 1.8 Structures of the diarylamidine minor groove binding drugs DAPI (top left), Berenil (top right) and Pentamidine (bottom). (reproduced from reference[19])

1.2.2 Intercalation

Intercalation occurs when an aromatic planar molecule slides between two base pairs in DNA. The drug is held in place by forming π-π stacking interactions with the bases situated above and below the binding site[21]. As the aromatic molecule inserts into the DNA it causes the double helix to unwind slightly causing the DNA strand to lengthen by 3.4 Å[22]. This lengthening leads to conformational changes in the sugar molecules present in the sugar-phosphate backbone and overall nucleotide structure at the intercalation site[22,23]. As the DNA backbone is relatively inflexible, once one molecule has intercalated onto the DNA, another molecule can't insert into the adjacent site as it would result in too much strain in the DNA. This is known as the 'neighbour exclusion principle'[15,21].

Doxorubicin (Figure 1.9) is an anthracycline antibiotic that was developed in the 1960's. It has been very effective at treating solid tumours and acts *via* intercalation. Ethidium bromide and Rhodamine (Figure 1.9) are further examples of planar aromatic molecules that bind *via* intercalation. They are both fluorescent dyes that are used in fluorescence microscopy[24]. A range of inorganic intercalators have also been developed, including ruthenium(II)[25][26] and rhodium(II) octahedral[27] complexes and platinum(II) square planer complexes[28]. Ethidium bromide has also been attached to a platinum(II) complex (Figure 1.9) as a potential intercalator, resulting in a molecule able to bind to DNA *via* intercalation and coordination[24].

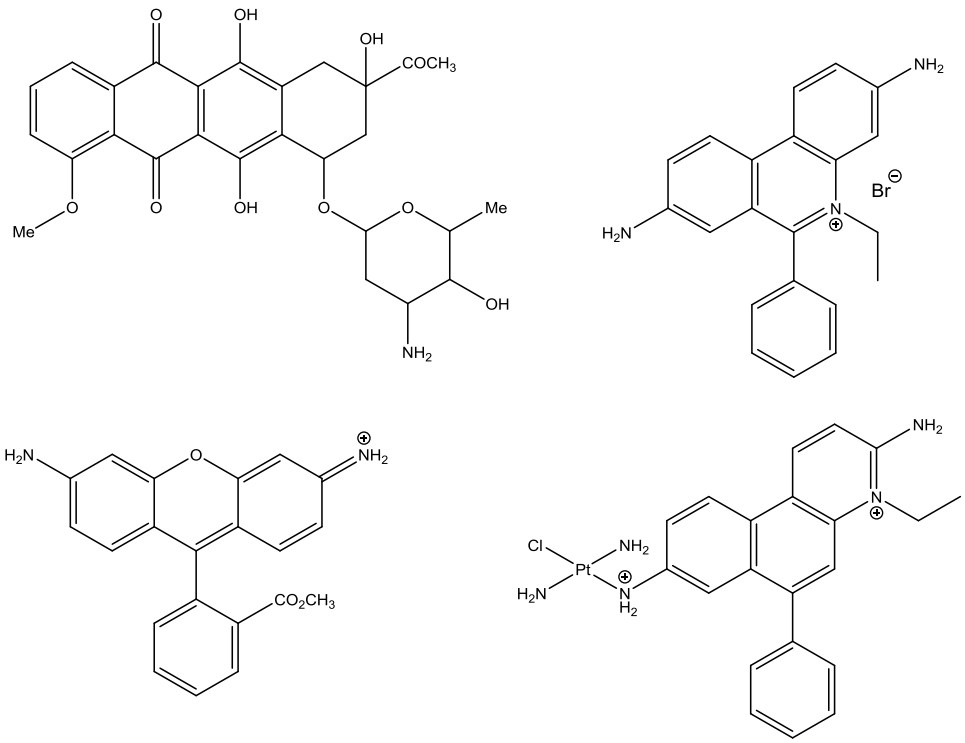

Figure 1.9 Structure of the intercalating agents Doxorubicin (top left), Ethidium Bromide (top right), Rhodamine 123 (bottom left) and an ethidium bromide platinum complex (bottom right) (Reproduced from reference [24])

1.2.3 Alkylating agents

Alkylating agents act by forming covalent bonds with DNA bases. They normally favour binding at the N7 position of the purine bases. Nitrogen mustards are a class of cytotoxic chemotherapy agents and are based on the chemical warfare agent mustard gas. Chlorambucil and bendamustine are chemotherapeutic nitrogen mustards. They form aziridinium rings *via* displacement of a chloride ion. The aziridinium ring then attacks at the N7 position of a guanine bases [29]. The formation and attack of another aziridinium ring results in an interstand crosslink. Cyclophosphamide is the most commonly used nitrogen mustard, it requires metabolism by hepatic cytochrome P450 enzymes for it to become active and is used to treat leukaemia and Hodgkin's disease [30]. Another classic example of a successful alkylating agent is cisplatin and its counterpart's oxaliplatin, nedaplatin and carboplatin (discussed further in section 1.3.1).

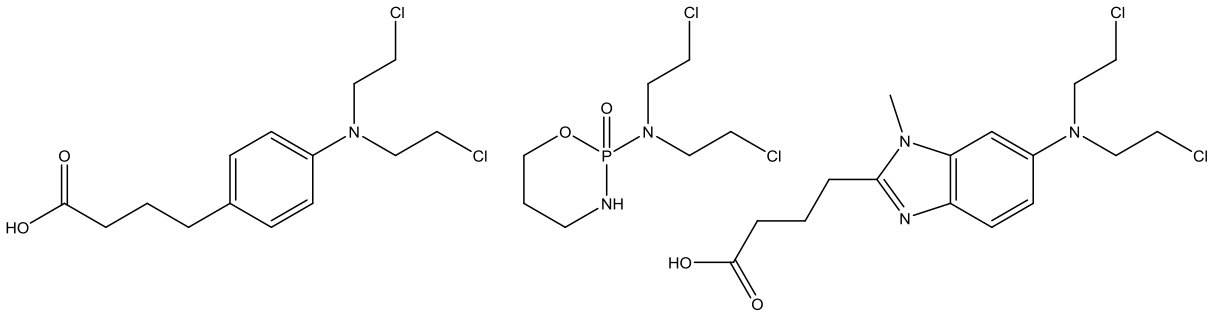

Figure 1.10 Structure of the nitrogen mustards Chlorambucil (left), Bendamustine (centre) and Cyclophosphamide (right) (Reproduced from reference [31])

1.2.4 Backbone binders

Backbone binding molecules recognize functional groups on the sugar phosphate backbone of DNA. The sugar phosphate back bone is oxygen rich and polyanionic, making it a target for cationic molecules that can form hydrogen bonds with the phosphate oxygens. Few synthetic molecules act as backbone binders. However, the triplatinNC complex designed by Farrell *et al.* binds selectivity to the oxygen rich backbone. The complex binds by forming hydrogen bonds between its amine groups and oxygen molecules of the phosphate backbone [32] (Figure 1.11). Recently a range of non-steroidal anti-inflammatory drugs have been bound to copper to enhance their anti-cancer activity. It is thought that these molecules act by binding to the DNA backbone, their sensitivity changes with alteration to the backbones structure and hydration.

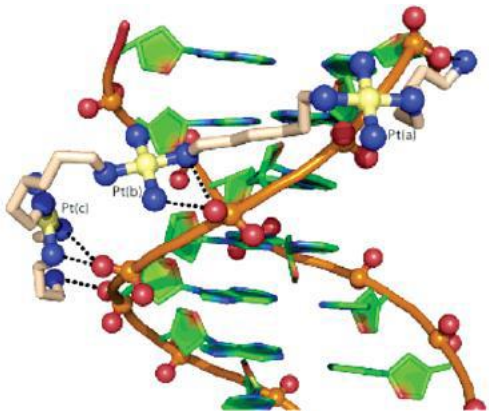

Figure 1.11 Model of triplatinNC binding to oxygen molecules in the sugar phosphate backbone. The dashed lines indicate hydrogen bonding between the NH3 molecules of triplatinNC and oxygen-phosphate molecules on the DNA. (Taken from reference [33])

1.2.5 Targeting DNA quadruplex structures

As previously discussed the vast majority of DNA in the body exists in the B conformation, with some adopting the A, Z, quadruplex and junction forms. These unusual structures are all advantageous targets for DNA recognition. Quadruplex recognition can be achieved by loop binding, π-stacking, or central channel binding. Randazzo *et al.* have shown that distamycin A (Figure 1.12) can selectively bind to the groove of the quadruplex in a 4:1 binding mode with the parallel quadruplex $[(TGGGGT)]_4$. π-Stacking ligands sit on top of the quadruplex. They are generally large flat aromatic compounds, such as TMPyP4 which is able to stabilize a G-quadruplex structure. Thiazole orange is another π-stacking molecule; it also sits on the face of the quadruplex. Due to it fluorescent properties it is used in displacement assays for testing new compounds as quadruplex binders. Metal based quadruplex binders have also been developed, such as the platinum based complexes by Che *et al*. (Figure 1.13). The platinum metal center keeps the ligands in a square planar geometry allowing the molecule to bind externally in an end-stacking mode at the terminal face of the quadruplex.

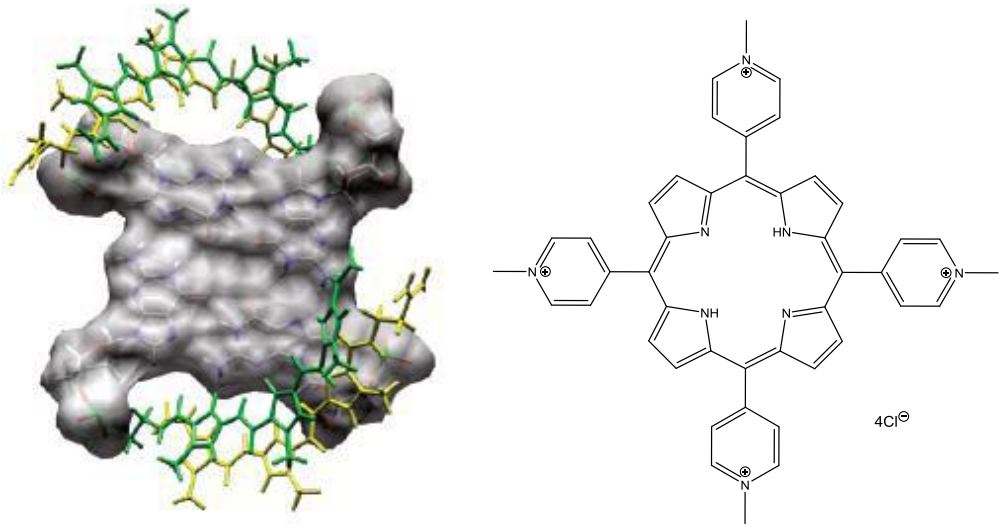

Figure 1.12 (Left) Model of the G3 tetrad showing the 4:1 binding of distamycin A, whose structures is depicted in yellow and green. (Taken from reference [34]) (Right) Structure of TMPyP4, a π-stacking quadruplex ligand (Reproduced from reference [35])

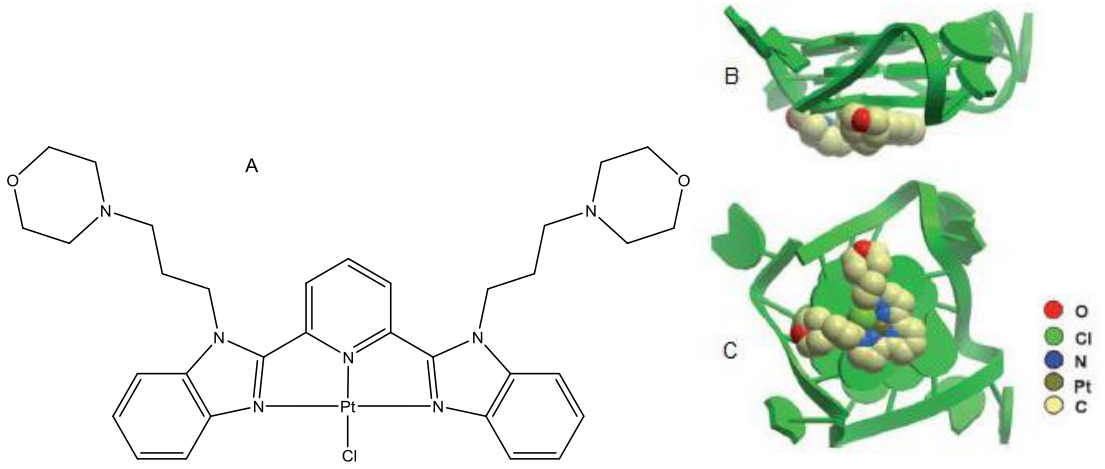

Figure 1.13 Sturcture of the platinum complex designed by Che *et al* (A), models of this complex binding to the face of a G-quadruplex of c-myc DNA, side view (B), top view (C) (A - reproduced; B and C - Taken from reference [15])

1.2.6 Targeting DNA junctions

The Holliday junction is important in genetic recombination, although few synthetic agents bind to the four-way junction. The proteins responsible for this recombination of genetic material are the Ruv proteins A, B and C[36]. RuvA consists of four sub units (Figure 1.14), this tetrameric protein binds to the Holliday junction and targets the hexameric RuvB protein to the junction[37]. It is these proteins that are responsible for branch migration of the Holliday junction. The heterodimeric DNA-binding protein Integration Host Factor (IHF) is able to bind to the Holliday junction[38]. IHF is found in *E. coli*, it regulates around 120 genes and many DNA-protein interactions[39]. IHF is also able to bind to the minor groove of DNA and the phosphate backbone.

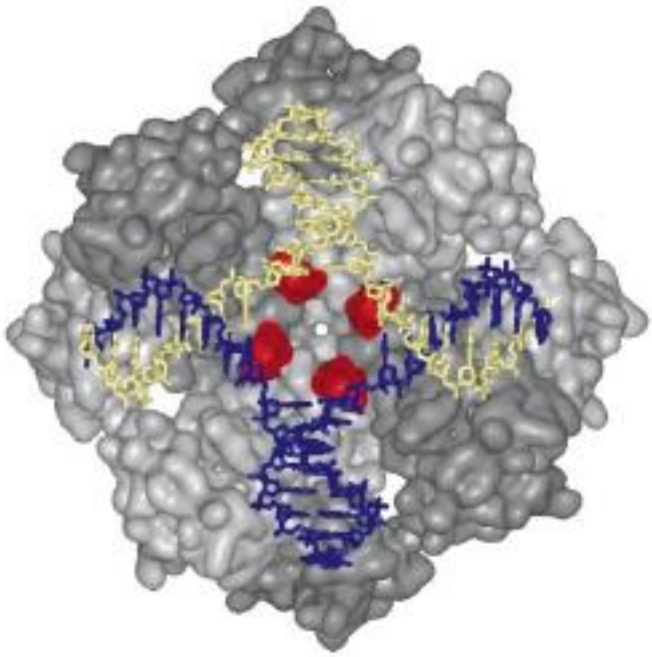

Figure 1.14 Model showing the protein RuvA (grey) binding to a Holliday junction. (Taken from reference [40])

Targeting of three-way junctions can be achieved by the supramolecular helicates discussed further in section 1.5.1. The metallo-cylinder has an unprecedented mode of binding as it binds non-covalently to the center of three way junctions (Figure 1.15). The cylinder does not undergo any significant conformational changes upon binding in the hydrophobic cavity of the three-way junction. The cylinder has twelve aromatic rings, resulting in a large aromatic surface, leading to the formation of π-stacking interactions with DNA bases in the junction. The cylinder is also tetracationic resulting in electrostatic interaction between the cylinder and the polyanionic backbone. These forces along with van der Waals interaction's and short range hydrogen bonds give rise to the cylinder's ability to bind non-covalently to the DNA.

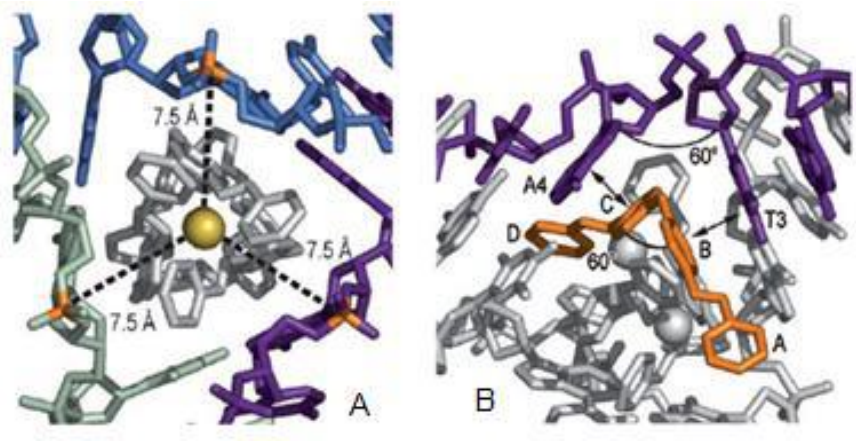

Figure 1.15 Model showing the electrostatic interactions between the iron metal centre and the phosphate group of the backbone (A). Model showing the π-stacking interactions between phenyl groups in the cylinder and the bases in DNA, as indicated by the double headed arrows (B). (Taken from reference [41])

1.3 Metallo anti-cancer drugs

This most successful chemotherapeutic agent used to date is cisplatin. Cisplatin is a platinum based complex whos effects on E. coli were first was discovered in 1965 by Barnett Rosenburg. Its clinic application was approved in 1978 for the treatment of testicular and ovarian cancer. Cisplatin has a number of side effects and drawbacks which have led to the development of a number of platinum analogues and interest in other metal centers as discussed below.

1.3.1 Platinum based anti-cancer drugs

The first platinum based metallo drug to be discovered was cisplatin, in the 1960's[42]. It is comprised of a Pt(II) metal center with two ammonia ligands and two labile chlorine ligands. This small molecule is able to enter cells by diffusing across the cell membrane and also *via* Cu transport proteins. Cisplatin is an alkylating agents (although it platinates rather than alkylates, is it referred to as an alkylating agent in clinic) and forms intrastrand links on the N7 position of purine bases in DNA (Figure 1.16). It has a preference for binding to guanine adducts over adenine adducts, with the majority of

intrastrand crosslinks being formed between GG bases (60-65%) and GA bases (22-30%)[43]. It is these DNA adducts that cause inhibition of DNA replication, arrest of the G2 phase of the cell cycle and apoptosis[44]. The distortion it induces in DNA structure (a 45° kink) is recognized by DNA binding proteins, which either initiate DNA repair mechanisms or signal to initiate apoptosis[45]. The discovery of cisplatin revolutionized anticancer treatment and gave rise to an increase in testicular cancer survival rates [46][47].

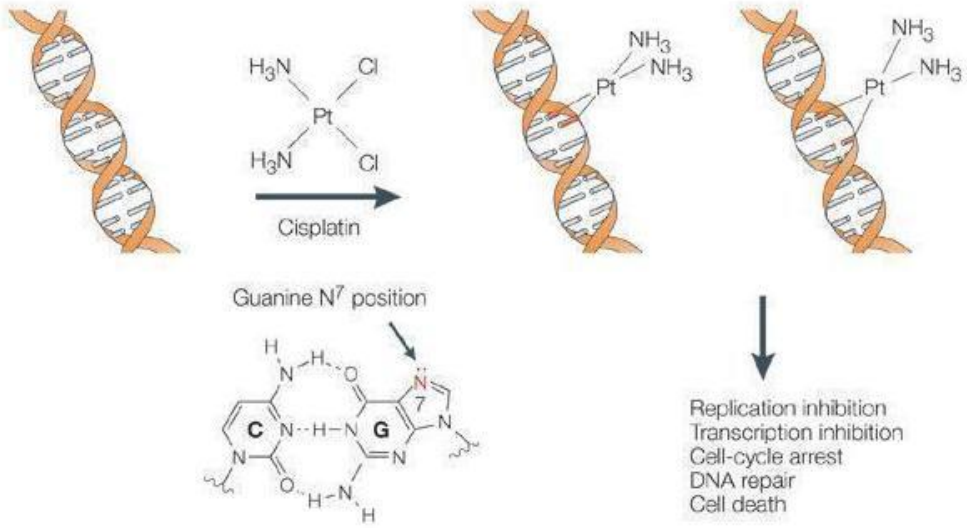

Figure 1.16 Schematic diagram showing how cisplatin forms intrastrand crosslinks at the N7 position of two guanine bases on the same strand of DNA, resulting in inhibition of replication and apoptosis. (Taken from reference [48])

However, cisplatin causes a lot of unpleasant side effects which are thought to be due to the complex binding to proteins [42]. Some cancers are also resistant to the effects of cisplatin whilst other tumours develop resistance after prolonged exposure to the drug. All of these pit falls have led to the development of new platinum based anti-cancer drugs including Carboplatin, Satraplatin, Oxaliplatin and Nedaplatin [49] (Figure 1.17).

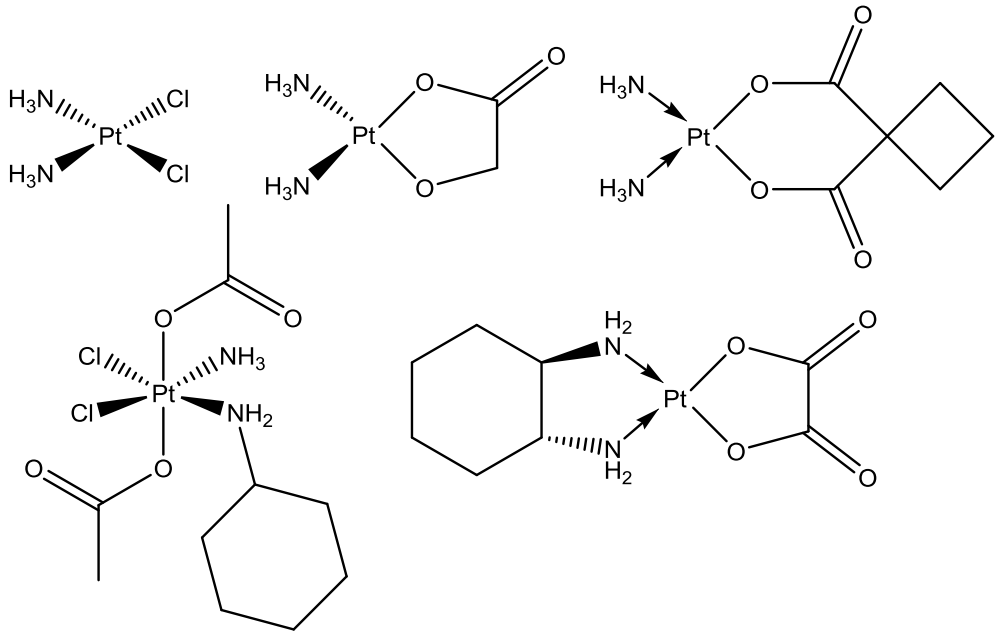

Figure 1.17 Structure of cisplatin (top left) Nedaplatin (top centre), Carboplatin (top right), Satraplatin (bottom left) and Oxaliplatin (bottom right) (Reproduced from reference [49]).

1.3.2 Non-platinum metal based drugs

Due to the success of platinum based anticancer drug in clinic other metal based complexes were developed. Changing from platinum to a different transition metal allows different geometric complexes to be developed. This could alter the metal complex's mode of action overcoming one of the main drawbacks with cisplatin, which is that cells become resistance to the drug. Changes in coordination number and geometry could also have the potential to increase specificity for cancer cells. The use of a metal complex over organic complexes is the ability to easily impart a charge to the complex. This can be useful for electrostatic binding to the DNA.

1.3.3 Iron based anti-cancer drugs

Iron is an abundant metal found in *vivo* and is required for many biological processes; including DNA synthesis, cell growth and proliferation and is vital in the oxygen transport chain. Iron is also regarded as a DNA damaging metal. This feature makes it a popular

target for synthesizing anti-cancer agents[50]. Iron's biological compatibility and low cost makes it a useful metal center for developing metallo-drugs. Cancer cells also have a higher requirement for iron than normal cells. Depletion of iron in tumors leads to hypoxic areas and ultimately cell apoptosis[51].

A novel approach to chemotherapy developed by Richardson *et al*. is to administer iron chelators, which bind to the free iron *in-situ* in the cancer cell, causing the cell to go into apoptosis, but limited damage to free normal tissues[51] .

The mononuclear polypyridyl complexes developed by Chen *et al*. (Figure 1.18) are fluorescent, allowing their cellular localisation to be monitored[52]. The increase of planarity in the polypyridyl iron(II) complexes leads to a increase in lipophilicity and cellular uptake[52]. The ability for the complex to be uptake more effectively leads to improved anticancer efficacy.

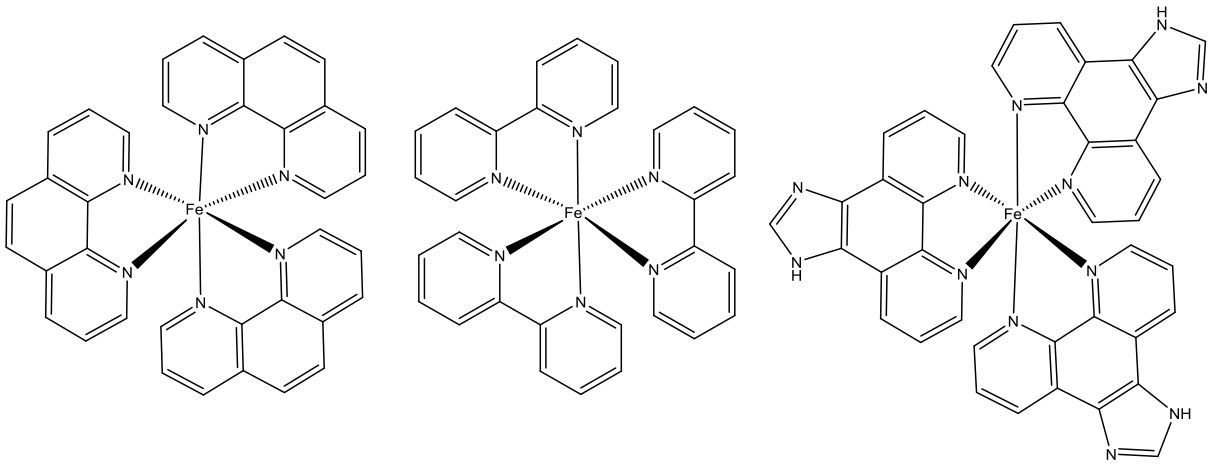

Figure 1.18 Structure of the monocular polypyridyl iron(II) complexes developed by Chen *et al*. (Reproduced from reference [52]).

A range of pentadentate pyridyl iron(II) complexes have been developed (Figure 1.19). They show higher cytotoxicity in a range of human cancer cell lines than cisplatin[53]. The

complexes have been tested on HeLa cells and induced apoptosis after 18 hours of treatments[53]. An iron(III) complex has been developed with two 5-nitro-8-hydroxylquinoline ligands and is thought to bind to DNA *via* an intercalative binding mode[50]. In T-24 cells it shows lower cytotoxicity that cisplatin and is thought to act *via* a mitochondria-mediated apoptotic pathway[50]. Iron complexes formed with the glycopeptide bleomycin been shown to cause double stand breaks in DNA[54].

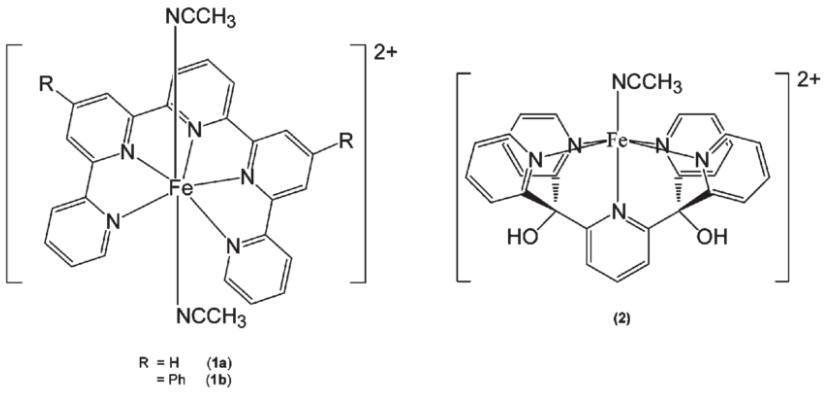

Figure 1.19 Structure of the pentadentate pyridyl iron(II) complexes developed by Che *et al*. (Taken from reference [53])

1.3.4 Ruthenium based anti-cancer drugs

Ruthenium has the ability to mimic iron in biological systems by binding to biomolecules such as human transferrin, serum and other proteins[55]. This property makes ruthenium-based drugs less toxic than platinum based drugs. Ruthenium can exhibit a number of oxidation states, has ligand exchange rates comparable to platinum and favors an octahedral geometry[55]. This is in contrast to the square planer geometry of platinum in cisplatin, hopefully leading to a different mode of action and reactivity.

A range of polypyridyl-Ruthenium based complexes have been developed, with a view to the polypyridyl ligand intercalating with DNA. A number of these complexes are also

photoluminescent allowing their localisation to be monitored, leading to the creation of DNA-targeted anticancer drugs[56].

The ruthenium based complex *trans*-[tetrachlorobis(1*H*-indazole)ruthenate(III)] (KP1019) has been shown to be affective against a range of cancers (Figure 1.20). Clinical trials have been undertaken with KP1019[57]. The complex induces DNA damage and apoptosis in colon cancer cells as well as inhibiting proliferation in ovarian cancer cells[58]. KP1019 is thought to bind to transferrin once it is administered. This could be useful in targeting tumour cells due to their high expression of transferrin receptors[55].

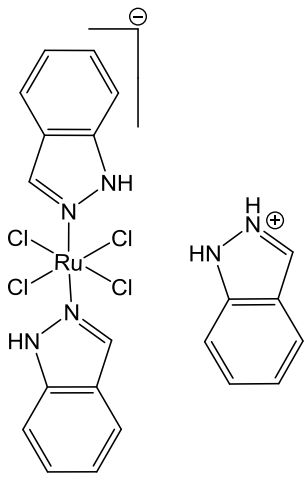

Figure 1.20 Structure of the ruthenium complex KP1019 (Taken from reference [58]).

A tetrapyridyl ruthenium based prodrug has been developed that is activated *in-situ* by green light (Figure 1.21). Treatment of A549 and A431 cells show a 22 fold increase in cytotoxicity after irradiation with green light at 520nm compared to cell treatment in the dark[59]. The *trans*-ruthenium complex is activated by a ligand photo-substitution reaction, its trans monodenate sulphur ligands are replaced by water molecules upon irradiation[59].

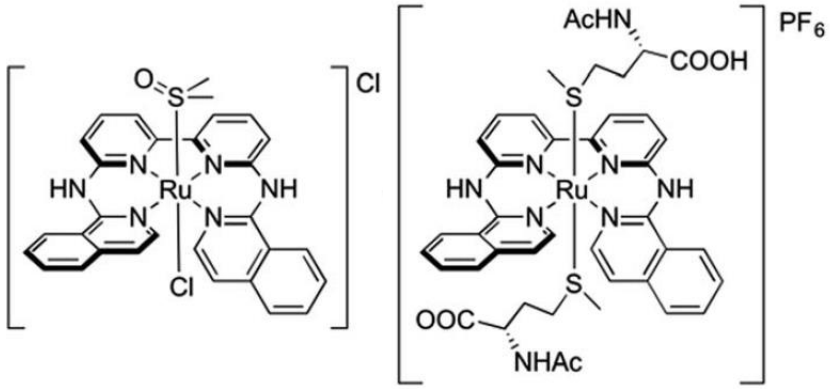

Figure 1.21 Structure of the ruthenium prodrugs developed by Bonnet *et al*. (Taken from reference [59]).

1.3.5 Nickel based anti-cancer drugs

Nickel has been used as a metal center for the development of novel anti-cancer drugs as it is a first row transition metal and can support a multitude of coordination numbers and geometry's. These changes in geometry from the square planar geometry of cisplatin will hopefully lead to complexes that act *via* a different mode of action, overcoming the resistance mechanism that arise from long-term cisplatin treatment.

Two novel nickel based complex's containing disalicylidene chelating ligands have been developed by Bal-Demirci *et al*[60]. (Figure 1.22). These complexes where tested against K562 leukemia cells and are shown to be cytotoxic against these cells, whilst being nontoxic to normal mononuclear cells at their IC_{50} doses[60]. These complexes induce their cytotoxic effect by triggering apoptotic pathways, as they are shown to cause between 75 and 78% DNA fragmentation in K562 cells[60].

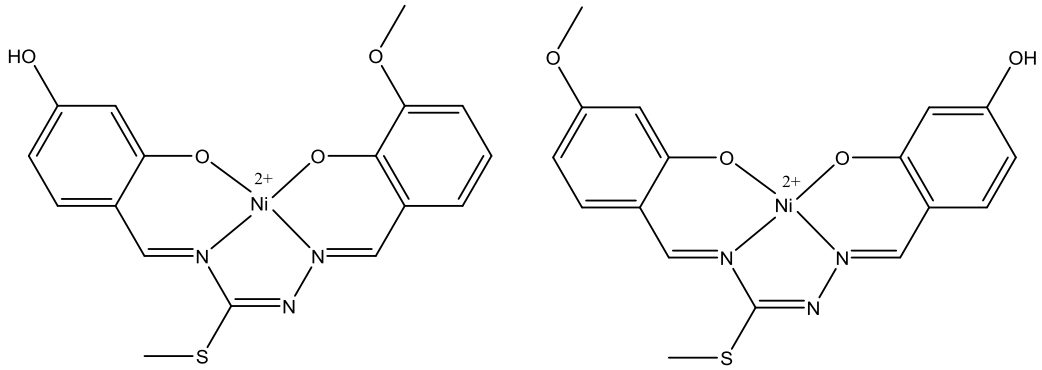

Figure 1.22 Structure of the nickel(II) complexes designed by Bal-Demirci *et al*. (Reproduced from reference [60]).

A courmarin based nickel(II) complex has been developed by Zhu *et al*. (Figure 1.23) and was tested against PC3, HepG2 and HL60 cancer cell lines, showing the greatest affect against HepG2 cells[61]. It is thought that the complex interacts with DNA by a form of non calssical intecalation, as there is a lack of red shift in the electronic spectra upon complex binding to DNA. There is however an observed hyperchromism in the electronic spectum showning the active participation of courmarin moieteies in associating with the DNA. The toxicity of the free ligand was also tested aginst the same cancer cell lines and the IC50 value was considerably higher than that of the metal complexes, showing that the inclusion of a metal improved the toxictiy and potentially alters the complex mode of action.

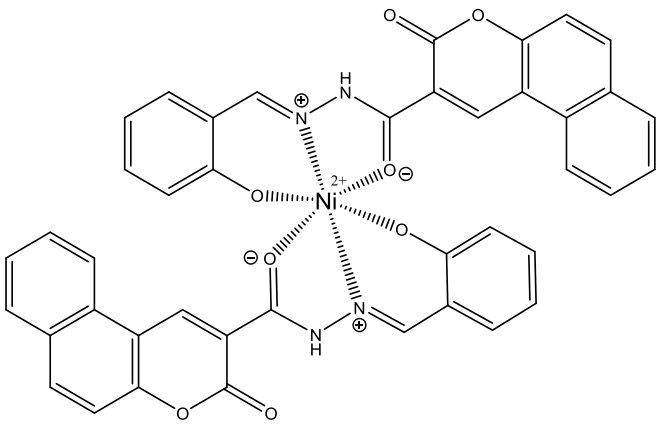

Figure 1.23 Structure of the courmarin based nickel(II) complex developed by Zhu *et al*. (Reproduced from reference [61]).

1.3.6 Copper based anti-cancer drugs

Copper is an endogenous metal and as such is thought to be less toxic to the body than non-essential metals such as platinum [62]. Copper is essential for the function of an array or proteins and enzymes that are involved in energy metabolism, respiration and DNA synthesis. Copper complexes have also been shown to poses antibacterial, antifungal, antiviral and anti-inflammatory properties[63]. Another advantage for designing copper based drugs is their ability to enter the cell by copper transporters, meaning they can be effectively internalized into the cell without the need to attached them to cell penetrating peptides.

One hypothesis for copper complexes anti-cancer activity, is due to their ability to form reactive oxygen species. The hydroxyl radical (OH) is thought to be the main species responsible for causing DNA damage in cells under oxidative stress[63] [64].

The Marzano group have developed a range of copper(I) complexes with triazolyborate ligands (Figure 1.24). When tested against A549 cells these showed activity rates that cisplatin under the same conditions, with IC-50 vales up to 26 fold lower than that of cisplatin [65].

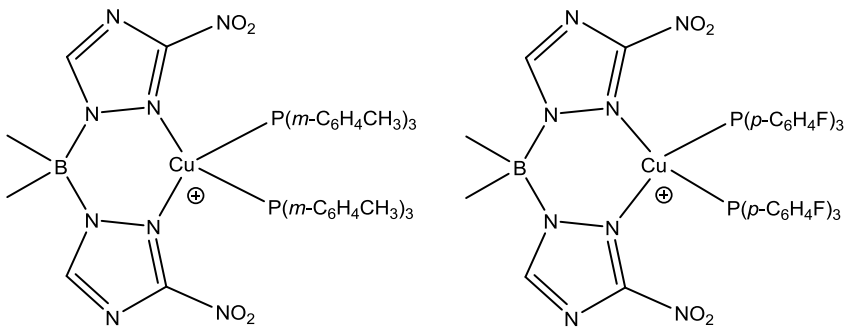

Figure 1.24 Structure of the triazolyborate copper(I) complexes designed by the Marzano group [63].

A range of copper(I) complexes containing hydrophilic alkyl phosphine ligands have been developed by Santini *et al.*[66] (Figure 1.25). Reducing the lipophilicity of the overall molecule increased the cytotoxic activity for this series of copper(I) compounds. These compounds were tested against a variety of cancer cell lines, but showed the highest cytotoxic effect if A549 and HCT-15 tumour cells, showing better cytotoxic activity than cisplatin. This result shows that these copper(I) complex are able to overcome intrinsic cisplatin resistance that occurs in these cell lines and acts *via* a different mechanism of action. It is though that the copper(I) complexes have a different target site that acts through impairment of ubiquitin-proteasome degradation pathways[66].

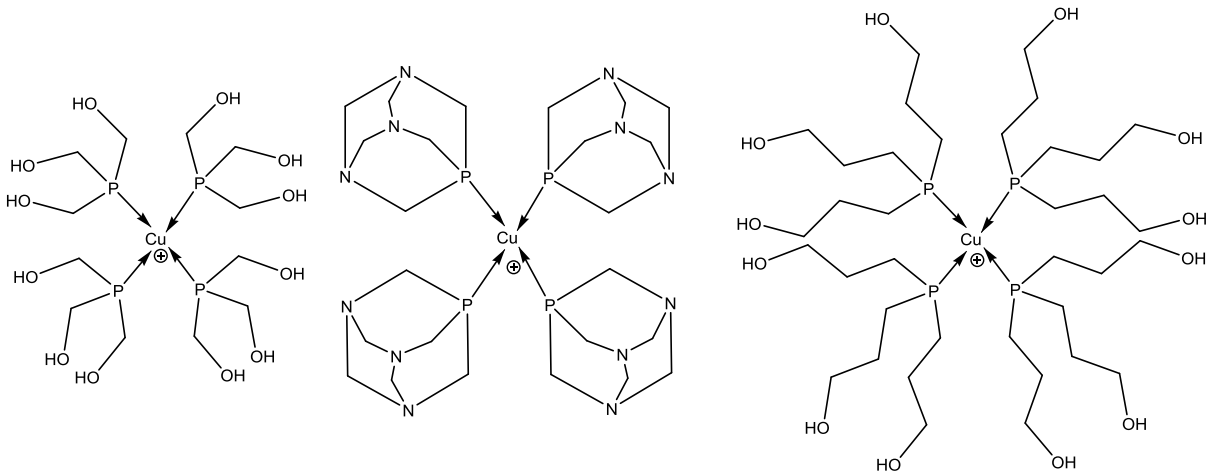

Figure 1.25 Structure of the hydrophilic copper(I) complexes designed by Santini *et al.* (Reproduced from reference [66]).

1.4 Fluorescent probes.

The addition of a fluorescent probe allows drugs to be monitored using fluorescence confocal microscopy. This allows the localisation and uptake of drugs to be observed over time inside cells. This can be achieved by the addition of an organic fluorophore or a biotin molecule - the biotin moiety can then bind to a streptavidin complex attached to a fluorophore. The use of a fluorescent marker has been used to achieve a greater

understanding in the mode of action of a number of drugs used in clinic including cisplatin [67][68][69][70].

1.4.1 Fluorescent dye-anticancer drug conjugates

Carboxyfluorescein diacetate (CFDA) has been grafted into a cisplatin analogue (Figure 1.26). The CFDA moiety is non fluorescent; after administration to live cells the acetate group is hydrolyzed by esterases and the complex becomes fluorescent [70]. After 2-3 hours the complex accumulates in the nucleus as observed by fluorescence microscopy. It has been argued that a large lipophilic fluorophore would scientifically change the pharmacokinetic properties of the complex, meaning it can't accurately be compared to cisplatin[71][72].

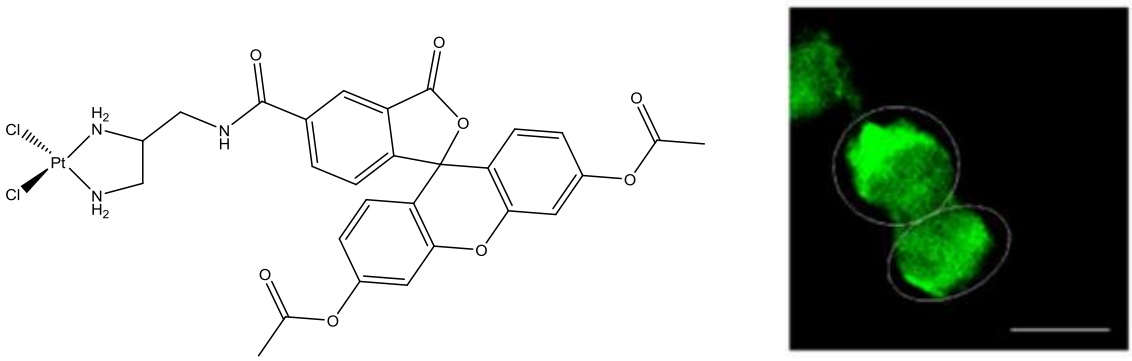

Figure 1.26 Structure of the fluorescent cisplatin analogue CFDA-Pt developed by Molenaar *et al.* (Reproduced from reference [70]), and its localisation in cisplatin resistance A2780 cells (scale bar 10µM) (Taken from reference [69]).

Tamoxifen is used in the treatment of breast cancer; it has been covalently bound to the fluorescent dye nitro-2-1,3-benzoxadiazol-4-yl (NBD), forming the compound FLTX1[73], (Figure 1.27). NBM is commonly used as a biomarker in hydrophobic environments[74]. FLTX1 was designed so that the triphenyl moiety in tamoxifen can bind to the active site of the estrogen receptor protein, without being affected by the NBD moiety [73]. FLTX1

shows near identical pharmacological properties to tamoxifen, showing the addition of the fluorophore has little impact on its binding[73].

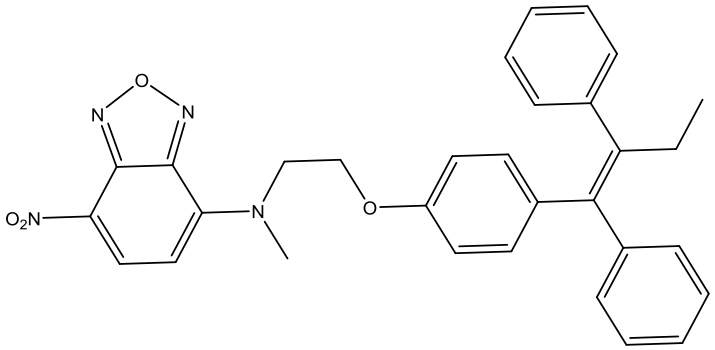

Figure 1.27 Structure of the Tamoxifen and nitro-2-1,3-benzoxadiazol-4-yl (NBD) dye complex FLTX1 (Reproduced from reference [73]).

1.5 Supramolecular chemistry

Supramolecular chemistry has been defined by Lehn as the chemistry of molecular assemblies and of the intramolecular bond [75,76]. Supramolecular chemistry studies the weak and reversible non-covalent interactions between molecules, including van der Waals forces, π-π interactions, hydrogen bonding, hydrophobic forces and electrostatic effects. Such structures are formed from organic ligands bound to metal cations forming a variety of shapes through self-assembly, including cages[77], knots[78] and helicates[79] (discussed below). These structures have been used in an array of applications including the formation of cages [80], MRI agents [81] and anti-cancer drug delivery systems [82].

1.5.1 Metallo supramolecular helicates

Metallo supramolecular helicates are formed from the spontaneous self-assembly of organic ligand strands wrapping around cationic metal ions. These complex can be double, triple, tetra or multi stranded. The design of the ligand and its binding sites dictates the shape that is forms. The helicate ligand is made up of the desired number of binding site, which are separated by a spacer. The spacer must be flexible enough to allow

the ligand to form a helical complex, but also rigid enough to prevent coordination of other binding site to the same metal ion. Helicates can be formed using homo or heterotopic ligands. Homo topic ligands have the same metal binding sites; heterotopic ligands have different metal binding sites. The use of heterotopic ligands leads to the formation of two different isomers, head to head (HH) or head to tail (HT)[83] (Figure 1.28).

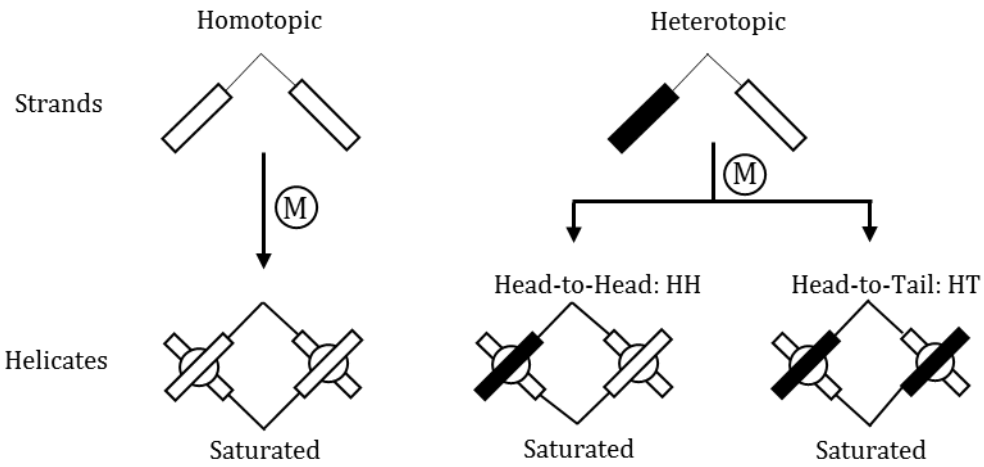

Figure 1.28 Schematic diagram showing the formation of helicates using homotopic and heterotopic ligands (Taken from reference [83])

Metallo helicates are chiral due to the way in which the ligand wraps around the metal ions in a helical fashion. Helicity is a special case of chirality. When viewed down the helical axis the ligands can wrap round the metal ions clockwise and are called right handed (P or plus) or anti-clockwise, left handed helix (M or minus) [83]. The use of an achiral ligands leads to the formation of a racemic mixture of M and P enantiomers, which can be separated using chiral chromatography [84] (Figure 1.29).

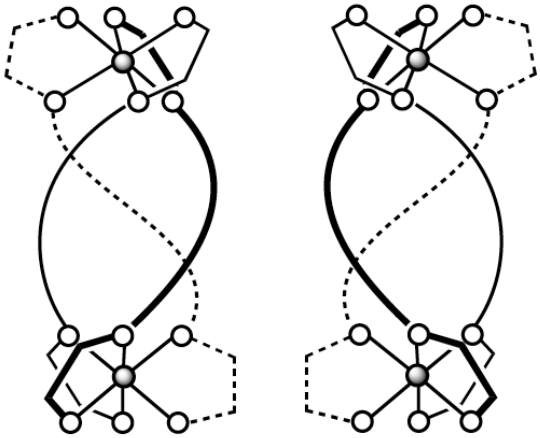

Figure 1.29 Helicity of a dinuclear triple stranded helicate, P (left) and M (right). (Taken from reference [84])

A number of helical complex have been developed that interact with DNA and have been tested as potential anti-cancer agents. Two novel double stranded helicates have been synthesized by Adamski *et al*. using quaterpyridine and copper(I) and silver(I) salts [79].

1.5.2 Supramolecular metallo cylinder.

The Hannon group has developed a supramolecular helicate comprised of three bis-pyridylimine ligands wrapped around two cationic metal centers (Figure 1.30). Its cylindrical shape gives rise to its name as a metallo-cylinder. The ligand is synthesized using inexpensive commercially available starting materials and can be made into a complex by the addition of an iron salt, in a one-pot synthesis reaction.

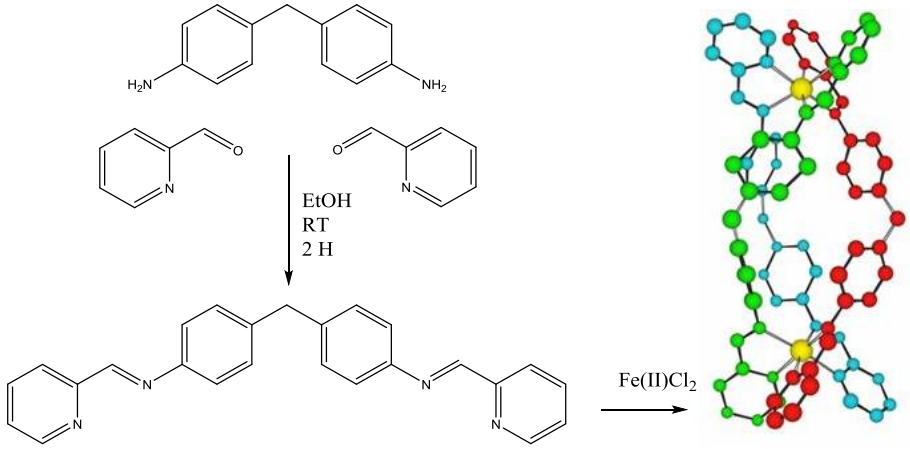

Figure 1.30 The molecular structure and synthesise of the parent ligand and the triple stranded, dinuclear, tetracatioinc supramolecular iron(II) cylinder.

The size of the metallo cylinder is comparable to that of the naturally occurring zinc finger proteins, (2nm in length by 1 nm in diameter). The metallo helicate has a 4+ charge, causing the complex to be attracted to the anionic backbone of DNA. The size of the complex allows the cylinder to bind in the major groove of B-DNA, spanning 5 base pairs, and its strong cationic nature gives rise to a strong binding constant in excess of 10^7 M^{-1} at 20mM NaCl with *ct*-DNA. When the complex binds in the major groove of B-DNA it induces a structural change in the DNA, allowing the cylinder to act as a cytostatic and potent apoptotic agent. Atomic force microscopy (AFM) has also shown that the cylinder causes dramatic intramolecular coiling of linearized plasmid DNA upon treatment with the cylinder [85] (Figure 1.31). The cylinder is also able to unwind duplex DNA with an unwinding angle of 27 °.

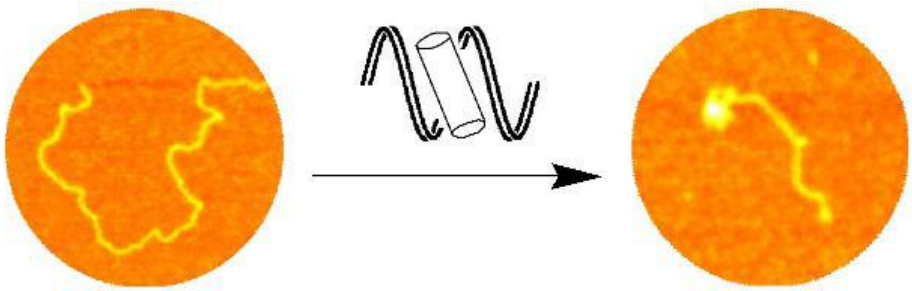

Figure 1.31 AFM image of linearized plasmid DNA before treatment and after treatment with the iron cylinder, causing dramatic intramolecular coiling of the DNA (Taken from reference [85]).

The metallo-cylinder was crystallized with a palindromic hexanucleotide sequence and showed an unprecedented mode of DNA recognition [41]. The DNA had formed a three-way Y-shaped junction with a hydrophobic hollow center that was occupied by the metallo-cylinder, Figure 1.32. The helicate is held in place by an electrostatic-dipole interaction between itself, due to being tetracationic, and the anionic DNA phosphate groups. The phenyl rings in the central spacer of the ligands form π-stacking interactions with the thymine and adenine bases in the junction [41]. An example of a Y-shaped junction is a DNA replication fork. These are formed whenever DNA is processed, prodominently

during transcription and replication. The ability to block DNA processing leads to cytostasis at low molecular concentrations and apoptosis at slight higher concentrations in numerous cell lines [86][87]. The metallo helicate is also able to bind the central cavity of RNA three-way junction, stabilizing the structure [88].

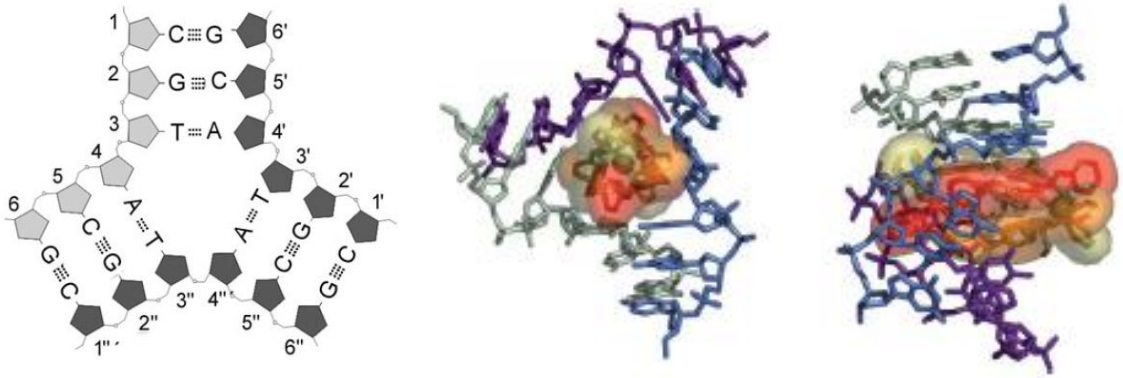

Figure 1.32 (Left) Schematic structure of the three-way junction formed using a palindromic hexanucleotide sequence. Model showing the metallo cylinder residing in the hollow cavity of the three way junction, top view (Centre), side view (right) (Taken from reference [41]).

The metallo-cylinder is synthesised using an achiral ligand, leading to the formation of a racemic mixture or right handed (P) and left handed (M) enantiomers (Figure 1.33). Both enantiomers are *rac* isomers as the stereochemistry is the same around the metal ions. It is possible to separate these enantiomers by chromatography on cellulose using 20mM sodium(I) chloride as eluent, with the M enantiomer being eluted first [89] (Figure 1.33).

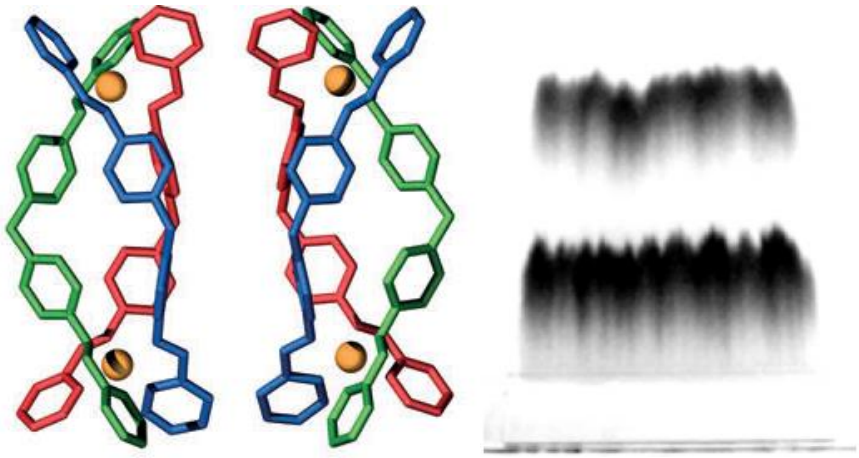

Figure 1.33 Structure of the P (left) and M (right) enantiomers of the iron(II) metallo cylinder [88]. Enantiomeric separation of P and M enantiomers on cellulose paper, eluted with 20 mM sodium chloride (Taken from reference [89]).

The P and M enantiomers of the metallo cylinder have been shown to have different effects on DNA and hence different binding modes. Through static light scattering and AFM experiments it has been shown that the M enantiomer is more effective at condensing DNA than the P enantiomer [90]. The P and M enantiomers are both able to cause supercoiling of DNA, whilst having very little effect of the base to base interactions that are monitored by CD, as such they resemble histone that DNA condenses around to pack into chromosomes [91]. The P enantiomer of the nickel metallo cylinder has been shown to preferentially bind to G-quadruplex DNA over duplex DNA [92]. In the presence of sodium(I) ions, the P enantiomer can also convert G-quadruplex structures from an antiparallel to a hybrid conformation (Figure 1.34).

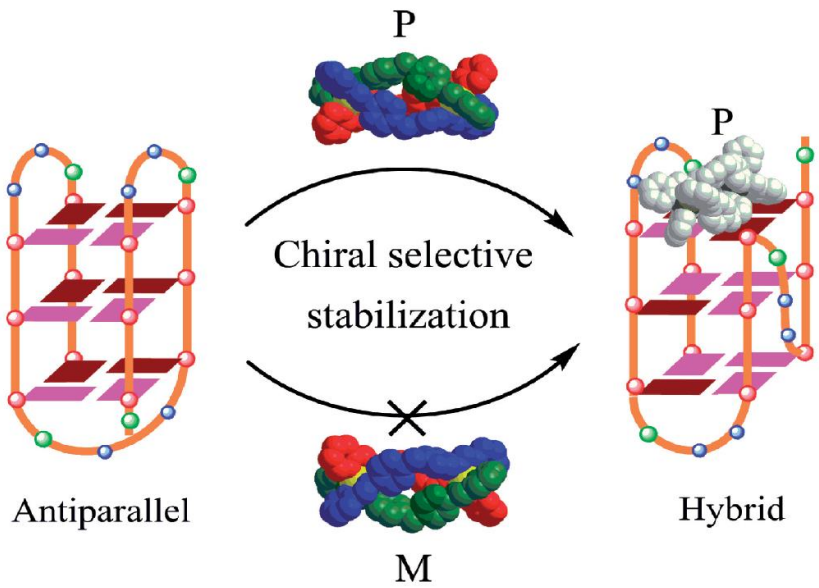

Figure 1.34 Diagram showing the P enantiomer stabilising a G-quadruplex and its ability to change an antiparallel conformation to a Hybrid in the presence of sodium ions (Taken from reference [92]).

A number of modifications have been made to the parent ligand structure to try and improve specificity and cytotoxicity, Figure 1.35. The parent ligand (1 in Figure 1.35) has been reacted with a number of metals including iron(II), nickel(II), cobalt(II), ruthenium(II), copper(I) and silver(I). Reactions with copper(I) and silver(I) salts leads to the formation of a double stranded dinuclear structure [93]. In solution these complexes

form an equilibrium of cyclophane (box) and helicate structure [94]. The addition of ethyl groups on the central spaced (ligand 7, Figure 1.35) lead to the formation of an exclusive helical structure upon reaction with copper(I) salts [95]. The copper(I) cylinders have a decreased 2+ charge, compared to the 4+ parent iron cylinder. Charge is in important factor for complexes binding to DNA, and as such the copper(I) complex binds less strongly than their iron(II) analogues [95]. The dicationic copper(I) cylinder doesn't cause coiling of DNA like its iron(II) tetracationic counterpart. It is thought that charge is also an important factor in bending and coiling DNA [95].

A silver(I) metallo-cylinder has also been prepared using ligand 8 (Figure 1.35). This double stranded dinuclear complex contains a major and minor groove within its structure [96].

An extended triple-stranded tetracationic iron(II) metallo-cylinder has been developed using ligand 6 (Figure 1.35). The addition of two ketimine groups in the spacer leads to a longer and slightly wider helicate than that formed using the parent ligand [97]. This iron (II) complex bind in the major grove of DNA, causing some bending and coiling of the DNA, but the effect is much less dramatic than that of the parent cylinder [97]. This effect shows that DNA coiling isn't just a consequence of the complex change but also the size and shape, with the parent cylinder interacting more strongly with the major groove.

Ruthenium based metallo-cylinders have been prepared using the parent ligand (ligand 1) and a bisazopyridine ligand (ligand 9 Figure 1.35). The parent ruthenium(II) metallo cylinder is of near identical shape and size of the iron(II) based parent complex [87]. This complex is able to bind to the major groove or DNA and cause dramatic coiling like its iron(II) counterpart [87]. The ruthenium analogue is highly stable due to the kinetic stability of the ruthenium(II) to nitrogen bond, which allows its cellular affects to be

attributed to the complex rather than its constituent components. The synthesis of this complex is laborious and produces low yields of pure triple stranded product (~1%). The parent ligand and *cis*-[$Ru(DMSO)_4Cl_2$] are heated to reflux for 5 days at 200°C, forming an array of products including triple stranded and polymeric stands products. Double stranded ruthenium complexes have been developed using a bisazopyridine ligand ($Ru_2Cl_4L_2$), (ligand 9, Figure 1.35) with five possible geometric isomers (three *cis* and two *trans*) [98]. Out of the possible conformations *cis*-α and *trans*-γ show the highest cytotoxicity in HBL100 and T47D cell lines [98].

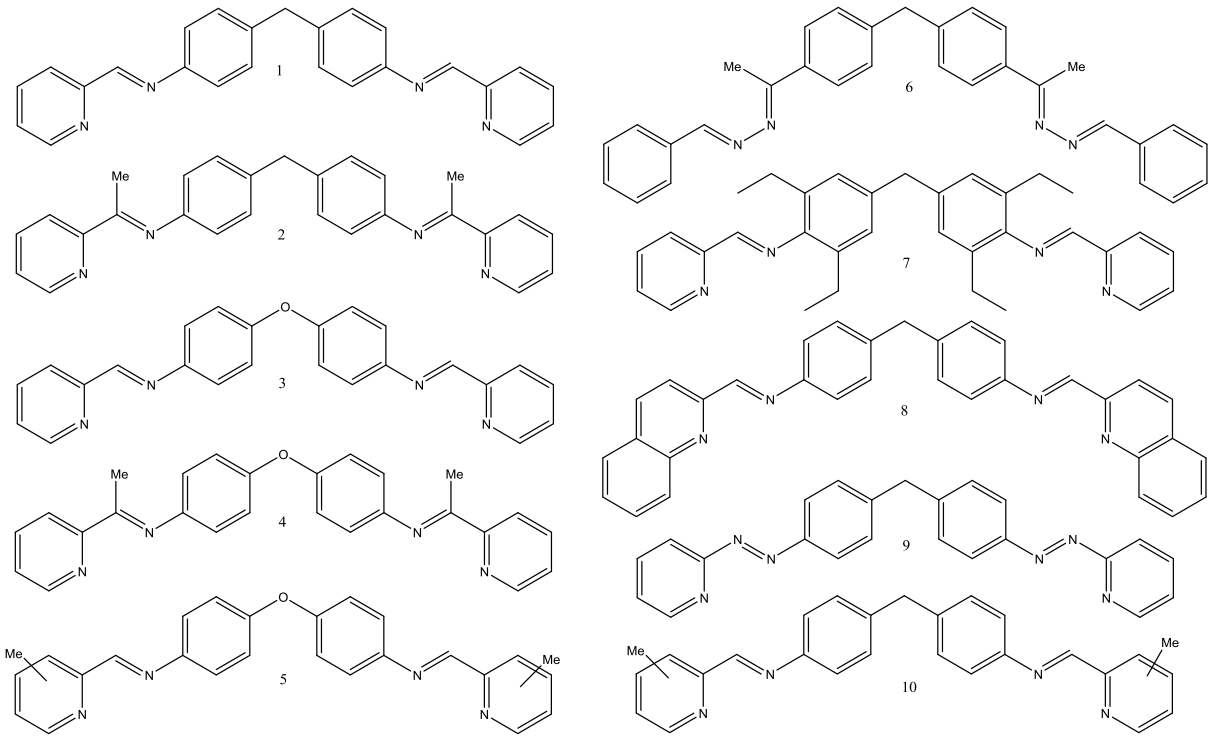

Figure 1.35 Structure of the parent ligand (1) and it modifications. (Ligands 5 and 10 contain a Me group in the 3,4,5 positons) (Reproduced from references [99][96][93][98][95][97])

Chiral arginine residues have been grafted onto the parent cylinder (Figure 1.36), this enhanced the complexes recognition of DNA three way junctions [100]. These complexes have shown increased cytotoxic activity against cancer cell lines compared to their parent counterpart [100]. The addition of chiral moieties allows the formation of pure enantiomeric products.

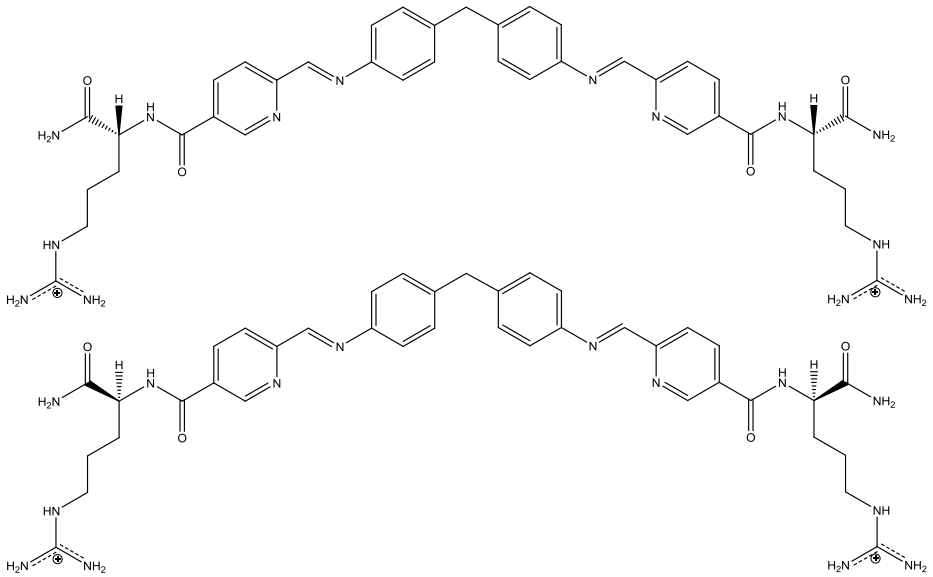

Figure 1.36 Structure of parent ligand modified with L-arginine (top) and D-Arginine (bottom) residues (Reproduced from reference [100]).

1.6 Thesis aims

The work undertaken in this thesis is an extension of the research conducted on the supramolecular helicates discussed in section 1.5.2. The aim of the work discussed herein is to develop a novel supramolecular helicate functionalised with organic fluorophores. This is to allow the localisation and uptake of the complex to be examined and gain a greater understanding of its mechanism of action. Their stability with be monitored by UV vis experiment and their DNA binding properties will be probed using circular dichroism.

The use of synchrotron imaging techniques will be employed to observe the localisation of the parent cylinder. Elemental maps will be produced, to obtain the location of the cytoplasm and nucleus of the cell. Iron maps with show iron rich areas within the sample, which can be overlaid with those of the cytoplasm and nucleus to allow the irons location to be determined. XANES scan will allow the oxidation state of the iron to be compared against a number or prepared iron standards, making it possible to check that the iron is still bound to the complex.

1.7 References

[1] M. W. Karaman, J. G. Hacia, *J. Hered.* **2003**, *94* , 432–433.

[2] H. Lodish, A. Berk, L. Zipursky, P. Matsudaira, D. Baltimore, J. Darnell, *Molecular Cell Biology. 4th Edition*, **2000**.

[3] S. L. Naylor, R. B. Weiss, **1990**.

[4] P. M. LoRusso, D. Weiss, E. Guardino, S. Girish, M. X. Sliwkowski, *Clin. Cancer Res.* **2011**, *17*, 6437–6447.

[5] B. A. Teicher, J. H. Doroshow, *N. Engl. J. Med.* **2012**, *367*, 1847–1848.

[6] R. Dahm, *Dev. Biol.* **2005**, *278*, 274–288.

[7] L. Pray, *Nat. Educ.* **2008**, *1*, 100.

[8] B. Alberts, A. Johnson, J. Lewis, M. Raff, K. Roberts, P. Walter, *Molecular Biology of the Cell, 4th Edition*, Garland Science, New York, **2002**.

[9] R. R. Sinden, *DNA Structure and Function*, **1994**.

[10] P. L. Hamilton, D. P. Arya, *Nat. Prod. Rep.* **2012**, *29*, 134.

[11] E. N. Nikolova, E. Kim, A. A. Wise, P. J. O'Brien, I. Andricioaei, H. M. Al-Hashimi, *Nature* **2011**, *470*, 498–502.

[12] L. Stefan, B. Bertrand, P. Richard, P. Le Gendre, F. Denat, M. Picquet, D. Monchaud, *ChemBioChem* **2012**, *13*, 1905–1912.

[13] S. Burge, G. N. Parkinson, P. Hazel, A. K. Todd, S. Neidle, *Nucleic Acids Res.* **2006**, *34*, 5402–5415.

[14] Y. Chen, D. Yang, *Curr. Protoc. Nucleic Acid Chem.* **2012**, 1–17.

[15] M. J. Hannon, *Chem. Soc. Rev.* **2007**, *36*, 280–295.

[16] S. J. McBryant, B. Gedulin, K. R. Clemens, P. E. Wright, J. M. Gottesfeld, *Nucleic Acids Res.* **1996**, *24*, 2567–2574.

[17] X. Tang, I. J. Dmochowski, *Mol. Biosyst.* **2007**, *3*, 100–110.

[18] A. C. G. Hotze, N. J. Hodges, R. E. Hayden, C. Sanchez-Cano, C. Paines, N. Male, M. K. Tse, C. M. Bunce, J. K. Chipman, M. J. Hannon, *Chem. Biol.* **2008**, *15*, 1258–1267.

[19] P. G. Baraldi, A. Bovero, F. Fruttarolo, D. Preti, M. A. Tabrizi, M. G. Pavani, R. Romagnoli, *Med. Res. Rev.* **2004**, *24*, 475–528.

[20] S. Y. Breusegem, R. M. Clegg, F. G. Loontiens, *J. Mol. Biol.* **2002**, *315*, 1049–1061.

[21] B. A. D. Neto, A. A. M. Lapis, *Molecules* **2009**, *14*, 1725–1746.

[22] H. Ihmels, D. Otto, in (Ed.: F. Würthner), Springer Berlin Heidelberg, Berlin, Heidelberg, **2005**, pp. 161–204.

[23] C. Medhi, J. B. O. Mitchell, S. L. Price, A. B. Tabor, *Biopolymers* **1999**, *52*, 84–93.

[24] H.-K. Liu, P. J. Sadler, *Acc. Chem. Res.* **2011**, *44*, 349–359.

[25] J. P. Hall, K. O'Sullivan, A. Naseer, J. a Smith, J. M. Kelly, C. J. Cardin, *Proc. Natl. Acad. Sci. U. S. A.* **2011**, *108*, 17610–4.

[26] K. K. Patel, E. A. Plummer, M. Darwish, A. Rodger, M. J. Hannon, *J. Inorg. Biochem.* **2002**, *91*, 220–229.

[27] C. L. Kielkopf, K. E. Erkkila, B. P. Hudson, J. K. Barton, D. C. Rees, *Nat. Struct. Biol.* **2000**, *7*, 117–121.

[28] K. B. Garbutcheon-Singh, P. Leverett, S. Myers, J. R. Aldrich-Wright, *Dalt. Trans.* **2013**, 918–926.

[29] A. Polavarapu, J. A. Stillabower, S. G. W. Stubblefield, W. M. Taylor, M. H. Baik, *J. Org. Chem.* **2012**, *77*, 5914–5921.

[30] A. Emadi, R. J. Jones, R. A. Brodsky, *Nat Rev Clin Oncol* **2009**, *6*, 638–647.

[31] J. A. Hartley, J. P. Bingham, R. L. Souhami, *Nucleic Acids Res.* **1992**, *20*, 3175–3178.

[32] J. Malina, N. P. Farrell, V. Brabec, *Angew. Chemie - Int. Ed.* **2014**, *53*, 12812–12816.

[33] S. Komeda, T. Moulaei, K. K. Woods, M. Chikuma, N. P. Farrell, L. D. Williams, *J. Am. Chem. Soc.* **2006**, *128*, 16092–16103.

[34] L. Martino, A. Virno, B. Pagano, A. Virgilio, S. Di Micco, A. Galeone, C. Giancola, G. Bifulco, L. Mayol, A. Randazzo, *J. Am. Chem. Soc.* **2007**, *129*, 16048–16056.

[35] A. Siddiqui-Jain, C. L. Grand, D. J. Bearss, L. H. Hurley, *Proc. Natl. Acad. Sci. U. S. A.* **2002**, *99*, 11593–8.

[36] S. C. West, *J. Bacteriol.* **1996**, *178*, 1237–1241.

[37] T. Nishino, M. Ariyoshi, H. Iwasaki, H. Shinagawa, K. Morikawa, *Structure* **1998**, *6*, 11–21.

[38] S. Ho, **2013**.

[39] M. Freundlich, N. Ramani, E. Mathew, a Sirko, P. Tsui, *Mol. Microbiol.* **1992**, *6*, 2557–2563.

[40] S. M. Ingleston, M. J. Dickman, J. A. Grasby, D. P. Hornby, G. J. Sharples, R. G. Lloyd, *Eur. J. Biochem.* **2002**, *269*, 1525–1533.

[41] A. Oleksi, A. G. Blanco, R. Boer, I. Usón, J. Aymamí, A. Rodger, M. J. Hannon, M. Coll, *Angew. Chemie - Int. Ed.* **2006**, *45*, 1227–1231.

[42] R. a Alderden, M. D. Hall, T. W. Hambley, *J. Chem. Educ.* **2006**, *83*, 728–734.

[43] K. Woźniak, J. Błasiak, *Acta Biochim. Pol.* **2002**, *49*, 583–596.

[44] C. M. Sorenson, M. a Barry, A. Eastman, *J. Natl. Cancer Inst.* **1990**, *82*, 749–755.

[45] Z. H. Siddik, *Oncogene* **2003**, *22*, 7265–79.

[46] L. H. Einhorn, *Proc. Natl. Acad. Sci. U. S. A.* **2002**, *99*, 4592–5.

[47] N. Hanna, L. H. Einhorn, **2014**, *32*.

[48] D. Wang, S. J. Lippard, *Nat Rev Drug Discov* **2005**, *4*, 307–320.

[49] M. G. Apps, E. H. Y. Choi, N. J. Wheate, *Endocr. Relat. Cancer* **2015**, *22*, R219–R233.

[50] H. R. Zhang, T. Meng, Y. C. Liu, Q. P. Qin, Z. F. Chen, Y. N. Liu, H. Liang, *Synthesis, Structure Characterization and Antitumor Activity Study of a New iron(III) Complex of 5-Nitro-8-Hydroxylquinoline (HNOQ)*, **2016**.

[51] D. R. Richardson, D. S. Kalinowski, S. Lau, P. J. Jansson, D. B. Lovejoy, *Biochim. Biophys. Acta - Gen. Subj.* **2009**, *1790*, 702–717.

[52] J. Chen, Z. Luo, Z. Zhao, L. Xie, W. Zheng, T. Chen, *Biomaterials* **2015**, *71*, 168–177.

[53] E. L.-M. Wong, G.-S. Fang, C.-M. Che, N. Zhu, *Chem. Commun.* **2005**, 4578–80.

[54] B. Roy, C. Tang, M. P. Alam, S. M. Hecht, *Biochemistry* **2014**, *53*, 6103–6112.

[55] M. a Jakupec, M. Galanski, V. B. Arion, C. G. Hartinger, B. K. Keppler, *Dalton Trans.* **2008**, 183–194.

[56] H. A. Wee, P. J. Dyson, *Eur. J. Inorg. Chem.* **2006**, 4003–4018.

[57] G. Süss-Fink, *Dalt. Trans.* **2010**, *39*, 1673–1688.

[58] S. K. Stevens, A. P. Strehle, R. L. Miller, S. H. Gammons, K. J. Hoffman, J. T. McCarty, M. E. Miller, L. K. Stultz, P. K. Hanson, *Mol. Pharmacol.* **2013**, *83*, 225–34.

[59] V. H. S. van Rixel, B. Siewert, S. L. Hopkins, S. H. C. Askes, A. Busemann, M. A. Siegler, S. Bonnet, *Chem. Sci.* **2016**, *7*, 4922–4929.

[60] T. Bal-Demirci, G. Congur, A. Erdem, S. Erdem-Kuruca, N. Özdemir, K. Akgün-Dar, B. Varol, B. Ülküseven, *New J. Chem.* **2015**, *39*, 5643–5653.

[61] T. Zhu, Y. Wang, W. Ding, J. Xu, R. Chen, J. Xie, W. Zhu, L. Jia, T. Ma, *Chem. Biol. Drug Des.* **2015**, *85*, 385–393.

[62] C. Marzano, M. Pellei, F. Tisato, C. Santini, *Anti-Cancer Agents Med. Chem. Anti-Cancer Agents)* **n.d.**, *9*.

[63] M. Plotek, K. Dudek, A. Kyziol, *Chemik* **2013**, 2–6.

[64] D. Scibior-Bentkowska, H. Czeczot, *Postpy Hig. i Med. doświadczalnej* **2009**, *63*, 58–72.

[65] C. Marzano, M. Pellei, S. Alidori, A. Brossa, G. G. Lobbia, F. Tisato, C. Santini, *J. Inorg. Biochem.* **2006**, *100*, 299–304.

[66] C. Santini, M. Pellei, G. Papini, B. Morresi, R. Galassi, S. Ricci, F. Tisato, M. Porchia, M. P. Rigobello, V. Gandin, et al., *J. Inorg. Biochem.* **2011**, *105*, 232–240.

[67] J. J. Criado, E. R. Fernandez, J. L. Manzano, A. Alonso, S. Barrena, M. Medarde, R. Pelaez, M. D. Tabernero, A. Orfao, *Bioconjug. Chem.* **2005**, *16*, 275–282.

[68] E. Rodriguez-Fernandez, J. L. Manzano, A. Alonso, M. J. Almendral, M. Perez-Andres, A. Orfao, J. J. Criado, *Curr. Med. Chem.* **2009**, *16*, 4314–4327.

[69] G. V Kalayda, C. H. Wagner, I. Buss, J. Reedijk, U. Jaehde, *BMC Cancer* **2008**, *8*, 175.

[70] C. Molenaar, J.-M. Teuben, R. J. Heetebrij, H. J. Tanke, J. Reedijk, *J. Biol. Inorg. Chem.* **2000**, *5*, 655–665.

[71] M. Hall, M. Okabe, D.-W. Shen, X.-J. Liang, M. M. Gottesman, *Annu. Rev. Pharmacol. Toxicol.* **2008**, *48*.

[72] M. D. Hall, C. T. Dillon, M. Zhang, P. Beale, Z. Cai, B. Lai, A. P. J. Stampfl, T. W. Hambley, *J. Biol. Inorg. Chem.* **2003**, *8*, 726–732.

[73] F. Lahoz, C. J. Oton, D. Lopez, J. Marrero-Alonso, A. Boto, M. Diaz, *Org. Electron. physics, Mater. Appl.* **2013**, *14*, 1225–1230.

[74] F. Lahoz, C. J. Oton, D. Lopez, J. Marrero-Alonso, A. Boto, M. Diaz, *Opt. Lett.* **2012**, *37*, 4756–4758.

[75] J.-M. Lehn, *Angew. Chem. Int. Ed.* **1988**, *27*, 89–112.

[76] J. W. Steed, J. L. Atwood, P. A. Gale, in *Supramol. Chem.*, John Wiley & Sons, Ltd, **2012**.

[77] J. Ujma, M. De Cecco, O. Chepelin, H. Levene, C. Moffat, S. J. Pike, P. J. Lusby, P. E. Barran, *Chem. Commun.* **2012**, *48*, 4423–4425.

[78] J.-F. Ayme, J. E. Beves, D. A. Leigh, R. T. McBurney, K. Rissanen, D. Schultz, *Nat Chem* **2012**, *4*, 15–20.

[79] A. Adamski, M. A. Fik, M. Kubicki, Z. Hnatejko, D. Gurda, A. Fedoruk-Wyszomirska, E. Wyszko, D. Kruszka, Z. Dutkiewicz, V. Patroniak, *New J. Chem.* **2016**

[80] D. M. Dalton, S. R. Ellis, E. M. Nichols, R. A. Mathies, F. Dean Toste, R. G. Bergman, K. N. Raymond, *J. Am. Chem. Soc.* **2015**, *137*, 10128–10131.

[81] Y. Chen, Q. Zhu, Y. Tian, W. Tang, F. Pan, R. Xiong, Y. Yuan, A. Hu, *Polym. Chem.* **2015**, *6*, 1521–1526.

[82] H. Gheybi, M. Adeli, *Polym. Chem.* **2015**, *6*, 2580–2615.

[83] C. Piguet, G. Bernardinelli, G. Hopfgartner, *Chem. Rev.* **1997**, *97*, 2005–2062.

[84] J. J. Jodry, J. Lacour, *Chemistry* **2000**, *6*, 4297–304.

[85] M. J. Hannon, V. Moreno, M. J. Prieto, E. Moldrheim, E. Sletten, I. Meistermann, C. J. Isaac, K. J. Sanders, A. Rodger, *Angew. Chemie Int. Ed.* **2001**, *40*, 879–884.

[86] C. Ducani, A. Leczkowska, N. J. Hodges, M. J. Hannon, *Angew. Chemie - Int. Ed.* **2010**, *49*, 8942–8945.

[87] G. I. Pascu, A. C. G. Hotze, C. Sanchez-Cano, B. M. Kariuki, M. J. Hannon, *Angew. Chemie* **2007**, *119*, 4452–4456.

[88] S. Phongtongpasuk, S. Paulus, J. Schnabl, R. K. O. Sigel, B. Spingler, M. J. Hannon, E. Freisinger, *Angew. Chemie - Int. Ed.* **2013**, *52*, 11513–11516.

[89] M. J. Hannon, I. Meistermann, C. J. Isaac, C. Blomme, J. R. Aldrich-Wright, A. Rodger, *Chem. Commun.* **2001**, 1078–1079.

[90] J. Malina, M. J. Hannon, V. Brabec, *Chem. - A Eur. J.* **2015**, *21*, 11189–11195.

[91] I. Meistermann, V. Moreno, M. J. Prieto, E. Moldrheim, E. Sletten, S. Khalid, P. M. Rodger, J. C. Peberdy, C. J. Isaac, A. Rodger, et al., *Proc. Natl. Acad. Sci. U. S. A.* **2002**, *99*, 5069–5074.

[92] H. Yu, X. Wang, M. Fu, J. Ren, X. Qu, *Nucleic Acids Res.* **2008**, *36*, 5695–5703.

[93] M. J. Hannon, L. J. Childs, *Supramol. Chem.* **2004**, *16*, 7–22.

[94] M. J. Hannon, C. L. Painting, A. Jackson, J. Hamblin, W. Errington, *Chem. Commun.* **1997**, 1807–1808.

[95] L. J. Childs, J. Malina, B. E. Rolfsnes, M. Pascu, M. J. Prieto, M. J. Broome, P. M. Rodger, E. Sletten, V. Moreno, A. Rodger, et al., *Chem. - A Eur. J.* **2006**, *12*, 4919–4927.

[96] M. J. Hannon, C. L. Painting, N. W. Alcock, **1999**, *2*, 2023–2024.

[97] C. Uerpmann, J. Malina, M. Pascu, G. J. Clarkson, V. Moreno, A. Rodger, A. Grandas, M. J. Hannon, *Chem. - A Eur. J.* **2005**, *11*, 1750–1756.

[98] A. C. G. Hotze, B. M. Kariuki, M. J. Hannon, *Angew. Chemie - Int. Ed.* **2006**, *45*, 4839–4842.

[99] J. M. C. Kerckhoffs, J. C. Peberdy, I. Meistermann, L. J. Childs, C. J. Isaac, C. R. Pearmund, V. Reudegger, S. Khalid, N. W. Alcock, M. J. Hannon, et al., *Dalt. Trans.* **2007**, *2*, 734–742.

[100] L. Cardo, V. Sadovnikova, N. Hodges, M. Hannon, S. Phongtongpasuk, *Chem. Commun.* **2011**, *47*, 6575–6577.

Chapter 2

2 Pyridylimine cylinders

2.1 Introduction and aims

As discussed in Chapter 1, the parent metallo-cylinder designed by the Hannon group is comprised of three bipyridylimine ligands and two metal centres[1]. The complex is of a similar size to the naturally occurring zinc-finger proteins, and as such is able to bind in the major groove[2] of DNA and also three-way junctions[3][4]. Cell testing of the parent metallo-cylinder has shown it to be cytotoxic against several different cell lines and unlike many commonly used platinum based drugs, such as Cisplatin, it has been shown to be non-genotoxic[5].

The main aim of this work is to gain a greater understanding of where the metallo-cylinder localises within cells and how quickly it enters them. One of the main drawbacks of the metallo-cylinder is its lack of traceability within cells. To overcome this its iron metal centers have been studied using synchrotron imaging (see chapter 4), but ideally a luminescent cylinder would be developed that's localisation could be monitored using fluorescence confocal microscopy. Ruthenium analogues of the metallo-cylinder have been created, but only in very low yields (around 1%) and are weakly luminescent[6].

2.2 Molecular design

An attractive way to address this challenge would be to produces a scaffold ligand for the cylinder which could easily be functionalised with a variety of fluorescent groups. One way to add a catalogue of fluorophores to the ligand would be through click chemistry, which occurs when an azide and alkyl group react in the presence of a copper catalyst to produce a triazole ring. An alkyl or azide group would need to first be added to the end of

the ligands pyridyl group. A synthetic preparation for alkyl functionalisation has already been developed in the group and employs the use of a Sonogashira reaction[7]. The 5 position on the pyridyl group was chosen as the site of modification. This increases the length of the cylinder but has the least effect on the complex DNA binding[8]. Modification in the 6 position was not considered, as this would add steric hindrance near the site of metal coordination and prevent octahedral coordination to first row transition metals. Modification in the 3 position increases the width of the complex and has been show to weaken the DNA binding[8]. Modification in the 4 position hasn't been explored before as functionalisation as this site is synthetically challenging.

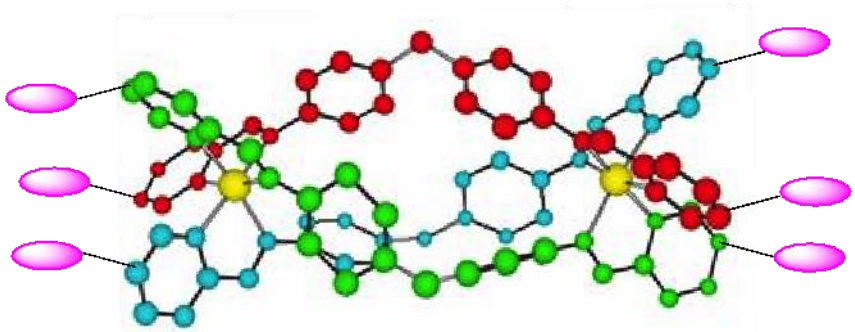

Figure 2.1 Molecular design of a flourophore functionalised pyridylimine based metallo complex

2.3 Sonogashira reaction

The Sonogashira reaction was developed by Kenkichi Sonogashira[9]. It is a cross coupling reaction that forms a new carbon-carbon bond. The reaction occurs between a terminal alkyne and an aryl or vinyl halide[9]. It is a double catalytic cycle mechanism (Scheme 2.1) that employs a zerovalent palladium complex such as $Pd(PPh_3)_4$ and a copper(I) halide salt. Palladium(II) pre-catalysts can also be used such as $Pd(PPh_3)_2Cl_2$, as they have a greater long-term stability for storage[10]. These are reduced in-situ by a phosphine or amine group[10]. The reaction is conducted under basic conditions using triethylamine as a solvent which neutralises the hydrogen-halide byproduct produced during the reaction

and facilitates in the formation of a key copper acetylide. If a Pd(II) catalyst is used it is first reduced in situ to Pd(0), this species then undergoes oxidative addition with the aryl-halide. The CuI salt forms a π-alkyne complex, making the terminal alkyne proton more acidic. In the presence of triethylamine, the π-alkyne complex is deprotonated forming copper acetylide. The alkyne group then undergoes transmetallation from the copper to the palladium metal catalyst, reforming the copper halide catalyst. Trans-cis isomerization occurs on the palladium metal, followed by reductive elimination, leading to formation of the new carbon-carbon bond and regeneration of the Pd(0) catalyst.

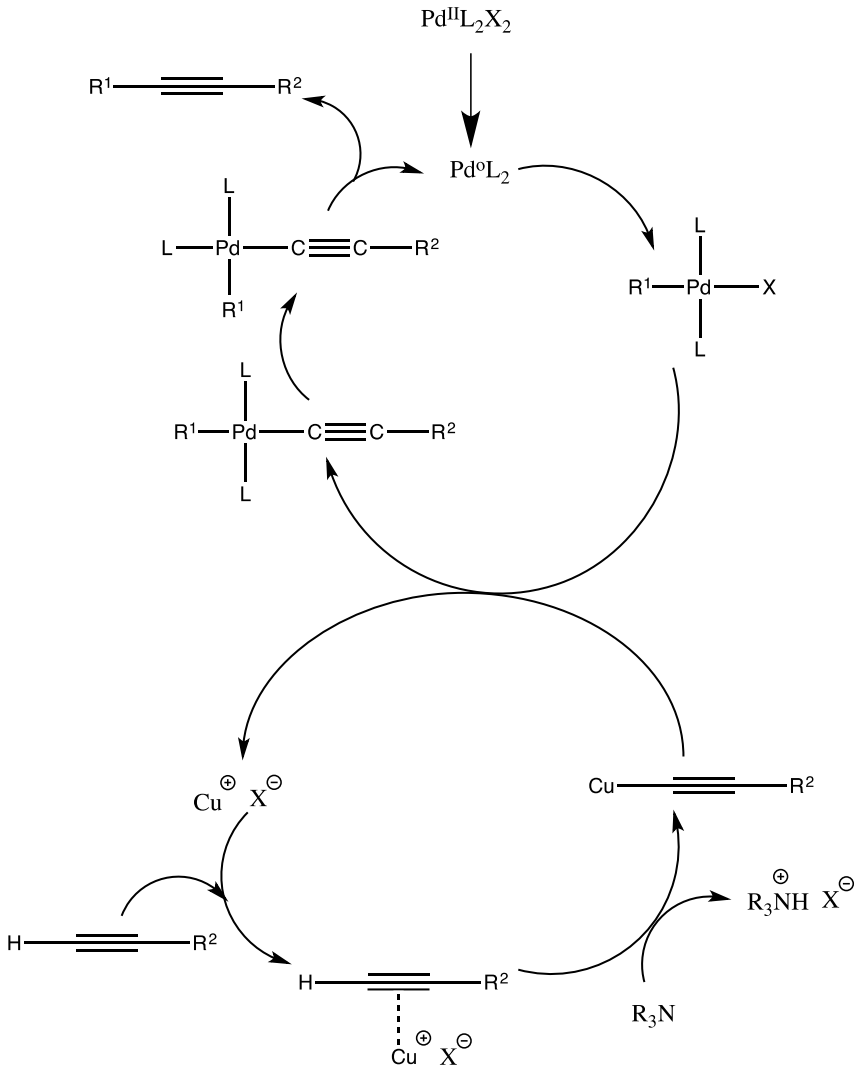

Scheme 2.1 Sonogashira reaction cycle

2.4 Click chemistry

Click chemistry is a cycloaddition reaction between an azide and an alkyne, leading to the formation of a five membered triazole ring. Click reaction are generally catalyzed by a copper(I) catalyst, however copper(II) is usually used and reduced *in-situ* using sodium ascorbate as it is non-air sensitive and can be used in aqueous conditions[11]. Click reactions can also proceed un-catalysed (copper free click chemistry) by using a highly strained alkyne in an 8 membered ring, the reaction proceeds due to the ring strain of the triple bond being decreased when it is reduced to a double bond[12]. The advantage of click chemistry over Huisgen 1,3-cycloaddition is that only the 1,4-substituted product is produced. This is in contrast to the Huisgen 1,3-cycloaddition which proceeds under thermal conditions and produces a mixture of the 1,5 and 1,4 regioisomers[13]. Another advantage of the click reaction is that it can proceed under mild reaction conditions, in aqueous solution. If a Cu(II) catalyst is used it is first reduced to a Cu(I) species with a slight excess of sodium ascorbate. The excess stops the formation of oxidative homocoupling products. It has recently been proposed that the mechanism proceeds through a mononuclear catalytic species, π,σ-bis(copper) acetylide and a bis(metallated) traizole complex[14]. It has also been suggested that the bis(Cu) cycle is kinetically favoured but both the mono and bis pathways are active in the reaction[14].

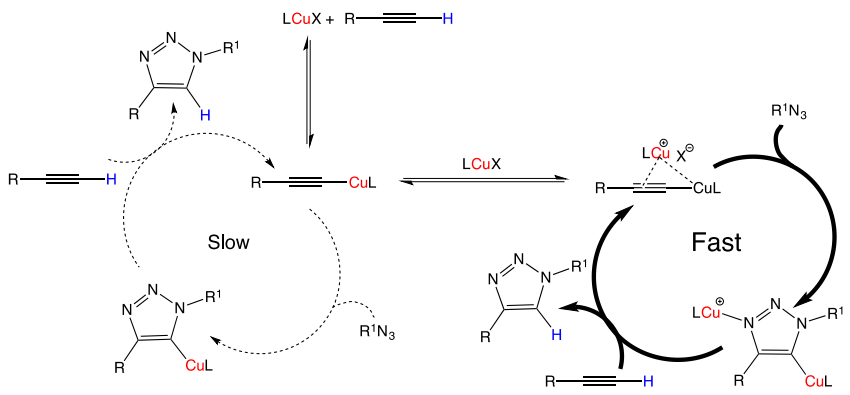

Scheme 2.2 Copper catalysed click chemistry reaction cycle (redrawn from reference [14])

2.5 Synthesis of coumarin ligand and complexes.

Coumarin was chosen due to its small size and biocompatibility. The small size should give the least steric hindrance at the terminal ends of the metallo-cylinder, allowing the ligand to undergo coordination to the metal centers. The size of the fluorophore will also have an effect on the solubility of the final product, as the metallo-cylinder will be comprised of three ligands with 3 fluorophores at the end of the cylindrical structure, this increase is size has been shown to have an effect on solubility. Coumarin dyes can also be easily modified; it was shown by Wang *et al.* that functionalisation in the 7th position can affect the fluorescent properties of the molecule upon triazole formation[15]. The addition of a diethylamine group at the 7th position was shown to give a strong fluorescent signal upon triazole formation with variety of alkyl functionalised phenyl compounds[15]. The diethylamine group is electron donating and increases the fluorescence[15].

2.5.1 Synthesis of 5-ethynyl-2-formylpyridine.

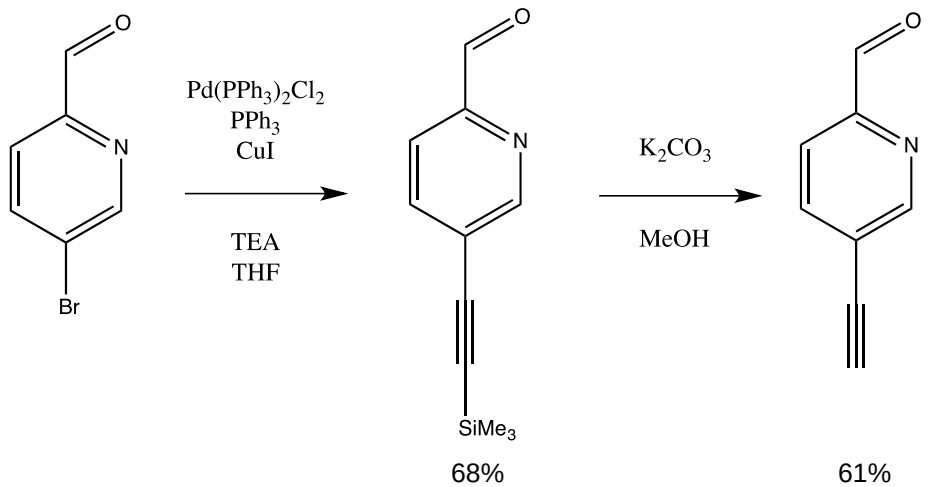

Scheme 2.3 Synthesis of 5-ethynyl-2-formylpyridine

5-Ethynyl-2-formylpyridine is not commercially available so was produced through a two-step reaction using the literature preparation[16] (Scheme 2.3). Firstly, a Sonogashira reaction was employed; 5-bromopyridine-2-carboxaldehyde was reacted with

trimethylsilylacetylene using a palladium bistriphenylphosphine dichloride catalyst, that was reduced *in-situ* using triphenylphosphine. Copper(I) iodide was used to catalyse the second part of the cyclic mechanism discussed above. Triethylamine was used as the main solvent to neutralize any acidic species produced during the reaction. Anhydrous THF was also used to help solubilized the palladium catalyst and 5-bromopyridine-2-carboxaldehyde. The procedure was modified to use anhydrous triethylamine and the reaction temperature was dropped from 80°C to 60°C, with stirring under argon for 5 hours. The work up conditions were also changed to eliminate the need for neutralization and extraction. Instead the solvent was removed in *vacuo* and the crude was dissolved in chloroform, filtered to remove the palladium catalyst and purified by flash column chromatography on silica with DCM as eluent. The product was triturated with petroleum ether to give pure product of 5-Trimethylsilylethynyl-2-formyl pyridine (68% yield). 5-Trimethylsilylethynyl-2-formyl pyridine was then stirred overnight in methanol with potassium carbonate to remove the silyl protecting group. Pure product was then obtained *via* flash column chromatograph on silica using DCM with a 61% yield. Both steps were fully characterised by ^{1}H NMR, ^{13}C NMR and ESI mass spectrometry, which were both consistent with literature data[16]. The ^{1}H NMR (Figure 2.2) confirms formation of the product by the singlet peak at 0.26 ppm, accounting for the $SiMe_3$ (Figure 2.2, a). Deprotection of the alkyne is confirmed by the loss of this peak and the formation of the H_5 peak at 3.5 (Figure 2.2, b), representing the alkyne proton.

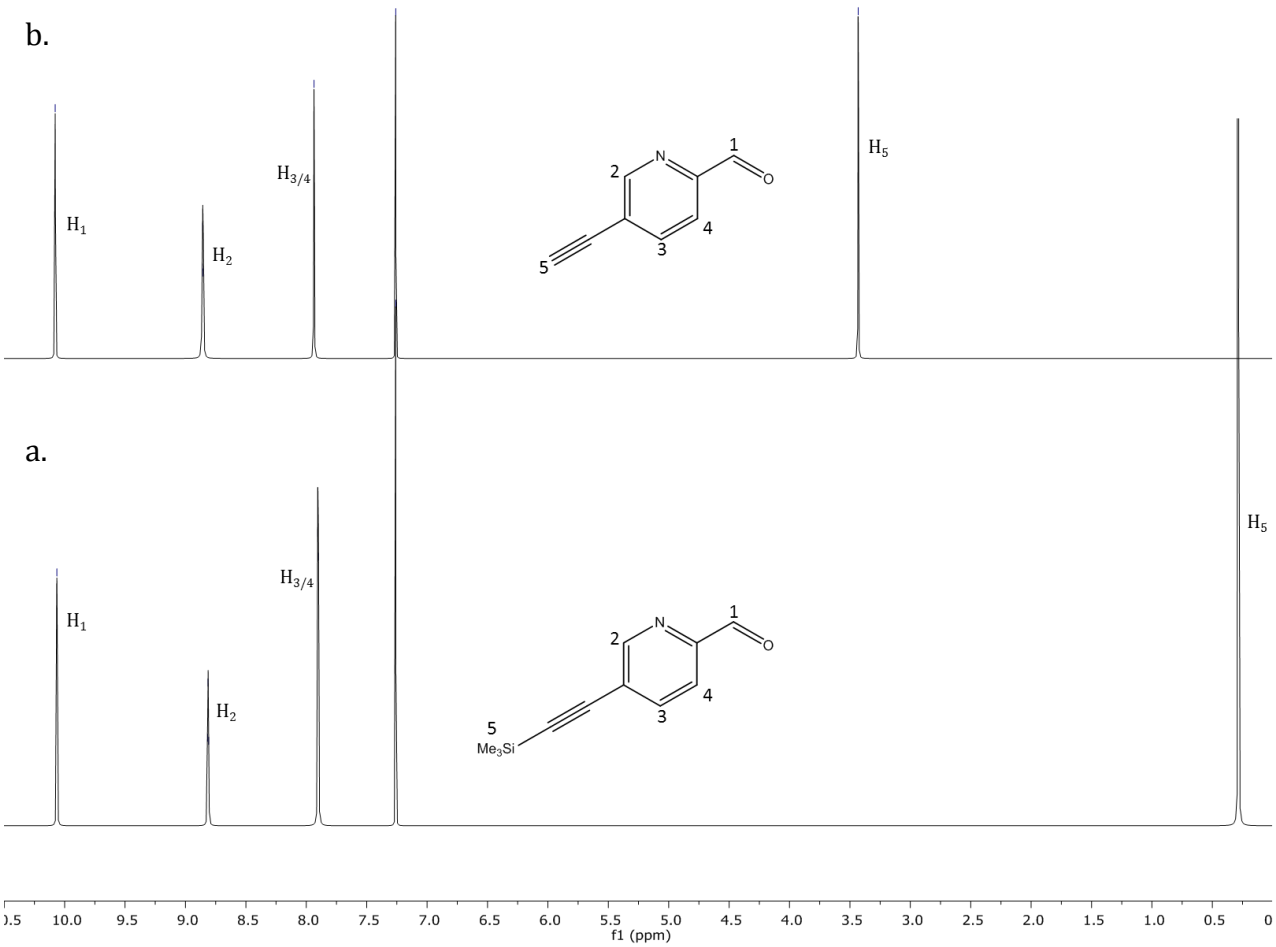

Figure 2.2 ^{1}H NMR (300 MHz, $CDCl_3$, 298 K) of 5-trimethylsilylethynyl-2-formyl pyridine (a) and 5-ethynyl-2-formylpyridine (b).

2.5.2 Synthesis of 3-azido-7-diethylaminocoumarin

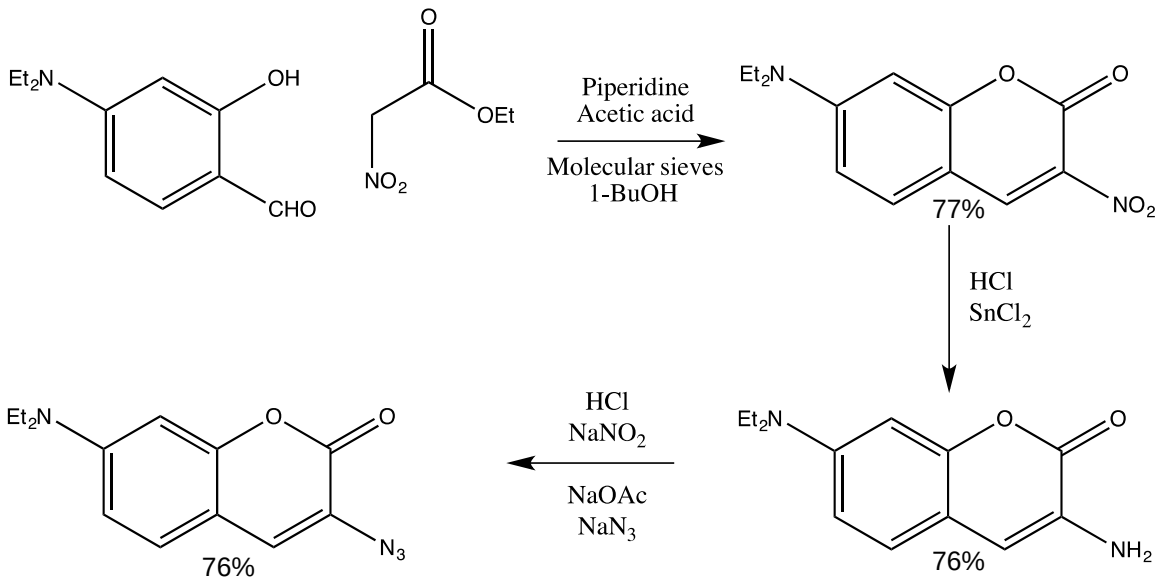

Scheme 2.4 Synthesis of 3-azido-7-diethylaminocoumarin

3-Azido-7-diethylaminocoumarin was not commercially available. It was synthesised *via* a three step synthesis (Scheme 2.4)[15]. 4-Diethylamino salicylaldehyde and ethyl nitroacetate were heated at reflux for 24 hours in anhydrous 1-butanol, under argon with molecular sieves and a catalytic amount of piperidine and acetic acid. Upon cooling, an orange solid was collected and dissolved in DMF at 80°C. The solution was hot filtered to remove molecular sieves, and ice cold water was added to the filtrate. 3-Nitro-7-diethylamino coumarin precipitated out of the solution as an orange solid, 77% yield.

The nitro group was then reduced to an amine by stirring in hydrochloric acid with stannous chloride dihydrate at RT for 4 hours. Yielding 3-Amino-7-diethylamino coumarin as a yellow solid in 76% yield.

The amine group was then converted to an azide group using nitrous acid to give the diazonium salt and then treated in-situ with sodium azide to give a golden brown product in 76% yield. The compound was characterized by ^{1}H and ^{13}C NMR and ESI mass spectrometry and was consistent with literature data. The ^{1}H NMR spectrum of all three steps is shown in Figure 2.3. All proton environments integrate correctly for all three NMR spectra. The formation of 3-nitro-7-diethylaminocoumarin is confirmed by the H_6 proton, which shows the carbon ring in the product has successful formed (Figure 2.3 a). There is a peak shift in the ^{1}H NMR spectra of 3-amino-7-diethylaminocoumarin, a broad NH_2 peak also appears at 4.8 ppm, confirming conversion of the NO_2 group to NH_2 (Figure 2.3, b). The NH_2 peak disappears in the ^{1}H NMR spectra of 3-azido-7-diethylaminocoumarin, showing formation of the desired product (Figure 2.3, c).

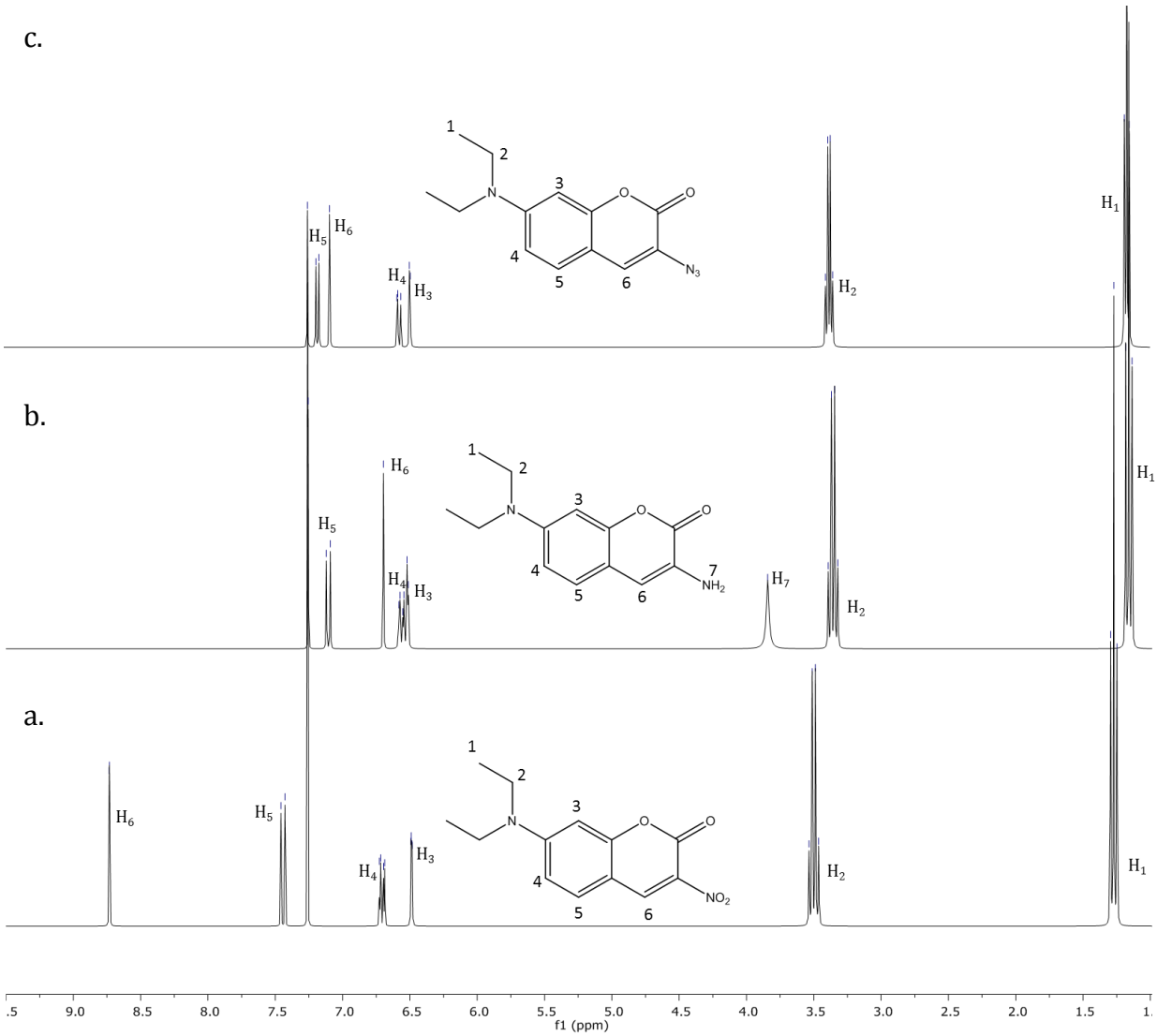

Figure 2.3 ^{1}H NMR (300 MHz, $CDCl_3$, 298 K) of 3-nitro-7-diethylaminocoumarin (a), 3-amino-7-diethylaminocoumarin (b), 3-azido-7-diethylaminocoumarin (c)

2.5.3 Synthesis of 5-(1-(7-(diethylamino)-2-oxo-2H-chromen-3-yl)-1H-1,2,3-triazol-4-yl)picolinaldehyde

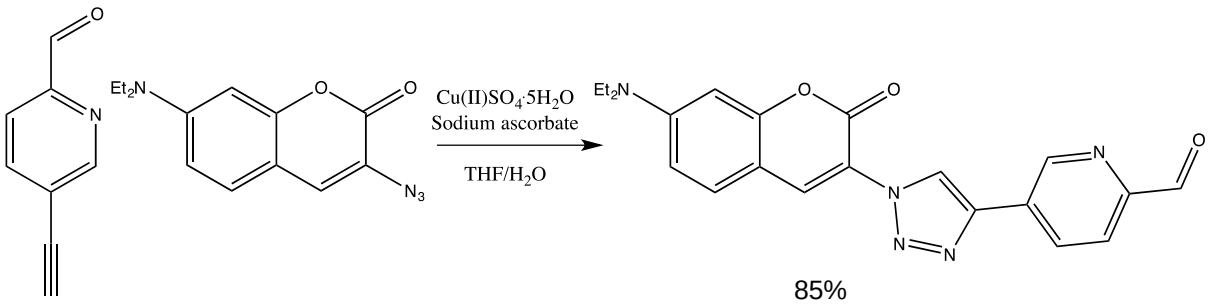

Scheme 2.5 Synthesis of 5-(1-(7-(diethylamino)-2-oxo-2H-chromen-3-yl)-1H-1,2,3-triazol-4-yl)picolinaldehyde

A click reaction was undertaken between 3-azido-7-diethylaminocoumarin and 5-ethynyl-2-formylpyridine (Scheme 2.5). Both starting materials were dissolved in THF and water (5:1). A freshly prepared solution of copper(II) sulphate was added, followed by a sodium(I) ascorbate solution to reduce the Cu(II) *in-situ* to Cu(I). Upon addition of sodium(I) ascorbate the solution darkened. The flask was covered in foil and stirred in the dark for 72 hours. The reaction was monitored by TLC. After 48 hours there was still a mixture of starting materials as well as product, so the reaction was left for a further 24 hours. After this there was still starting materials left, an aliquot of the sample was taken and checked by ^{1}H NMR showing 15% starting material to product. The reaction was stopped and ice cold water was added. The resulting yellow precipitate was collected by filtration and washed with ice-cold water to remove residual copper(II) salts and sodium(I) ascorbate. The crude product was then purified by flash column chromatography. 5-ethynyl-2-formylpyridine was eluted off using ether and some product was eluted washing DCM. However, a lot of product stuck to the column, as evident from the yellow colour of the silica, after 2 L of DCM had been used to elute the column, the collected fractions were placed under a UV lamp and were fluorescent, showing they contained the clicked product, the yield collected was lower than expected. The purification was modified in subsequent reactions. After collection by filtration the solid was washed with water – to remove copper salts and sodium ascorbate, ethanol – to remove coumarin azide starting material, ether – to remove 5-ethynyl-2-formylpyridine. The product was then washed through using chloroform and the filtrate was concentrated to dryness to afford pure product as a bright yellow powder with an 85 % yield. The purified product was then fully characterised by ^{1}H NMR and ^{13}C NMR and ESI mass spectrometry. The ^{1}H NMR spectrum confirms formation of the product (Figure 2.4). The loss of the alkyne proton peak and formation of the triazole ring proton, H_7, show the click reaction has been successful.

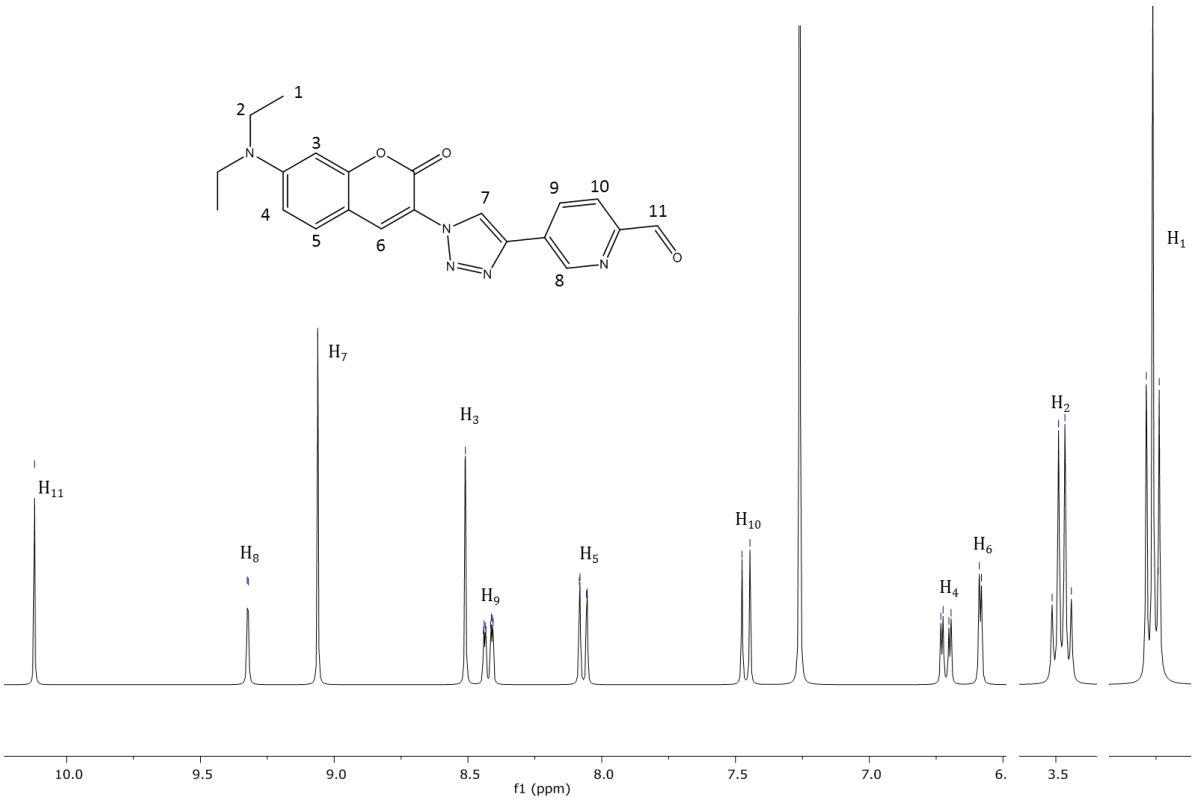

Figure 2.4 ^{1}H NMR (300 MHz, $CDCl_3$, 298 K) of 5-(1-(7-(diethylamino)-2-oxo-2H-chromen-3-yl)-1H-1,2,3-triazol-4-yl)picolinaldehyde

3-Azido-7-diethylcoumarin isn't fluorescent, as its fluorescence is quenched by the electron rich α-nitrogen of the azide group[15]. Upon 'clicking' the azide forms a triazole ring. The α-nitrogen is now in a ring and is unable to quench the fluorescence (Figure 2.5)[15]. This characteristic allows the reaction to be monitored by TLC, viewed under UV light - a fluorescent spot is present on the TLC plate after successful 'clicking' of the staring materials.

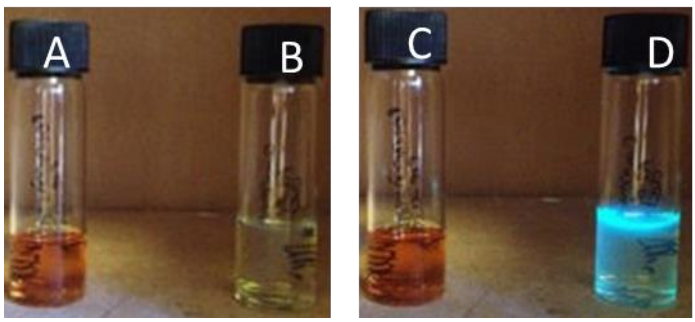

Figure 2.5 A coumarin azide, B clicked coumarin pyridine ring in 5th position, C - A exposed to UV light, D – B exposed to UV light.

2.5.4 Synthesis of L^{C5}

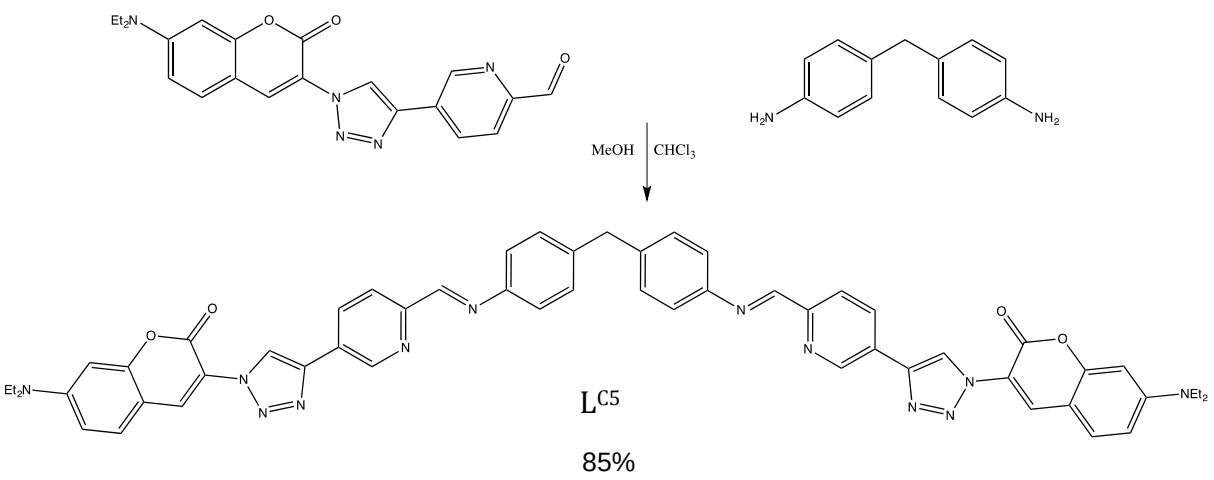

Scheme 2.6 Synthesis of L^{C5}

The newly formed clicked coumarin product was then incorporated into a bidentate ligand, with the capability of forming an iron metallo cylinder complex (Scheme 2.6). The ligand L^{C5} was prepared by suspending 5-(1-(7-(diethylamino)-2-oxo-2H-chromen-3-yl)-1H-1,2,3-triazol-4-yl)picolinaldehyde in methanol. Chloroform was added to aid dissolution. 4,4′-Methylenedianiline was dissolved in a small amount of methanol and added dropwise to the stirred solution. The reaction was stirred for 24 hours in the dark to prevent the possibility of photobleaching the coumarin dye. A yellow precipitate formed that was collected by filtration, washed with methanol to remove any unreacted 4,4′-methylenedianiline, followed by further washing with diethyl ether to help dry the powder. The product was obtained in a 85% yield. The purified product was then fully characterised using ^{1}H NMR that was fully assigned using 2D COSY and NOSEY experiments. ESI mass spectrometry and ^{13}C NMR were then under taken and fully assigned using a 2D HSQC experiment. The ^{1}H NMR spectra (Figure 2.6) confirms formation of the ligand, evidenced by formation of the imine peak at 8.7ppm and loss of the aldehyde peak from the starting material, proving that the condensation reaction has been successful.

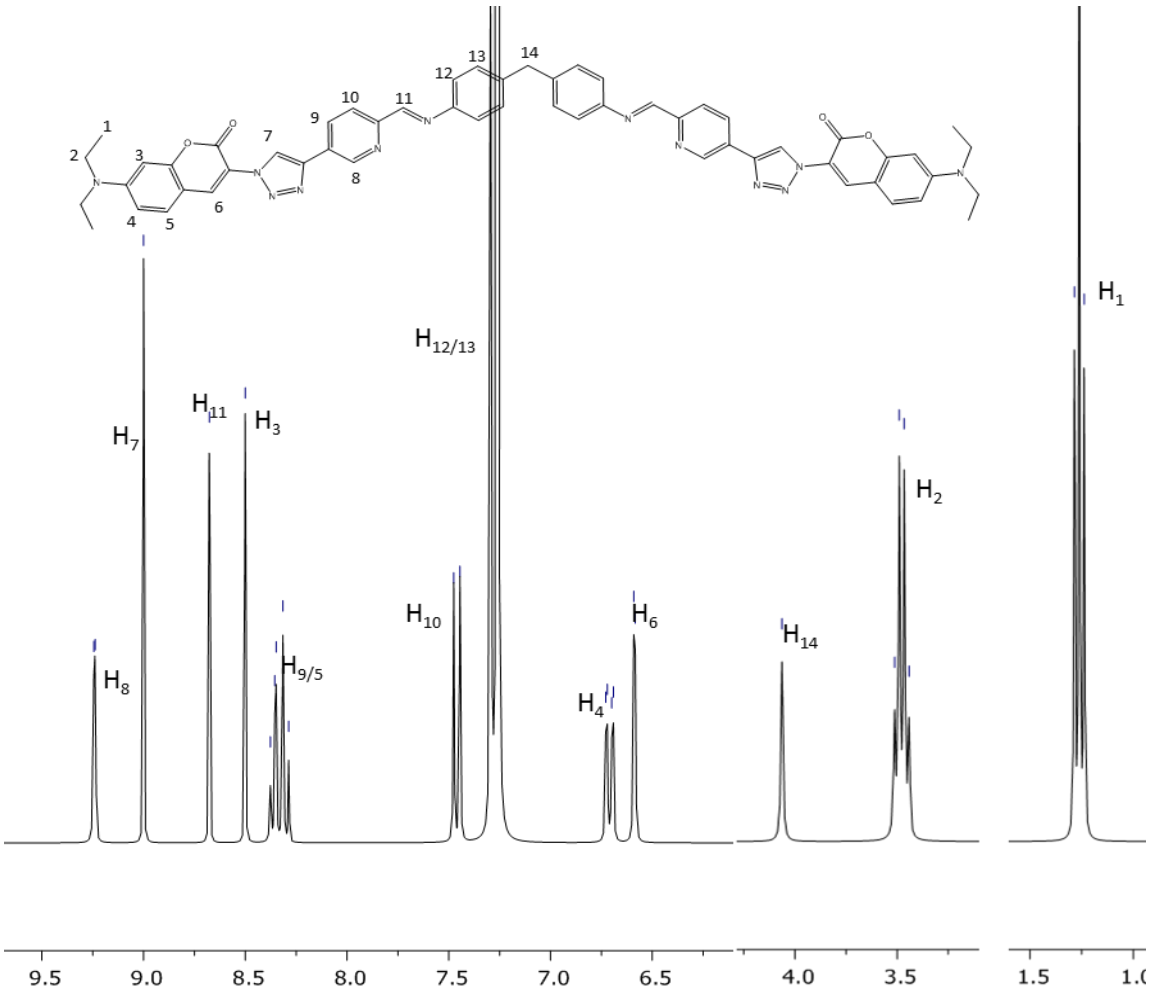

Figure 2.6 ^{1}H NMR (300 MHz, $CDCl_3$, 298 K) of L^{C5}

2.5.5 Synthesis of $(L^{C5}{}_3Fe_2)[PF_6]_4$

The newly developed fluorescent ligand was then used to produce a triple stranded dinuclear iron complex. L^{C5} was suspended in methanol, a stoichiometric amount of iron(II) chloride in a 3:2 ratio, was dissolved in methanol. This solution was added dropwise to the stirred ligand. Upon addition of metal salt the solution turned green. An excess of metanolic ammonium hexafluorophosphate was added to precipitate the complex from solution. The solid was collected by filtration, washed with methanol to remove any unreacted iron salt and diethyl ether to dry. The product was obtained in a 56% yield and characterised by ^{1}H NMR and ESI mass spectrometry. The ^{1}H NMR confirms formation of the product due to the broad nature of the peaks. The aromatic

protons of the ligand become inequivalent upon binding to the metal and are represented as two board peaks in the NMR spectrum (Figure 2.7). The formation of a multicharged species is also evident in the mass spectrum, where the M^{4+} peak can be observed at 733.60.

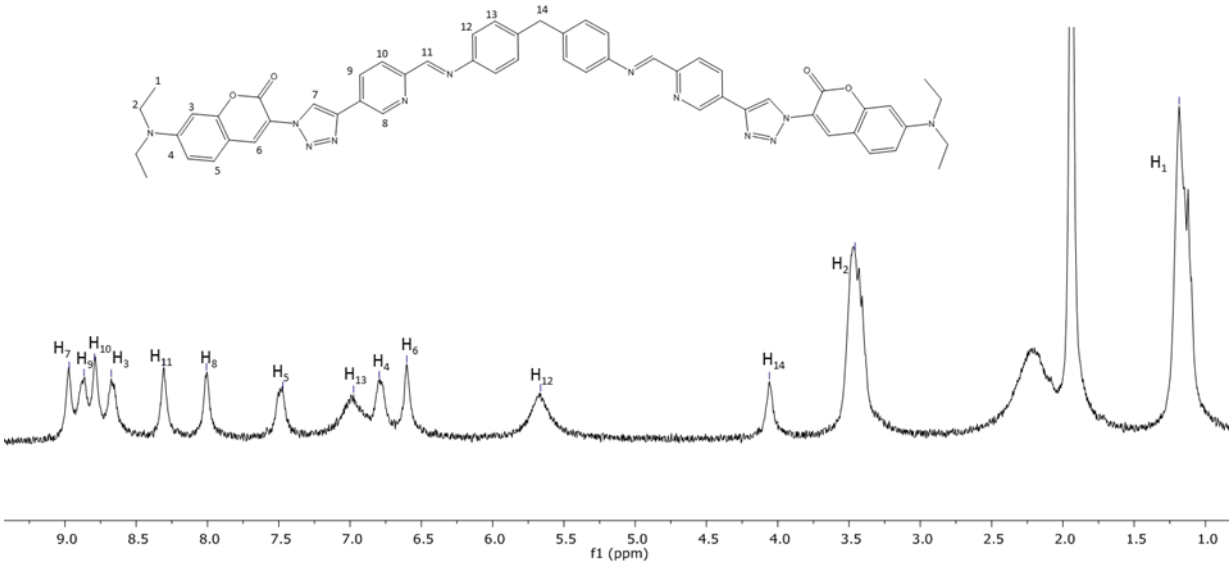

Figure 2.7 ^{1}H NMR (300 MHz, CD_3CN, 298 K) of $[L^{C5}{}_3Fe_2][PF_6]_4$

2.5.6 Attempted Synthesis if $(L^{C5}{}_3Ru_2)4PF_6$

Previously in the Hannon group a weakly luminescent ruthenium(II) cylinder has been synthesised[6]. This has been shown to be more stable than the iron(II) cylinder due to its strong Ru-N bond. Unfortunately, during the reaction, a number of side products are formed, leading to a low yield of triple stranded product, of around 1%. An attempt to make a ruthenium(II) cylinder using L^{C5} was undertaken, to increase stability of the resulting complex compared to the iron cylinder, when in contact with aqueous solution. Ru(II) chloride was firstly converted to $Ru(DMSO)_4Cl_2$, to increase its reactivity. L^{C5} was dissolved in anhydrous ethylene glycol and heated to 200˚C. $Ru(DMSO)_4Cl_2$ was added to the hot solution. Upon addition of the metal salt the solution turned dark red. The reaction was heated in the dark for 5 days at 200˚C. Upon cooling methanol was added and the

solution was filtered to remove any polymerized side products. Ammonium hexafluorophosphate was added to covert the counterion from Cl^- to PF_6^-. The resulting solid was collected by filtration and concentrated. Numerous attempts to purify the complex were under taken *via* flash column chromatograph with silica and alumina as the solid phase, with a variety of eluents; unfortunately, no pure product could be obtained.

2.6 Synthesis and design of dansyl ligands and complexes.

Due to the instability of the coumarin complex when in contact with aqueous media or solution, dansyl was explored as an alternative fluorophore, like coumarin, dansyl is also quite a small fluorophore. Large fluorophores on the cylinder are likely to adversely affect the cylinder's formation and DNA binding. A short polyethylene glycol (PEG3) linker was also introduced between the fluorophore and triazole, in the hope of aiding solubility. The increase in distance between the ends of the metallo-cylinder and the fluorophore would decrease any steric repulsion caused from the close proximity of the three fluorescent groups at the ends of the cylinder, and might minimise any π-π stacking effects leading too self-quenching of the fluorescence.

2.6.1 Synthesis of dansyl-PEG3-azide

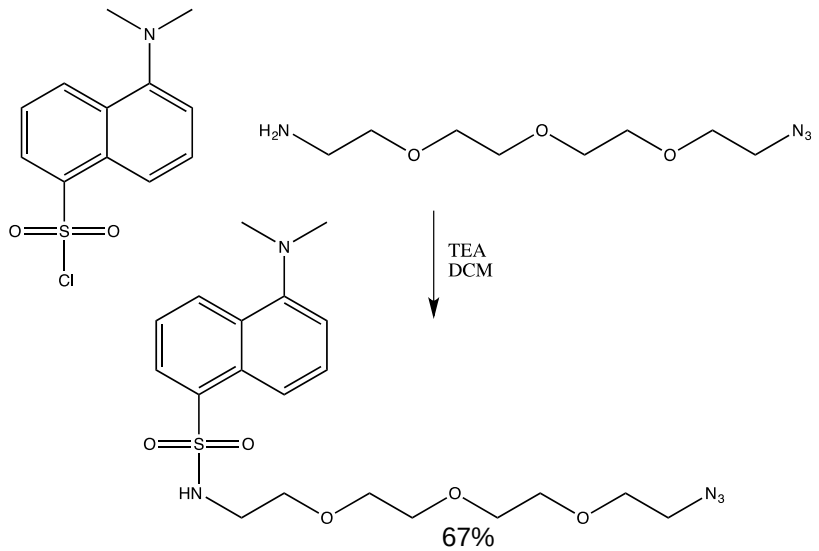

Scheme 2.7 Synthesis of dansyl-PEG3-azide

Dansyl chloride was dissolved in anhydrous DCM under argon with a small amount of anhydrous triethylamine[17]. 11-Azido-3,6,9-trioxaundecan-1-amine was added dropwise and the reaction stirred in the dark for 15 hours at room temperature. A saturated solution of sodium carbonate was added to quench the reaction. The solution was extracted using DCM and the crude product was purified using flash column chromatography using 2% methanol in DCM, giving a 67% yield. The bright yellow oil was fully characterised using ^{1}H NMR, ^{13}C NMR and ESI mass spectrometry, which were all consistent with literature data[17]. The ^{1}H spectra confirms formation of the product as the peaks correctly integrate to the correct number for each proton environment (Figure 2.8). The NH peak H_7, correctly integrates for one proton, showing conversion from NH_2 to NH. The $[M+Na]^+$ peak at 474.12 is also observed in the mass spectra, confirming product formation.

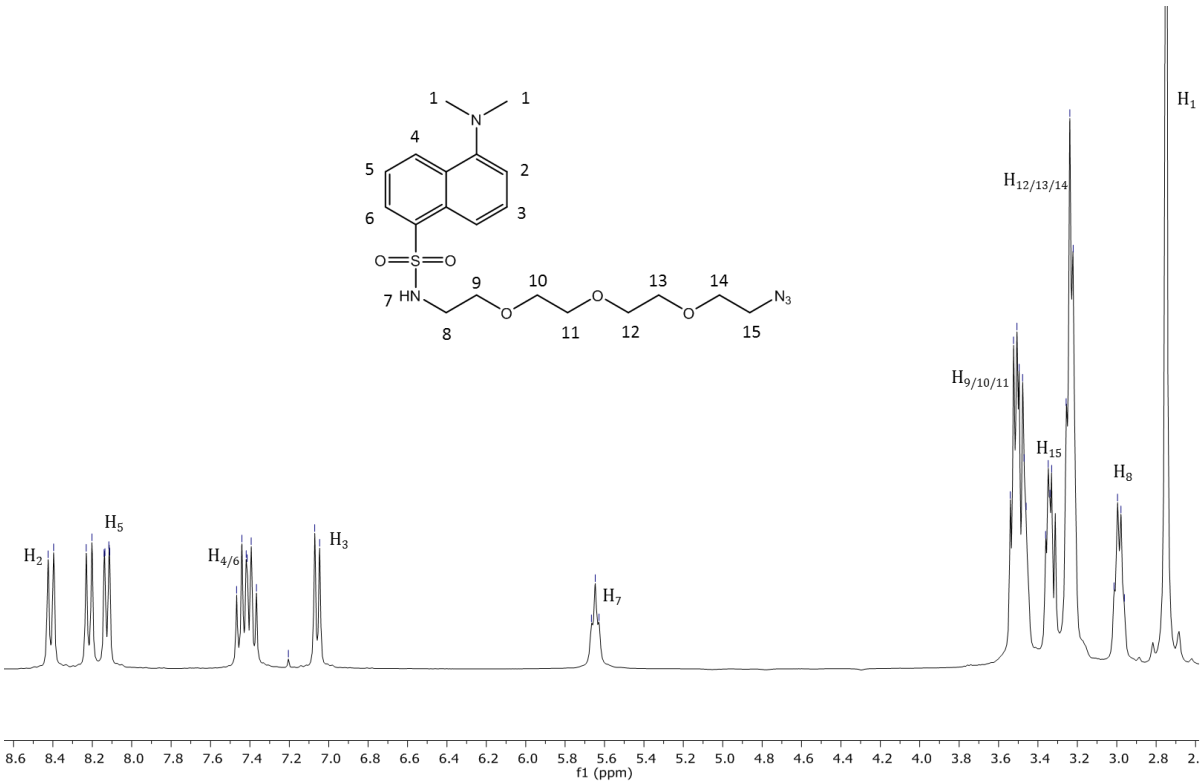

Figure 2.8 ^{1}H NMR (300 MHz, $CDCl_3$, 298 K) of dansyl-PEG3-azide.

2.6.2 Synthesis of 5-(dimethylamino)-N-(2-(2-(2-(2-(4-(6-formylpyridin-3-yl)-1H-1,2,3-triazol-1-yl)ethoxy)ethoxy)ethoxy)ethyl)naphthalene-1-sulfonamide

The newly formed azide functionalised dansyl group was grafted onto the pyridyl ring *via* a copper catalysed click reaction (Scheme 2.8)

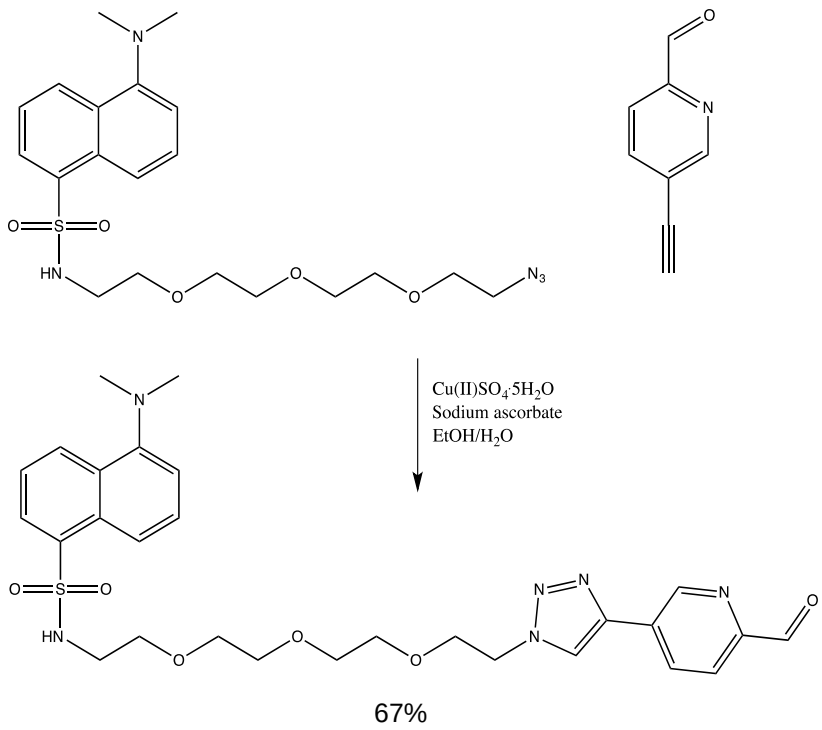

Scheme 2.8 Synthesis of 5-(dimethylamino)-N-(2-(2-(2-(2-(4-(6-formylpyridin-3-yl)-1H-1,2,3-triazol-1-yl)ethoxy)ethoxy)ethoxy)ethyl)naphthalene-1-sulfonamide

A click reaction was performed using dansyl-PEG3-azide and 5-ethynyl-2-formylpyridine were dissolved in ethanol and water (5:1). A fresh solution of copper sulphate pentahydrate in water, was added, followed by a solution of sodium ascorbate. Upon addition of sodium ascorbate the solution changed colour from yellow to orange-red. The reaction was stirred under argon for 18 hours in the dark. The solution was diluted with water, extracted with DCM and the organic fractions concentrated and purified by flash column chromatography on silica using DCM to produce the product as a yellow powder in a 67% yield. The pure product was then fully characterised using ESI MS, ^{1}H NMR and

^{13}C NMR. The ^{1}H NMR spectra (Figure 2.9) confirms formation of the product by the formation of the triazole peak H_{17} and loss of the alkyne peak from the starting material.

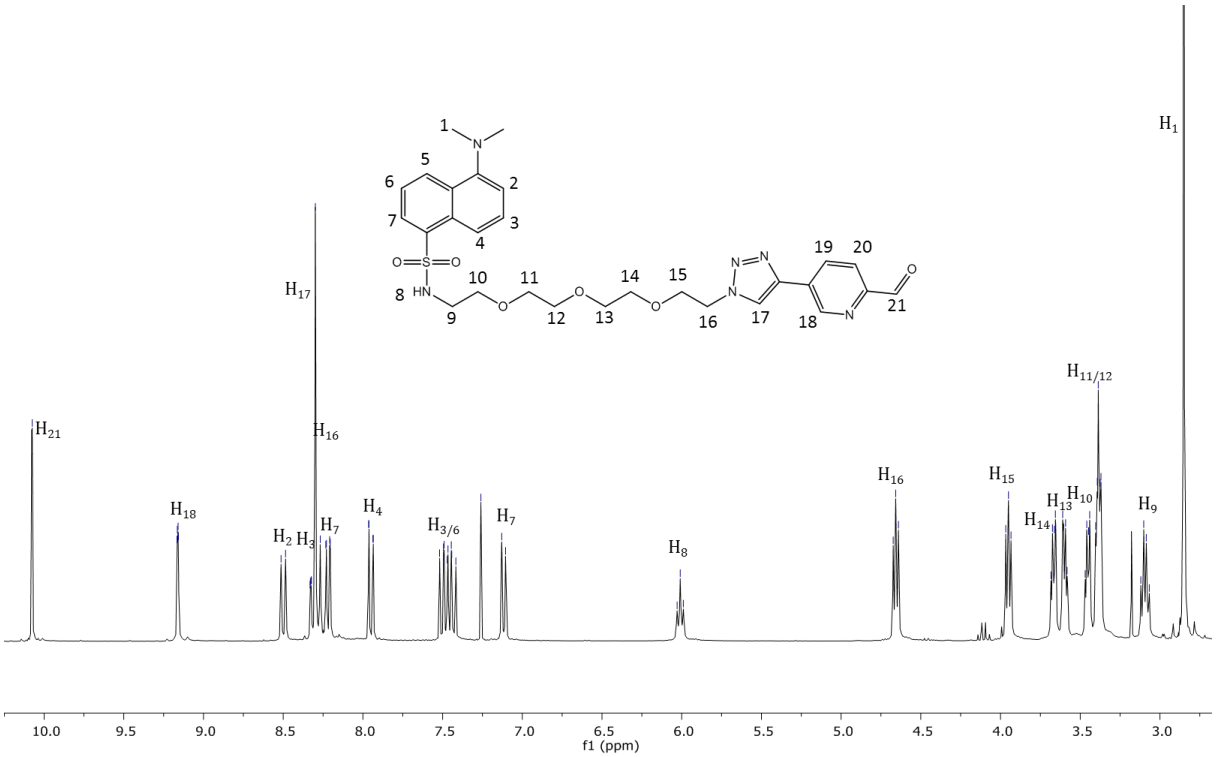

Figure 2.9 ^{1}H NMR (300 MHz, $CDCl_3$, 298 K) of 5-(dimethylamino)-N-(2-(2-(2-(2-(4-(6-formylpyridin-3-yl)-1H-1,2,3-triazol-1-yl)ethoxy)ethoxy)ethoxy)ethyl)naphthalene-1-sulfonamide

2.6.3 Synthesis of L^{D5}

The newly developed dansyl functionalised pyridine ring was then incorporated into a bidentate fluorescent ligand (Scheme 2.9), with the potential to form a metallo-cylinder complex.

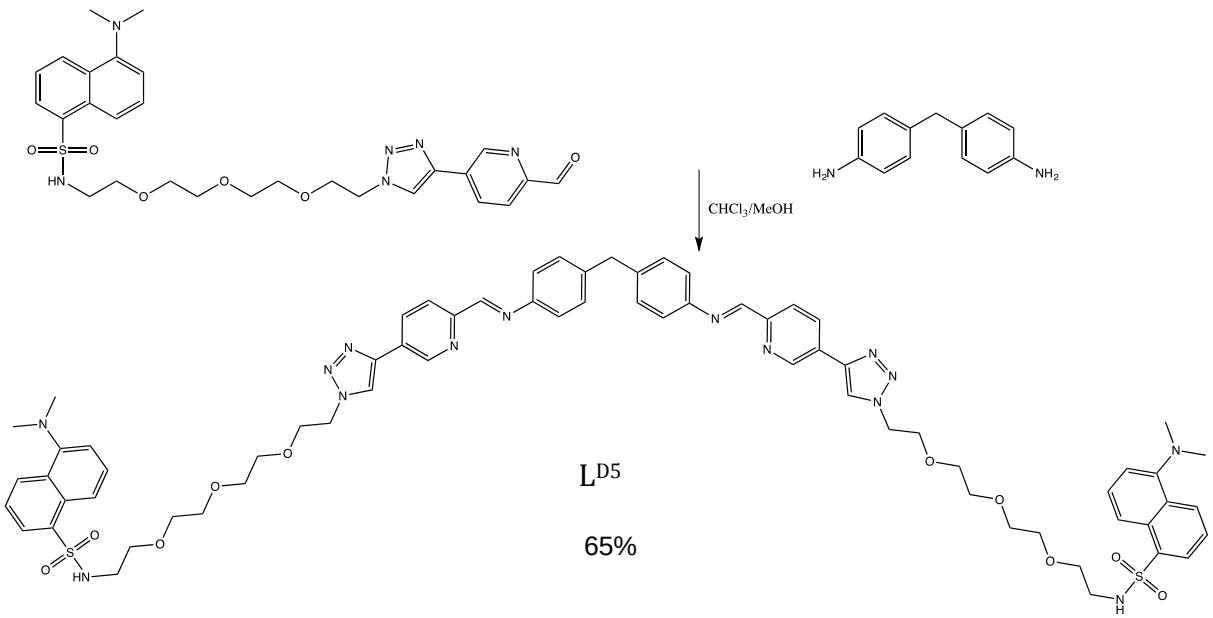

Scheme 2.9 Synthesis of L^{D5}

The ligand L^{D5}, was produced by dissolving 5-(dimethylamino)-N-(2-(2-(2-(2-(4-(6-formylpyridin-3-yl)-1H-1,2,3-triazol-1-yl)ethoxy)ethoxy)ethoxy) ethyl)naphthalene-1-sulphonamide in a mixture of chloroform and methanol (1:2). A solution of 4,4′-methylenedianiline in methanol was added dropwise to the stirred solution. The reaction was stirred at room temperature for 24 hours with the exclusion of light. After 16 hours of stirring an oily residue had stuck to the side of the round bottom flask, a small amount of methanol was added to the flask and the solution was sonicated for 5 minutes to dissolve the residue back into solution. Following this, the reaction was then stirred for a further 8 hours. An excess amount of diethyl ether was added to precipitate out the product, which was then collected rapidly *via* filtration and dried to afford L^{D5} as a brown solid with a 65% yield. The product was fully characterised using ^{1}H NMR that was fully

assigned using 2D COSY and NOESY NMR experiments. ^{13}C NMR experiments were undertaken that were fully assigned using a 2D HSQC NMR experiment. ESI mass spectrometry was then analyzed and showed the product peak. The ^{1}H NMR spectra (Figure 2.10) confirms formation of the ligand L^{D5}, due to the formation of the imine peak H_{21} and loss of the aldehyde peak from the starting material, confirming the condensation reaction has been successful.

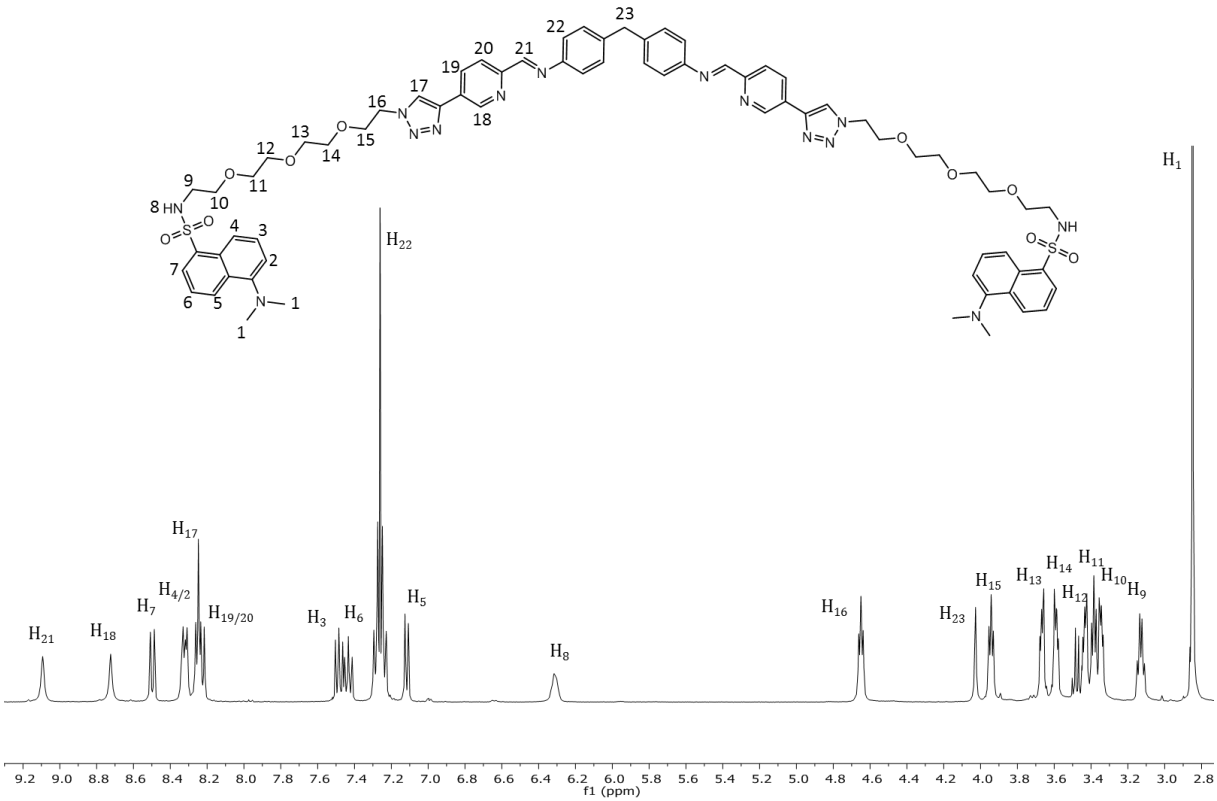

Figure 2.10 ^{1}H NMR (300 MHz, $CDCl_3$, 298 K) of L^{D5}

2.6.4 Synthesis of $[L^{D5}{}_3Fe_2][PF_6]_4$

The newly developed fluorescent ligand L^{D5} was used to form a triple stranded di nuclear metallo-cylinder. L^{D5} was reacted with iron(II) chloride in a stoicheometric 3:2 ration. L^{D5} was suspended in methanol followed by the dropwise addition of iron(II) chloride in methanol. Upon addition of the metal salt, the solution turned a deep purple, the characteristic colour of the triple stranded parent metallo-cylinder, who's colour arises from a strong MLCT band. An excess of methanolic ammonium hexafluorophosphate was

added to precipitate the complex. The solid was collected and washed with methanol to remove any unreacted ligand, water to remove excess NH_3PF_6 and diethyl ether to dry the solid. The product was produced in an 82% yield and characterised using ^1H NMR and ESI mass spectrometry. The ^1H NMR confirms formation of the product due to the broad shape of the proton peaks. The aromatic protons of the ligand become inequivalent upon binding to the metal and are represented as two broad peaks in the NMR spectrum (Figure 2.11). The formation of a multicharged species is also evident in the mass spectrum, where the M^{4+} peak can be observed at 1023.8.

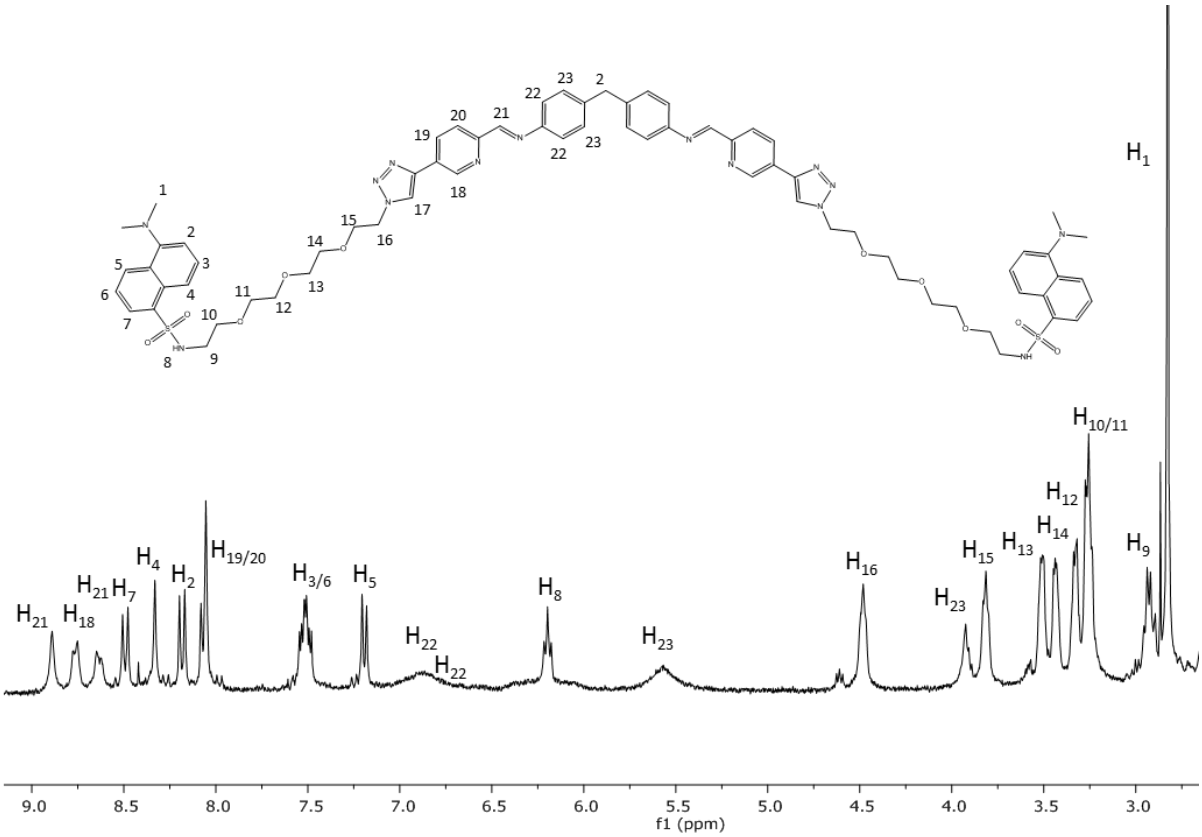

Figure 2.11 ^1H NMR (300 MHz, CD_3CN, 298 K) of $[L^{D5}{}_3Fe_2][PF_6]_4$

2.7 Functionalisation in the fourth position

Complexes synthesised using L^{C5} were unstable in aqueous solution, this is thought to be due to the steric hindrance of the fluorescent groups being held in close proximity at the end of metallo-cylinder. It was hoped that moving to the fourth position would give more

room at the end of the metallo-cylinder and reduce any steric repulsion between the fluorescent groups and hence improve stability (Figure 2.12). Up until now functionalisation in the fourth position hasn't been undertaken, this has been due to the synthetic difficulties of adding functional groups at this position. However, addition at the third position has been shown to increase the width of the cylinder complex and decrease its DNA binding ability[8]. It is hoped that the addition of a fluorophore at the fourth position will have a minimal effect on the DNA binding properties but improve the stability of the complex.

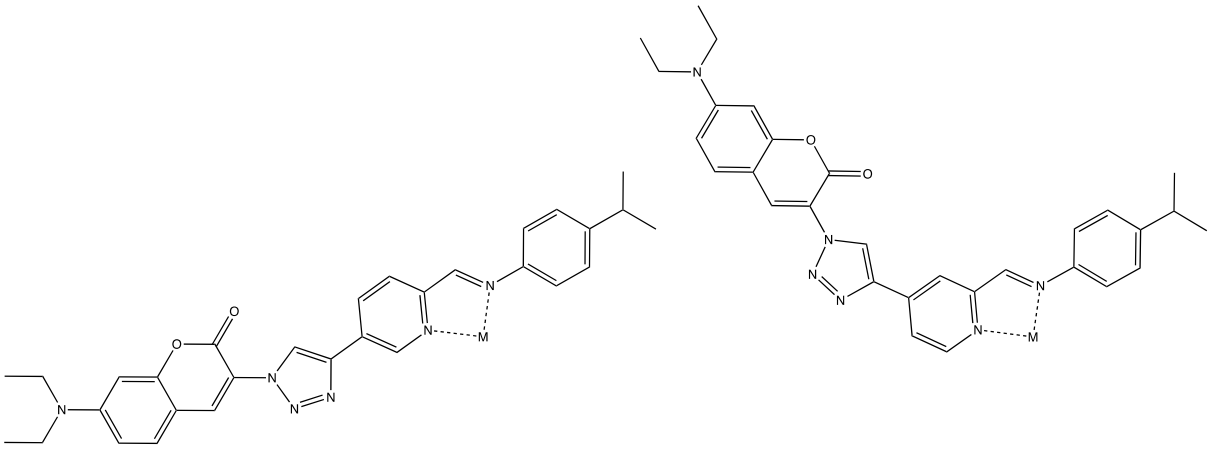

Figure 2.12Structural difference of fluorescent modification at the 5th position of the pyridyl ring (left) and the 4th position of the pyridyl ring (right).

2.7.1 Synthesis of 4-ethynyl-2-formylpyridine

4-Bromopyridine-2-carbaldehyde was commercially available from Fluorochem, this was used to add an alkyl group *via* the same 2 step synthetic route described in Section 2.5.1 (Scheme 2.10). 4-Trimethylsilylethynyl-2-formyl pyridine was successfully produced in a 63% yield and converted to 4-ethynyl-2-formylpyridine, giving a 59% yield . The products were fully characterised using ESI mass spectrometry, ^{1}H NMR and ^{13}C NMR. The ^{1}H NMR spectrum confirms the addition of the $SiMe_3$ group, by the presence of the H_5 peak at 0.25 ppm (Figure 2.13, a). The successful deprotection of this group is confirmed by the formation of the alkyne peak H_5 at 3.5 ppm (Figure 2.13, b).

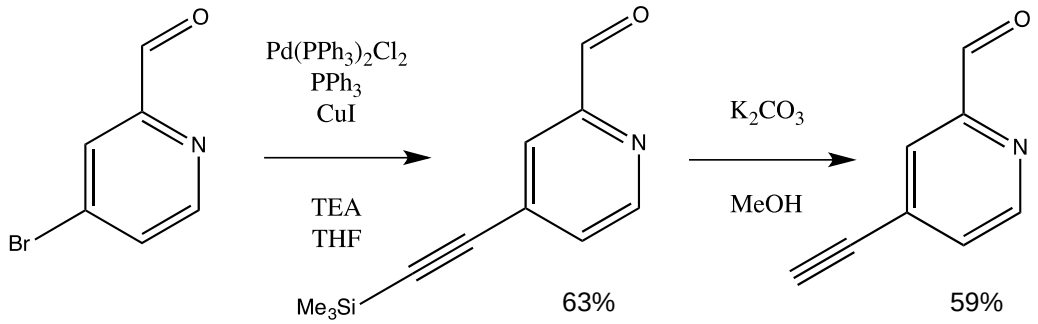

Scheme 2.10 Synthesis of 4-ethynyl-2-formylpyridine

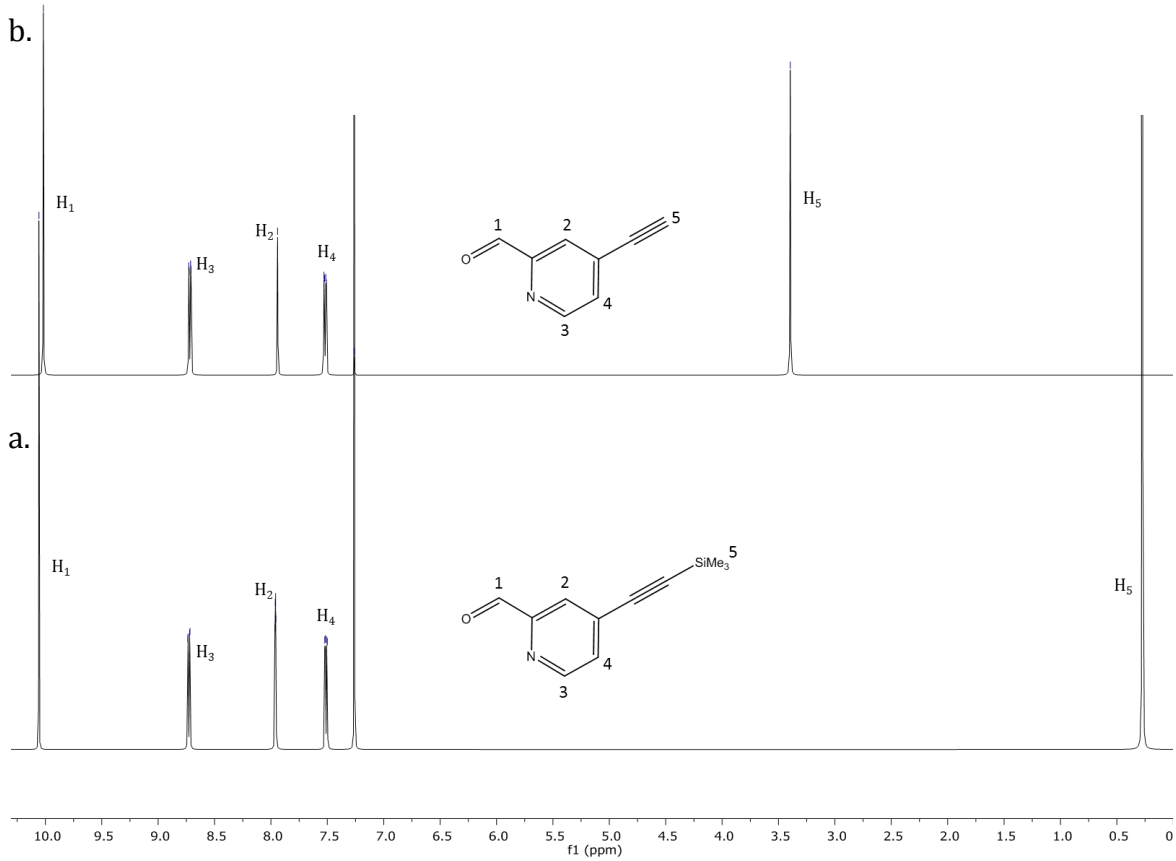

Figure 2.13 ^{1}H NMR (300 MHz, $CDCl_3$, 298 K) of 5-trimethylsilylethynyl-2-formyl pyridine (a) and 4-ethynyl-2-formylpyridine (b).

2.7.2 Synthesis of clicked courmarin product in fourth position.

The newly developed compound, 4-ethynyl-2-formylpyridine, was used in the production of a fluorescent ligand precursor. A click reaction was undertaken using the same synthetic procedure described in Section 2.5.3. 4-Ethynyl-2-formylpyridine and 3-azido-7-diethylaminocoumarin were dissolved in THF and water, the reaction was catalyzed by copper(II) sulphate pentahydrate, reduced *in-situ* to copper(I) using sodium(I) ascorbate

(Scheme 2.11). The bright yellow product was produced in a 73 % yield and fully characterised by ESI mass spectrometry, ^{1}H NMR and ^{13}C NMR.

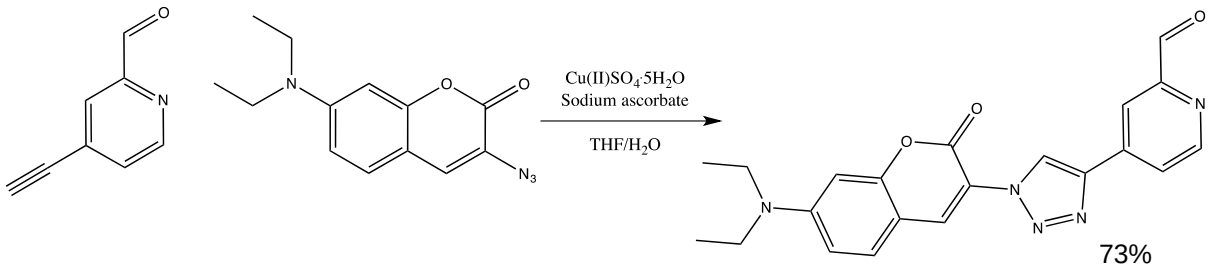

Scheme 2.11 Synthesis of 5-(1-(7-(diethylamino)-2-oxo-2H-chromen-3-yl)-1H-1,2,3-triazol-4-yl)picolinaldehyde

The ^{1}H NMR spectra (Figure 2.14) confirms the click reaction has been successful by formation of the triazole peak, H_7 and loss of the alkyne peak from the starting material.

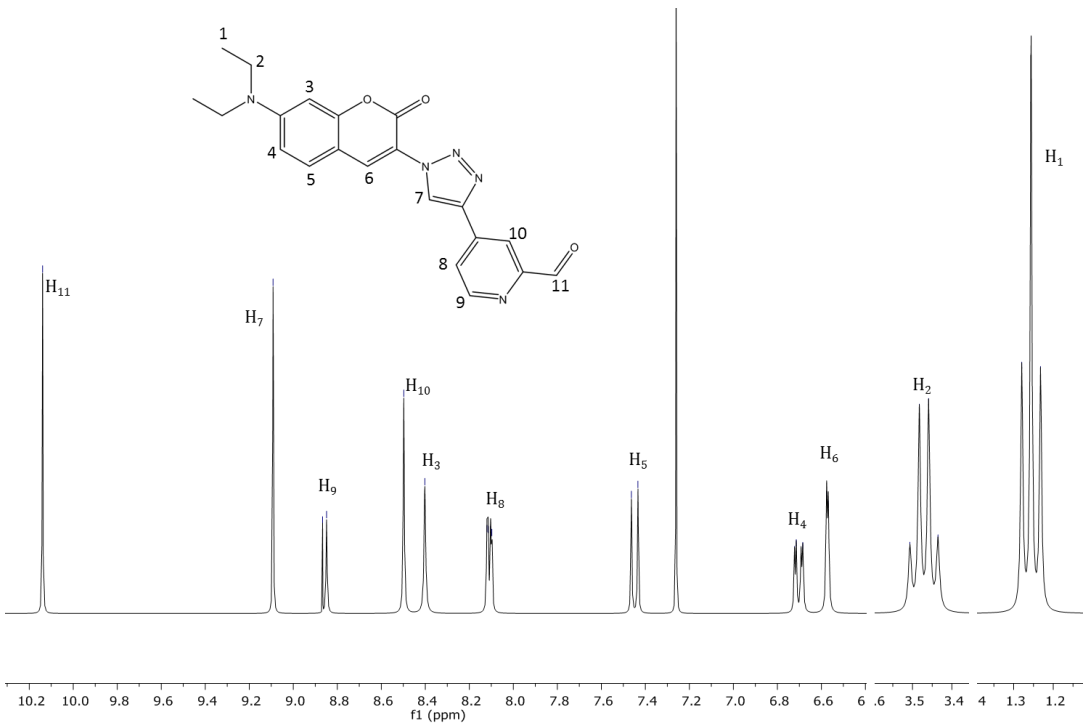

Figure 2.14 ^{1}H NMR (300 MHz, $CDCl_3$, 298 K) of the pyridine ring functionalised in the 4 position with a coumarin fluorophore.

2.7.3 Synthesis of L^{C4}

The newly synthesised pyridine ring functionalised in the 4th position with a coumarin fluorophore was then used in the formation of a ligand L^{C4} (

Scheme 2.12).

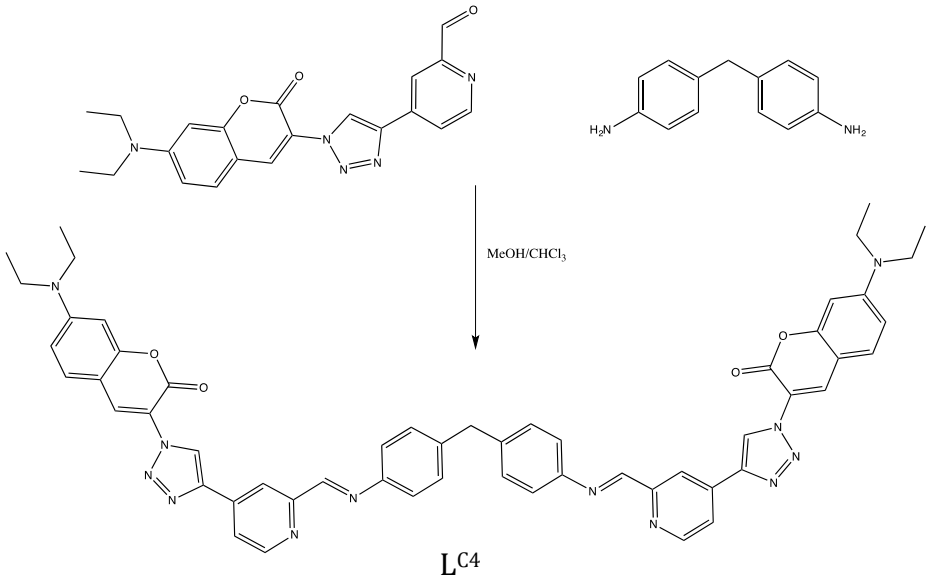

L^{C4}

71%

Scheme 2.12 Synthesis of L^{C4}

L^{C4} was produced by using the same synthetic procedure described in Section 2.5.4. The condensation reaction between the coumarin clicked product in position 4 and 4,4′-methylenedianiline was undertaken in methanol and chloroform. After stirring for 24 hours, the product was collected in a 71% yield and fully characterised using ESI mass spectrometry and ^{1}H NMR and ^{13}C NMR. 2D COSY and NOESY experiments were used to fully assign the proton NMR. A HSQC experiment was used to fully assign the carbon NMR spectrum.

Confirmation of the condensation reaction is evident in the ^{1}H NMR spectra of L^{C4}, by the formation of the imine proton peak, and loss of the aldehyde peak from the starting material.

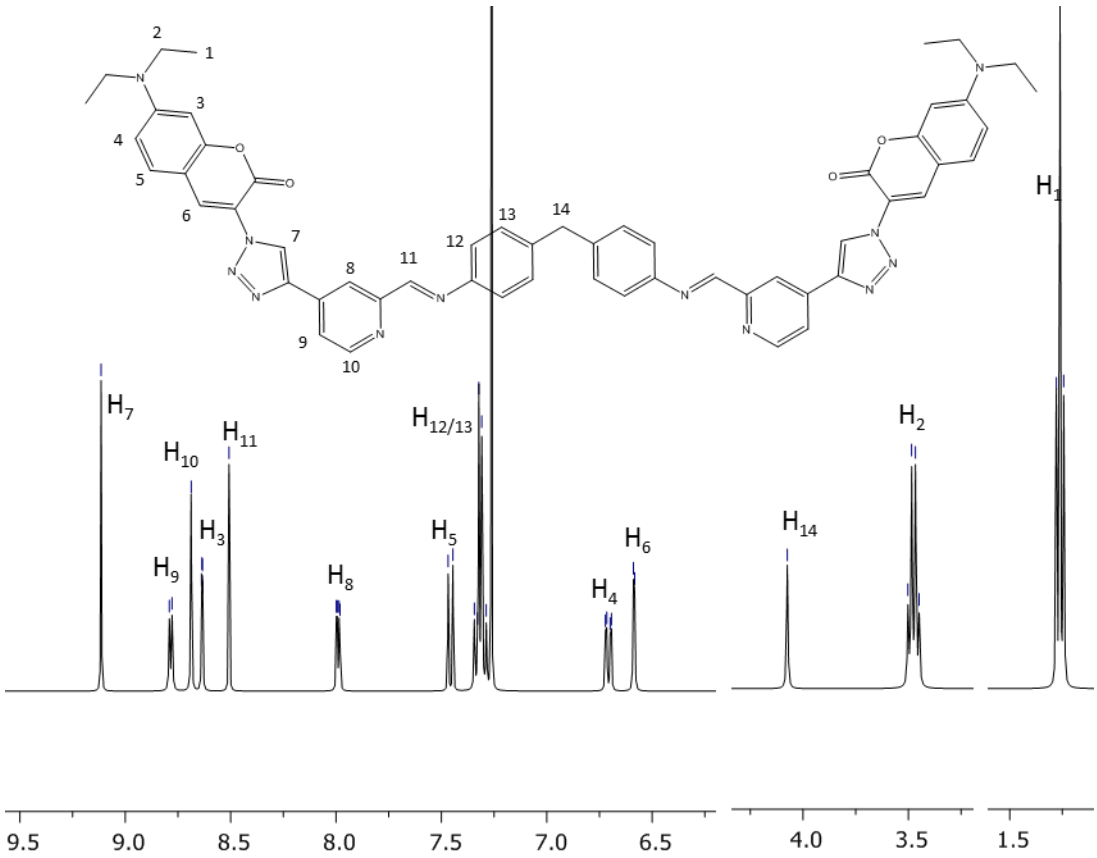

Figure 2.15 ^{1}H NMR (300 MHz, $CDCl_3$, 298 K) of L^{C4}

2.7.4 Synthesis of $[L^{C4}{}_3Fe_2][PF_6]_4$

The newly developed fluorescent ligand L^{C4}, was then used to produce a triple stranded dinuclear iron complex. L^{C4} was suspended in methanol, a stoichiometric amount of iron chloride, in a 3:2 ratio, was dissolved in methanol. This solution was added dropwise to the stirred ligand. Upon addition of metal salt the solution turned green. An excess of methanolic ammonium hexafluorophosphate was added to precipitate the complex from solution. The solid was collected by filtration, washed with methanol to remove any unreacted iron salt and diethyl ether to dry. The product was produced in a 58% yield and characterised by ^{1}H NMR and ESI mass spectrometry. The ^{1}H NMR confirms formation of the product due to the broad nature of the peak. The aromatic protons of the ligand become inequivalent upon binding to the metal and are represented as two board peaks in the NMR spectrum (Figure 2.16). The formation of a multicharged species is also evident in the mass spectrum, where the M^{4+} peak can be observed at 733.49.

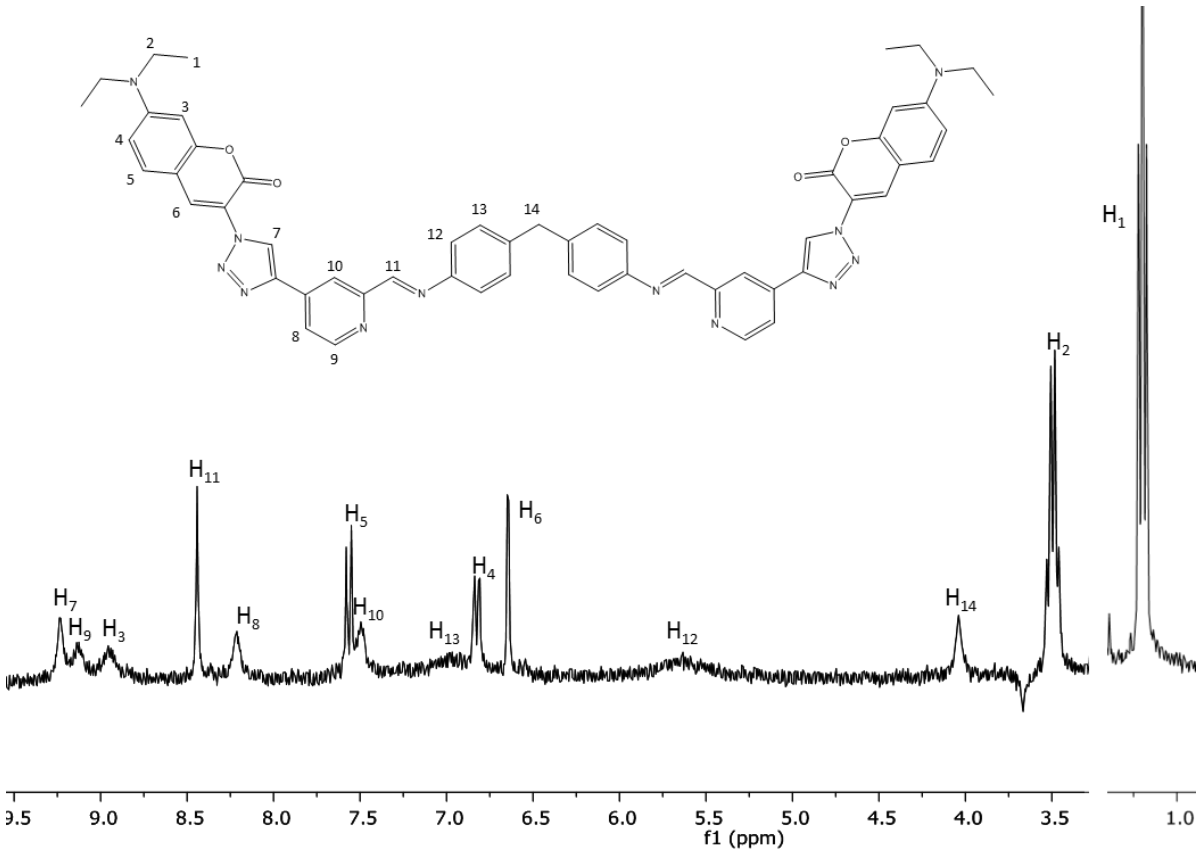

Figure 2.16 ^{1}H NMR (300 MHz, CD_3CN, 298 K) of $[L^{C4}{}_3Fe_2][PF_6]_4$

2.7.5 Synthesis of clicked dansyl in fourth position

Dansyl-PEG3-azide was 'clicked' to 4-ethynyl-2-formylpyridine using the same synthetic procedure described in Section 2.6.2 (Scheme 2.13). The product was precipitated and collected by filtration, giving a 59% yield, followed by full characterisation using ESI mass spectrometry and ^{1}H NMR and ^{13}C NMR. The ^{1}H NMR spectra (Figure 2.17) confirms the click reaction has been successful, due to formation of the imine proton peak, H_{16}, and loss of the alkyne peak from the starting material.

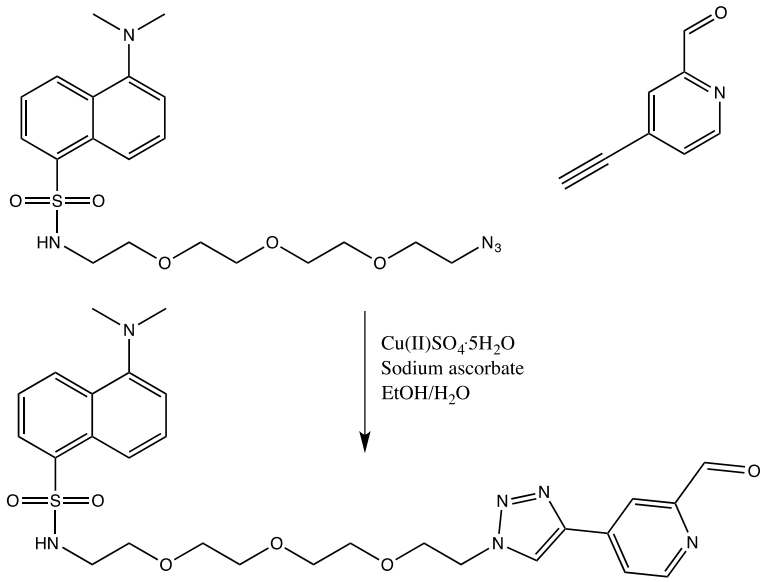

Scheme 2.13 Synthesis of 4-(dimethylamino)-N-(2-(2-(2-(2-(4-(6-formylpyridin-3-yl)-1H-1,2,3-triazol-1-yl)ethoxy)ethoxy)ethoxy)ethyl)naphthalene-1-sulfonamide

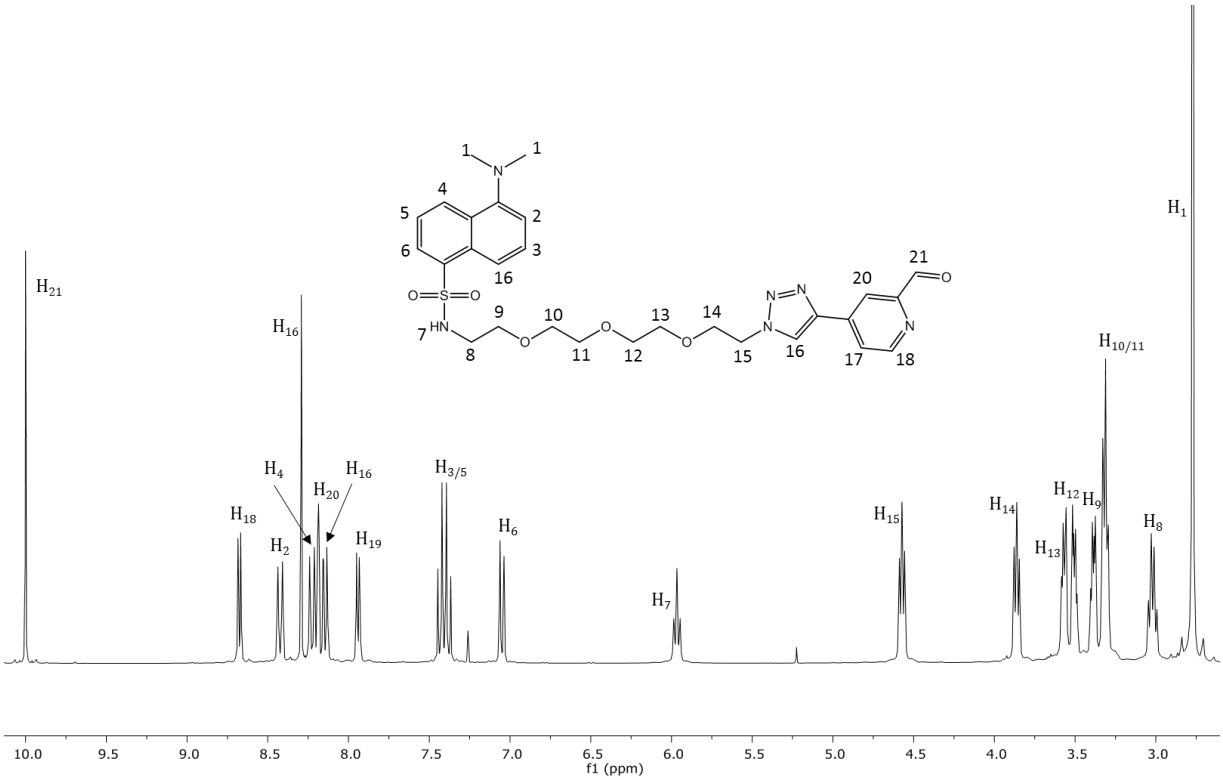

Figure 2.17 ^{1}H NMR (300 MHz, $CDCl_3$, 298 K) of 4-(dimethylamino)-N-(2-(2-(2-(2-(4-(6-formylpyridin-3-yl)-1H-1,2,3-triazol-1-yl)ethoxy)ethoxy)ethoxy)ethyl)naphthalene-1-sulfonamide

2.7.6 Synthesis of L^{D4}

The newly produced pyridyl ring, functionalised in the 4 position with a dansyl fluorophore, was then used to produce a bidentate ligand, L^{D4} (

Scheme 2.14). This ligand will be used to produce a metallo cylinder complex.

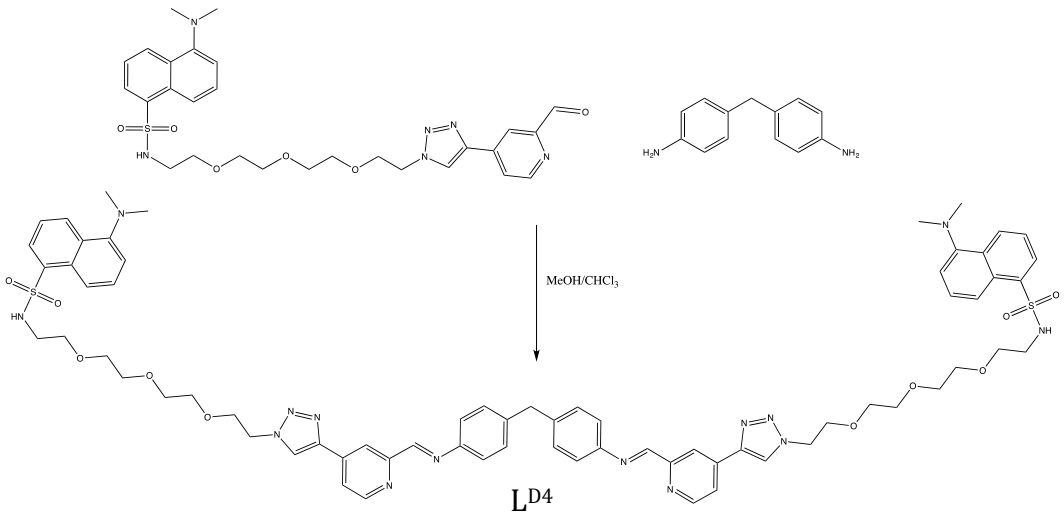

L^{D4}

68%

Scheme 2.14 Synthesis of L^{D4}

L^{D4} was synthesised *via* a condensation reaction between 4,4′-methylenedianiline and clicked dansyl product in position 4. The reactants were stirred in methanol and chloroform. The product was precipitated from solution using diethyl ether, collected by filtration and dried to give a 68% yield. The solid was characterised using ^{1}H NMR that was fully assigned using 2D COSY and NOESY NMR experiments. ^{13}C NMR experiments were undertaken that were fully assigned using a 2D HSQC NMR experiment. ESI mass spectrometry was then analyzed and showed the product peak.

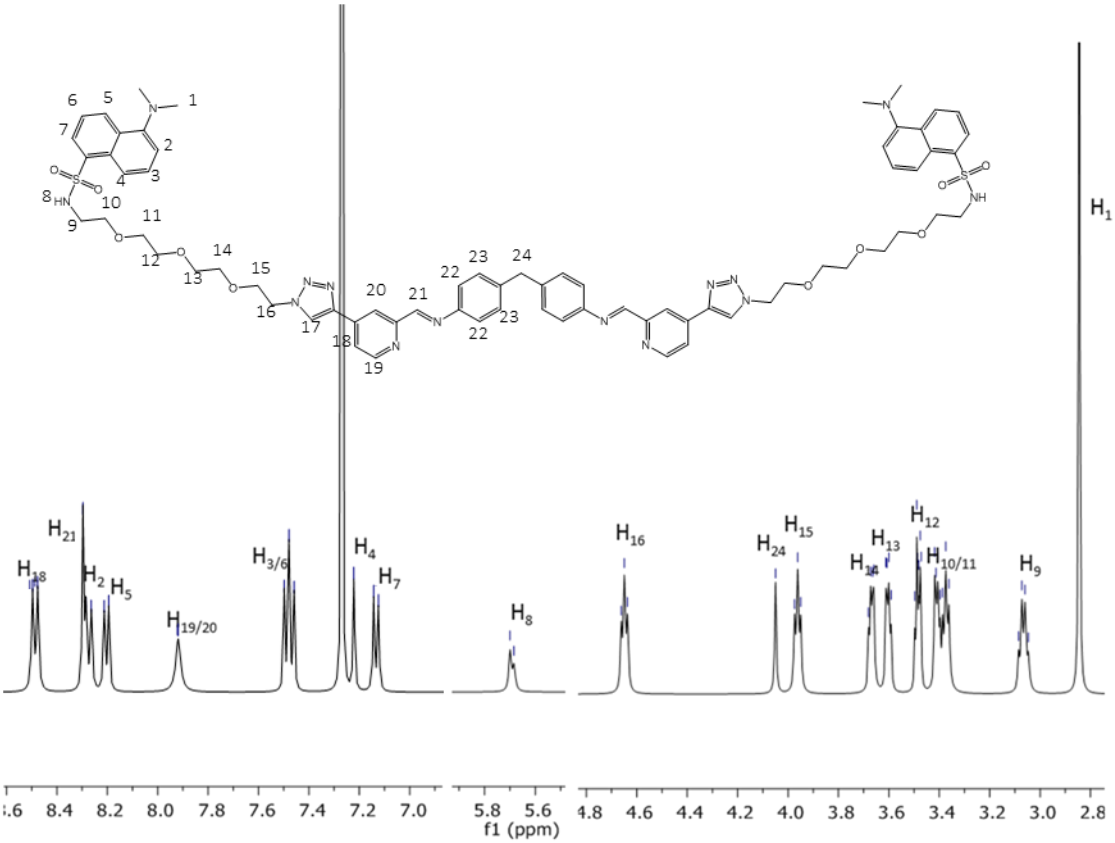

Figure 2.18 ^{1}H NMR (300 MHz, $CDCl_3$, 298 K) of L^{D4}

2.7.7 Synthesis of $[L^{D4}{}_3Fe_2][PF_6]$

The newly developed ligand, L^{D4}, was used to produce a triple stranded, dinuclear metallo iron complex. L^{D4} was reacted with iron(II)chloride in a 3:2 ratio following the same procedure described in Section 2.6.4. Upon addition of the iron(II) salt the solution turned bright purple. An excess methanolic solution of ammonium hexafluorophosphate was added, leading to precipitation of the complex, caused by counter ion exchange with the chloride. The solid was collected by filtration, washed with methanol to remove unreacted ligand, water to remove excess NH_3PF_6 and ether to dry the solid. The product was collected in a 72% yield and fully characterised using ^{1}H NMR and ESI mass spectrometry.

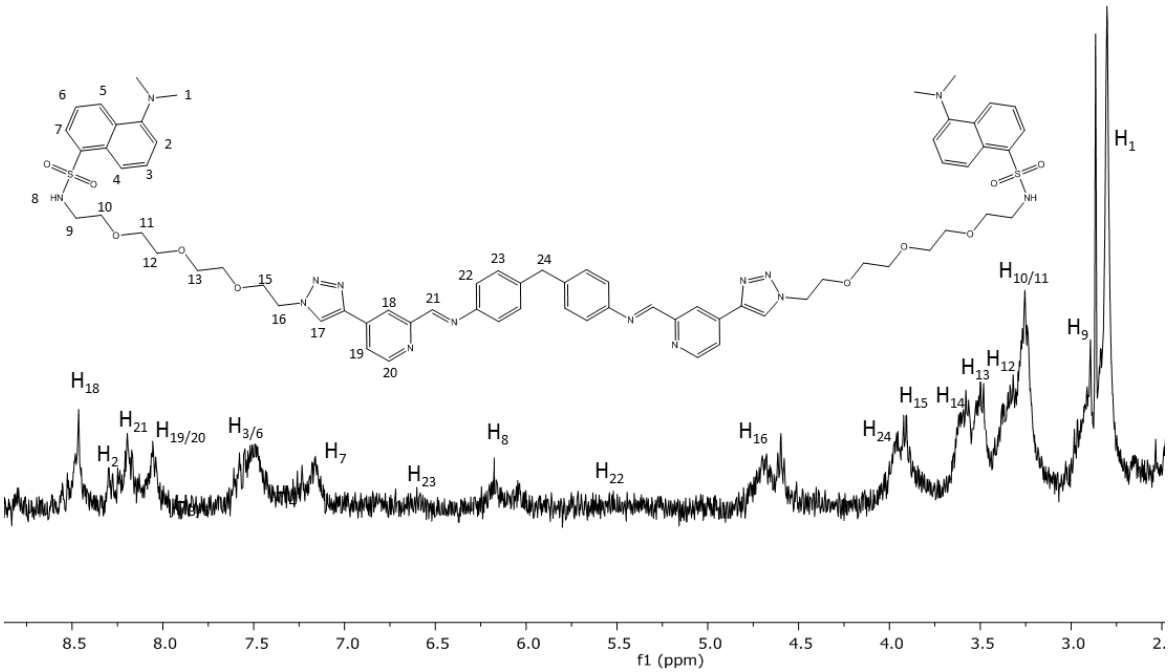

Figure 2.19 ^{1}H NMR (300 MHz, CD_3CN, 298 K) of $[L^{D4}{}_3Fe_2][PF_6]$.

2.8 Attempted synthesis of 5-azidopyridine-2-carbaldehyde.

Attempts to convert 5-bromopyridine-2-carbaldehyde to 5-azidopyridine-2-carbaldehyde were undertaken (Figure 2.20). This would potentially allow the metallo cylinder to react with a highly strained 8 membered ring copper-free click compound in *vivo* [18]. This could also lead to the cylinder being reacted with just one florescent group after cylinder formation, rather than having to functionalise the ligand prior to complex assembly. Another advantage of using copper free click chemistry, is the ease of purification, as there shouldn't be any unreacted starting material due to the high reactivity of the DBCO (dibenzocyclooctyl) ring.

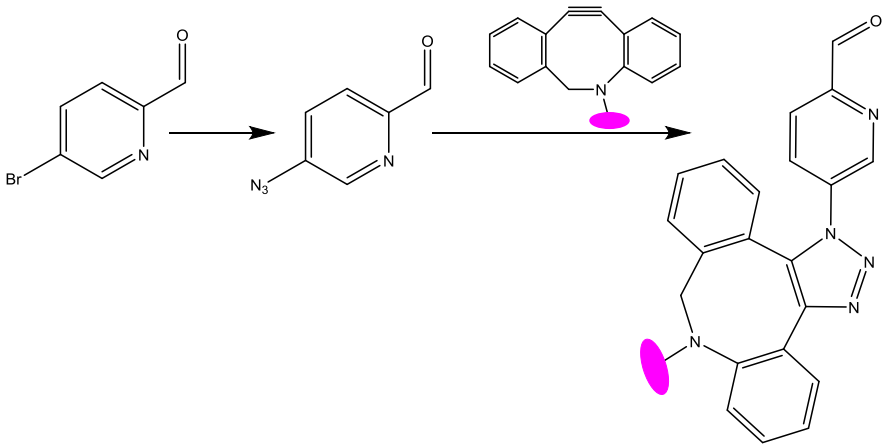

Figure 2.20 Conversion of the bromine group to an azide capable of undergoing copper free click reactions with DBCO modified fluorophores (depicted in pink).

5-Bromopyridine-2-carbaldehyde was stirred with sodium azide in water at 60˚C for 48 hours, followed by extraction into ethyl acetate. The solvent was removed in vacuo and the product analysed by ^{1}H NMR and ESI mass spectrometry. Both were consistent with unreacted 5-bromopyridine-2-carboxaldehyde, no product peaks were observed.

2.9 Attempted synthesis of $[L^{TB5}{}_3Ru_2][PF_6]_4$

Attempted to click onto an alkyne functionalized iron metallo-cylinder have been previously made, but proved unsuccessful, as the cylinder wasn't stable enough to undergo post cylinder-formation clicking. To overcome this, the synthesis of a ruthenium triple bond functionalised complex was undertaken, due to the increased stability of the ruthenium to nitrogen bond. 5-Ethynyl-2-formylpyridine was suspended in ethanol and a dropwise solution of 4,4′-methylenedianiline was added, producing a white precipitate. The solid was stirred for 18 hours at room temperature and collected by filtration. Washed with methanol to remove unreacted starting material then washed with ether to aid drying. The ligand L^{TB5}, was produced in an 84% yield and fully characterised using ^{1}H NMR, ^{13}C NMR and mass spectrometry. The ^{1}H NMR spectra confirms formation of the product by the presence of an imine peak and loss of the aldehyde peak from the starting material.

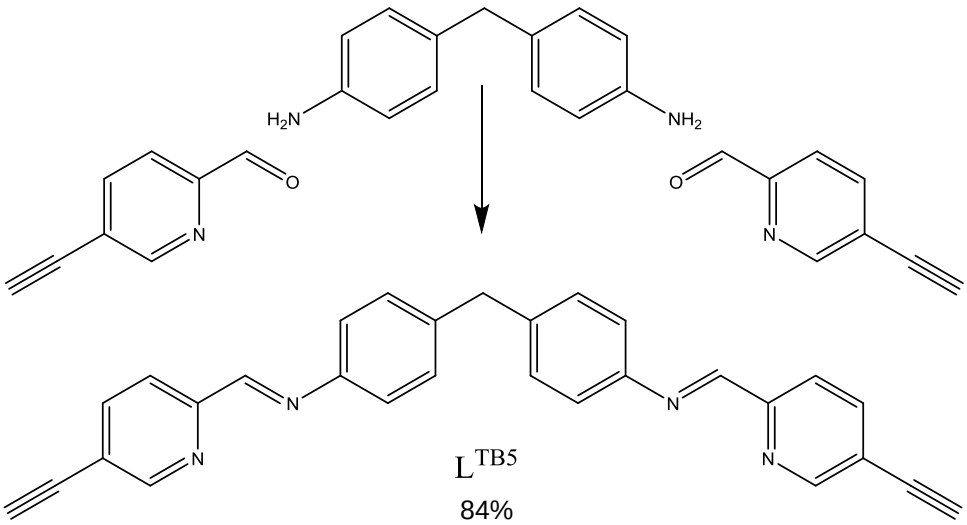

Scheme 2.15 Synthesis of ligand L^{TB5}

The ligand L^{TB5}, was suspended in ethylene glycol and heated to 200°C. $Ru(DMSO)_4Cl_2$ was added to the solution, upon its addition the solution turned a dark red colour. The reaction was heated at 200°C for 5 days. The reaction was cooled to room temperature, methanol was added and the solution was filtered to remove polymeric products. A solution of ammonium hexafluorophosphate was added to precipitate the product from the methanol, ethylene glycol mixture. The solid was collected and dissolved in acetonitrile. Numerous attempts to purify the product were undertaken, on silica, alumina and cellulose, with various eluents. Unfortunately no pure product could be obtained.

2.10 Attempted click reaction

A number of fluorophores have been successfully functionalised with azide groups to allow them to undergo click reactions with 5-ethynyl-2-formylpyridine and 4-ethynyl-2-formylpyridine (Figure 2.21). Numerous attempts to click Fluorescein isothiocyanate (FITC) have been undertaken, the solvent systems, catalysts and reaction times have all been altered but unfortunately no click products could be obtained.

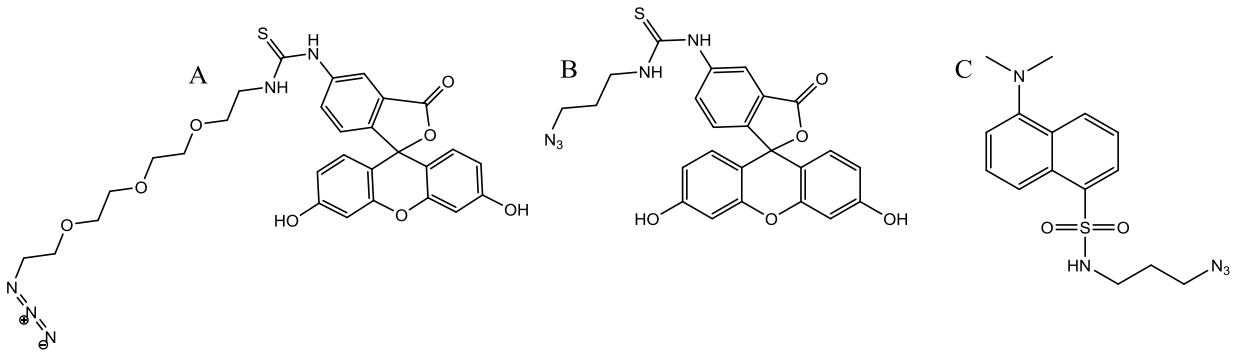

Figure 2.21 A. FITC-PEG3-azide, B. FITC-C3-azide and C. dansyl-C3-azide

Biotin azide has been synthesised, with the prospect of clicking it on to the alkyne functionalised pyridine ring. This will be turned into a ligand and subsequently a metallo cylinder complex. The addition of the biotin molecule will allow the complex to be located during cellular uptake by the use of a fluorescently tagged streptavidin molecule. Numerous attempts were made to click biotin-PEG-3 azide with 5-ethynyl-2-formylpyridine. The solvent system and catalyst were both changed, but no product was produced.

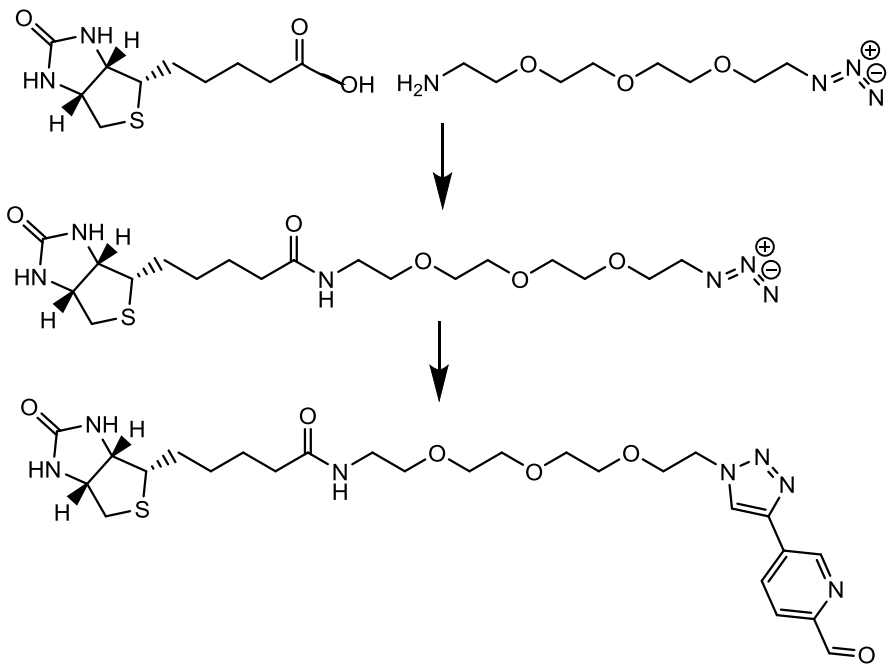

Figure 2.22 Biotin functionalised pyridyl ring

2.11 Stability studies

The stability of the complexes, was monitored in a mixture of solvents – acetonitrile to aid complex solubility's, and water – to mimic the aqueous cell environment. This was to examine how stable the complexes would be in an aqueous environment and how suitable they would be for cellular uptake studies.

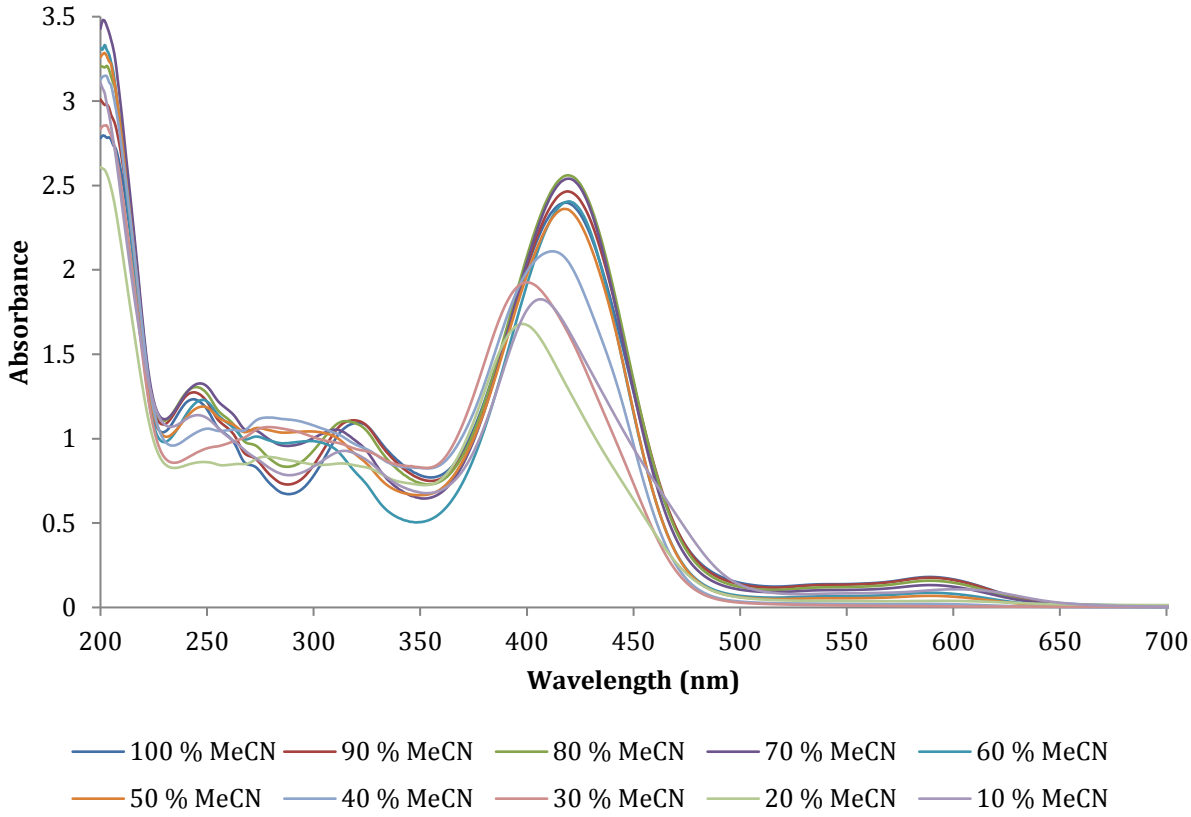

Figure 2.23 Stability of 100 µM $[L^{C5}{}_3Fe_2][PF_6]_4$ in acetonitrile/water in increasing gradient

This complex $[L^{C5}{}_3Fe_2][PF_6]_4$ degrades when water concentration is increased, this is also evident in Figure 2.31, where the complex has precipitated out of solution. This means the complex cannot be used for long treatments in aqueous environments, and any effects observed from the complex may be attributed to the ligand or the release of iron within the cell.

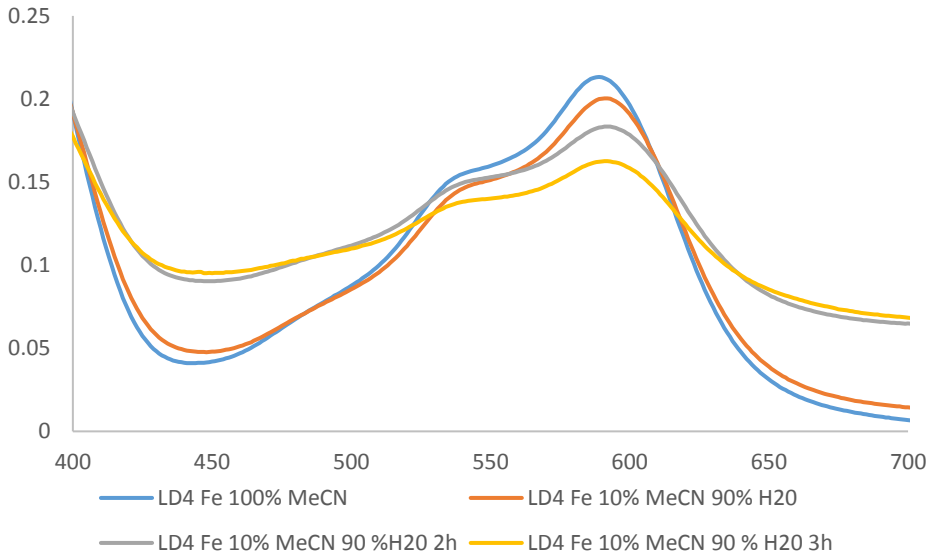

Figure 2.24 Stability of 10 µM $[L^{D4}{}_3Fe_2][PF_6]_4$ in acetonitrile or acetonitrile/water (1:9)

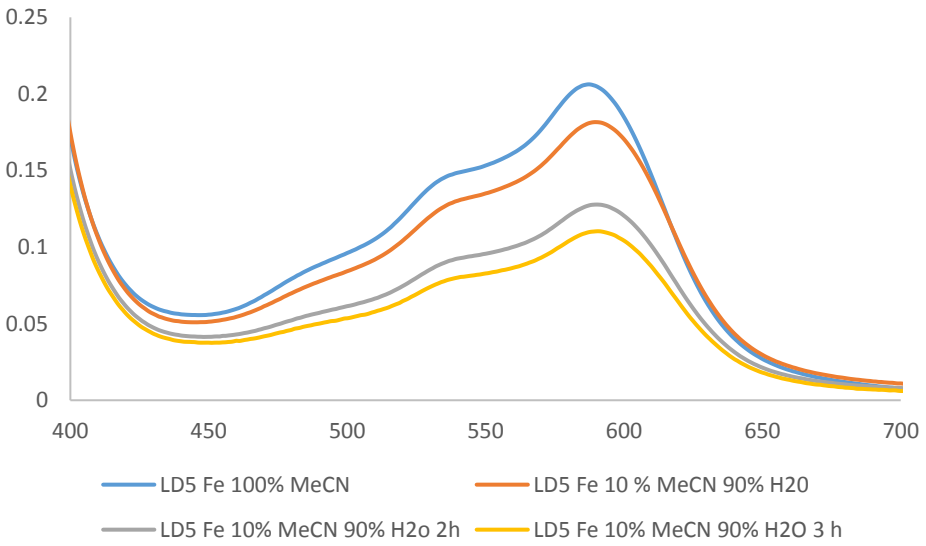

Figure 2.25 Stability of 10 µM $[L^{D5}{}_3Fe_2][PF_6]_4$ in acetonitrile or acetonitrile/water (1:9)

The stability of the dansyl iron complexes was examined be a similar method (Figure 2.25 and Figure 2.25). The complex was dissolved in acetonitrile and its UV-vis spectrum was compared to the sample dissolved in 10% MeCN and water. It can be seen that $[L^{D4}{}_3Fe_2][PF_6]_4$ has greater stability, this may be attributed to the increased distance between the fluorescent groups at the ends of the cylinder, reducing any steric hindrance and repulsion effects experienced by three fluorescent groups held in close proximity.

2.12 Fluorimeter studies

Fluorescence studies have been conducted to examine if the iron based complexes are fluorescent after complex formation. The complexes were dissolved in acetonitrile and their excitation and emission spectra are shown below. Upon complex formation it can be observed that all four complex still exhibit an emission peak.

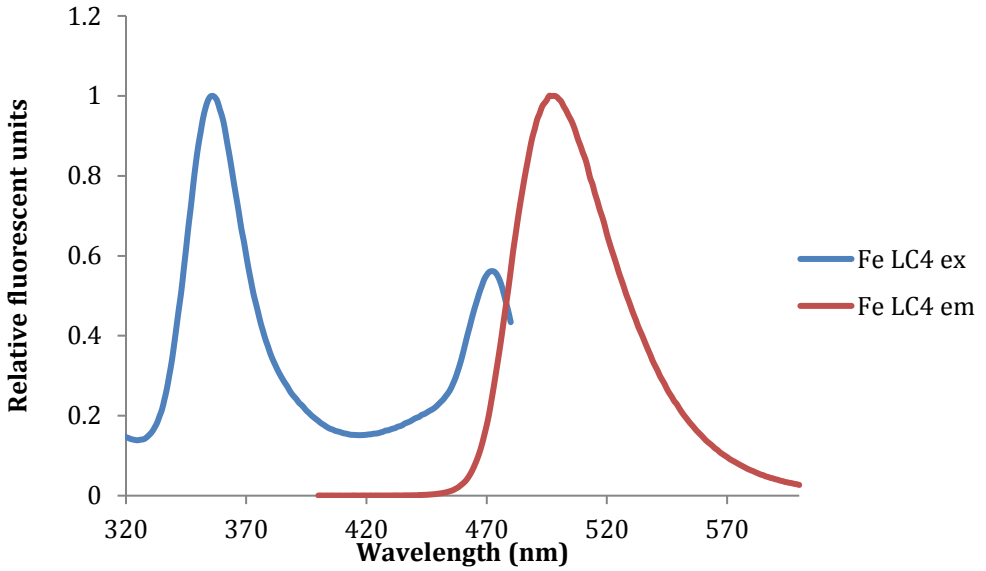

Figure 2.26 Normalized emission and excitation spectrum of $[L^{C4}{}_3Fe_2][PF_6]_4$ in acetonitrile.

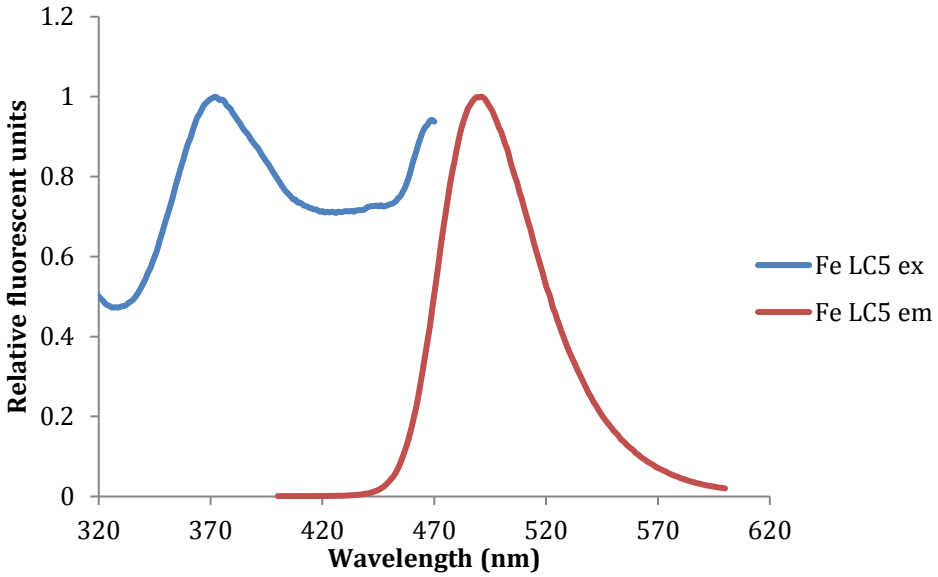

Figure 2.27 Normalized emission and excitation spectrum of $[L^{C5}{}_3Fe_2][PF_6]_4$ in acetonitrile.

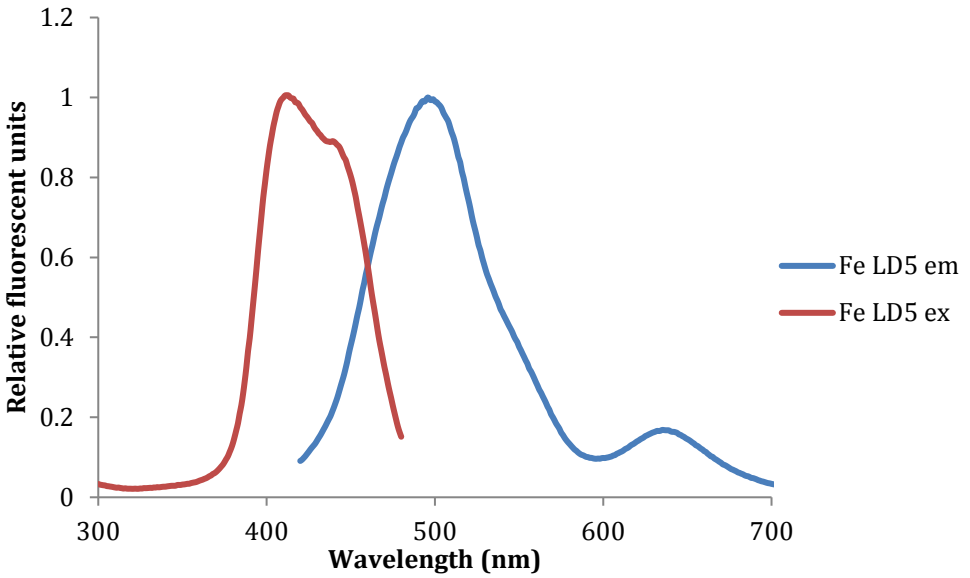

Figure 2.28 Normalized emission and excitation spectrum of $[L^{D5}{}_3Fe_2][PF_6]_4$ in acetonitrile.

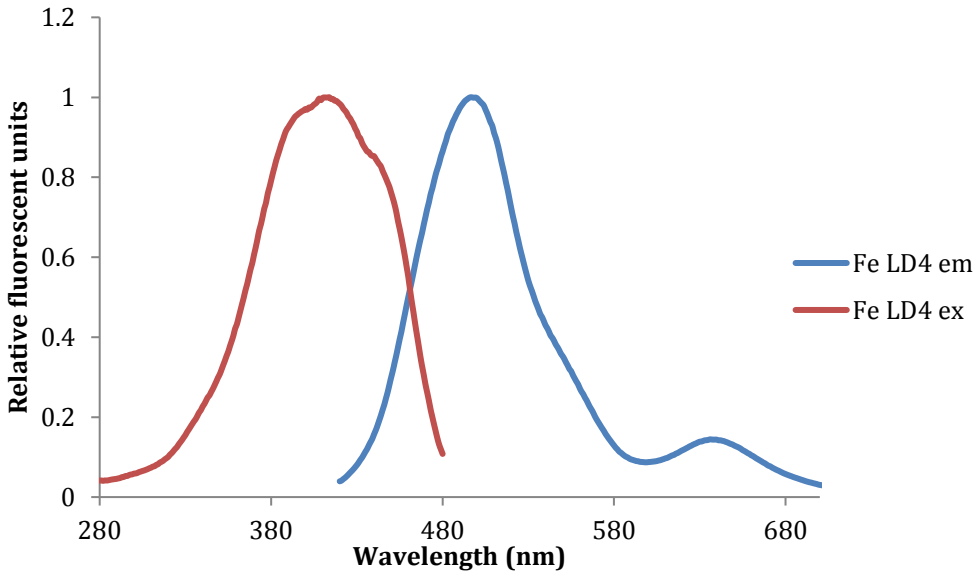

Figure 2.29 Normalized emission and excitation spectrum of $[L^{D4}{}_3Fe_2][PF_6]_4$ in acetonitrile.

2.13 Imaging

Imaging experiments were undertaken using the coumarin functionalised iron cylinder $[L^{C5}{}_3Fe_2][PF_6]_4$, to examine if the compound could be visualised using fluorescence microscopy (Figure 2.32). MDA-231 cells were seeded into MatTek dishes, at a density of 300,000 cells per dish, and left to adhere for 24 hours. The media was removed, cells were washed with PBS and clear imaging media was added. The MatTek dish was placed on the heated stage of the Nikon A1R Inverted Confocal/TIRF microscope and the cells were focused. An image was taken of the cells before treatment to examine their morphology

and check they had an elongated natural shape before treatment and they were still adhered to the MatTek dish. The compound was added directly to the MatTek dish and time course imaging was under taken, with an image being taken every minute, for 20 minutes (Figure 2.32). An increase in fluorescence in the blue channel was observed, this is from the coumarin moiety on the complex. It it believed that the complex enters cells and is then degraded. With the increase in fluorescence being attributed to the breakdown of the complex, leaving the free ligand being imaged. This is reminiscent of the work by Chen *et al*. discussed in chapter 1; where polypyridyl iron complexes were thought to be fluorescent[19], but as observed in other studies, these complexes have no emission profile[20]. It is assumed the fluorescence in their imaging studies is also caused by compound degradation, and it is in fact free ligand being imaged.

The imaging experiment was repeated and cells were also stained with draq 5, (red nuclear stain), to examine if the complex enters the nucleus (Figure 2.30). After 20 minutes, it was observed that the degraded complex remains located in the cytoplasm, with no co-localisation observed between coumarin and draq 5.

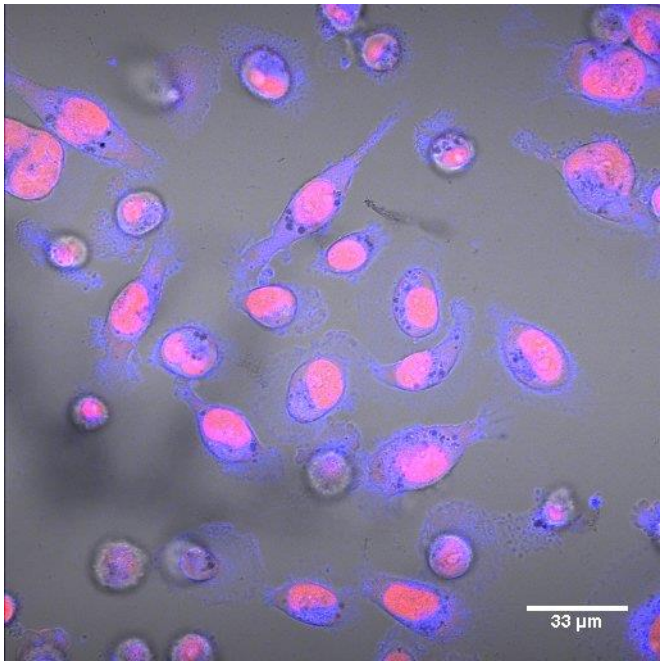

Figure 2.30 MDA-231 cells treated with 100 µM $[L^{C5}{}_3Fe_2][PF_6]_4$ with 3% MeCN in clear imaging media, over 20 minutes with the nucleus stained with draq 5.

The degradation of the complex is further confirmed by precipitation of the complex in the MatTek dish at the end if the experiment as shown in Figure 2.31.

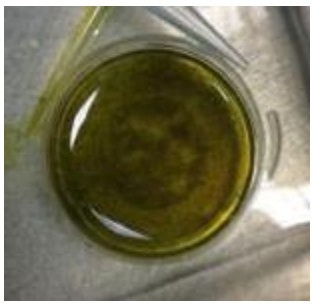

Figure 2.31 MatTek dish containing MDA-231 cells after treatment with 100 µM $[L^{C5}{}_3Fe_2][PF_6]_4$ with 3% MeCN in clear imaging media, over 20 minutes.

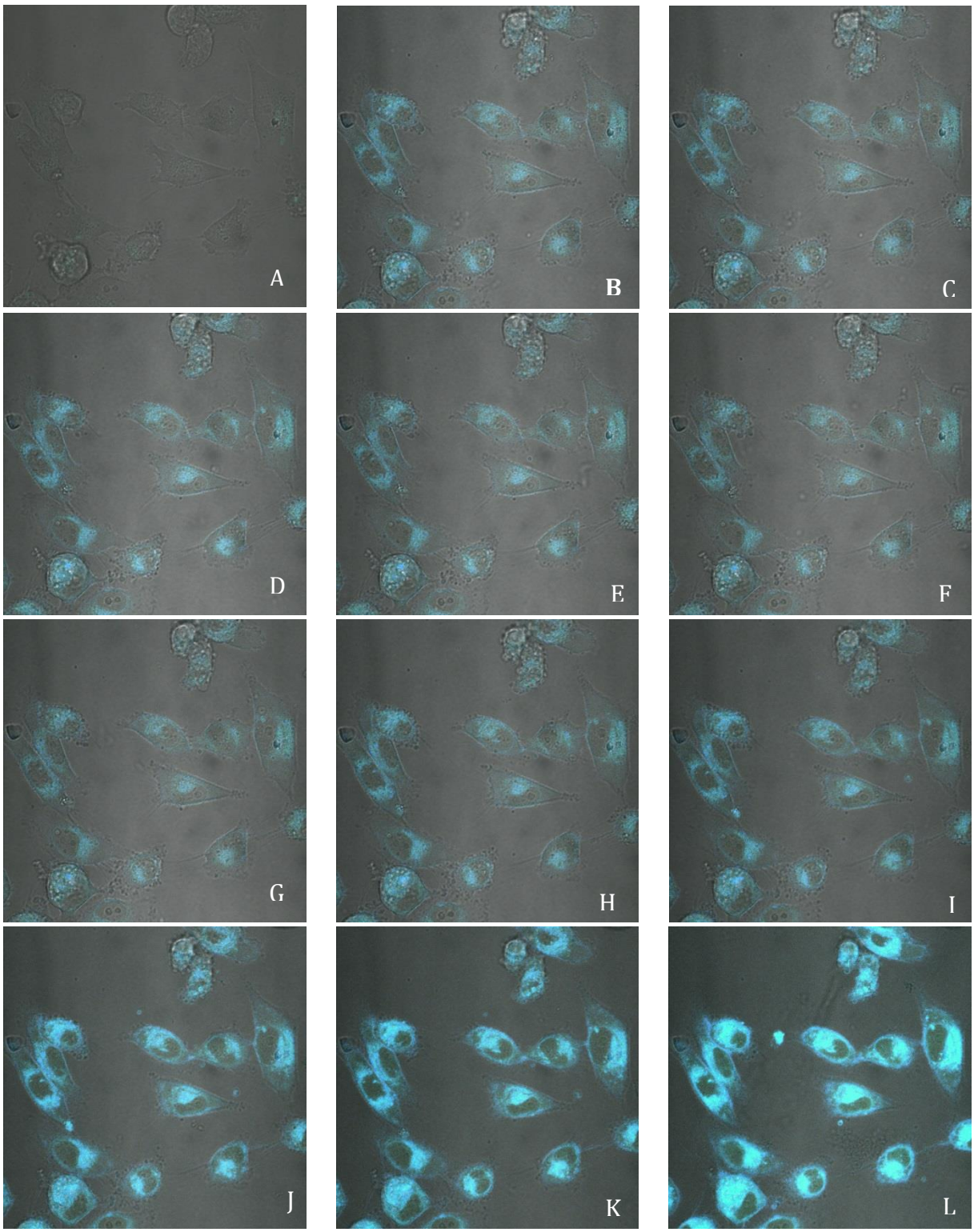

Figure 2.32 MDA-231 cells treated with 100 μM $[L^{C5}{}_3Fe_2][PF_6]_4$ with 3% MeCN in clear imaging media, over 20 minutes. A 0 min, B 1 min, C 2 min, D 3 min, E 4 min, F 5 min, G 6 min, H 7 min, I 8 min, J 11 min, K 15 min, L 20 min

2.14 Conclusions and future work

In conclusion four novel fluorophore functionalised ligands have been created and characterised. L^{C5}, L^{C4}, L^{D5} and L^{D5} (Figure 2.33).

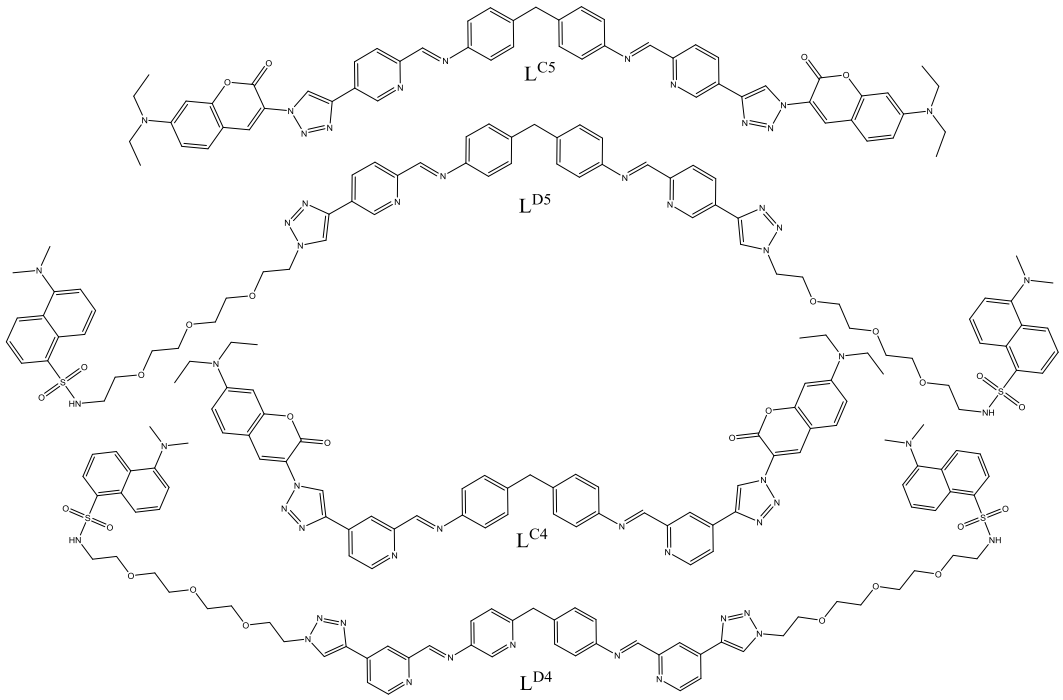

Figure 2.33 Structure of L^{C5}, L^{C4}, L^{D5} and L^{D5}

These ligands have been successfully used to form iron based metallo-cylinder complexes, $[L^{C5}{}_3Fe_2][PF_6]_4$, $[L^{D5}{}_3Fe_2][PF_6]_4$, $[L^{C4}{}_3Fe_2][PF_6]_4$ and $[L^{D4}{}_3Fe_2][PF_6]_4$. There stability has been examined in aqueous solution using UV-vis experiments and their fluorescence has been examined with fluorimeter studies. The complexes are not stable over long periods of time when in aqueous solution. Fluorescence confocal imaging was undertaken using $[L^{C5}{}_3Fe_2][PF_6]_4$ in MDA-231 cell, however the observed fluorescence is attributed to degradation of the complex, with the released ligands fluorescence being observed.

In future work stability studies would be undertaken for longer period of time, along with NMR experiments to examine complex degradation over time in aqueous solution. CD binding studies would be under taken to explore the binding properties of all complexes. Imaging studies using dansyl functionalised complex would be undertaken to explore if

complexes fluorescence can be observed using fluorescence confocal microcopy. Fluorimeter experiments would be undertaken following the addition of water to see if the fluorescence signal increase upon degradation of the complex, as observed in fluorescence microcopy. Further attempts to click biotin and FITC on to the cylinder ligand would be attempted.

2.15 References

[1] M. J. Hannon, C. L. Painting, A. Jackson, J. Hamblin, W. Errington, *Chem. Commun.* **1997**, 1807–1808.

[2] C. Ducani, A. Leczkowska, N. J. Hodges, M. J. Hannon, *Angew. Chemie - Int. Ed.* **2010**, *49*, 8942–8945.

[3] A. Oleksi, A. G. Blanco, R. Boer, I. Usón, J. Aymamí, A. Rodger, M. J. Hannon, M. Coll, *Angew. Chemie - Int. Ed.* **2006**, *45*, 1227–1231.

[4] S. Phongtongpasuk, S. Paulus, J. Schnabl, R. K. O. Sigel, B. Spingler, M. J. Hannon, E. Freisinger, *Angew. Chemie - Int. Ed.* **2013**, *52*, 11513–11516.

[5] A. C. G. Hotze, N. J. Hodges, R. E. Hayden, C. Sanchez-Cano, C. Paines, N. Male, M. K. Tse, C. M. Bunce, J. K. Chipman, M. J. Hannon, *Chem. Biol.* **2008**, *15*, 1258–1267.

[6] G. I. Pascu, A. C. G. Hotze, C. Sanchez-Cano, B. M. Kariuki, M. J. Hannon, *Angew. Chemie* **2007**, *119*, 4452–4456.

[7] J. A. Norman, Functionalised Iron(II) Supramolecular Helicates: Design, Synthesis and DNA Binding Studies, University of Birmingham, **2012**.

[8] J. C. Peberdy, J. Malina, S. Khalid, M. J. Hannon, A. Rodger, *J. Inorg. Biochem.* **2007**, *101*, 1937–1945.

[9] K. Sonogashira, in *Handb. Organopalladium Chem. Org. Synth.*, John Wiley & Sons, Inc., **2003**, pp. 493–529.

[10] L. Yin, J. Liebscher, *Chem. Rev.* **2007**, *107*, 133–173.

[11] S. L. Presolski, V. P. Hong, M. G. Finn, *Curr. Protoc. Chem. Biol.* **2011**, *3*, 153–162.

[12] J. C. Jewetta, C. R. Bertozzi, *Chem Soc Rev* **2010**, *39*, 1272–1279.

[13] F. Amblard, J. H. Cho, R. F. Schinazi, *Chem Rev* **2009**, *109*, 4207–4220.

[14] L. Jin, D. R. Tolentino, M. Melaimi, G. Bertrand, *Sci. Adv.* **2015**, 1–5.

[15] K. Sivakumar, F. Xie, B. M. Cash, S. Long, H. N. Barnhill, Q. Wang, *Org. Lett.* **2004**, *6*, 4603–4606.

[16] C. Rajadurai, A. Ivanova, V. Enkelmann, M. Baumgarten, *J. Org. Chem.* **2003**, *68*, 9907–9915.

[17] H. Egami, S. Kamisuki, K. Dodo, M. Asanuma, Y. Hamashima, M. Sodeoka, *Org. {&} Biomol. Chem.* **2011**, *2*, 7667–7670.

[18] J. M. Baskin, J. A. Prescher, S. T. Laughlin, N. J. Agard, P. V. Chang, I. A. Miller, A. Lo, J. A. Codelli, C. R. Bertozzi, *Proc. Natl. Acad. Sci. U. S. A.* **2007**, *104*, 16793–7.

[19] J. Chen, Z. Luo, Z. Zhao, L. Xie, W. Zheng, T. Chen, *Biomaterials* **2015**, *71*, 168–177.

[20] Johanna, "Comparing Tris-2,2'-bipyridine Complexes of Iron (II) and Ruthenium (II) through Spectroscopy and Electrochemistry," **.**

Chapter 3

3 Imidazolimine cylinders

3.1 Introduction

The parent ligand system (discussed in chapters 1 and 2) has been modified by swapping the pyridylimine system to an imidazolimine system (Figure 3.1). The addition of the NH groups on the ligand scaffold will allow functional groups to be added to the structure by utilising a simple condensation reaction. 4,4′-Methylenedianiline is used as the spacer in both ligand systems, meaning the distance between the binding sites in kept constant. The modification from pyridyl to imidazole rings causes little difference in the width and diameter of the triple stranded dinuclear complexes formed upon reaction of the ligands with metal(II) salts. As such they should both bind in a similar manner to DNA, with the ability to bind in the Major grove of B-DNA and DNA and RNA three-way junction.

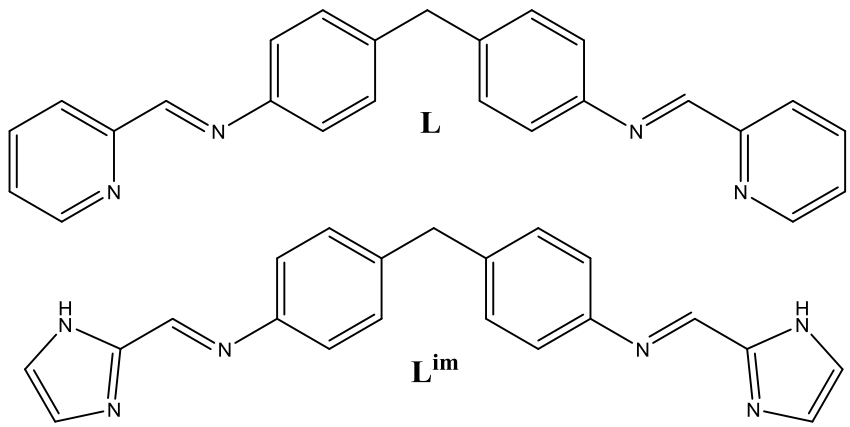

Figure 3.1 Pyridylimine parent ligand L and imidazoleimine parent ligand L^{im}

The modified ligand is synthesized by the same simple condensation reaction in methanol at room temperature, with two drops of glacial acetic acid as catalyst (Figure 3.2). Upon reaction with an iron(II) or nickel(II) salt; a dinuclear, triple stranded, tetra cationic complex is formed (Figure 3.2, right).

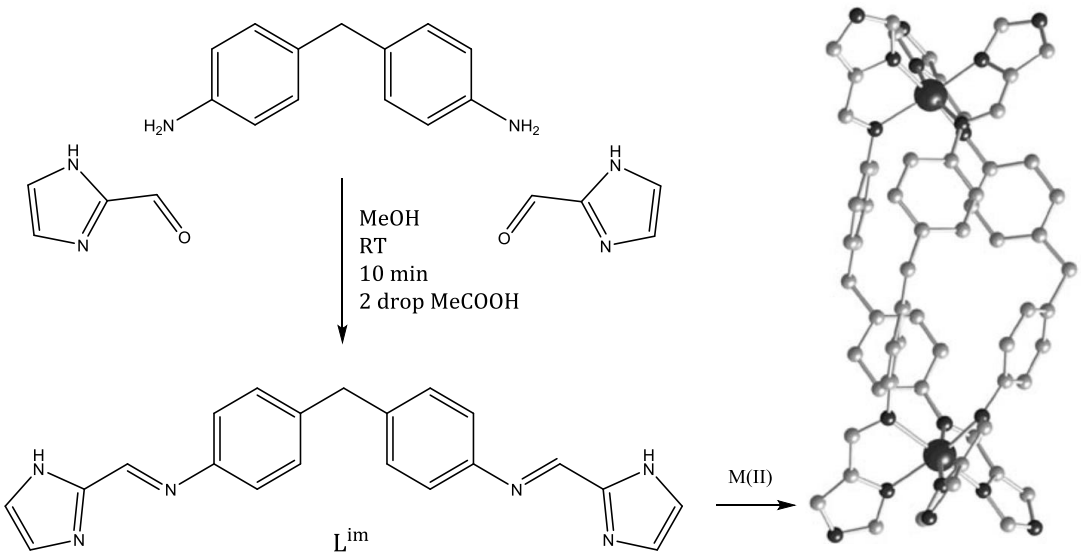

Figure 3.2 Synthesis of the parent imidazole ligand (L^{im}) and formation of a dinuclear, triple stranded, tetra cationic complex $[M_2\ ^{im}{}_3]^{4+}$ [1]

The bisimidazolimine ligands have additional hydrogen donor groups (NH), these are located at the exterior of the complex structure and engage in hydrogen bonding with anions and solvent molecules [1]. The most striking difference between the imidazole and pyridyl based systems is the spin-crossover property exhibited in the imidazole complexes.

Spin-crossover is observed in d^4, d^5, d^6 and d^7 metal ions, two different electron configurations are possible in the octahedral ligand field, high spin and low spin. Changes between the spin states can be caused by temperature, pressure, light irradiation or influence of a magnetic field. The iron(II) metal center of the imidazolimine complex is d^6 therefore both high spin and low spin states are possible (Figure 3.3).

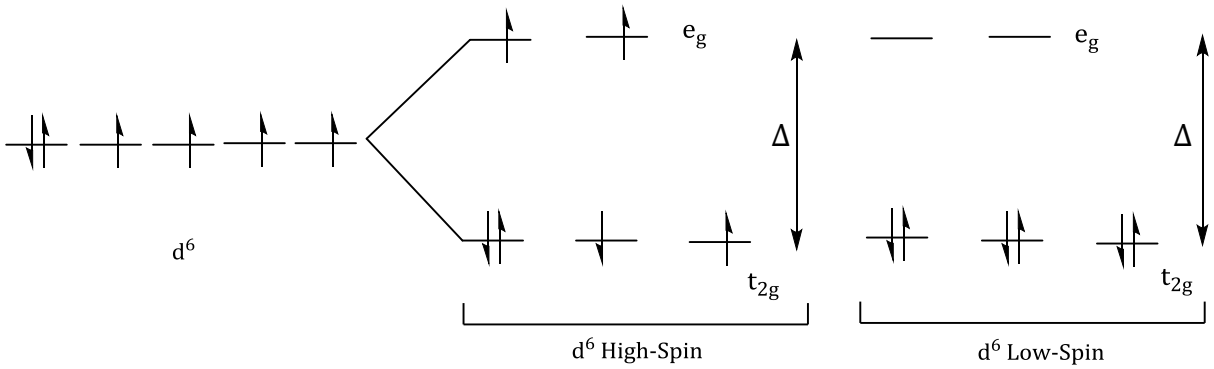

Figure 3.3 Crystal field splitting of a d^6 electron configuration into high-spin and low-spin states.

The overlay of the pyridyl (black) and imidazole (white) nickel(II) complex structures shows that their structures are very similar (Figure 3.4)[1]. d^8 Nickel(II) complexes do not exhibit spin-crossover, eliminating the effects of spin transitions on the structure. The replacement of the six membered pyridyl ring to the five membered imidazole ring causes slight differences at the ends of the cylinder, due to the change in size of the rings[1]. However, this does not have a dramatic effect on the length or diameter of the nickel(II) complexes[1]. As there is very little change in the length and diameter of the complex and the charge is the same as the pyridylimine based iron and nickel systems, it is hypothesized that the complexes will bind in a similar fashion, residing in the major groove of DNA[2] and DNA[3] / RNA[4] three way junctions.

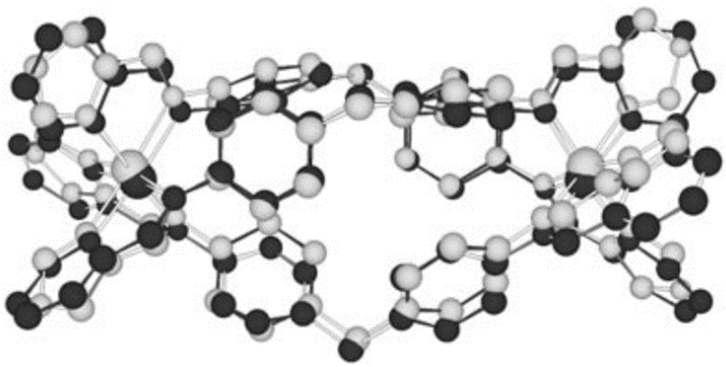

Figure 3.4 Overlay of the structures of the pyridylimine Ni(II) (black)[5] and the imidazolimine Ni(II) complex (white)[1].

3.2 Molecular design

Azide and alkyne containing chains with be grafted on to the imidazole ring *via* their NH component. This will be achieved by a condensation reaction. This would allow a copper catalyzed click reaction to be utilized to add a fluorescent organic dye to the imidazole ligand (Figure 3.5). Incorporation of an azide chain will allows copper free click reactions to be undertake, using a highly strain triple bond in an eight membered ring. This would give the potential for the complex to bind to DNA and be tagged with a biotin molecule or fluorophore after binding.

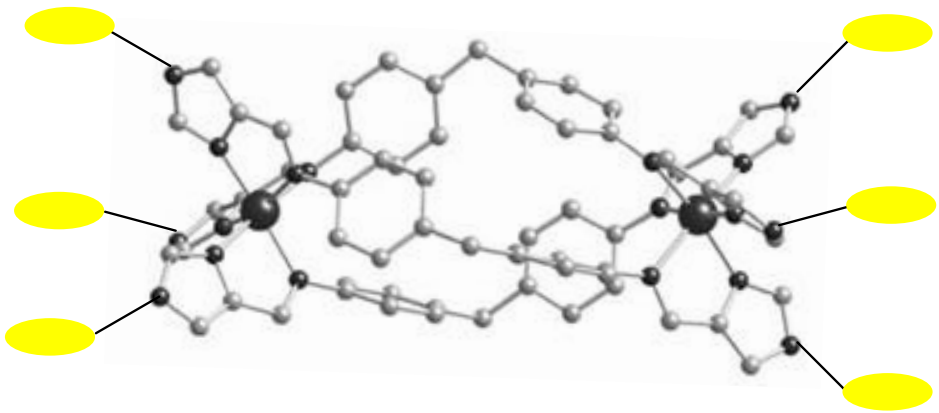

Figure 3.5 Addition of fluorophore/biotion molecules to the NH position of the imidazole rings.

3.3 Synthesis of azide functionalised ligands and complexes

The development of an azide functionalised ligand will allow fluorescent groups to be click onto the ligand, using cooper catalysed click chemistry or copper free click chemistry. It is hoped that the short carbon chain will allow larger fluorophores to be 'clicked' to the imidazole complex. It is anticipated that the increased distance from the ligand will not impeded cylinder formation and reduce any steric hindered caused between the close proximity of bulky fluorophore or biotin moieties.

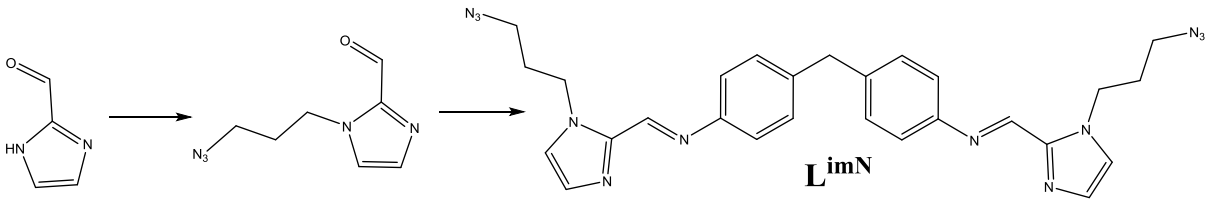

Figure 3.6 Synthesis of ligand L^{imN}

3.3.1 Synthesis of azide imidazole

The three carbon chain linker was synthesized in a two-step reaction, Scheme 3.1. Firstly 3-chloropropan-1-ol was heated to reflux was sodium azide and potassium iodide in water for 24 hours. The reaction was cooled and extracted with diethyl ether and the organic fraction dried over sodium sulphate. The solution was carefully concentrated under reduced pressure to afford the produce as a yellow oil in an 82% yield. The compound was fully characterised by ^{1}H NMR and ^{13}C NMR and MS.

3-Azidopropan-1-ol was then converted to 3-azidopropyl methanesulphonate. The starting material was dissolved in tetrahydrofuran and triethylamine and the solution cooled to 0°C. Mesyl chloride was added dropwise to the reaction mixture and the solution was warmed to room temperature and stirred for three hours. Dichloromethane and a saturated sodium bicarbonate solution were added to the reaction mixture; the organic layer was separated, washed, dried and concentrated to afford 3-azidopropyl methanesulphonate as a colourless oil in an 76% yield; which was fully characterised by ^{1}H NMR and ^{13}C NMR and MS.

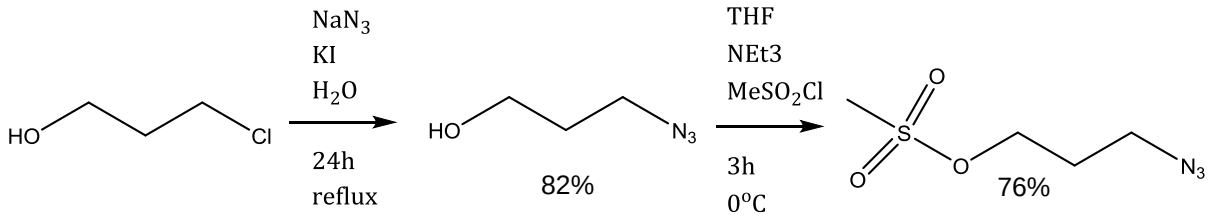

Scheme 3.1 Two-step synthesis of the short azido functionalised chain linker 3-azidopropyl methanesulfonate

Imidazole-2-carboxaldehyde and potassium carbonate were dissolved in anhydrous DMF, Scheme 3.2. 3-Azidopropyl methanesulphonate was added dropwise to the stirred solution and the reaction was stirred at room temperature under an argon atmosphere for 18 h. The suspension was filtered to remove the potassium carbonate and the filtrate diluted with water. The solution was extracted with diethyl ether and the organic layer was separated, dried and concentrated to afford 1-(3-azidopropyl1H-imidazole-2-carbaldehyde) as a yellow oil in an 67% yield. The compound was fully characterized by by ^{1}H and ^{13}C NMR and MS. The ^{1}H NMR is shown in Figure 3.7 and shows loss of the NH imidazole peak, indicating product formation has been successful. The proton peaks also integrate correctly for each proton environment.

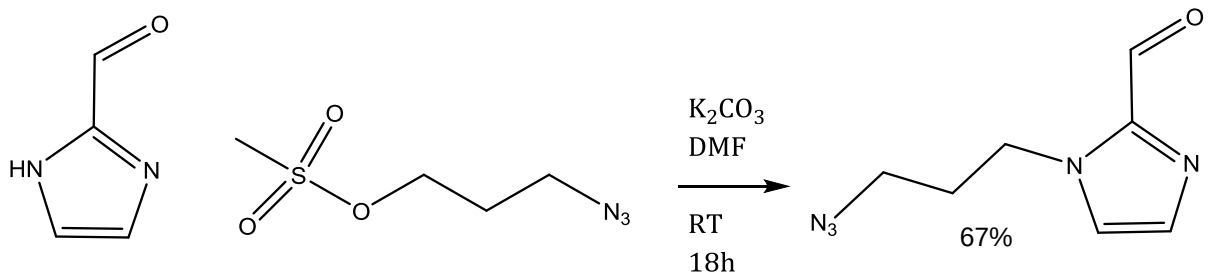

Scheme 3.2 Systhesis of 1-(3-azidopropyl)-1H-imidazole-2-carbaldehyde.

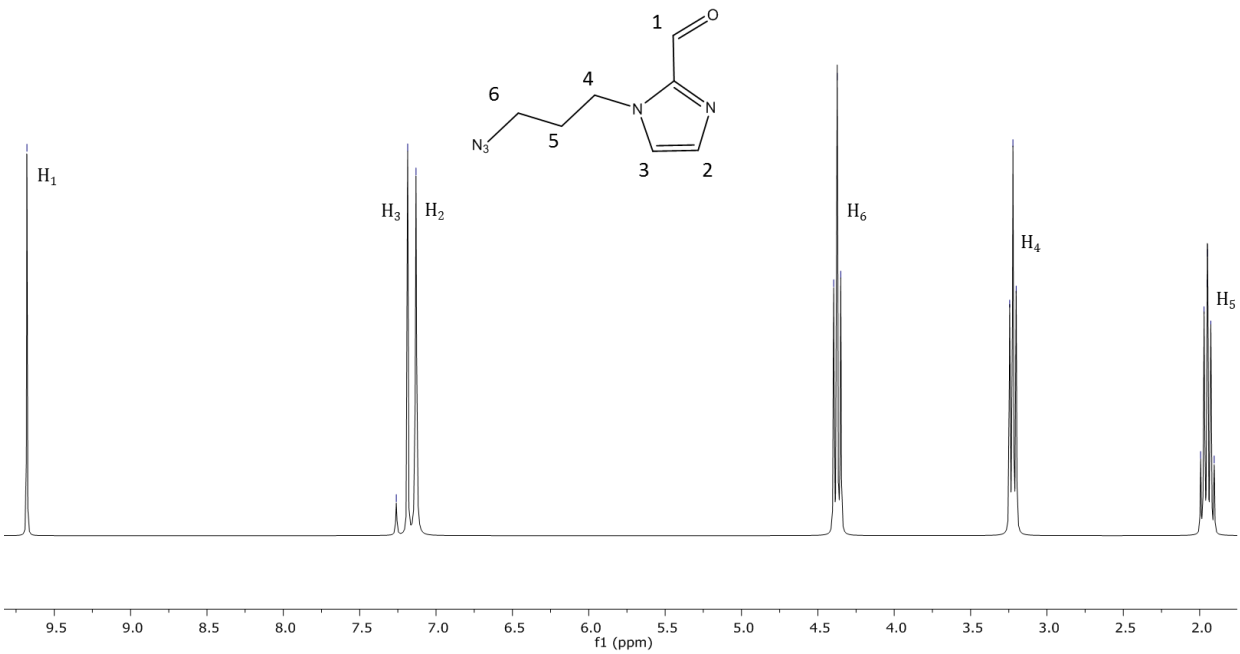

Figure 3.7 ^{1}H NMR (300 MHz, $CDCl_3$, 298 K) of 1-(3-azidopropyl)-1H-imidazole-2-carbaldehyde.

3.3.2 Synthesis of azide functionalised imidazole ligand L^{imN}

The newly synthesised azide functionalised imidazole group was then incorporated into the full ligand, L^{imTB}, which will allow formation of the metallo cylinder. The azide functionalised imidazole ligand (L^{imTB}) was successfully synthesized *via* a condensation reaction. 1-(3-Azidopropyl)-1H-imidazole-2-carbaldehyde was dissolved in ethanol, and 4,4′-methylenedianiline was dissolved in ethanol and added dropwise to the stirred solution. The reaction was stirred for 18 hours at room temperature. The white precipitate was collected by filtration, washed and dried to afford Ligand L^{imN} in a 64% yield, Scheme 3.3.

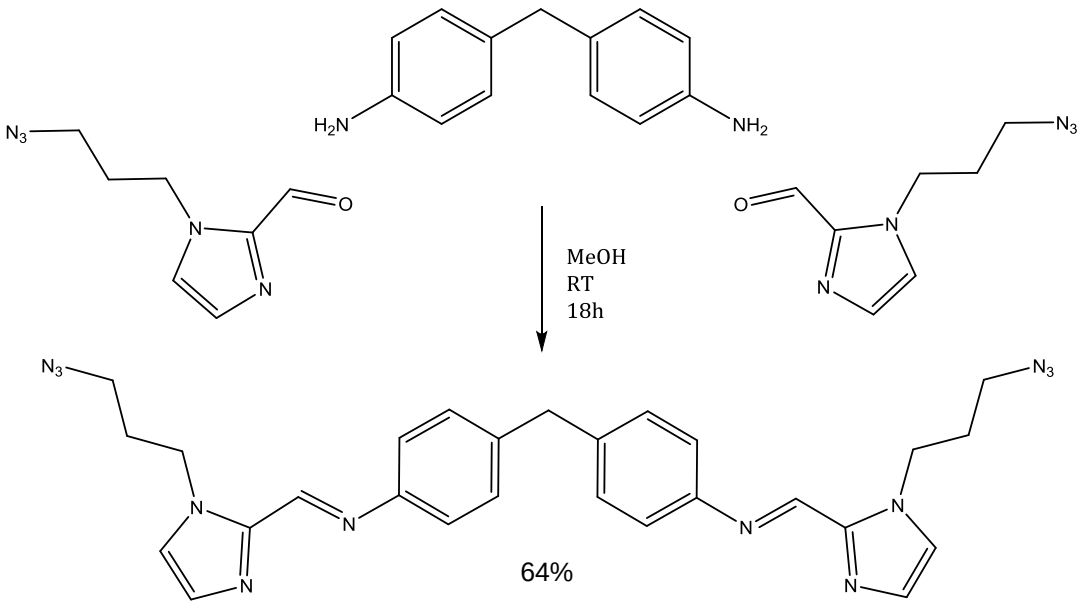

Scheme 3.3 Synthesis of the azide functionalised imadazole ligand L^{imN}, through the reaction of 1-(3-azidopropyl)-1H-imidazole-2-carbaldehyde and 4,4′-methylenedianiline.

The ligand was fully characterised and the ^{1}H NMR spectra is shown in Figure 3.8. The loss of the aldehyde peak from the starting material and the formation of the imine bond, (H_4 Peak at 8.55ppm) confirm the formation of the product. The bridge protons of the spacer are clearly visible (H_1 4ppm) and the azide chain is intact (H_9, H_7 and H_8)

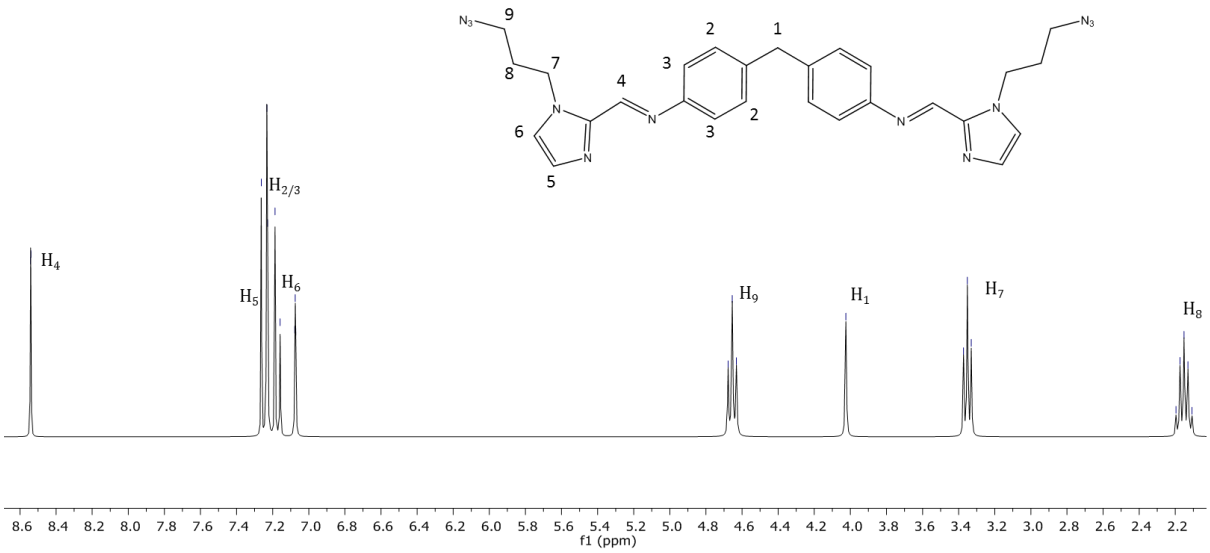

Figure 3.8 ^{1}H NMR (300 MHz, $CDCl_3$, 298 K) of the azide functionalised imidazole ligand L^{imN}.

3.3.3 Synthesis of $[L^{imN}{}_3Fe_2][\ PF_6]_4$

The newly synthesised azide functionalised ligand, L^{imN} was used to develop an iron based triple stranded, dinuclear metal complex. The alkyne functionalised ligand L^{imN} was suspended in methanol, a methanolic solution of iron(II) chloride was added dropwise to the stirred solution. Upon addition of the metal salt the solution turned a deep wine red colour (Figure 3.9), showing formation of the metal complex. This colour is characteristic of iron imidazole cylinders, due to the MLCT band observed at 550nm. The complex was precipitated from solution by the addition of ammonium hexafluorophosphate, collected, washed and dried to afford the product. The complex exhibits spin-cross over and is paramagnetic. Due to this property the complex was characterized using long range paramagnetic ^{1}H NMR and MS. Formation of the product is confirmed by the $(M)^{4+}$ at 418.02 (Figure 3.10), observed in the mass spectrum, showing the presence of a multi charge species.

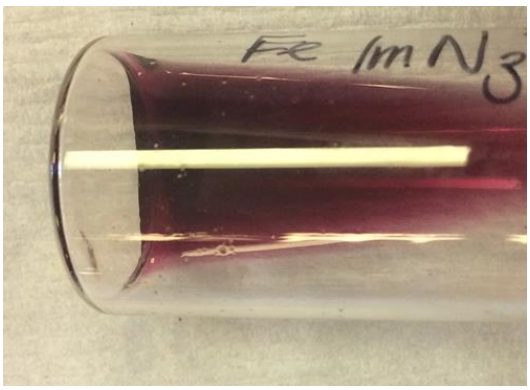

Figure 3.9 Deep wine red solution of $[L^{imN_3}Fe_2][PF_6]_4$ in acetonitrile.

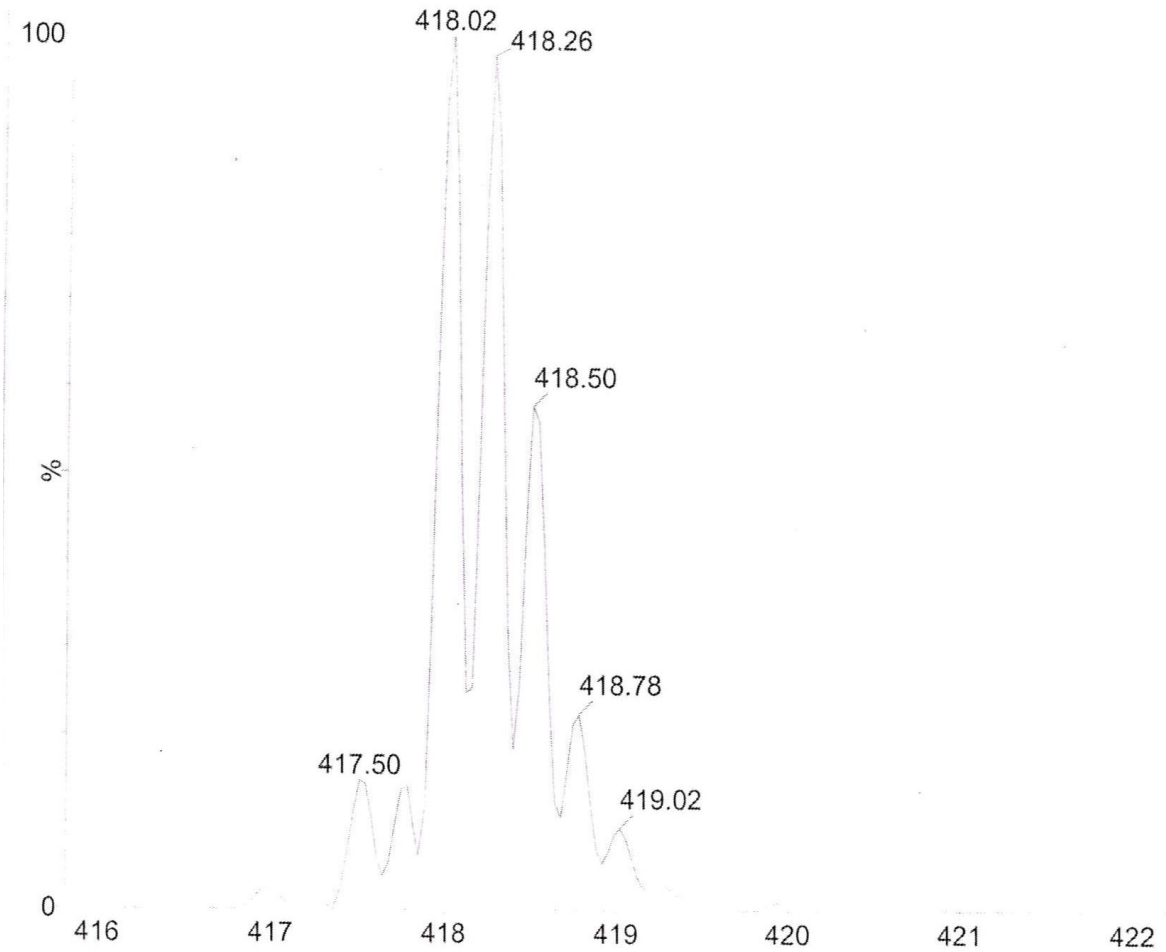

Figure 3.10 Mass Spectra of $[L^{imN_3}Fe_2][PF_6]_4$, showing the $(M)^{4+}$ complex peak at 418.02.

3.3.4 Synthesis of $[L^{imN_3}Ni_2][PF_6]_4$

The Ligand, L^{imTB} was also used to from a triple stranded nickel based metallo cylinder. L^{imTB} was suspended in methanol and a solution of nickel(II) chloride was added. Upon

addition of the nickel slat the solution turned orange. The complex was precipitated from solution by the addition of ammonium hexafluorophosphate. The solid was collected and characterized using mass spectrometry. Formation of the product is confirmed by the $(M)^{4+}$ at observed 419.80 in the mass spectrum.

3.4 Synthesis of alkyne functionalised ligands and complexes

The development of an alkyne functionalised ligand will allow fluorescent groups to be clicked onto the ligand

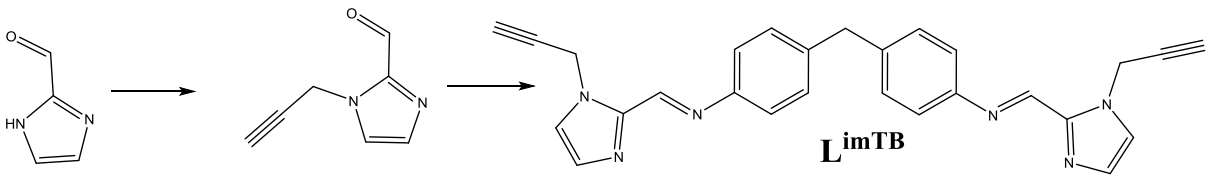

Figure 3.11 Synthesis of ligand L^{imTB}

3.4.1 Synthesis of alkyne imidazole

Imidazole-2-carboxaldehyde and potassium carbonate were suspended in anhydrous DMF. Propargyl bromide (80% w.v in toluene stabilised with MgO) was added dropwise to the stirred solution and the reaction mixture was stirred for 18 hours at room temperature under an atmosphere of argon. The suspension was filtered to remove potassium carbonate and the filtrate diluted with water. The solution was extracted with diethyl ether, dried and concentrated to afford 1-(prop-2-yn-1-yl)-1H-imidazole-2-carbaldehyde as a yellow oil, in a 69% yield, Scheme 3.4.

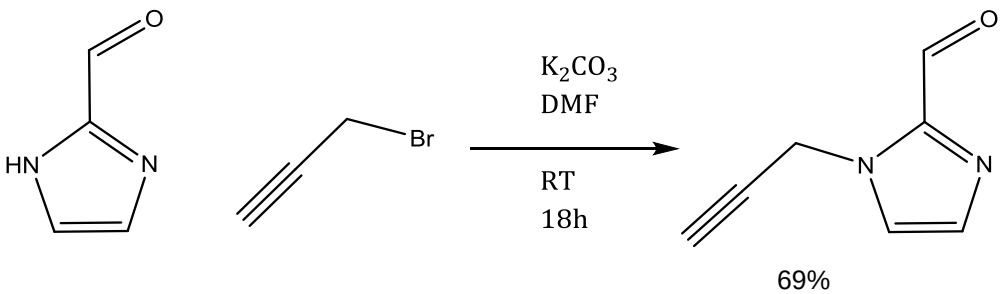

Scheme 3.4 Synthesis of 1-(prop-2-yn-1-yl)-1H-imidazole-2-carbaldehyde.

1-(Prop-2-yn-1-yl)-1H-imidazole-2-carbaldehyde was fully characterised and the ^{1}H NMR spectra is shown below. The loss of the NH imidazole peak confirms the reaction has been successful, the proton environments integrate correctly to show the alkyne linker is attached to the imidazole ring, Figure 3.12.

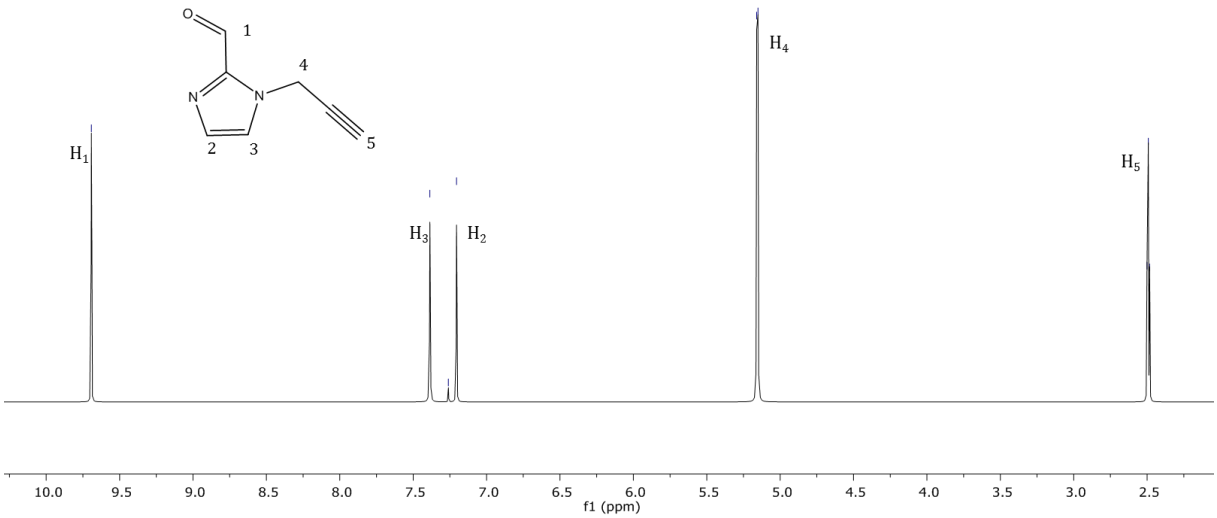

Figure 3.12 ^{1}H NMR (300 MHz, $CDCl_3$, 298 K) of 1-(prop-2-yn-1-yl)-1H-imidazole-2-carbaldehyde

3.4.2 Synthesis of alkyne functionalised imidazole ligand L^{imTB}

The alkyne functionalised imidazole group will be used to develop a bidentate ligand that will be utilized in the formation of a metallo cylinder complex. The alkyne functionalised imidazole ligand L^{imTB} has been successfully synthesised *via* a condensation reaction. 1-(Prop-2-yn-1-yl)-1H-imidazole-2-carbaldehyde was dissolved in ethanol, an ethanolic solution of 4,4′-methylenedianiline was added dropwise to the stirred solution. The reaction was stirred at room temperate for 18 hours, forming an off white precipitate, Scheme 3.5. The precipitate was collected, washed and dried to afford the alkyne imidazole ligand L^{imTB}, in an 82% yield.

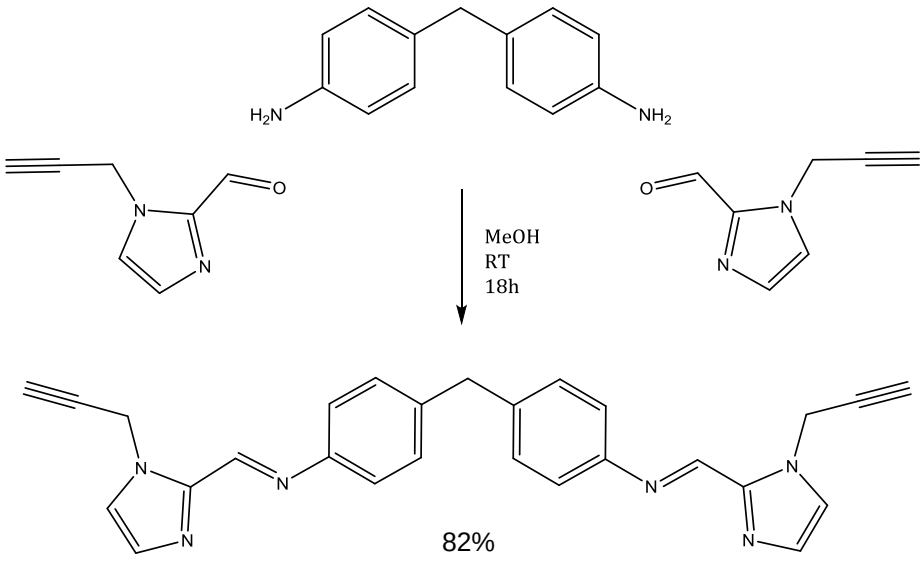

Scheme 3.5 Synthesis of the alkyne functionalised imadazole ligand L^{imTB}, through the reaction of 1-(prop-2-yn-1-yl)-1H-imidazole-2-carbaldehyde and 4,4′-methylenedianiline.

The alkyne functionalised imidazole ligand L^{imTB} was fully characterised and the ^1H NMR spectra is shown below (Figure 3.13). The formation of the imine bond, H_4, is shown by the proton peak at 8.5 ppm, the loss of the aldehyde peak from the starting material also shows the reaction has been successful. The bridging protons from the spacer are clearly visible around 4.0 ppm and the alkyne linker peaks are visible 3.4 ppm and 5.45 ppm, showing the linker is attached to the imidazole ring.

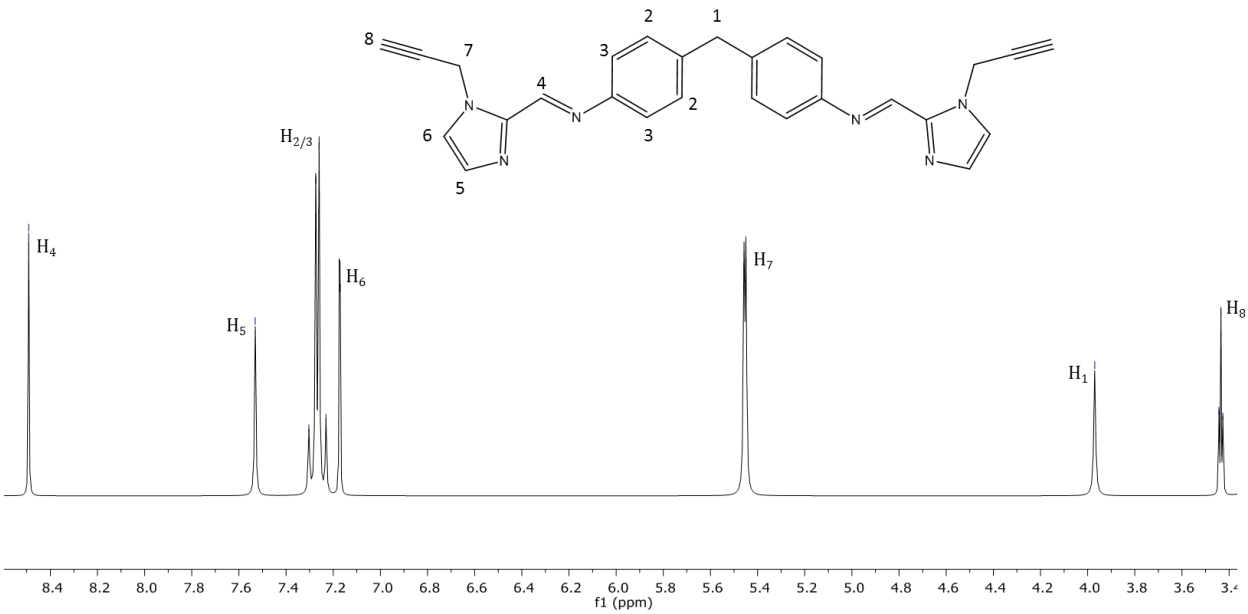

Figure 3.13 ^1H NMR (300 MHz, $CDCl_3$, 298 K) of alkyne functionalised imidazole ligand L^{imTB}.

3.4.3 Synthesis of $[L^{imTB}{}_3Fe_2][\ PF_6]_4$

The alkyne functionalise imidazole ligand L^{imTB} was used to produce an iron based, triple stranded, dinuclear, metallo cylinder complex. The alkyne functionalised ligand L^{imTB} was suspended in methanol, a methanolic solution of iron(II) chloride was added dropwise to the stirred solution. Upon addition of the metal salt the solution turned a deep wine red colour, indicating formation of the metal complex. The reaction was shown to be successful by the presence of the $(M)^{4+}$ observed in the mass spectrum at 350.81.

3.4.4 Synthesis of $[L^{inTB}{}_3Ni_2][\ PF_6]_4$

The nickel metallo cylinder was synthesised using the alkyne modified ligand L^{imTB}. The triple bond functionalised imidazole ligand L^{imTB} was suspended in methanol and reacted with a methanolic solution of $NiCl_2\ 6H_2O$ (3:2, ligand:metal ratio). Upon addition of the metal salt the solution turned an orange colour. The ES mass spectra shows the complex peak $(M)^{4+}$ at 352.13 (Figure 3.14).

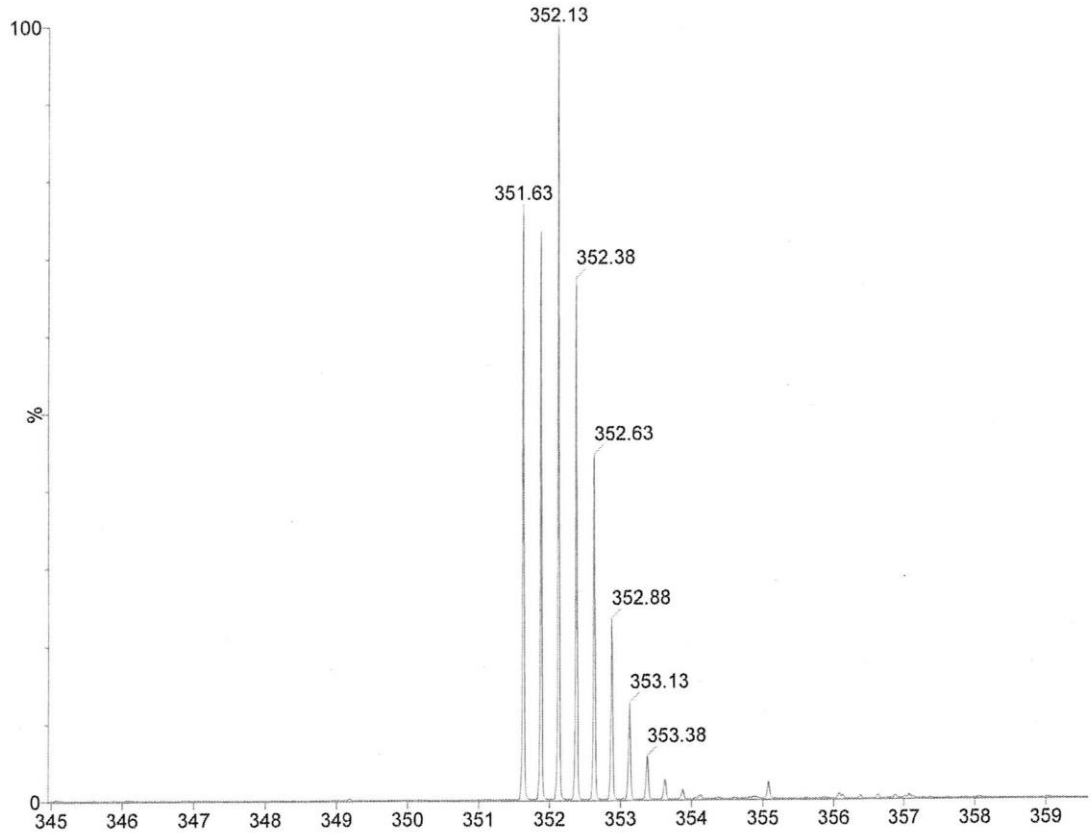

Figure 3.14 Mass Spectra of $[L^{imTB}{}_3Ni_2][PF_6]_4$, showing the $(M)^{4+}$ complex peak at 352.13.

3.5 'Click' reactions with imidazole ligands

After confirming the modified imidazole ligands could successful form both the iron and nickel metallo cylinder, attempts were made to click a fluorophore to the modified imidazole ligand.

A click reaction was undertaken with 1-(prop-2-yn-1-yl)-1H-imidazole-2-carbaldehyde and coumarin azide . The alkyne functionalised imidazole compound and coumarin azide was dissolved in THF and water (5:1). The reaction mixture was stirred, an aqueous solution of $CuSO_4.5H_2O$ was added, followed by an aquesous soltion of soadium ascorbate. Upon additon of the sodium ascorbate the solution turned a deep red colour, indicating Cu(II) has been reduced to Cu(I) *in-situ*. The reaction was stirred at room temperature in the dark for 48 hours. Ice cold water was added to precipitate the product, which was

rapidly collected by filtration. The solid was washed with ethanol and ether then dried to afford the product as a yellow solid. The product was collected in a 33% yield and characterised using ^{1}H NMR and MS. The product peak can be observed by mass spectrometry at 393.5, $M+H^{+}$ peak.

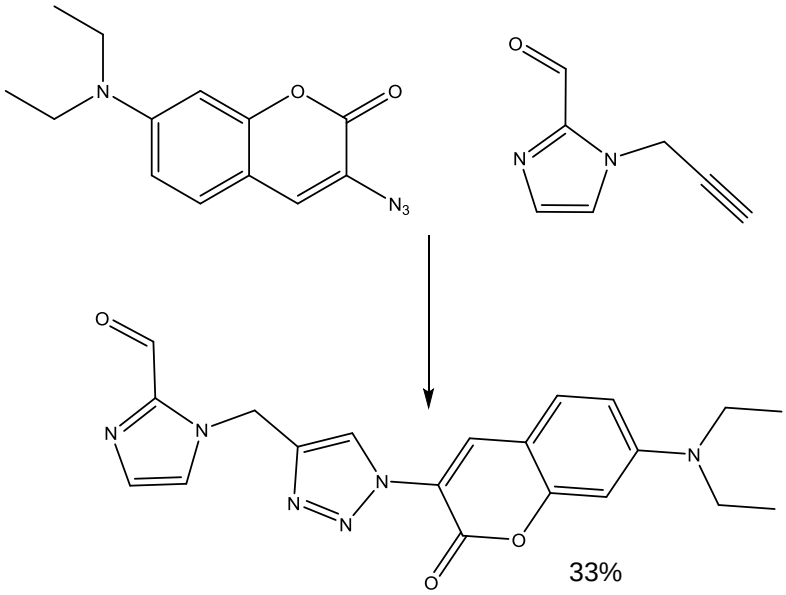

Scheme 3.6 The 'click' reaction of 1-(prop-2-yn-1-yl)-1H-imidazole-2-carbaldehyde and coumarin azide.

The 'clicked' coumarin functionalised imidazole compound was reacted with 4,4′-methylenedianiline *via* a condensation reaction, to form a florescent ligand. The coumarin functionalised imidazole compound was suspended in methanol, a methanolic solution of 4,4′-methylenedianiline was added dropwise to the stirred suspension. The reaction was stirred for 18 hours in the dark, producing a pale yellow precipitate. The product was collected by filtration and washed with methanol and ether, then dried. The ligand was produced in an 82% yield and characterised using ^{1}H NMR and mass spectrometry, which showed the product peak at 948.2 $[M+H]^{+}$.

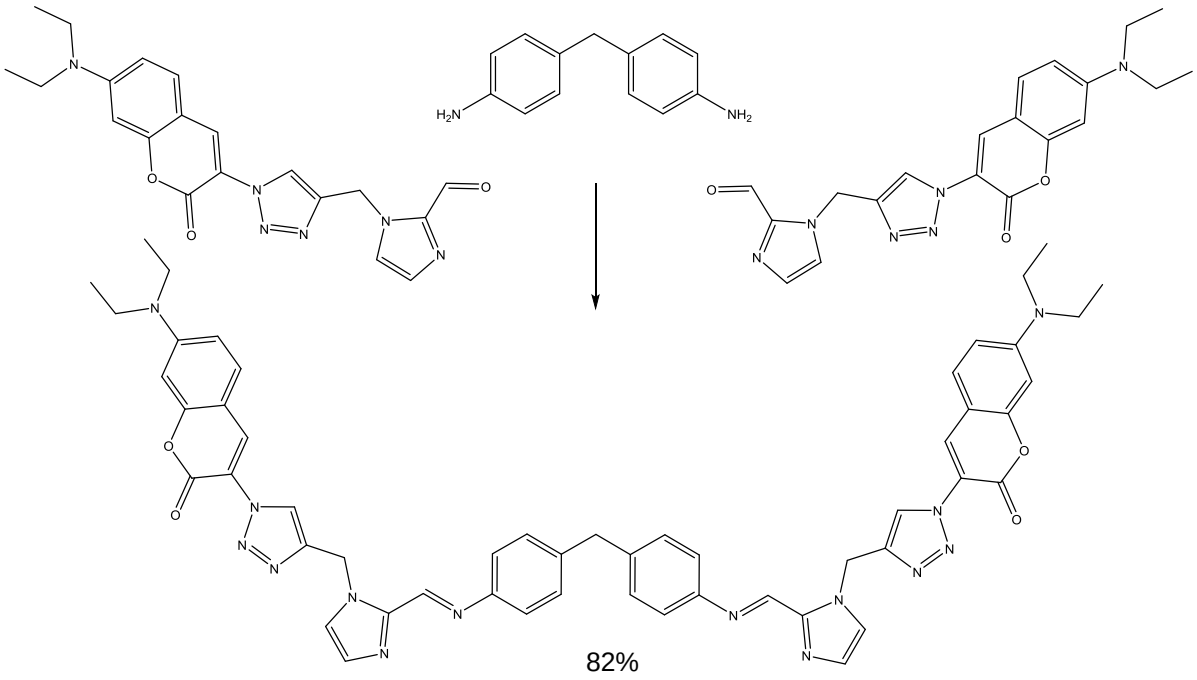

Scheme 3.7 Condensation reaction between the coumarin functionalised imidazole ring and 4,4′-methylenedianiline to form ligand L^{imC}

The fluorescent functionalised imidazole ligand, L^{imC}, was successfully used to form two triple strand dinuclear complexes $[L^{imC}{}_3Fe_2][PF_6]_4$ and $[L^{imC}{}_3Ni_2][PF_6]_4$. Both were synthesised by suspension of the ligand in methanol, followed by addition of the metal chloride salt, then precipitation of the complex with ammonium hexafluorophosphate. The addition of the fluorophore hasn't hindered complex formation. Both complexes are paramagnetic, making them difficult to fully characterise using ^{1}H NMR. The mass spectra of each complex shows the presence of the $[M]^{+4}$ 738.23 and 739.65 respectively for each complex.

3.6 Copper free click reactions

The modification of the imidazole ring with an azide linker allows to be used in copper free click (CFC) chemistry. This utilizes the high ring strain in the eight membered ring of dibenzocyclooctyne (DBCO), allowing it to form a triazole ring with an azide group without a copper catalyst. Two CFC reactions were under taken, one with a DBCO-PEG4 biotin group and one with a DBCO-cy5 dye (Figure 3.15).

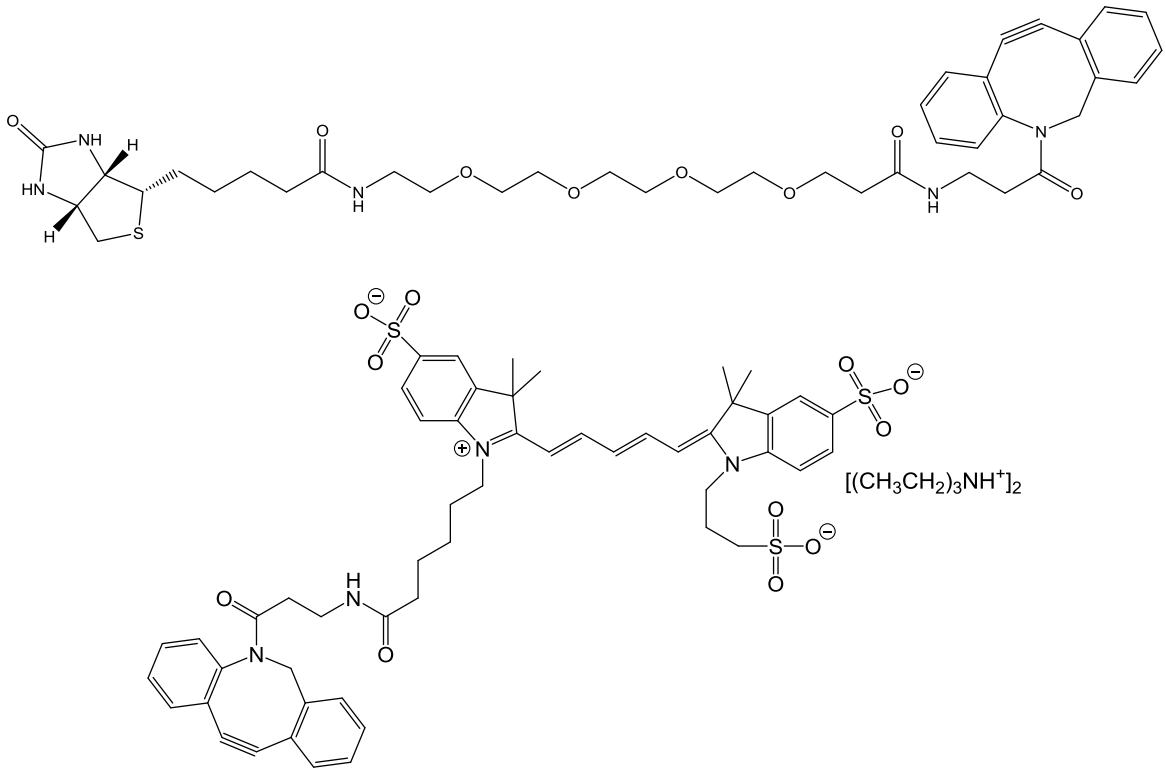

Figure 3.15 Structure of DBCO-PRG4-biotin (top) and DBCO-cy5 (bottom)

1-(3-Azidopropyl)-1H-imidazole-2-carbaldehyde was dissolved in methanol followed by the dropwise addition of DBCO-PEG-4 biotin in methanol. The reaction was stirred for 12 hours and the solvent evaporated to dryness. Mass spectrometry was used to analyse the sample, but unfortunately no product peaks could be found. The experiment was also performed with DBCO-Cy5, the reaction was stirred in the dark for 12 hours and the sample analysed using mass spectrometry. Unfortunately, no product peaks were observed; only 1 mg of DBCO-Cy5 was purchase due to its price, ^{1}H NMR experiment were performed on the sample but the signal was weak and no clear product peaks were visible.

3.7 Synthesis of $[L^{im}_3Ru_2][PF_6]_4$

Attempts to 'post click' a fluorophore onto the alkyne modified imidazole iron cylinder complex have been undertaken, but the iron cylinder degraded during the click process. The ruthenium cylinder is highly stable due to the strong Ru - N bond between the d^6 Ru

and the ligand. It was hoped that after the parent imidazole ruthenium complex had been formed, one side chain could be added to the complex. This side chain could subsequently undergo click reactions to allow just one fluorescent tag to be grafted onto the complex, as opposed to the six fluorophores that are present if they are attached during ligand synthesis. The reduction from six to one fluorescent group should reduce any steric hinderence and repulsion that occurs when three fluorophores are held in close proximity to each end of the cylinder. This reduction would also decrease the overall size of the complex enabling it to bind to DNA in a more similar manner to the parent complex, whilst also increasing its solubility and stability in aqueous solution.

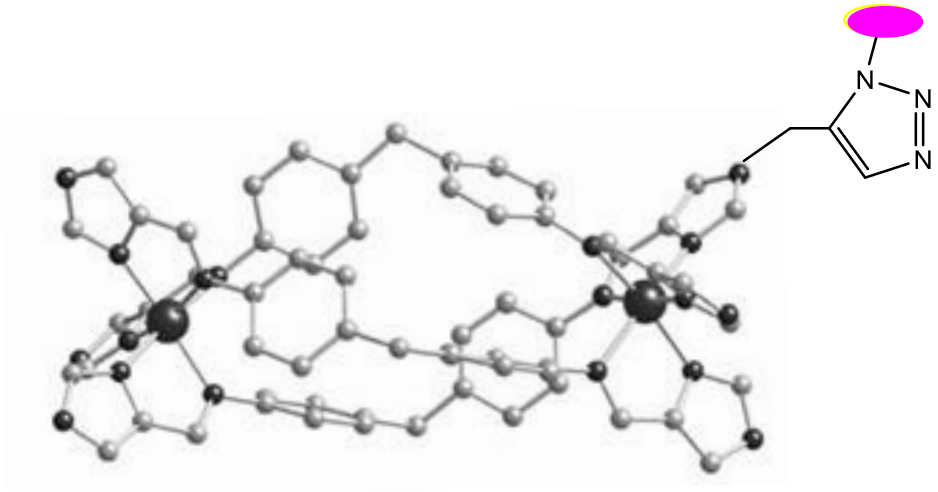

Figure 3.16 Proposed structure of the parent ruthenium imidazole complex functionalised by post complex modification to allow the addition of a single fluorophore or 'tag (shown in pink)'

3.7.1 Synthesis of L^{im}

The parent imidazole ligand L^{im} was synthesized *via* the condensation reaction between imadazole-2-carboxadlehyde and 4,4′-methylenedianiline (Scheme 3.8). Imidazole-2-carboxadlehyde was dissolved in methanol, a methanolic solution of 4,4′-methylenedianiline was added in a dropwise fashion. The reaction was stirred at room temperature for 18 hours, producing a white precipitate. The product was collected by filtration, washed with cold methanol and ether and dried, to afford the product as a white

solid. The ligand was produced in an 95% yield and fully characterised by ^{1}H NMR, ^{13}C NMR and ESI-MS.

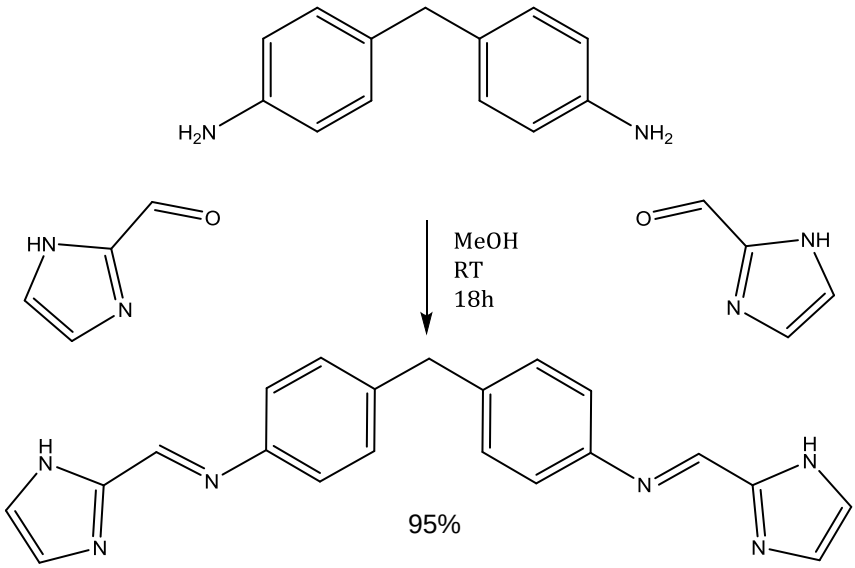

Scheme 3.8 Condensation reaction of imidazole-2-carboxadlehyde with 4,4′-methylenedianiline

3.7.2 Attempted synthesis of $[L^{im}_3Ru_2][\ PF_6]_4$

Once the imidazole ligand L^{im} was synthesized, the formation of $[L^{im}_3Ru_2][\ PF_6]_4$ was attempted. The imidazole ligand L^{im} was dissolved in ethylene glycol and the solution heated to 200°C under argon atmosphere. Once the reaction was at 200°C $Ru(DMSO)_4Cl_2$ was added to the flask *via* a side arm. Upon addition of the ruthenium salt the reaction turned dark red in colour. The reaction was heated at 200 °C for 6 days. The reaction was cooled and a solution of ammonium hexafluorophosphate was added; the solution was left to stir overnight. The solid precipitate was collected, washed with water to remove excess NH_3PF_6, followed by ether to dry the solid and remove water. The solid was dissolved in a minimal amount of acetonitrile and precipitated using ether to produce a fine powder that was collected, washed with ether and dried. The crude product was stirred in ethanol overnight and filtered to remove large polymeric compounds. The

filtrate was concentrated to dryness leaving an orange solid. Numerous attempts to purify this compound were undertaken using column chromatography. Varying both the solid phase (silica, alumina) and the solution phase (acetonitrile, water), no pure product could be obtained.

3.8 Conclusions and future work

In conclusion three novel ligand systems have been developed, L^{imTB}, L^{imN} and L^{imC} (Figure 3.17), each has been characterised by ^{1}H NMR, ^{13}C NMR and mass spectrometry.

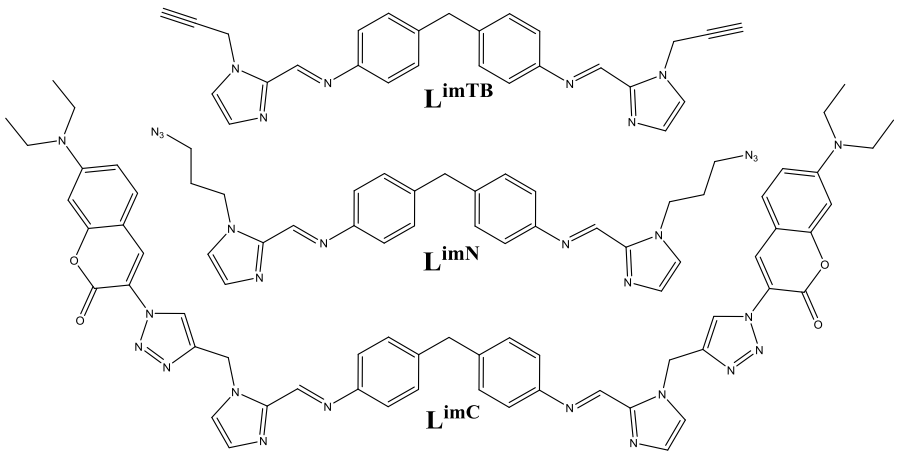

Figure 3.17 Newly synthesised ligand L^{imTB}, L^{imN} and L^{imC}

These have been reacted with iron(II) and nickel(II) salts to form six new complexes, which have been charcterised by ^{1}H NMR.

Attempts to synthesize a ruthenium(II) parent complex has been undertaken but proved unsuccessful.

Attempts to graft biotin and Cy5 onto the ligand precursor utilizing copper free click chemistry have been undertaken but proved unsuccessful.

In future work, stability and DNA binding studies of the newly synthesised complexes developed in this chapter will be completed.

Studying the complexes stability in aqueous solution overtime will give an insight into their potentials for cellular work. Secondly, circular dichroism and linear dichroism experiments would be performed to examine the complexes ability to bind and interact with ct-DNA.

A variety of different fluorophore can be grafted onto the alkyne and azide functionalised cylinder *via* click chemistry. The alkyne moiety could also be utilized in sonogashira cross coupling reaction to add a fluorophore.

Scaling up the ruthenium(II) cylinder synthesis described in section 3.7.2, may yield enough product to attempt to couple the alkyne group onto the complex as proposed.

A ruthenium(II) complex would be synthesized with ligand L^{imTB}, with the intention of 'clicking' a fluorophore onto the ligand, after complex formation. Unfortunately an azide modified ruthenium(II) cylinder cannot be attempted due to the explosive nature of azide's at high temperature, the ruthenium(II) cylinder is formed at 200°C, so this would be a dangerous experiment.

3.9 References

[1] F. Tuna, M. R. Lees, G. J. Clarkson, M. J. Hannon, *Chem. - A Eur. J.* **2004**, *10*, 5737–5750.

[2] C. Ducani, A. Leczkowska, N. J. Hodges, M. J. Hannon, *Angew. Chemie - Int. Ed.* **2010**, *49*, 8942–8945.

[3] A. Oleksi, A. G. Blanco, R. Boer, I. Usón, J. Aymamí, A. Rodger, M. J. Hannon, M. Coll, *Angew. Chemie - Int. Ed.* **2006**, *45*, 1227–1231.

[4] S. Phongtongpasuk, S. Paulus, J. Schnabl, R. K. O. Sigel, B. Spingler, M. J. Hannon, E. Freisinger, *Angew. Chemie - Int. Ed.* **2013**, *52*, 11513–11516.

[5] M. J. Hannon, C. L. Painting, A. Jackson, J. Hamblin, W. Errington, *Chem. Commun.* **1997**, 1807–1808.

Chapter 4

4 Synchrotron Imaging Techniques

4.1 Introduction

In this chapter the cellular accumulation and uptake of the parent iron pyridylimine based complex will be examined using synchrotron imaging techniques. How the light is produced and used for imaging is now explained

4.1.1 Synchrotron systems and radiation

Synchrotron light has a unique set of characteristics - high brilliance, high intensity, sharp focus and tenability - giving it a wide range of applications in a variety of research areas including health care, engineering, archaeology and astrophysics.

The synchrotron light source consists of a circular storage ring, and a linear accelerator. A linear accelerator and booster is used to accelerate the electrons to their final energy before they are magnetically injected into the storage ring, where they are kept at a constant speed[1].

The electrons traveling around the linear accelerator are produced by an electron gun. A high voltage cathode is heated under vacuum, this gives the electrons in the cathode sufficient energy to undergo thermionic emission and escape from the surface of the materials; these electrons are accelerated by earthed anodes. This stream of electrons has an energy of 90,000 electron volts (90 KeV), these electrons are accelerated by a linear accelerator to 100,000,000 electron volts using radio frequency cavities[1].

Electrons with an energy of 0. 1GeV are injected into the booster synchrotron from the linear accelerator[1]. Dipole magnets are used to bend the electron beam around the curves of the stadium-shaped track, whilst radio frequency voltage sources accelerate the electrons around the straight sections of the track.

Electrons are then magnetically 'kicked' out of the booster ring into the storage ring. The storage ring is made of twenty-four straight sections, which are angled together to form a

loop. Dipole magnets curve the beam between adjacent straight sections in the storage ring. The entire system is held under a vacuum to minimise electrons scattering off air molecules. Electrons are held in the storage ring at a constant speed with an energy of 3 GeV. As electrons circulate the storage ring they produce synchrotron radiation, this radiation is projected at a tangent to the electron storage ring and is captured in beamlines. Beamlines can originate at bends in the storage ring or on the straight sections at insertion devices. Synchrotron light firstly enters the front end, where light is extracted from the storage ring and focused into a beamline, it then enters the optics hutch were the desired wavelengths are selected and focused. This focused light then passes to the experimental hutch where the X-rays interact with the sample and are detected using X-ray cameras.

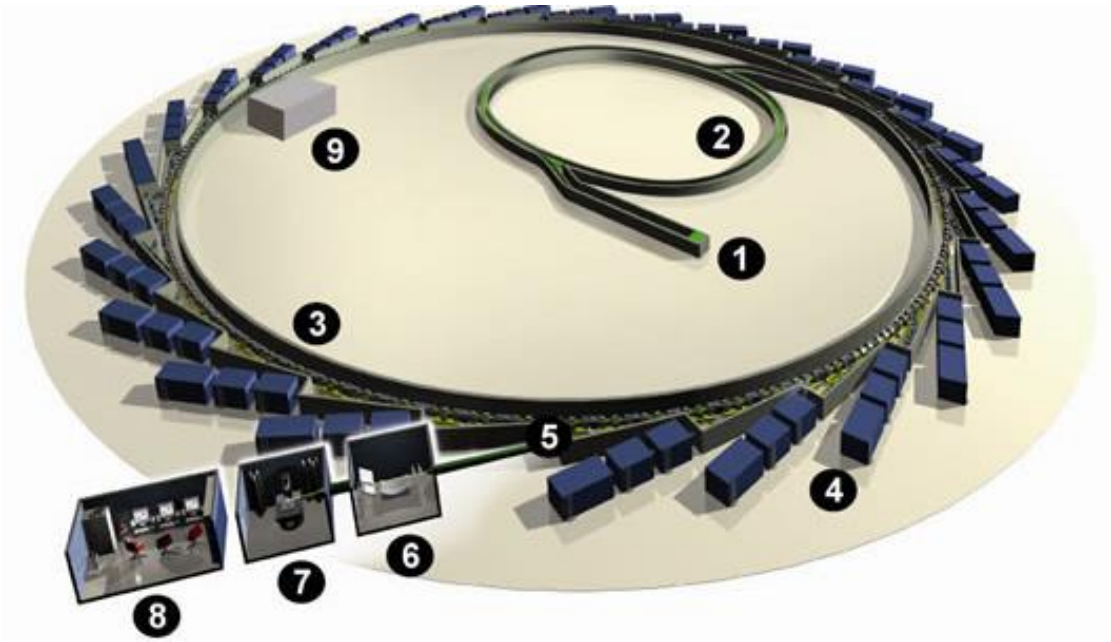

Figure 4.1 Layout of the Diamond Light Source in Oxfordshire. 1- injection systems, electron gun and linear accelerator. 2 – booster synchrotron, 3 – storage ring, 4 - beam lines, 5 – font ends, 6 – optics hutch, 7 – experimental hutch, 8 – control cabin, 9 – radio frequency cabin[1].

4.1.2 XRF and XANES

Two techniques are used to analyse the uptake and composition of the metallo cylinder - X-Ray Fluorescence (XRF) and X-Ray Absorption Near-Edge Structure (XANES). XRF is used to analyse quantitatively the composition of a material. The sample is bombarded

with high-energy X-rays, causing ionisation of the sample's constituent atoms. During ionisation, one or more of the atom's inner shell electrons is ejected from its shell, causing the electronic structure of the atom to become unstable. Electrons in higher energy orbitals fall down to fill the hole left behind. As the electron falls to fill the hole, it releases energy in the form of a photon *i.e.* a characteristic 'secondary' X-ray. These secondary X-rays are detected and allow elemental maps to be produced. Each element has electronic orbitals with characteristic energies; there are a limited number of ways that the higher energy electron can fall to fill the lower energy level. The main transitions are called K_α (L to K transitions), K_β (M to K transitions) and L_α (M to L transitions). Each of these transitions yield a fluorescent photon that has a characteristic energy equal to the difference in energy of the initial and final orbital. The wavelengths of radiation are then separated, allowing the intensities of each characteristic radiation to be directly related to the amount of each element in the material. An example spectrum so shown in Figure 4.2.

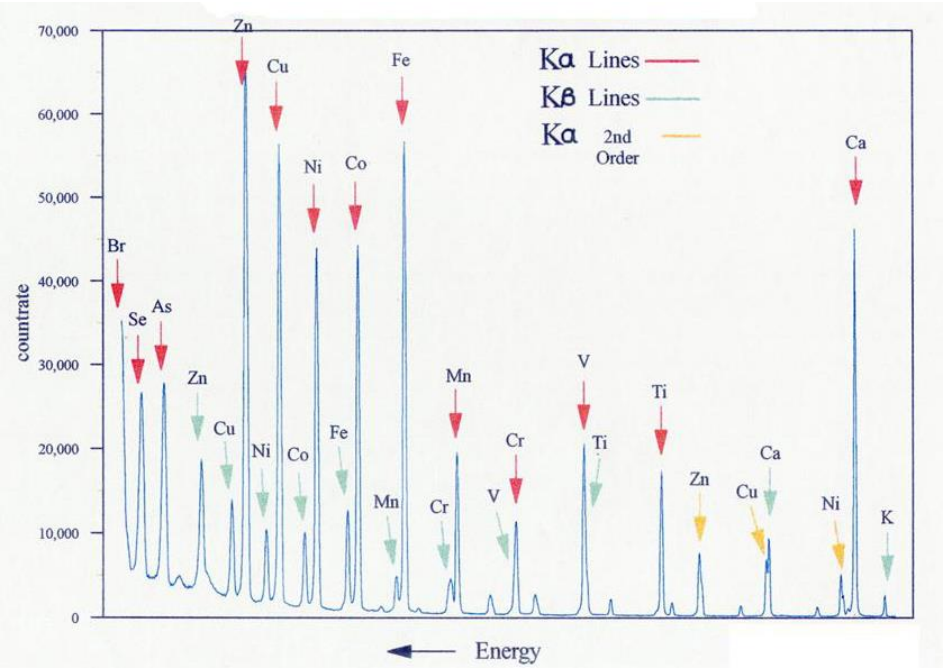

Figure 4.2 Wavelength dispersive XRF spectrum.

XANES is a form of X-ray absorption spectroscopy (XAS) which is used to examine the coordination structure of atoms. The energy of the synchrotron beam is tuned through the absorption edge of the element of interest and modulations in the absorption are measured. Modulations near the absorption edges are caused by photoelectron transitions. As discussed previously an X-ray interacts with the sample by photo absorption into a core level of the atom. This is followed by photoelectron emission, leaving a core hole in the atom that is filled by an electron from another level, releasing an X-ray or emission of an Auger electron. These modulations give information about the chemical state and local symmetry of the element. Using this information, the oxidation state of the element can be examined, for example Fe(II) and Fe(III) metal atoms can be differentiated between. As well as the geometry, for example allowing octahedral and square planar platinum centers to be distinguished between. For metal atoms in the absorption region, the photoelectron is excited to the first unoccupied level above the Fermi level. XANES spectroscopy allows the properties of an unknown sample to be compared against a set of standards. An example of this is from samples of soil and concrete that have been compared against a set of plutonium standards. XANES spectra of four plutonium standards at different oxidation states were recorder (Pu(III), Pu(IV), Pu(V) and Pu(VI)). The set of standards were compared against the soil and concrete samples, it can be seen from the spectrum, that the plutonium in the soil and concrete has a Pu(IV) oxidation state due to the alignment and identical shape of their individual XANES spectra (Figure 4.3)[2].

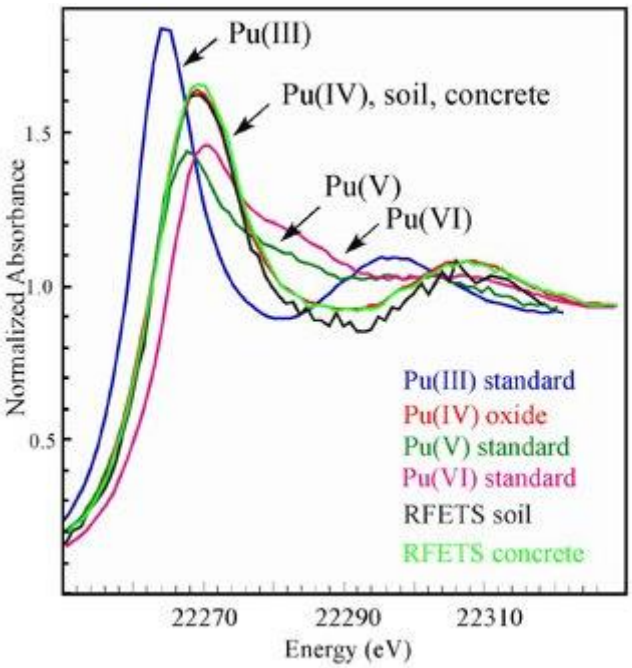

Figure 4.3 XANES spectra of plutonium in soil and concrete against a set of plutonium standards at different oxidation states. (Image taken from reference[2]).

4.1.3 Synchrotron XRF and XANES imaging applications

Synchrotron imaging has been used to examine the cellular distribution of platinum(IV) complexes in A2780 ovarian cancer cells[3]. Micro-XANES of the treated cells was used to ensure the prodrug had been reduced *in-situ* for Pt(IV) to Pt(II)[3]. Cells were seeded and treated with freshly prepared platinum solutions. After treatment, cells were washed, trypsinised and re-suspended in ammonium acetate. Cells were mounted onto Fromvar film in a Teflon frame and frozen in liquid nitrogen cooled liquid isopentane. XRF imaging produced elemental maps of Cl, K, Ca, Cu, Zn and Pt were recorded, and show nuclear localisation of the Pt complex after 24 hours of treatment (Figure 4.4)[3].

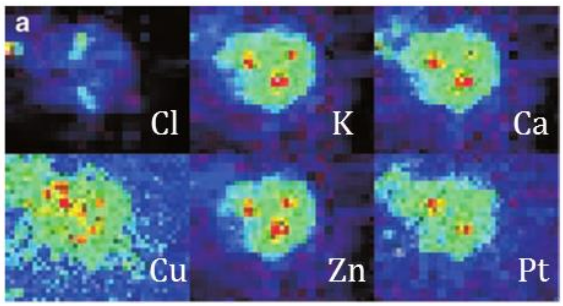

Figure 4.4 Elemental maps of Cl, K, Ca, Cu, Zn and Pt respectively obtained by XRF imaging of A2780 cells treated with *cis*-[$PtCl_4(NH_3)_2$] (Image taken from reference[3]).

The micro-XANES spectra on treated A2780 cells shows platinum is present in the cells. The Pt(IV) complex *cis*-[$PtCl_4(NH_3)_2$] shows a single peak in the first derivative, similar to that observed for cisplatin, indicating the complex has been reduced to Pt(II)(Figure 4.5)[3].

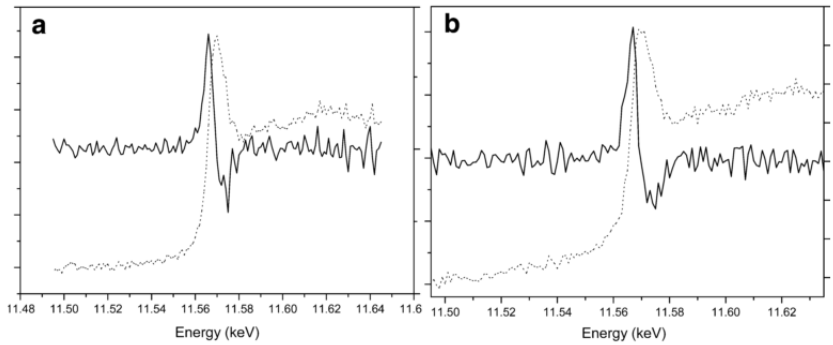

Figure 4.5 XANES spectra (solid line) and first derivative (dotted line) of *cis*-[$PtCl_2(NH_3)_2$] (a) *cis*-[$PtCl_4(NH_3)_2$] (b) through A2780 cells after 24 hours of treatment (Image taken from reference [3]).

XANES experiments have also been used to probe the oxidation state and coordination environment of cobalt complexes, following treatment of cancer cells[4]. Cells were plated and treated. After treatment cells were washed with PBS, trypsinised and re-suspended in ammonium acetate, followed by dehydration in ethanol and 2 days of freeze drying. The solid cell pellet was then subjected to XANES experiments. It can be observed that [Co(diNOsar)]Br_3 (diNOsar = dinitrosarcophagine) (Figure 4.6) possess the same shaped XANES curve before and after administration to cells; this indicates the complex stays intact after 24 hours in the cell environment, as it possess the same oxidation state and

coordination geometry (Figure 4.7)[4]. This is in comparison to [Co(acac)$_3$] (Figure 4.6) which showed an altered XANES spectrum after cell treatment; indicating that the complex had lost ligands and potentially degraded inside the cell (Figure 4.7)[4].

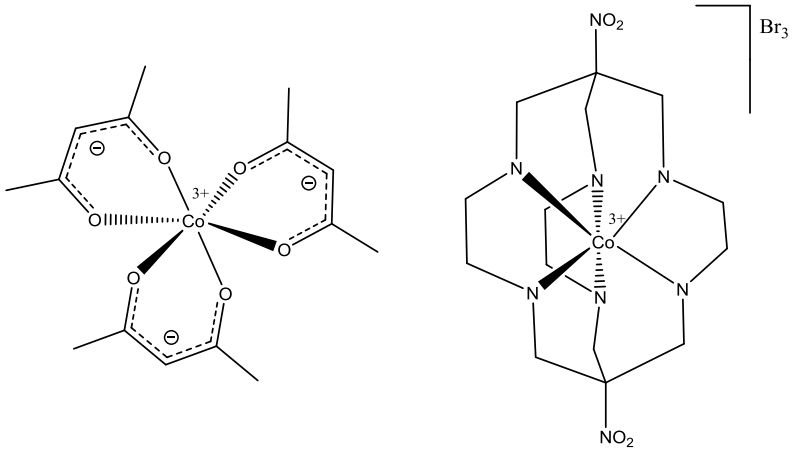

Figure 4.6 Structure of [Co(acac)$_3$] (left) and [Co(diNOsar]Br$_3$ (right).

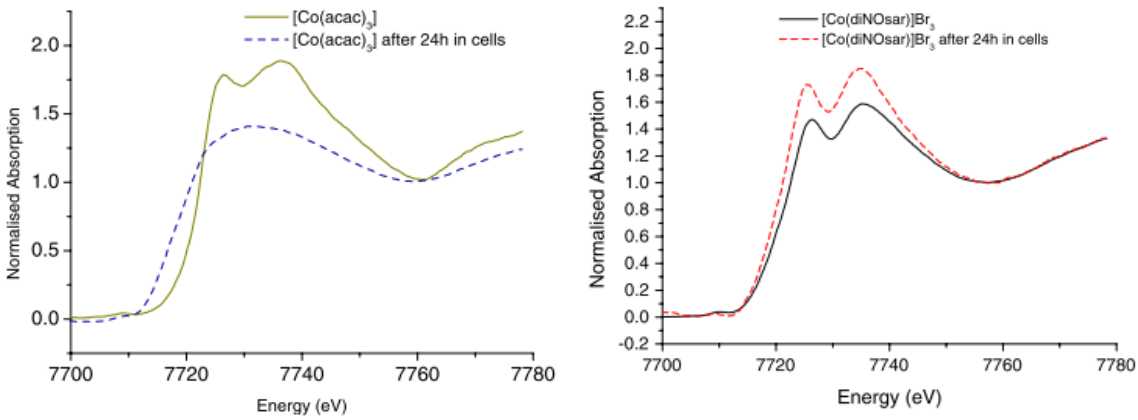

Figure 4.7 XANES spectra of [Co(acac)$_3$] before and after administration to A2780 cells for 24 hours (left). XANES spectra of [Co(diNOsar)Br$_3$] before and after administration to A2780 cells for 24 hours (right) (Image taken from reference [4]).

4.1.3 Aims

The aim of this experiment is to prepare samples of cancer cells that have been treated with different concentrations of parent metallo-cylinder (previously described in chapter 2) for different periods of time. Samples will be examined using XRF imaging to produce elemental maps of – potassium(I) to distinguish outline of the cell (due to the high levels of potassium(I) in the cytoplasm); zinc, to observe the nucleus; chlorine, as this is the

complex counter ion, as well as a common ion throughout the cell; and finally, iron, the metal centre of the metallo-cylinder. These elemental maps will then be overlaid to determine if iron is inside the cell and subsequently inside the nucleus.

XANES experiments will then be taken for iron containing areas of the cell and compared to iron containing standards that will be prepared, to analyse whether the iron metallo-cylinder retains its structure once inside the cell.

4.2 Sample preparation

4.2.1 Iron(II) metallo-cylinder complex preparation

Firstly, the parent ligand was prepared *via* a condensation reaction between 2-pyridinecarbaldehyde and 4,4′-methylenedianiline in a 2:1 ratio[5]. The starting materials were stirred at room temperature for 18 hours in ethanol. The product was collected by filtration, washed with methanol and diethyl ether and dried. The compound was characterised by ^{1}H NMR (Figure 4.8), ^{13}C NMR and MS. The ligand was then dissolved in methanol. Upon addition of $FeCl_2$ the solution changed to a bright purple colour, producing the metallo cylinder complex. The bright purple colour of the complex is due to the MLCT band at 575 nm. NH_4PF_6 was added to precipitate the product, which was collected by filtration, washed with water, methanol and ether and dried to produce the product. Dowex was used to change the counter ion from a PF_6^- to a Cl^- counter ion. The product was filtered and the solvent removed to produce the parent metallo cylinder complex $[Fe_2L_3]Cl_4$. The complex was characterised by ^{1}H NMR (Figure 4.8) and MS.

Figure 4.8 ^{1}H NMR (300 MHz, $CDCl_3$, 298 K) of the parent ligand (bottom) and ^{1}H NMR (300 MHz, CD_3OD, 298 K) complex $[Fe_2L_3]Cl_4$ (top).

4.2.2 Biological sample preparation

MDA-231 (breast cancer) and A2780 (ovarian cancer) cell lines were selected for this experiment due to their large nuclei. This gave a large target area to be imaged for colocalisation studies. Both cell lines were removed from liquid nitrogen storage and placed into DMEM (Dulbecco's Modified Eagle Medium) and RPMI-1640 (Roswell Park Memorial Institute Medium) respectively. After 12 hours the media was removed, cells washed with PBS, new media added. Cells where left to reach 80% confluency before cell passage. Cells were passaged twice before use.

Round sapphire discs were used as the substrate to grow cells on as they have a good thermal shock resistance, low thermal expansion coefficient, extreme surface hardness

and low fluorescence. These properties make sapphire ideal for use in a cryostat as the extreme temperature doesn't affect it. Sapphire discs also have excellent optical qualities and transmittance over a wide spectral range, allowing cells to be clearly viewed using the camera attached to the beamline. The sapphire discs were sterilised in 70% ethanol, and then left to air-dry in a laminar flow hood. A disc was placed into each well of a 6 well plate, before each well was seeded with 10,000 cells which were left to adhere to the disc overnight. The adherence of cells was checked using a Leica DMIL light microscope. Fresh solution of iron cylinder was prepared using DMEM and RPMI-1640 media. The media in each well was removed, the cells washed with PBS and fresh media added containing the desired concentration of metallo cylinder (20μM or 100μM). The treated discs were placed back into the incubator for their desired treatment time (30 min, 4 h or 24 h). The treatment media was removed and the cells were washed three times with PBS to remove any residual metallo cylinder from the surface of the disc. A super cooled slurry of dry ice and methanol was prepared. The discs were snap frozen by hovering them just over the surface of the methanol bath with tweezers for 1 second, then submerging them into the bath for 5-10 seconds, once removed the discs were placed in a clean, labelled, 6 well plate. Snap freezing was used to fix the cells to remove the need for a chemical fixative such as ammonium acetate. This was to allow the cells to stay in as natural a state as possible. Plates were stored in a -80°C freezer until they were needed (no longer than 1 week) and then transported to the Diamond Light Source on dry ice.

4.3 XRF and XANES beam line Set up

All elemental mapping and XANES spectroscopy was conducted on beamline I18 at the Diamond Light Source in Oxfordshire. The schematic of beam line I18 is shown in Figure 4.9. The beamline passes through 3 slits, toroid, monochromator, HR mirrors and KB

focusing mirrors before it hits the sample. These devices highly focus the beam, giving it a size and spatial resolution of 2µm x 2µm.

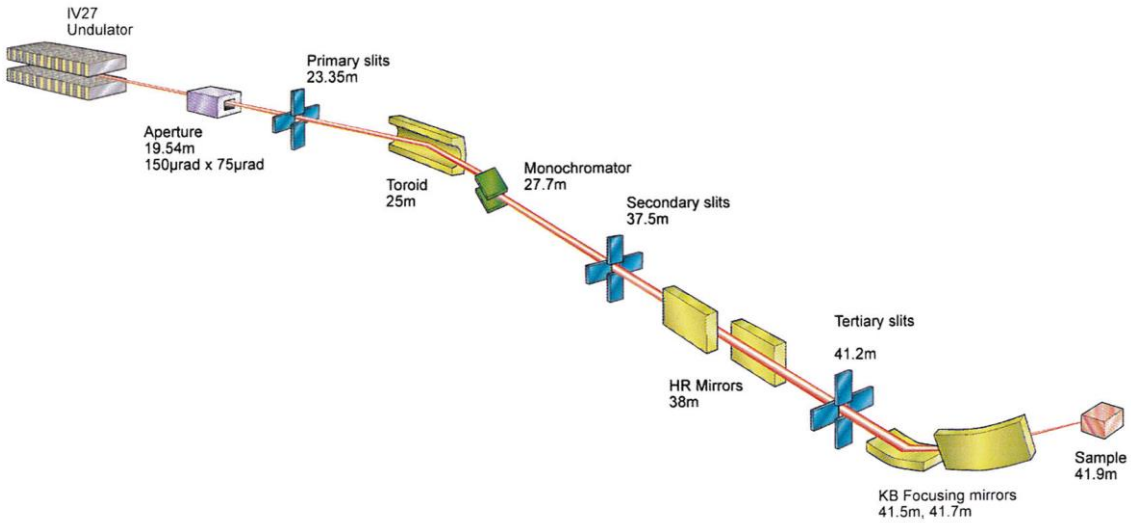

Figure 4.9 Set up of beamline I18 as its focused onto the sample, giving it a beam size of 2µm x 2µm[1].

The sapphire disc was attached to an aluminium disc using super glue. The aluminium disc was subsequently mounted by a clip onto the face of the He/N_2 cryostat (Figure 4.10). The copper back of the cryostat allows uniform heat distribution.

Figure 4.10 Aluminium disc with a sapphire disc glued into place (left). The base plate of the cryostat showing the metal clip used to hold the aluminium disc in place during the experiment.

A cover is then placed onto the front of the sample. The cryostat is mounted to a motorised stage to allow movement of the sample in the X-Y plane so the sample can be focused from the control cabin. A stream of nitrogen is blown onto the face of the cryostat to stop ice formation on the front of the sample during the experiment. The detector is held at a 45° angle to the sample, with the beamline and camera directly facing the sample (Figure 4.11).

Figure 4.11 Experimental beamline set up on beamline I18 at the Diamond Light Source. The face plate of the cyrostat sample holder (A). Side view of the experimental set up (B). Front view of the experimental set up, with the blue top line blowing a stream of nitrogen across the sample to stop ice formation(C). Arm of the cryostat, covered in ice. The X-ray detector at a 45°C angle to the sample. The camera and beamline are located directly opposire the sample. Experimental hatch (D).

4.4 XRF and XANES results

MDA-231 and A2780 cells were used for the experiment as they have large nuclei and the results can be used in collaboration with previously obtained MTT data and hoechst displacement studies undertaken using these cell lines. During the experimental procedure, cells are firstly located using a camera, and an area of interest is selected and focused upon (the cells of interest are highlighted in red in the subsequent camera images). Areas are selected so that 2-4 cells, that have an elongated healthy shape are selected. Ideally the cells are spaced out enough to allow a clear cell edge to be defined, but also within a small enough area to make effective use of beam time. Elemental maps of the area shown below take up to 3 hours to be produced by the X-ray beam raster scanning across the sample.

Elemental maps of iron are taken to examine the location of iron rich deposits within and around the cell. Chlorine, potassium and zinc maps are acquired to determine the location of the cells, due to their high concentrations within cell cytoplasm. These are subsequently used to produce overlay images of chlorine and iron to deduce if iron has been internalised, and if so its localisation within the cell.

Elemental maps from samples of MDA-231 cells treated with 100 μM parent metallo cylinder for 24 hours are shown in Figure 4.12 and Figure 4.13. The iron maps show low levels of iron within the sample. From the overlay images it can be observed that iron (shown in blue) accumulates around the edge of the cells but is not observed inside the cells. This is the longest treatment time that cells are exposed to the metallo cylinder. Only small areas of the sapphire disc area are imaged and cells that have effectively taken up the complex may have undergone apoptosis and been washed from the window during the PBS washing stage of sample preparation.

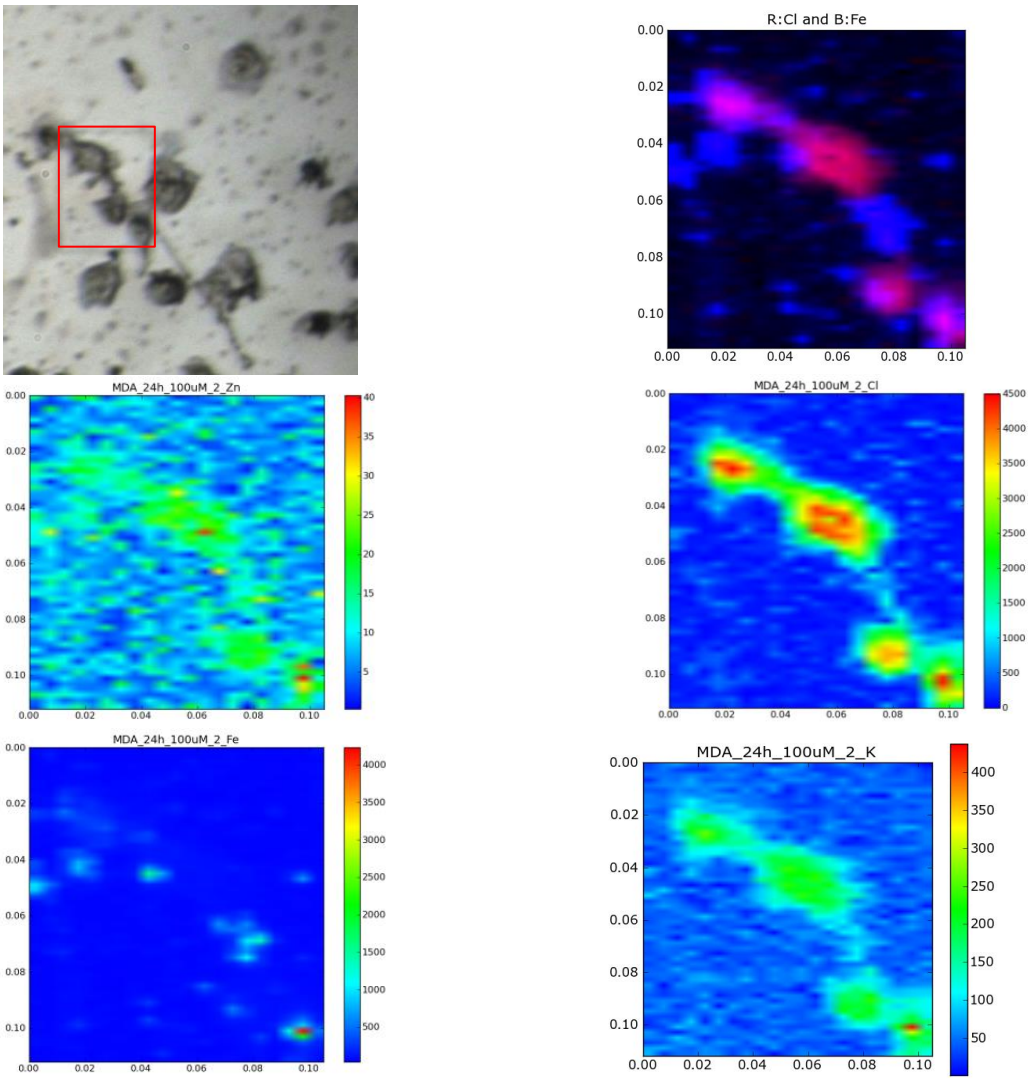

Figure 4.12 MDA-MB-231 cells, grown on sapphire windows, treated with 100μM parent iron(II) cylinder $[Fe_2L_3]Cl_4$ for 24 h, followed by snap freezing fixation. Camera image of the MDA-231 cells to be mapped using XRF microscopy. Elelmntal maps of Zn, Fe, Cl and K producing using XRF synchrotron microscopy. Overlay of Cl and Fe elemental maps.

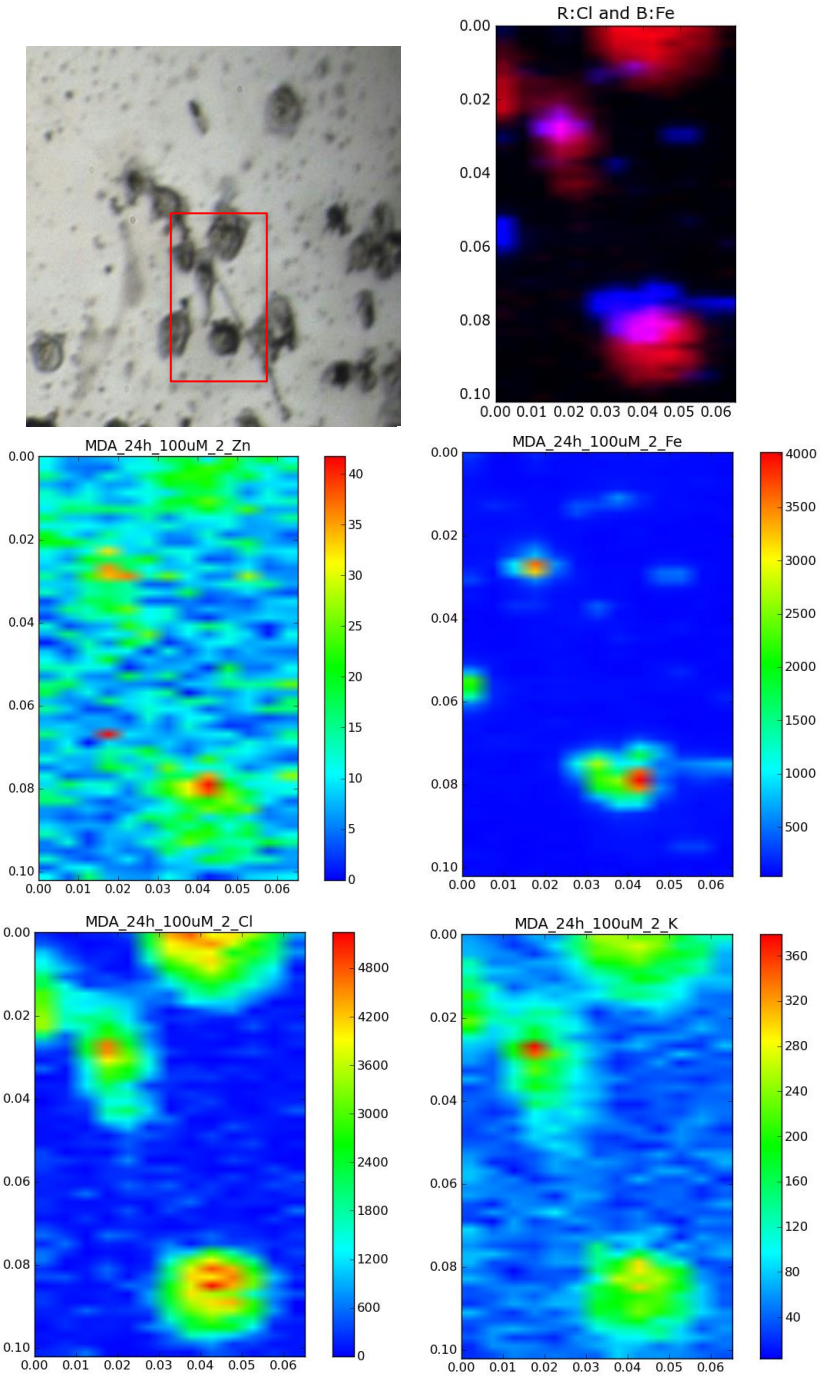

Figure 4.13 MDA-MB-231 cells grown on sapphire windows, treated with 100μM parent iron(II) cylinder $[Fe_2L_3]Cl_4$ for 24 h followed by snap freezing fixation. Camera image of the MDA-231 cells to be mapped using XRF microscopy. Elemental maps of Zn, Fe, Cl and K producing using XRF synchrotron microscopy. Overlay of Cl and Fe elemental maps.

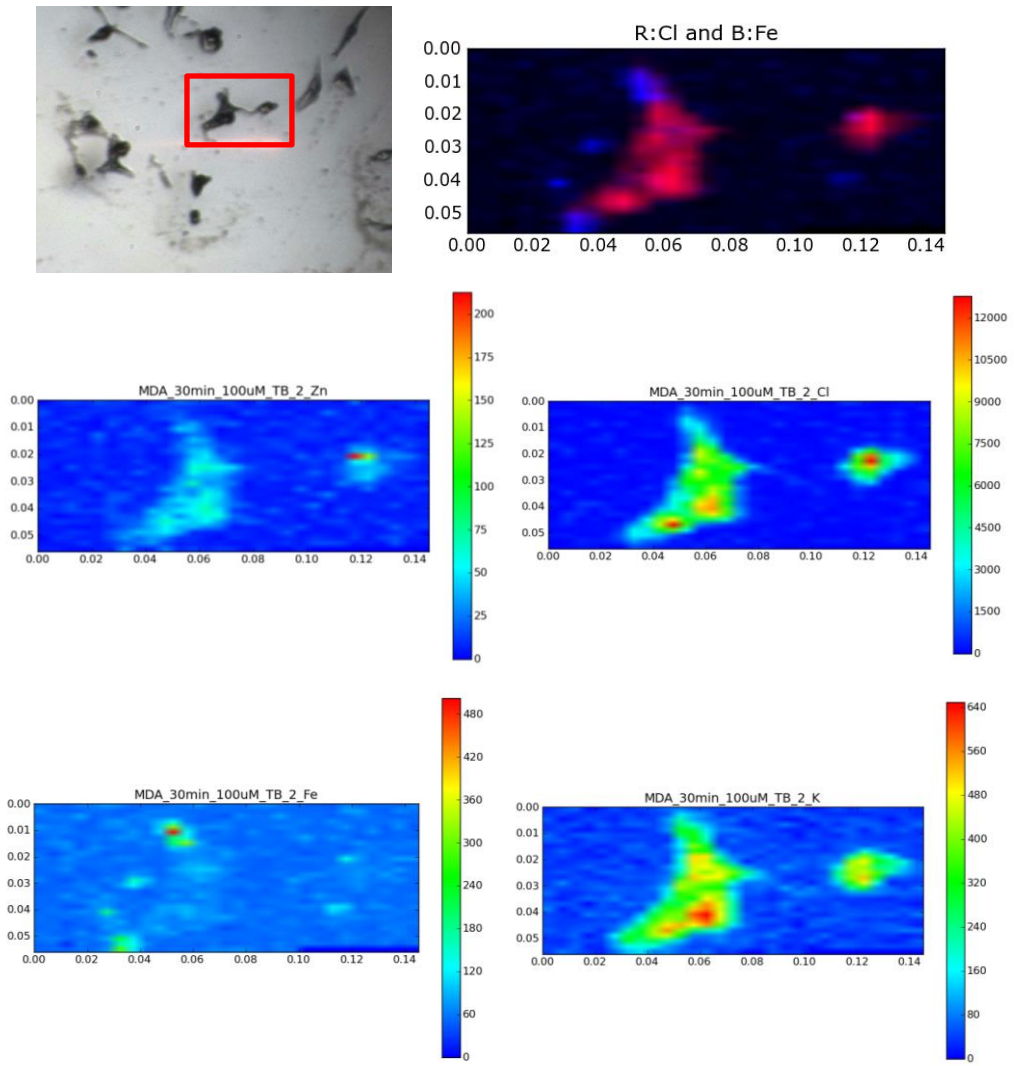

Figure 4.14 MDA-MB-231 cells grown on sapphire windows, treated with 100μM parent iron(II) cylinder $[Fe_2L_3]Cl_4$ for 0.5 h followed by snap freezing fixation. Camera image of the MDA-231 cells to be mapped using XRF microscopy. Elemental maps of Zn, Fe, Cl and K producing using XRF synchrotron microscopy. Overlay of Cl and Fe elemental maps.

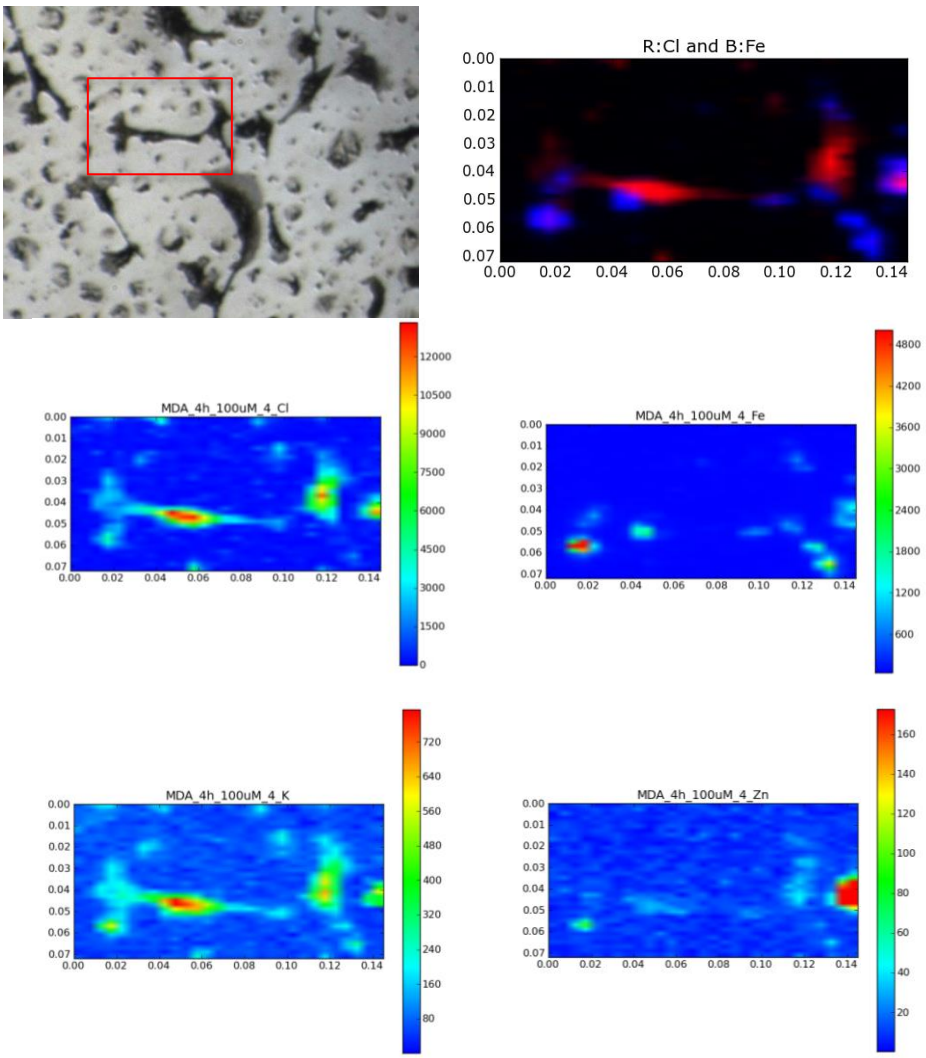

Figure 4.15 MDA-MB-231 cells grown on sapphire windows, treated with 100μM parent iron(II) cylinder $[Fe_2L_3]Cl_4$ for 4 h followed by snap freezing fixation. Camera image of the MDA-231 cells to be mapped using XRF microscopy. Elemental maps of Zn, Fe, Cl and K producing using XRF synchrotron microscopy. Overlay of Cl and Fe elemental maps.

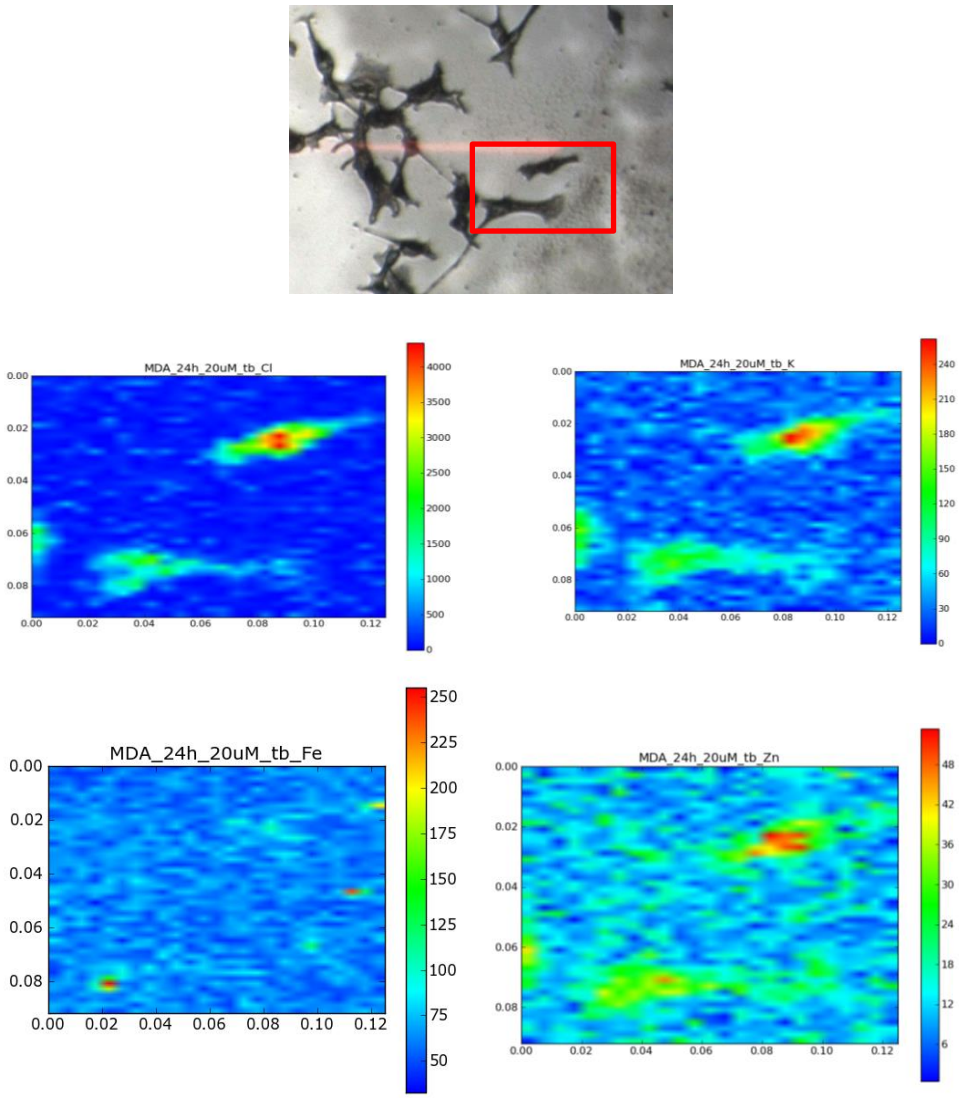

Figure 4.16 MDA-MB-231 cells grown on sapphire windows, treated with 20μM parent iron(II) cylinder $[Fe_2L_3]Cl_4$ for 24 h followed by snap freezing fixation. Camera image of the MDA-231 cells to be mapped using XRF microscopy. Elemental maps of Zn, Fe, Cl and K producing using XRF synchrotron microscopy. Overlay of Cl and Fe elemental maps.

MDA-231 cells were treated with 20 μM parent iron cylinder for 30 minutes. In Figure 4.17 the iron and chlorine maps are overlaid. It can be observed there is stong colocalistaion of iron and chlorine in two of the smaller cells. The cells appear too have iron within them and have balled up in to a spherical shape. As observed within the camera image. This suggests that the cells that have uptaken the iron complex are entering apoptosis, indicated by their loss of enlogated morphology.

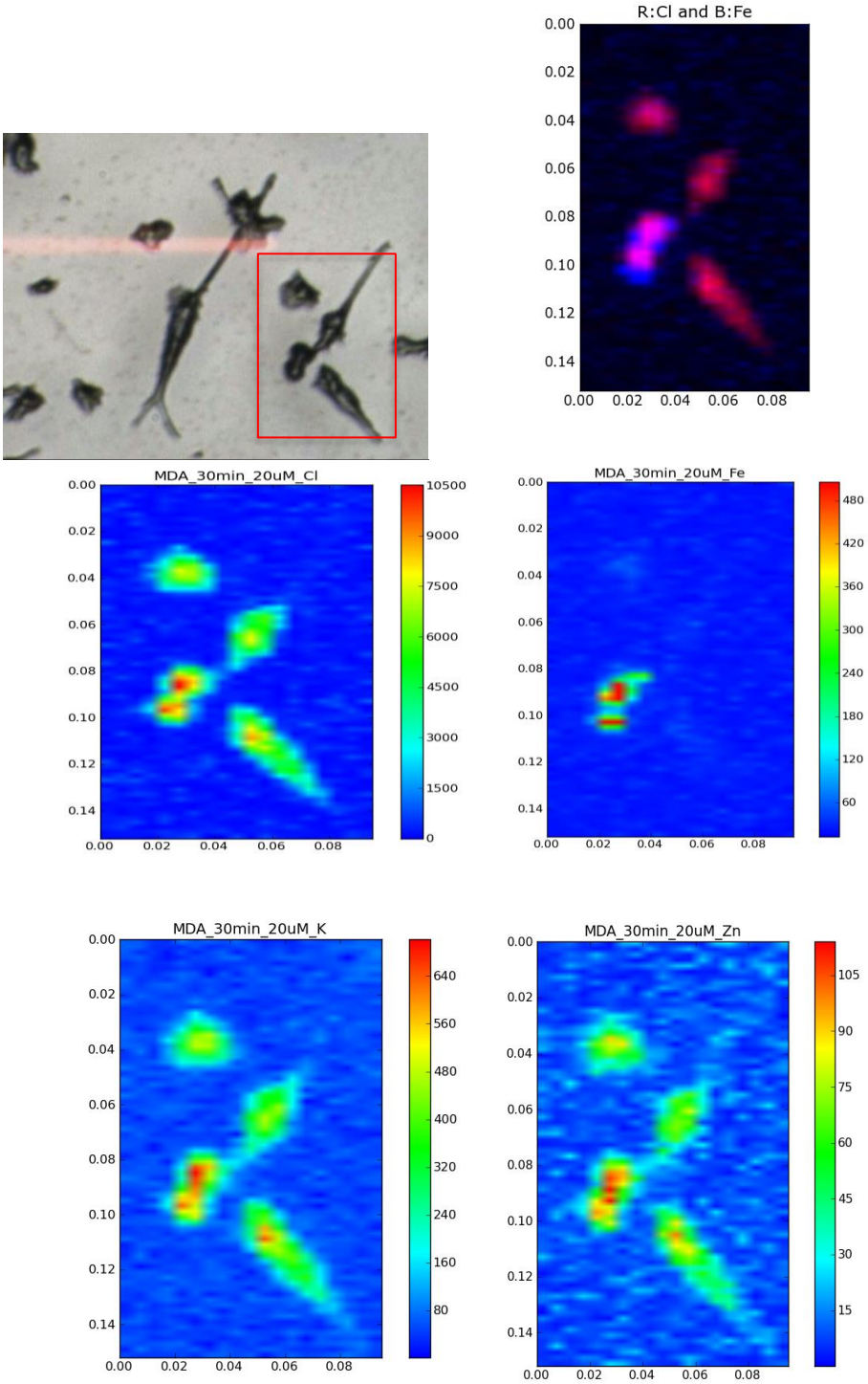

Figure 4.17 MDA-MB-231 cells grown on sapphire windows, treated with 20μM parent iron(II) cylinder $[Fe_2L_3]Cl_4$ for 0.5 h followed by snap freezing fixation. Camera image of the MDA-231 cells to be mapped using XRF microscopy. Elemental maps of Zn, Fe, Cl and K producing using XRF synchrotron microscopy. Overlay of Cl and Fe elemental maps.

A2780 cells have also been imaged and mapped after treatment with the metallo cylinder. A2780 cells treated with 100 μM parent iron cylinder ($[Fe_2L_3]Cl_4$) for 30 minutes are shown in Figure 4.18, Figure 4.19 and Figure 4.20 and when compared to MDA-231 cells treated under the same conditions (Figure 4.14); they show a higher level of iron uptake. Over laying the iron and chloride elemental maps shows that the iron is inside the cell, this is particularly evident in Figure 4.18.

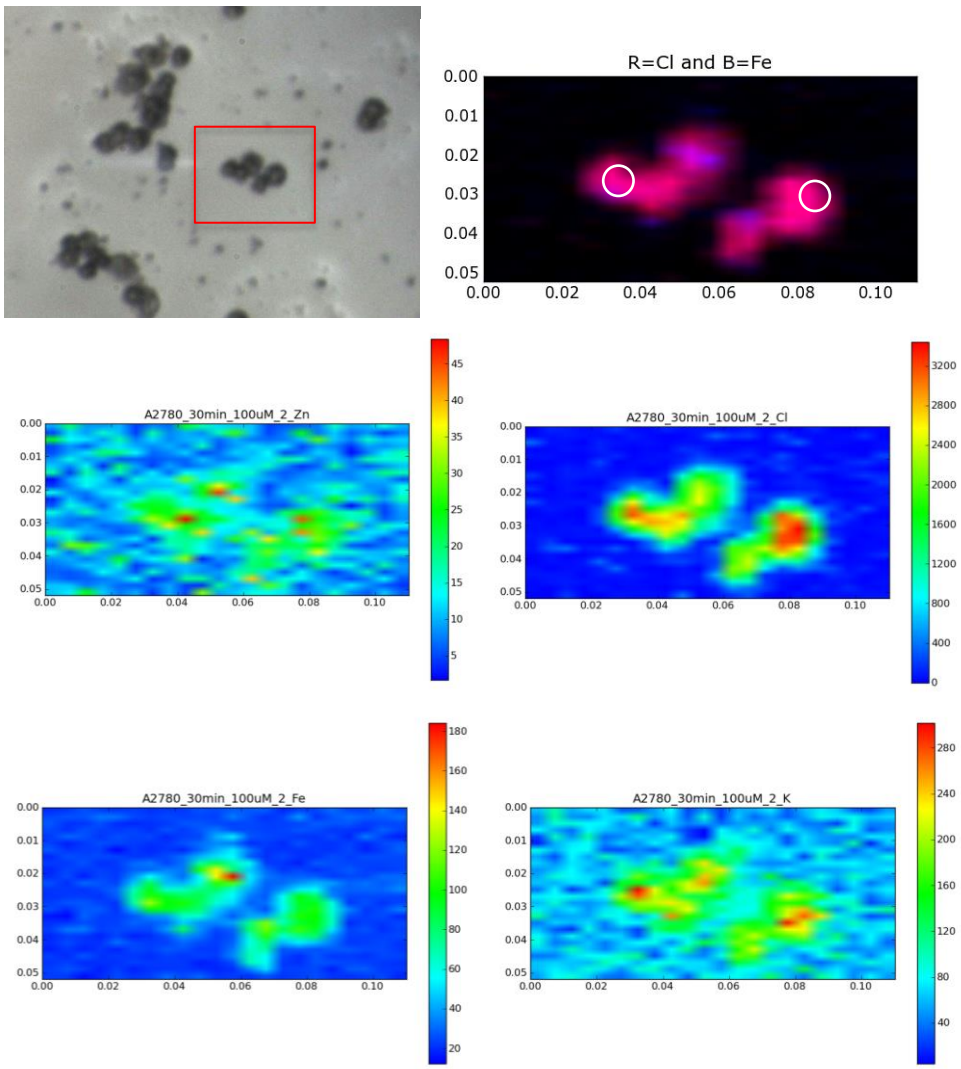

Figure 4.18 A2780 cells grown on sapphire windows, treated with 100μM parent iron(II) cylinder $[Fe_2L_3]Cl_4$ for 0.5 h followed by snap freezing fixation. Camera image of the A2780 cells to be mapped using XRF microscopy. Elemental maps of Zn, Fe, Cl and K producing using XRF synchrotron microscopy. Overlay of Cl and Fe elemental maps.

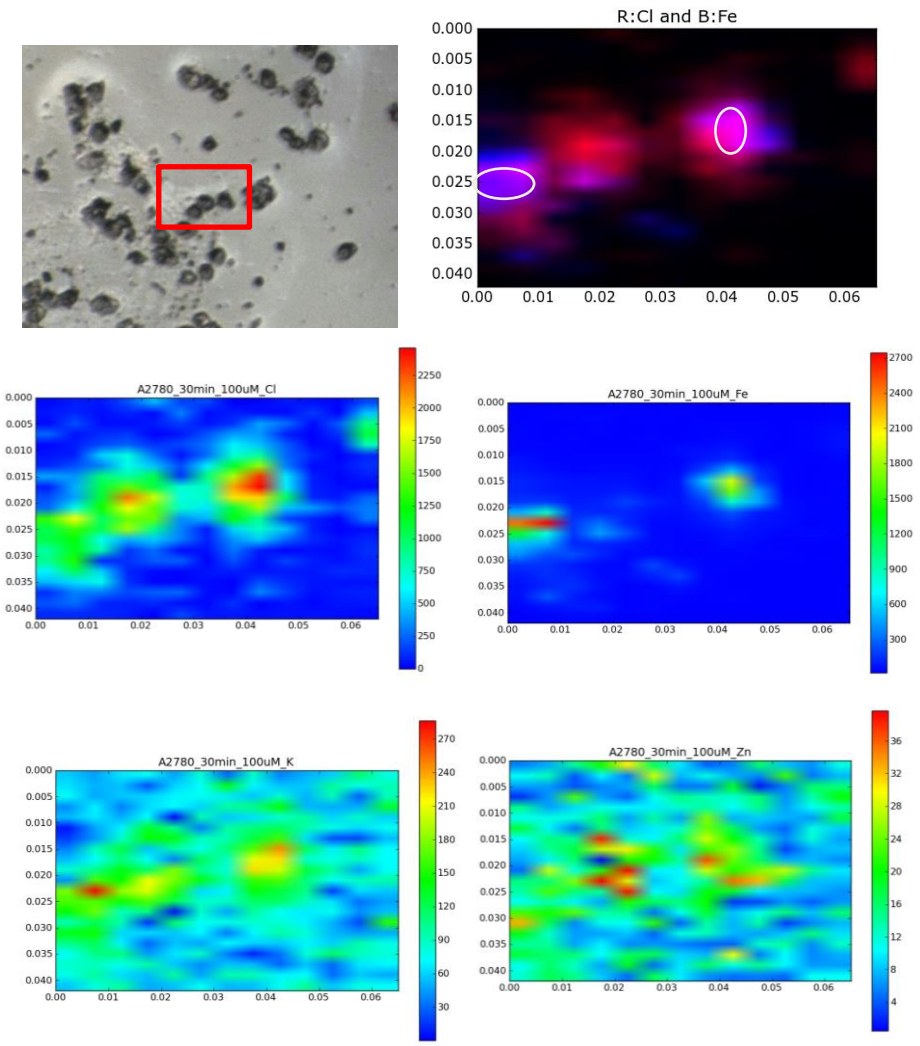

Figure 4.19 A2780 cells grown on sapphire windows, treated with 100µM parent iron(II) cylinder $[Fe_2L_3]Cl_4$ for 0.5 h followed by snap freezing fixation. Camera image of the A2780 cells to be mapped using XRF microscopy. Elemental maps of Zn, Fe, Cl and K producing using XRF synchrotron microscopy. Overlay of Cl and Fe elemental maps.

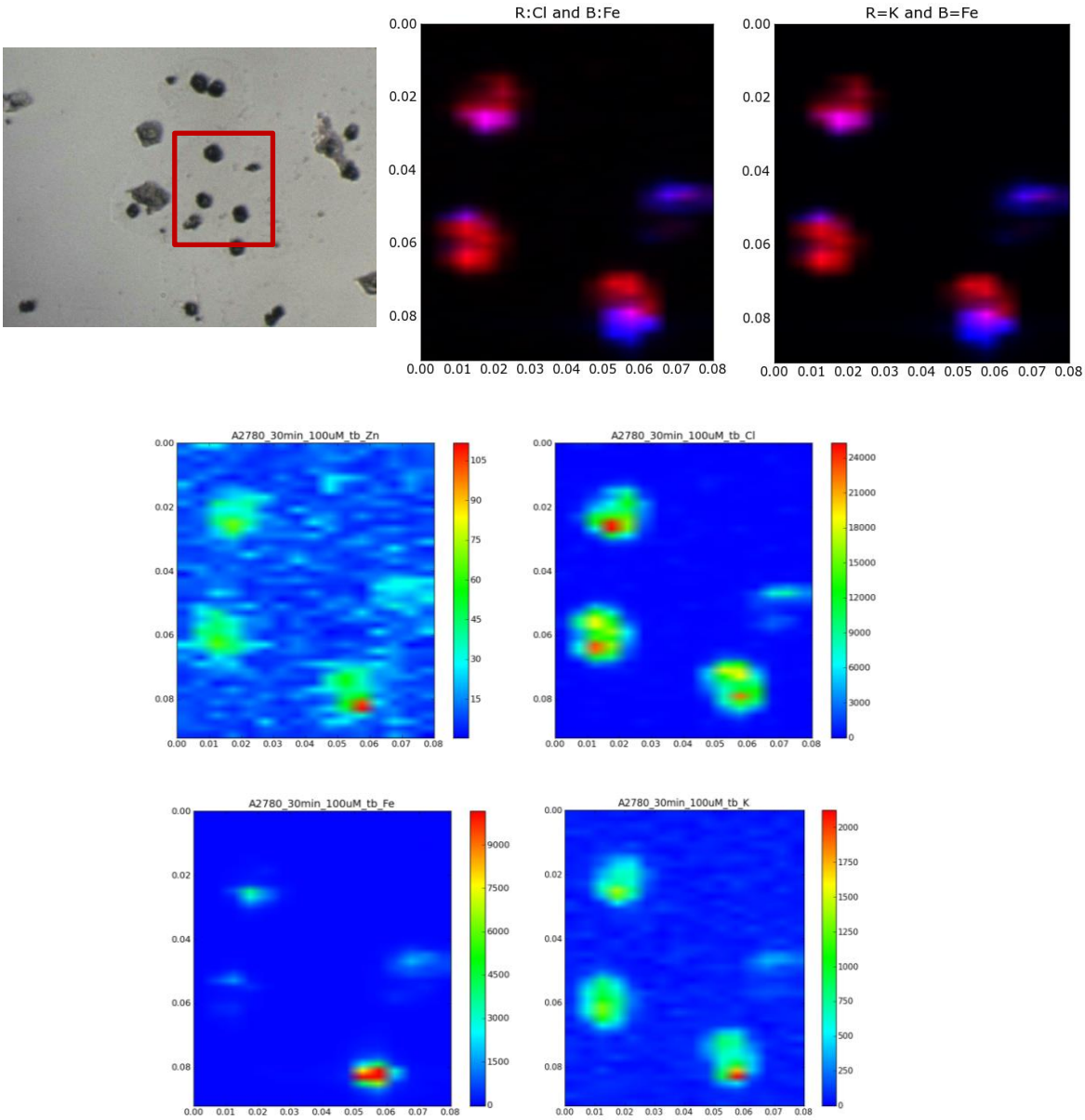

Figure 4.20 A2780 cells grown on sapphire windows, treated with 100μM parent iron(II) cylinder $[Fe_2L_3]Cl_4$ for 0.5 h followed by snap freezing fixation. Camera image of the A2780 cells to be mapped using XRF microscopy. Elemental maps of Zn, Fe, Cl and K producing using XRF synchrotron microscopy. Overlay of Cl and Fe elemental maps.

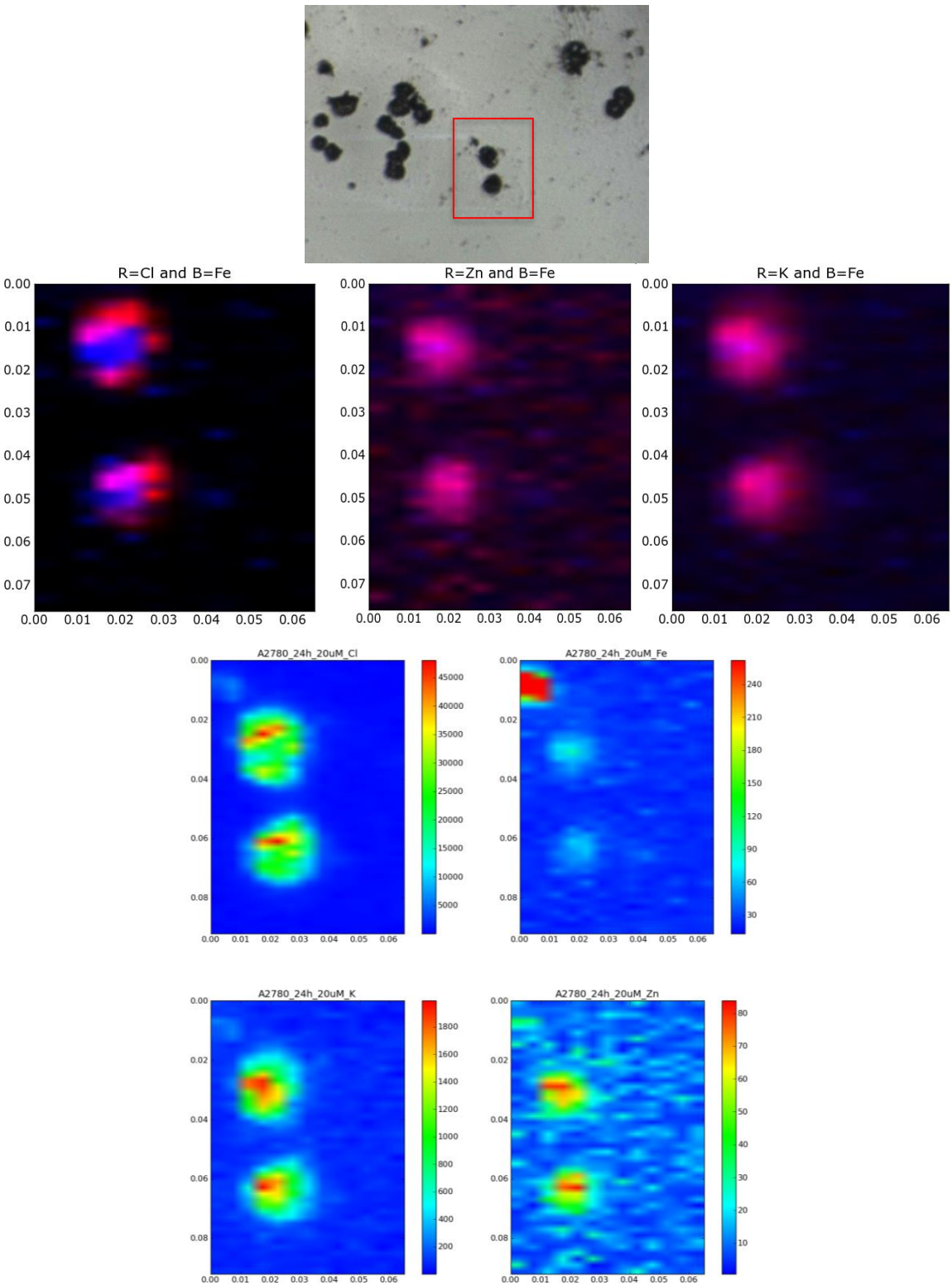

Figure 4.21 A2780 cells grown on sapphire windows, treated with 20µM parent iron(II) cylinder $[Fe_2L_3]Cl_4$ for 24 h followed by snap freezing fixation. Camera image of the A2780 cells to be mapped using XRF microscopy. Elemental maps of Zn, Fe, Cl and K producing using XRF synchrotron microscopy. Overlay of Cl and Fe elemntal maps.

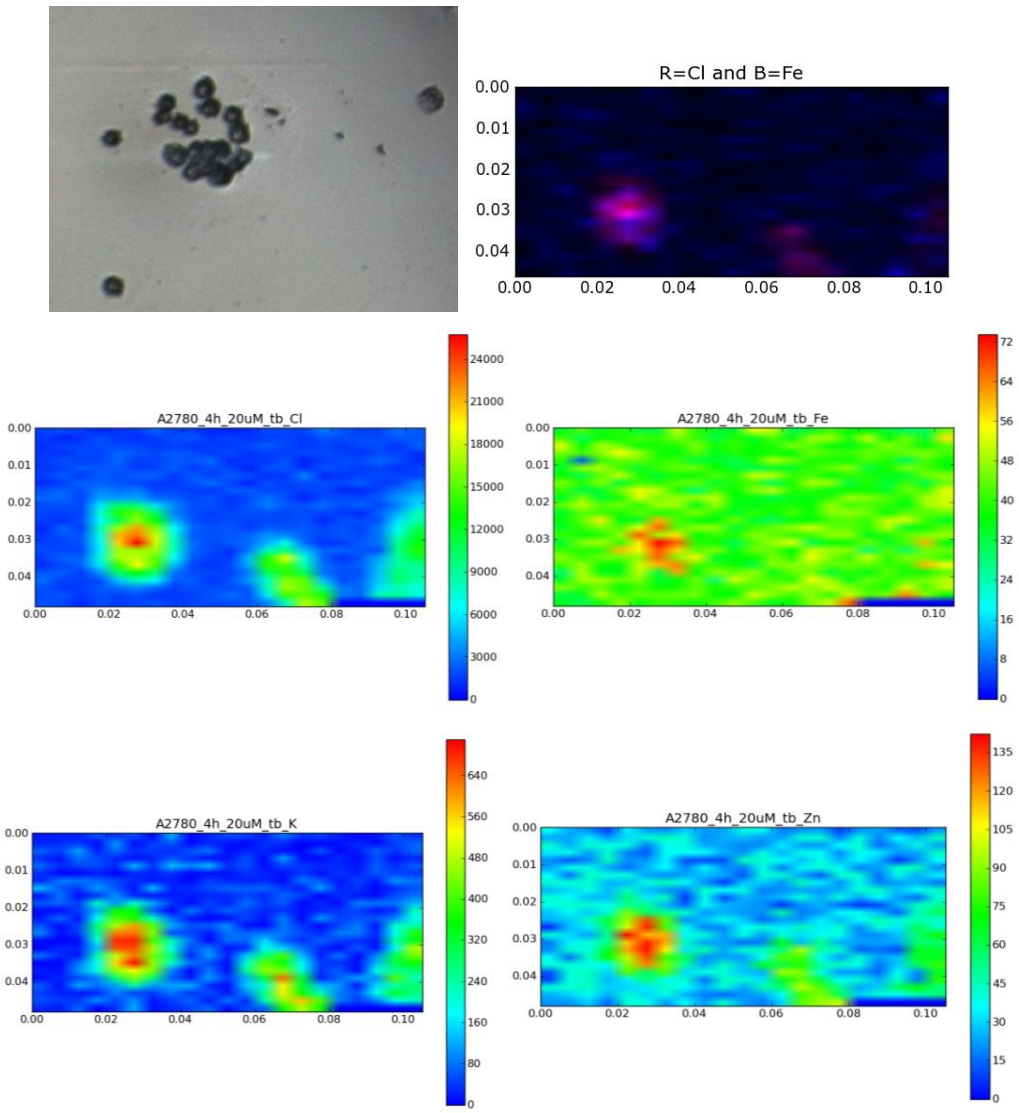

Figure 4.22 A2780 cells grown on sapphire windows, treated with 20μM parent iron(II) cylinder $[Fe_2L_3]Cl_4$ for 4 h followed by snap freezing fixation. Camera image of the A2780 cells to be mapped using XRF microscopy. Elemental maps of Zn, Fe, Cl and K producing using XRF synchrotron microscopy. Overlay of Cl and Fe elemental maps.

Control samples of cells treated with iron(II) chloride were prepared using the procedure described previously (4.2.2 Biological sample preparation). Cells were treated with $FeCl_2$ at 40 μM and 200 μM, double the concentration used for the metallo-cylinder, to account for the two metal centers within the iron(II) cylinder. In A2780 cells treated with iron(II) chloride at 40 μM for 24 hours it can be observed that iron is associated around the edges of the sample. Samples treated with a high dose of $FeCl_2$ shows an iron distriburtion that correlated with zinc distribution, indicating the iron has been taken up into the cell. The distribution appears similar to that observed for cells treated with the complex at 100 μM (Figure 4.19)

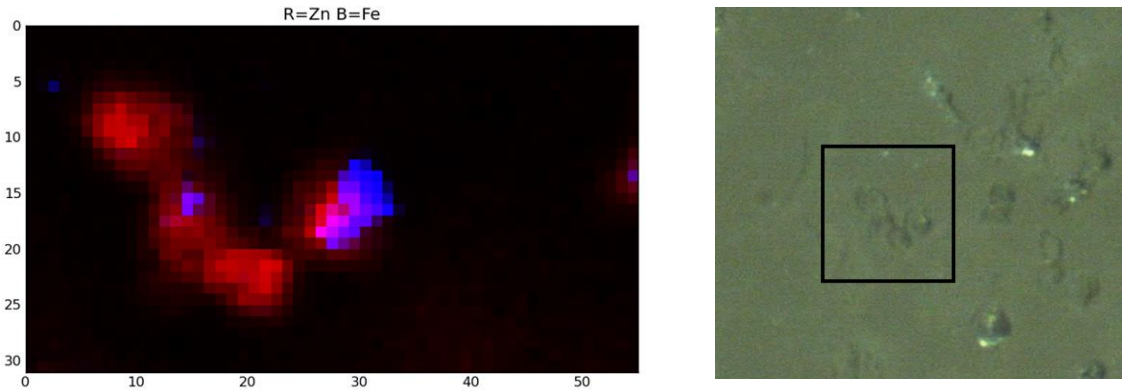

Figure 4.23 A2780 cells grown on sapphire windows, treated with 40µM iron(II) chloride $FeCl_2$ for 24 h followed by snap freezing fixation. Camera image of the A2780 cells to be mapped using XRF microscopy. Overlay of Zn and Fe elemental maps.

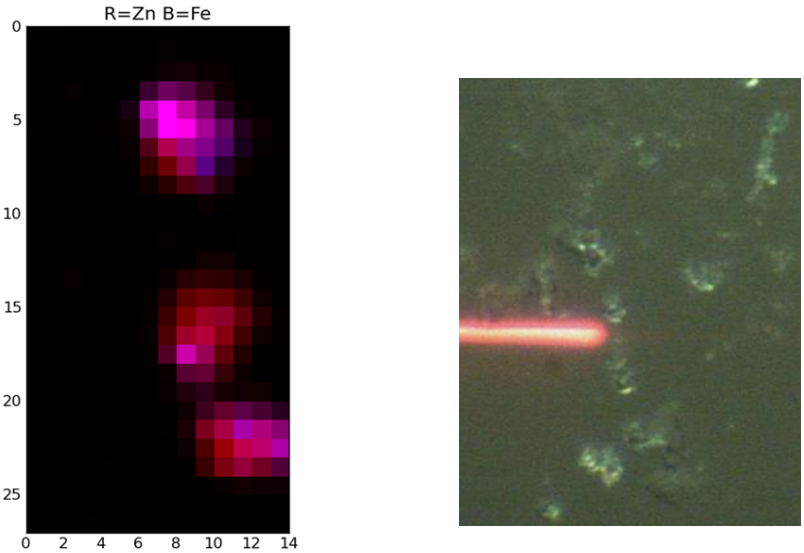

Figure 4.24 A2780 cells grown on sapphire windows, treated with 200µM iron(II) chloride $FeCl_2$ for 24 h followed by snap freezing fixation. Camera image of the A2780 cells to be mapped using XRF microscopy. Overlay of Zn and Fe elemental maps.

Elemental map overlays of MDA-231 cells treated with $FeCl_2$ at 40 µM for 4 hours shows very little correlation between iron and the cellular distribution of zinc. Iron appears to be distributed around the cell and hasn't been internalised within the cell. This corresponds with the distribution of iron seen in MDA-MB-231 complex treated samples (Figure 4.12 - Figure 4.17).

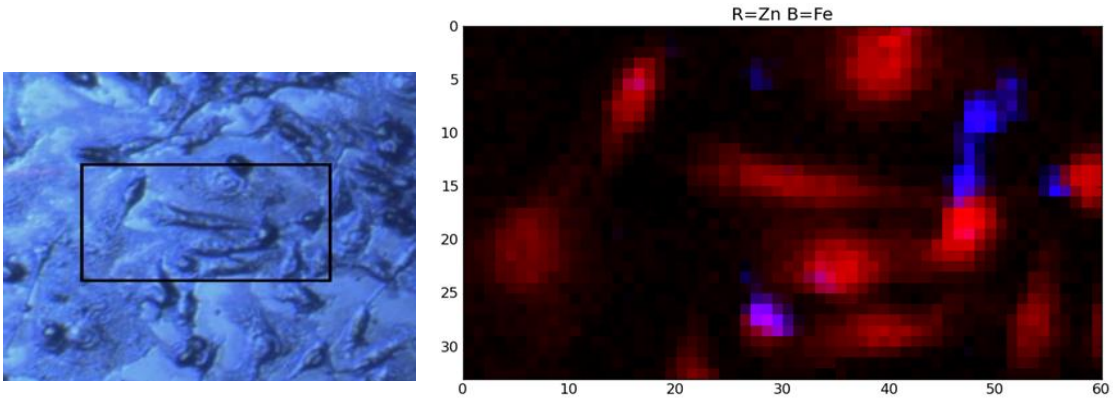

Figure 4.25 MDA-231 cells grown on sapphire windows, treated with 40µM iron(II) chloride $FeCl_2$ for 4 h followed by snap freezing fixation. Camera image of the MDA-231 cells to be mapped using XRF microscopy. Overlay of Zn and Fe elemental maps.

XANES scans were taken through an iron containing area in A2780 cells treated with the metallo cylinder $[L_3Fe_2][Cl]_4$ for 4 hours. The obtained spectra (Graph 4.1) shows a similar shape to the iron standards of metallo cylinder bound to ct-DNA and iron (II) phosphate. This indicated that iron inside the cell has a 2^+ oxidation state and is appears intact within the cell.

During the experiment the cryostat broke, which meant that XANES scan couldn't be obtained, as the process would cause too much damage to the cells at room temperature. This meant that iron rich areas in the elemental maps couldn't be further investigates to examine the ions coordination environment and oxidation state, which would allow examination of the stability of the complex.

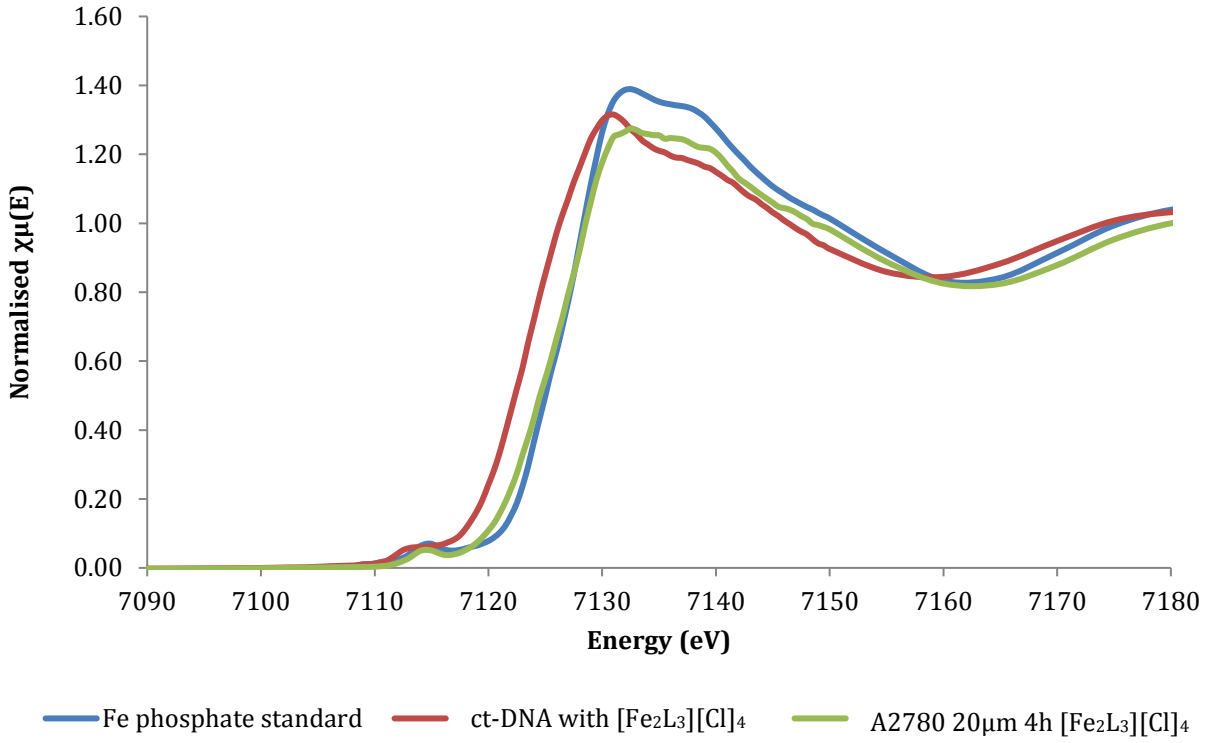

Graph 4.1 XANES spectrum, taken of iron(II) standards of iron phosphate, iron metallo cylinder bound to ct-DNA and through an iron rich area of an A2780 cell sample treated with metallo cylinder for 4 hours at 20 μM.

4.5 Bromine cylinders

Bromine modified cylinders were developed to allow co-localisation experiments of bromine and iron to be undertaken. This will give insight into whether the cylinder remains intact once inside the cell. A strong correlation in the elemental maps for bromine and iron would suggest the complex remains intact. Whereas if no correlation is observed, the complex has degraded and the ligand has 'fallen off' the metal ion.

4.5.1 Synthesis of bromine cylinders

5-bromo-2-pyridnecarbldehyde was dissolved in methanol, followed by the dropwise addition of 4,4′-methylenedianiline dissolved in methanol (

Figure 4.26). The solution was stirred for 20 hours at room temperature; producing a white precipitate that was collected by filtration. The ligand (L^{Br5}) was obtained in an 83% yield and fully characterised using ^{13}C NMR, MS and ^{1}H NMR (Figure 4.27). In ^{1}H NMR the

imine peak (H_4) can be observed as a strong singlet, the loss of the aldehyde peak from the starting material confirms the condensation reaction has been successful.

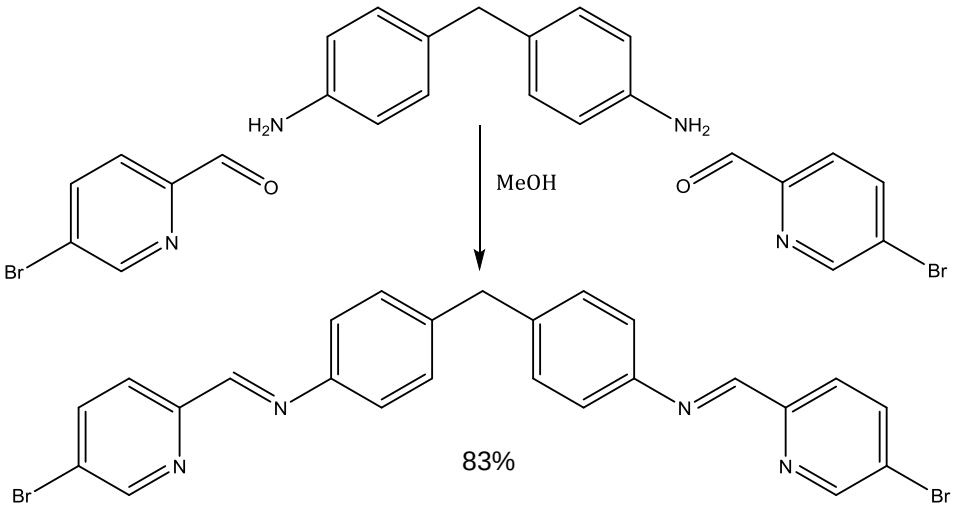

Figure 4.26 Synthesis of bromine functionalised ligand L^{Br5}.

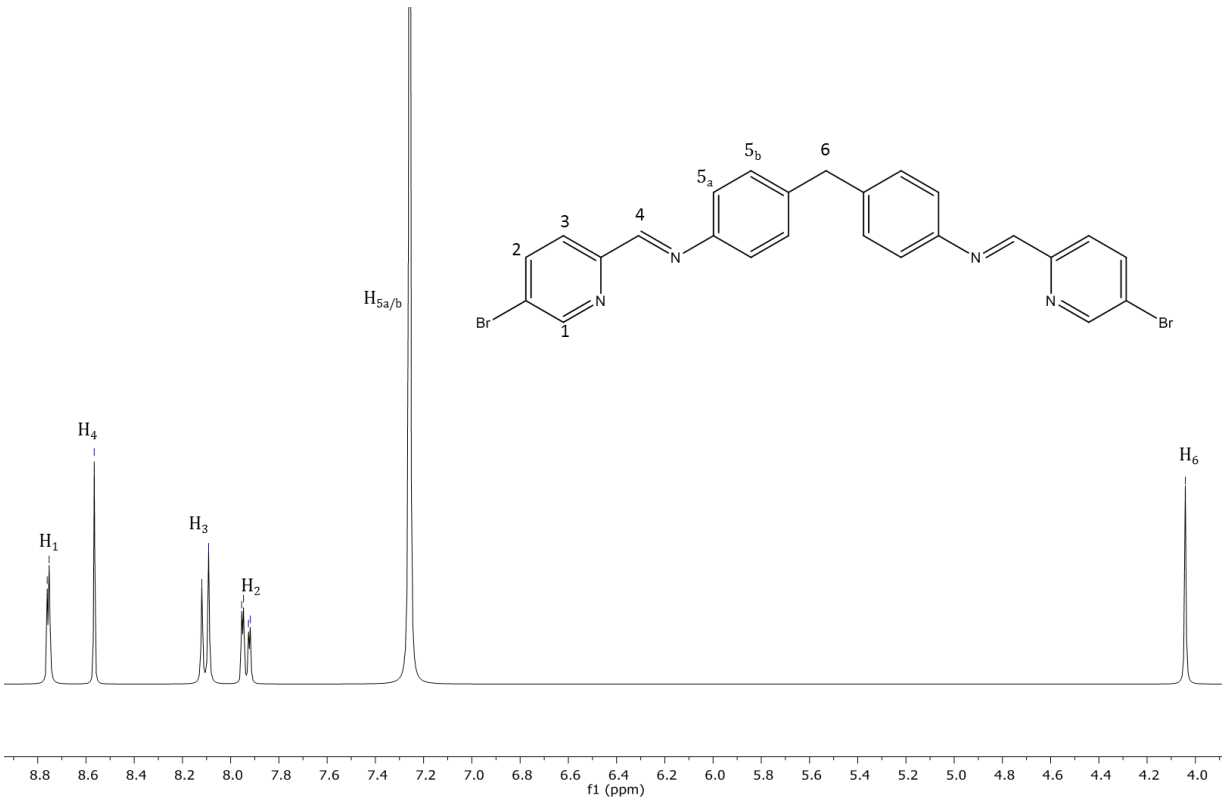

Figure 4.27 ^{1}H NMR (300 MHz, $CDCl_3$, 298 K) of the pyridylimine ligand functionalised in the 5th with bromine L^{Br5}.

The ligand L^{Br5} was suspended in methanol and $FeCl_2$ (dissolved in methanol) was added dropwise to the stirred ligand. Upon addition of the metal salt, the solution turned a characteristic purple colour, showing formation of a metal complex due to the MLCT band at 573nm, giving rise to the intense colour. The product was precipitated from solution by the addition of ammonium hexafluorophosphate, collected and dried. The product was obtained in an 84% yield and fully characterised; the ^{1}H NMR spectra (Figure 4.28) shows the formation of the product, indicated by the broad peaks for H_{5a} and H_{5b}. In the ligand these hydrogens are equivalent, indicated by the strong singlet peak at 7.26 ppm in the ^{1}H NMR (Figure 4.27). Upon coordination to the metal, these protons become inequivalent and occupy two different environments, shown by the two board singlets in the complex ^{1}H NMR (Figure 4.28).

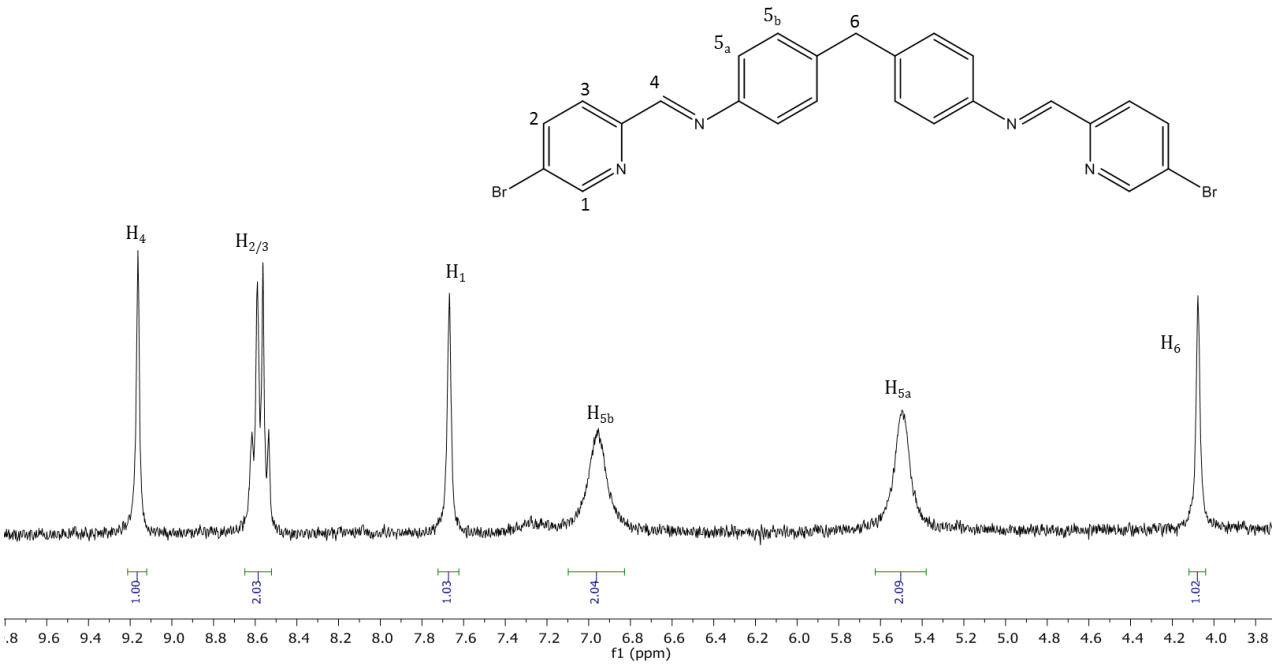

Figure 4.28 ^{1}H NMR (300 MHz, MeCN, 298 K) of the complex $[Fe_2L^{Br5}{}_3][PF_6]_4$.

To further examine the stability of the complex the bromine functionalised group was also synthesised at the 4th positon of the pyridine ring. The ligand, L^{Br4}, was prepared as described above using 4-bromo-2-pyridnecarbldehyde and 4,4′-methylenedianiline in a 2:1 ratio, giving an 88% yield of product (

Figure 4.29). Confirmation of ligand L^{Br4} formation is shown by the ^1H NMR (Figure 4.30), appearance the imine peak (H_4) and loss of the aldehyde peak, prove the condensation reaction was successful.

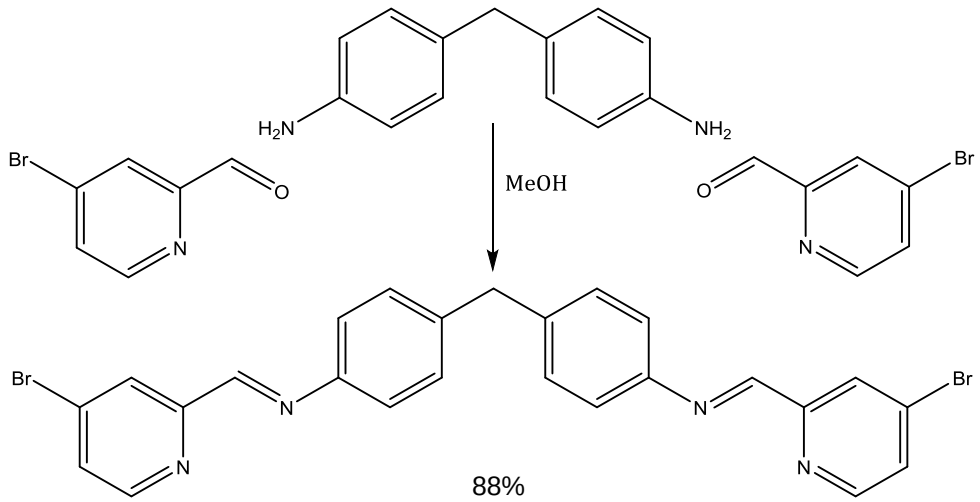

Figure 4.29 Synthesis of the bromine functionalised ligand L^{Br4}, with Br in the 4th position of the pyridine ring.

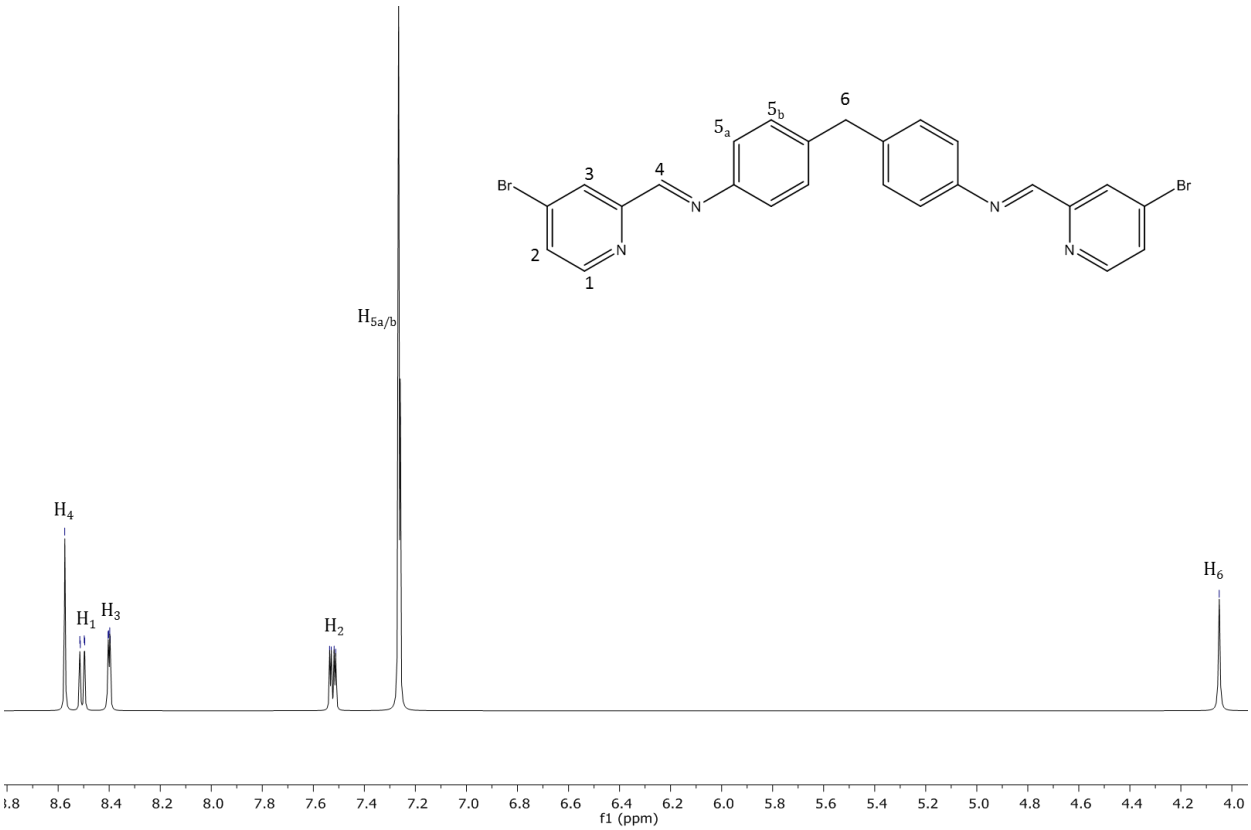

Figure 4.30 ^1H NMR (300 MHz, $CDCl_3$, 298 K) of the pyridylimine ligand functionalised in the 4th position with bromine.

The ligand L^{Br4} was reacted with $FeCl_2$ as described above. The ^1H NMR of the complex (Figure 4.31) shows the aromatic protons have split into two broad peaks (H_{5a} and H_{5b}), showing coordination to the metal centres causing them to be inequivalent.

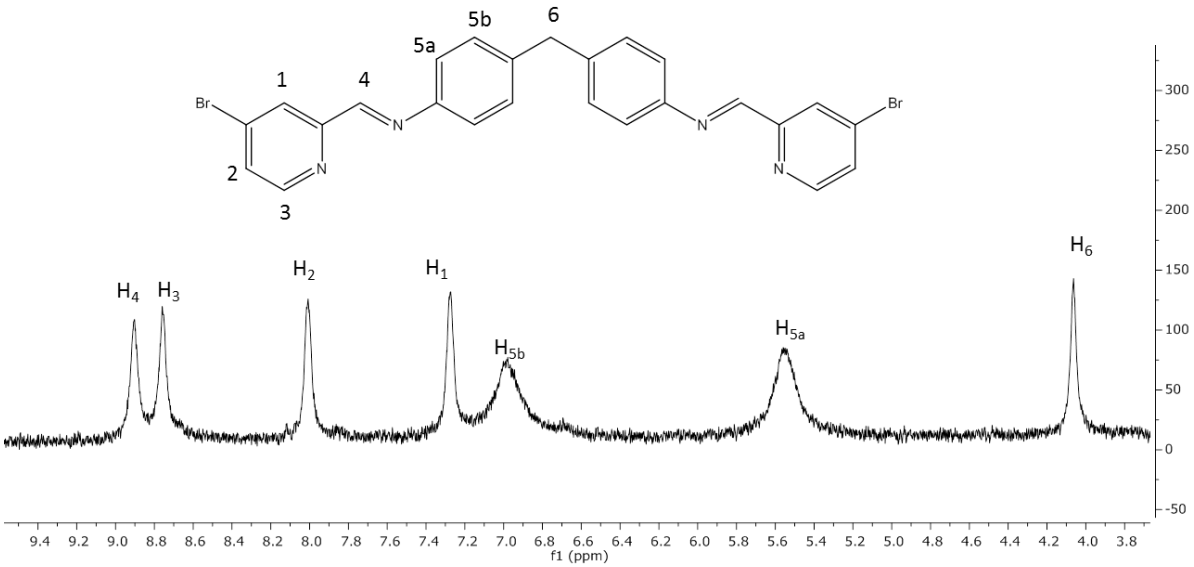

Figure 4.31 ^1H NMR (300 MHz, MeCN, 298 K) of the complex $[Fe_2L^{Br4}{}_3][PF_6]_4$.

4.5.2 Stability of bromine cylinders

UV-vis stability studies were undertaken to assess if the complexes were stable in an aqueous environment, which is essential for effective cellular uptake and treatment. 100 μM solution of $[Fe_2L^{Br5}{}_3][PF_6]_4$ and $[Fe_2L^{Br4}{}_3][PF_6]_4$ was prepared in 3% acetonitrile/water mixture. The acetonitrile was used to dissolve the complex, and diluted to 100 μM using ultra-pure milliQ water. A background of acetonitrile/water mixture (3:97) was run before experimental measurements were taken. UV-vis spectra were taken of the complex solutions over 4 hours, at 1 h time points (Graph 4.2) for complex $[Fe_2L^{Br5}{}_3][PF_6]_4$ and over 6 hours for complex $[Fe_2L^{Br4}{}_3][PF_6]_4$. Between measurements the complexes was left inside the machine in the dark at room temperature.

The peak at 575 nm represents the MLCT band of the complex; for this to be present the ligand has to be bound to the metal. Observed over time, the intensity of the peak decreases for $[Fe_2L^{Br5}{}_3][PF_6]_4$, and after 4 hours the double humped shape of the broad

peak has almost flattened out. The loss of the MLCT band indicates the complex is degrading within the time scale of the experiment, in aqueous solution. This indicated degradation of the complex and that it is unstable in aqueous solution over. Upon removal of the sample from the UV-vis machine the solution has a very faint purple hue compared to the deep purple colour observed when the complex is first formed, further confirming the degradation of the complex and loss of the MLCT band.

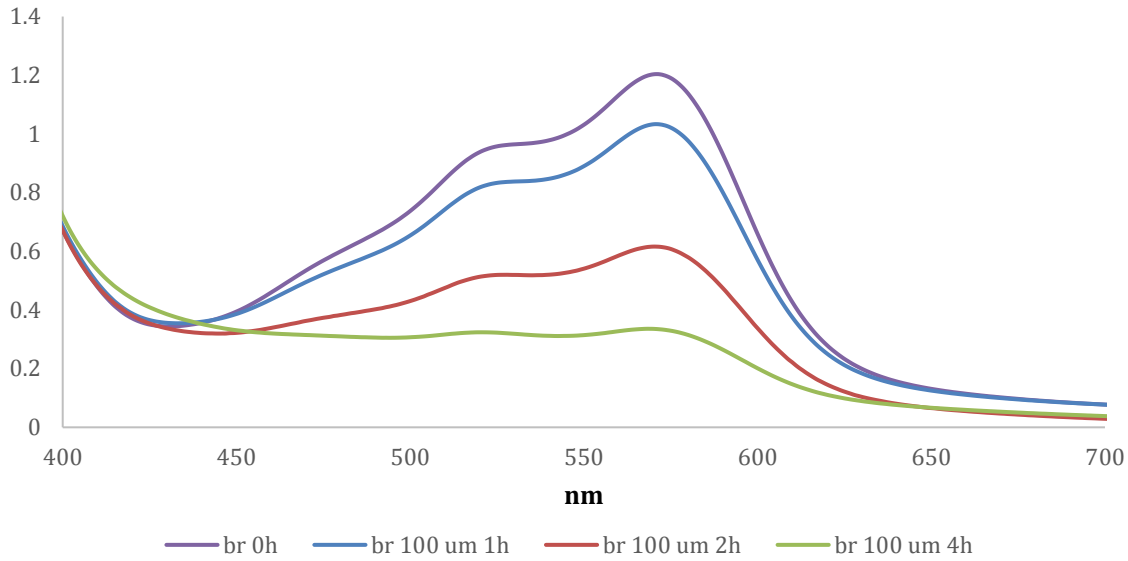

Graph 4.2 Stability of 100 µm Fe(II) bromine-5 cylinder over 4 hours in MeCN/milliQ water (3:97).

The UV-vis stability study was repeated with $[Fe_2L^{Br5}_3][PF_6]_4$ with the addition of 30 µM ct-DNA. The addition of ct-DNA greatly improves stability of the complex. The defined double humped shape from 500-600nm is still observed after 12 hours. This may be due to the complex binding to the major groove of DNA and being stabilised by the electrostatic forces holding it in place. After 78 hours the MLCT peak at 575nm still has an intensity above 1, in comparison to the intensity of the peak after 4 hours without ct-DNA, where the intensity drops below 0.3.

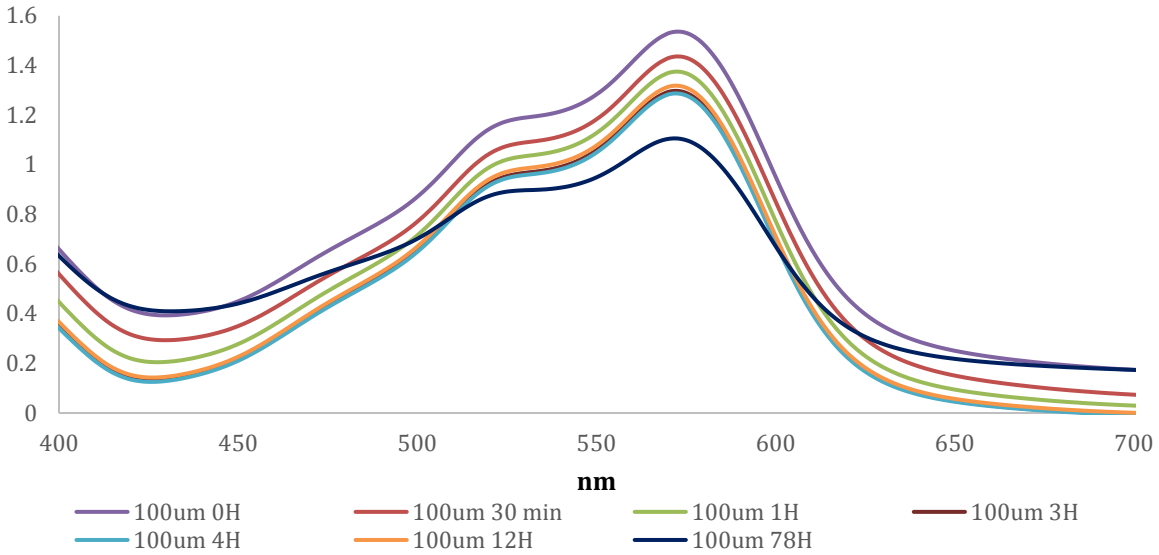

Graph 4.3 Stability of 100 µm Fe(II) bromine-5 cylinder over 78 hours in MeCN/milliQ water (3:97) with 30 µm ct-DNA.

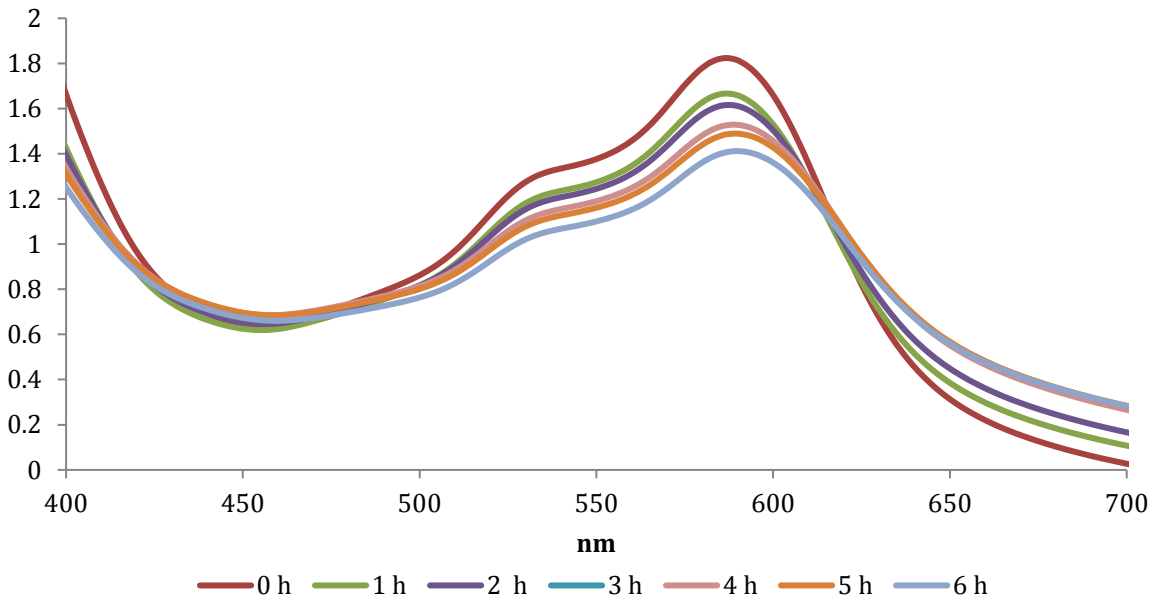

Graph 4.4 Stability of 100 µm Fe(II) bromine-4 cylinder over 6 hours in MeCN/milliQ water (3:97).

The iron(II) bromine functionalised complex $[Fe_2L^{Br4}{}_3][PF_6]_4$ shows increased stability in its UV-vis spectrum in acetonitrile/water (3:97), compared to complex $[Fe_2L^{Br5}{}_3][PF_6]_4$ (Graph 4.4). After 6 hours a well-defined MLCT band is still observed, with maxima at 590nm. This increase in stability is due to the increased spaced distance between the bromide groups at the ends of the complex (Figure 4.32 Structure of LBr4 and LBr5). Any repulsion effects caused to the close proximity of three bromine groups has been reduced.

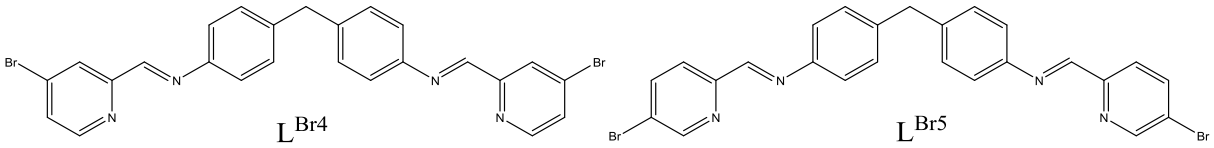

Figure 4.32 Structure of L^{Br4} and L^{Br5}

4.5.3 Synchrotron XRF imaging of bromine cylinders

Once the relative stabilities of the bromine cylinders were analysed, synchrotron imaging samples were prepared as described previously (4.2.2 Biological sample preparation). Except the bromine modified complex was dissolved in MeCN and added to the cell media in the 6 well plate. The volume of MeCN was kept at 3% during dilution with cell media. Samples were washed after treatment and snap frozen as described above (4.2.2 Biological sample preparation). Only short treatment periods were undertaken, ranging from 30 minutes to 4 hours. This was due to the instability of the complexes in aqueous media as discussed in section 4.2.2 . As shown by the UV-vis experiments the complexes are stabilised upon binding to DNA. However, in a cellular environment the complex needs to enter the cell and reach the nucleus or mitochondria before it is able to bind to DNA and increase its stability.

MDA cells were used due to their large nucleus, this gave a large target area to be mapped and deduce if the complex has entered the nucleus. The cells of interest are shown in Figure 4.33 and are highlighted in the red box. The redline is the synchrotron beamline on the sapphire disc.

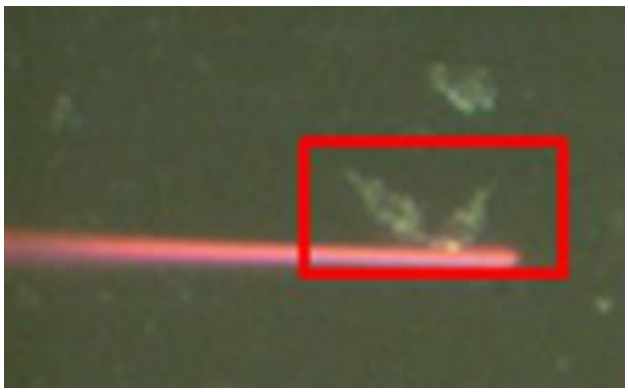

Figure 4.33 Camera image of MDA cells grown on a sapphire window treated with 100 µm $[Fe_2L^{Br5}{}_3][PF_6]_4$ for 30 min, snap frozen and held at liquid nitrogen temperature by a cryostat. The image was recorded on I18 at Diamond Light Source. The red box shows the cells used to produce elemental maps.

Elemental maps of Zn, Cl, Fe and Br were taken across the sample. The outline of the cells can clearly be observed in the Cl and Zn map of the sample and correlates with the cell shape observed in the camera image. The elongated shape and morphology of the cells observed on the camera image shows that were healthy, adhered and in a healthy state before snap freezing. This confirms that the small volume of acetonitrile used to administer the complex has had little effect on the cells. The elemental iron map (Figure 4.34) shows the presence of iron inside the cell after treatment with $[Fe_2L^{Br5}{}_3][PF_6]_4$ for 30 minutes. The bromide maps also show the presence of bromine inside the cell but also in defined clusters around the perimetre of the cell. This suggests that some of the complex has degraded before being uptaken by the cells. Although there is iron and bromide inside the cell there is no strong co-localisation between the two. This suggests that the complex has degraded before reaching the nucleus, where it could have been stabilised by binding to the DNA.

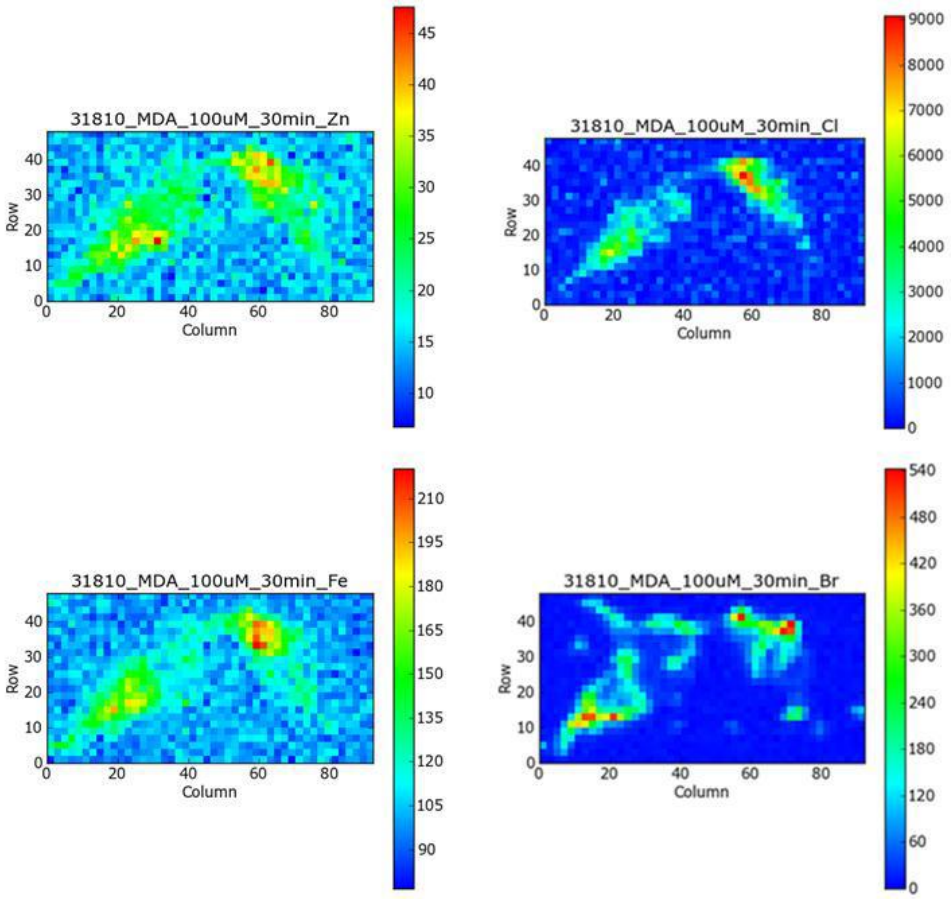

Figure 4.34 Elemental maps of chlorine, zinc, iron and bromine produced by x-ray synchrotron imaging of MDA-MB-231 cells treated with 100 µm $[Fe_2L^{Br5}{}_3][PF_6]_4$ for 30 min, shown above in the red box in Figure 4.33.

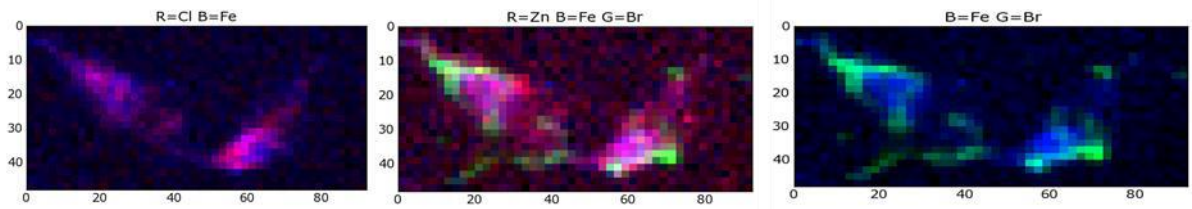

Figure 4.35 The overlay of chlorine and iron elemental maps of MDA-231 cells treated with 100 µm $[Fe_2L^{Br5}{}_3][PF_6]_4$ for 30 min, that show iron inside the cell. The overlay of zinc, iron and bromine maps showing the presence of bromine inside the cell. The overlay of iron and bromine inside the cell, however there seems to be little correlation between the distribution of iron and bromine.

A2780 cells have been treated with the iron bromine complex $[Fe_2L^{Br4}{}_3][PF_6]_4$ at 20 µM concentration for 30 minutes, to allow the maps obtained, to be comparable to those produced following treatment of $[Fe_2L^{Br5}{}_3][PF_6]_4$. A2780 cells have also been treated with the bromine functionalised ligand L^{Br4}, it examine if bromine distribution is comparable to that observed in $[Fe_2L^{Br4}{}_3][PF_6]_4$ treated cells.

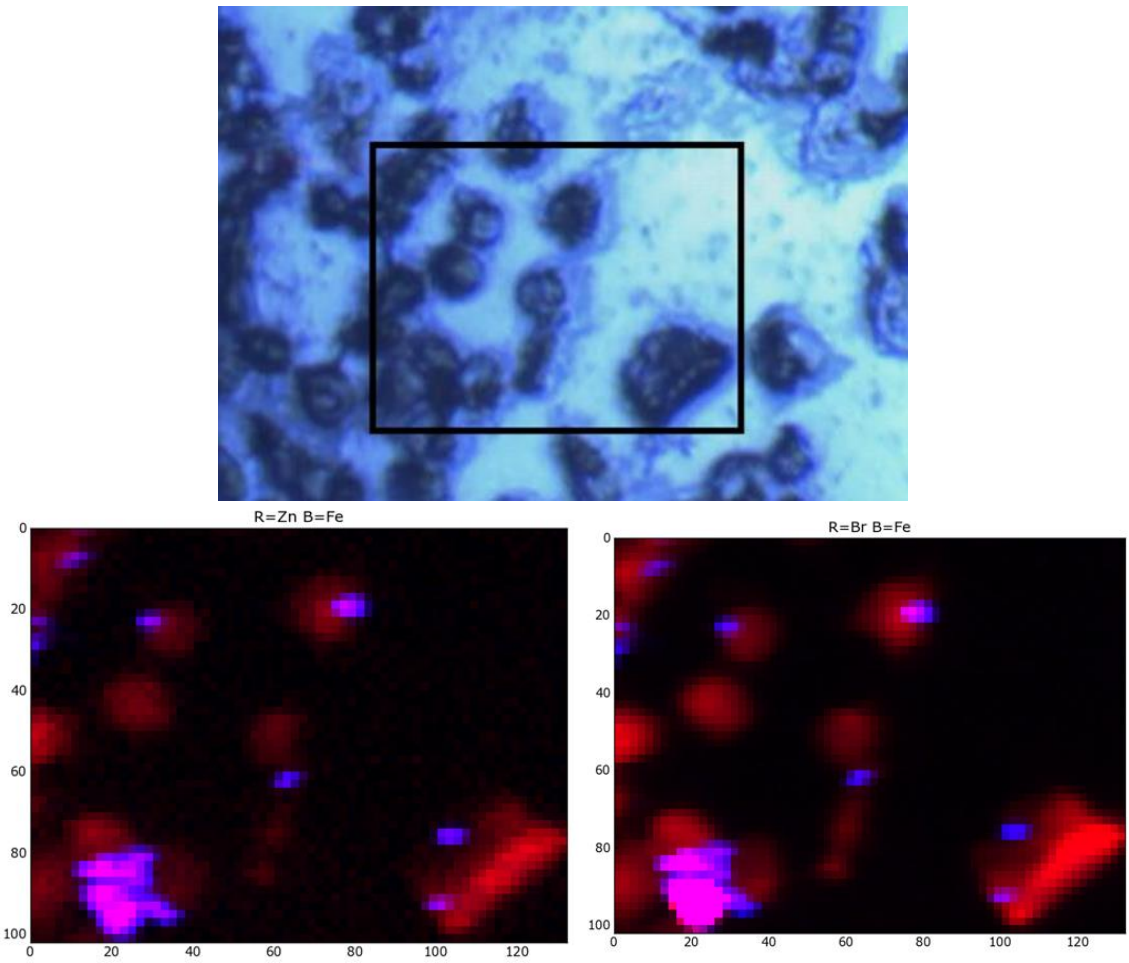

Figure 4.36 A2780 cells grown on sapphire windows, treated with 100 µM $[Fe_2L^{Br4}{}_3][PF_6]_4$ for 0.5 h followed by snap freezing fixation. Camera image of the A2780 cells to be mapped using XRF microscopy. Overlay of Zn and Fe elemental maps, and Br and Fe elemental maps.

In A2780 cells treated with the complex, there is weak correlation between the distribution of bromine and iron throughout the cell. Bromine appears to be distributed through the whole cell and shows strong correlation with the distribution of zinc, whilst iron is in defined regions. This is surprising due to the greater stability observed by the $[Fe_2L^{Br4}{}_3][PF_6]_4$ complex in aqueuos enviroment, in comparison to is 5th position counterpart. In UV-vis experiments the complex appears realative stable for up to six hours, and the cell sample has only been tretaed for 30 minutes. The complex may have been uptake into the cell and broken down inside the cell due to components within the cell. In comparison the bromine distribution in ligand (L^{Br4}) treated cells, at 100 µM for 30 minutes, appears to bein well defined regions that show little correclation with the

zinc maps, indicating bromine is out side of the cell. This would again suggest that the complex enters cells intact, then degrades, leaving bromine inside the cells.

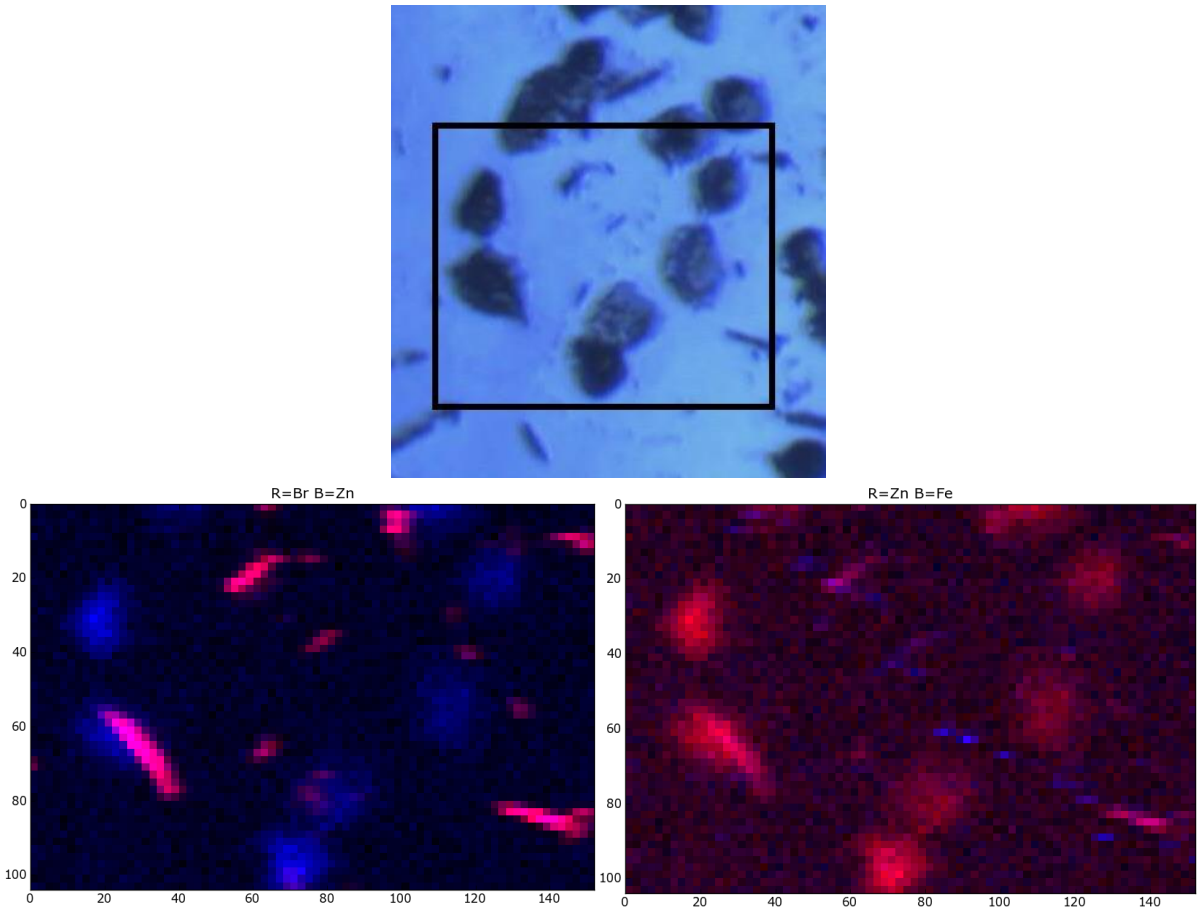

Figure 4.37 A2780 cells grown on sapphire windows, treated with 100 µM Ligand-L^{Br4} for 0.5 h followed by snap freezing fixation. Camera image of the A2780 cells to be mapped using XRF microscopy. Overlay of Zn and Fe elemental maps, and Br and Zn elemental maps

4.6 Cryo soft x-ray tomographic imaging

4.6.1 Introduction

Beamline B24 is a full field transmission microscope, which allows biological samples to be tomographically imaged under near physiological conditions. This technique uses soft X-rays around 500eV in the 'water window'. The 'water window' is the region between the K-absorption edges of carbon at 284eV and oxygen at 543eV. Between these two energies oxygen is virtually transparent to x-rays, however carbon is highly absorbing. This gives rise to natural contrast in the sample between the carbon containing organelles/structures of the cell and the vitreous ice surrounding the sample. This allows

biological samples to be imaged with a resolution of around 30-40nm. The data collected in the water window allows features such as membranes and mitochondria structures to be clearly visualised. This technique allows transmission electron miscopy style images to be obtained without the need for cell fixation, staining with heavy metals or sectioning. Samples are plunge frozen, allowing samples to be 'fixed' without the need for chemicals, therefore cells can be viewed in as close to a natural physiological state as possible. The images obtained are from 3D data collected on whole unstained biological cells.

4.6.2 Literature examples of cryo soft X–ray tomographic imaging

Cryo soft X-ray tomography (cryo-SXT) provides 3D nanoscale information from unstained, cryopreserved whole cells. G361 (malignant melanoma cells) have been cryo preserved and imaged using cryo soft X-ray tomography. The images produced show clear well defined organelle structures, including the nucleus, cell membrane, mitochondria, endoplasmic reticulum, nuclear envelope and nuclear pores[6]. These images show cells in as close a natural state as possible, due to removal of chemical fixation.

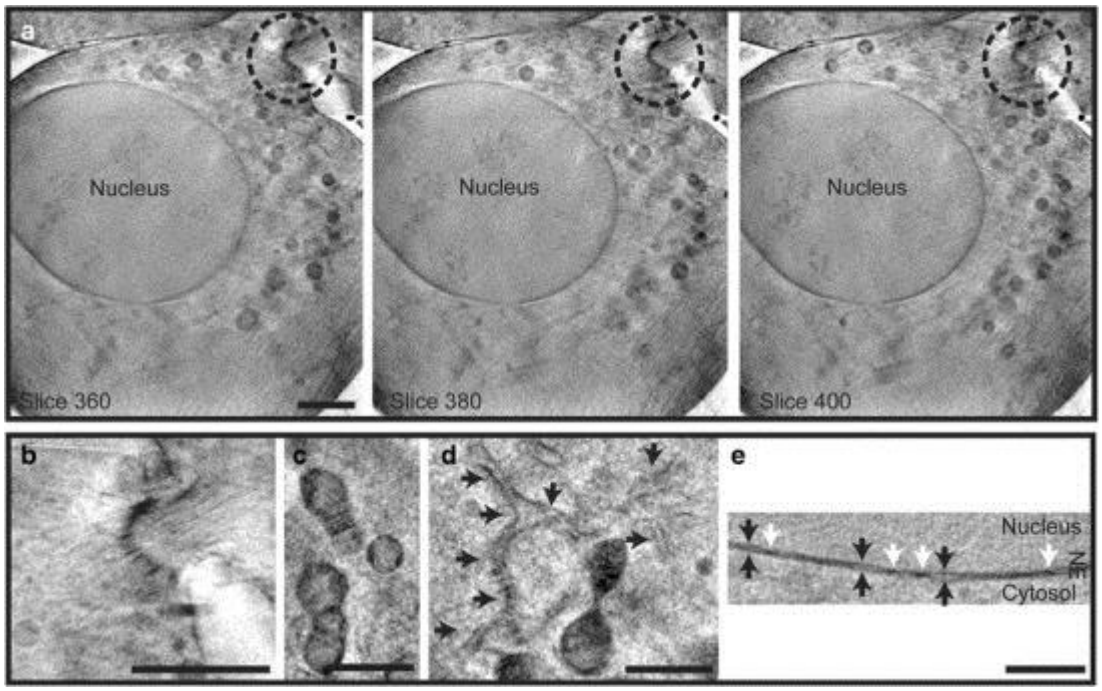

Figure 4.38 a. Images from a reconstructed tomogram of dividing G361 cells taken using Cryo-SXT (Soft X-ray Tomography). The nucleus, cell membrane and intercellular bridge (circled). b. magnification of the intercellular bridge. c. mitochondria with christae. d. Endoplasmic reticulum (arrows). e. nuclear envelope (white arrows indicate nuclear pores). (Images taken from reference[6]).

This technique also allows yeast ultrastructure to be imaged, which has previously proved difficult due to its thick cell wall[7]. The cell wall is traditionally removed prior to chemical fixation, disrupting the cells native structure[7]. Cryo fixation and soft X-ray tomography allows the internal vesicles to be clearly imaged and 3D models of the cell to be produced.

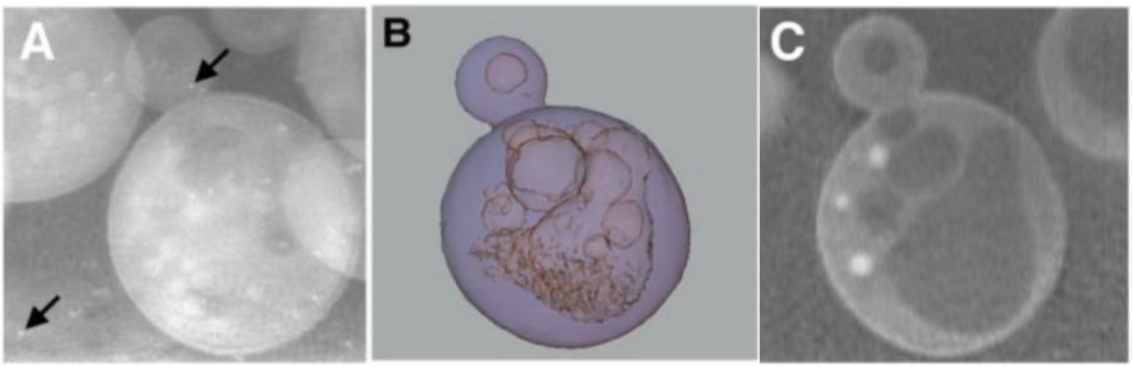

Figure 4.39 A. X-ray image of *Saccharomyces cerevisiae* (arrows show gold fiducial markers used in the alignment of tomographic images) B. Reconstructed data of yeast cells (in A. and C) using transparent surface analysis showing internal vesicles. C. computer generated image section from reconstructed data (dense lipid droplets appear white, organelles and large vacuoles appear dark due to their low density. (Image taken from reference[7]).

Cryo-SXT has been used in correlation with cryo-fluorescence microscopy to allow whole cell imaging of endosomes and autosomes in mammalian Hek293 cells. Early endosomes were located by using an anti-transferrin receptor antibody conjugated to 10nm gold nanoparticles; these have been segmented in Figure 4.40, and represented in yellow, with the up taken gold nanoparticles visible as black dots inside the endosome[8]. The fluorescent marker GFP (green florescent protein) was attached to LC3(Atg8); an autophagy specific protein recruited to forming autophagosomes. Red fluorescent protein (RFP) was attached to Atg9; an autophagy transmembrane specific protein essential in the formation of early autophagosomal structures. GFP-LC3 and RFP-Atg9 were located using a cryo-fluorescence stage in the laboratory. Cryo-SXT images were produced at the synchrotron to obtain the cellular ultrastructure. The 3D ultrastructure of endocytic and

autophagic structure was mapped and showed clusters of omegasomes coming from 'hotspots' on the endoplasmic reticulum[8]. Cryo-SXT and cryo-fluorescence microscopy can be used in conjunction with immunogold markers to analyse cellular process that would be inaccessible using other imaging modalities[8].

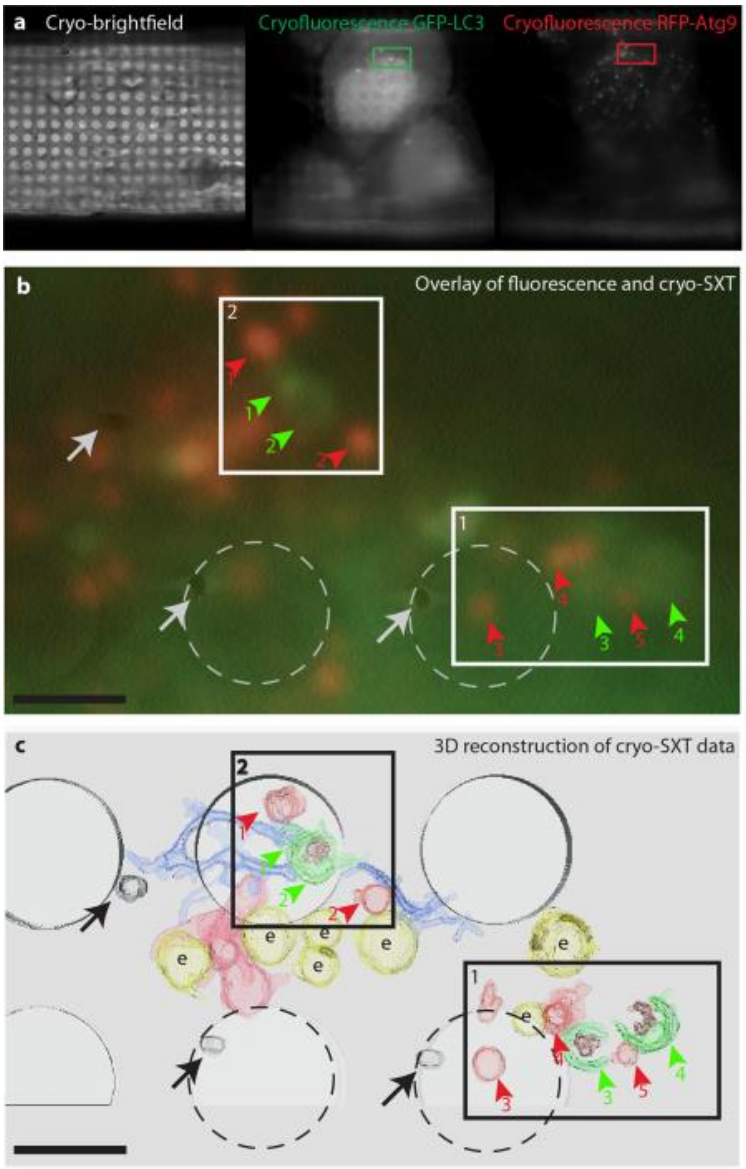

Figure 4.40 Cryo – CLXM of omegasomes in starved HeK293 cells. a. the cryo bright field, cryofluorescence GFP-LC3, cryofluorescence RFP-Atg9 image. b. overlay of the fluorescent green and red channels (red arrows RFP, green arrows GFP, Quantifoil holes indicated in white). c. 3D reconstruction of cryo-SXT data, with features being manually segmented and rendered using Amira Software. (Quantifoil holes shown as grey circles, gold fiducials indicted by grey arrows, Atg9-VTC-red, LC3-positive omegasomes – green, endosomes – yellow containing anti-TfnR-gold – shows as black dots inside the endosome, endoplasmic reticulum – blue)((Images taken from reference [8])

4.6.3 Aims

The aim of this experimental is to obtain whole cell images of cells treated with parent metallo iron(II) cylinder. To examine the effects, it has on the morphology of the cell. The advantage of this technique is the removal of chemical fixation; allowing cells to be viewed in a natural physiological state. This means any changes in the cell morphology can be attributed to the metallo cylinder rather than chemical fixation.

4.6.4 Sample preparation for cryo soft X–ray tomographic imaging

HeLa and MDA-231 cells were seeded into MatTek dishes and left to adhere for 24 hours. Cells were stained with the membrane dye DiI and z-stacks were taken of the cells to ascertain their thickness. The height of 10 separate cells was taken and used to calculate an average thickness for each cell type. MDA -231 cells had an average height of 14 μm, and Hela cells an average height of 9μm. This technique has a cell thickness limit of 5-10μm, which eliminated MDA-231 cells from the experiment. Hela cells were used as they were within the thickness limit.

Cells were grown directly on gold 3mm TEM grids; covered with carbon Quantifoil film, with holes of 2 nm, separated by 2 nnm. The TEM grids were sterilised by dipping in 70% ethanol, then air dried in a laminar flow hood. One grid was placed in each well of a six well plate. Hela cells were seeded at 20,000 cells per well in 3 mL of media, as the grid needs to have a final confluence below 20%. Cells were treated with metallo cylinder at 20 μM concentration for 24 hours or 4-hour time points. The grids were gently washed with PBS and fresh media was added. The well plates where then plunge frozen by Paul Stanley (University of Birmingham, materials and metallurgy). Each disc was removed from the well plate with tweezers and placed in the plunge freezer (Figure 4.41). Samples were blotted from behind for 2 seconds to remove excess moisture from the sample that was drawn from the front of the sample through the holes in the Quantifoil film. The disc

was then plunged into liquid nitrogen cooled liquid ethane for vitrification. Grids were transferred into cryo TEM grid storage boxes, which were subsequently placed into a dry shipper and at liquid nitrogen temperature. Samples were transported to the Diamond Light Source and imaged within 2 days of preparation.

Figure 4.41 Photos of the Cryoplunge 3 used to plunge freezer gold TEM grids in liquid nitrogen cooled liquid ethane.

4.6.5 Beamline set-up

During the experiments, the beam line was still under construction therfore these were some of the first experiments to be conducted on beamline B24. As the beamline was still under construction it was not connected to the synchrotron; therefore, X-rays were generated by a nitrogen plasma source. The schematic setup of the beamline is shown in Figure 4.42, the beam passes through the shield wall and is deflected through a variable line spacing – plain grating monochromator (VLS-PGM) by a horizontal deflection torroidal mirror. The beam is directed to the focal point of the PGMs exit slits. The beam is then focused onto the sample grid by a capillary condenser. A 40 nm zone plate then refocuses the resulting image onto a CCD direct detector.

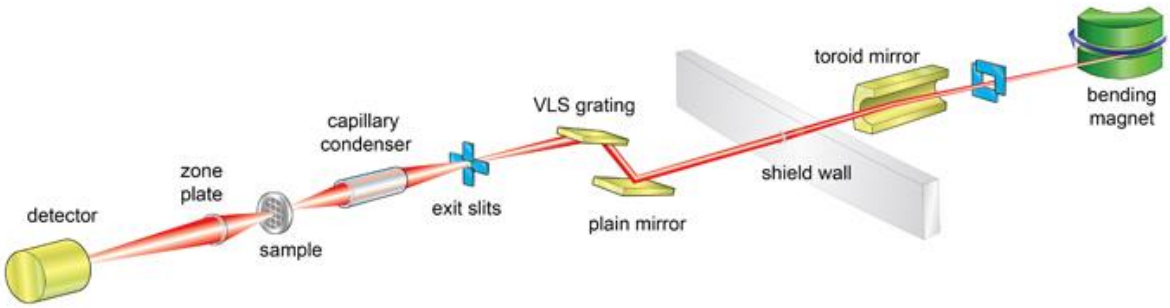

Figure 4.42 Schematic layout of beamline B24 at the Diamond Light Source.

The sample is fitted in to the sample holders, which can hold four TEM grids, this is done under liquid nitrogen (Figure 4.43). The sample holder arm is then inserted into the machine and the chamber is kept at constant cryo-temperature throughout the experiment. The sample is then exposed to soft X-rays and the signal obtained at the detector is used to generate the image.

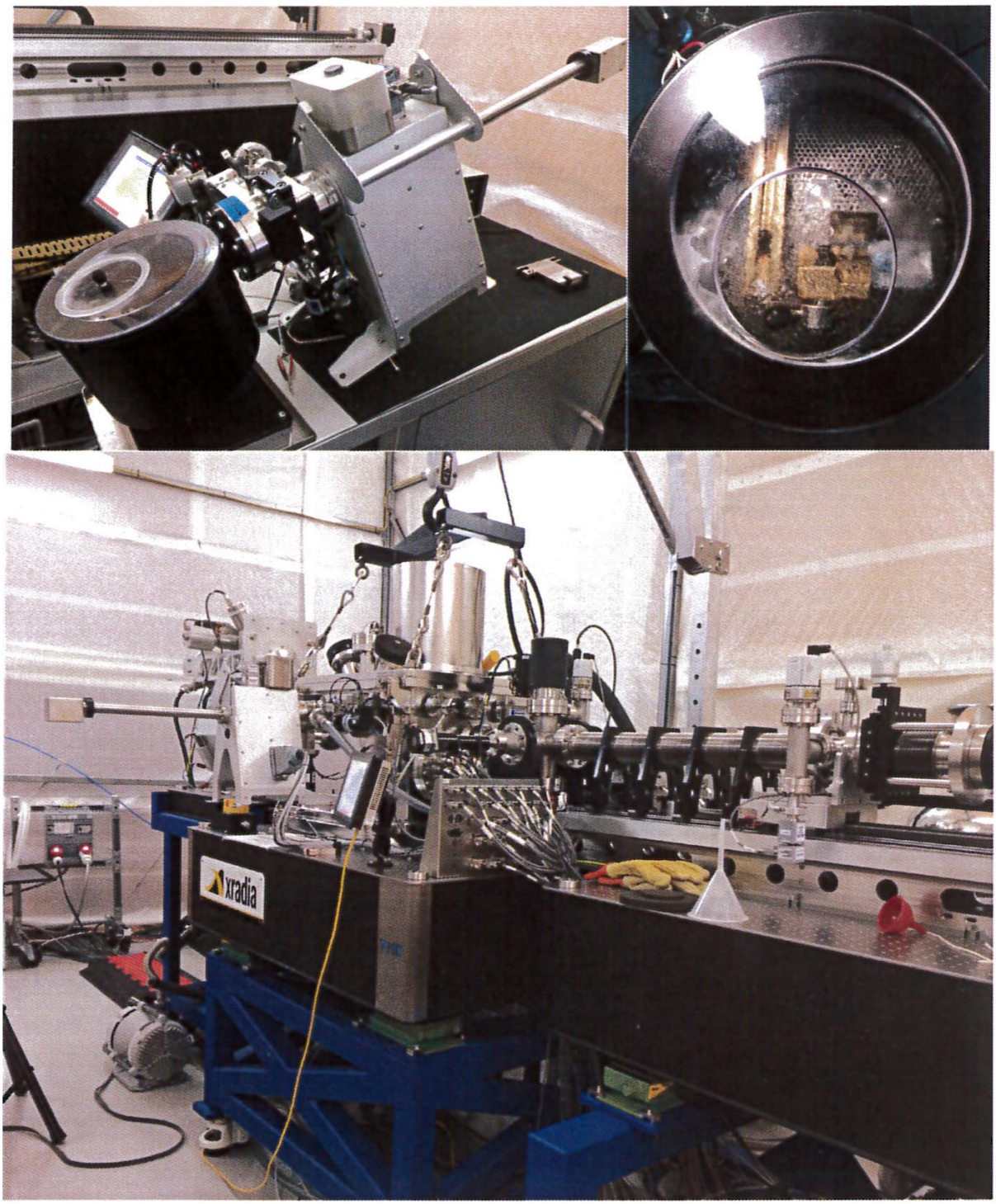

Figure 4.43 Images of the experimental beamline set up on beamline B24 at the Diamond Light Source.

4.6.6 Results of cryo soft X–ray tomographic imaging

Sample preparation for this technique proved challenging, in particular the plunge freezing. As observed in Figure 4.44 some samples were covered with a thick layer of ice, this is due to inefficient blotting; caused by either over confluent cells or too short a blot

time. In other samples where plunge freezing was successful the cells appear to be dying as they appear spherical and have lost their defined elongated morphology. Unfortunately, the plunge freezing facility is located a distance from the cell incubator, meaning cells are out of the incubator for a considerable time prior to plunge freezing. Every effort was made to maintain the cells temperature, transporting them in a thick walled polystyrene box lined with tin foil, containing filled sealed boxes of warm water in an attempt to maintain the temperature. The plunge freezer is also only used sporadically and due to the flammable nature of ethane gas, Paul Stanley plunge froze the samples on my behalf. This didn't allow me to develop the technique of plunge freezing for future samples.

Attempts to image the spherical HeLa cells were undertaken, but the cells proved too thick for the technique, their increased thickness is probably due to them balling up. A second batch of samples was prepared using HeK cells as these are thinner with an average thickness 5µm. However, plunge freezing of these samples was also challenging and the cells again looked spherical in morphology.

Beamline B24 is now fully operational and has been joined to the synchrotron. The facility now has a dedicate plunge freezer and cell culture facility meaning future samples can be cultured, treated and plunge frozen all at one location with expert advice on sample preparation at hand. This technique has the ability to produce clear images as seen in the literature, with the main draw back for my experiments being plunge freezing. I believe this could be overcome by undertaking all stages of the experiment at Diamond Light Source. The Hannon group has also recently purchased a cryo stage that can be attached to an inverted microscope. This would allow samples to be screened at cryo temperature at the university prior to taking samples to Diamond. This would allow good quality samples be identified prior to vising Diamond, so that the beam time would be used focusing on good quality samples. A fluorescence cube has also been fitted to the beamline

now that it is fully operational. The parent ruthenium cylinder is weakly fluorescent; the fluorescence of ruthenium complexes is increased in samples at liquid nitrogen temperatures. As these experiments are conducted at cryo temperature, dual experiments could be undertaken. Gathering TEM style images showing structural details and morphological change as well as fluorescence experiments so that the localisation of the cylinder could be observed.

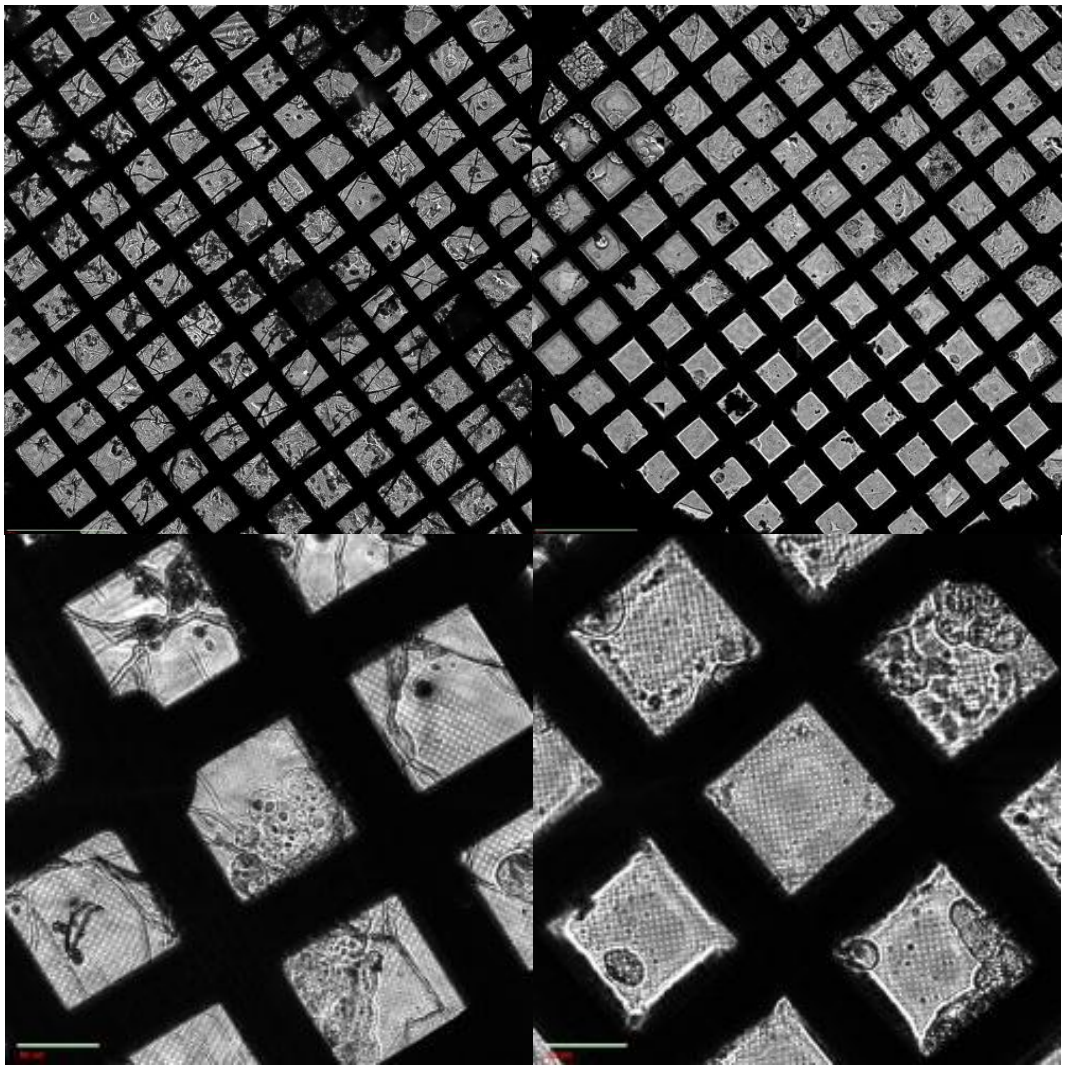

Figure 4.44 A. shows the layer of ice that is covering the TEM grid after plunge freezing with ice cracks visible in the sample. B. shows a sample that has been successfully plunge frozen, however, the zoom in of this sample C. shows that the cells balled up and have started to go into apoptosis. D. shows a zoom in of the ice layer on the TEM grid.

4.7 Conclusion and future work

In conclusion elemental maps of MDA-231 and A2780 cells have been successfully produced for a variety of complex treatment concentrations and time points. Sample preparation on sapphire discs and cell fixation using 'snap' freezing in cooled methanol has been successful.

Two novel bromine functionalised ligands have been successfully synthesised and characterised using ^{1}H NMR, ^{13}C and mass spectrometry.

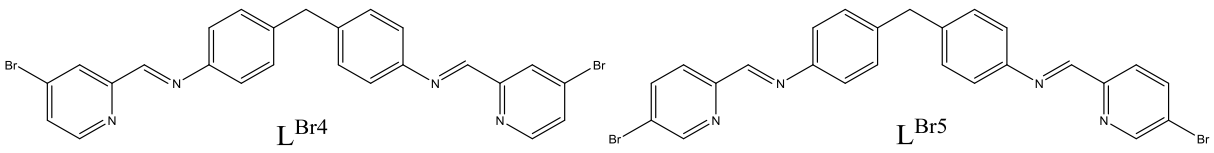

Figure 4.45 Structure of L^{Br4} and L^{Br5}

These have been successfully reacted with iron(II) chloride to form two novel complexes, which have been characterised using ^{1}H NMR and mass spectrometry. Their stability has also been tested in aqueous solution, and an increase in stability occurs by moving bromine from the 5th to the 4th position of the pyridine ring. The cellular uptake of these complexes has also been explored in MDA-231 and A2780 cell *via* synchrotron imaging, by the production of elemental maps.

Attempts to prepare TEM-grid sample has also been undertaken, with attempts to image these samples using cryo-SXT. Whilst cell growth and treatment was successful, plunge freezing was the major down fall in sample preparation.

In Future work cryo-SXT samples would be prepared at the Diamond Light Source to assure plunge freezing was undertaken correctly and eliminate the need to transport samples. Cells would also be treated with the ruthenium parent complex $[L^{p}{}_{3}Ru_{2}][PF_{6}]_{4}$, which has already been successfully synthesised (Figure 4.46). This would also dual

fluorescent and cryo-SXT images to be contained and overlaid. These images would allow localisation of the complex and morphological changes, which occur due to complex treatment, to be examined at the same time.

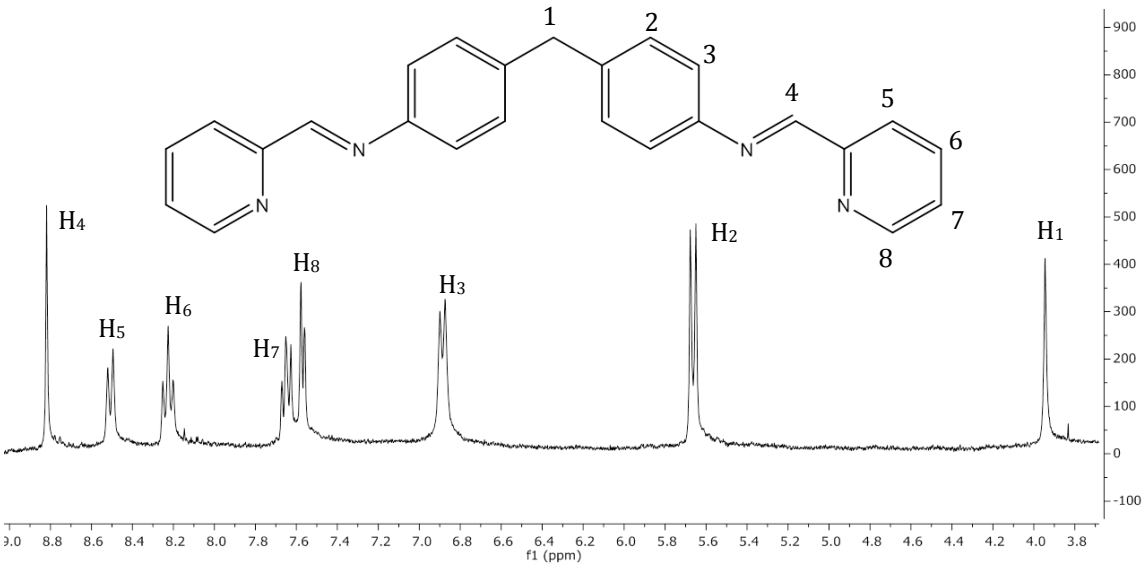

Figure 4.46 ^{1}H NMR (300 MHz, MeCN, 298 K) of $[L_3Ru_2][PF_6]_4$

More XANES experiment would be undertaken through iron containing areas of cells treated with the iron metallo-cylinder, to allow comparison to iron standards. Very few XANES measurements were taken during I18 beamline experiments, due to the technical difficulties experienced at the facility.

4.8 References

[1] "www.diamond.ac.uk,"

[2] D. L. Clark, **2006**, 2–4.

[3] M. D. Hall, C. T. Dillon, M. Zhang, P. Beale, Z. Cai, B. Lai, A. P. J. Stampfl, T. W. Hambley, *J. Biol. Inorg. Chem.* **2003**, *8*, 726–732.

[4] P. D. Bonnitcha, M. D. Hall, C. K. Underwood, G. J. Foran, M. Zhang, P. J. Beale, T. W. Hambley, *J. Inorg. Biochem.* **2006**, *100*, 963–971.

[5] M. J. Hannon, C. L. Painting, A. Jackson, J. Hamblin, W. Errington, *Chem. Commun.* **1997**, 1807–1808.

[6] R. Carzaniga, M. C. Domart, L. M. Collinson, E. Duke, *Protoplasma* **2014**, *251*, 449–458.

[7] C. A. Larabell, M. A. Le Gros, *Mol. Biol. Cell* **2004**, *15*, 957–962.

[8] E. M. H. Duke, M. Razi, A. Weston, P. Guttmann, S. Werner, K. Henzler, G. Schneider, S. A. Tooze, L. M. Collinson, *Ultramicroscopy* **2014**, *143*, 77–87.

Chapter 5

5 Experimental

5.1 General experimental

All solvents and commercially available reagents were purchased from Sigma-Aldrich, Fisher Scientific and VWR and were used without further purification. Deuterated NMR solvents were purchased from Goss Scientific and were used without further purification.

NMR spectra were recorder using a Bruker AVIII300 (300 MHz) and AVIII400 (400 MHz) spectrometer. Chemical shift (δ) are reported in parts per million (ppm), spectra are calibrated to the reference peak of the deuterated NMR solvent ($CDCl_3$ – 7.26/77.16 ppm, CD_3CN – 1.94/118.26 ppm, DMSO – 2.50/39.52 ppm, $(CD_3)_2CO$ – 2.05/29.84 ppm, CD_30D – 3.31/ 49.00 ppm, 1H and 13C respectively). NMR spectra were assigned based on the chemical shift and coupling constants, COSY, NOESY and HSQC experiments were used where necessary. Coupling constants (*J*) are quoted to the nearest 0.1 Hz and peak multiplicities are singlet (s), doublet (d) , triplet (t), quartet (q), quintet (qu) and multiplet (m).

Electrospray Ionisation Mass Spectrometry (ESI-MS) was performed on a Micromass LCT TOF Mass Spectrometer, with peaks shown as *m/z* values and reported in Daltons.

UV-Vis spectra were recoded using a Cary 500 Varian spectrometer, using quartz cuvettes with a 1cm path length.

Fluorescence emission and excitation spectra were recorded using a Shimadzu RF-5301 PC spectrofluorophotometer, using a quartz cuvettes with a 1cm path length.

Thin layer Chromatography (TLC) was carried out on pre-coasted aluminium sheets (Silica Gel 60 F254), retention factors (Rf) are reported with relation to the solvent used to elute the plate, TLC spots were visualised using a hand held UV fluorescence light (254

nm). Flash column chromatography was performed using Merck 60 silica gel, with particle size 40-63 μm.

5.1.1 Preparation of 5-trimethylsilylethynyl-2-formyl pyridine

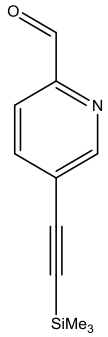

An oven-dried schlenk flask was charged with 5-bromopyridine-2-carbaldehyde (966 mg, 5.30 mmol), copper iodide (76 mg, 0.40 mmol), palladium bistriphenylphosphine dichloride (141 mg, 0.20 mmol) and triphenylphosphine (60 mg, 0.22 mmol). Anhydrous triethylamine (30 mL) and anhydrous THF (8 mL) were added and the reaction was stirred at room temperature under argon for 20 min resulting in a yellow suspension. Trimethylsilylacetylene (1 mL, 6.11 mmol) was injected into the flask drop wise at room temperature. The reaction was then heated at 60 °C for 5 h under an argon atmosphere. The solvent from the crude was removed and the crude extracted with chloroform, filtered and concentrated to give a brown solid. The solid was purified by column chromatographed on silica gel eluted with DCM. The product containing fractions were combined and concentrated to dryness. The solid was extracted with petroleum-ether (boiling range 40-60 °C), filtered and the solvent removed to give 5-Trimethylsilylethynyl-2-formyl pyridine as a pale beige solid (0.741 g, 68%). ^{1}H NMR (300 MHz, $CDCl_3$): δ 0.28(s, 9H, H^9), 7.90 (d, 2H, $^{4}J_{H\text{-}H}$ = 1.3 Hz, H^{3+4}), 8.81 (t, 1H, $1^{4}J_{H\text{-}H}$ = 1.4 Hz, H^6), 10.1 (s, 1H, H^{al}). ^{13}C {^{1}H} NMR (100 MHz, $CDCl_3$): δ 192.9, 153.2, 151.3, 140.1, 125.0, 121.2, 103.0, 101.0, 41.7. Rf (DCM) 0.53. ESIMS *m/z* calculated for 203.08 M^+; observed 203.1 $[M+H]^+$ .The ^{1}H NMR data was consistent with that described in the literature.

5.1.2 Preparation of 5-ethynyl-2-formylpyridine

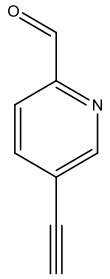

To a solution of 5-trimethylsilylethynyl-2-formyl pyridine (0.700 g, 3.45 mmol) in methanol (50 mL) was added potassium carbonate (0.068 g, 0.49 mmol); the solution was stirred overnight at room temperature. Ethyl acetate (200 mL) was added and the solution washed with water (2 x 25 mL), brine (25 mL), dried over $MgSO_4$ and the solvent evaporated to dryness. The crude was purified by column chromatography on silica gel eluted with DCM to afford 5-ethynyl-2-formylpyridine as a white solid (0.277 g, 61%): ^{1}H NMR (300 MHz, $CDCl_3$): δ 3.42 (s, 1H, H8), 7.94 (d, 2H, $^4J_{H-H}$ = 0.9 Hz, H3+4), 8.86 (t, 1H, $^4J_{H-H}$ = 1.4 Hz, H6), 10.08 (s, 1H, H^{al}). ^{13}C {^{1}H} NMR (100 MHz, $CDCl_3$): δ 192.5, 153,0, 151.5, 140.1, 123.6, 120.9, 84.0, 79.7. Rf (DCM) 0.57. ESIMS: m/z 131.04 M^+; Observed 154.0 $[M+Na]^+$. The ^{1}H NMR data was consistent with that described in the literature.

5.1.3 Preparation of 4-trimethylsilylethynyl-2-formyl pyridine

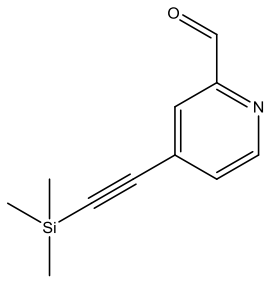

An oven-dried schlenk flask was charged with 4-bromopyridine-2-carbaldehyde (900 mg, 4.84 mmol), copper iodide (80 mg, 0.42 mmol), palladium bistriphenylphosphine dichloride (140 mg, 0.2 mmol) and triphenylphosphine (40 mg, 0.15 mmol). Anhydrous triethylamine (30 mL) and anhydrous THF (8 mL) were added and the reaction was stirred at room temperature under argon for 20 min resulting in a yellow suspension. Trimethylsilylacetylene (1 mL, 6.11 mmol) was injected into the flask drop wise at room temperature. The reaction was then heated at 60 °C for 5 h under an argon atmosphere. The solvent from the crude was removed and the crude extracted with chloroform, filtered and concentrated to give a brown solid. The solid was purified by column chromatographed on silica gel eluted with DCM. The product containing fractions were combined and concentrated to dryness. The solid was extracted with petroleum-ether

(boiling range 40-60 °C), filtered and the solvent removed to give 4-Trimethylsilylethynyl-2-formyl pyridine as a pale beige solid (0.573 g, 63%). ^{1}H NMR ^{1}H NMR (300 MHz, $CDCl_3$): δ 1.57 (s, 1H,), 7.51 (dd, 1H), 7.96 (d, 1H), 8.73 (d, 1H), 10.06 (s, 1H) . ^{13}C {^{1}H} NMR (100 MHz, $CDCl^3$): δ 193.3, 165.4, 153.1, 150.5, 133.1, 130.0, 124.4, 102.5, 101.3, 69.9 ESIMS m/z calculated for M^+ 203.08 ; observed 203.1 $[M+H]^+$.

5.1.4 Preparation of 4-ethynyl-2-formylpyridine

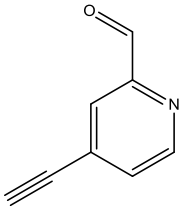

To a solution of 4-trimethylsilylethynyl-2-formyl pyridine (550 mg, 2.71 mmol) in methanol (50 mL) was added potassium carbonate (60 mg, 0.43 mmol); the solution was stirred overnight at room temperature. Ethyl acetate (200 mL) was added and the solution washed with water (2 x 25 mL), brine (25 mL), dried over $MgSO_4$ and the solvent evaporated to dryness. The crude was purified by column chromatography on silica gel eluted with DCM to afford 4-ethynyl-2-formylpyridine as a white solid (209 mg, 59%): ^{1}H NMR (300 MHz, $CDCl_3$): δ 3.40 (s, 1H), 7.52 (dd, 1H), 7.94 (s, 1H) 8.72 (d, 1H), 10.02 (s, 1H). ^{13}C {^{1}H} NMR (100 MHz, $CDCl^3$): δ 192.7, 152.8, 150.2, 131.8, 129.9, 124.1, 83.6, 80.0. ESIMS: m/z M^+ 131.04; Observed 154.0 $[M+Na]^+$.

5.1.5 Preparation of 3-nitro-7-diethylamino coumarin

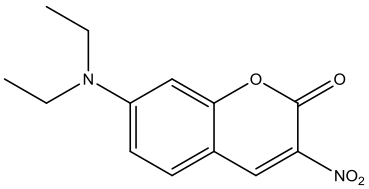

An oven-dried 100 ml three-necked round bottom flask equipped with stir bar, argon inlet and condenser was evacuated and back filled with argon. The flask was then charged with 4-diethylamino salicylaldehyde (1.400 g, 7.20 mmol), ethyl nitroacetate (0.8 mL, 7.20 mmol) and molecular sieves 4 Å (100 mg) and the flask fitted with a rubber septum. Anhydrous 1-butanol (20 mL), piperidine (0.1 mL) and acetic acid (0.2 mL) were added and the mixture refluxed for 24 h. Upon cooling room temperature, an orange solid formed that was collected by filtration and dissolved in DMF (20 mL) at 80°C. The

solution was filtered to remove the molecular sieved. Ice cold water (100 mL) was added to the filtered and precipitated 3-nitro-7-diethylamino coumarin as an orange solid that was collect and dried in a desiccator overnight (1.470 g, 77%).^{1}H NMR (300 MHz, $CDCl_3$): δ 1.27 (t, 6H, $^{3}J_{H-H}$ = 7.2 Hz, H11), 3.50 (q, 4H, $^{3}J_{H-H}$ = 7.2 Hz, H10), 6.48 (d, 1H, $^{4}J_{H-H}$ = 2.4 Hz, H9), 6.71 (dd, 1H, $^{3}J_{H-H}$ = 8.8 Hz, $^{4}J_{H-H}$ = 2.4 Hz, H7), 7.44 (dd, 1H, $^{3}J_{H-H}$ = 9.2 Hz, H6), 8.72 (s, 1H, H4). ^{13}C {^{1}H} NMR (100 MHz, $CDCl^3$): δ 12.58, 45.66, 96.98, 106.35, 111.23, 132.68, 143.47, 153.58, 154.68, 158.92. ESIMS m/z calculated for 262.10 M^+; observed 263.13 $[M+H]^+$. The ^{1}H NMR data was consistent with that described in the literature

5.1.6 Preparation of 3-amino-7-diethylamino coumarin

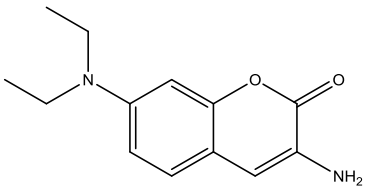

Hydrochloric acid (15 mL, 32%) and stannous chloride dehydrate (4.800 g, 21.36 mmol), in order, were added to a 50 ml round bottom flask equipped with a stir bar. 3-Nitro-7-diethylamino coumarin (0.800 g, 3.05 mmol) was added to the solution in small portions over ten minutes. The reaction was stirred at room temperature for 4 h and then poured onto 60 g of ice. The solution was made basic using sodium hydroxide solution (5 M) and the resulting solution extracted with diethyl ether (2 x 100 mL). The organic layers were combined and washed with water (50 mL) dried over anhydrous sodium sulphate and concentrated under reduced pressure. The residue was triturated with hexane producing a precipitate which was collected and dried to give 3-amino-7-diethylaminocoumarin as a bright yellow solid (0.540 g, 76%). ^{1}H NMR (300 MHz, $CDCl_3$): δ 1.18 (t, 6H, $^{3}J_{H-H}$ = 7.2 Hz, H11), 3.37 (q, 4H, $^{3}J_{H-H}$ = 7.2 Hz, H10), 3.85 (bs, 2H, NH2), 6.53 (d, 1H, $^{4}J_{H-H}$ = 2.4 Hz, H9), 6.57 (dd, 1H, $^{3}J_{H-H}$ = 8.8 Hz, $^{4}J_{H-H}$ = 2.0 Hz, H7), 6.70 (s, 1H, H4), 7.11 (d, 1H, $^{3}J_{H-H}$ = 8.8 Hz, H6). ^{13}C {^{1}H} NMR (100 MHz, $CDCl^3$): δ 12.64, 44.79, 98.21, 109.48, 109.83, 126.09, 127.68, 147.65, 151.78, 160.46. ESIMS m/z calculated for 232.12

M^+; observed 233.16 $[M+H]^+$. The ^1H NMR data was consistent with that described in the literature.

5.1.7 Preparation of 3-azido-7-diethylaminocoumarin

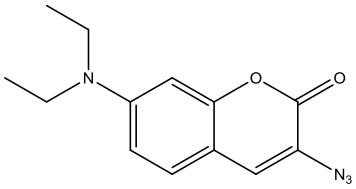

7-Diethylamino-3-amino coumarin (0.300 g, 1.29 mmol) was dissolved in hydrochloric acid (12 mL, 16%) and the solution cooled to 0 °C. A solution of sodium nitrite (0.090 g, 1.29 mmol) was slowly added and the reaction mixture stirred at 0 °C for 1 h. A solution of sodium acetate (6.000 g) in water (15 ml) was then added to adjust the pH to 4. Sodium azide (0.171 g, 2.64 mmol) was added in small portions over ten minutes and the resulting solution stirred at 0 °C for 5 h. The reaction was rapidly filtered and the precipitated washed with ice cold water and dried under vacuum to give 3-Azido-7-diethylaminocoumarin as a golden solid (0.25 g, 76%). ^1H NMR (300 MHz, $CDCl_3$): δ 1.20 (t, 6H, $^3J_{H-H}$ = 7.2 Hz, H11), 3.40 (q, 4H, $^3J_{H-H}$ = 7.2 Hz, H10), 6.50 (d, 1H, $^4J_{H-H}$ = 2.4 Hz, H9), 6.58 (dd, 1H, $^3J_{H-H}$ = 8.8 Hz, $^4J_{H-H}$ = 2.4 Hz, H7), 7.10 (s, 1H, H4), 7.19 (d, 1H, $^3J_{H-H}$ = 8.8 Hz, H6). ^{13}C {^1H} NMR (100 MHz, $CDCl^3$): δ 12.58, 44.94, 97.54, 108.17, 109.58, 119.76, 127.73, 128.29, 149.98, 154.32, 158.54. ESIMS m/z calculated for 258.11 M^+; observed 259.2 $[M+H]^+$. The ^1H NMR data was consistent with that described in the literature.

5.1.8 Preparation of 4-(1-(7-(diethylamino)-2-oxo-2H-chromen-3-yl)-1H-1,2,3-triazol-4-yl)picolinaldehyde

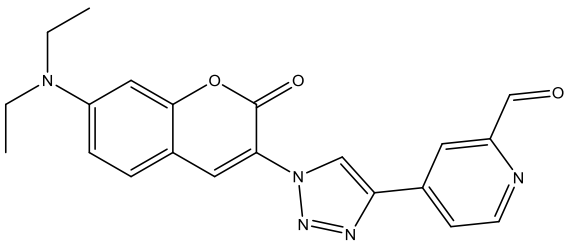

A mixture of 3-azido-7-diethylaminocoumarin (0.200 g, 0.77 mmol) and 4-ethynyl-1-formylpyridine (0.100 g, 0.77 mmol) were dissolved in THF and water (5:1, 10 mL). A freshly prepared 1 M solution of sodium ascorbate (136 µl, 0.136 mmol) in water was added followed by a freshly prepared 7.5% solution of copper (II) sulphate

pentahydrate (112 µl, 0.034 mmol) in water. The mixture was stirred in the dark at room temperature for 72 h. Ice cold water (50 ml) was added to the reaction and the precipitate was rapidly collected by filtration. The solid was washed with ethanol (200 mL), diethyl ether (200ml). The product was then washed through into a separate flask with chloroform (200 mL) and the solvent evaporated to dryness to afford 4-(1-(7-(diethylamino)-2-oxo-2H-chromen-3-yl)-1H-1,2,3-triazol-4-yl)picolinaldehyde as a yellow solid (218 mg, 73%). ^{1}H NMR (300 MHz, $CDCl_3$): δ 1.26 (t, 6H, $^{3}J_{H-H}$ = 7.2 Hz, H19), 3.47 (q, 4H, $^{3}J_{H-H}$ = 7.2 Hz, H18), 6.58 (d, 1H, $^{4}J_{H-H}$ = 2.4 Hz, H11), 6.70 (dd, 1H, $^{3}J_{H-H}$ = 9.0 Hz, $^{4}J_{H-H}$ = 3 Hz, H13), 7.45 (d, 1H, $^{3}J_{H-H}$ = 9.0 Hz, H14), 8.11 (dd, 1H, $^{3}J_{H-H}$ = 6 Hz, $^{3}J_{H-H}$ = 3 Hz H3), 8.40 (s, 1H, H4), 8.50 (s, 1H, H16), 8.86 (d, 1H, $^{3}J_{H-H}$ = 6.0 Hz) 9.09 (s, 1H, H8), 10.14 (s, 1H, H^{im}). ^{13}C {^{1}H} NMR (100 MHz, $CDCl^{3}$):12.57, 45.22, 97.15, 107.07, 110.40, 116.35, 118.23, 122.50, 123.93, 130.35, 134.96, 139.49, 144.33, 151.04, 151.99, 153.59, 156.07,156.96,193.36. δ. ESIMS m/z calculated for 389.15 M^{+}; observed 390.2 $[M+H]^{+}$

5.1.9 Preparation of 5-(1-(7-(diethylamino)-2-oxo-2H-chromen-3-yl)-1H-1,2,3-triazol-4-yl)picolinaldehyde

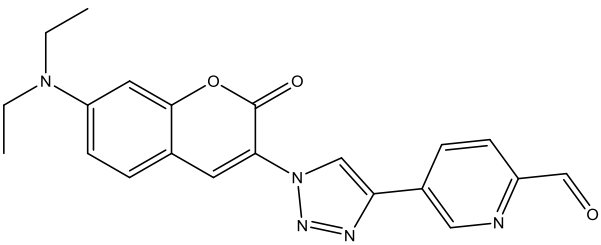

A mixture of 3-azido-7-diethylaminocoumarin (0.400 g, 0.77 mmol) and 5-ethynyl-1-formylpyridine (0.200 g, 0.77 mmol) were dissolved in THF and water (10 mL, 5:1). A freshly prepared 1 M solution of sodium ascorbate (272 µL, 0.272 mmol) in water was added followed by a freshly prepared 7.5% solution of copper (II) sulphate pentahydrate (224 µL, 0.068 mmol) in water. The mixture was stirred in the dark at room temperature for 72 h. Ice cold water (50 mL) was added to the reaction and the precipitate was rapidly collected by filtration. The solid was washed with ethanol (200 mL), diethyl ether (200mL). The p4roduct was then washed through into a separate flask with chloroform (200 mL) and

the solvent evaporated to dryness to afford 5-(1-(7-(diethylamino)-2-oxo-2H-chromen-3-yl)-1H-1,2,3-triazol-4-yl)picolinaldehyde as a yellow solid (509 mg, 85%). ^{1}H NMR (300 MHz, $CDCl_3$): δ 1.26 (t, 6H, $^{3}J_{H-H}$ = 7.2 Hz, H19), 3.48 (q, 4H, $^{3}J_{H-H}$ = 7.2 Hz, H18), 6.58 (d, 1H, $^{4}J_{H-H}$ = 2.4 Hz, H11), 6.71 (dd, 1H, $^{3}J_{H-H}$ = 9.0 Hz, $^{4}J_{H-H}$ = 2.4 Hz, H13), 7.46 (d, 1H, $^{3}J_{H-H}$ = 9.0 Hz, H14), 8.07 (d, 1H, $^{3}J_{H-H}$ = 8.1 Hz, H3), 8.42 (dd, 1H, $^{3}J_{H-H}$ = 8.1 Hz, $^{4}J_{H-H}$ = 1.2 Hz, H4), 8.51 (s, 1H, H16), 9.06 (s, 1H, H8), 9.32 (d, 1H, $^{4}J_{H-H}$ = 1.2 Hz, H6), 10.12 (s, 1H, H^{al}). ^{13}C {^{1}H} NMR (100 MHz, $CDCl^{3}$): δ 12.43, 45.08, 97.07, 106.99, 110.29, 121.79, 122.01, 130.21, 130.57, 133.64, 134.82, 147.38, 151.88, 151.99, 152.08, 153.67, 155.96, 156.89, 192.89. ESIMS m/z calculated for 389.15 M^{+}; observed 390.2 $[M+H]^{+}$

5.1.10 Preparation of L^{C5}

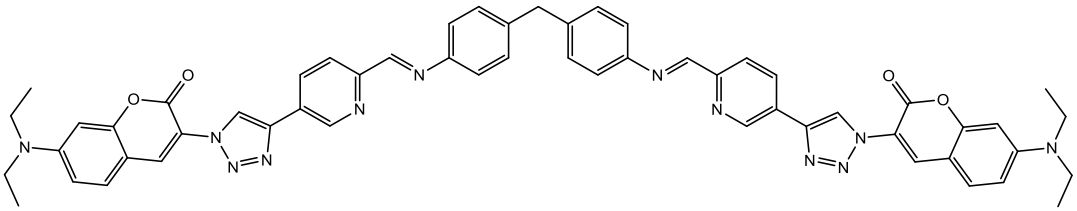

5-(1-(7-(diethylamino)-2-oxo-2H-chromen-3-yl)-1H-1,2,3-triazol-4-yl)picolinaldehyde (500 mg, 1.28 mmol) was dissolved in a mixture of chloroform (5 mL) and methanol (10 mL). A solution of 4,4′-methylenedianiline (128 mg, 0.64 mmol in methanol 4 mL) was added dropwise to the stirred reaction. The reaction was stirred for 24 hours in the dark at room temperature. The product was collected by filtration, washed with methanol (100 mL), diethyl ether (100 mL) and dried under vacuum to afford L^{C5} as a dark brown solid (511 mg, 85%). ^{1}H NMR (300 MHz, $CDCl_3$): δ 1.26 (t, 6H), 3.48 (q, 2H), 4.09 (s, 1H), 6.59 (d, 1H), 6.71 (dd, 1H), 7.29 (s, 4H), 7.46 (d, 1H), 8.33 (m, 2H), 8.50 (s, 1H), 8.68 (s, 1H), 9.00 (s, 1H), 9.24 (d, 1H). ESIMS m/z calculated for 941.07 M^{+}; observed 942.2 $[M+H]^{+}$

5.1.11 Preparation of $[Fe_2L^{C5}{}_3][PF_6]_4$

Ligand L^{C5} (100mg, 0.11 mmol) was suspended in methanol (5mL). $Fe(II)Cl_2{\cdot}4H_2O$ (30 mg 0.08 mmol) was dissolved in methanol (2 mL), this was added dropwise to the stirred

Ligand L^{C5} solution. Upon addition of the metal salt the solution turned dark green with a purple hue. The reaction was stirred for 48 hours in the dark at room temperature. A saturated methanolic solution of ammonium hexafluorophosphate was added (1 mL) and the complex precipitated from solution. The solid was collected by filtration and washed with cold methanol (50 mL) and diethyl ether (50 mL). The green solid was dried under reduced pressure to afford $[Fe_2L^{C5}{}_3][PF_6]_4$ (72 mg, 56%). ^{1}H NMR (300 MHz, CD_3CN): δ 1.24 (t, 6H), 3.58 (q, 4H), 4.11 (s, 1H), 5.94 (bs, 2H), 6.63 (s, 1H), 6.88 (d, 1H), 7.12 (bs, 1H), 7.61 (bs, 1H), 8.41 (s, 1H), 9.00 (s, 1H), 9.09 (d, 1H), 9.42 (s, 1H). ESIMS m/z observed $[M+H]^{+4}$ 733.60.

5.1.12 Preparation of L^{C4}

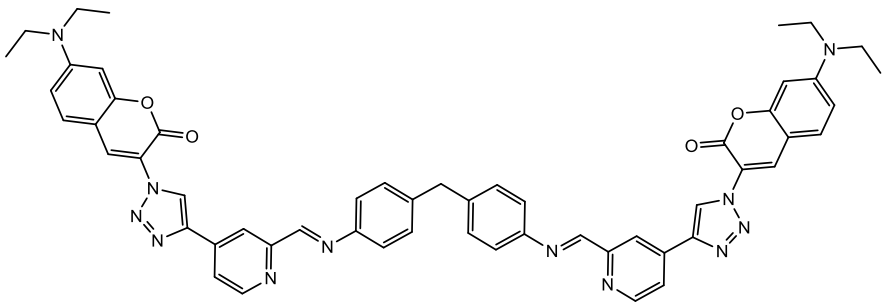

4-(1-(7-(diethylamino)-2-oxo-2H-chromen-3-yl)-1H-1,2,3-triazol-4-yl)picolinaldehyde (150 mg, 0.38 mmol) was dissolved in a mixture of chloroform (5 mL) and methanol (10 mL). A solution of 4,4′-methylenedianiline (38 mg, 0.19 mmol in methanol 4 mL) was added dropwise to the stirred reaction. The reaction was stirred for 24 hours in the dark at room temperature. The product was collected by filtration, washed with methanol (100 mL), diethyl ether (100 mL) and dried under vacuum to afford L^{C4} as a dark brown solid (127 mg, 71%). ^{1}H NMR (300 MHz, $CDCl_3$): 1.26 (t, $^3J_{H-H}$ = 6.0 Hz, 6H), 3.47 (q, $^3J_{H-H}$ = 6.0 Hz 4H), 4.07 (s, 1H), 6.58, (d, $^3J_{H-H}$ = 6.0 Hz, 1H), 6.70 (dd, $^3J_{H-H}$ = 9.0 Hz, 1H), 7.31 (d, $^3J_{H-H}$ = 3 Hz, 4H), 7.45 (d, $^3J_{H-H}$ = 9.0 Hz, 1H), 7.98 (dd, $^3J_{H-H}$ = 6.0 Hz, 1H), 8.50 (s, 1H), 8.63 (s, 1H), 8.68 (s, 1H), 8.78 (d, $^3J_{H-H}$ = 6.0 Hz, 1H). 9.11 (s, 1H). δ ^{13}C {1H} NMR (100 MHz, $CDCl_3$):

δ 12.58 45.21, 97.18, 107.14, 110.34, 115.5, 118.31, 121.38, 121.65, 122.37, 129.96, 130.31, 134.90, 138.85, 139.99, 145.03, 149.07, 150.51, 151.91, 155.51, 156.05, 159.84. ESIMS m/z calculated for 941.07 M^+; observed 942.2 $[M+H]^+$.

5.1.13 Preparation of $[Fe_2L^{C4}{}_3][PF_6]_4$

Ligand L^{C4} (100mg, 0.11 mmol) was suspended in methanol (5mL). $Fe(II)Cl_2 \cdot 4H_2O$ (30 mg 0.08 mmol) was dissolved in methanol (2 mL), this was added dropwise to the stirred Ligand L^{C4} solution. Upon addition of the metal salt the solution turned dark green with a purple hue. The reaction was stirred for 48 hours in the dark at room temperature. A saturated methanolic solution of ammonium hexafluorophosphate was added (1 mL) and the complex precipitated from solution. The solid was collected by filtration and washed with cold methanol (50 mL) and diethyl ether (50 mL). The green solid was dried under reduced pressure to afford $[Fe_2L^{C4}{}_3][PF_6]_4$ (74 mg, 58%).^{1}H NMR (300 MHz, CD_3CN): 1.20 (t, 6H), 3.50 (q, 4H), 4.05 (s, 1H), 5.62 (bs, 2H), 6.64 (d, 1H), 6.81 (dd, 1H), 6.97 (bs, 2H), 7.48 (s, 1H), 7.57 (d, 1H), 8.21 (bs, 1H), 8.44 (s, 1H), 8.95 (bs, 1H), 9.13 (bs, 1H), 9.23 (bs, 1H). ESIMS m/z observed 733.49 $[M+H]^{4+}$.

5.1.14 Preparation of dansyl-PEG_3-azide

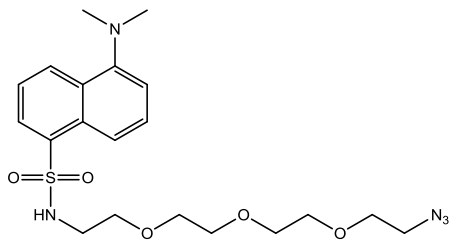

Dansyl chloride (1000 mg, 3.7 mmol) was dissolved in anhydrous dichloromethane (10 mL). Anhydrous triethylamine (560 µL, 1.8 mmol) and 11-azido-3,6,9-trioxaundecan-1-amine (806 µL, 1.1 eq, 4.07 mmol) were added and the reaction stirred for 15 h under argon at room temperature in the dark. A saturated aqueous solution of $NaHCO_3$ (20 mL) was added and the reaction was extracted with dichloromethane (3 x 50 mL). The organic fractions were combined, dried over $MgSO_4$, filtered and the solvent evaporated to dryness. The residue was purified using column chromatography on silica gel eluted with 2% MeOH in DCM. The product

fractions were combined and the solvent evaporated to afford dansyl-PEG$_3$-azide (1.18 g, 67%) as a bright yellow oil. ^{1}H NMR (300 MHz, $CDCl_3$): δ 8.51(d, 1H, $^3J_{H-H}$ = 8.52), 8.29 (d, 1H, $^3J_{H-H}$ = 8.67), 8.22 (dd, 1H, $^3J_{H-H}$ = 7.29, $^4J_{H-H}$ = 1.23), 7.52 (m, 2H), 7.16 (d, 1H, $^3J_{H-H}$ = 7.05 Hz), 5.60 (t, 1H, $^3J_{H-H}$ = 5.88), 4.09 (q, 1H, $^3J_{H-H}$ = 7.14), 3.61 (m, 6H), 3.47 (m, 2H), 3.35 (m, 6H), 3.08 (q, 2H, $^3J_{H-H}$ = 5.70), 2.86 (s, 6H).δ ^{13}C {^{1}H} NMR (100 MHz, $CDCl_3$): δ 42.87, 45.22, 50.43, 68.96, 69.80, 69.98, 70.18, 70.35, 115.0, 118.76, 123.11, 129.05, 129.44, 129.65, 130.12, 135.03, 151.72. MALDI-MS m/z calculated 451.19; observed M^+ 451.12, $[M+Na]^+$ 474.12, $[M+K]^+$490.02

5.1.15 Preparation of 5-(dimethylamino)-N-(2-(2-(2-(2-(4-(6-formylpyridin-3-yl)-1H-1,2,3-triazol-1-yl)ethoxy)ethoxy)ethoxy)ethyl)naphthalene-1-sulfonamide

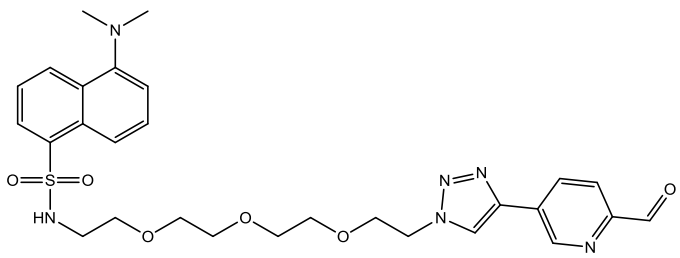

Dansyl-PEG3-azide (588 mg, 1.3 mmol) and 5-ethynyl-2-formylpyridine (143 mg, 1.09 mmol) were dissolved in a mixture of ethanol and water (5:1 , 20 mL). Sodium ascorbate (400 µl of a 1M solution) and copper (II) sulphate pentahydrate (200 µl of a 1M solution) were added and the reaction was stirred for 18 h in the dark at room temperature under an argon atmosphere. The reaction was diluted with water (15 mL) and the solution extracted with dichloromethane (3 x 50mL). The organic fractions were combined, dried over $MgSO_4$ and concentrated to dryness. The residue was purified by column chromatograph on silica gel eluted with DCM. The product containing fractions were combined, evaporated to dryness to afford the product as a yellow oil (425 mg, 67%). ^{1}H NMR (300 MHz, $CDCl_3$): δ δ 8.51(d, 1H, $^3J_{H-H}$ = 8.52), 8.29 (d, 1H, $^3J_{H-H}$ = 8.67), 8.22 (dd, 1H, $^3J_{H-H}$ = 7.29, $^4J_{H-H}$ = 1.23), 7.52 (m, 2H), 7.16 (d, 1H, $^3J_{H-H}$ = 7.05 Hz), 5.60 (t, 1H, $^3J_{H-H}$ = 5.88), 4.09 (q, 1H, $^3J_{H-H}$ = 7.14), 3.61 (m, 6H), 3.47 (m, 2H), 3.38 (m, 6H), 3.09 (q, 2H, $^3J_{H-H}$ = 5.70), 2.85 (s, 6H). ^{13}C {^{1}H} NMR (100 MHz,

$CDCl^3$): δ 42.00, 44.4, 49.4, 68.2, 69.3 69.2, 69.3, 69.4, 114.1, 117.9, 122.2, 127.1, 128.3, 128.6, 128.6, 129.4, 130.0, 132.4,134.1, 142.5, 146.2, 150.9, 191.8 ESIMS m/z calculated M+ 582.6, observed [M+H]+ 583.6

5.1.16 Preparation of 4-(dimethylamino)-N-(2-(2-(2-(2-(4-(2-formylpyridin-4-yl)-1H-1,2,3-triazol-1-yl)ethoxy)ethoxy)ethoxy)ethyl)naphthalene-1-sulfonamide

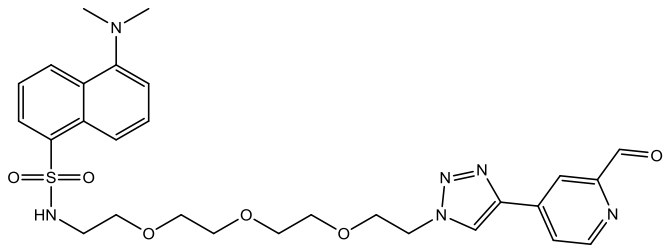

Dansyl-PEG3-azide (100 mg, 0.22 mmol) and 4-ethynyl-2-formylpyridine (30 mg, 0.22 mmol) were dissolved in a mixture of ethanol and water (5:1 , 20 mL). Sodium ascorbate (200 µl of a 1M solution) and copper (II) sulphate pentahydrate (100 µl of a 1M solution) were added and the reaction was stirred for 18 h in the dark at room temperature under an argon atmosphere. The reaction was diluted with water (15 mL) and the solution extracted with dichloromethane (3 x 50mL). The organic fractions were combined, dried over MgSO4 and concentrated to dryness. The residue was purified by column chromatograph on silica gel eluted with DCM. The product containing fractions were combined, evaporated to dryness to afford the product as a yellow oil (75mg, 59%). ^{1}H NMR (300 MHz, $CDCl_3$): δ 2.77 (s, 6H), 3.02 (m, 2H), 3.31 (m, 4H), 3.39 (m, 2H), 3.50 (m, 2H), 3.57 (m, 2H), 3.86 (t, 2H), (4.57 (t, 2H), 6.13 (t, 1H), 7.05 (dd, 1H), 7.41 (dt, 2H), 7.94 (dd, 1H), 8.14 (dd, 1H), 8.19 (d, 1H), 8.23 (d, 1H), 8.29 (s, 1H), 8.42 (d, 1H), 8.68 (dd, 1H), 10.00 (s, 1H). ESIMS m/z calculated M+ 582.6, observed [M+H]+ 583.7

5.1.17 Preparation of L^{D5}

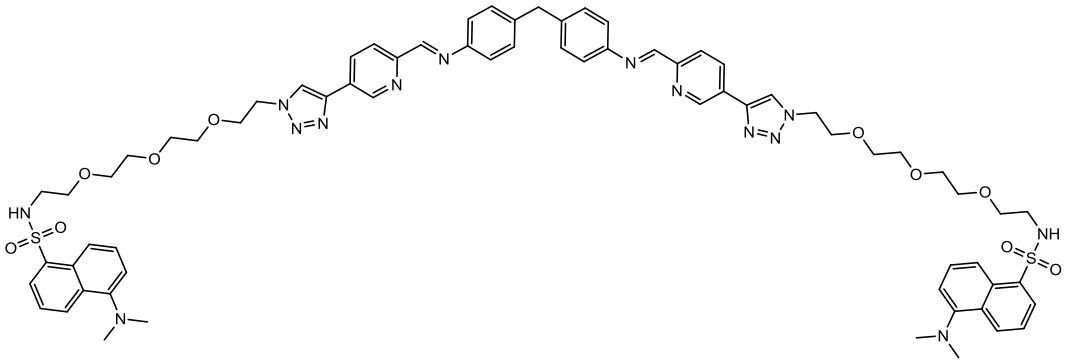

5-(dimethylamino)-N-(2-(2-(2-(2-(4-(6-formylpyridin-3-yl)-1H-1,2,3-triazol-1-yl)ethoxy)ethoxy)ethoxy) ethyl)naphthalene-1-sulfonamide (300 mg, 0.51 mmol) was dissolved in a mixture of chloroform (5 mL) and methanol (10mL). A solution of 4,4′-methylenedianiline (51 mg, 0.25 mmol in 2 mL methanol) was added dropwise to the stirring reaction. The reaction was stirred for 24 h at room temperature in the dark. Methanol (10 mL) was added to the reaction and the solution was sonicated for 5 minutes to dissolve an oily residue that has built up on the side of the glass, the solution was stirred for a further 2 hours at room temperature in the dark. Diethyl ether (50 mL) was added to precipitate the product. The product was collected by filtration and dried under vacuum to afford L^{D5} as a brown solid (216 mg, 65%). ^{1}H NMR (300 MHz, $CDCl_3$): δ 2.85 (s, 6H), 3.13 (m, 2H), 3.37 (m, 4H), 3.44 (m, 2H), 3.60 (m, 2H), 3.67 (m, 2H), 3.95 (t, 2H), 4.03 (s, 1H), 4.66 (s, 2H), 6.32 (t, 1H), 7.12 (dd, 1H), 7.27 (s, 4H), 7.46 (ddd, 2H), 8.25 (m, 3H), 8.32 (m, 2H), 8.50 (d, 1H), 8.72 (s, 1H), 9.09 (dd, 1H). ^{13}C {^{1}H} NMR (100 MHz, $CDCl_3$): δ 43.18, 45.56, 50.49, 69.45, 70.22, 70.38, 70.51, 70.55, 115.27, 119.20, 121.71, 122.11, 122.35, 123.32, 128.26, 129.31, 129.93, 130.42, 133.56, 146.84, 159.54.

5.1.18 Preparation of $[Fe_2L^{D5}{}_3][PF_6]_4$

Ligand L^{D5} (100 mg, 0.075 mmol) was suspended in methanol (10 mL). $Fe(II)Cl_2{\cdot}4H_2O$ (9.98 mg, 0.05 mmol) was dissolved in methanol (2 mL), this was added dropwise to the stirred Ligand L^{D5} solution. Upon addition of the metal salt the solution turned purple. The reaction was stirred for 24 hours in the dark at room temperature. A saturated methanolic solution of ammonium hexafluorophosphate was added (1 mL) and the complex precipitated from solution. The solid was collected by filtration and washed with cold methanol (50 mL) and diethyl ether (50 mL). The purple solid was dried under reduced pressure to afford $[Fe_2L^{D5}{}_3][PF_6]_4$ (95 mg, 82%). ^1H NMR (300 MHz, CD_3CN): δ 2.83 (s, 6H), 2.93 (m, 2H), 3.26 (m , 4H), 3.33 (m, 2H), 3.43 (m, 2H), 3.51 (m, 2H), 3.81 (t, 2H), 3.93 (s, 4H), 4.48 (t, 2H), 5.58 (bs, 2H), 5.99 (t, 1H), 6.90 (bs, 2H), 7.20 (d, 1H), 7.52 (m, 2H), 8.06 (d, 2H), 8.18 (d, 1H), 8.32 (s, 1H), 8.50 (d, 1H), 8.64 (d, 1H), 8.77 (d, 8.77), 8.89 (s, 1H). ESIMS m/z observed at 1023.8 $[M+H]^{4+}$.

5.1.19 Preparation of L^{D4}

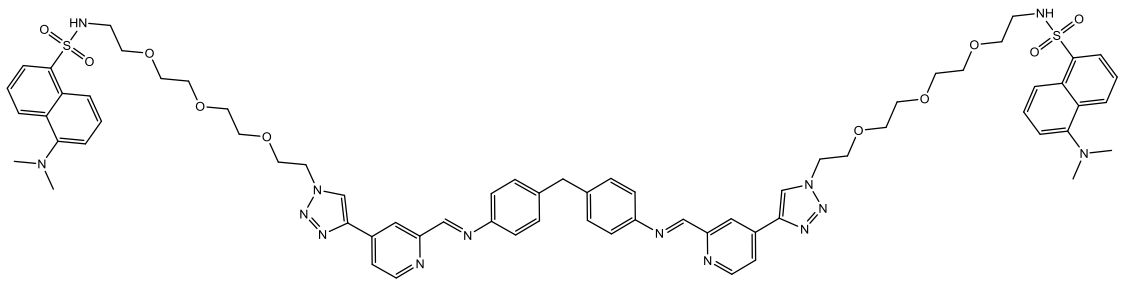

4-(dimethylamino)-N-(2-(2-(2-(2-(4-(6-formylpyridin-3-yl)-1H-1,2,3-triazol-1-yl)ethoxy)ethoxy)ethoxy) ethyl)naphthalene-1-sulfonamide (50 mg, 0.08 mmol) was dissolved in a mixture of chloroform (5 mL) and methanol (10mL). A solution of 4,4′-methylenedianiline (7.5 mg, 0.04 mmol in 2 mL methanol) was added dropwise to the stirring reaction. The reaction was stirred for 24 h at room temperature in the dark. Methanol (10 mL) was added to the reaction and the solution was sonicated for 5 minutes to dissolve an oily residue that has built up on the side of the glass. The reaction was

stirred for a further 2 hours at room temperature in the dark. Diethyl ether (50 mL) was added to precipitate the product. The product was collected by filtration and dried under vacuum to afford L^{D4} as a brown solid (36 mg, 68%). ^{1}H NMR (300 MHz, $CDCl_3$): δ 2.85 (s, 6H), 3.07 (t, 2H), 3.37 (t, 2H), 3.41 (m, 2H), 3.48 (m, 2H), 3.61 (m, 2H), 3.67 (m, 2H), 3.96 (t, 2H), 4.05 (s, 1H), 4.65 (t, 2H), 5.70 (t, 1H), 7.13 (d, 1H), 7.21 (s, 1H), 7.26 (s, 4H), 7.48 (t, 3H, 7.92 (s, 2H), 8.21 (dd, 1H), 8.28 (d, 1H), 8.31 (2, 1H), 8.50 (d, 1H). ^{13}C {^{1}H} NMR (100 MHz, $CDCl_3$): δ 43.20, 45.54, 50.64, 69.37, 69.50, 70.27, 70.42, 70.60, 115.29, 118.37, 119.04, 121.56, 128.37, 129.47, 129.95, 130.53.

5.1.20 Preparation of $[Fe_2L^{D4}{}_3][PF_6]_4$

Ligand L^{D4} (30 mg, 0.02 mmol) was suspended in methanol (10 mL). $Fe(II)Cl_2 \cdot 4H_2O$ (3 mg, 0.015 mmol) was dissolved in methanol (2 mL), this was added dropwise to the stirred Ligand L^{D4} solution. Upon addition of the metal salt the solution turned purple. The reaction was stirred for 24 hours in the dark at room temperature. A saturated methanolic solution of ammonium hexafluorophosphate was added (1 mL) and the complex precipitated from solution. The solid was collected by filtration and washed with cold methanol (50 mL) and diethyl ether (50 mL). The purple solid was dried under reduced pressure to afford $[Fe_2L^{D4}{}_3][PF_6]_4$ (25 mg, 72%). ^{1}H NMR (300 MHz, CD_3CN): δ 2.77 (s, 2H), 2.91 (m, 2H), 3.23 (m, 4H), 3.31 (m, 2H), 3.47 (m, 2H), 3.57 (m, 2H), 3.90 (m, 2H), 4.65 (m, 2H), 5.50 (bs, 2H), 6.15 (s, 1H), 6.70 (bs, 2H), 7.14 (s, 1H), 7.46 (s, 2H), 8.04 (s, 2H), 8.17 (s, 2H), 8.43 (s, 1H). ESIMS m/z observed at 1169.7 $[M+H]^{4+}$.

5.1.21 Preparation of L^{Br5}

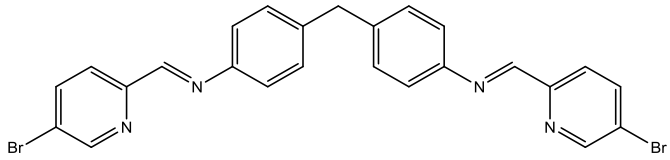

To a solution of 5-bromopydrinde-2-carboxaldehye (200 mg, 1.07 mmol) in methanol (30 mL) was added dropwise a solution of 4,4′-methylenedianiline (102 mg, 0.52 mmol in 2 mL methanol). The reaction was stirred at room temperature for 20 h. A white precipitate formed which was collected by filtration, washed with cold methanol (100 mL), diethyl ether (50 mL) and dried under vacuum to afford L^{Br5} as a white powder (230 mg, 83%). ^{1}H NMR (300 MHz, $CDCl_3$): δ 4.04 (1H, s), 7,26 (4H, s)7.94 (1H, dd, , $^{3}J_{H-H}$ = 9 Hz, $^{4}J_{H-H}$ = 3 Hz), 8.11 (1H, d, $^{3}J_{H-H}$ = 9 Hz), 8.57 (1H, s), 8.76 (1H, s). ^{13}C {^{1}H} NMR (100 MHz, $CDCl_3$): δ 41.26, 121.57, 122.95, 129.97, 139.49, 150.93, 158.95. ESIMS m/z observed at 535.00.

5.1.22 Preparation of $[Fe_2L^{Br5}{}_3][PF_6]_4$

Ligand L^{Br5} (100mg, 0.18 mmol) was suspended in methanol (10 mL). $Fe(II)Cl_2{\cdot}4H_2O$ (24 mg, 0.12 mmol) was dissolved in methanol (2 mL), this was added dropwise to the stirred Ligand L^{Br5} solution. Upon addition of the metal salt the solution turned purple. The reaction was stirred for 24 hours at room temperature. A saturated methanolic solution of ammonium hexafluorophosphate was added (1 mL) and the complex precipitated from solution. The solid was collected by filtration and washed with cold methanol (100 mL) and diethyl ether (50 mL). The purple solid was dried under reduced pressure to afford $[Fe_2L^{Br5}{}_3][PF_6]_4$ (115mg, 84%). ^{1}H NMR (300 MHz, CD_3CN): δ 4.08 (s, 1H), 5.51 (bs, 2H), 6.97 (bs, 2H), 7.66 (s, 1H), 8.59 (m, 2H), 9.17 (s, 1H).

5.1.23 Preparation of L^{Br4}

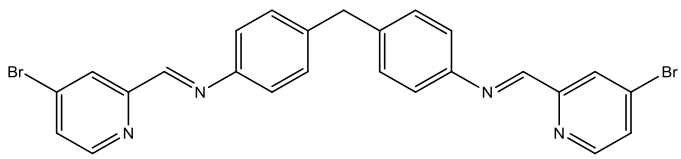

To a solution of 4-bromopydrinde-2-carboxaldehye (100 mg, 0.54 mmol) in methanol (10 mL) was added

dropwise a solution of 4,4′-methylenedianiline (50 mg, 0.25 mmol in 2 mL methanol). The reaction was stirred at room temperature for 20 h. A white precipitate formed which was collected by filtration, washed with cold methanol (100 mL), diethyl ether (50 mL) and dried under vacuum to afford L^{Br4} as a white powder (117 mg, 88%). ^{1}H NMR (300 MHz, $CDCl_3$): δ 4.05 (1H, s), 7.27 (4H, s) 7.52 (1H, dd, $^{3}J_{H-H}$ = 6 Hz, $^{4}J_{H-H}$ = 3 Hz), 8.40 (1H, d, $^{3}J_{H-H}$ = 1.5 Hz), 8.50 (1H, d, $^{3}J_{H-H}$ = 6 Hz), 8.57 (1H, s). ^{13}C {^{1}H} NMR (100 MHz, $CDCl_3$): δ 41.26, 121.63, 152.17, 128.30, 129.99, 150.42, 158.65. ESIMS *m/z* observed at 535.00

5.1.24 Preparation of $[Fe_2L^{Br4}{}_3][PF_6]_4$

Ligand L^{Br4} (100mg, 0.18 mmol) was suspended in methanol (10 mL). $Fe(II)Cl_2{\cdot}4H_2O$ (24 mg, 0.12 mmol) was dissolved in methanol (2 mL), this was added dropwise to the stirred Ligand L^{Br4} solution. Upon addition of the metal salt the solution turned purple. The reaction was stirred for 24 hours at room temperature. A saturated methanolic solution of ammonium hexafluorophosphate was added (1 mL) and the complex precipitated from solution. The solid was collected by filtration and washed with cold methanol (50 mL) and diethyl ether (50 mL). The purple solid was dried under reduced pressure to afford $[Fe_2L^{Br4}{}_3][PF_6]_4$ (109 mg, 79%). ^{1}H NMR (300 MHz, CD_3CN): δ 4.04 (s, 1H), 5.53 (bs, 1H), 6.96 (bs, 1H), 7.25 (s, 1H), 7.99 (s, 1H), 8.73 (s, 1H), 8.92 (s, 1H).

5.1.25 Preparation of 1-(prop-2-yn-1-yl)-1H-imidazole-2-carbaldehyde

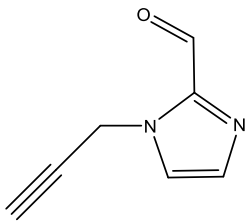

To a mixture of imidazole-2-carboxaldehyde (300mg, 3.12 mmol) and potassium carbonate (431 mg, 2.98 mmol) in anhydrous DMF (13 mL) was added propargyl bromide (80% w.v in toluene stabilised with MgO). The reaction was stirred at room temperature under an argon atmosphere for 18 h. The suspension was filtered and the filtrate diluted with water (20 mL). The solution was extracted with diethyl ether (3 x 50 mL), the organic layer dried over $MgSO_4$, filtered and the solvent evaporated to provide 1-(prop-2-yn-1-yl)-1H-imidazole-2-carbaldehyde

as a yellow oil (288 mg, 69 %). ^{1}H NMR (300 MHz, $CDCl_3$): δ 2.49 (1H, t, , $^{4}J_{H-H}$ = 3 Hz), 5.15 (2H, d, , $^{4}J_{H-H}$ = 3 Hz), 7.20 (1H, s), 7.39 (1H, s), 9.69 (1H, s). ^{13}C {^{1}H} NMR (100 MHz, $CDCl_3$): δ 182.1, 142.6, 131.6, 125.5, 76.1, 75.4, 37.2. ESIMS *m/z* calculated 134.13; observed 134.1 M^+, 135.1 $[M+H]^+$

5.1.26 Preparation of L^{TBim}

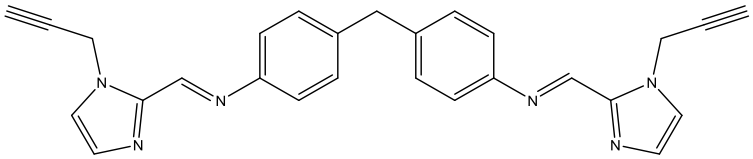

To a solution of 1-(prop-2-yn-1-yl)-1H-imidazole-2-carbaldehyde (150 mg, 0.84 mmol) dissolved in methanol (10 mL) was added dropwise a solution of 4,4′-methylenedianiline (83 mg, 0.42 mmol in 2 mL methanol). The reaction was stirred at room temperature for 18 h. A white precipitate formed that was collected by filtration, washed with cold methanol (50 mL) and diethyl ether (50 mL). The product was dried under vacuum to afford L^{TBim} as a white powder (148 mg, 82%). ^{1}H NMR (300 MHz, $CDCl_3$): δ 3.34 (1H, t, $^{4}J_{H-H}$ = 3 Hz), 3.97 (1H, s), 5.46 (1H, d, $^{4}J_{H-H}$ = 3 Hz), 7.17 (1H, s), 7.26 (4H, q, $^{3}J_{H-H}$ = 9 Hz), 7.53 (1H, s), 8.49 (1H, s). ^{13}C {^{1}H} NMR (100 MHz, $CDCl_3$): δ 150.7, 148.8, 142.5, 140.3, 130.5, 130.1, 125.4, 121.7, 79.4, 76.4, 44.6, 39.4 ESIMS *m/z* calculated 430.19, observed 431.2 $[M+H]^+$, 453.2 $[M+Na]^+$

5.1.27 Preparation of $[Fe_2L^{TBim}_3][PF_6]_4$

Ligand L^{TBim} (50 mg, 0.12 mmol) was suspended in methanol (10 mL). $Fe(II)Cl_2{\cdot}4H_2O$ (16mg, 0.08 mmol) was dissolved in methanol (2 mL), this was added dropwise to the stirred Ligand L^{TBim} solution. Upon addition of the metal salt the solution turned dark red. The reaction was stirred for 24 hours at room temperature. A saturated methanolic solution of ammonium hexafluorophosphate was added (1 mL) and the complex precipitated from solution. The solid was collected by filtration and washed with cold

methanol (50 mL) and diethyl ether (50 mL). The red solid was dried under reduced pressure to afford $[Fe_2L^{TBim}{}_3][PF_6]_4$ (44 mg, 56%). ESIMS m/z observed at 350.81 $[M+H]^{4+}$

5.1.28 Preparation of $[Ni_2L^{TBim}{}_3][PF_6]_4$

Ligand L^{TBim} (50 mg, 0.12 mmol) was suspended in methanol (10 mL). $Ni(II)Cl_2{\cdot}6H_2O$ (19 mg, 0.08 mmol) was dissolved in methanol (2 mL), this was added dropwise to the stirred Ligand L^{TBim} solution. Upon addition of the metal salt the solution turned orange. The reaction was stirred for 24 hours at room temperature. A saturated methanolic solution of ammonium hexafluorophosphate was added (1 mL) and the complex precipitated from solution. The solid was collected by filtration and washed with cold methanol (50 mL) and diethyl ether (50 mL). The orange solid was dried under reduced pressure to afford $[Ni_2L^{TBim}{}_3][PF_6]_4$ (36 mg, 45%). ESIMS m/z observed at 352.13 $[M+H]^{4+}$

5.1.29 Preparation of 3-azidopropan-1-ol

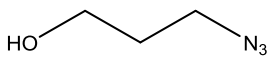

3-Chlororpropanol-1-ol (5g, 52.8 mmol) and sodium azide (8.5g, 130.7 mmol) were dissolved in water (65 mL). The solution was heated at 90 ^{O}C for 20 h. The solution was cooled to room temperature and diluted with diethyl ether (200 mL) and brine (200 mL). The organic fraction was separated, dried over Na_2SO_4 and carefully concentrated to afford 3-azidopropan-1-ol as colourless oil (4.47g, 82%). ^{1}H NMR (300 MHz, $CDCl_3$): δ 1.85 (2H, qu, $^3J_{H\text{-}H}$ = 6 Hz), 3.45 (2H, t, $^3J_{H\text{-}H}$ = 6 Hz)) 3.5 (1H, s, OH), 3.71 (2H, t , $^3J_{H\text{-}H}$ = 6 Hz)). ESIMS *m/z* calculated 101.11, observed 102.22 $[M+H]^+$

5.1.30 Preparation of 3-azidopropyl methanesulfonate

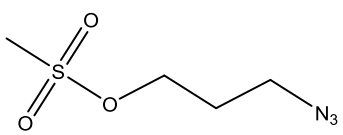

3-Azidopropan-1-ol (1.219 g, 12.1 mmol) was dissolved in a mixture of dry THF (25 mL) and triethylamine (2.5 mL), the solution was cooled to 0°C under argon. Mesyl chloride (1.5 mL) was added dropwise to the cooled solution and the mixture stirred for 1 h at 0 °C. The reaction mixture was then

slowly warmed to room temperature and stirred for 16 h. DCM (100 mL) and a saturated sodium bicarbonate solution (50 mL) were added to the reaction mixture. The organic layer was separated and washed with saturated sodium bicarbonate (2 x 50 mL), brine (50 mL) and dried over Na_2SO_4. The solvent was carefully removed to give 3-azidopropyl methanesulfonate as a colourless oil (1.647 mg, 76%). ^{1}H NMR (300 MHz, $CDCl_3$): δ 2.28 (2h, qu, $^3J_{H-H}$ = 6 Hz), 3.31 (3H, s), 3.75 (2H, t, $^3J_{H-H}$ = 6 Hz), 4.58 (2H, t, $^3J_{H-H}$ = 6 Hz). δ ESIMS m/z $[M+H]^+$ 180.2

5.1.31 Preparation of 1-(3-azidopropyl)-1H-imidazole-2-carbaldehyde

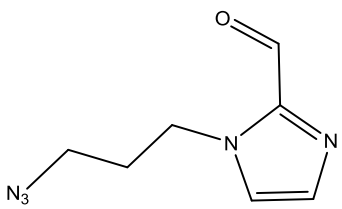

To a mixture of imidazole-2-carboxaldehyde (300mg, 3.125 mmol) and potassium carbonate (500 mg, 3.6 mmol) in anhydrous DMF (10 mL) was added 3-azidopropyl methanesulfonate. The reaction was stirred at room temperature under an argon atmosphere for 18 h. The suspension was filtered and the filtrate was diluted with water (20 mL). The solution was extracted with diethyl ether (3 x 50 mL), the organic layer dried over $MgSO_4$, filtered and the solvent evaporated to provide 1-(3-azidopropyl)-1H-imidazole-2-carbaldehyde as a yellow oil (374 mg, 67%). ^{1}H NMR (300 MHz, $CDCl_3$): δ 1.95 (2H, qu, $^3J_{H-H}$ = 6 Hz) 3.22 (2H, t, $^3J_{H-H}$ = 6 Hz), 4.37 (2H, t, $^3J_{H-H}$ = 6 Hz), 7.13 (1H, s), 7.19 (1H, s), 9.58 (1H, 2).

5.1.32 Preparation of L^{imN}

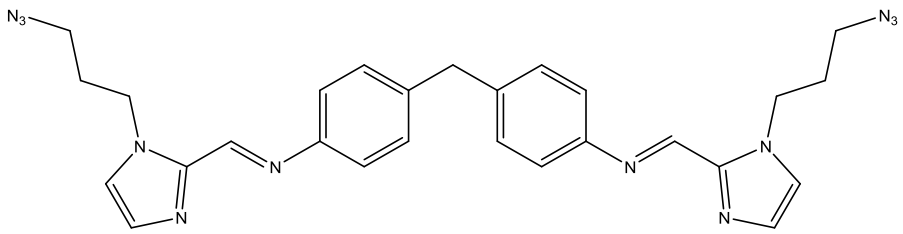

To a solution of 1-(3-azidopropyl)-1H-imidazole-2-carbaldehyde (150 mg, 0.84 mmol) dissolved in ethanol (10 mL) was added dropwise a solution of 4,4′-methylenedianiline (83

mg, 0.42 mmol in 2 mL ethanol). The reaction was stirred at room temperature for 18 h. A white precipitate formed that was collected by filtration, washed with cold methanol (100 mL) and diethyl ether (50 mL). The product was dried under vacuum to afford L^{imN} as a white powder (140mg, 64%). ^{1}H NMR (300 MHz, $CDCl_3$): δ 2.25 (q, 2H), 3.45 (t, 2H), 4.12 (s, 1H), 4.75 (t, 2H), 7.17 (s, 1H), 7.30 (d, 4H), 7.36 (s, 1H), 8.64 (s, 1H). ^{13}C {^{1}H} NMR (100 MHz, $CDCl_3$): δ 30.09, 45.27, 48.49, 115.49, 121.25, 124.93, 129.80, 129.94, 130.49, 139.77, 149.08, 150.61.

5.1.33 Preparation of $[Fe_2L^{imN}_3][PF_6]_4$

Ligand L^{imN} (50 mg, 0.09 mmol) was suspended in methanol (10 mL). $Fe(II)Cl_2{\cdot}4H_2O$ (12 mg, 0.06 mmol) was dissolved in methanol (2 mL), this was added dropwise to the stirred Ligand L^{imN} solution. Upon addition of the metal salt the solution turned dark red. The reaction was stirred for 24 hours at room temperature. A saturated methanolic solution of ammonium hexafluorophosphate was added (1 mL) and the complex precipitated from solution. The solid was collected by filtration and washed with cold methanol (50 mL) and diethyl ether (50 mL). The red solid was dried under reduced pressure to afford $[Fe_2L^{imN}_3][PF_6]_4$ (23 mg, 34%). ^{1}H NMR (300 MHz, CD_3CN): δ 3.09 (bs), 3.37 (s), 3.89 (s), 4.44 (s), 4.64 (bs), 6.58 (d), 6.90 (d), 7.26 (s), 8.49 (bs), 9.72 (s), 11.84 (bs), 15.17 (s), 17.32 (s), 53.14 (bs), 58.20 (bs), 96.78 (bs). ESIMS m/z observed at 418.02 $[M+H]^{4+}$.

5.1.34 Preparation of $[Ni_2L^{imN}_3][PF_6]_4$

Ligand L^{imN} (50 mg, 0.09 mmol) was suspended in methanol (10 mL). $Ni(II)Cl_2{\cdot}6H_2O$ (14 mg, 0.06 mmol) was dissolved in methanol (2 mL), this was added dropwise to the stirred Ligand L^{imN} solution. Upon addition of the metal salt the solution turned orange. The reaction was stirred for 24 hours at room temperature. A saturated methanolic solution of ammonium hexafluorophosphate was added (1 mL) and the complex precipitated from

solution. The solid was collected by filtration and washed with cold methanol (50 mL) and diethyl ether (50 mL). The orange solid was dried under reduced pressure to afford $[Ni_2L^{imN}{}_3][PF_6]_4$ (28 mg, 42%). ESIMS m/z observed at 419.80 $[M+H]^{4+}$.

5.1.35 Preparation of L

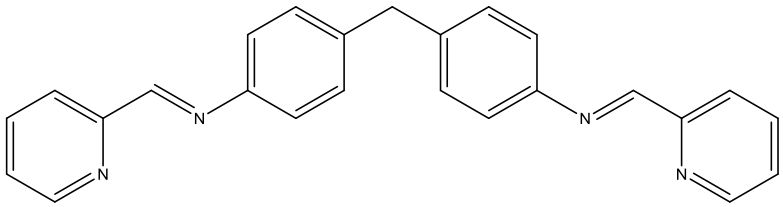

4,4′-Methylenedianiline (500 mg, 2.52 mmol) was dissolved in ethanol (50 mL), 2-pyridinecarbaldehyde (0.5 mL, 5.04 mmol) was added dropwise. A cream suspension formed and the reaction was stirred for 22 h at room temperature. The precipitate was collected by filtration, washed with methanol (50 mL), diethyl ether (20 mL) and dried under vacuum to afford L as a pale cream solid (872 mg, 92%). ^{1}H NMR (300 MHz, $CDCl_3$): δ 4.05 (s, 1H), 7.26 (s, 4H), 7.39 (ddd, 1H), 7.81 (dt, 1H), 8.20 (d, 1H), 8.62 (s, 1H), 8.71 (d, 1H). ESIMS m/z $[M+H]^+$ 377.6.

5.1.36 Preparation of $[Fe_2L_3]Cl_4$

Ligand L (100 mg, 0.26 mmol) was suspended in methanol (10 mL). $Fe(II)Cl_2{\cdot}4H_2O$ (35 mg, 0.17 mmol) was dissolved in methanol (2 mL), this was added dropwise to the stirred Ligand L solution. Upon addition of the metal salt the solution turned purple. The reaction was stirred for 24 hours at room temperature. A saturated methanolic solution of ammonium hexafluorophosphate was added (1 mL) and the complex precipitated from solution. The purple solid was collected by filtration and washed with cold methanol (50 mL) and diethyl ether (50 mL). The purple solid was suspended in methanol (20 mL) and stirred with dowex to exchange the counter ion. The solution was stirred for 6 hours at room temperature, then filtered to remove the dowex beads. The solution was

concentrated under vacuum, to a small volume ~ 2 mL. Diethyl ether (50 mL) was added to precipitate the complex from solution. The precipitate was collected by filtration and dried under reduced pressure to afford $[Fe_2L_3][Cl]_4$ as a purple solid (97 mg, 81%). ^{1}H NMR (300 MHz, MeOD): δ 4.05 (s, 1H), 5.61 (bs, 2H), 7.03 (bs, 2H), 7.44 (d, 1H), 7.84 (t, 1H), 8.48 (t, 1H), 8.68 (d, 1H), 9.14 (s, 1H).

5.1.37 Preparation of L^{im}

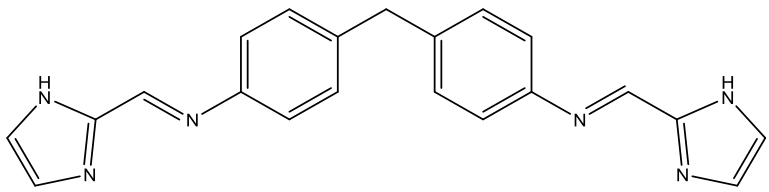

Imadazole-2-carboxaldehyde (500 mg, 5.2 mmol) was dissolved in methanol (20 mL). A solution of 4,4′-methylenedianiline (514 mg, 2.6 mmol) dissolved in methanol (2 mL) was added dropwise to the stirred solution forming a suspension. The reaction was stirred for 18 h at room temperature and the precipitate was collected by filtration, washed with cold methanol (50 mL) and diethyl ether (20 mL) and dried under vacuum to afford L^{im} as a white solid (874 mg, 95%). ^{1}H NMR (300 MHz, DMSO): 3.99 (s, 1H), 7.25 (d, 1H), 7.27 (s, 1H), 7.32 (s, 1H), 7.32 (d, 1H), 8.41 (s, 1H), 13.07 (bs, 1H).δ 13C {1H} NMR (100 MHz, DMSO): δ 154.4, 150.4, 131.2, 130.1, 121.6, 120.6, 40.6. ESIMS m/z $(M+H)^+$ 355.2

5.1.38 Preparation of 1-((1-(7-(diethylamino)-2-oxo-2H-chromen-3-yl)-1H-1,2,3-triazol-4-yl)methyl)-1H-imidazole-2-carbaldehyde

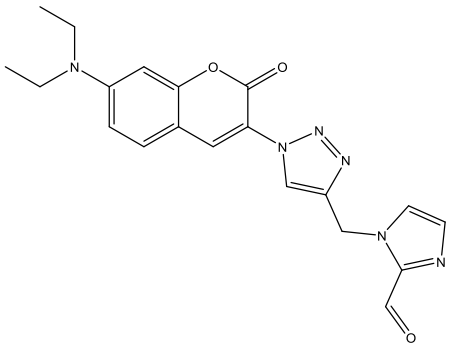

A mixture of 3-azido-7-diethylaminocoumarin (96 mg, 0.37 mmol) and 1-(prop-2-yn-1-yl)-1H-imidazole-2-carbaldehyde (50 mg, 0.37 mmol) were dissolved in THF and water (5:1, 10 mL). A freshly prepared 1 M solution of sodium ascorbate (34 µl, 0.034 mmol) in water was added followed by a freshly prepared 7.5% solution of copper (II) sulphate pentahydrate (28 µl, 0.0085 mmol) in water. The mixture was stirred in the dark at room temperature for 72 h. Ice cold water (20 ml) was added to the reaction and the precipitate was rapidly collected by filtration. The solid was washed with ethanol (20 mL), diethyl ether (20ml). The product was then washed through into a separate flask with chloroform (20 mL) and the solvent evaporated to dryness to afford 1-((1-(7-(diethylamino)-2-oxo-2H-chromen-3-yl)-1H-1,2,3-triazol-4-yl)methyl)-1H-imidazole-2-carbaldehyde as a yellow solid (48 mg, 33%). ^{1}H NMR (300 MHz, $CDCl_3$): δ 1.18 (t, 6H), 3.39 (q, 4H), 3.42 (s, 2H), 5.73 (s, 2H), 6.49 (d, 1H), 6.60 (dd, 1H), 7.33 (d, 1H), 8.26 (s, 1H), 8.52 (s, 1H), 9.80 (bs, 1H). ^{13}C {^{1}H} NMR (100 MHz, $CDCl_3$): δ 12.4, 42.3, 45, 97.1, 106.9, 110.1, 116.6, 124.0, 130.1, 135.1, 142.2, 142.7, 143.9, 151.7, 155.9, 156.8, 182.4.

5.1.39 Preparation of L^{imC}

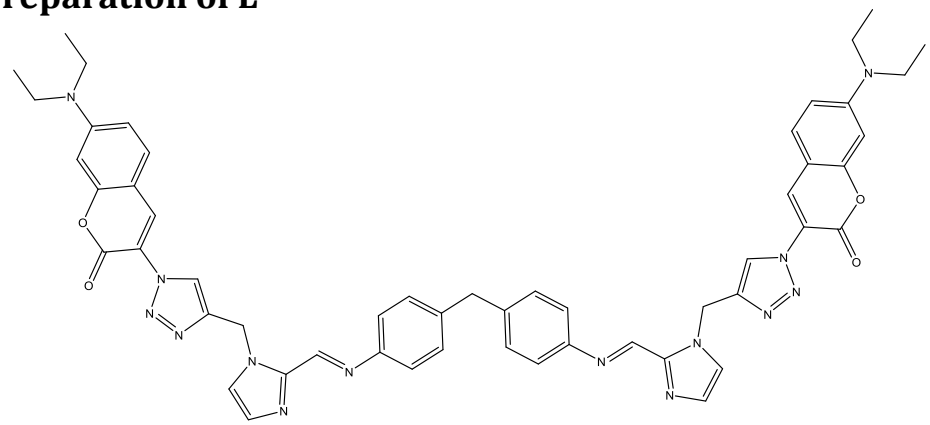

1-((1-(7-(diethylamino)-2-oxo-2H-chromen-3-yl)-1H-1,2,3-triazol-4-yl)methyl)-1H-imidazole-2-carbaldehyde (20 mg, 0.05 mmol) was dissolved in methanol (5 mL). 4,4′-Methylenedianiline (5 mg, 0.025 mmol) was dissolved in methanol (1 mL), and added dropwise to the stirred solution forming a suspension. The reaction was stirred for 18 h at room temperature and the precipitate was collected by filtration, washed with cold methanol (50 mL) and diethyl ether (20 mL) and dried under vacuum to afford L^{imC} as a yellow solid (19 mg, 82%). ^{1}H NMR (300 MHz, $CDCl_3$): δ 1.23 (t, 6H), 3.44 (q, 4H), 4.04 (s, 1H), 6.03 (s, 2H), 6.53 (s, 1H), 6.65 (d, 1H), 7.28 (s, 4H), 7.38 (d, 1H), 8.32 (s, 1H), 8.62 (s, 1H). ^{13}C {^{1}H} NMR (100 MHz, $CDCl_3$): δ12.42, 41.09, 45.00, 97.04, 106.95, 110.04, 116.72, 121.30, 123.85, 129.91, 130.01, 134.90, 139.68, 151.64, 155.85, 156.82. ESIMS m/z calculated 946.41, observed 947.4 $[M+H]^+$.

5.1.40 Preparation of $[Fe_2L^{imC}_3][PF_6]_4$

Ligand L^{imC} (8 mg, 0.008 mmol) was suspended in methanol (5 mL). $Fe(II)Cl_2{\cdot}4H_2O$ (1 mg, 0.005) was dissolved in methanol (1 mL), this was added dropwise to the stirred Ligand L^{imC} solution. Upon addition of the metal salt the solution turned dark red. The reaction was stirred for 24 hours at room temperature. A saturated methanolic solution of ammonium hexafluorophosphate was added (100 μ) and the complex precipitated from solution. The solid was collected by filtration and washed with cold methanol (5 mL) and

diethyl ether (5 mL). The red solid was dried under reduced pressure to afford $[Fe_2L^{imC}{}_3][PF_6]_4$ (4.1 mg, 43%). ESIMS m/z observed at 738.23 $[M+H]^{4+}$.

5.1.41 Preparation of $[Ni_2L^{imC}{}_3][PF_6]_4$

Ligand L^{imC} (8 mg, 0.008 mmol) was suspended in methanol (5 mL). Ni(II)$Cl_2 \cdot 6H_2O$ (1.3 mg 0.005) was dissolved in methanol (1 mL), this was added dropwise to the stirred Ligand L^{imC} solution. Upon addition of the metal salt the solution turned orange. The reaction was stirred for 24 hours at room temperature. A saturated methanolic solution of ammonium hexafluorophosphate was added (100 µl) and the complex precipitated from solution. The solid was collected by filtration and washed with cold methanol (5 mL) and diethyl ether (5 mL). The orange solid was dried under reduced pressure to afford $[Ni_2L^{imC}{}_3][PF_6]_4$ (3.8 mg, 40%). ESIMS m/z observed at 739.65 $[M+H]^{4+}$.

5.1.42 Preparation of dasnyl _C3_N3

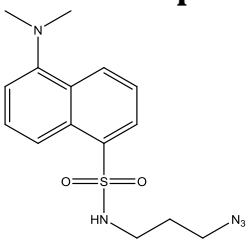

Dansyl chloride (200 mg, 0.74 mmol) was dissolved in anhydrous DCM (5 mL) and anhydrous triethylamine (103 µl, 0.74 mmol). The solution was cooled to 0 °C under argon before the addition of 3-azidopropylamine (300 µl). The reaction was stirred for 1 h at 0 °C before warming to room temperature and string for an additional 2 hours. The solvent was removed in vacuo and the crude product was purified by flash chromatograph on silica gel using DCM/MeOH (49:1) as eluent, to afford the product as a yellow oil (141.9 mg, 58 %). ^{1}H NMR (300 MHz, $CDCl_3$): δ 1.62 (2H, qu, $^3J_{H-H}$ = 6.6 Hz), 2.88 (6H, s), 2.97 (2H, q, $^3J_{H-H}$ = 6.6Hz), 3.22 (2H, t, $^3J_{H-H}$ = 6.3 Hz), 5.38 (1H, t, $^3J_{H-H}$ = 6.3 Hz), 7.17 (1H, d, $^3J_{H-H}$ = 7.5 Hz), 7.53 (2H, m), 8.25 (1H, dd, $^3J_{H-H}$ = 7.5 Hz, $^4J_{H-H}$ = 1.2 Hz), 8.31 (1H, d, $^3J_{H-H}$ = 8.4 Hz), 8.54 (1H, d, $^3J_{H-H}$ = 8.4 Hz). ^{13}C {^{1}H} NMR (100 MHz, $CDCl_3$): δ 28.82, 40.70, 45.44, 48.70, 115.30, 118.62, 123.21, 128.53, 129.56, 130.63, 134.46, 152.09. ESMS m/z calculated 333.13, found $[M+H]^+$ at 334.1.

5.1.43 Preparation of FITC_C3_N3

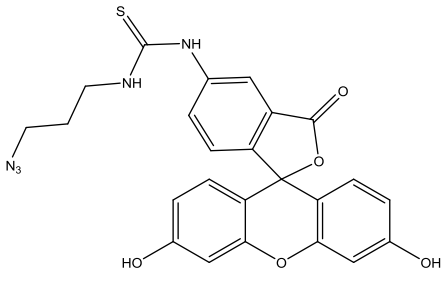

Fluorescein isothiocyanate isomer I (100 mg, 0.257 mmol) was suspended in anhydrous DCM (5mL) and anhydrous triethylamine (70 µl, 0.502 mmol). 3-Azidopropylamine (300 µl) was added dropwise, the solution was stirred under argon at room temperature for 48 h. The solvent was removed under reduced pressure and the residue purified using flash chromatography on silica gel using DCM/MeOH (9/1). The residue was dried under vacuum overnight to afford the product as an orange powder (66 mg, 53%) ^{1}H NMR (300 MHz, CD_3OD): δ 1.88 (2H, qu, $^{3}J_{H-H}$ = 6.6 Hz), 3.27 (1H, qu, $^{4}J_{H-H}$ = 1.8 Hz), 3.38 (2H, t, $^{3}J_{H-H}$ = 6.6 Hz), 3.66 (2H, t, $^{3}J_{H-H}$ = 6.9 Hz), 6.49 (1H, d, $^{4}J_{H-H}$ = 2.4 Hz), 6.52 (1H, d, $^{4}J_{H-H}$ = 2.4 Hz), 6.63 (1H, s), 6.64 (1H, s), 6.67 (1H, s), 6.70 (1H, s), 7.11 (1H, d, $^{3}J_{H-H}$ = 8.1 Hz), 7.69 (1H, dd, $^{3}J_{H-H}$ = 8.1 Hz, $^{4}J_{H-H}$ = 1.8 Hz), 8.07 (1H, d, $^{4}J_{H-H}$ = 1.8 Hz). ^{13}C {^{1}H} NMR (100 MHz, CD_3OD): δ 29.33, 43.06, 50.31, 103.56, 111.89, 114.33, 120.60, 126.16, 130.08, 130.19, 130.53, 131.50, 131.59, 142.27, 148.20, 154.60, 162.67, 171.37, 182.99. ESMS m/z calculated 489.11, found $[M+H]^+$ at 490.1.

5.1.44 Preparation of FITC_PEG3_N3

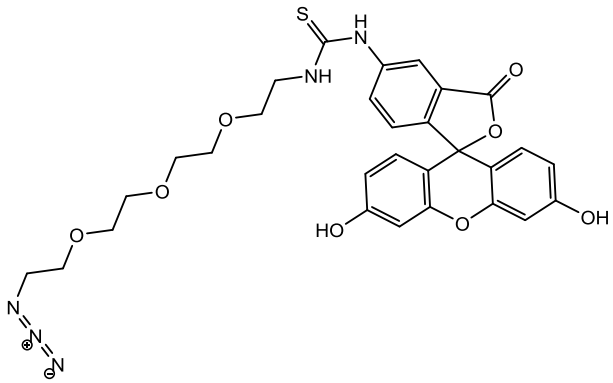

Fluorescein isothiocyanate isomer I (100 mg, 0.257 mmol) was suspended in anhydrous DCM (5mL) and anhydrous triethylamine (100 µl, 0.717 mmol). 11-azido-3,6,9-trioxaundecan-1-amine (200 µl, mmol) was added dropwise, the solution was stirred under argon at room temperature for 36 h. The solvent was removed under reduced pressure and the residue purified using flash chromatography on silica gel using DCM/MeOH (6/1). The residue was dried under vacuum overnight to afford the

product as an orange powder (75 mg, 48%)^{1}H NMR (400 MHz, CD_3OD): δ 3.28-3.26 (2H, m), 3.55-3.66 (14H, m), 3.76 (2H, bs), 6.49 (1H, d, $^{4}J_{H-H}$ = 2.4Hz), 6.51 (1H, d, $^{4}J_{H-H}$ = 2.8 Hz), 6.67 (1H, 2), 6.641 (1H, s), 6.644 (1H, s), 7.10 (1H, d, $^{3}J_{H-H}$ = 8.0 Hz), 7.73 (1H, d, $^{3}J_{H-H}$ = 8.0 Hz), 8.14 (1Hy, d, $^{4}J_{H-H}$ = 1.6 Hz). ^{13}C {^{1}H} NMR (100 MHz, CD_3OD): δ 45.45, 51.66, 62.14, 70.15, 70.99, 71.27, 71.39, 71.43, 71.47, 71.55, 103.55, 111.66, 113.67, 113.73, 113.99, 119.90, 125.89, 129.45, 130.16, 130.29, 130.41, 131.34, 131.44, 142.35, 148.68, 148.75, 154.32, 161.96, 171.23, 182.73.

5.1.45 Preparation of L^{TB5}

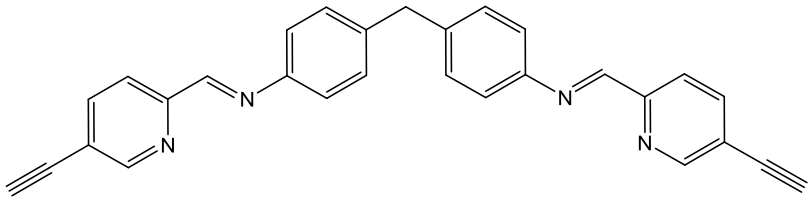

5-Ethynyl-2-formylpyridine (100 mg, 0.76 mmol) was dissolved in ethanol (20 mL). A solution of 4,4′-methylenedianiline (75 mg, 0.38 mmol) dissolved in ethanol (2 mL) was added dropwise to the stirred solution forming a suspension. The reaction was stirred for 18 h at room temperature and the precipitate was collected by filtration, washed with cold methanol (50 mL) and diethyl ether (20 mL) and dried under vacuum to afford L^{TB5} as a white solid (135 mg, 84%). ^{1}H NMR (300 MHz, CDCl): 3.34 (s, 1H), 4.05 (s, 1H), 7.25 (s, 4H), 7.88 (dd, 1H), 8.19 (dd, 1H), 8.61 (s, 1H), 8.79 (dd, 1H).

5.2 Cell culture experimental

5.2.1 General cell culture

DMEM (Dulbeccos Modified Eagles Medium with 4500mg glucose/L, 110mg sodium pyruvate/L, pyridioxine.HCl and $NaHCO_3$ and phenol red), PBS (Phosphate Buffered Saline – without sodium and magnesium chloride), FBS (Fetal Bovine Serum – heat inactivated, sterile filtered), L-Glutamine 200mM, Penicillin-Streptomycin - 10,000 units penicillin and 10 mg streptomycin/mL, trypsin-EDTA (0.5% trypsin, 0.2% EDTA, x 10 concentration) were all purchased from Sigma Aldrich and used as received. RPMI 1640 (Roswell Park Memorial Institute with 2000 mg glucose/L, Glutathione 1.0 mg/L and phenol red) and McCoys 5A media (3000 mg glucose/L, Bacto-Peptone 600mg/L Glutathione 0.5mg/L and phenol red) were purchased from GIBCO life technologies and used as received. All cell culture was performed in a sterile cell culture laminar flow cell culture hood. All solutions were warmed to 37 °C in a water bath prior to use.

5.2.2 Cell lines

MDA-231 human Caucasian breast adenocarcinoma (92020424) cultured using DMEM, A2780 human ovarian carcinoma (93112519) cultured using RPMI, U-2 OS Human Osteosarcoma (92022711) cultured using McCoys 5A, HeLa Human cervix epitheloid carcinoma (93021013) cultured using DMEM, HeK-293 Human Embryo Kidney (85120602) cultured using DMEM. All cell lines were obtained fro the European collection of cell culture (ECACC).

5.2.3 Cell media preparation

DMEM and RPMI were supplemented with FBS (10% v/v), penicillin (100 U/ml), streptomycin (100 µg/mL) and L-glutamine (2mM). McCoys 5A was supplemented with FBS (10% v/v), penicillin (100 U/ml) and streptomycin (100 µg/mL).

5.2.4 Cell culture passage

Cells were passaged once they reached 80% confluence. Media, Trypsin-EDTA and PBS were warmed to 37°C in a water bath. Old media was removed carefully, cells were then gently rinsed with PBS (10 mL), and the PBS removed. Trypin-EDTA (2 mL of a x1 solution) was added and then flask was returned to the incubater for 5 minutes. Cell detachment was monitored using a Leica DMIL light microscope. Once cells were fully detached, media was added to inhibit the trypsin-EDTA. The contents of the flask was transferred to a 15 mL falcon tube. The cell suspension was subjected to centrifugation in a Falcon 6/300 refrigerated centrifuge for 5 minutes at 1500 rpm at 20 °C. The supernatant was discarded and the cell pellet was resuspended in 1 mL of media. Fresh media (15 mL) was added to a new T75 flask along with 200 µL of the cell suspension. The flask was swirled gently to evenly distribute cells. The flask was then placed in an incubator at 37 °C with a 5% CO_2 atmosphere.

5.2.5 Cryopreservation of cells

Cell lines were preserved for future use by following cell passage up to centrifugation. The cell pellet was resuspended into 3 mL of freezing media (FBS and DMSO 10% v/v). 1 mL aliquots were placed into o-ring cryovials. Samples were placed in the -80°C freezer for 24 h and then transferred to a vapour phase liquid nitrogen tank for longterm storage.

5.2.6 Cell counting

The steps for cell passage were followed up to cell centrifugation and resuspension in 1 mL of media. 20 µL of the cell suspension was added to 180 µL of media in an eppindorf. A Hawksley BS.748 Neubauer haemocytometer with a 0.1 mm depth was sterilised with 70% ethanol along with a cover slip that was placed on top of the haemocytometer. 10 µL of the cell aliquot was pipetted onto each side of the haemocytometer. Cells were counted in the central square of the grid on both sides and an average was taken. The volume required for the desired number of cells was then calculated using the equation.

5.2.7 Sapphire disc sample preparation

35 mm Round sapphire discs (knights optical) were sterilised by placing them in a 70 % ethanol solution for 5 minutes, the air drying in a sterilpetri disc in a laminar flow hood. The discs were then dipped into PBS twice, followed by the applicable media for the cell type being used. One disc was then placed into each well in a sterile 6 well plate. Cells were counted using the above procedure and 300,000 cells were placed in each well and the total volume made up to 3 mL with media. The plates were then placed in an incubator at 37°C with 5% CO_2 for 24 hours to allow cells to adhere to the disc. Cells were the treated with the compound at the required concentration for the desired length of time. The media was then removed and the discs were gently washed twice with PBS to remove any residual media. The discs were then snap frozen using a dry ice and methanol slurry that had been allowed to cool down to -70°C. discs were firstly bolted from the side to remove the majority of PBS on the surface by capillary action. Discs where then hovered over the surface of the bath for a few seconds, submerged into the bath for 5 seconds, then placed into labelled 6 wells plates kept on a bed of dry ice. Samples where then stored in a -80°C freezer until use, when they were shipped to the diamond light source on dry ice.

5.2.8 TEM grid sample preparation

Gold TEM grids covered with an R2/2 quantifoil carbon film were sterilised by dipping in a 70% ethanol solution and then leaving them on a sterile surface to dry, until the ethanol had fully evaporated. One TEM grid was placed in each well of a 6 well plate. Cells were counted using the above procedure and 50,000 cell were placed into each well and the total volume made up to 3 mL using media. Plates were placed into and incubator at 37°C with 5% CO_2 for 24h for cells to adhere. Cells were then treated with compound at varying concentrations for the required length of time. Sampled were plunge frozen using a Joel Cy3 plunge freezer. Grids were removed from the well extremely carefully using opposable tweezers so as to not damage the quatifoil film. The sample were placed in the plunge freezer, blotted from behind for 2 seconds and then plunged in a solution of liquid nitrogen cooled liquid ethane. The sample was then transferred into cyro grid boxes whilst still submerged in liquid nitrogen. Sample grid boxes were stored at liquid nitrogen temperature in a dry shipper.

5.2.9 MatTek dish preparation

MatTek dishes were seeded with 300,000 cells per well and cells were left to adhere for 24 hours. The media was removed, cells were washed with PBS and clear media was added (without phenol red). The dish was transferred to the microscope, focused and an image taken before treatment. The complex was then added and an imaging time course was under taken.

Appendix

6 Appendix

6.1 NMR spectra of 5-trimethylsilylethynyl-2-formyl pyridine

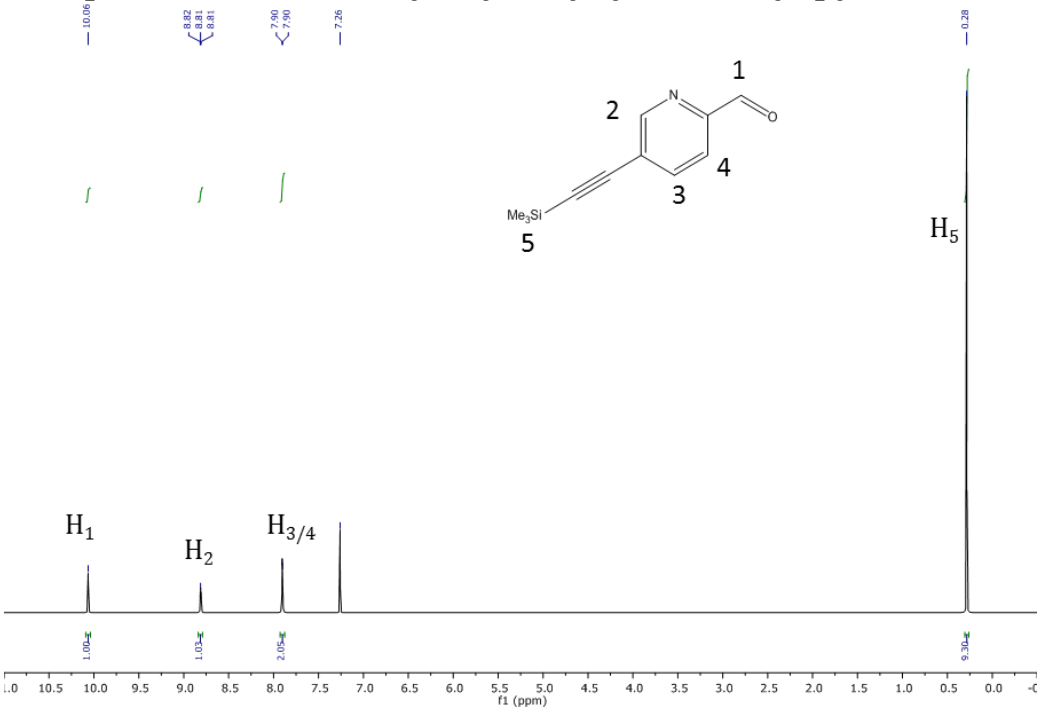

Figure 6.47 ^{1}H NMR spectrum of 5-trimethylsilylethynyl-2-formyl pyridine in $CDCl_3$

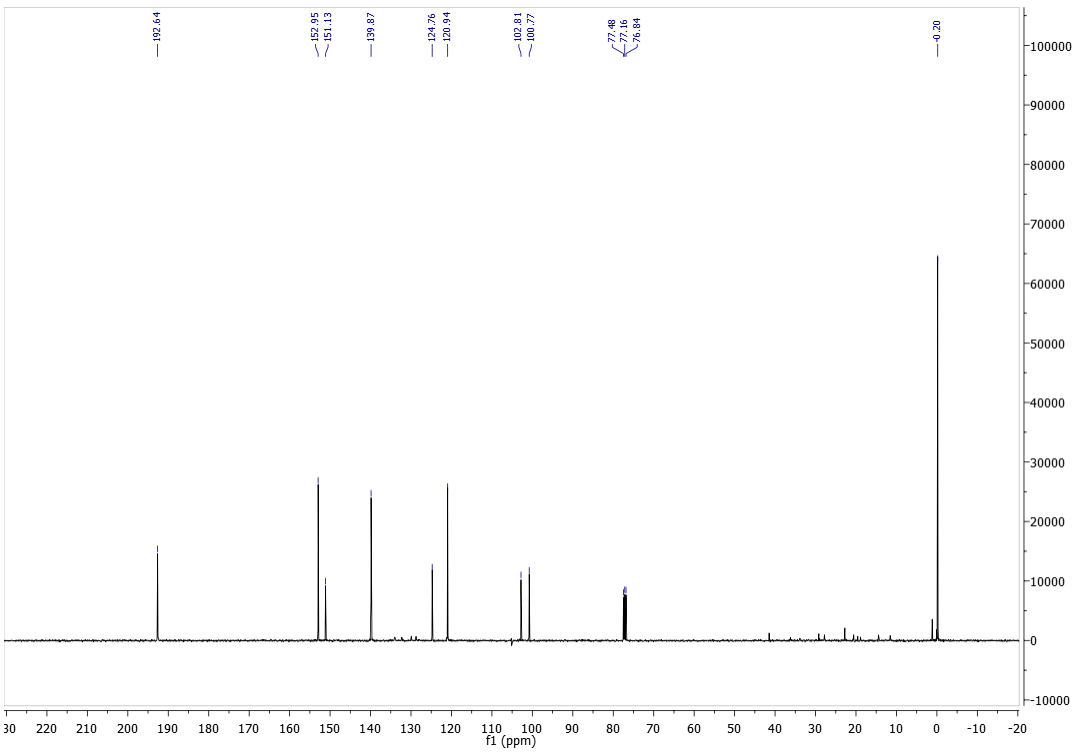

Figure 6.48 ^{13}C NMR spectrum of 5-trimethylsilylethynyl-2-formyl pyridine in $CDCl_3$

6.2 NMR spectra of 5-ethynyl-2-formylpyridine

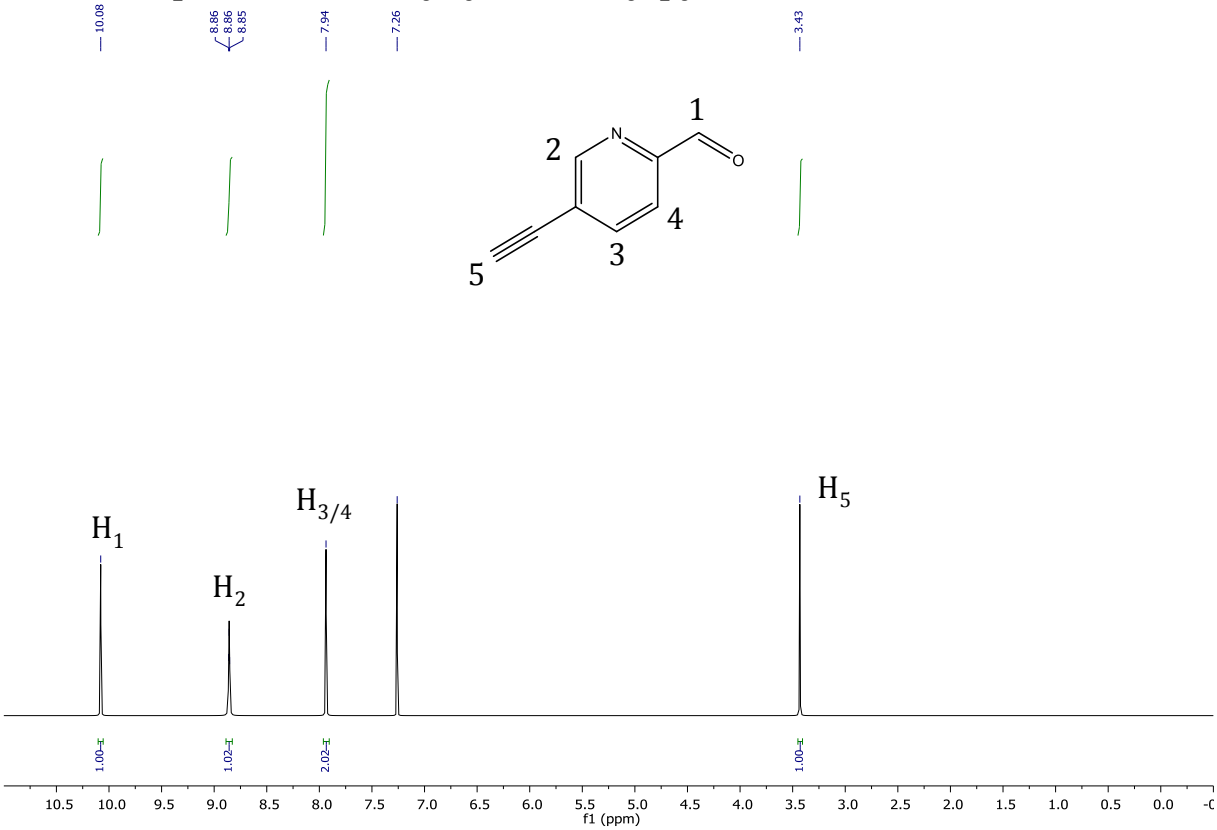

Figure 6.49 ^{1}H NMR spectrum of 5-ethynyl-2-formylpyridine in $CDCl_3$

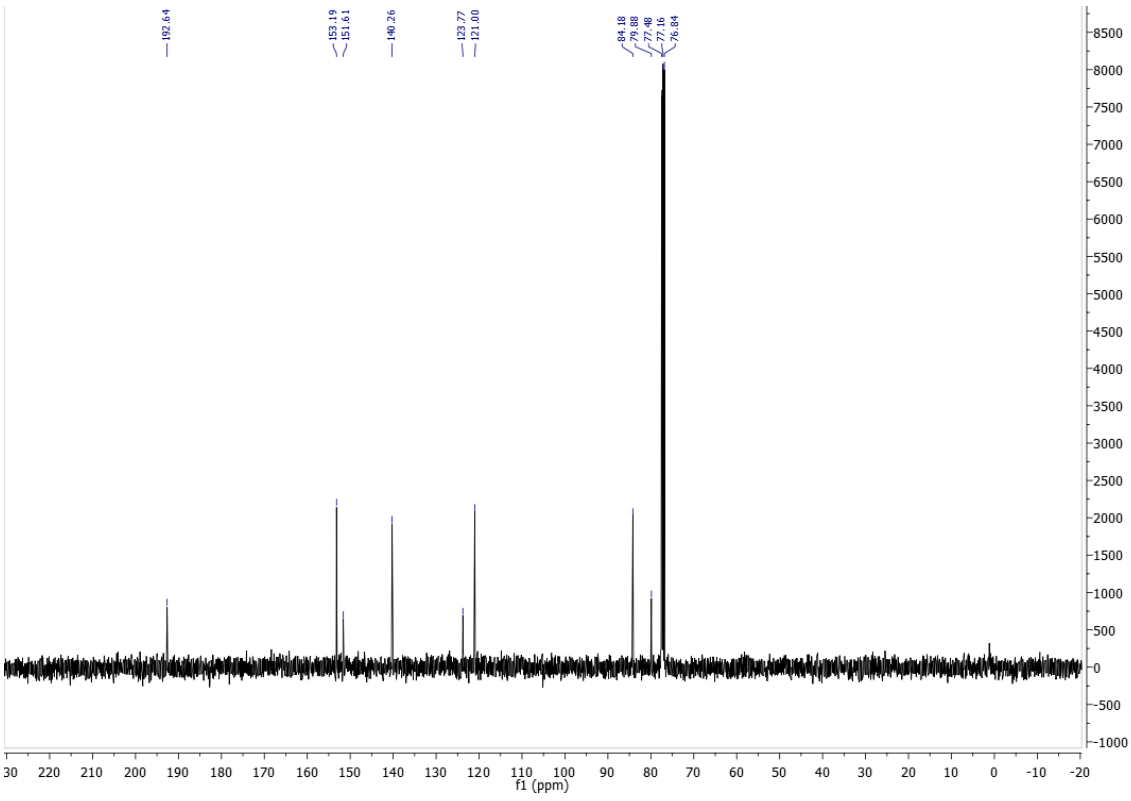

Figure 6.50 ^{13}C NMR spectrum of 5-ethynyl-2-formylpyridine in $CDCl_3$

6.3 NMR spectra of 4-trimethylsilylethynyl-2-formyl pyridine

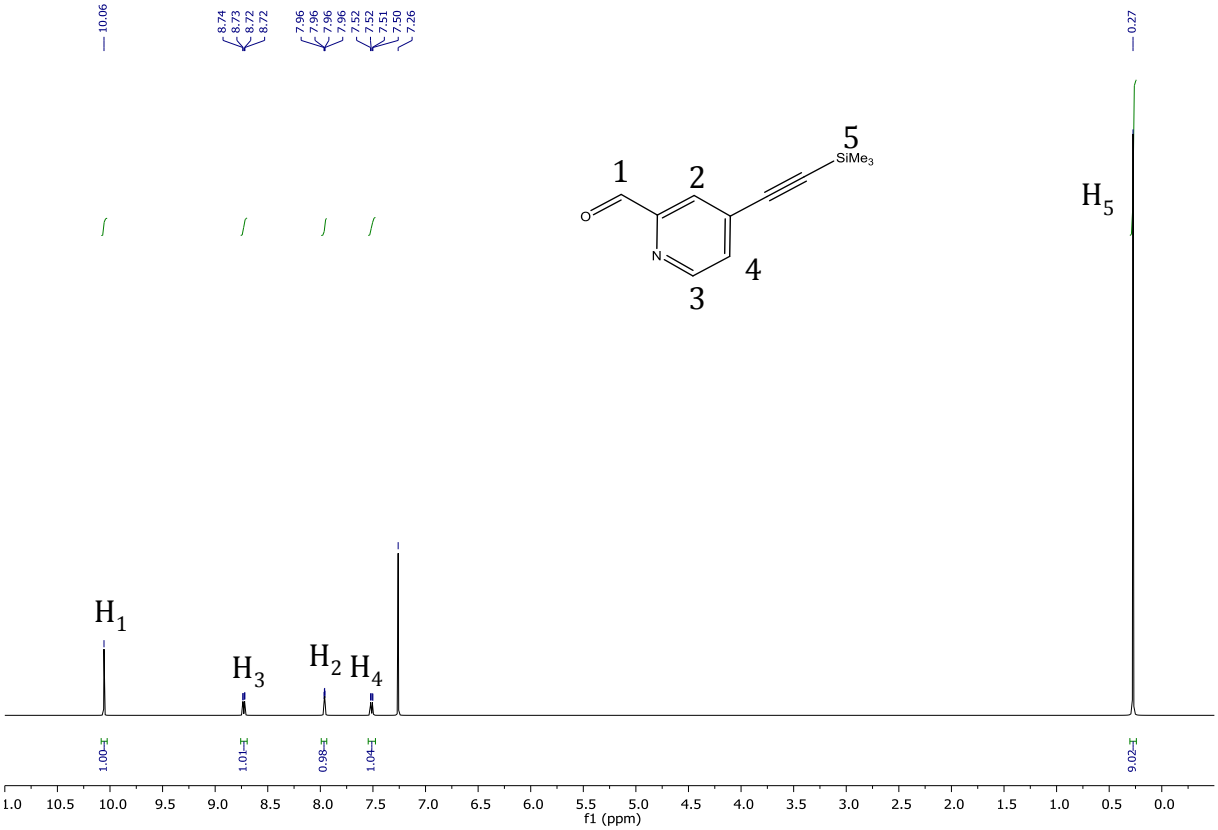

Figure 6.51 ^{1}H NMR spectrum of 4-trimethylsilylethynyl-2-formyl pyridine in $CDCl_3$

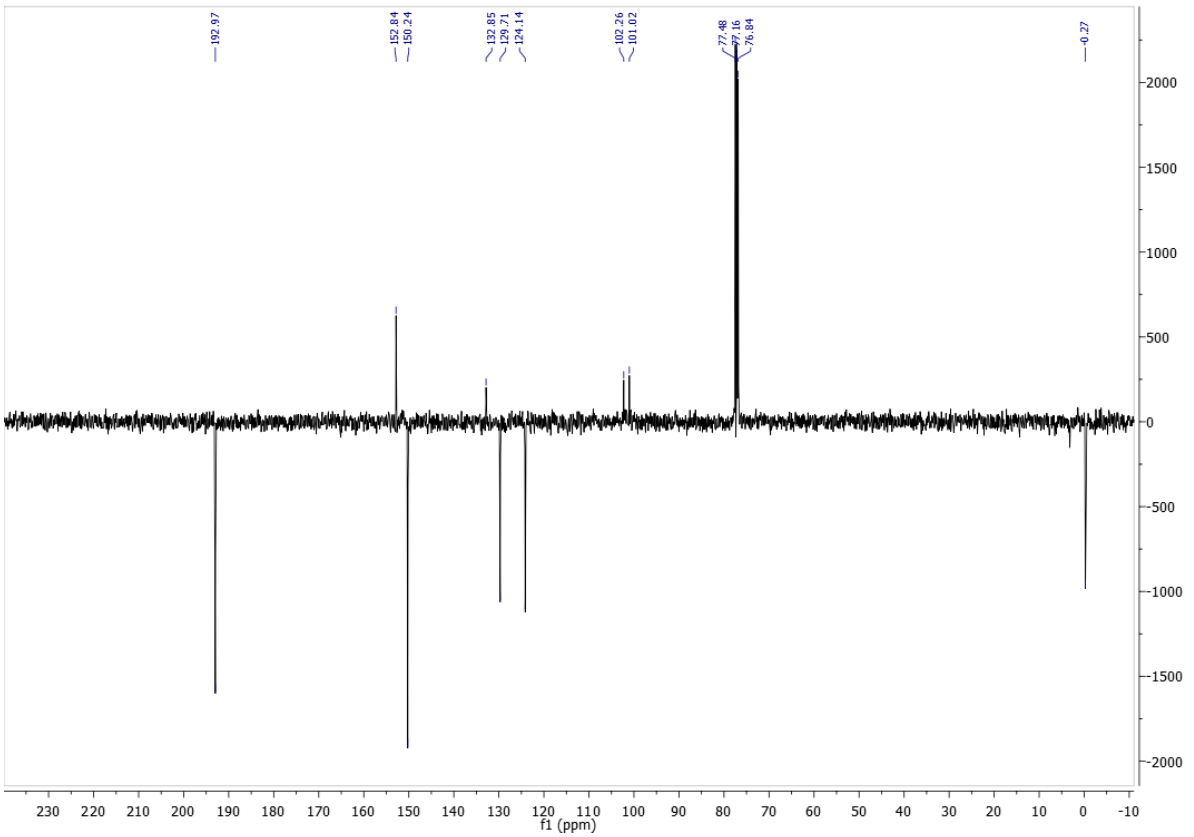

Figure 6.52 ^{13}C NMR spectrum of 4-trimethylsilylethynyl-2-formyl pyridine in $CDCl_3$

6.4 NMR spectra of 4-ethynyl-2-formylpyridine

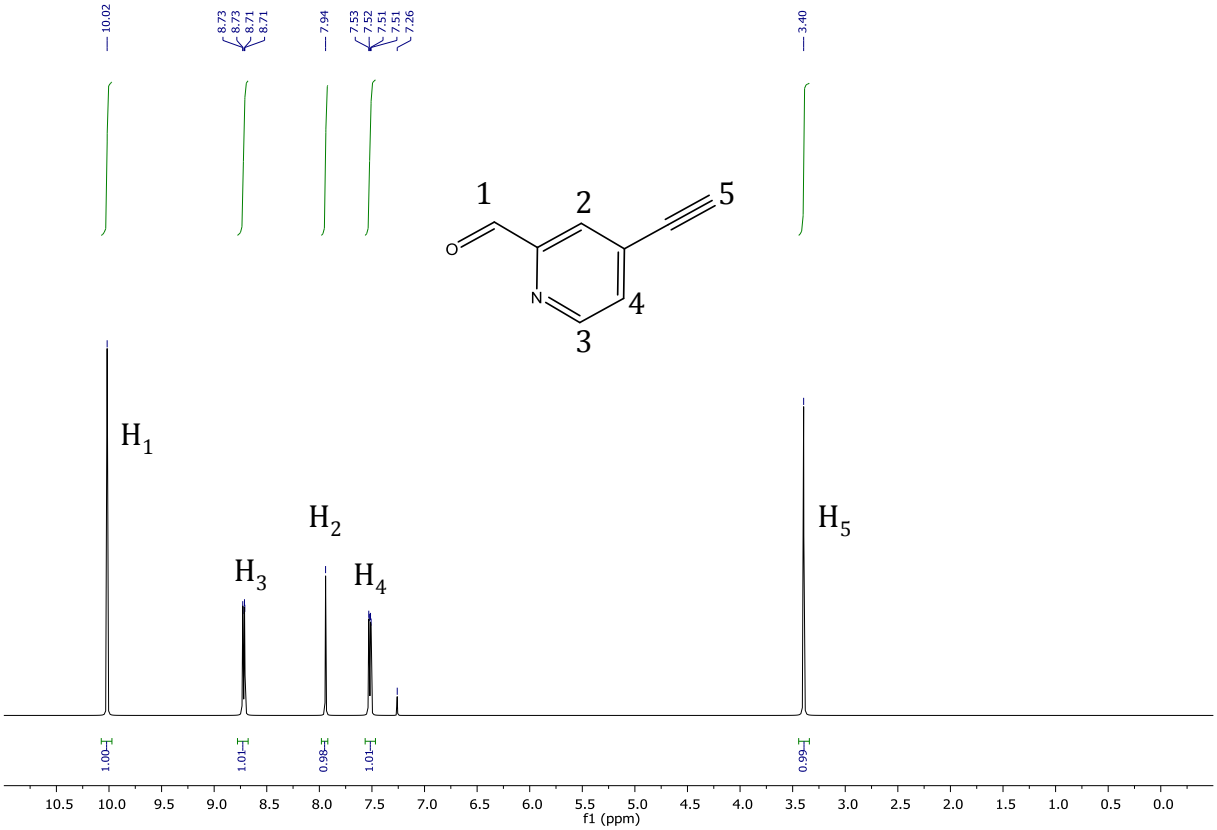

Figure 6.53 ^{1}H NMR spectrum of 4-ethynyl-2-formylpyridine in $CDCl_3$

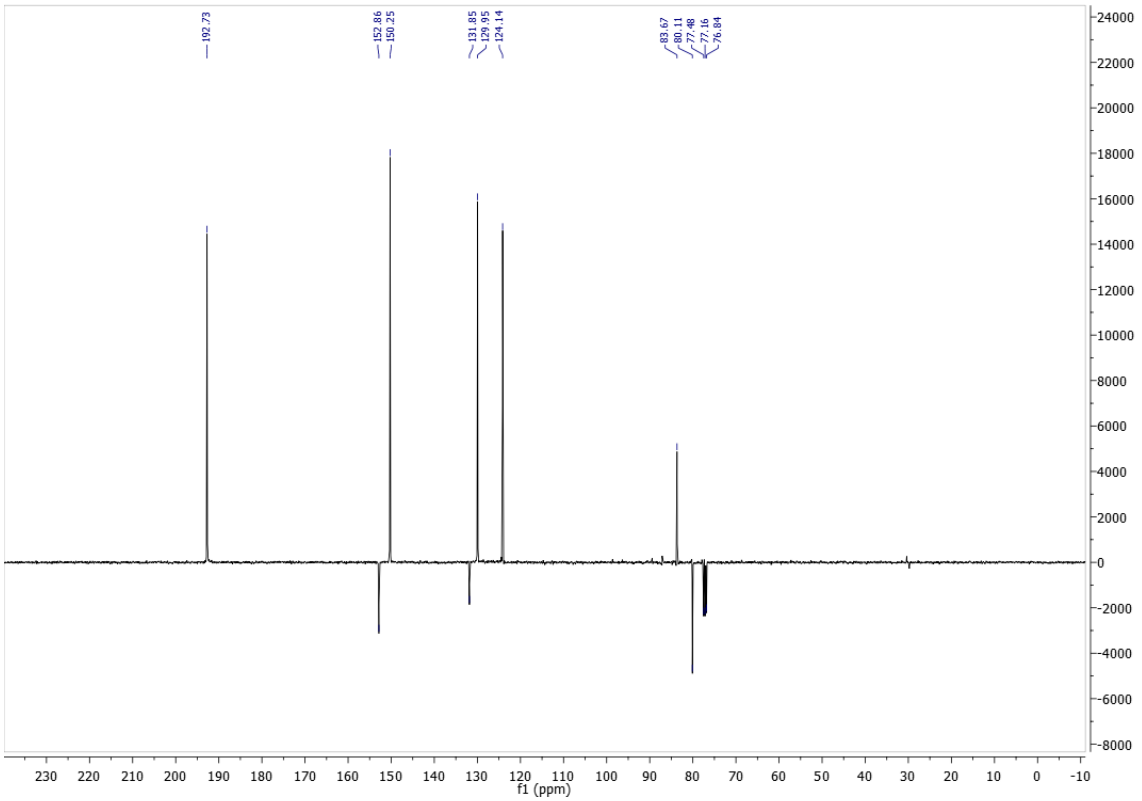

Figure 6.54 ^{13}C NMR spectrum of 4-ethynyl-2-formylpyridine in $CDCl_3$

6.5 NMR spectra of 3-nitro-7-diethylamino coumarin

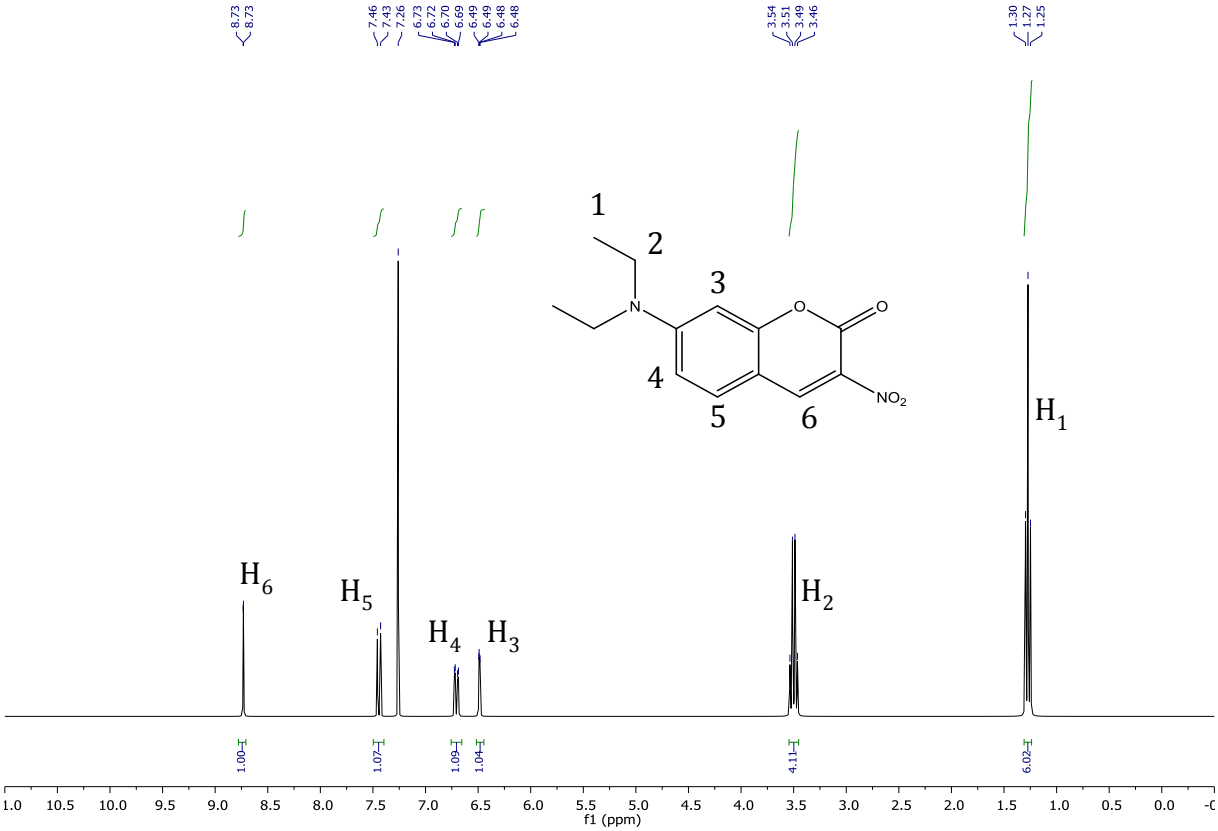

Figure 6.55 ^{1}H NMR spectrum of 3-nitro-7-diethylamino coumarin in $CDCl_3$

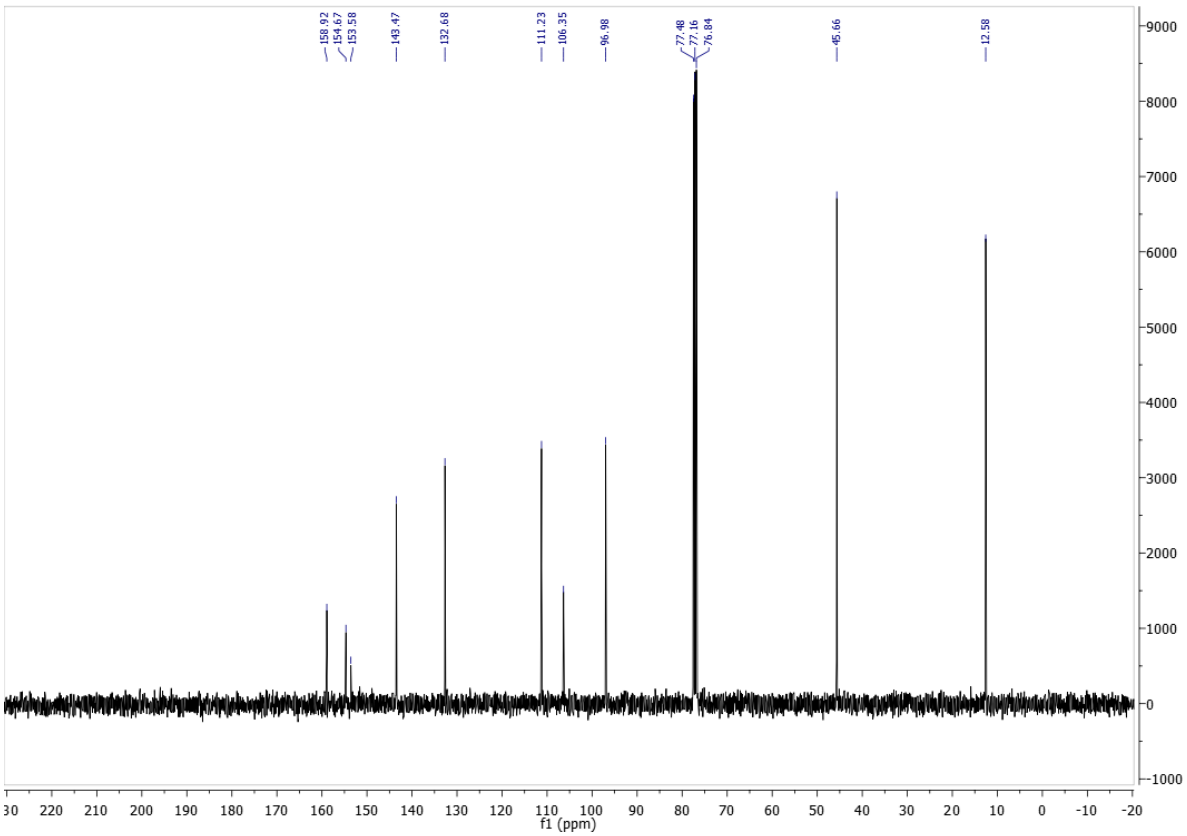

Figure 6.56 ^{13}C NMR spectrum of 3-nitro-7-diethylamino coumarin in $CDCl_3$

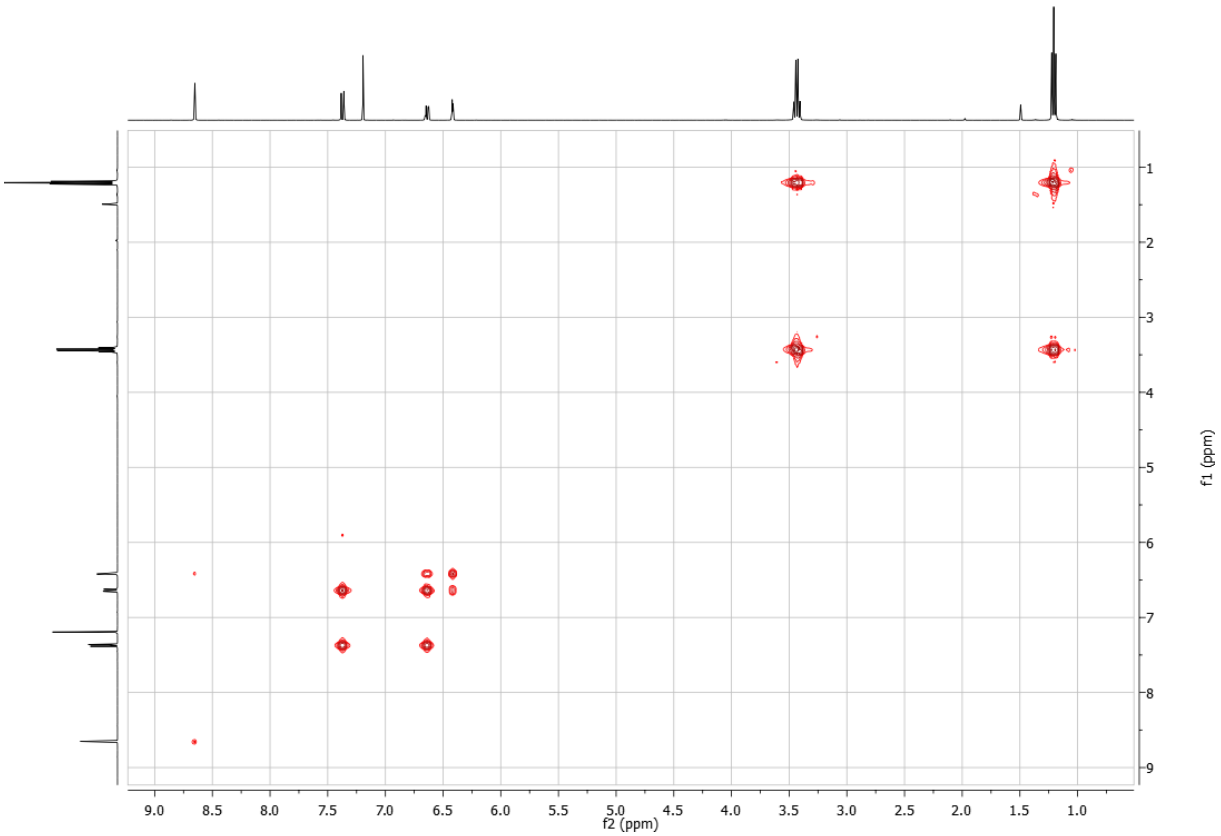

Figure 6.57 COSY NMR spectrum of 3-nitro-7-diethylamino coumarin in $CDCl_3$

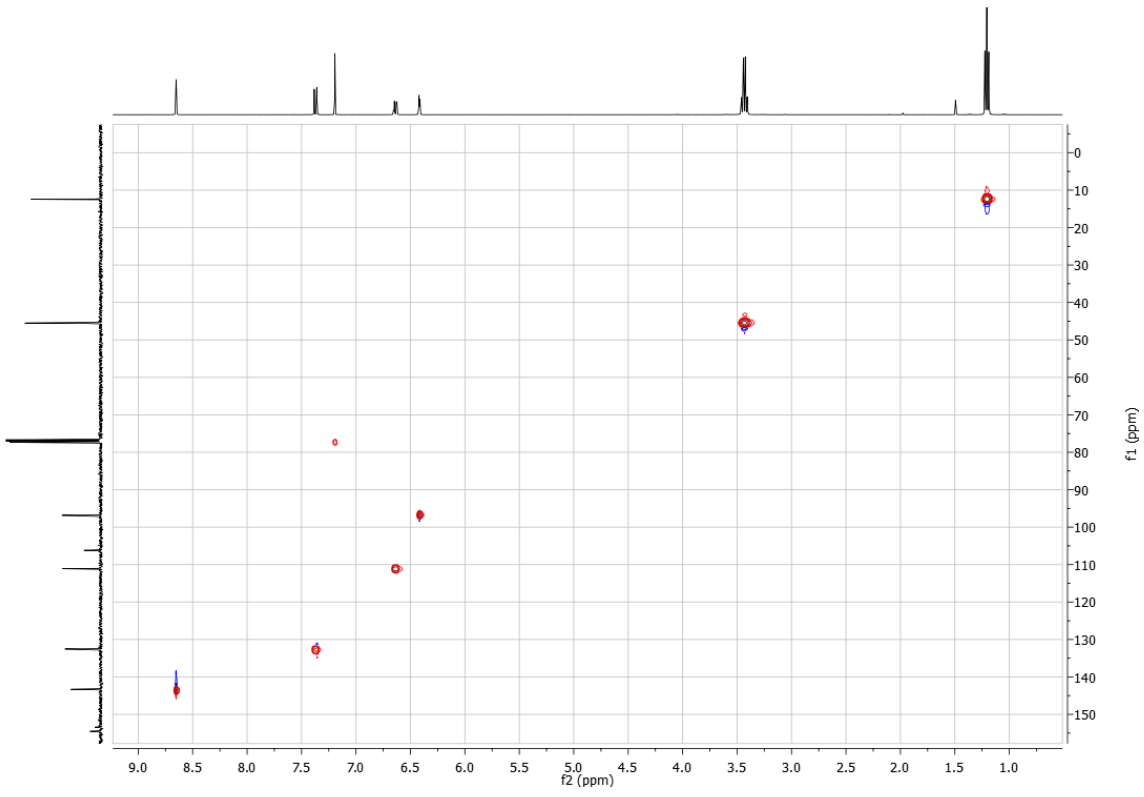

Figure 6.58 HSQC NMR spectrum of 3-nitro-7-diethylamino coumarin in $CDCl_3$

6.6 NMR spectra of 3-amino-7-diethylamino coumarin

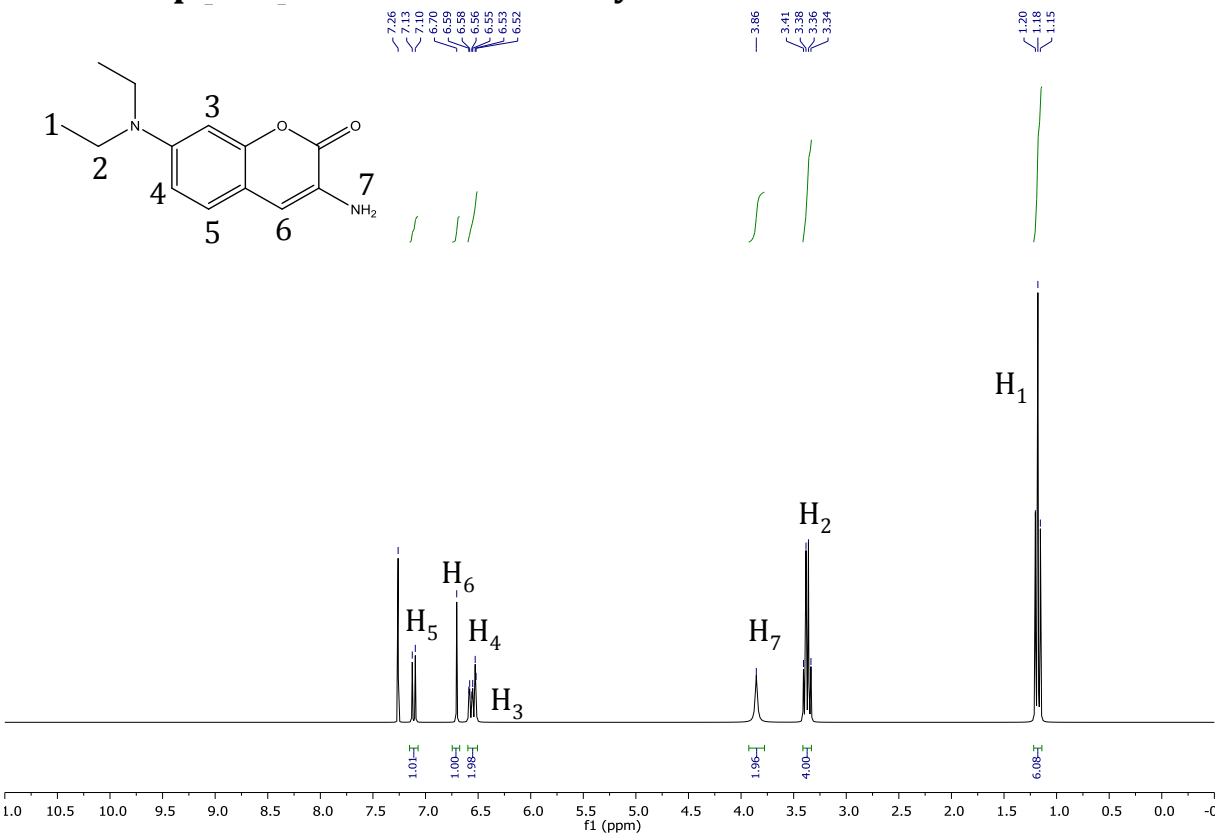

Figure 6.59 ^{1}H NMR spectrum of 3-amino-7-diethylamino coumarin in $CDCl_3$

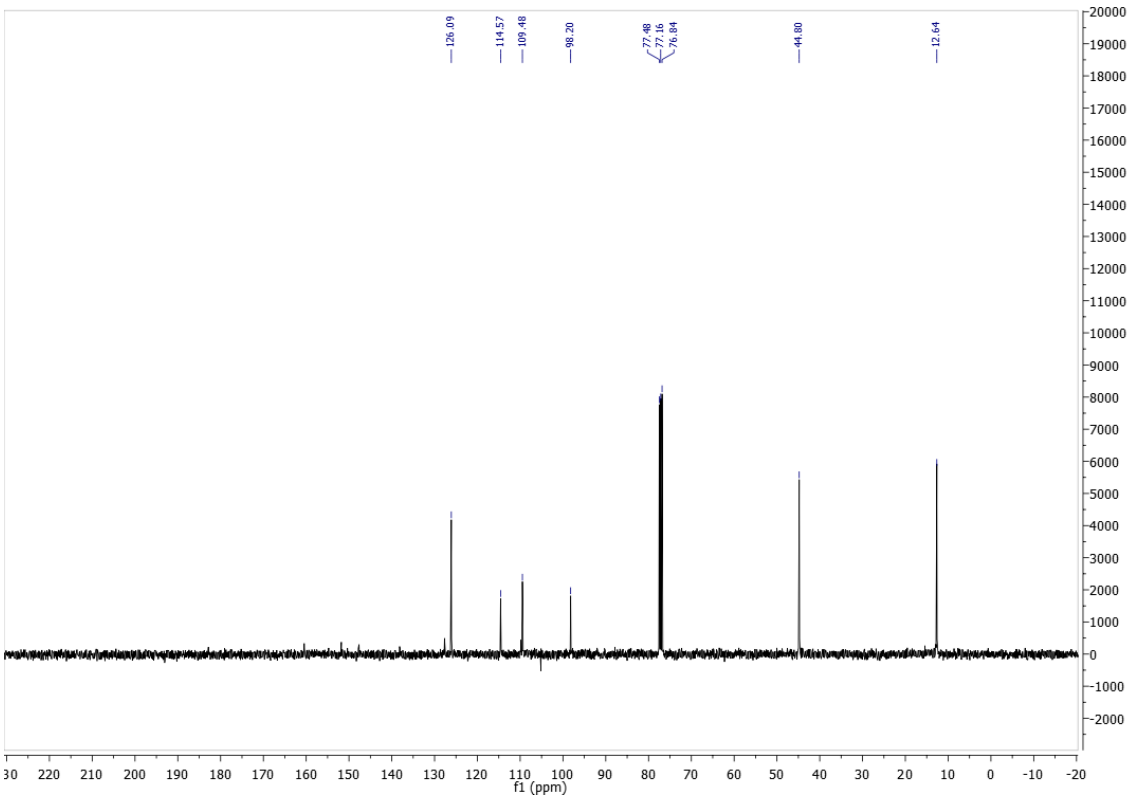

Figure 6.60 ^{13}C NMR spectrum of 3-amino-7-diethylamino coumarin in $CDCl_3$

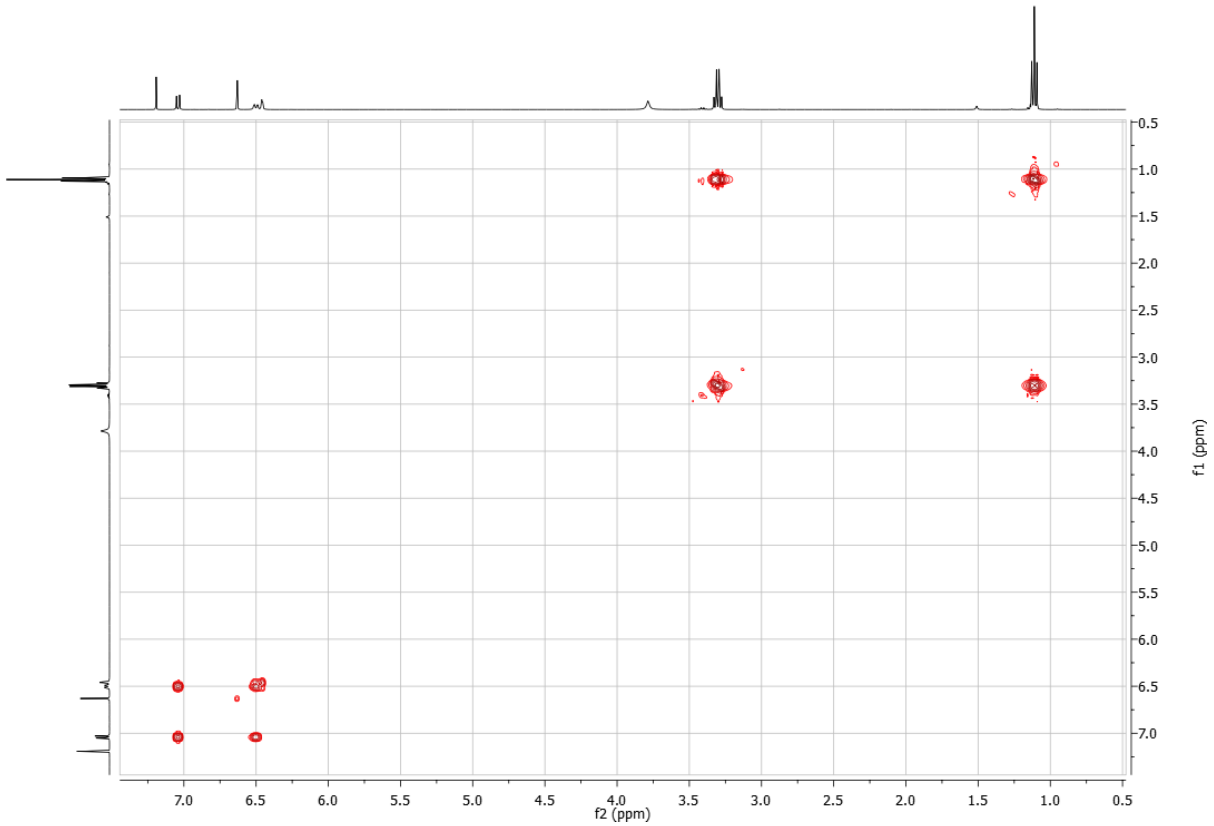

Figure 6.61 COSY NMR spectrum of 3-amino-7-diethylamino coumarin in CDCl3

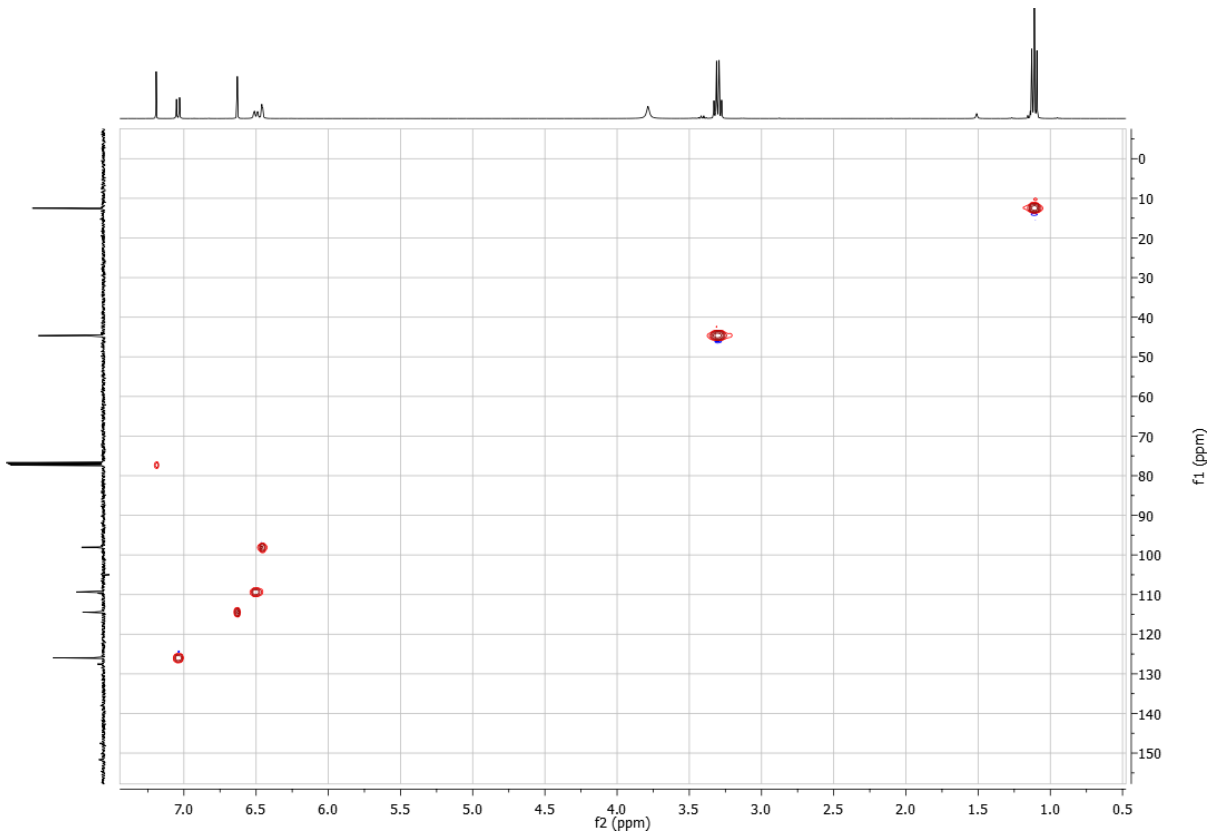

Figure 6.62 HSQC NMR spectrum of 3-amino-7-diethylamino coumarin in $CDCl_3$

6.7 NMR spectra of 3-azido-7-diethylaminocoumarin

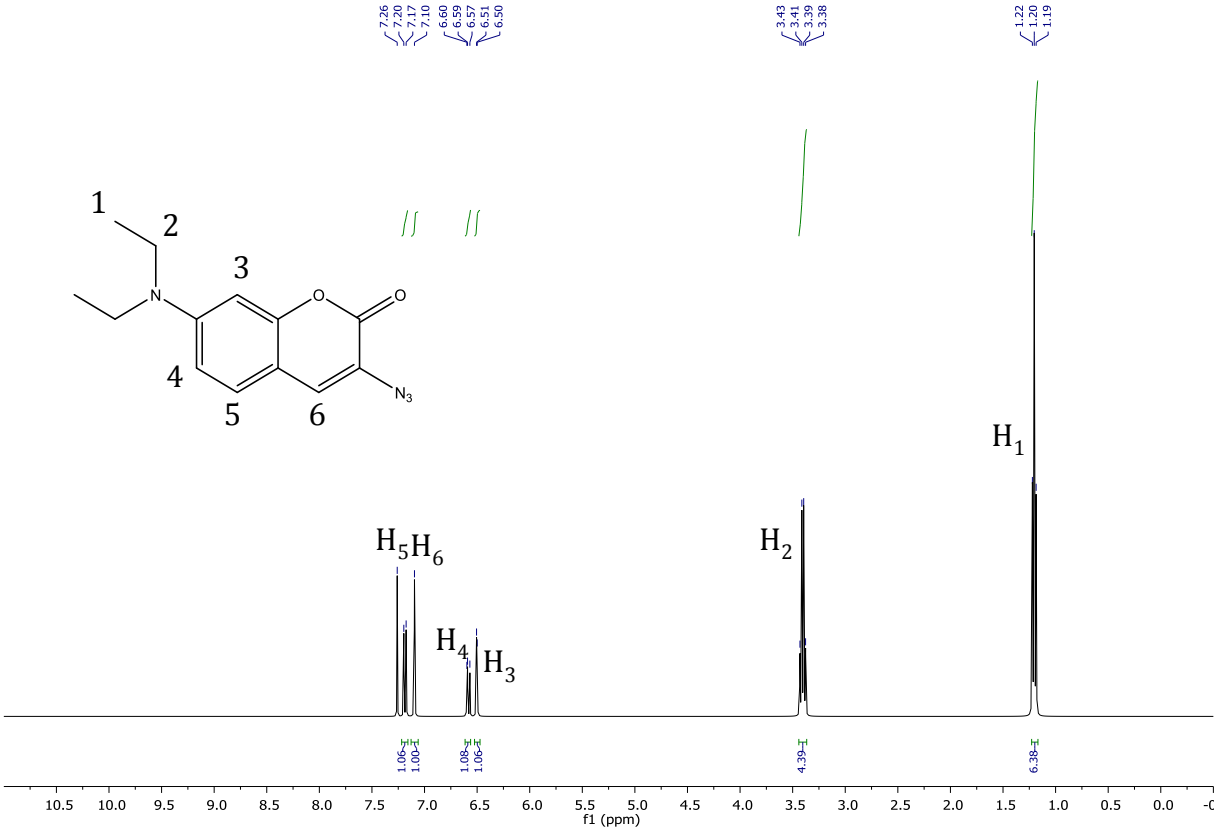

Figure 6.63 ^{1}H NMR spectrum of 3-azido-7-diethylaminocoumarin in $CDCl_3$

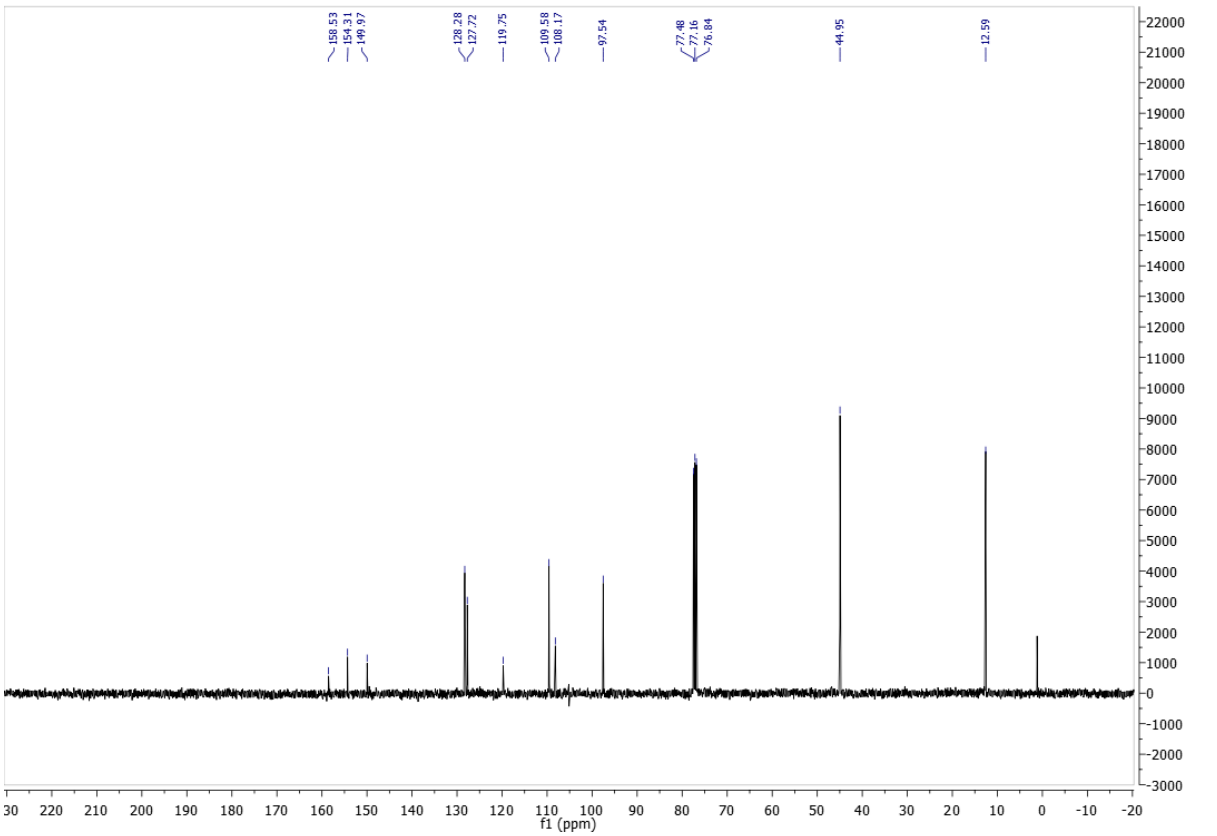

Figure 6.64 ^{13}C NMR spectrum of 3-azido-7-diethylaminocoumarin in $CDCl_3$

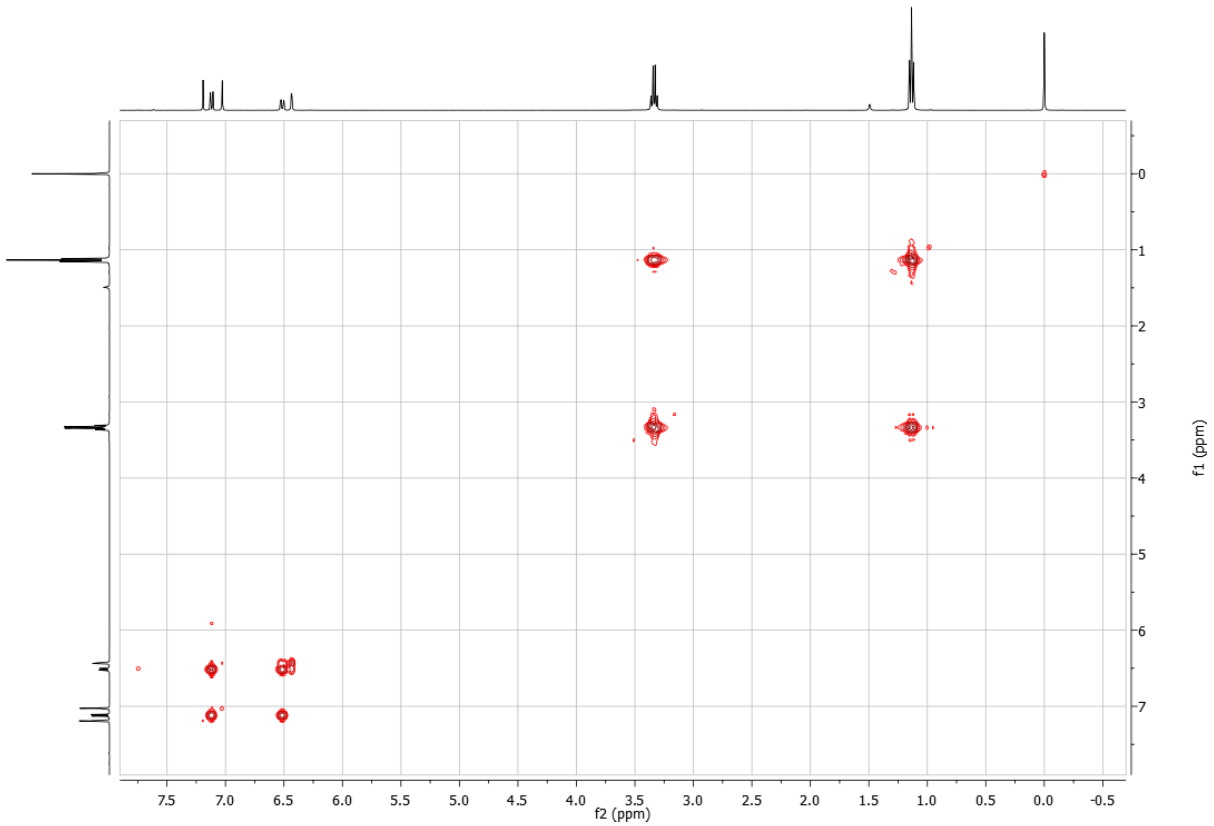

Figure 6.65 COSY NMR spectrum of 3-azido-7-diethylaminocoumarin in $CDCl_3$

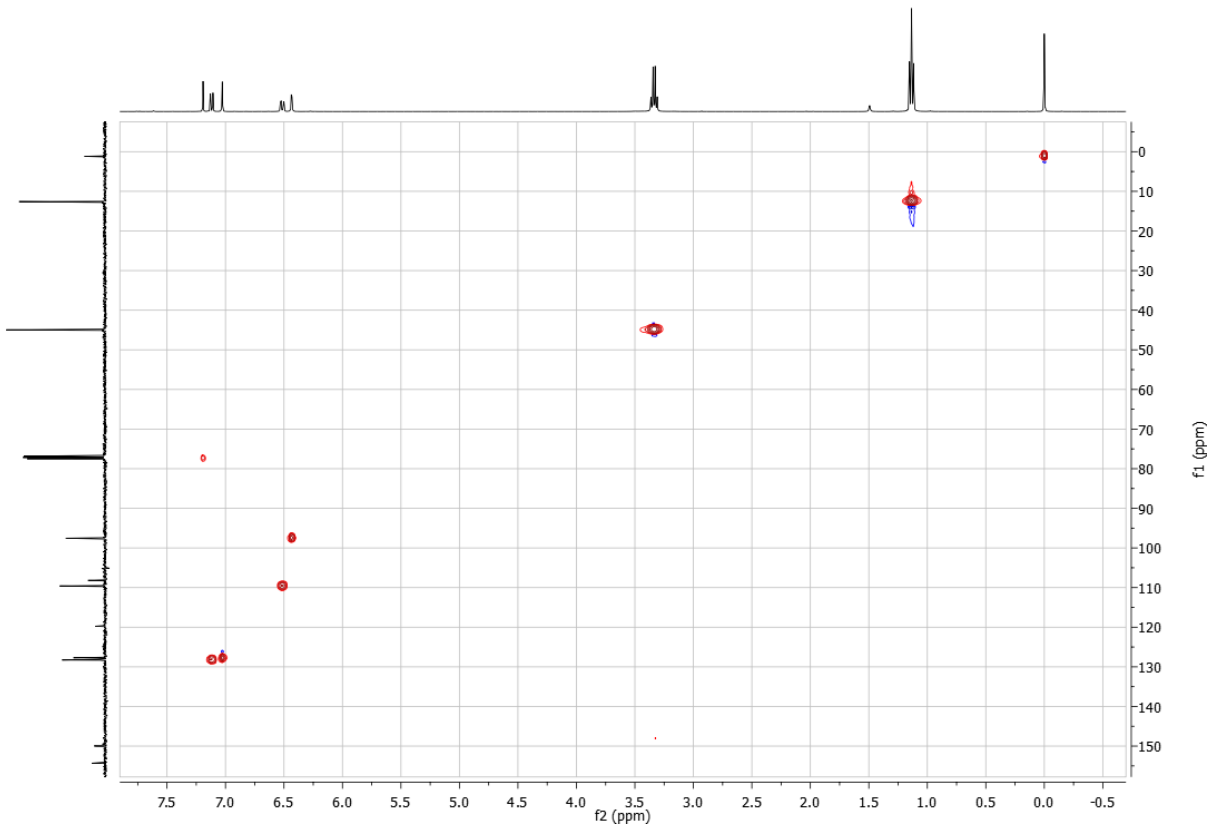

Figure 6.66 HSQC NMR spectrum of 3-azido-7-diethylaminocoumarin in $CDCl_3$

6.8 NMR spectra of 4-(1-(7-(diethylamino)-2-oxo-2H-chromen-3-yl)-1H-1,2,3-triazol-4-yl)picolinaldehyde

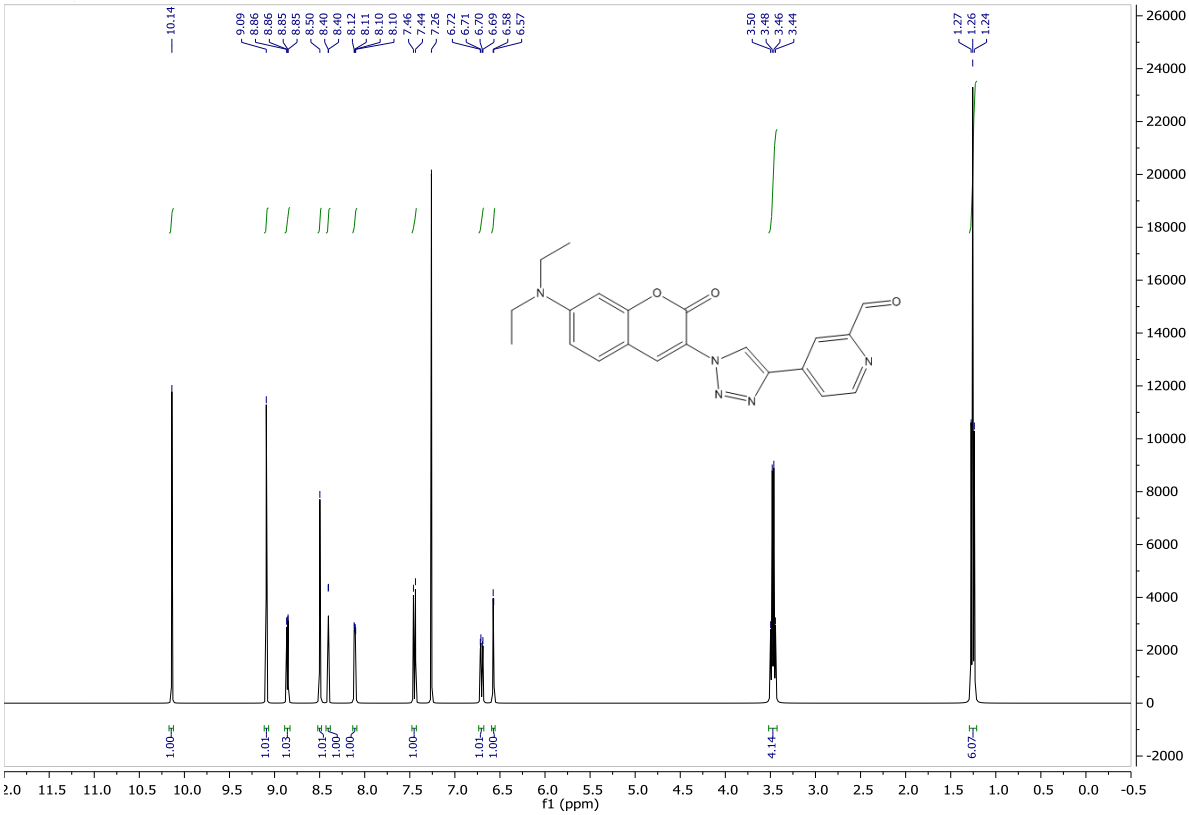

Figure 6.67 ^{1}H NMR spectrum of 4-(1-(7-(diethylamino)-2-oxo-2H-chromen-3-yl)-1H-1,2,3-triazol-4-yl)picolinaldehyde in $CDCl_3$

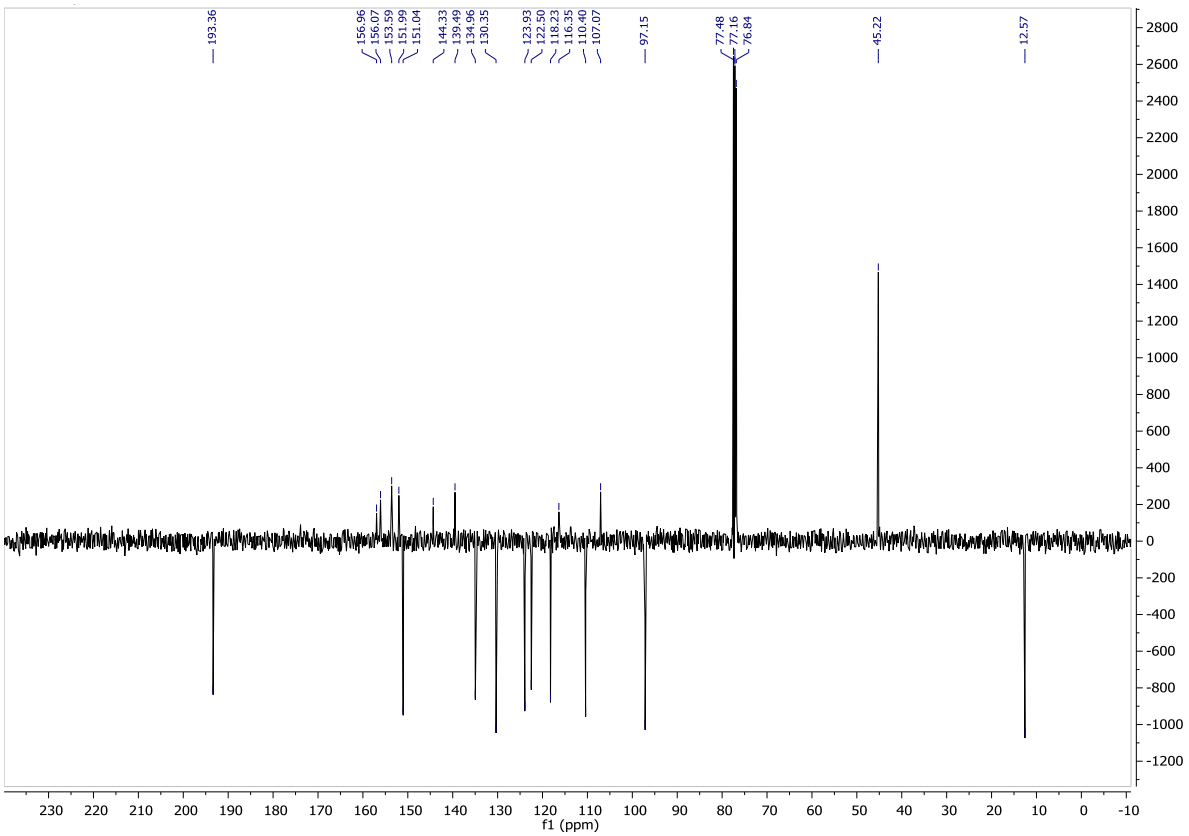

Figure 6.68 ^{13}C NMR spectrum of 4-(1-(7-(diethylamino)-2-oxo-2H-chromen-3-yl)-1H-1,2,3-triazol-4-yl)picolinaldehyde in $CDCl_3$

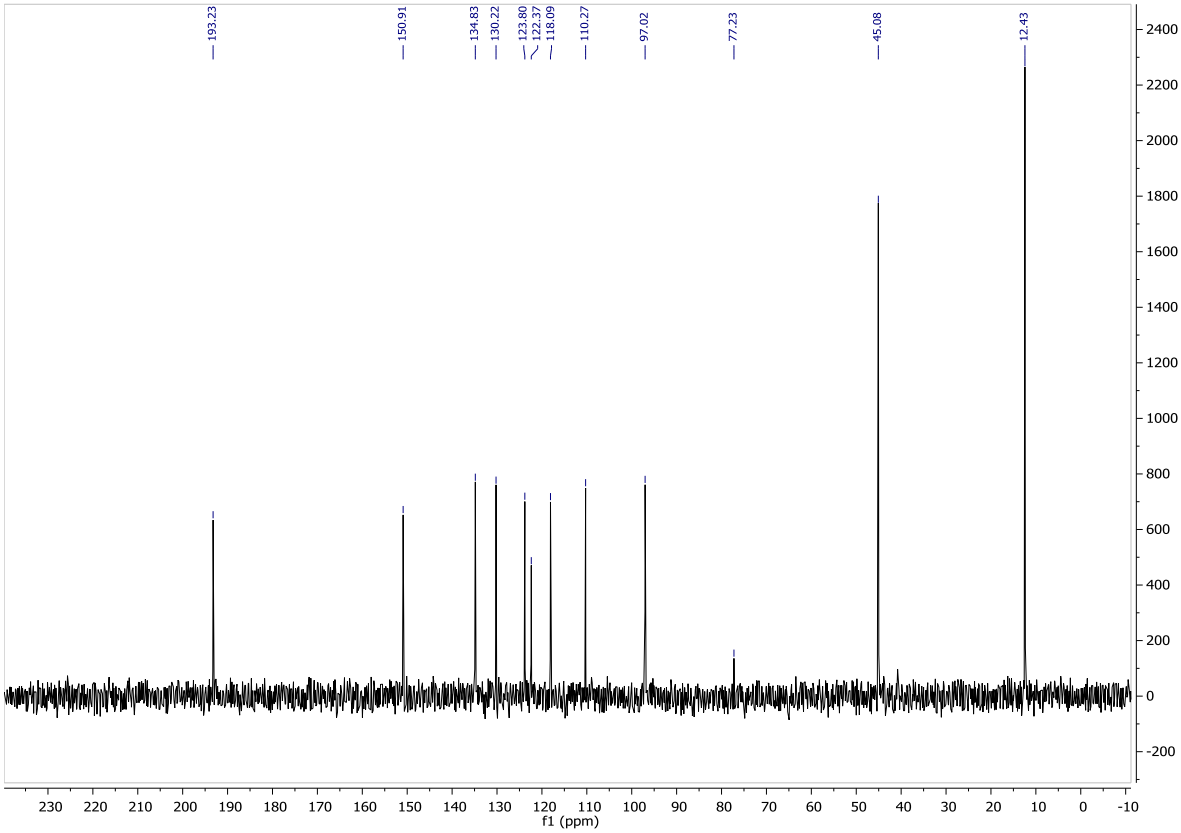

Figure 6.69 ^{13}C NMR spectrum of 4-(1-(7-(diethylamino)-2-oxo-2H-chromen-3-yl)-1H-1,2,3-triazol-4-yl)picolinaldehyde in $CDCl_3$

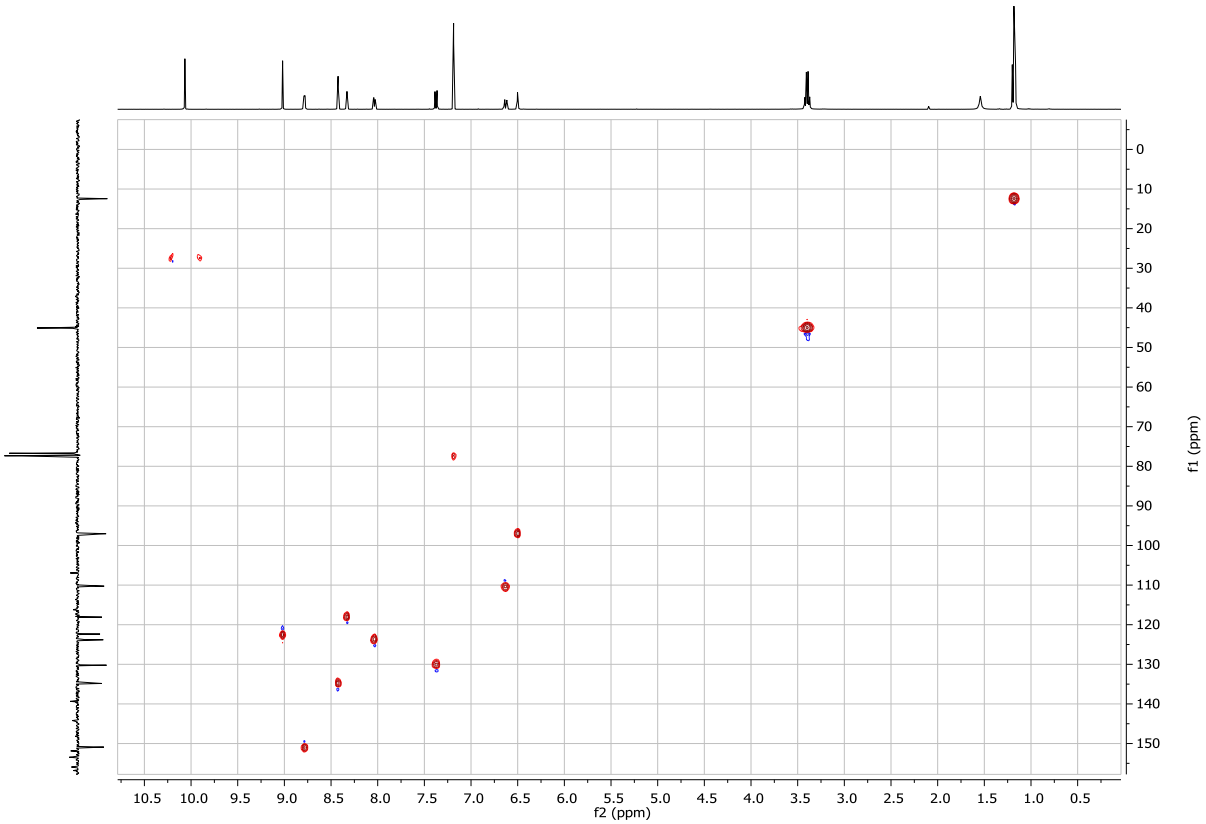

Figure 6.70 HSQC NMR spectrum of 4-(1-(7-(diethylamino)-2-oxo-2H-chromen-3-yl)-1H-1,2,3-triazol-4-yl)picolinaldehyde in $CDCl_3$

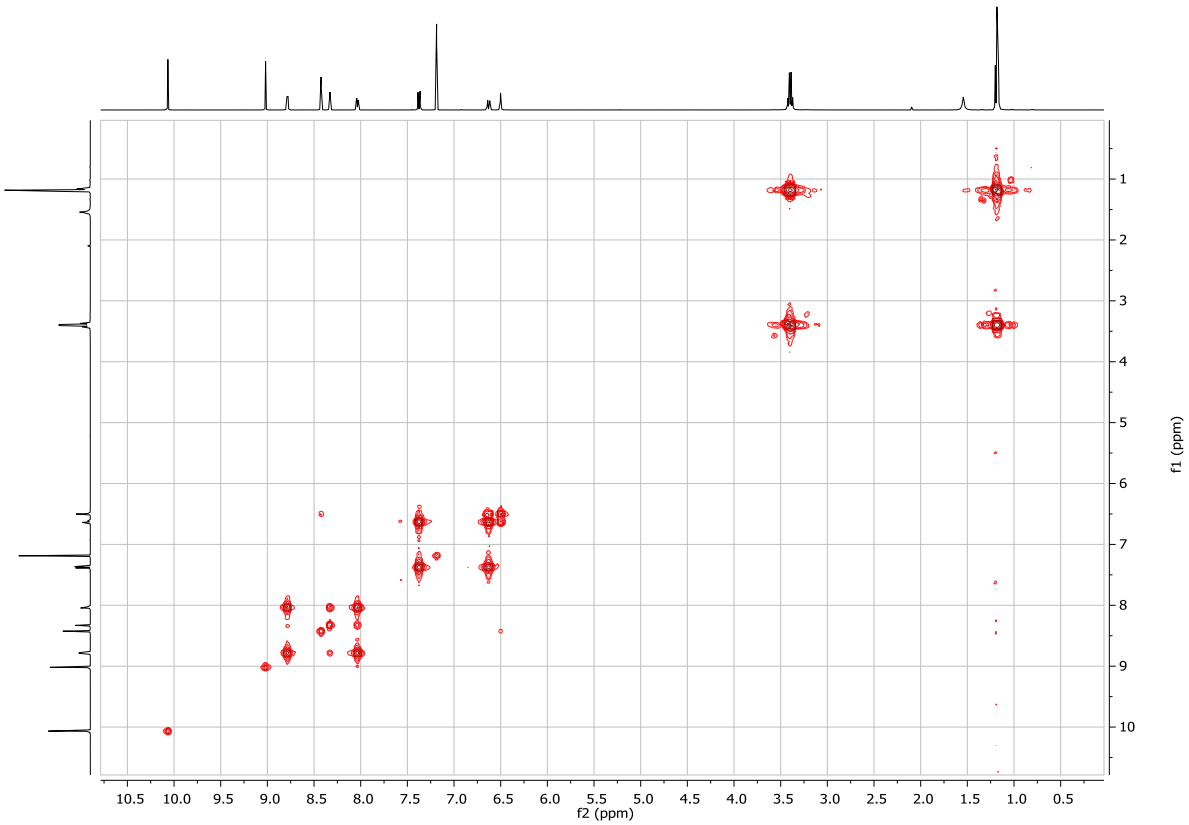

Figure 6.71 COSY NMR spectrum of 4-(1-(7-(diethylamino)-2-oxo-2H-chromen-3-yl)-1H-1,2,3-triazol-4-yl)picolinaldehyde in $CDCl_3$

6.9 NMR spectra of 5-(1-(7-(diethylamino)-2-oxo-2H-chromen-3-yl)-1H-1,2,3-triazol-4-yl)picolinaldehyde

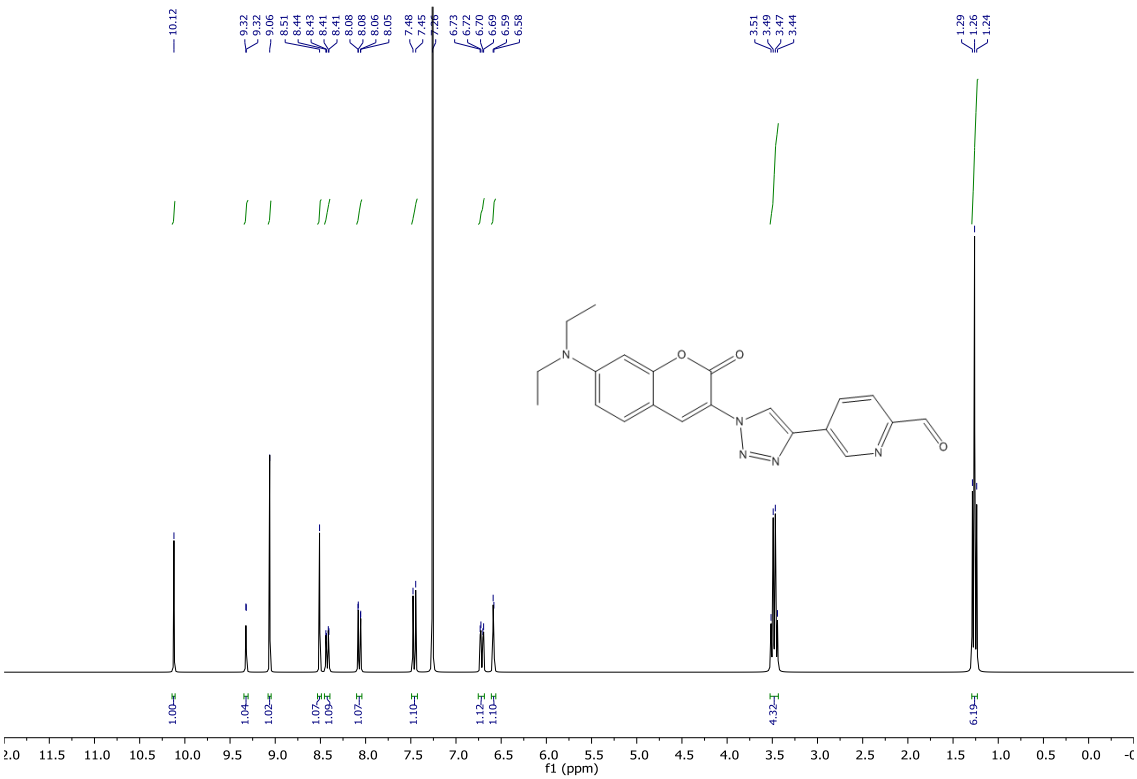

Figure 6.72 ^{1}H NMR spectrum of 5-(1-(7-(diethylamino)-2-oxo-2H-chromen-3-yl)-1H-1,2,3-triazol-4-yl)picolinaldehyde in $CDCl_3$

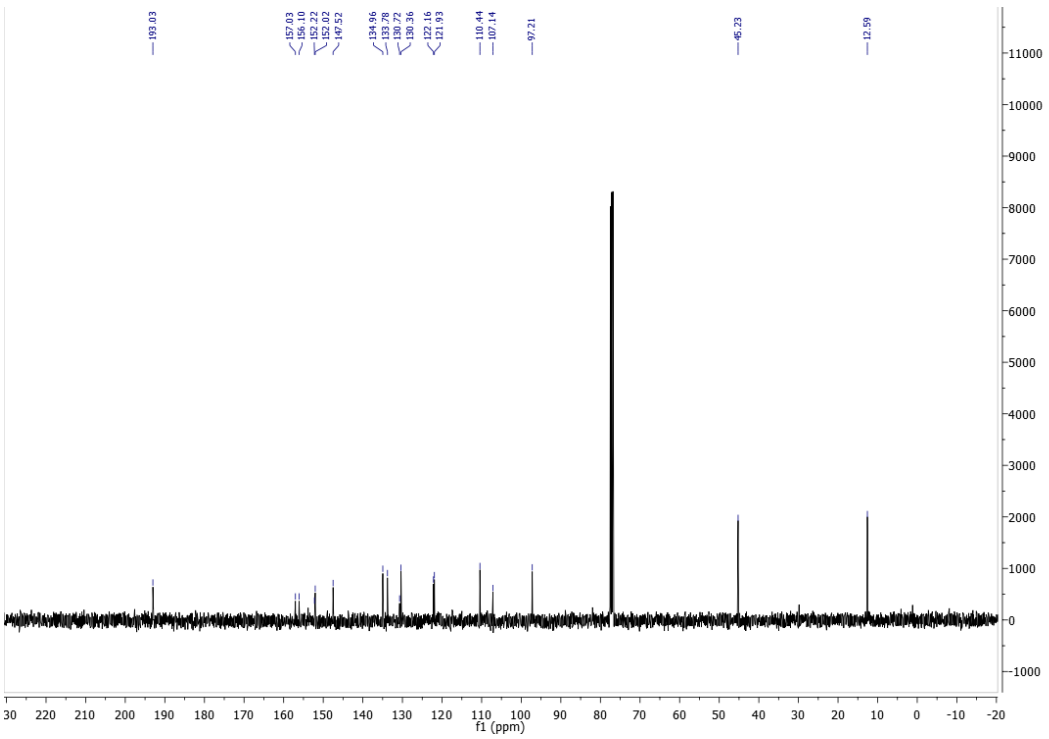

Figure 6.73 ^{13}C NMR spectrum of 5-(1-(7-(diethylamino)-2-oxo-2H-chromen-3-yl)-1H-1,2,3-triazol-4-yl)picolinaldehyde in $CDCl_3$

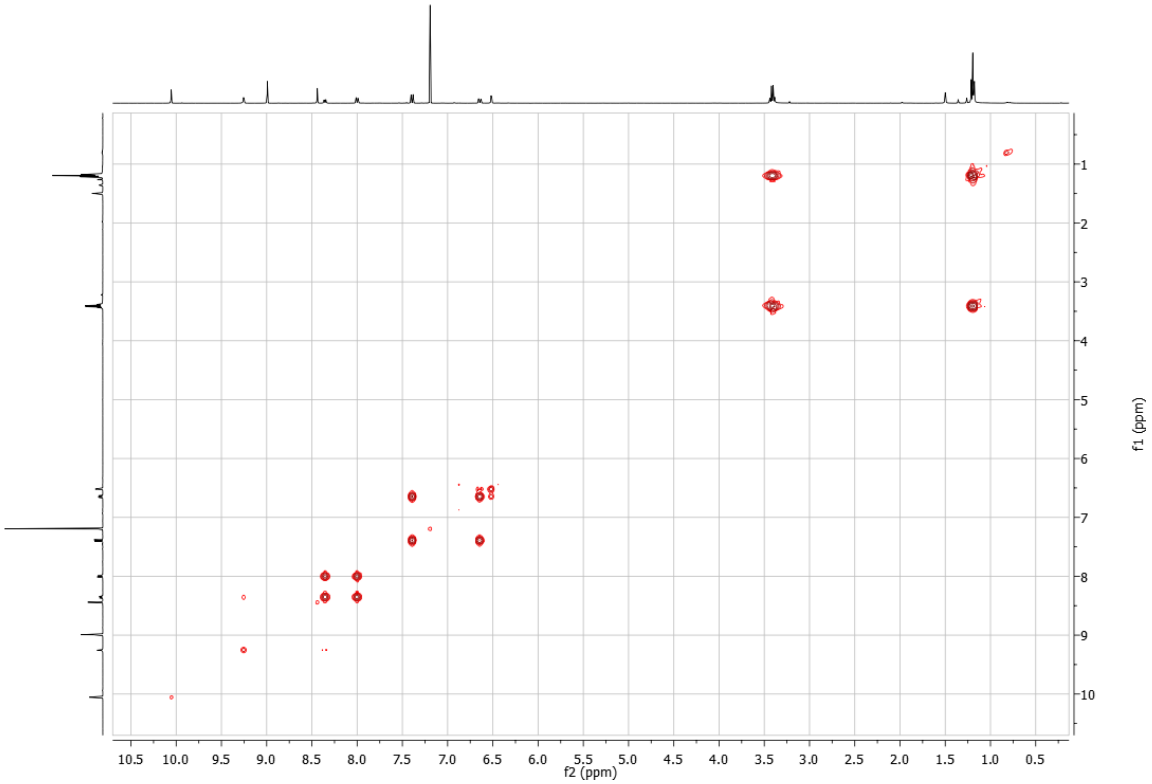

Figure 6.74 COSY NMR spectrum of 5-(1-(7-(diethylamino)-2-oxo-2H-chromen-3-yl)-1H-1,2,3-triazol-4-yl)picolinaldehyde in $CDCl_3$

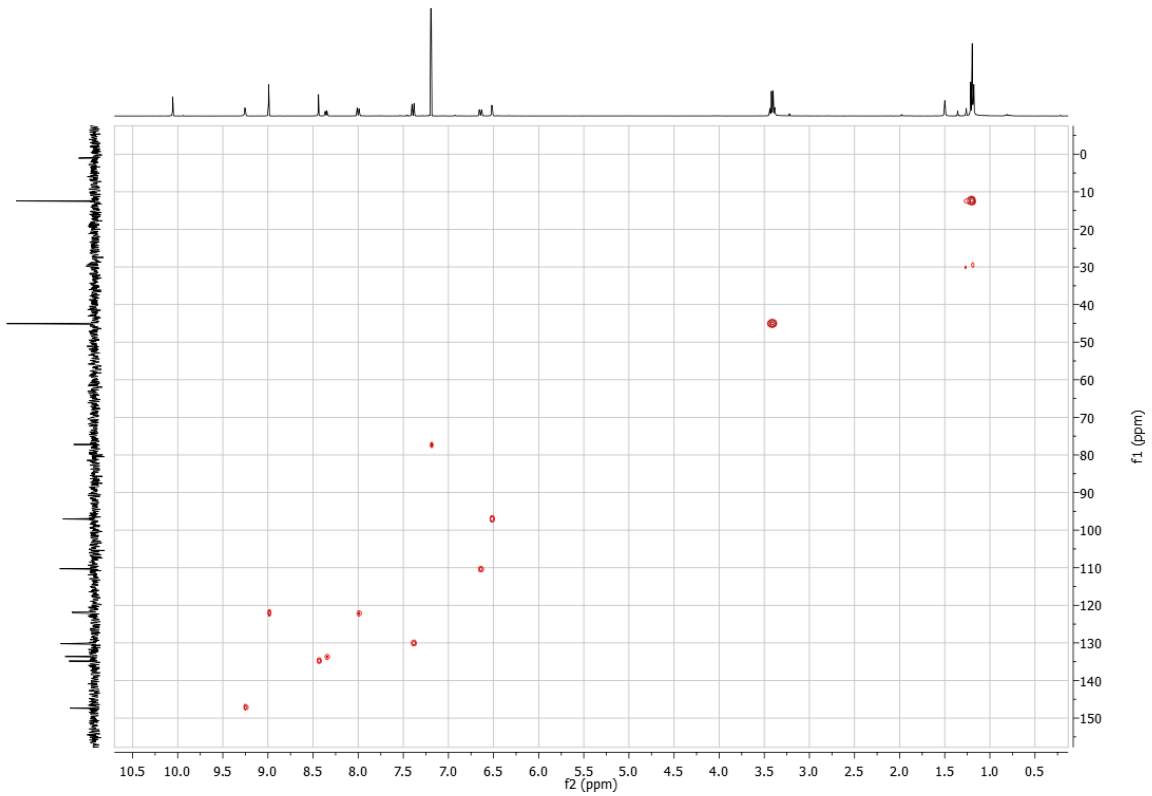

Figure 6.75 HSQC NMR spectrum of 5-(1-(7-(diethylamino)-2-oxo-2H-chromen-3-yl)-1H-1,2,3-triazol-4-yl)picolinaldehyde in $CDCl_3$

6.10 NMR spectra of L^{C5}

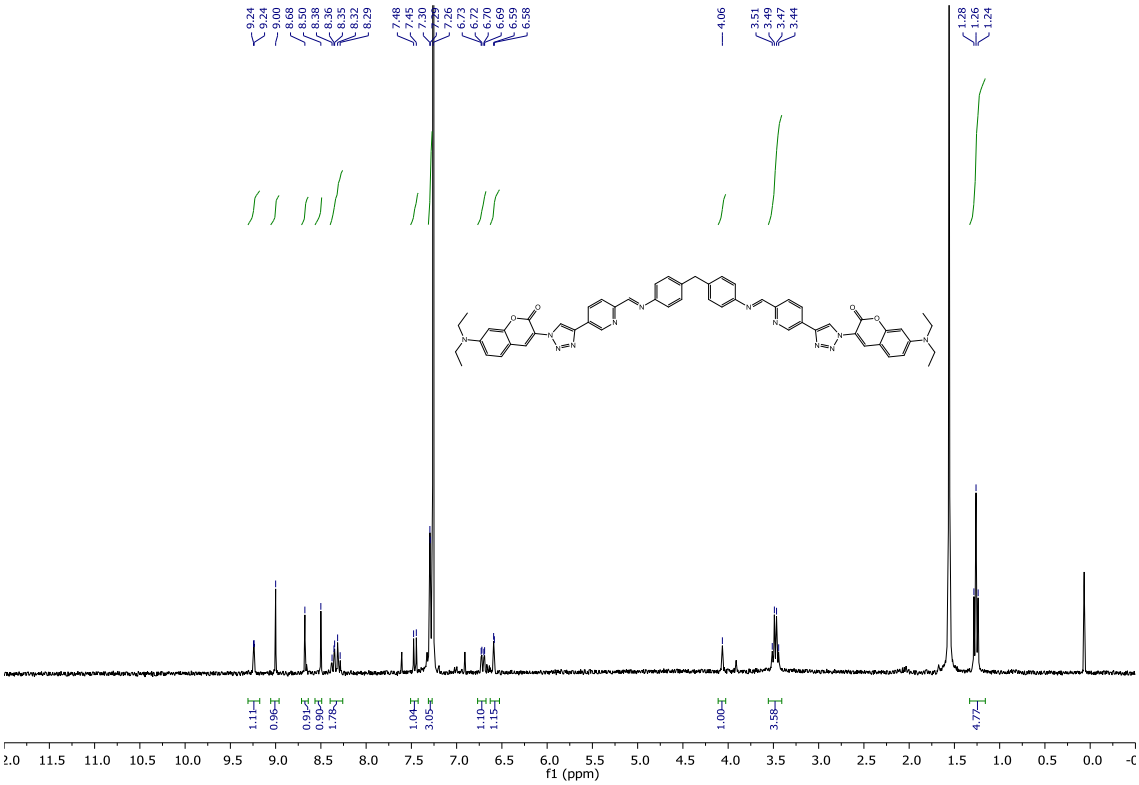

Figure 6.76 ^{1}H NMR spectrum of L^{C5} in $CDCl_3$

6.11 NMR spectra of $[Fe_2L^{C5}{}_3][PF_6]_4$

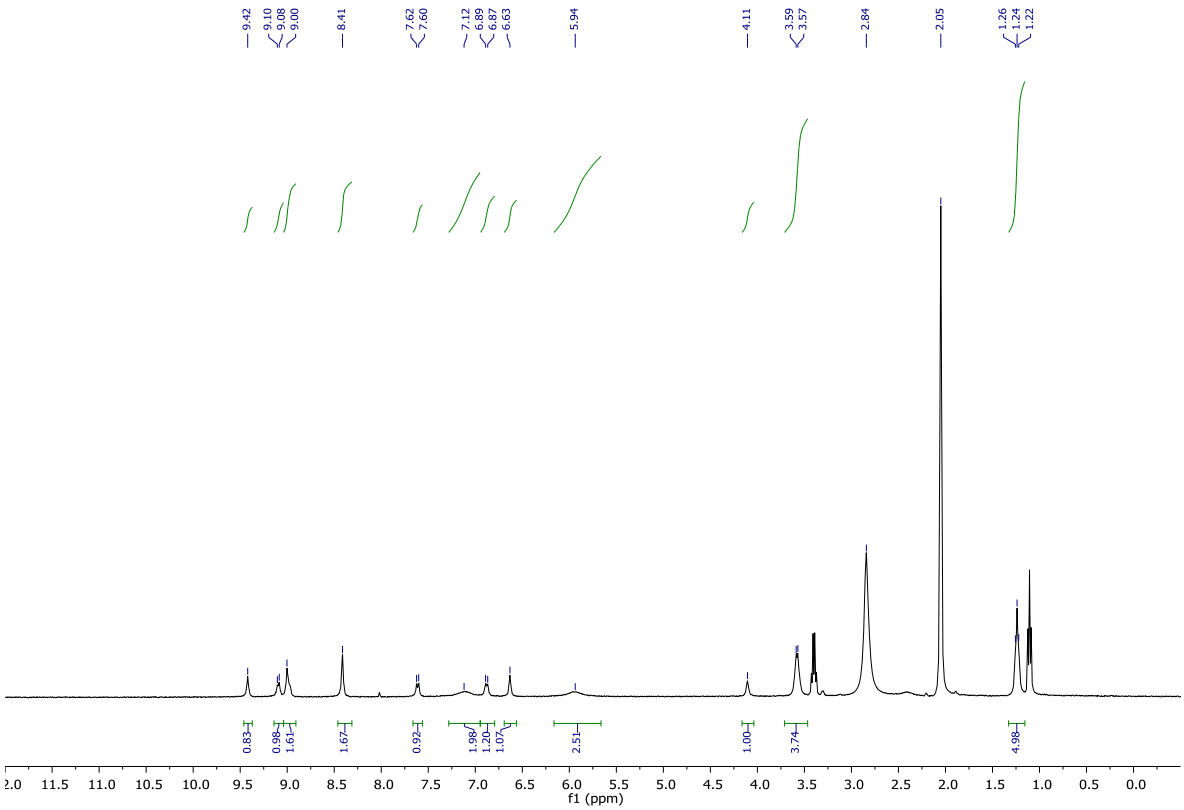

Figure 6.77 ^{1}H NMR spectrum of $[Fe_2L^{C5}{}_3][PF_6]_4$ in CD_3CN

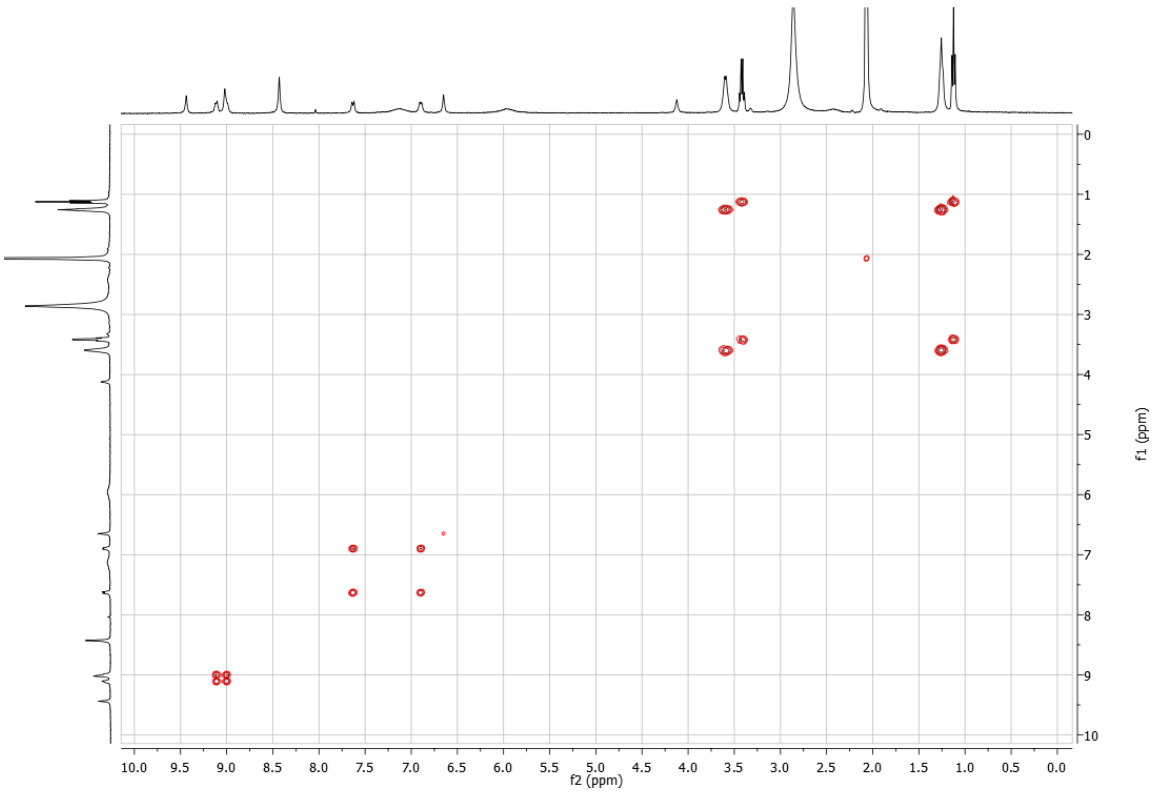

Figure 6.78 COSY NMR spectrum of $[Fe_2L^{C5}{}_3][PF_6]_4$ in CD_3CN

6.12 NMR spectra of L^{C4}

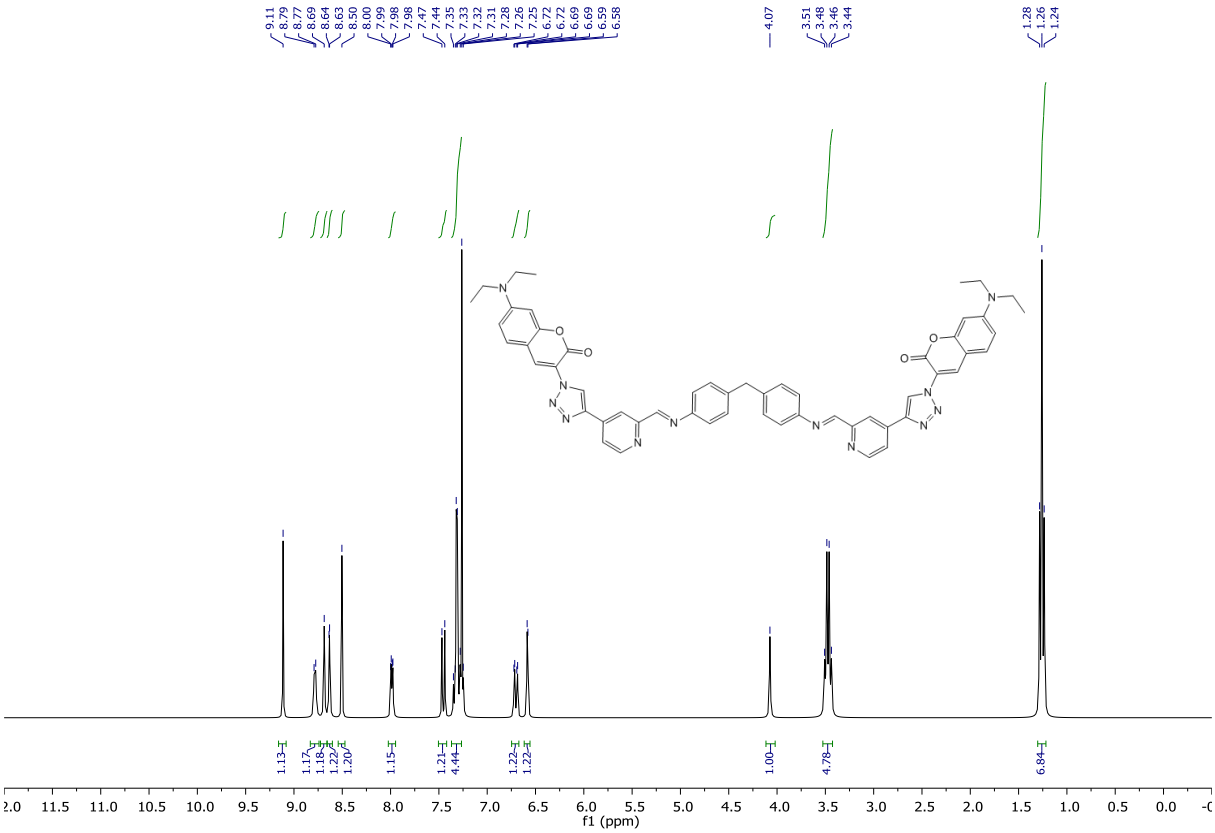

Figure 6.79 ^{1}H NMR spectrum of L^{C4} in $CDCl_3$

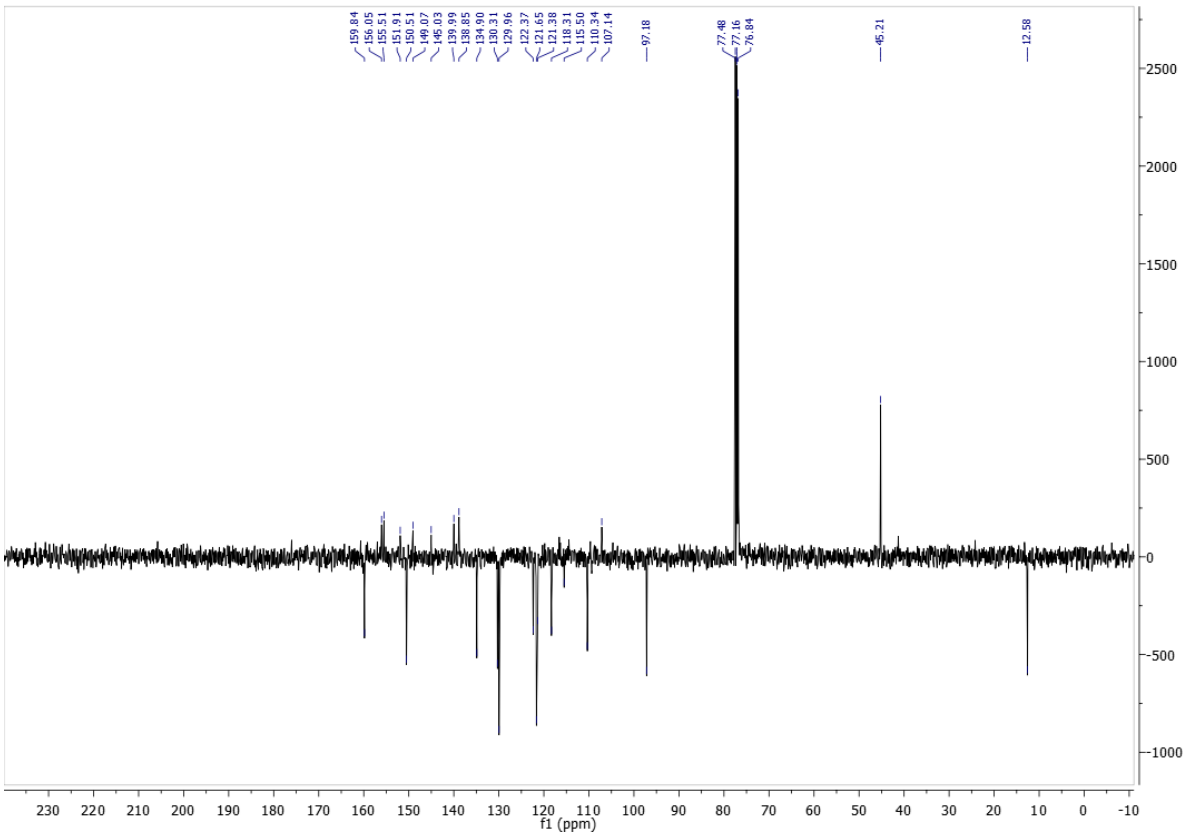

Figure 6.80 ^{13}C NMR spectrum of L^{C4} in $CDCl_3$

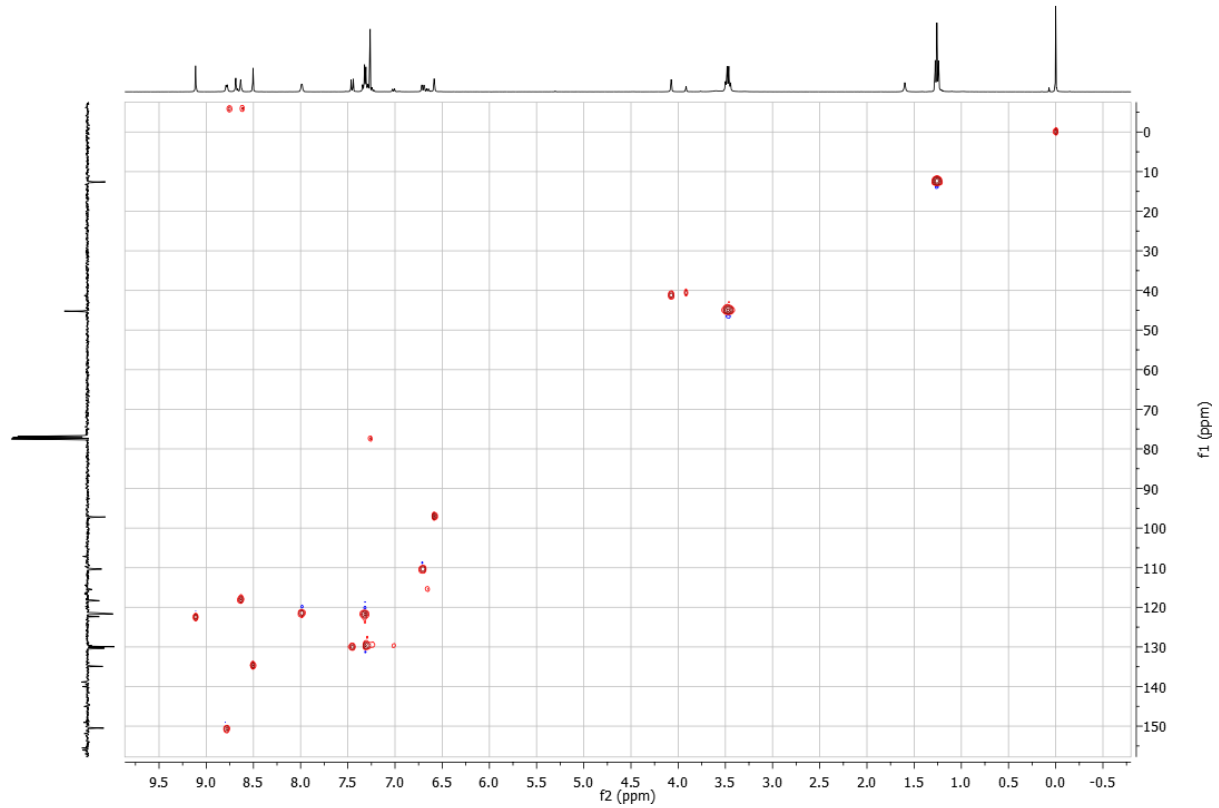

Figure 6.81 HSQC NMR spectrum of L^{C4} in $CDCl_3$

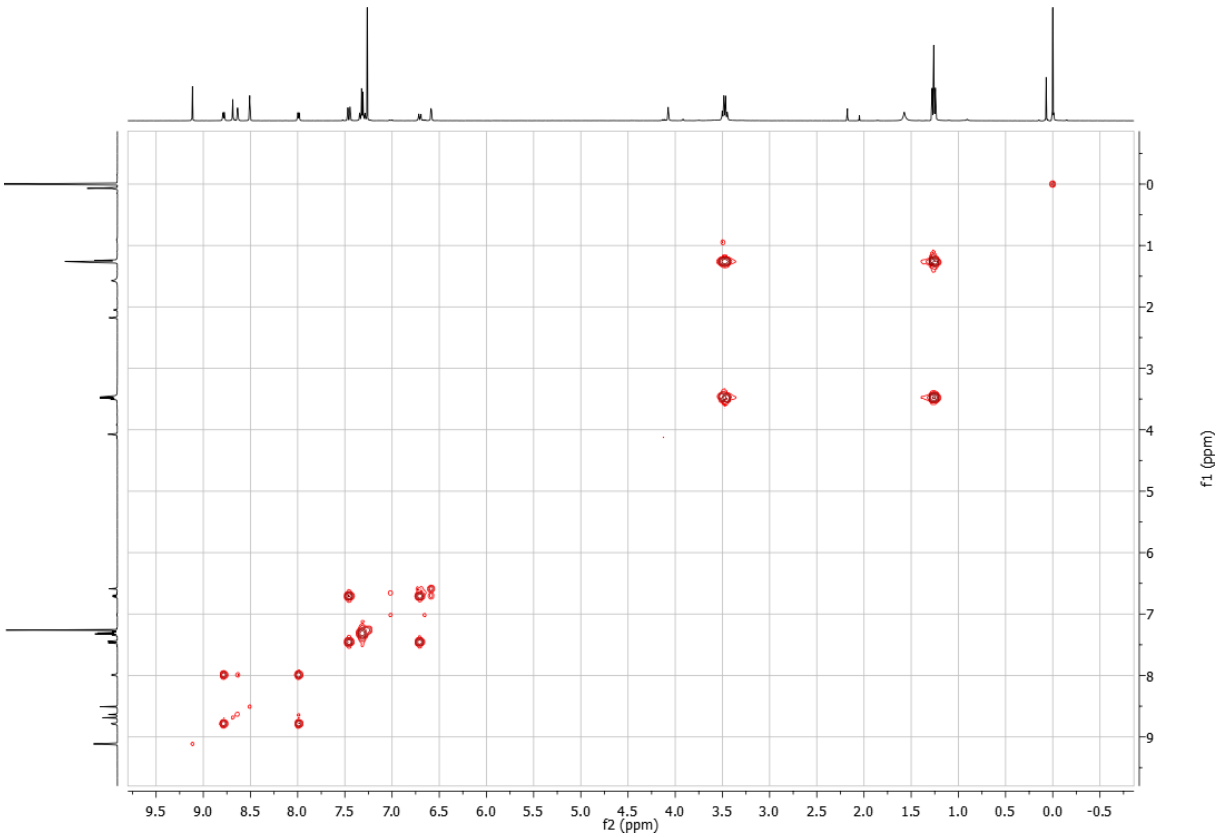

Figure 6.82 COSY NMR spectrum of L^{C4} in $CDCl_3$

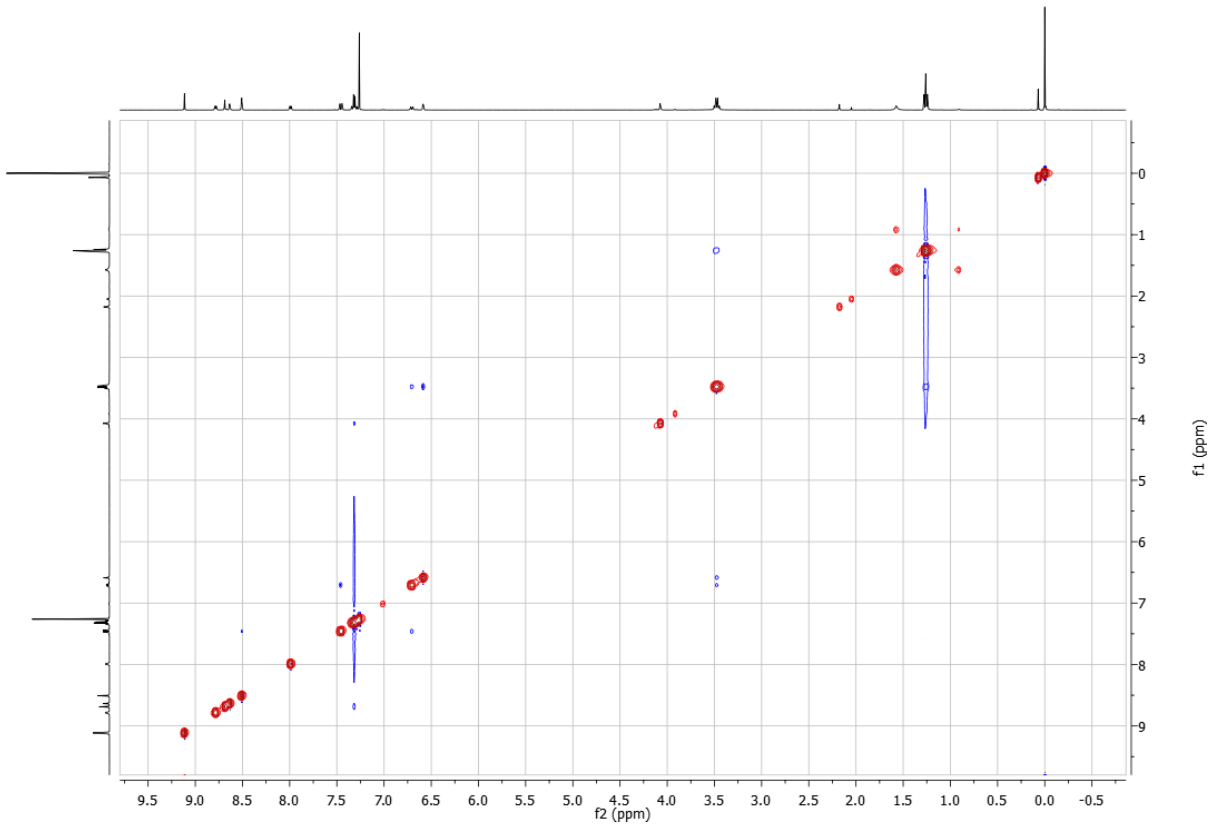

Figure 6.83 NOESY NMR spectrum of L^{C4} in $CDCl_3$

6.13 NMR spectra of $[Fe_2L^{C4}{}_3][PF_6]_4$

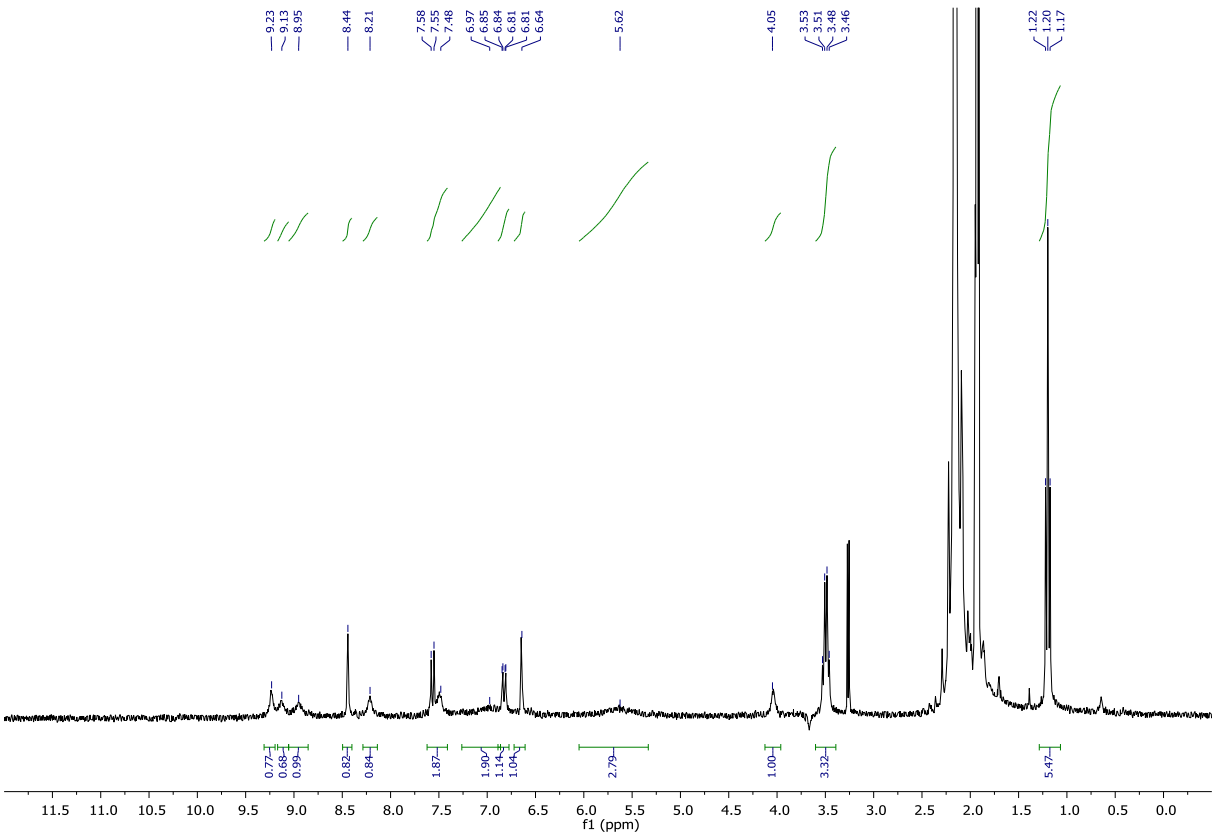

Figure 6.84 ^1H NMR spectra of $[Fe_2L^{C4}{}_3][PF_6]_4$ in CD_3CN

6.14 NMR spectra of dansyl-PEG$_3$-azide

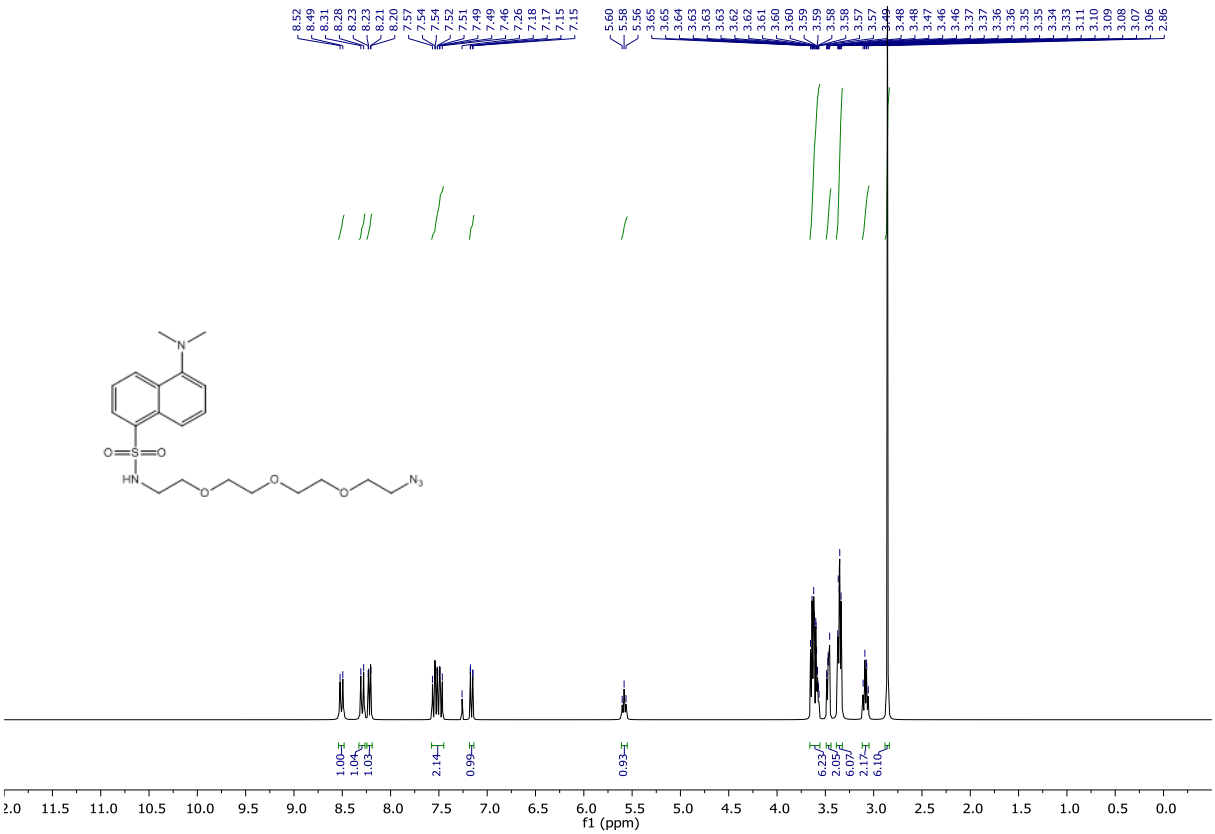

Figure 6.85 ^{1}H NMR spectrum of dansyl-PEG$_3$-azide in $CDCl_3$

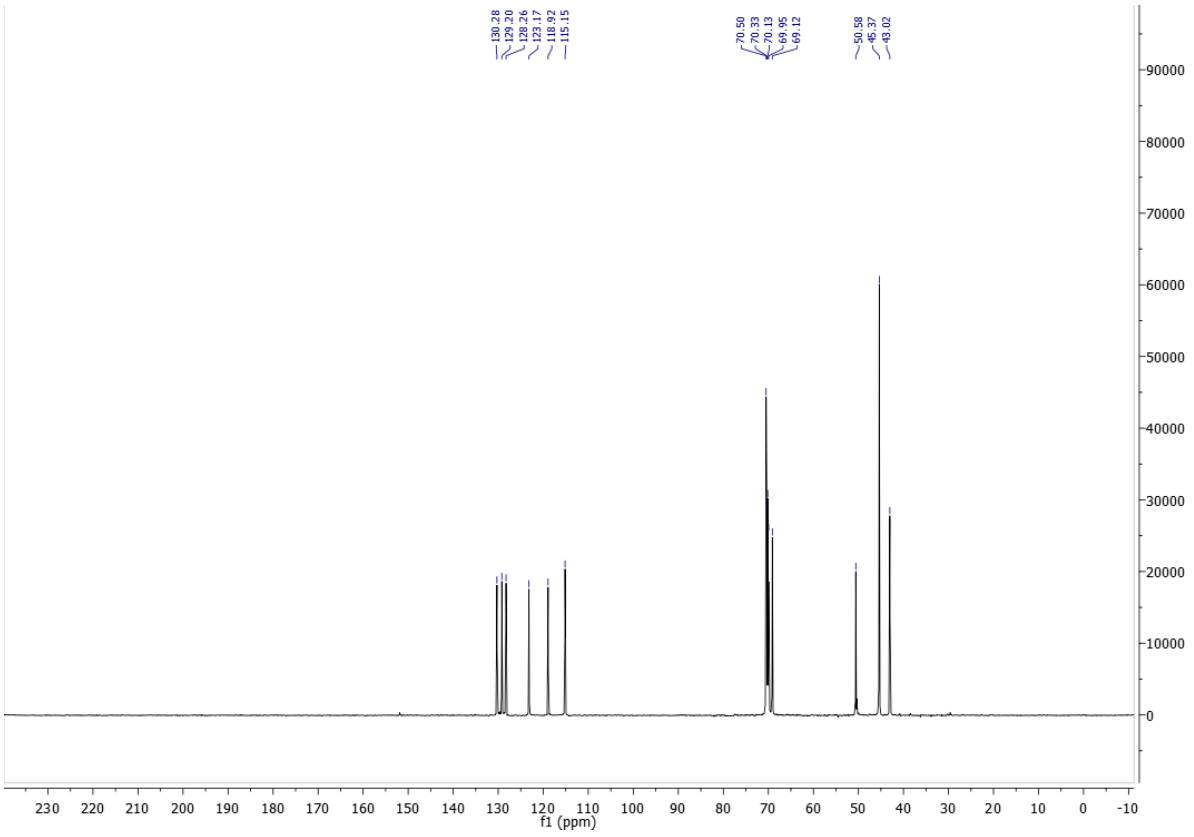

Figure 6.86 ^{13}C NMR spectrum of dansyl-PEG$_3$-azide in $CDCl_3$

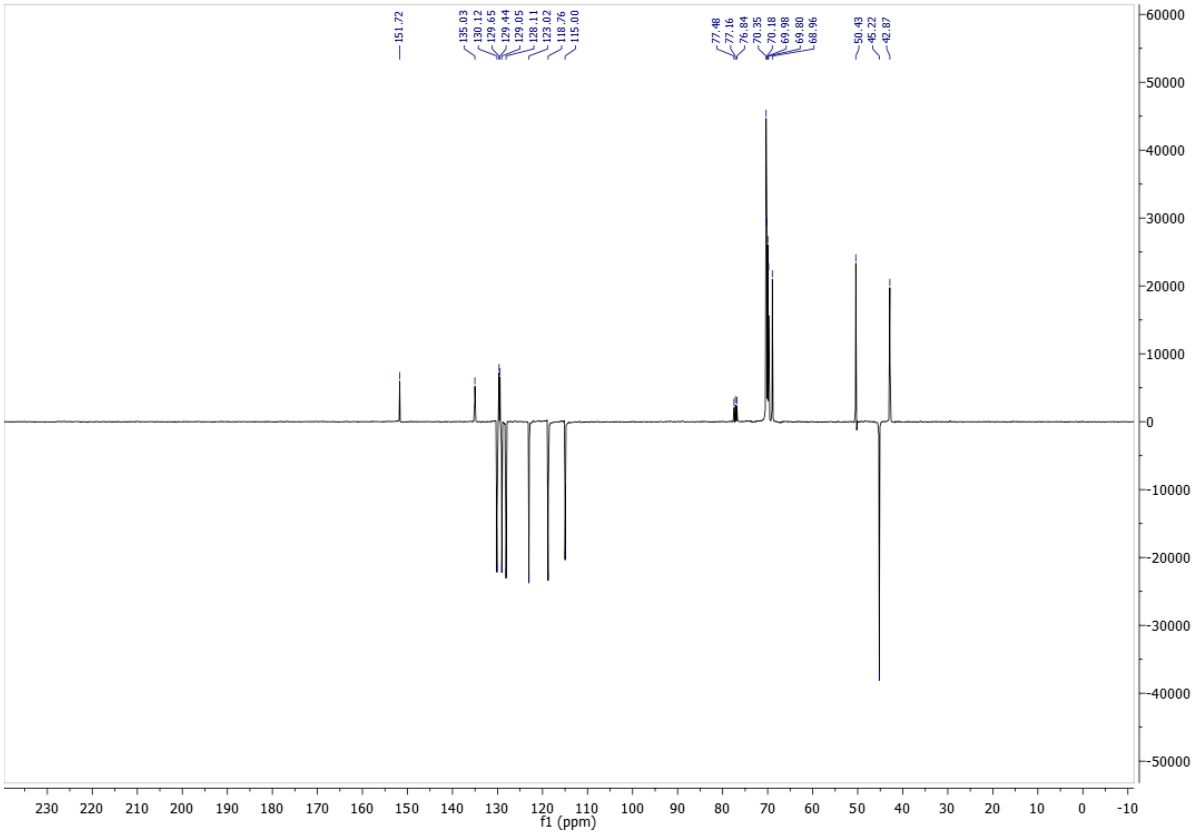

Figure 6.87 ^{13}C NMR spectrum of dansyl-PEG$_3$-azide in CDCl$_3$

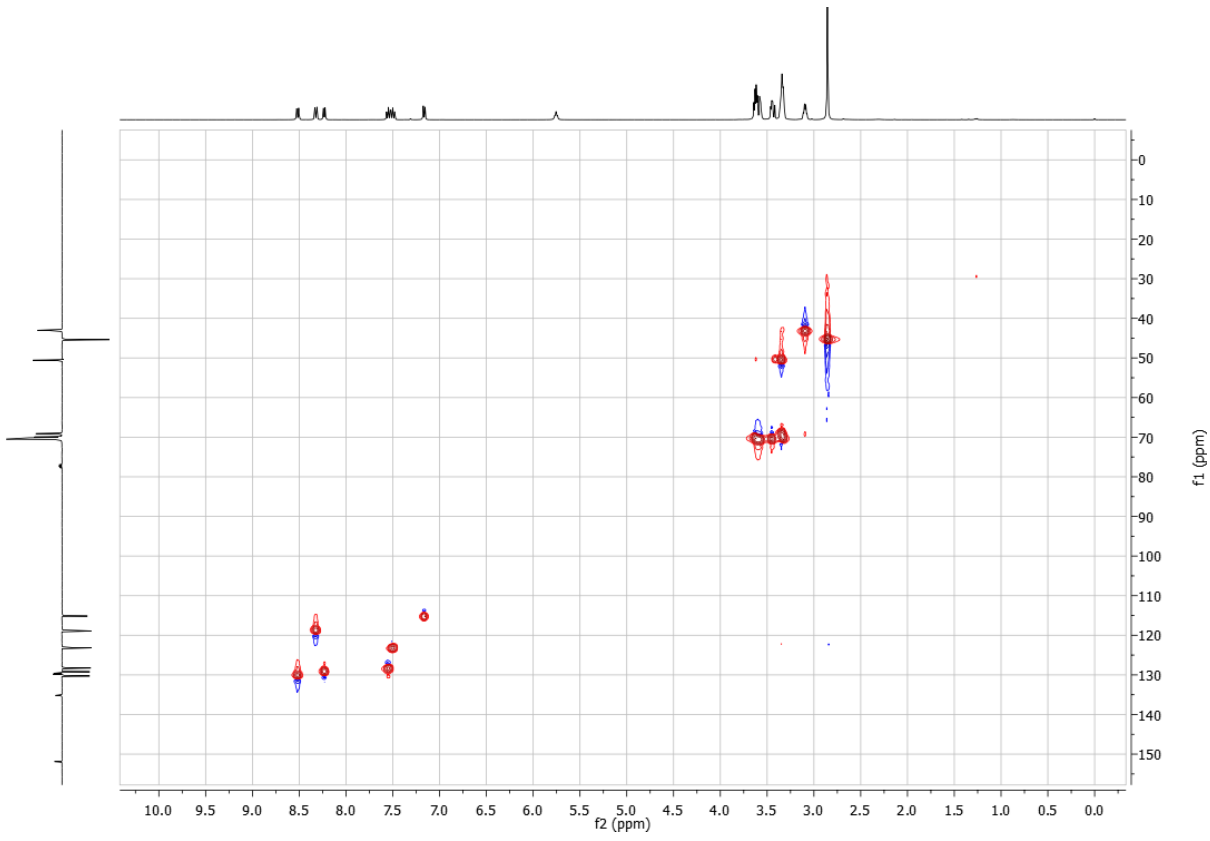

Figure 6.88 HSQC NMR spectrum of dansyl-PEG$_3$-azide in CDCl$_3$

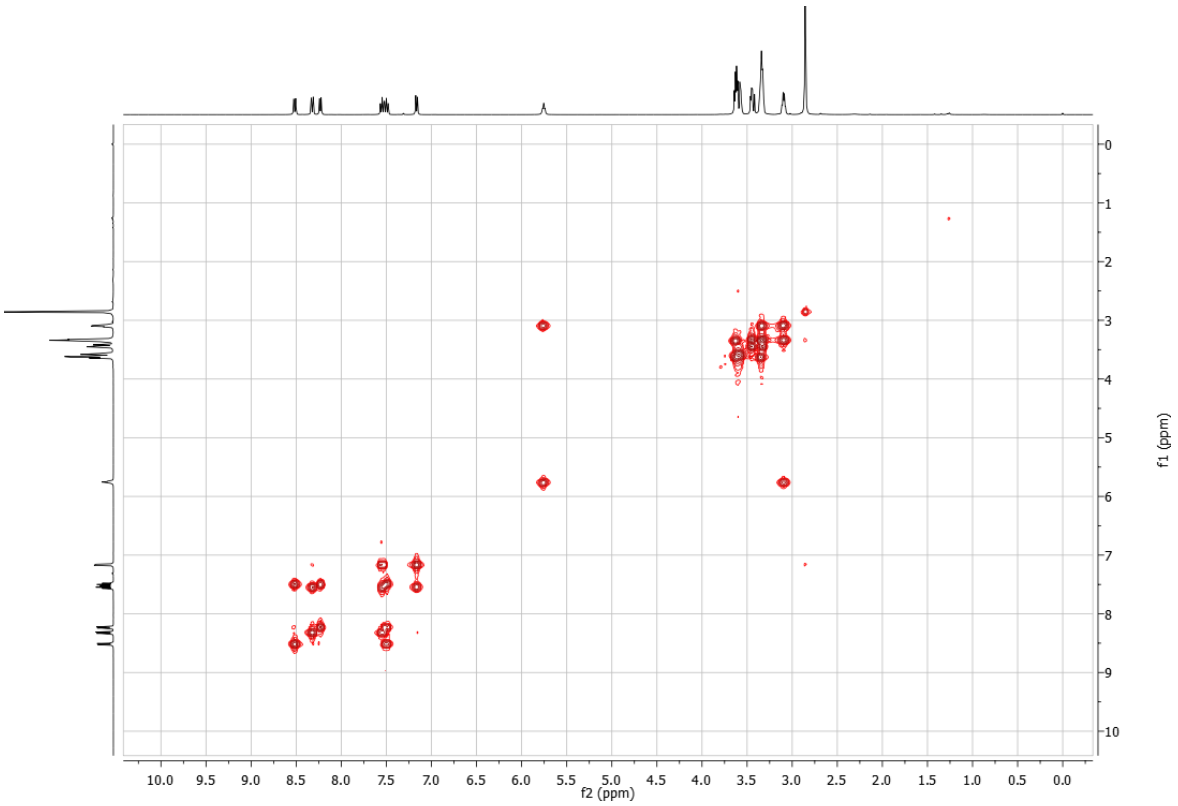

Figure 6.89 COSY NMR spectrum of dansyl-PEG$_3$-azide in CDCl$_3$

6.15 NMR spectra of 5-(dimethylamino)-N-(2-(2-(2-(2-(4-(6-formylpyridin-3-yl)-1H-1,2,3-triazol-1-yl)ethoxy)ethoxy)ethoxy)ethyl)naphthalene-1-sulfonamide

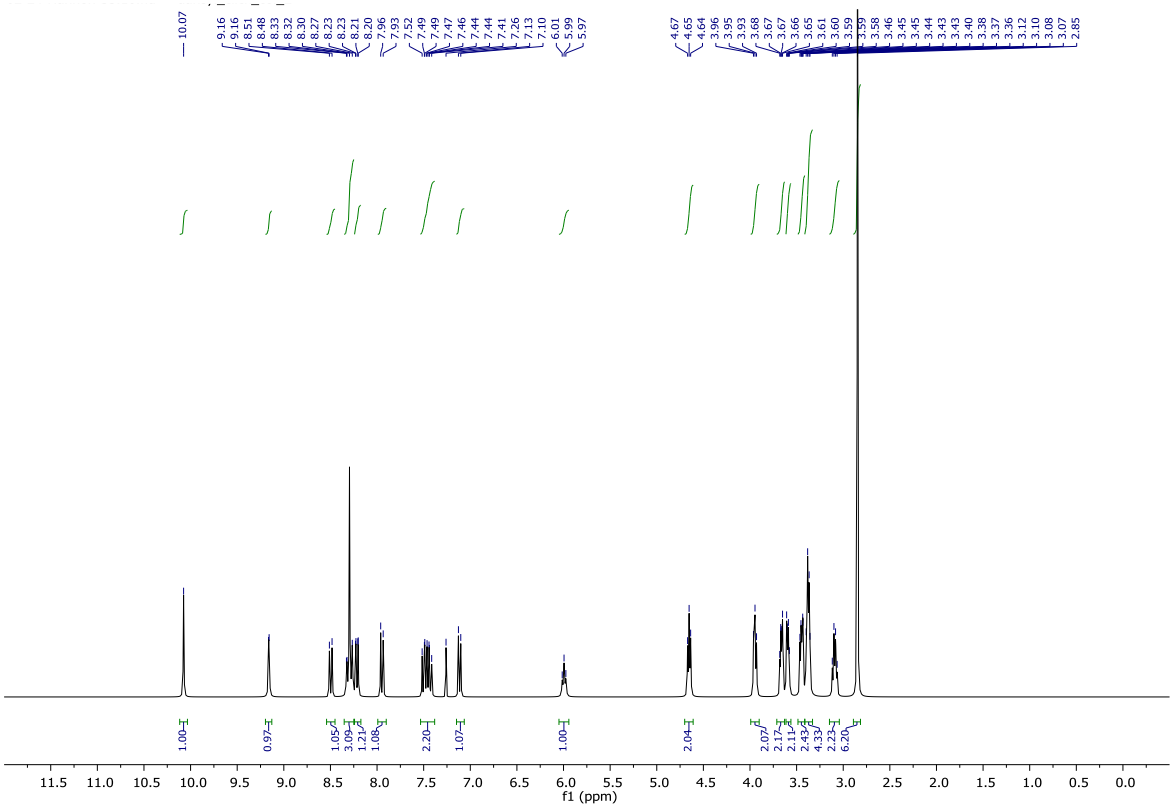

Figure 6.90 ^{1}H NMR spectrum of 5-(dimethylamino)-N-(2-(2-(2-(2-(4-(6-formylpyridin-3-yl)-1H-1,2,3-triazol-1-yl)ethoxy)ethoxy)ethoxy)ethyl)naphthalene-1-sulfonamide in $CDCl_3$

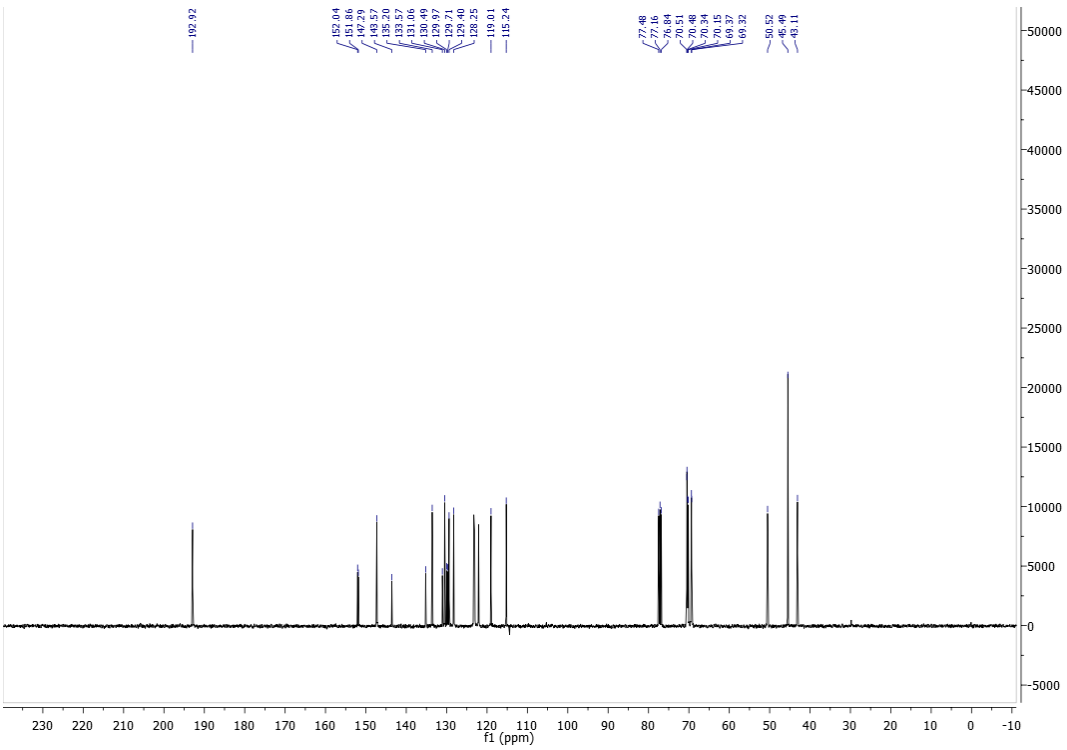

Figure 6.91 ^{13}C NMR spectrum of 5-(dimethylamino)-N-(2-(2-(2-(2-(4-(6-formylpyridin-3-yl)-1H-1,2,3-triazol-1-yl)ethoxy)ethoxy)ethoxy)ethyl)naphthalene-1-sulfonamide in $CDCl_3$

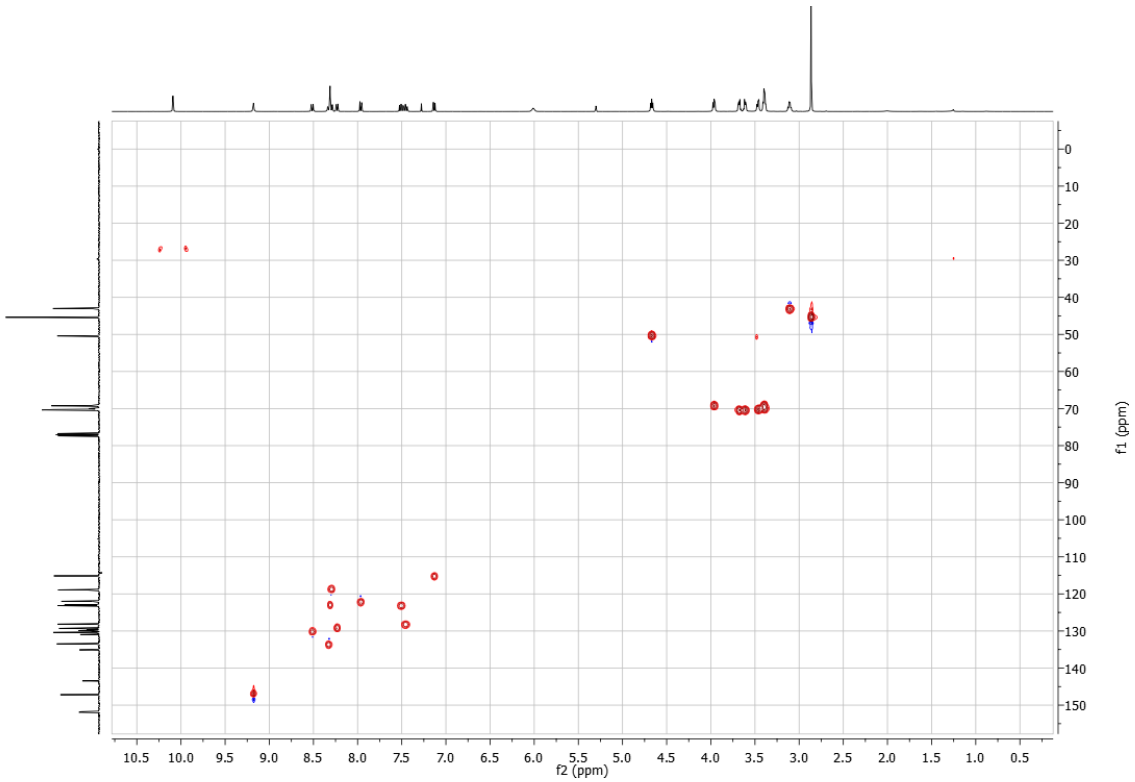

Figure 6.92 HSQC NMR spectrum of 5-(dimethylamino)-N-(2-(2-(2-(2-(4-(6-formylpyridin-3-yl)-1H-1,2,3-triazol-1-yl)ethoxy)ethoxy)ethoxy)ethyl)naphthalene-1-sulfonamide in $CDCl_3$

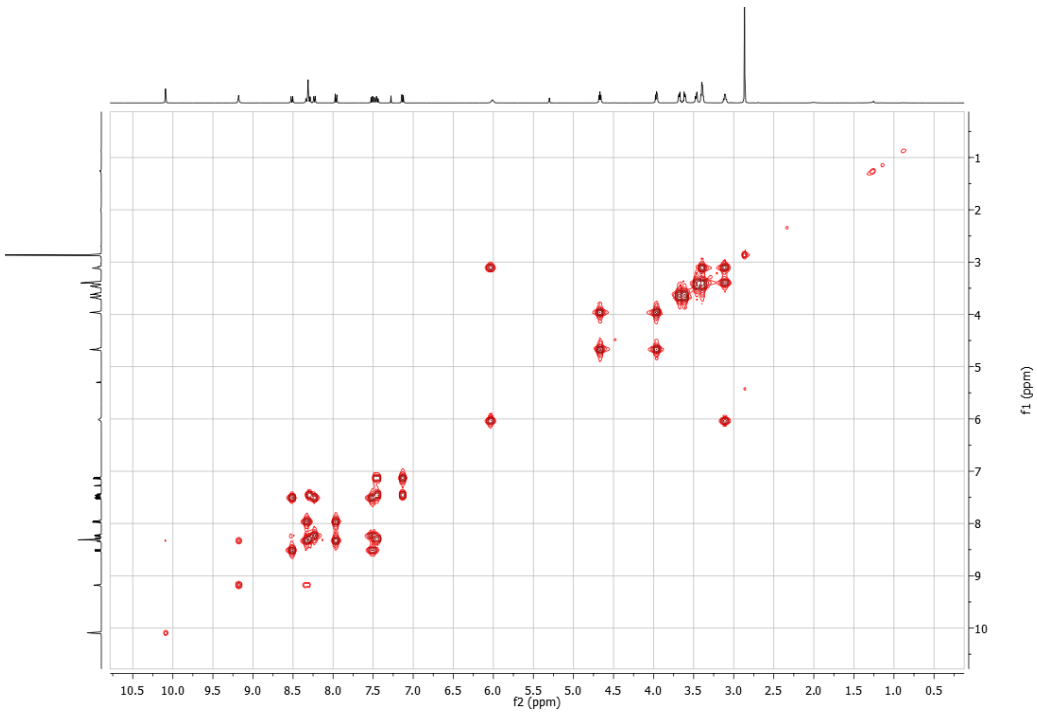

Figure 6.93 COSY NMR spectrum of 5-(dimethylamino)-N-(2-(2-(2-(2-(4-(6-formylpyridin-3-yl)-1H-1,2,3-triazol-1-yl)ethoxy)ethoxy)ethoxy)ethyl)naphthalene-1-sulfonamide in $CDCl_3$

6.16 NMR spectra of 4-(dimethylamino)-N-(2-(2-(2-(2-(4-(2-formylpyridin-4-yl)-1H-1,2,3-triazol-1-yl)ethoxy)ethoxy)ethoxy)ethyl)naphthalene-1-sulfonamide

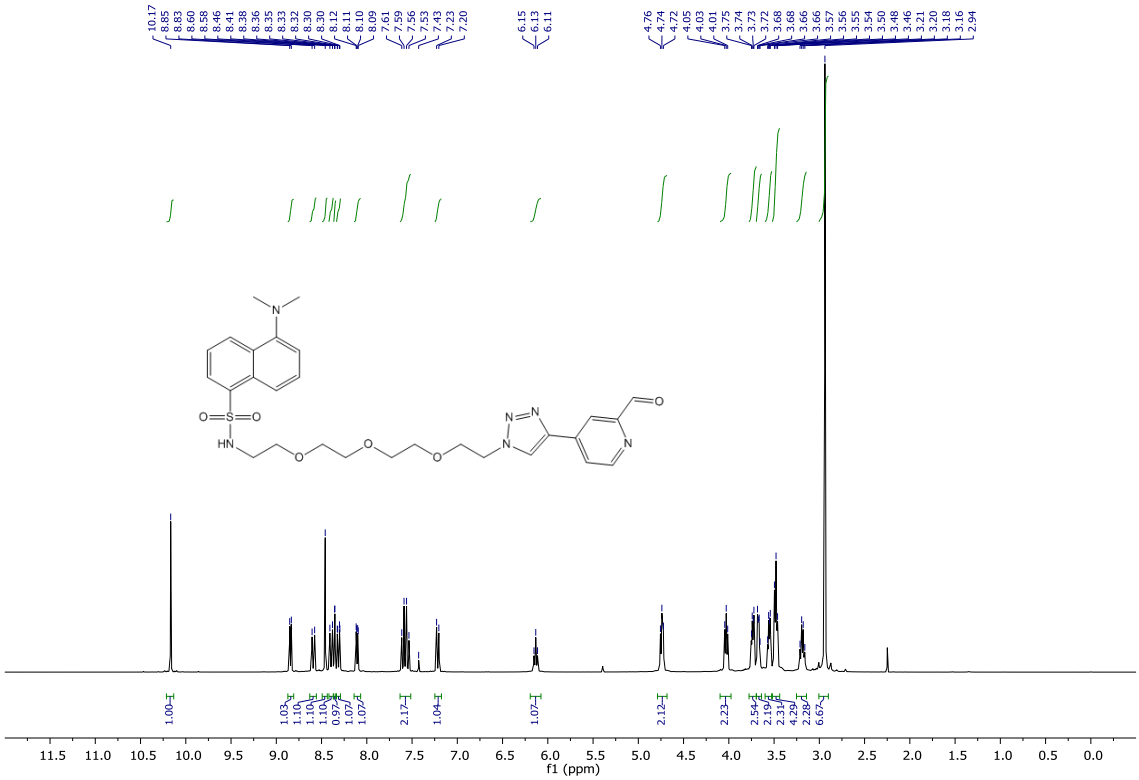

Figure 6.94 ^{1}H NMR spectra of 4-(dimethylamino)-N-(2-(2-(2-(2-(4-(2-formylpyridin-4-yl)-1H-1,2,3-triazol-1-yl)ethoxy)ethoxy)ethoxy)ethyl)naphthalene-1-sulfonamide in $CDCl_3$

6.17 NMR spectra of L^{D5}

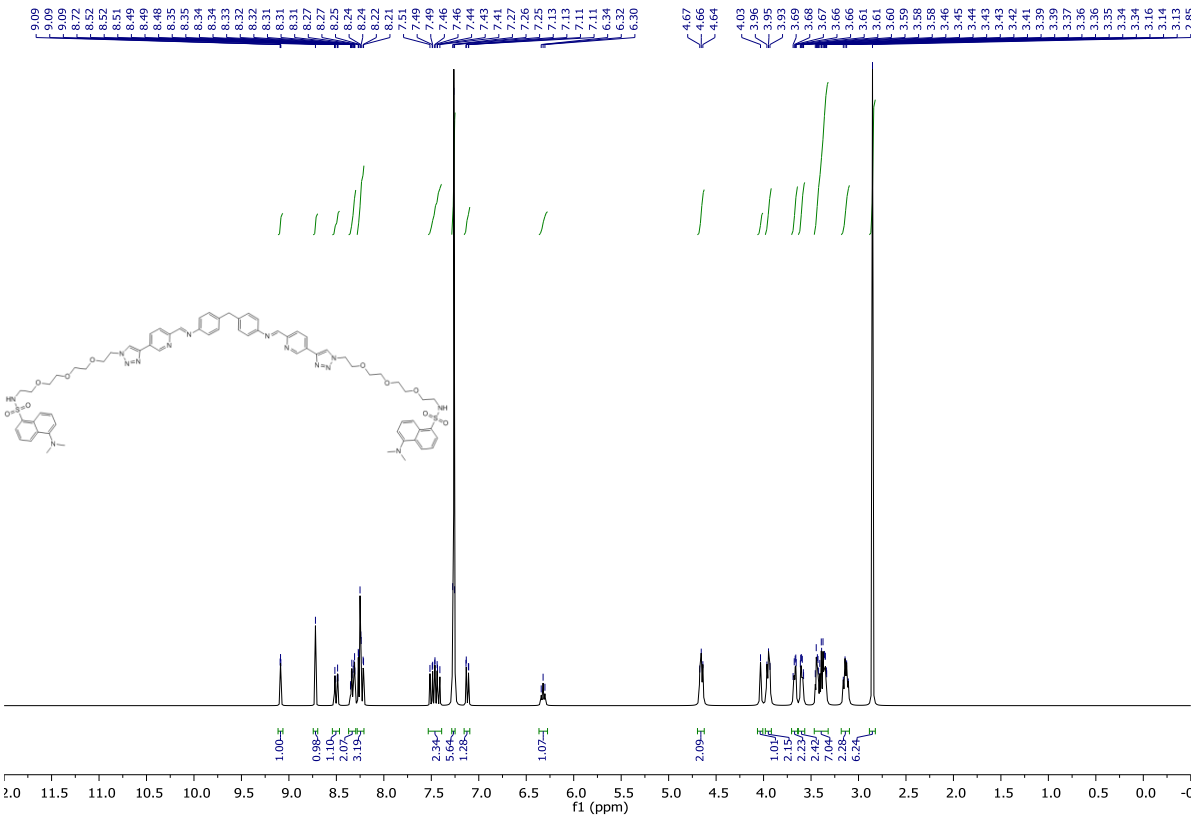

Figure 6.95 ^{1}H NMR spectrum of L^{D5} in $CDCl_3$

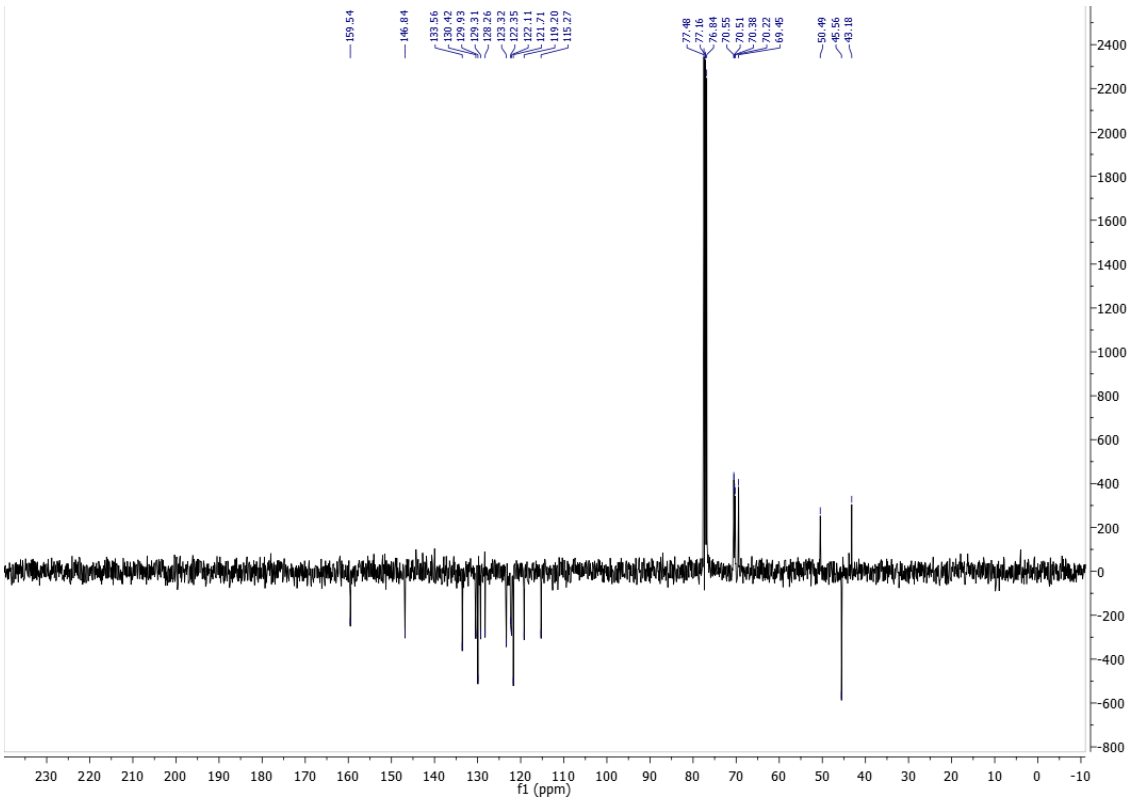

Figure 6.96 ^{13}C NMR spectrum of L^{D5} in $CDCl_3$

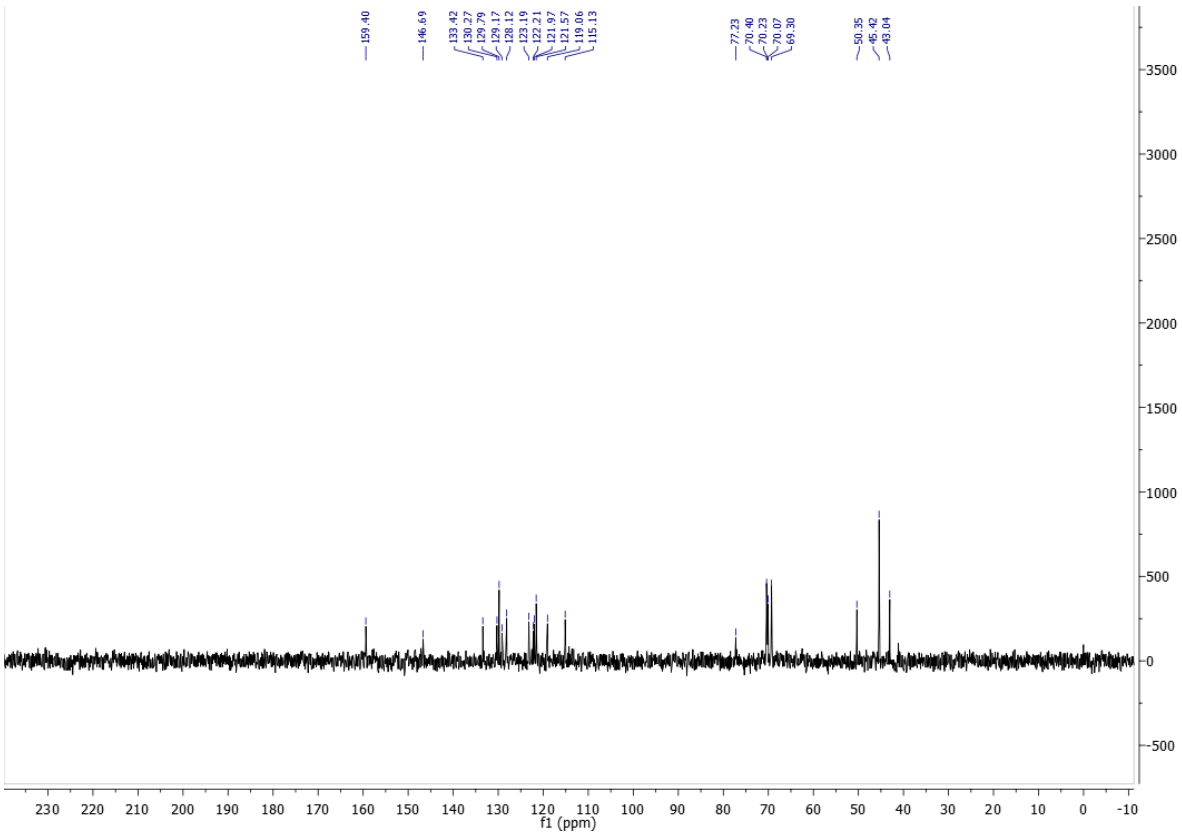

Figure 6.97 ^{13}C NMR spectrum of L^{D5} in $CDCl_3$

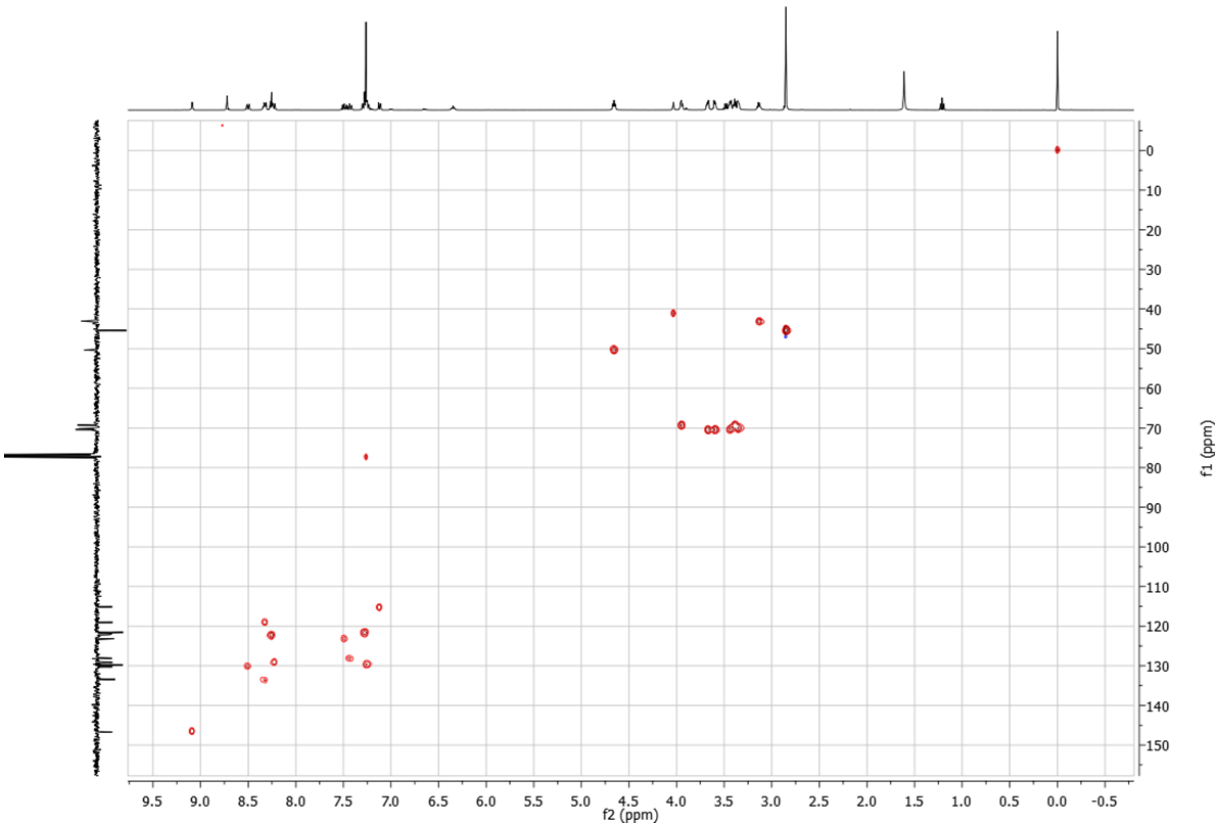

Figure 6.98 HSQC NMR spectrum of L^{D5} in $CDCl_3$

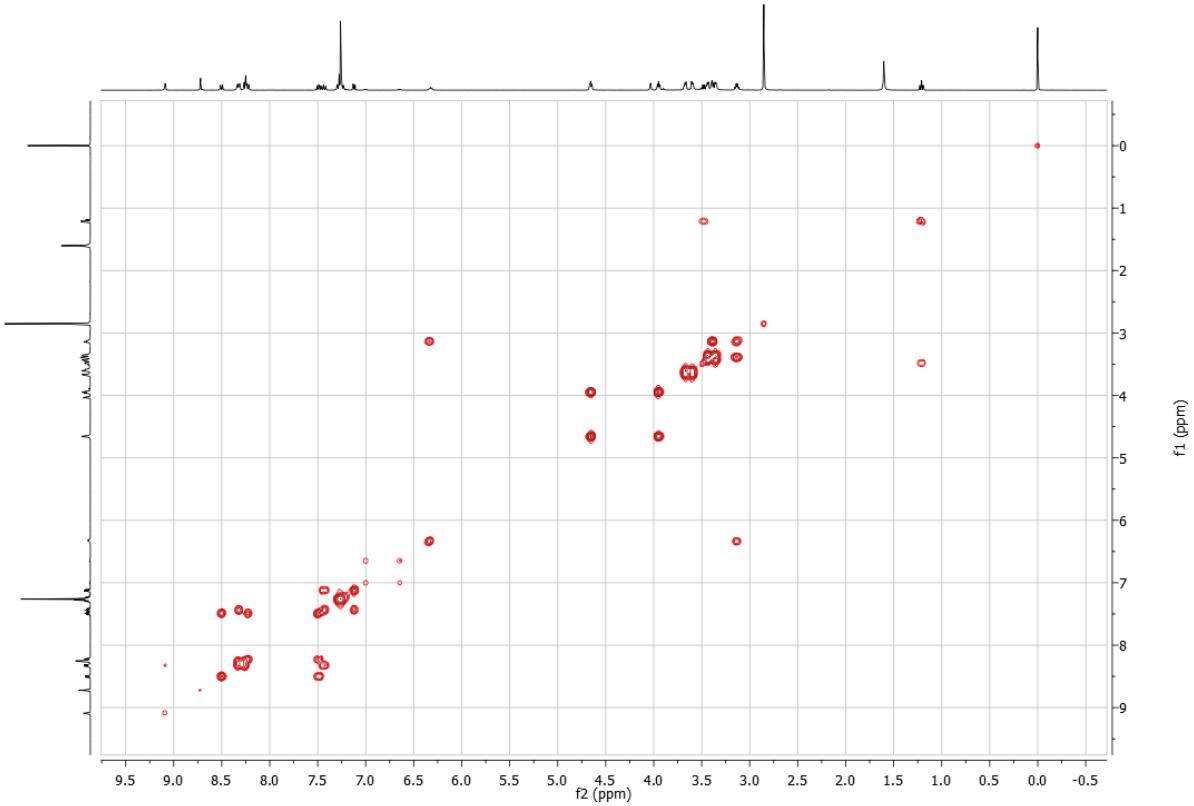

Figure 6.99 COSY NMR spectrum of L^{D5} in $CDCl_3$

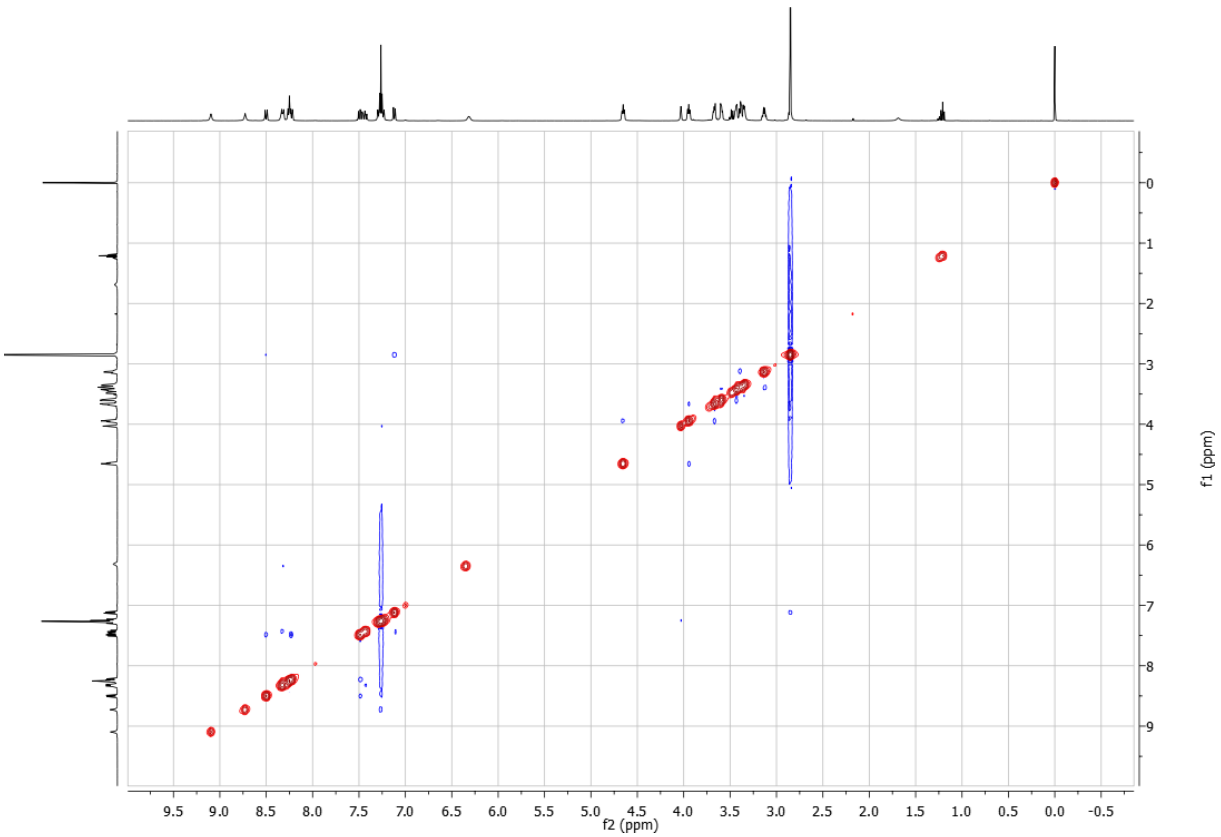

Figure 6.100 NOESY NMR spectrum of L^{D5} in $CDCl_3$

6.18 NMR spectra of $[Fe_2L^{D5}{}_3][PF_6]_4$

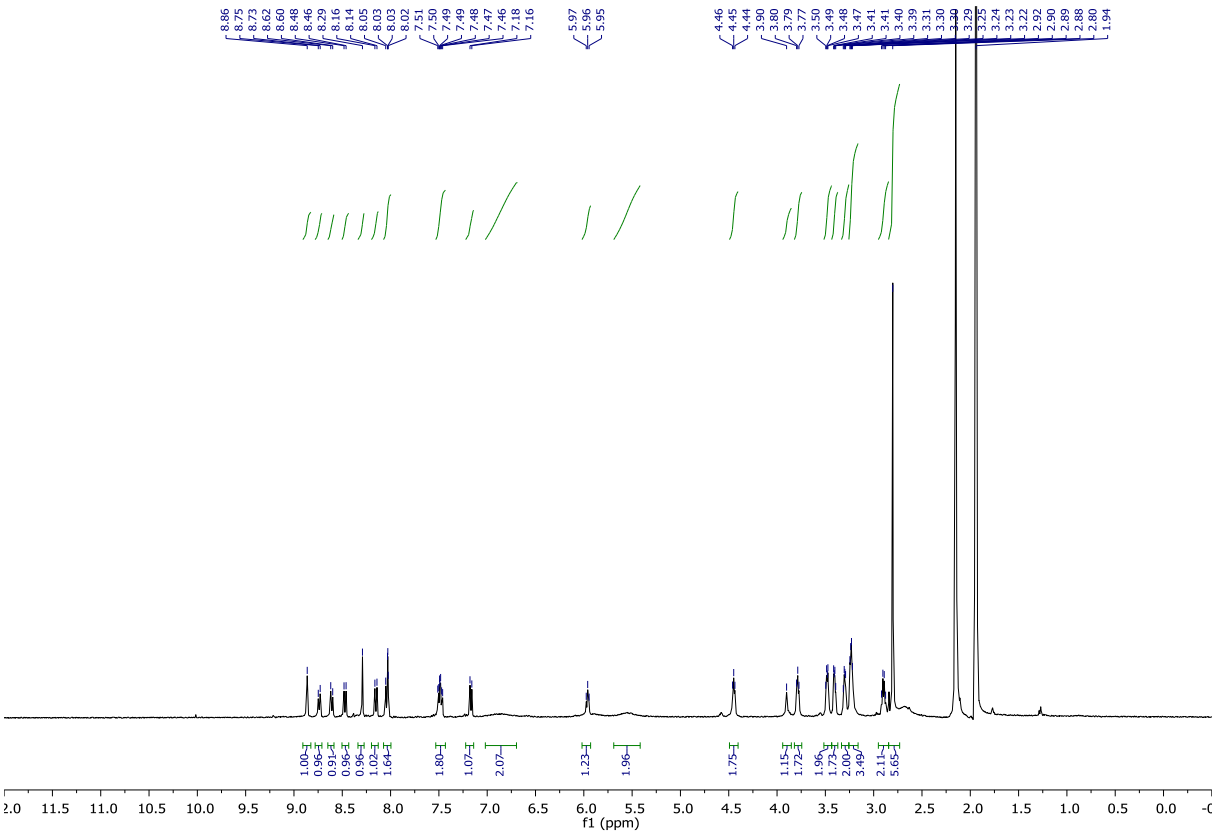

Figure 6.101 ^{1}H NMR spectrum of $[Fe_2L^{D5}{}_3][PF_6]_4$ in CD_3CN

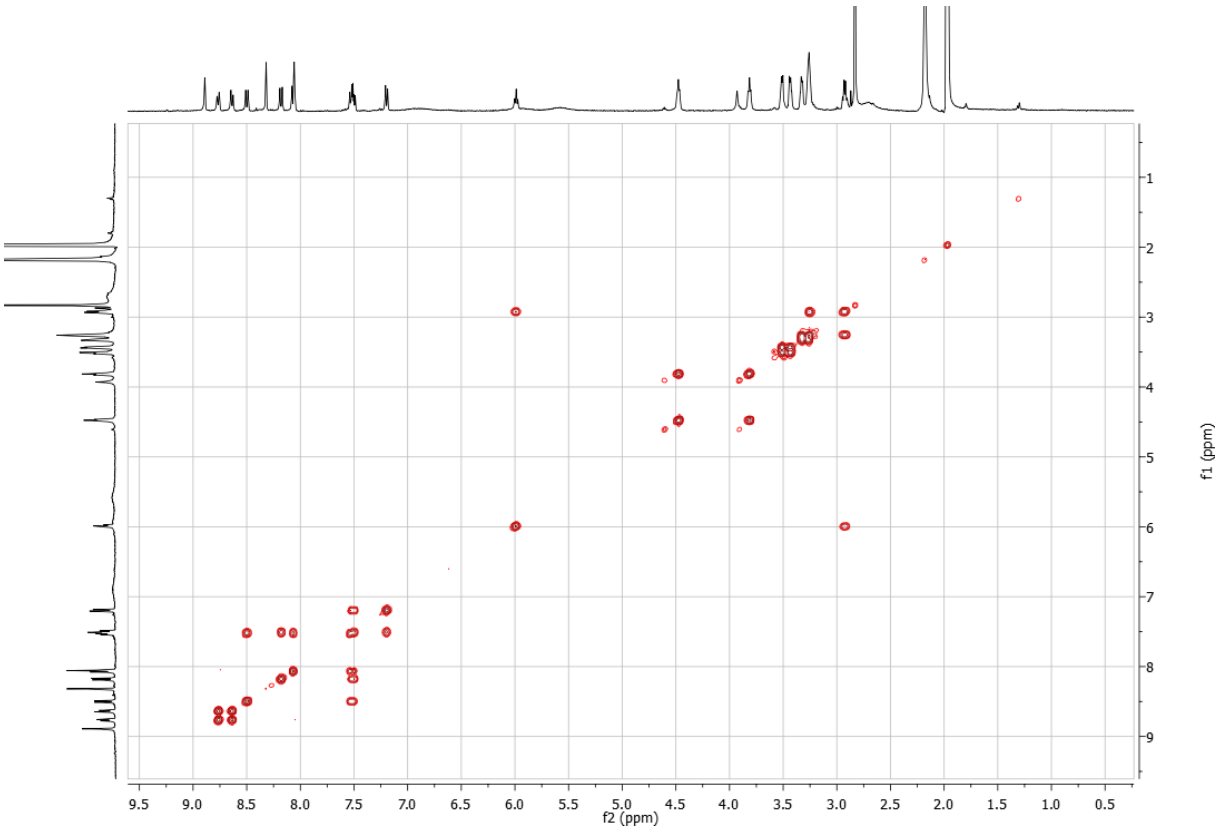

Figure 6.102 COSY NMR spectrum of $[Fe_2L^{D5}{}_3][PF_6]_4$ in CD_3CN

6.19 NMR spectra of L^{D4}

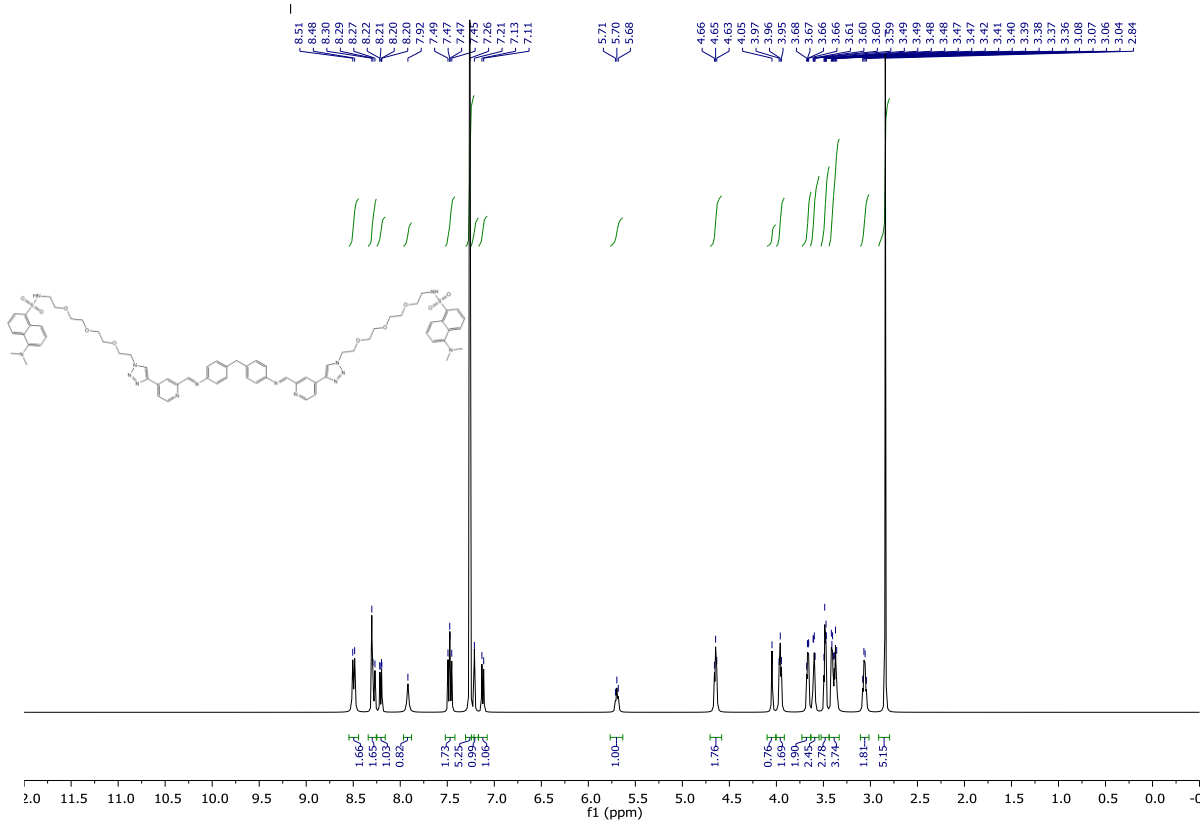

Figure 6.103 ^{1}H NMR spectrum of L^{D4} in $CDCl_3$

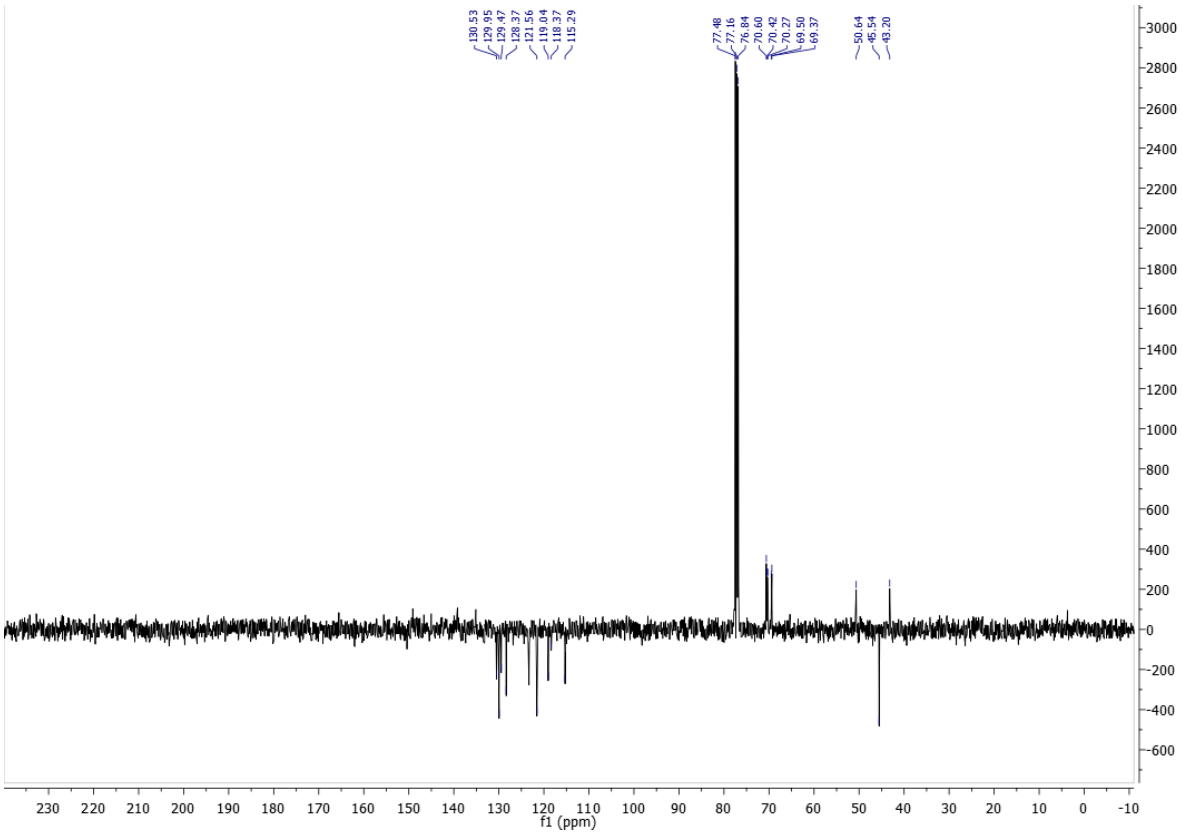

Figure 6.104 ^{13}C NMR spectrum of L^{D4} in $CDCl_3$

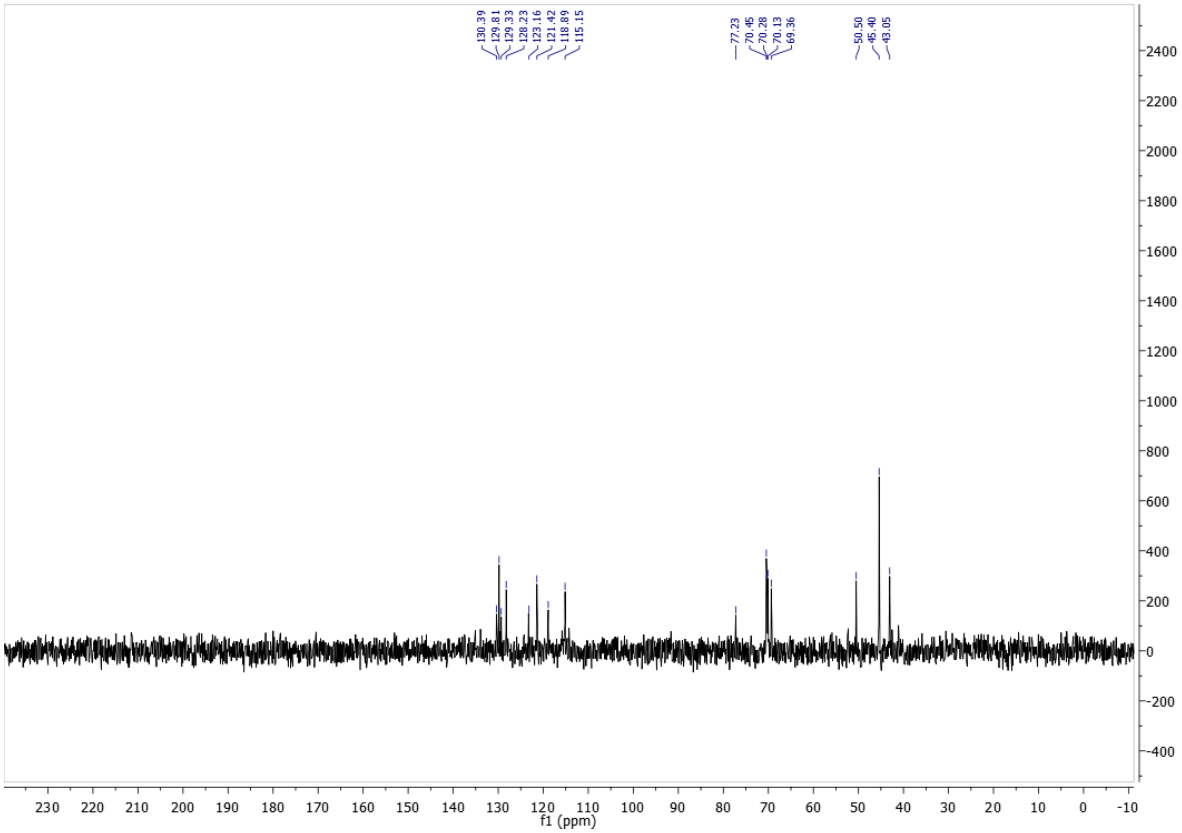

Figure 6.105 ^{13}C NMR spectrum of L^{D4} in $CDCl_3$

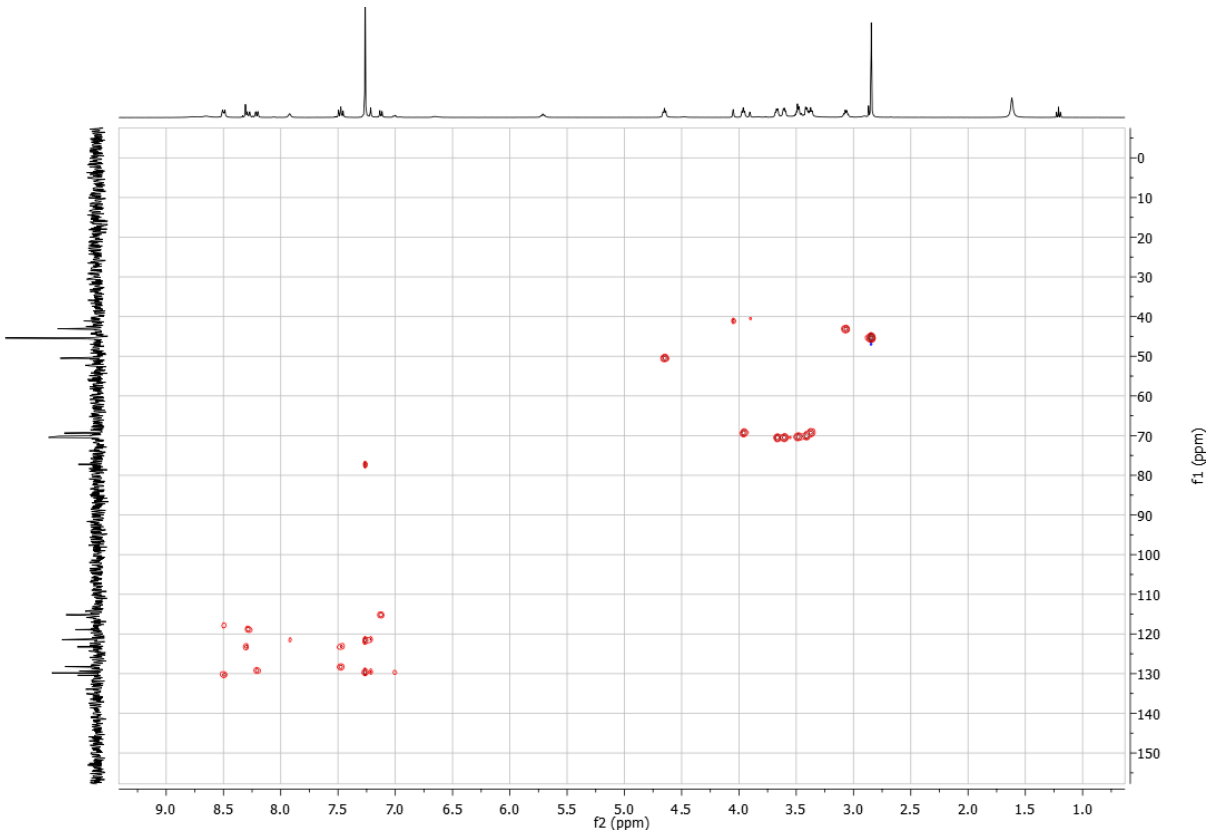

Figure 6.106 HSQC NMR spectrum of L^{D4} in $CDCl_3$

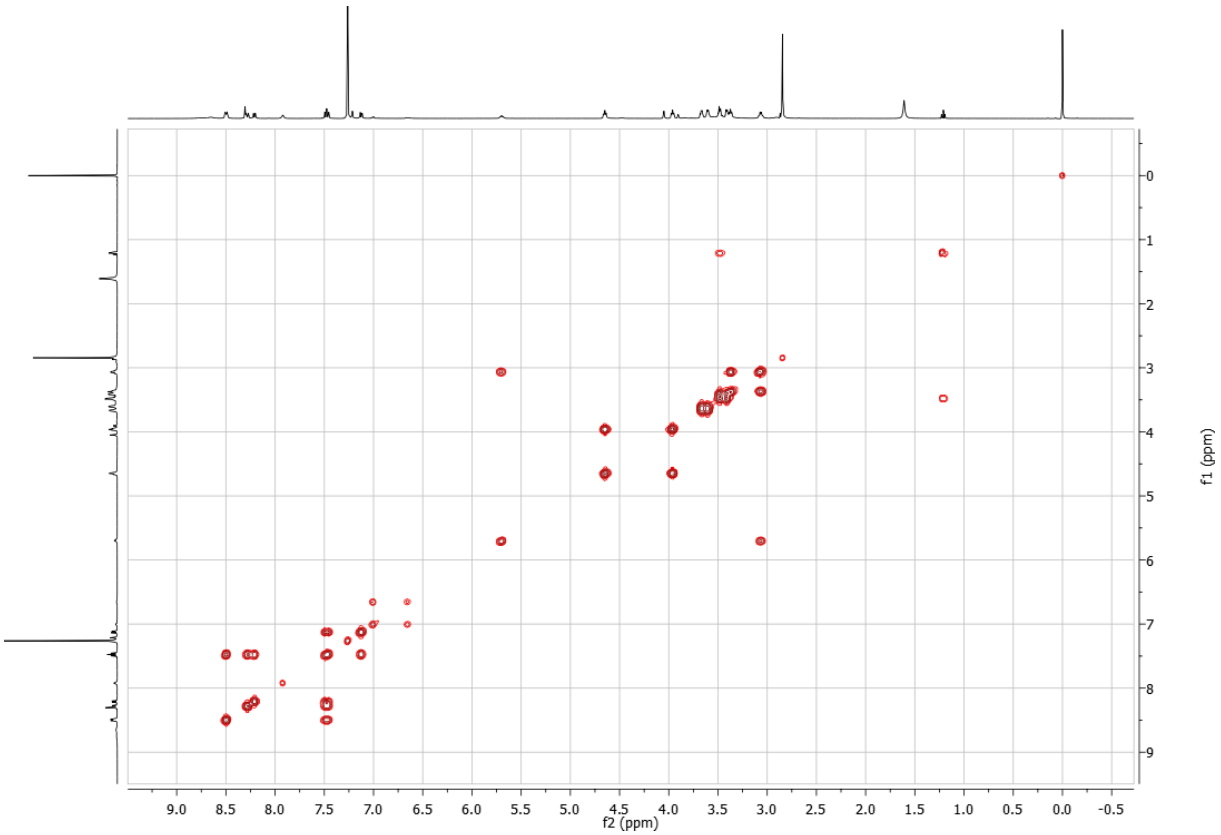

Figure 6.107 COSY NMR spectrum of L^{D4} in $CDCl_3$

6.20 NMR spectrum of $[Fe_2L^{D4}{}_3][PF_6]_4$

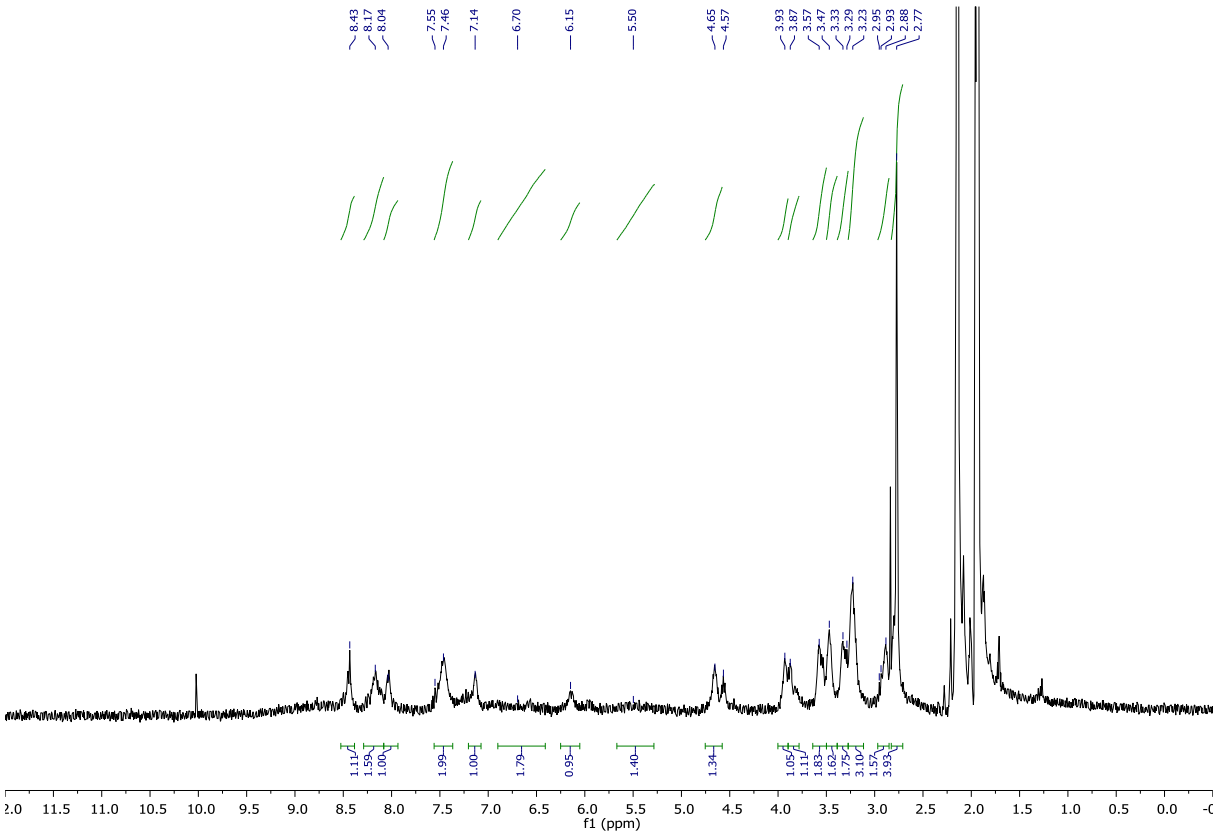

Figure 6.108 ^1H NMR spectrum $[Fe_2L^{D4}{}_3][PF_6]_4$ of CD_3CN

6.21 NMR spectra of L^{Br5}

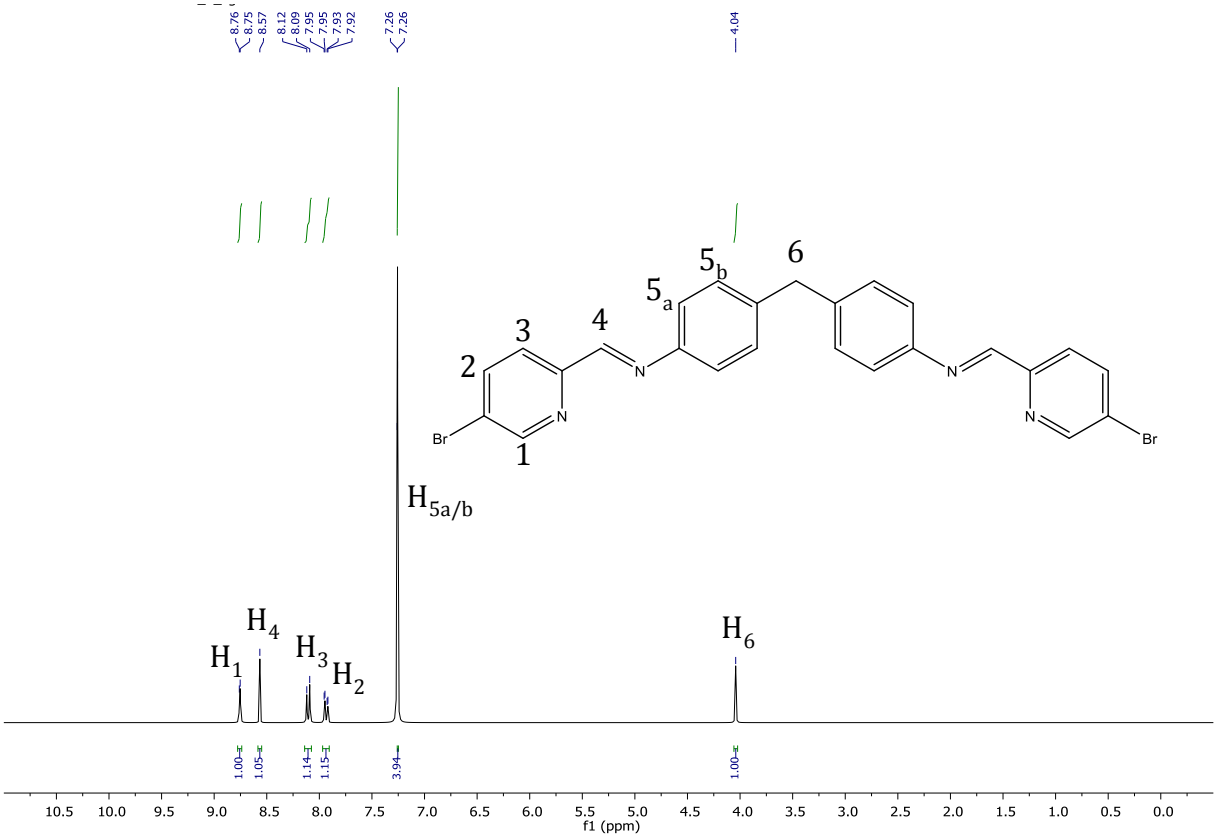

Figure 6.109 ^{1}H NMR spectrum of L^{Br5} in $CDCl_3$

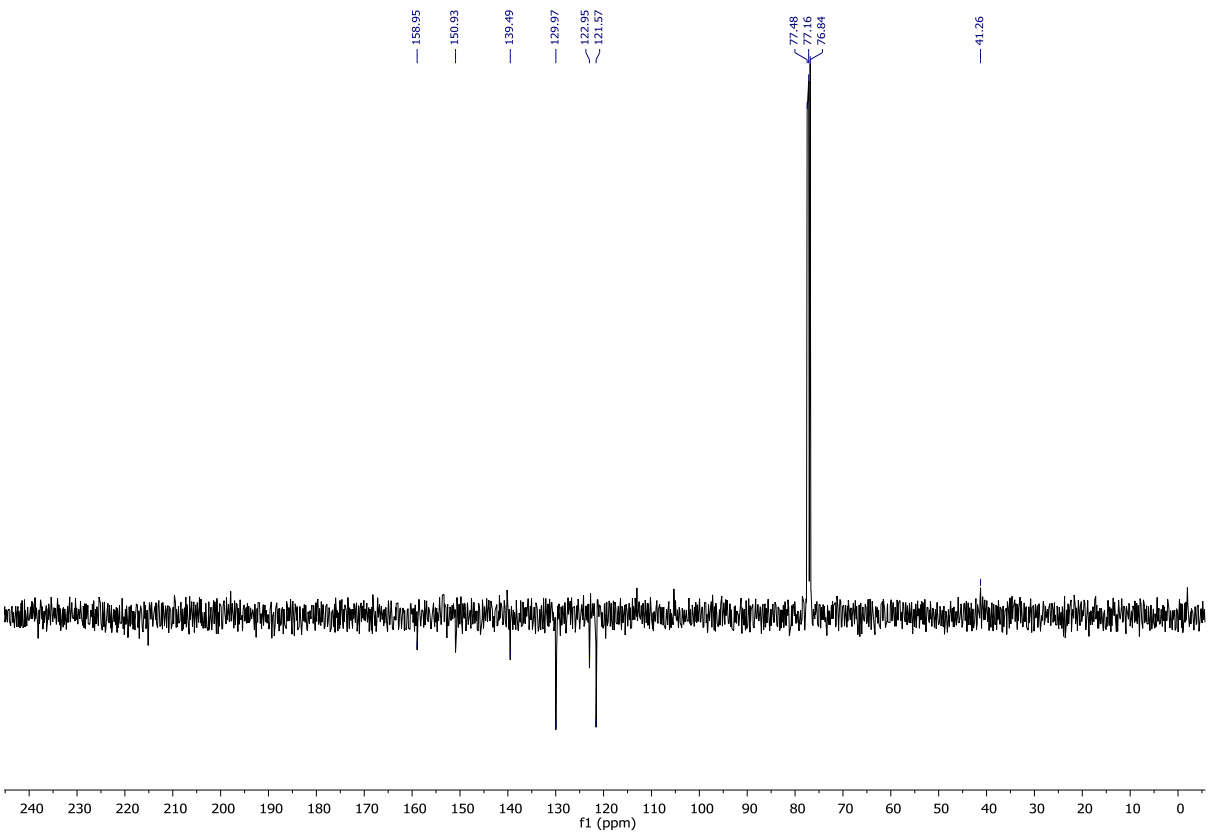

Figure 6.110 ^{13}C NMR spectrum of L^{Br5} in $CDCl_3$

6.22 NMR spectrum of $[Fe_2L^{Br5}_3][PF_6]_4$

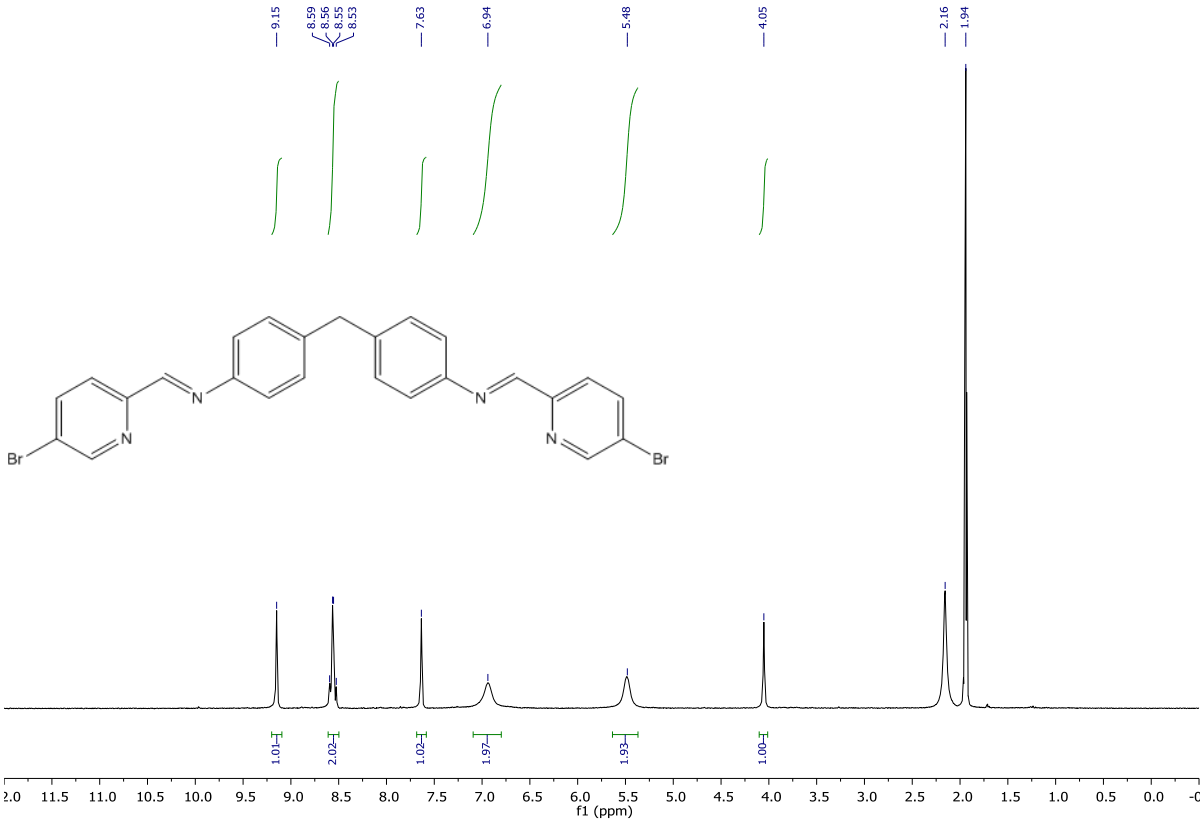

Figure 6.111 ^{1}H NMR spectrum of $[Fe_2L^{Br5}_3][PF_6]_4$ in CD_3CN

6.23 NMR spectra of L^{Br4}

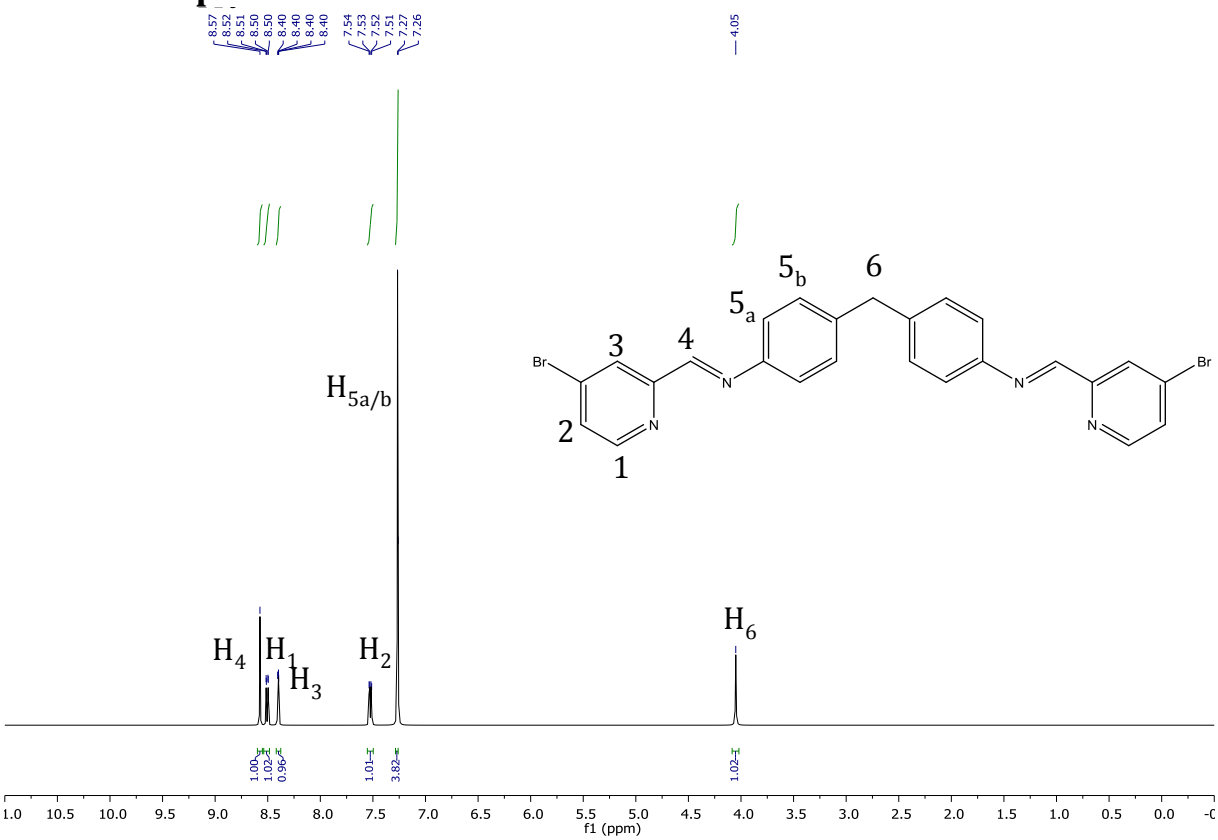

Figure 6.112 ^{1}H NMR spectrum of L^{Br4} in $CDCl_3$

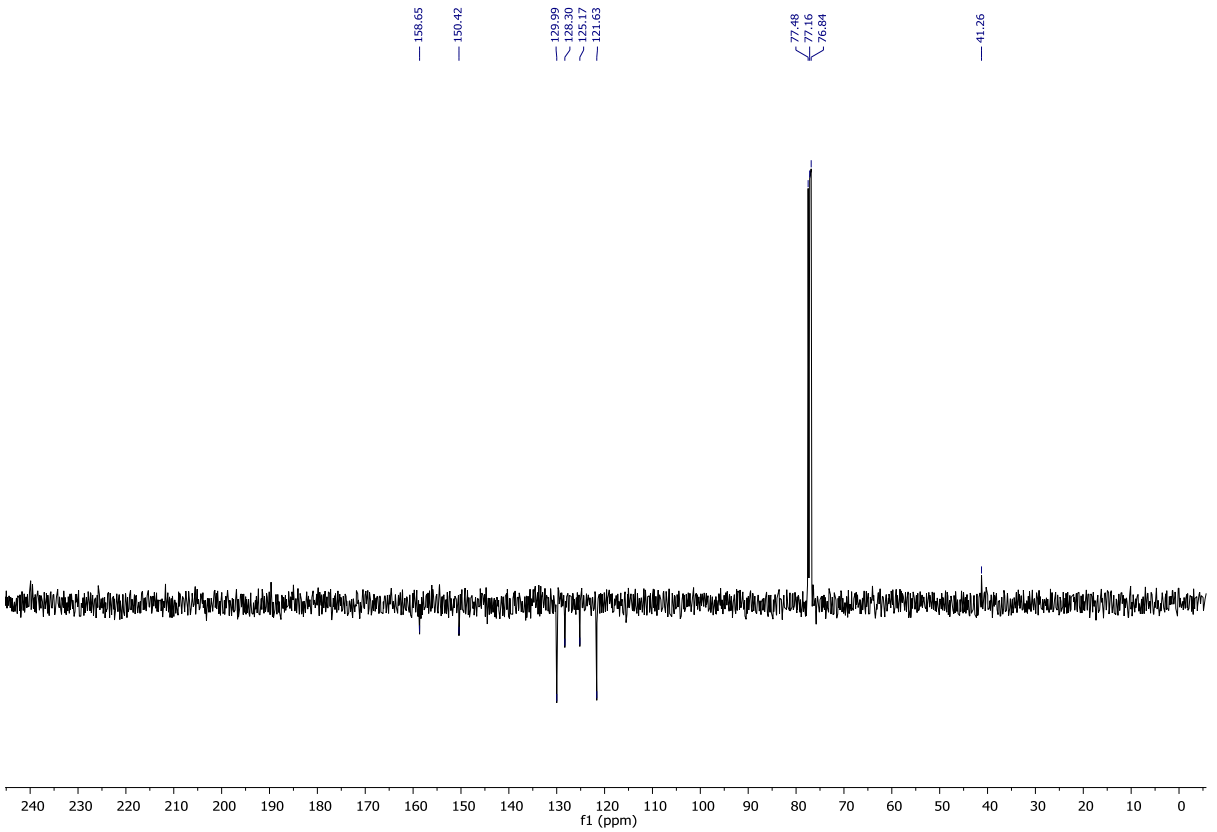

Figure 6.113 ^{13}C NMR spectrum of L^{Br4} in $CDCl_3$

6.24 NMR spectra of $[Fe_2L^{Br4}{}_3][PF_6]_4$

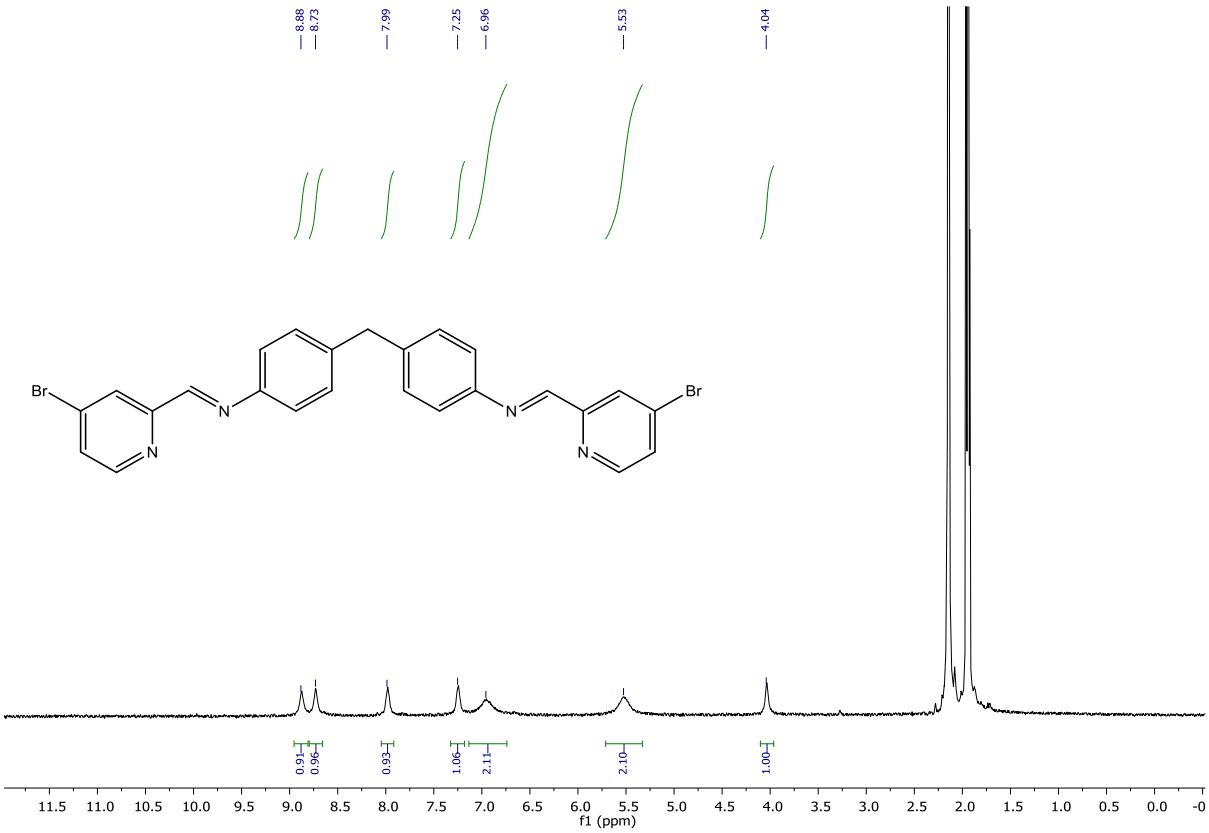

Figure 6.114 ^{1}H NMR spectrum of $[Fe_2L^{Br4}{}_3][PF_6]_4$ in CD_3CN

6.25 NMR spectra of 1-(prop-2-yn-1-yl)-1H-imidazole-2-carbaldehyde

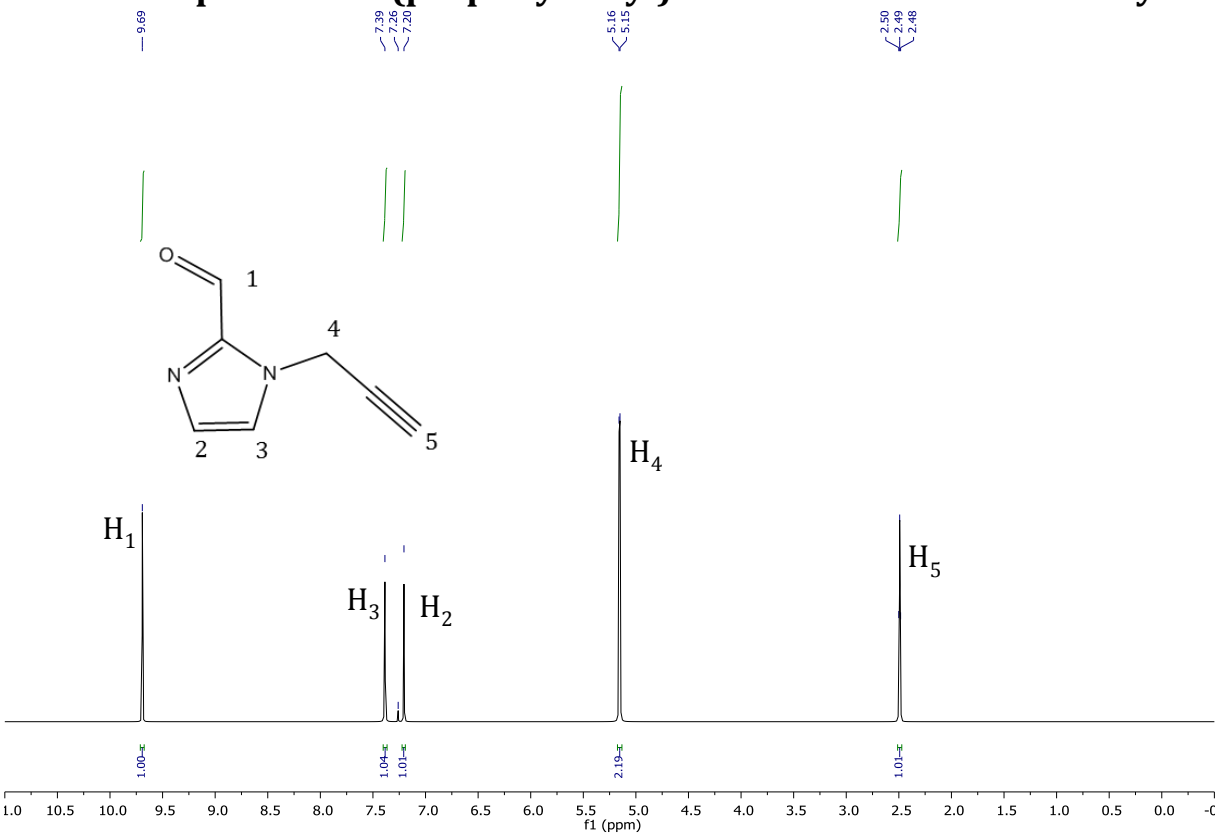

Figure 6.115 ^{1}H NMR spectrum of 1-(prop-2-yn-1-yl)-1H-imidazole-2-carbaldehyde in $CDCl_3$

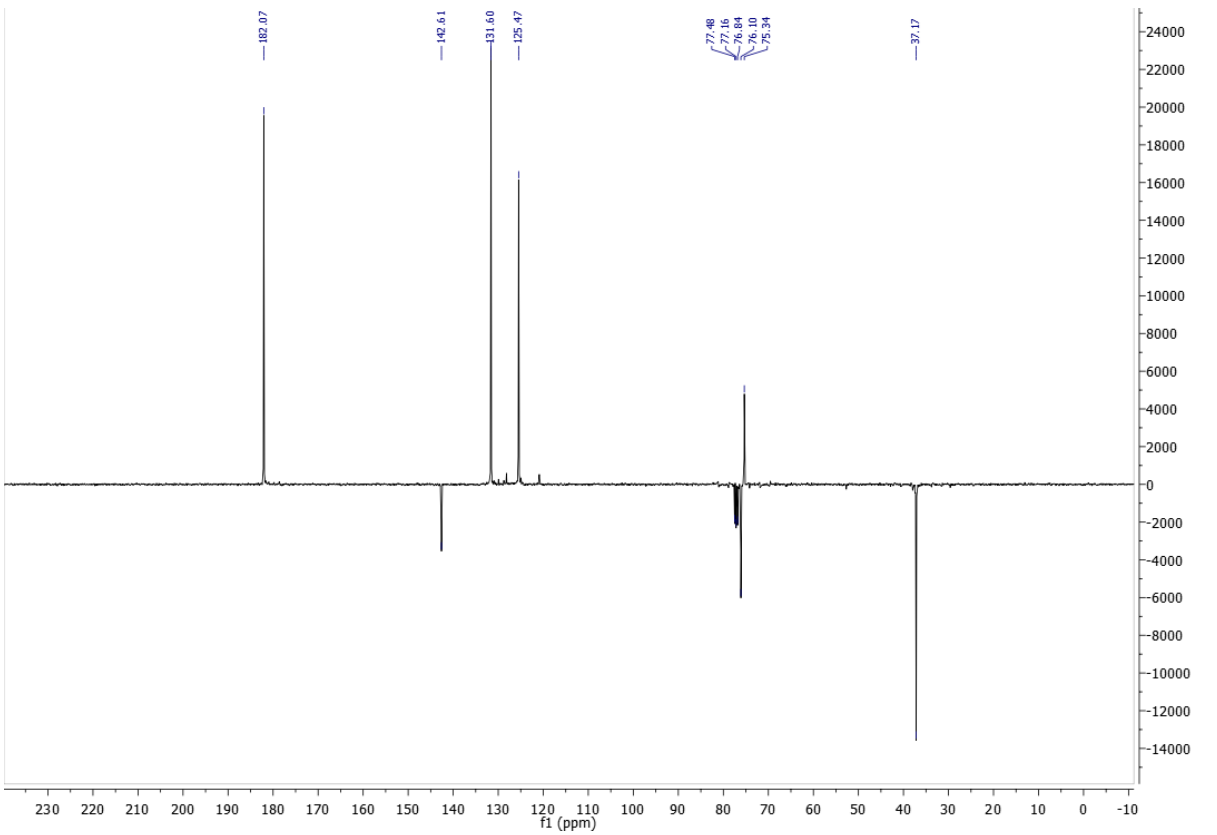

Figure 6.116 ^{13}C NMR spectrum of 1-(prop-2-yn-1-yl)-1H-imidazole-2-carbaldehyde in $CDCl_3$

6.26 NMR spectra of L^{TBim}

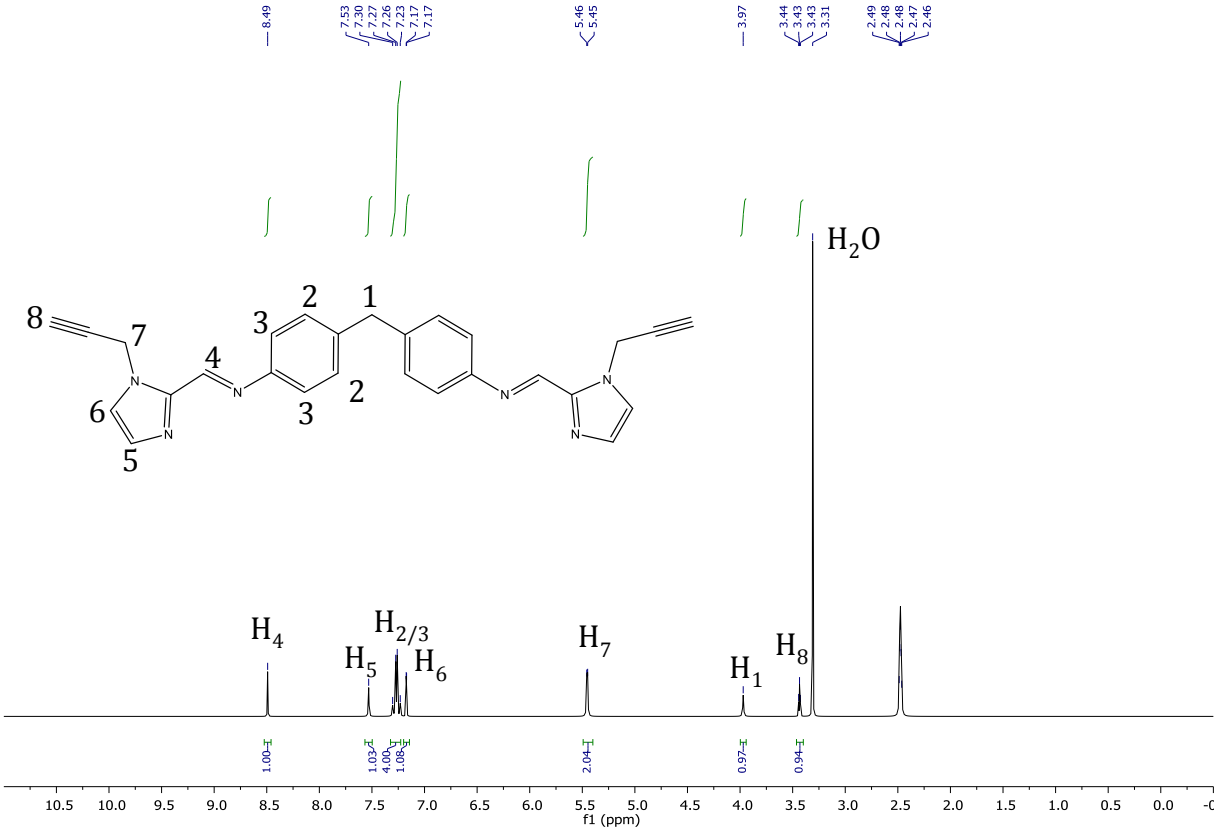

Figure 6.117 ^{1}H NMR spectrum of L^{TBim} in DMSO

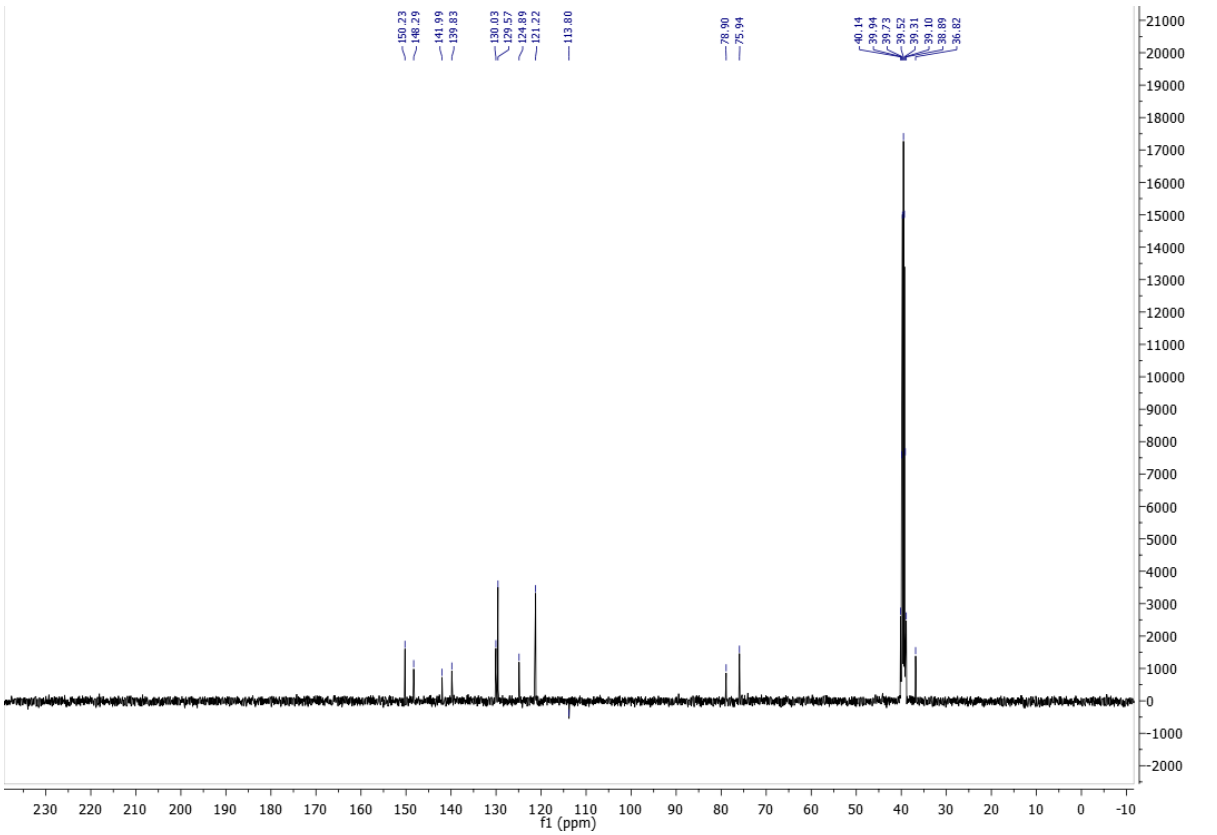

Figure 6.118 ^{13}C NMR spectrum of L^{TBim} in DMSO

6.27 NMR spectrum of 3-azidopropan-1-ol

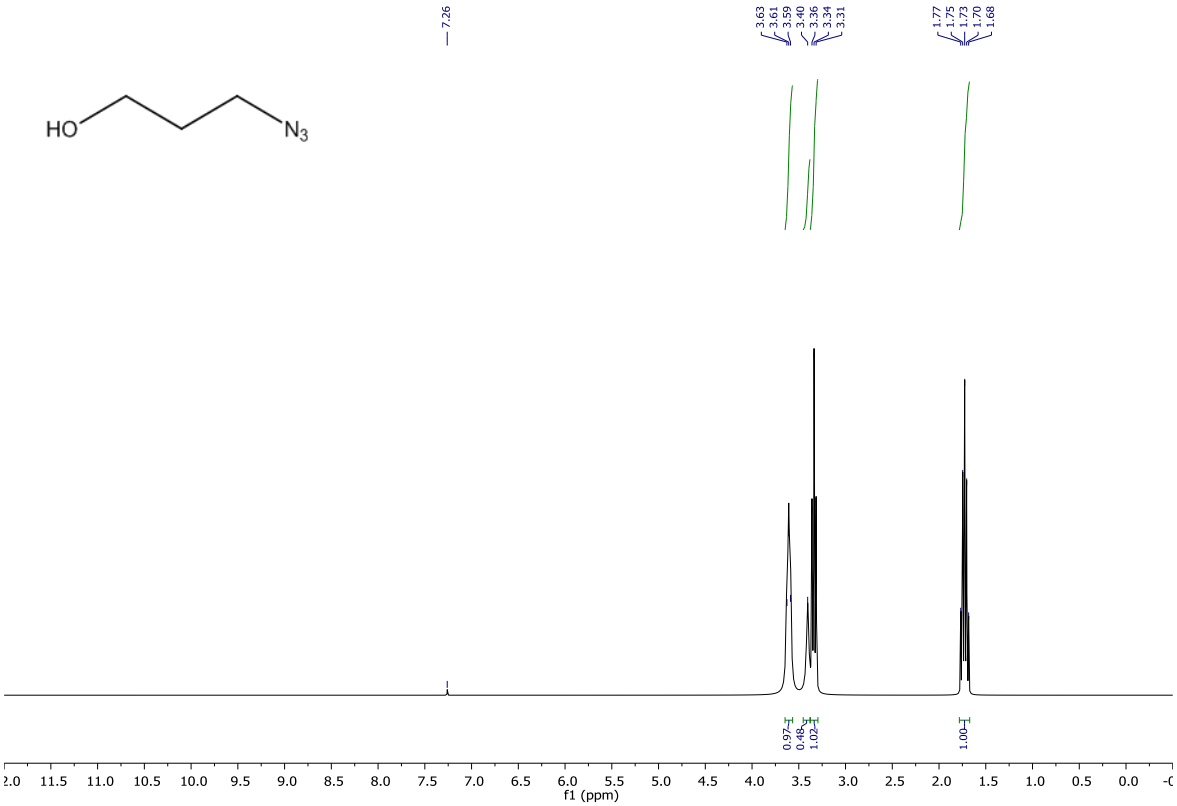

Figure 6.119 ^{1}H NMR spectrum of 3-azidopropyl methanesulfonate in $CDCl_3$

6.28 NMR spectrum of 3-azidopropyl methanesulfonate

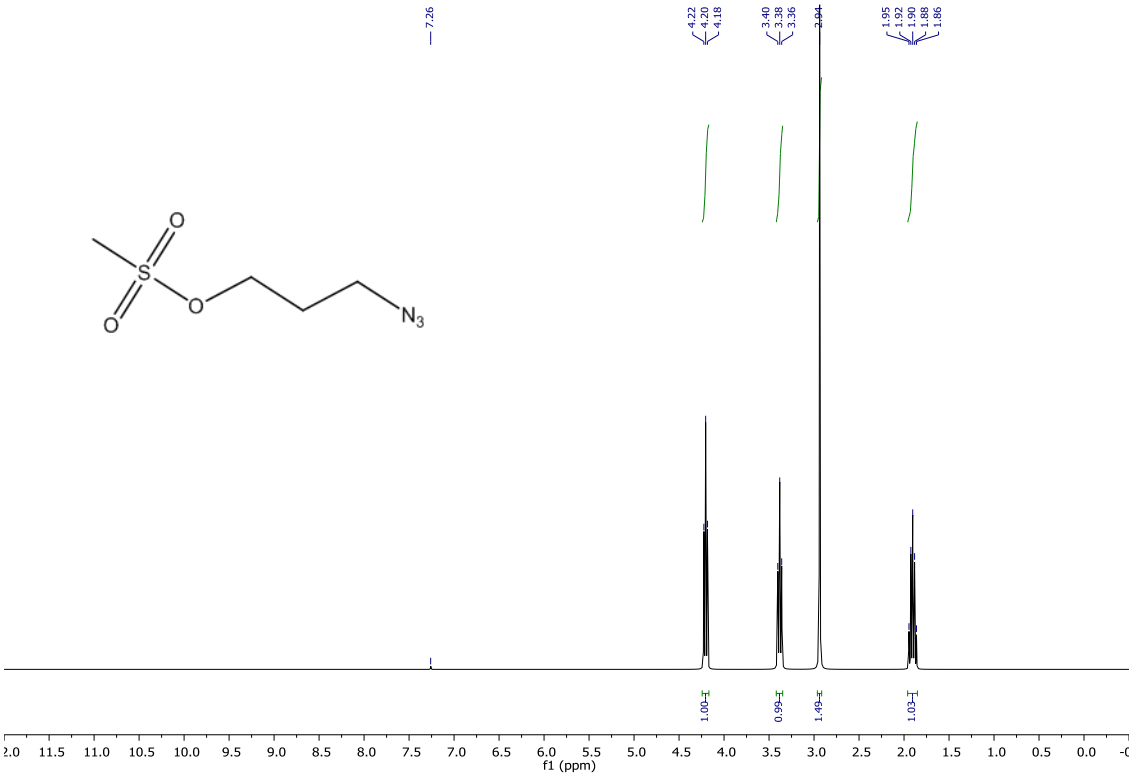

Figure 6.120 ^{1}H NMR spectrum of 3-azidopropyl methanesulfonate in $CDCl_3$

6.29 NMR spectra of 1-(3-azidopropyl)-1H-imidazole-2-carbaldehyde

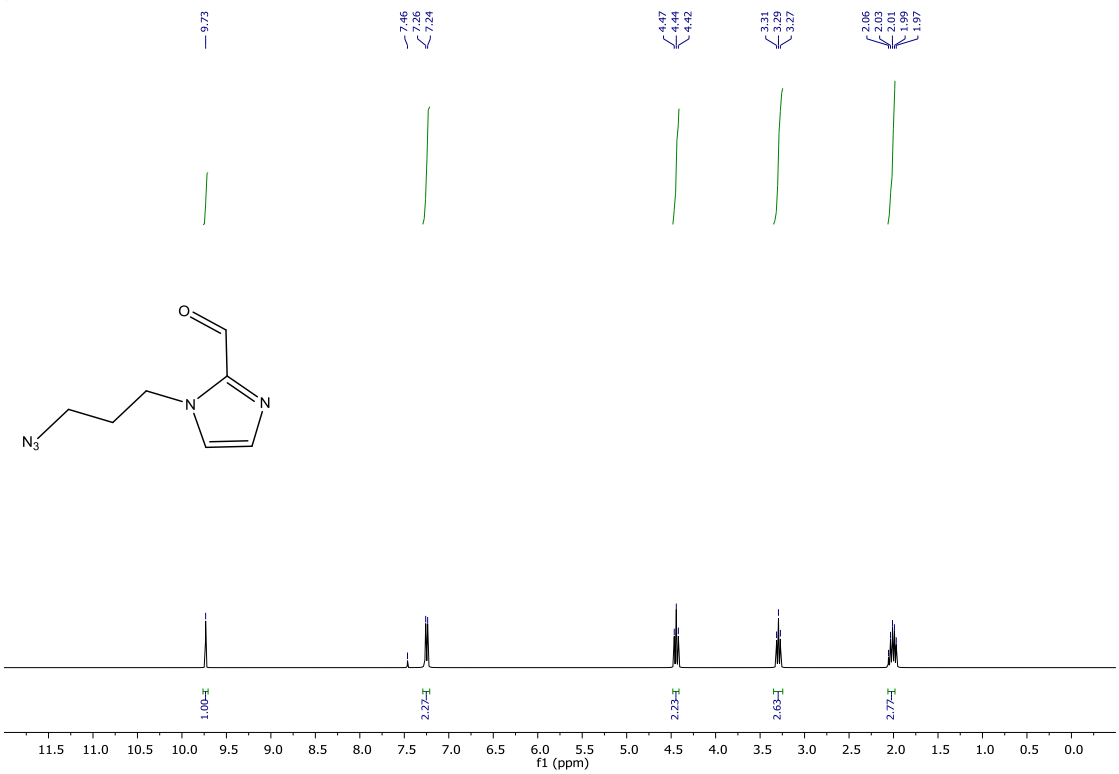

Figure 6.121 ^{1}H NMR spectrum of 1-(3-azidopropyl)-1H-imidazole-2-carbaldehyde in $CDCl_3$

6.30 NMR spectra of L^{Nim}

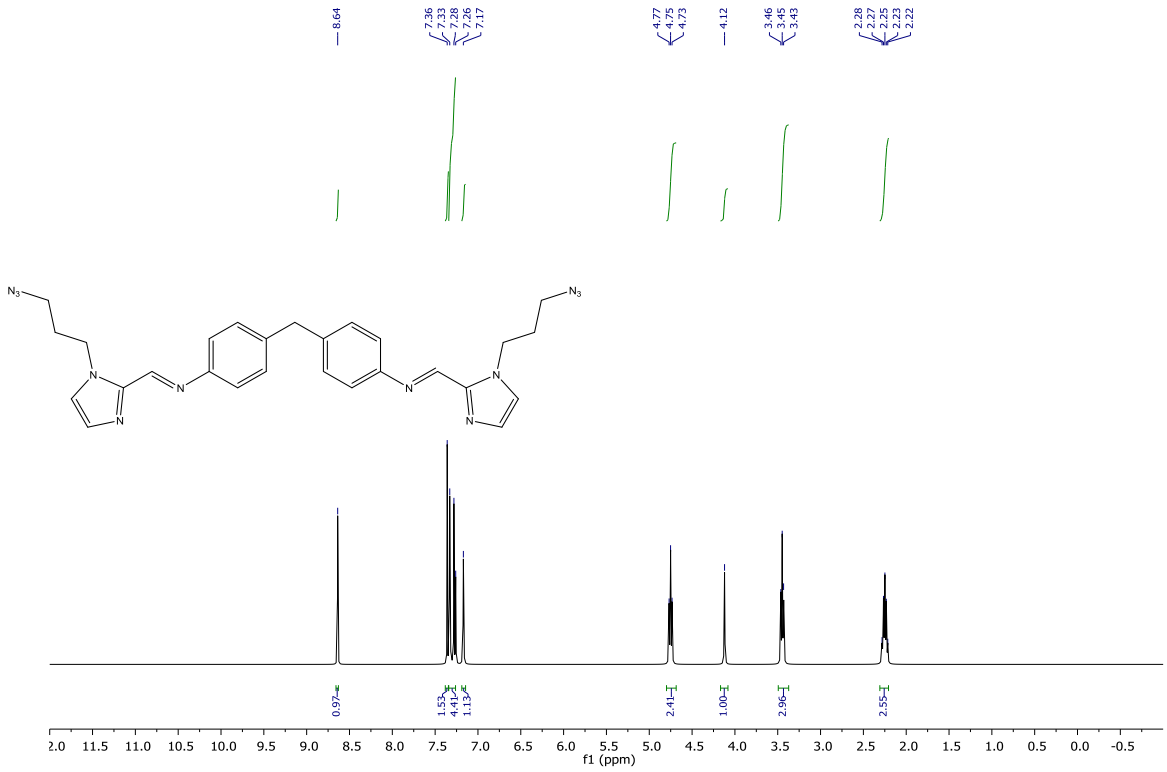

Figure 6.122 ^{1}H NMR spectrum of L^{Nim} in $CDCl_3$

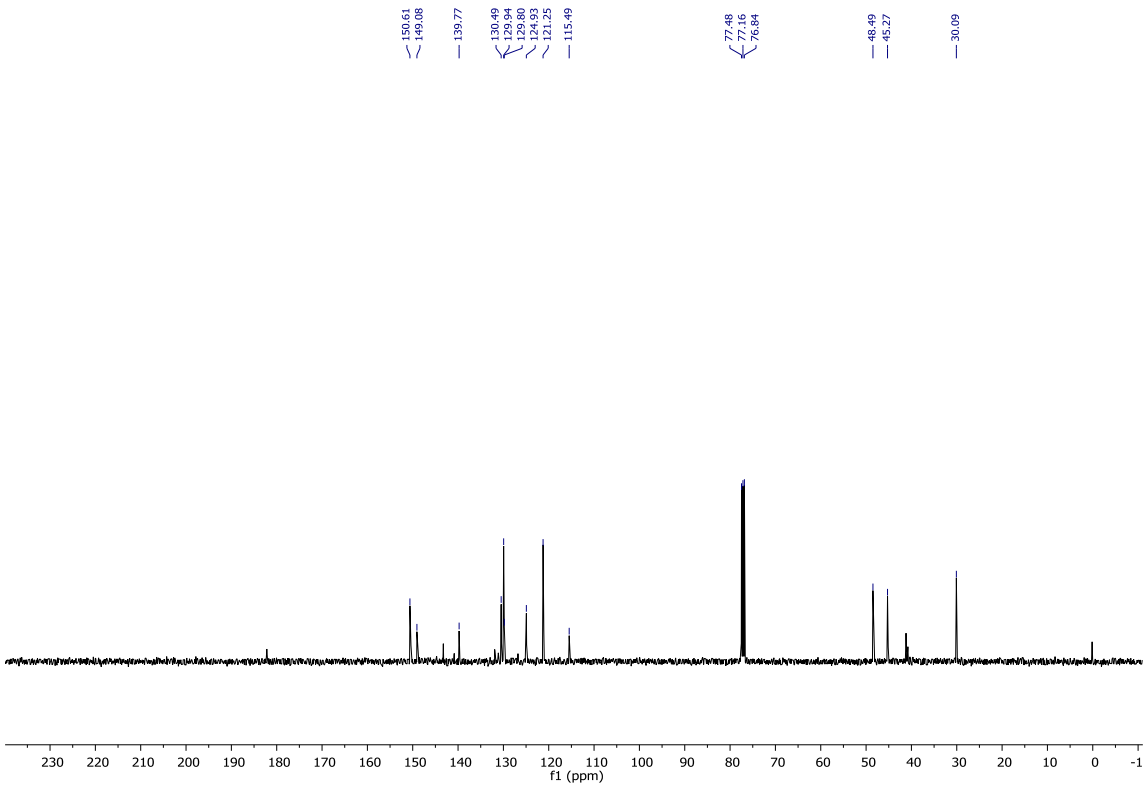

Figure 6.123 ^{13}C NMR spectrum of L^{Nim} in $CDCl_3$

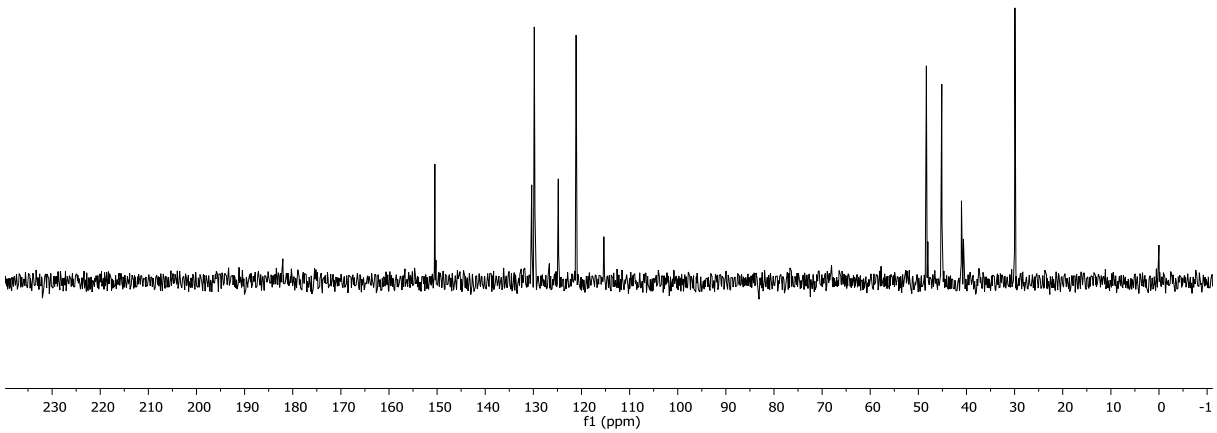

Figure 6.124 ^{13}C NMR spectrum of L^{Nim} in

6.31 NMR spectrum of $[Fe_2L^{Nim}{}_3][PF_6]_4$

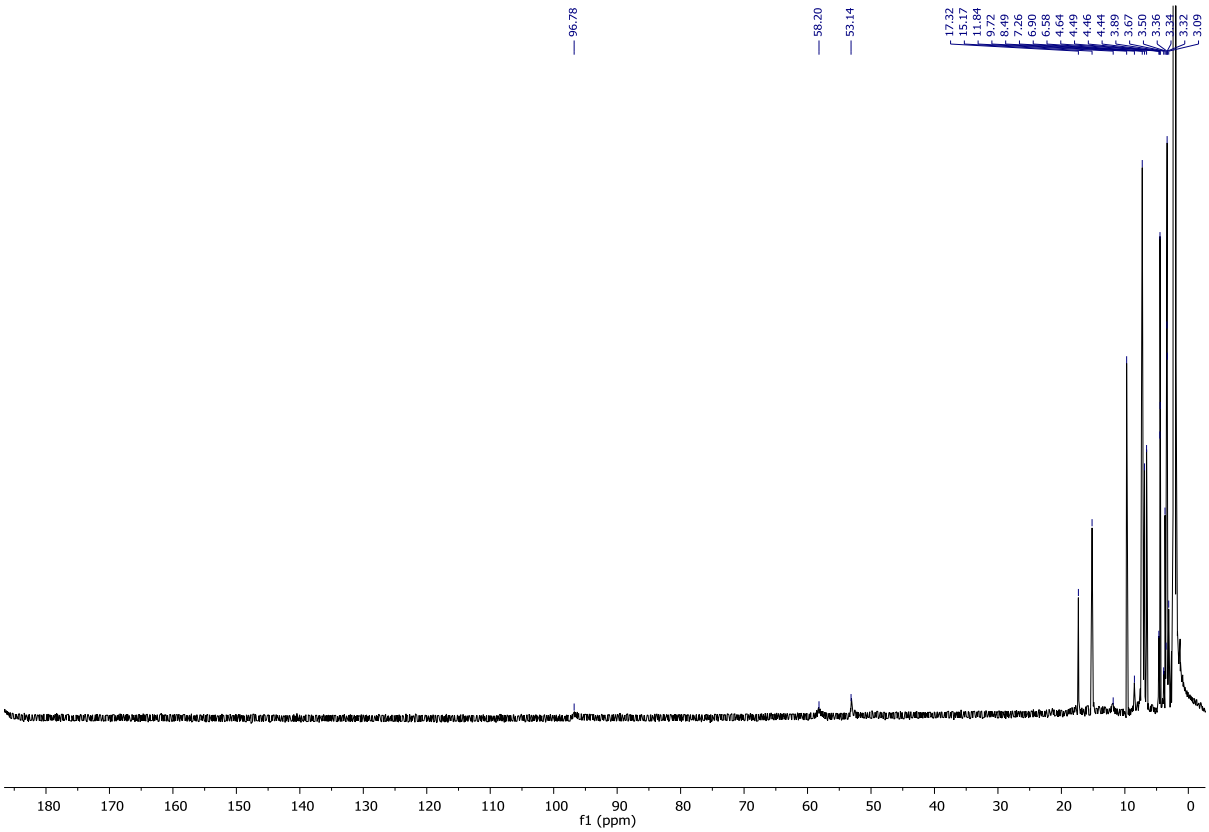

Figure 6.125 ^{1}H NMR spectrum of $[Fe_2L^{Nim}{}_3][PF_6]_4$ in CD_3CN

6.32 NMR spectra of 1-((1-(7-(diethylamino)-2-oxo-2H-chromen-3-yl)-1H-1,2,3-triazol-4-yl)methyl)-1H-imidazole-2-carbaldehyde

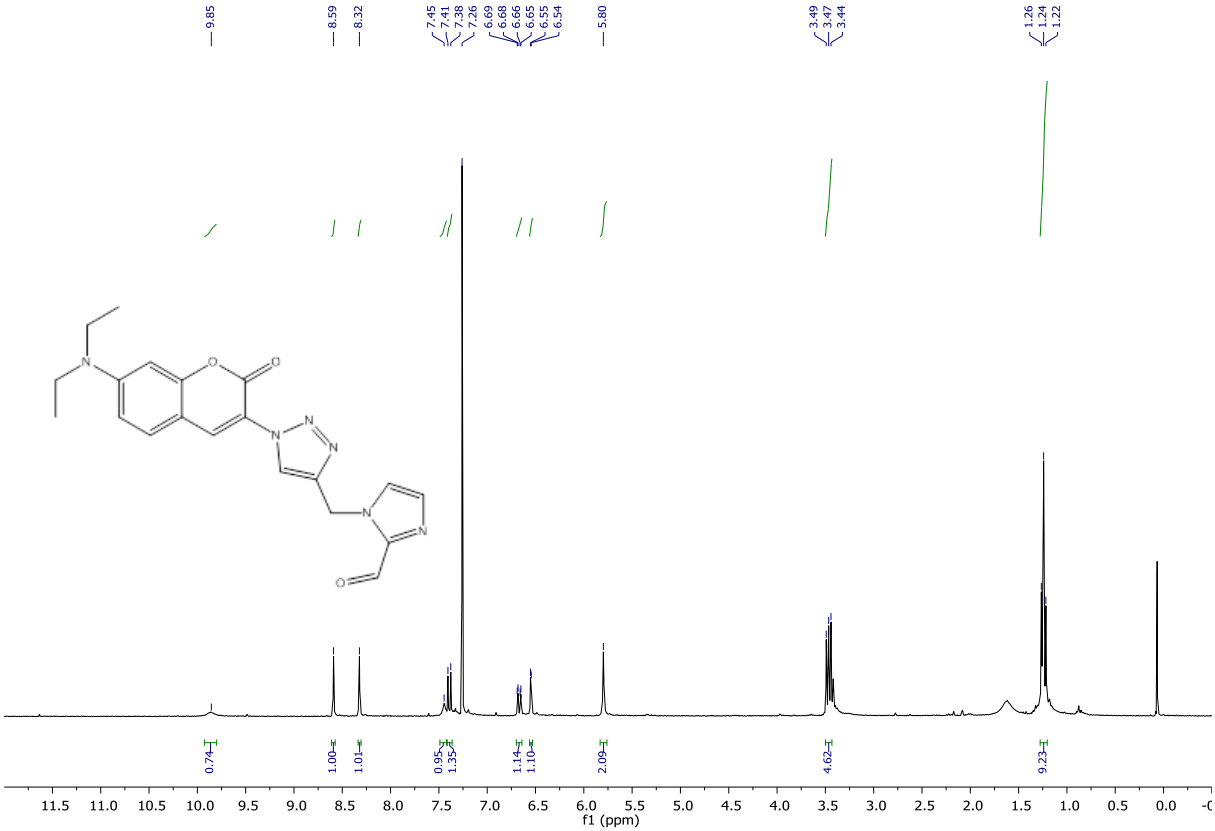

Figure 6.126 ^{1}H NMR spectrum of 1-((1-(7-(diethylamino)-2-oxo-2H-chromen-3-yl)-1H-1,2,3-triazol-4-yl)methyl)-1H-imidazole-2-carbaldehyde in $CDCl_3$

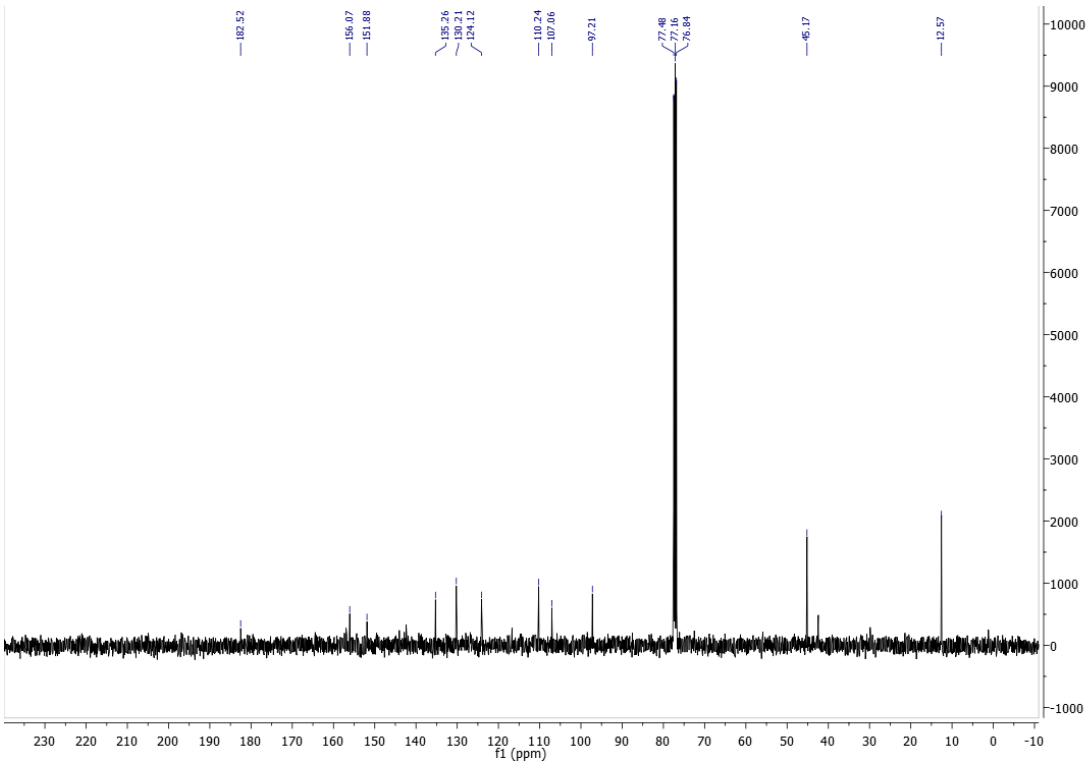

Figure 6.127 ^{13}C NMR spectrum of 1-((1-(7-(diethylamino)-2-oxo-2H-chromen-3-yl)-1H-1,2,3-triazol-4-yl)methyl)-1H-imidazole-2-carbaldehyde in $CDCl_3$

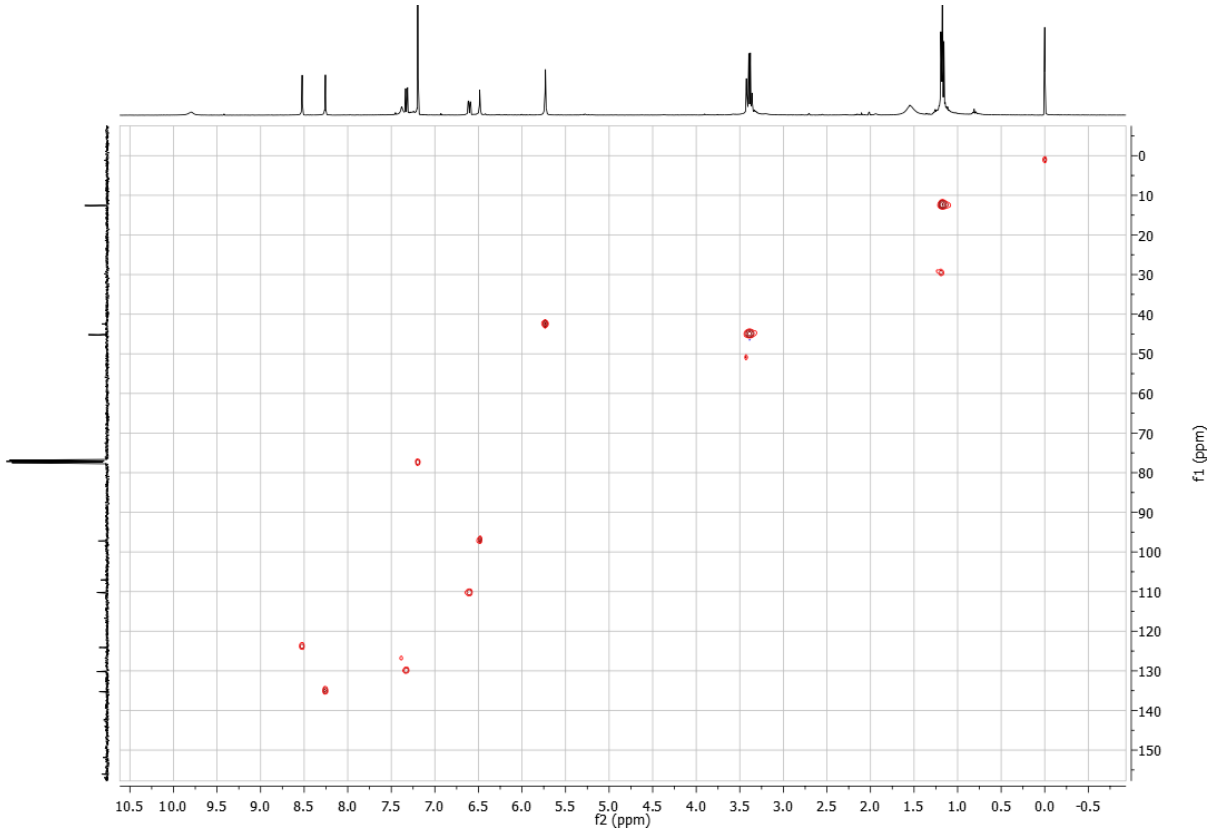

Figure 6.128 HSQC NMR spectrum of 1-((1-(7-(diethylamino)-2-oxo-2H-chromen-3-yl)-1H-1,2,3-triazol-4-yl)methyl)-1H-imidazole-2-carbaldehyde in $CDCl_3$

6.33 NMR spectra of L^{imC}

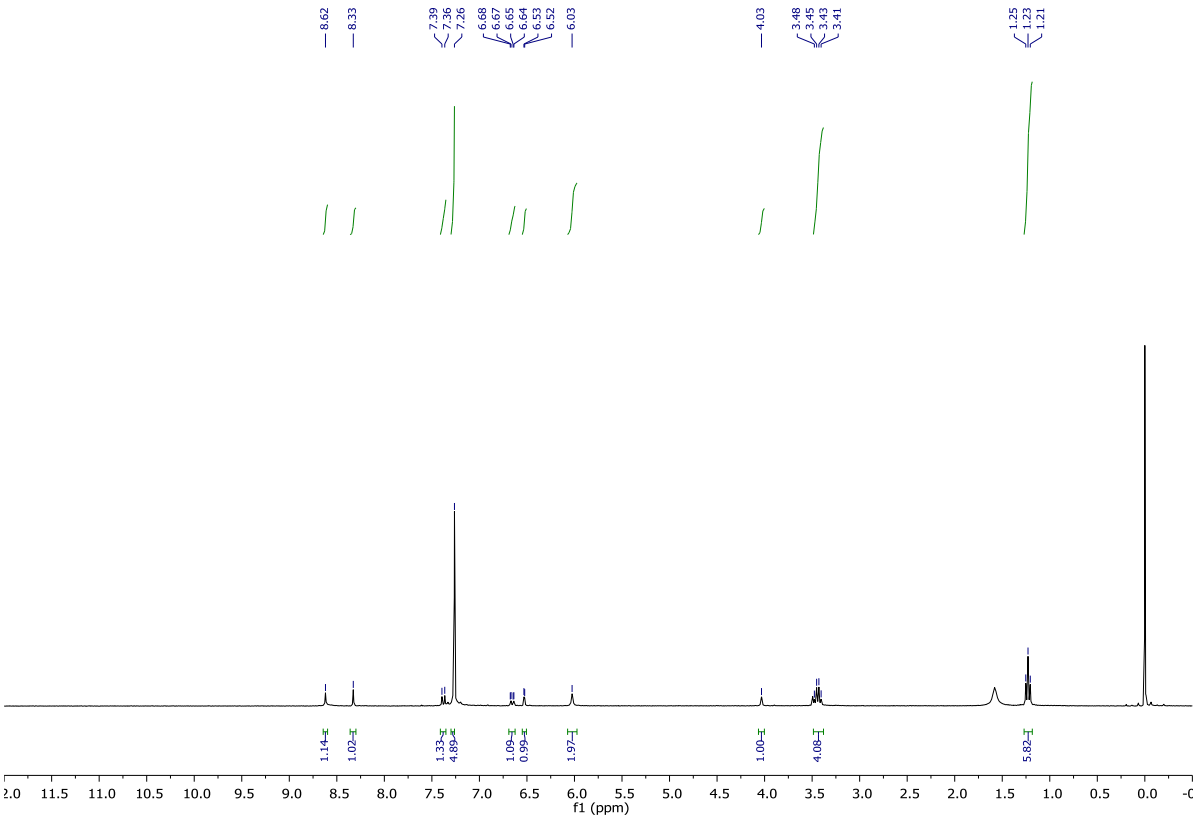

Figure 6.129 ^{1}H NMR spectrum of L^{imC} in $CDCl_3$

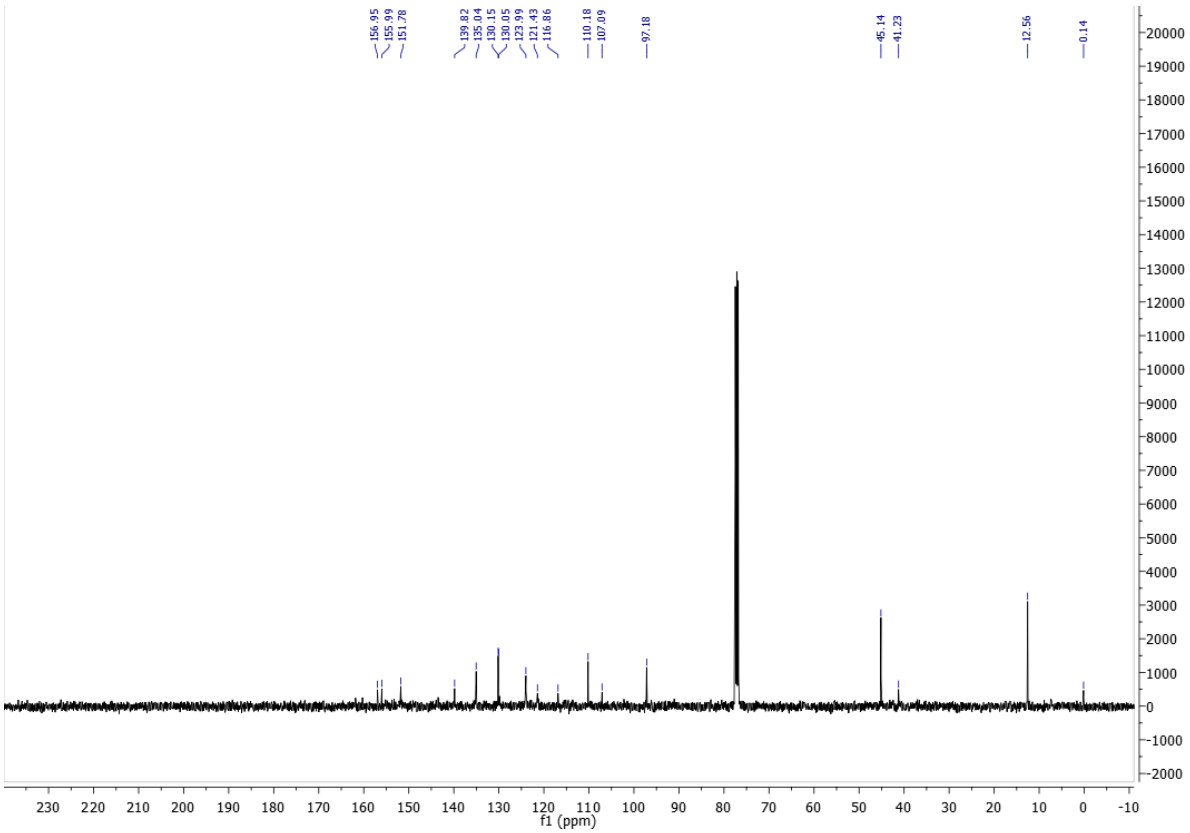

Figure 6.130 ^{13}C NMR spectrum of L^{imC} in $CDCl_3$

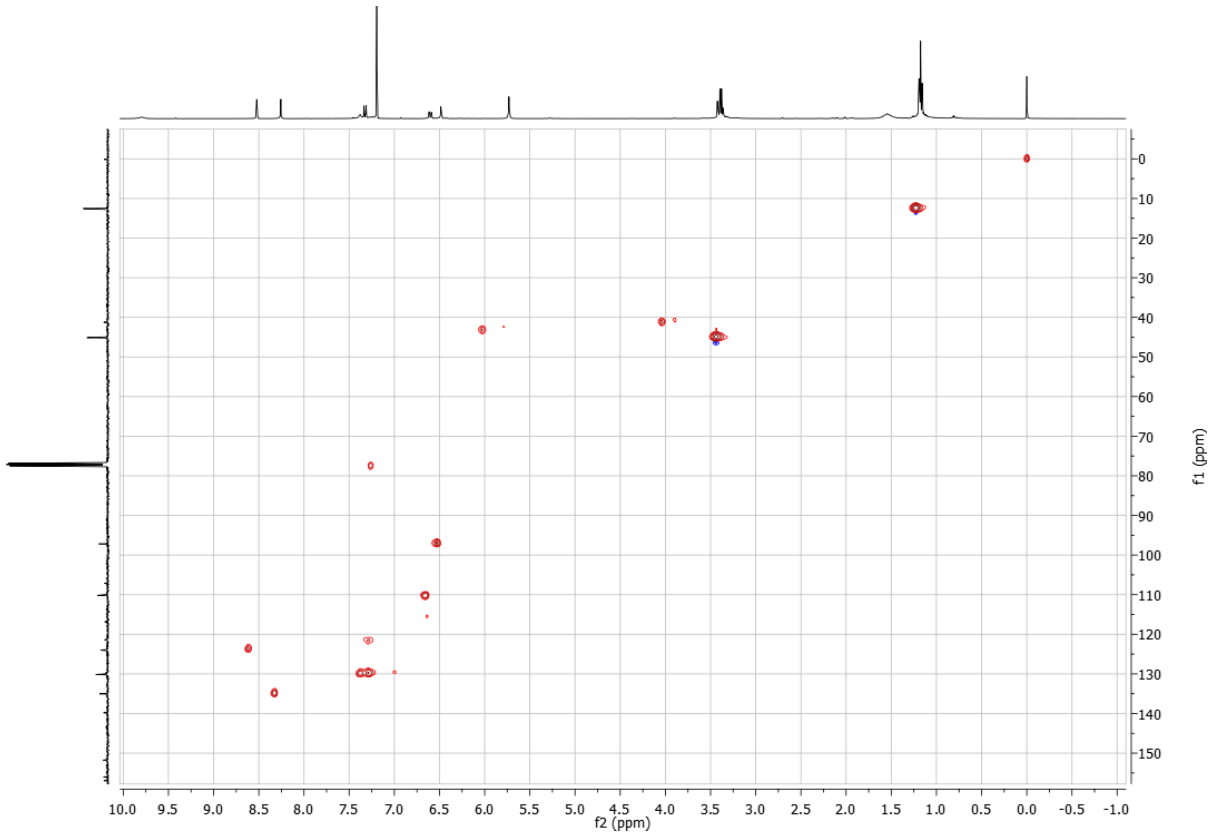

Figure 6.131 HSQC NMR spectrum of L^{imC} in $CDCl_3$

6.34 NMR spectrum of L

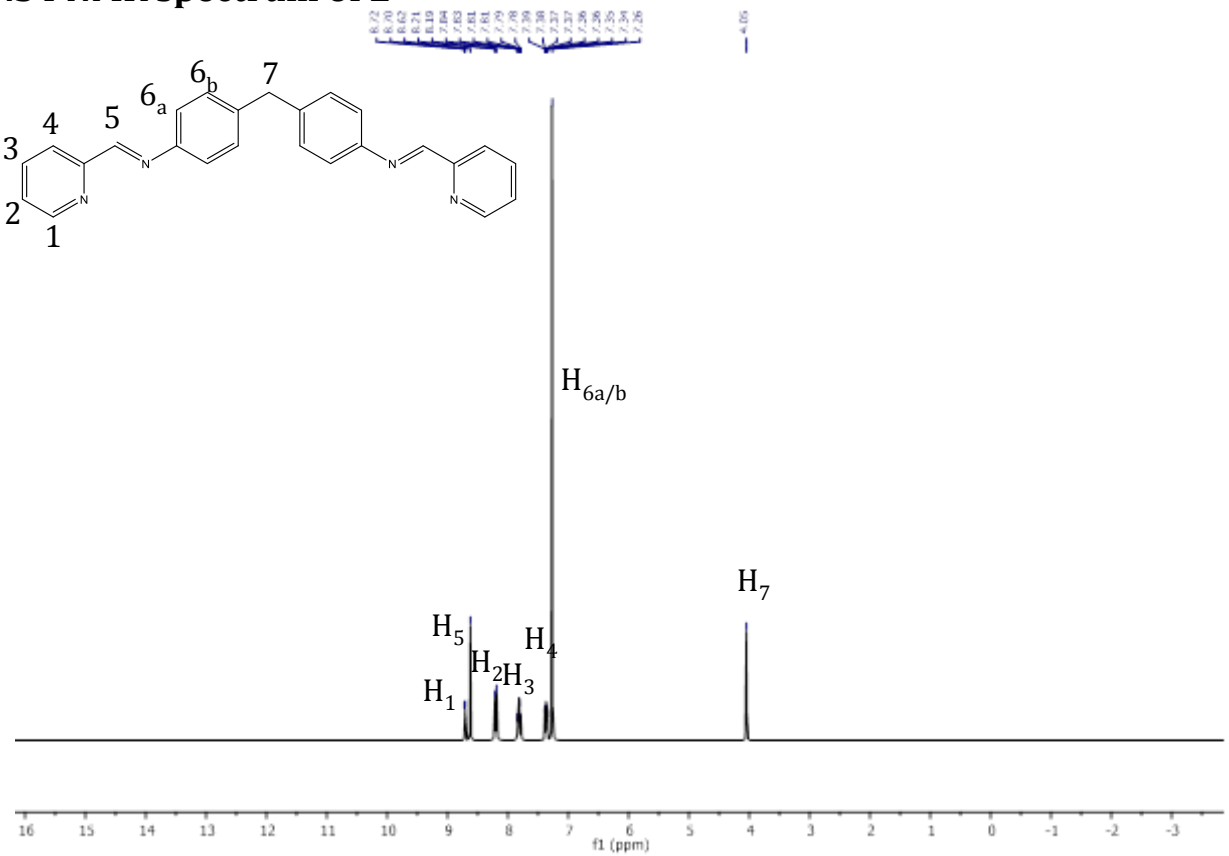

Figure 6.132 ^{1}H NMR spectrum of L in $CDCl_3$

6.35 NMR spectrum of $[Fe_2L_3]Cl_4$

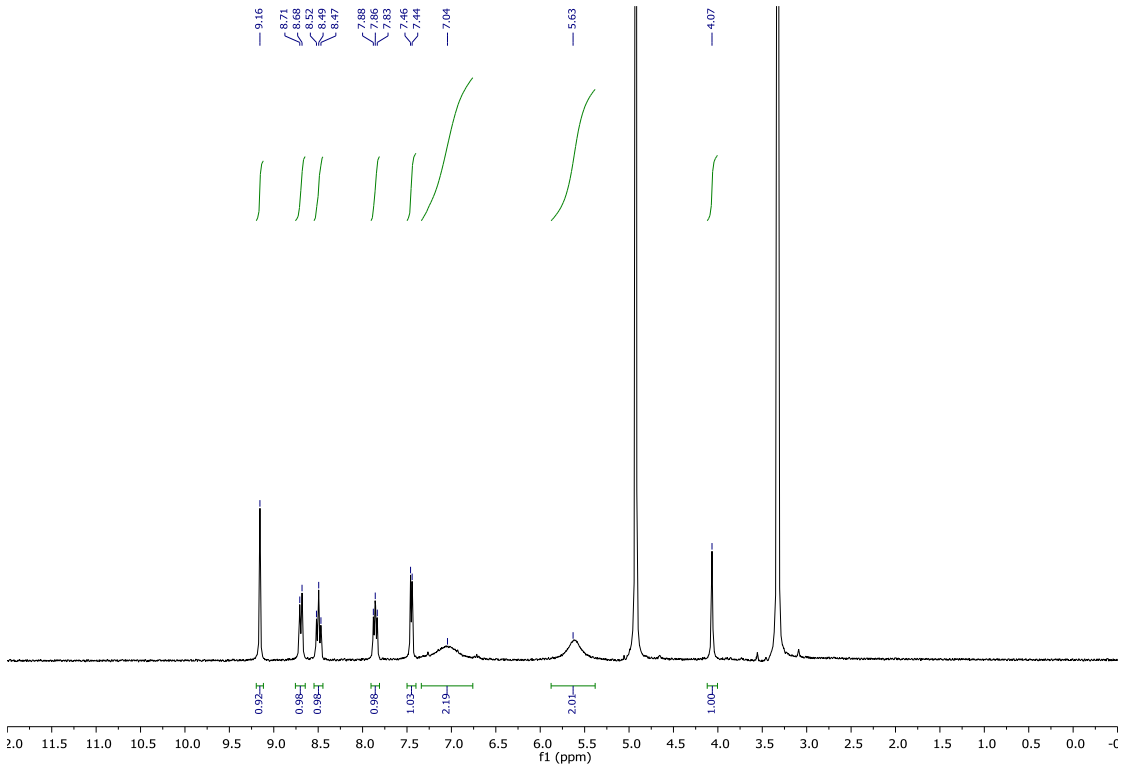

Figure 6.133 ^{1}H NMR spectrum of $[Fe_2L_3]Cl_4$ in CD_3CN

6.36 NMR spectra of L^{im}

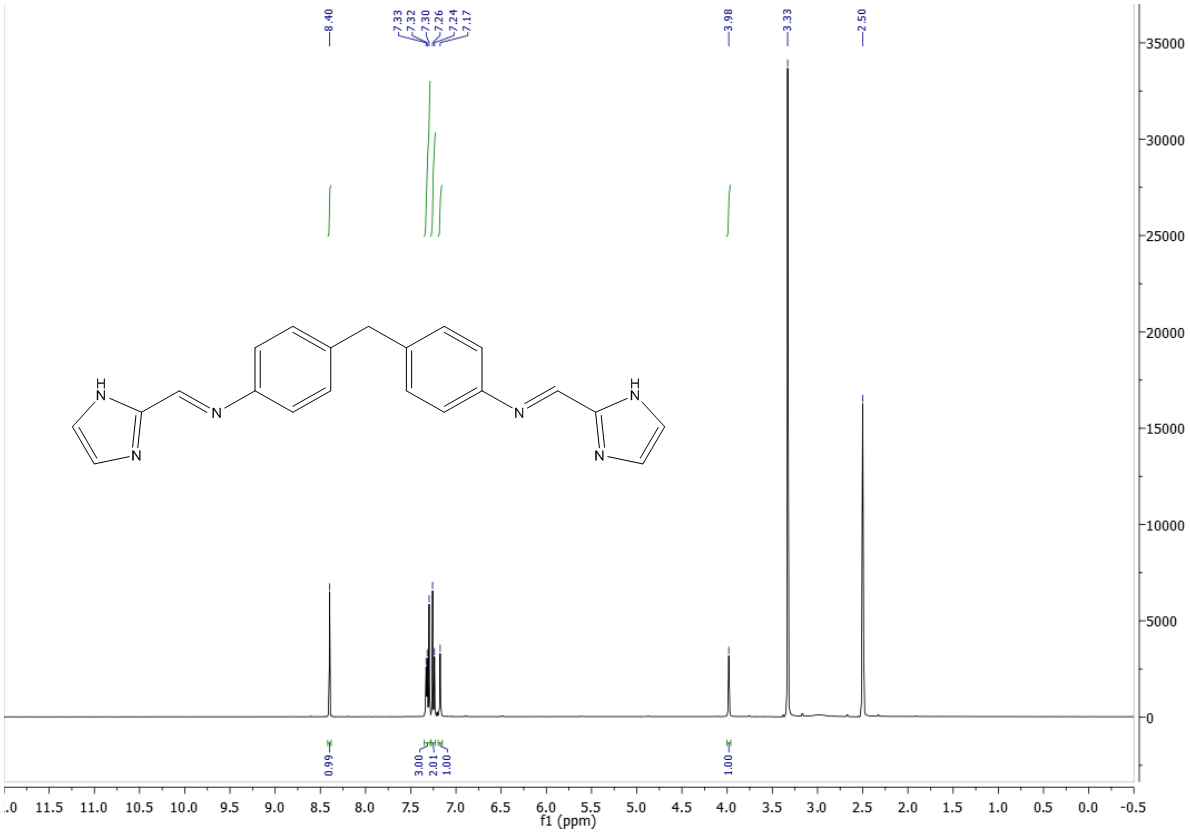

Figure 6.134 ^{1}H NMR spectrum of L^{im} in DMSO

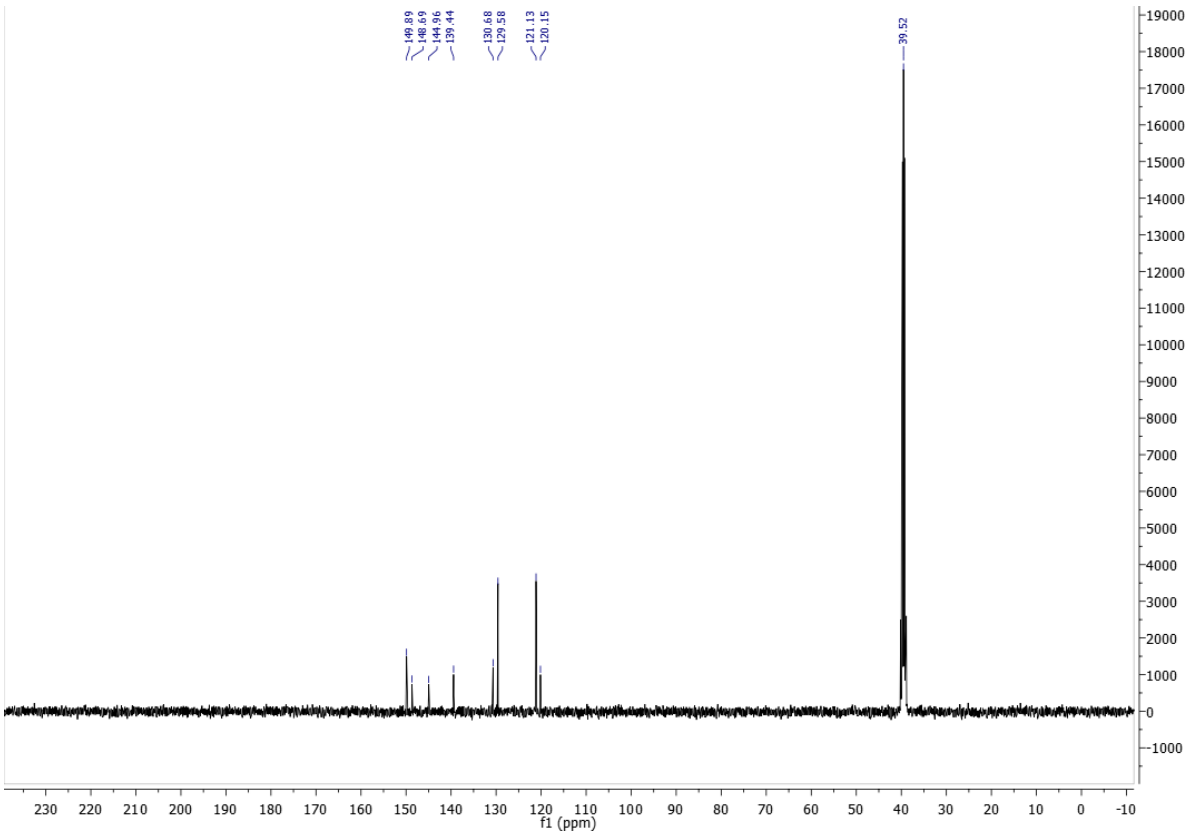

Figure 6.135 ^{13}C NMR spectrum of L^{im} in DMSO

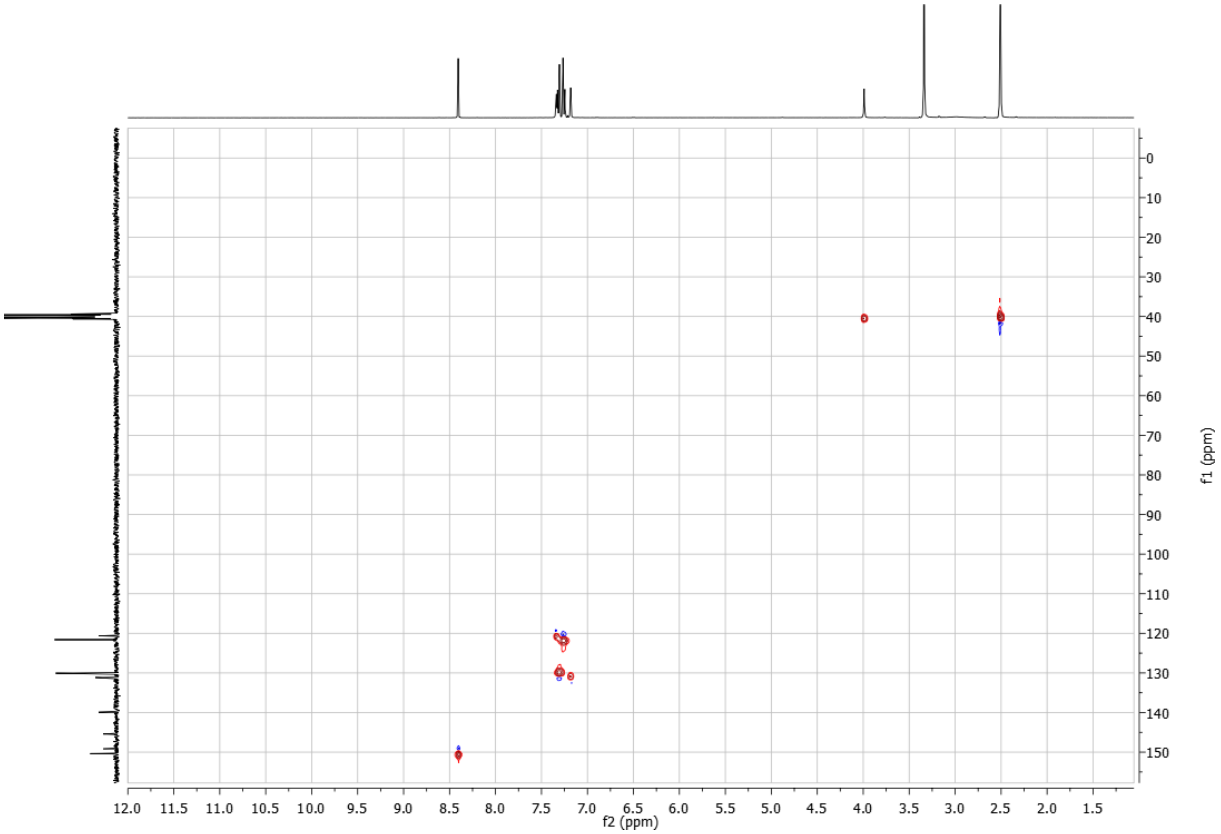

Figure 6.136 HSQC spectrum of L^{im} in DMSO

6.37 NMR spectra of dansyl _C3_N_3

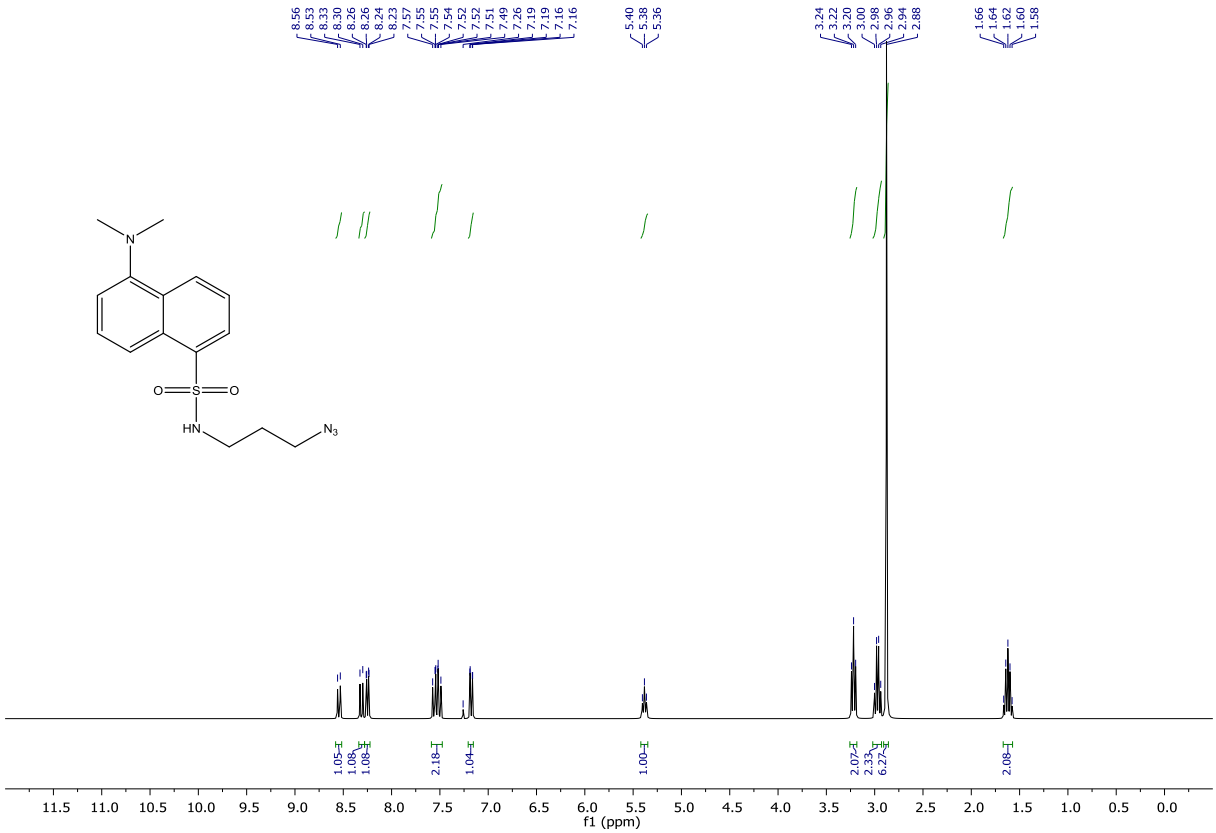

Figure 6.137 ^{1}H NMR spectrum of Dansyl _C3_N_3 in $CDCl_3$

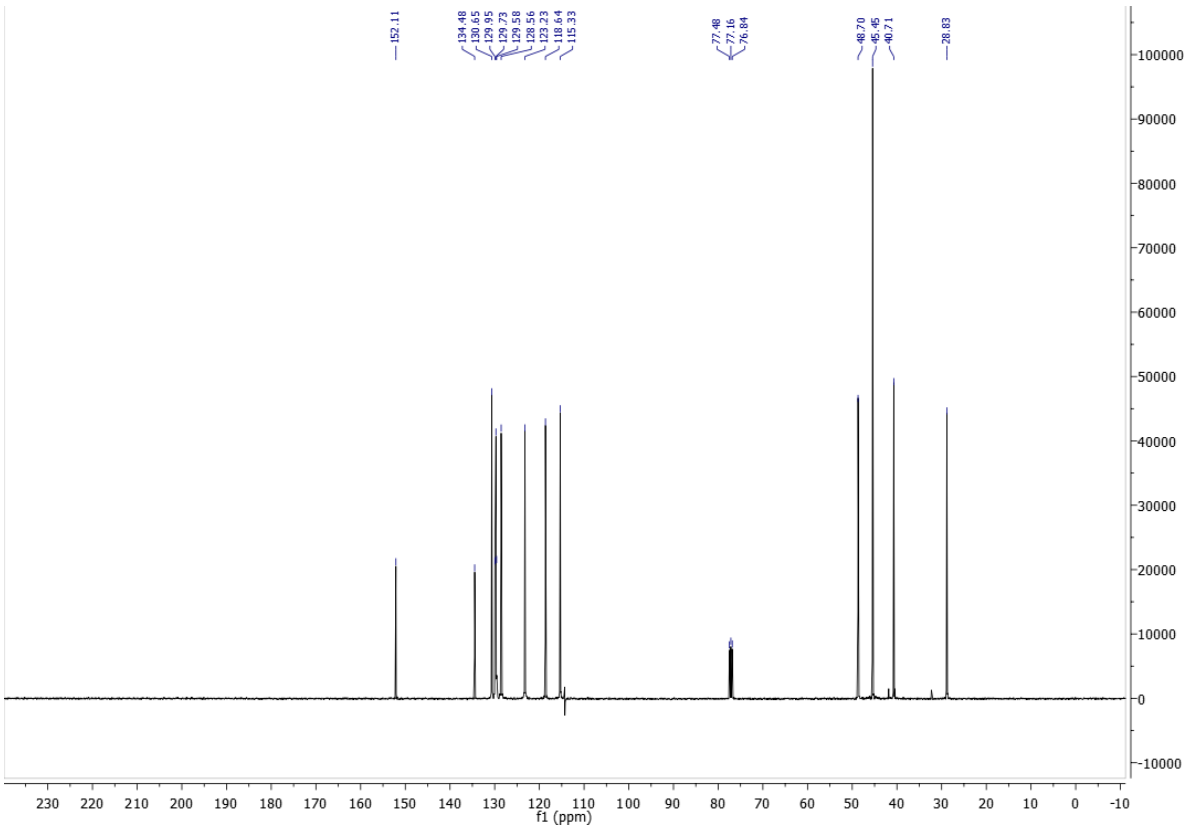

Figure 6.138 ^{13}C NMR spectrum of Dansyl _C3_N_3 in $CDCl_3$

6.38 NMR spectra of FITC_C3_N_3

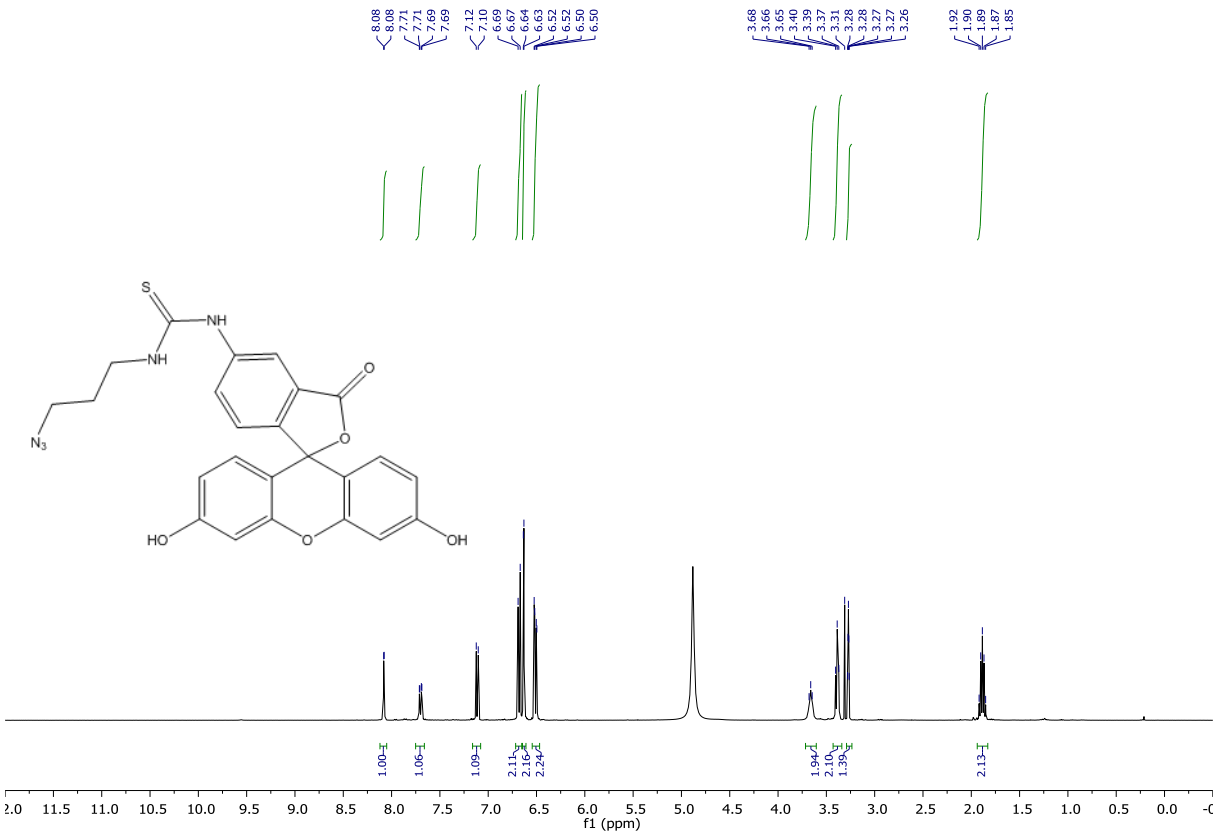

Figure 6.139 ^{1}H NMR spectrum of FITC _C3_N_3 in MeOD

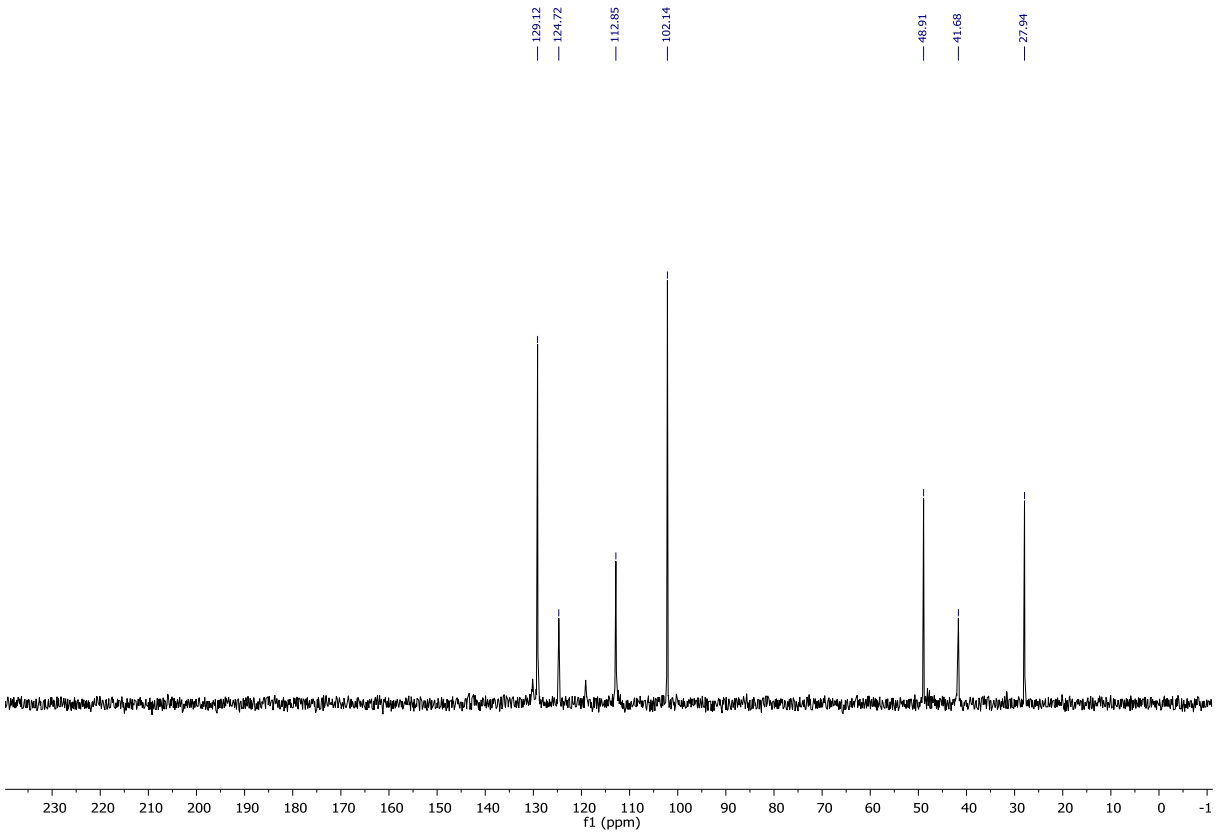

Figure 6.140 ^{13}C NMR spectrum of FITC_C3_N_3 in MeOD

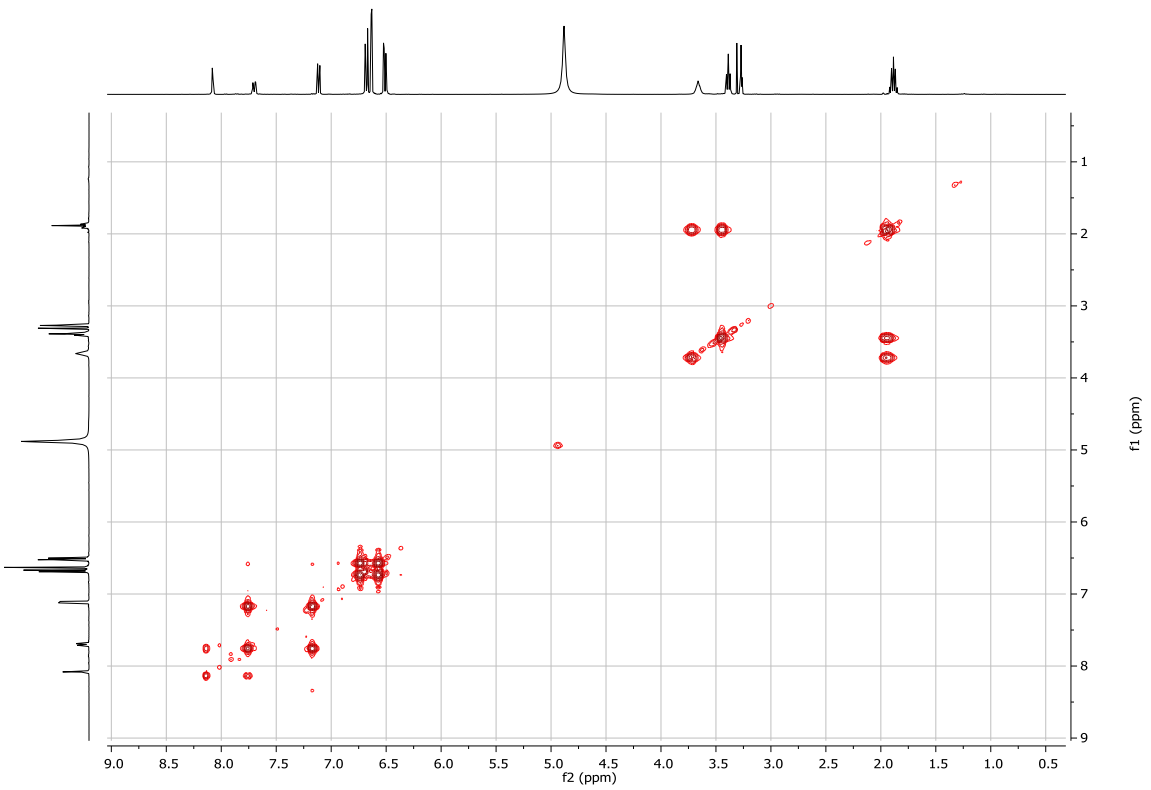

Figure 6.141 COSY NMR spectrum of FITC _C3_N_3 in MeOD

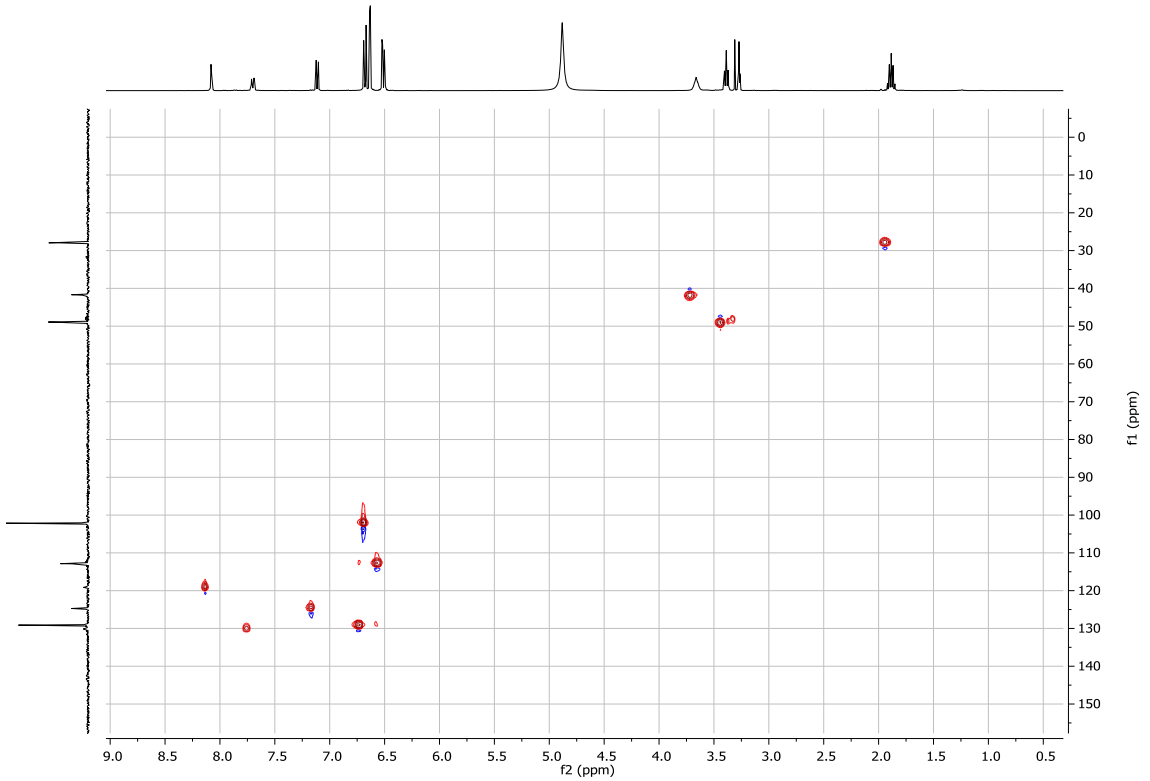

Figure 6.142 HSQC NMR spectrum of FITC _C3_N_3 in MeOD

6.39 NMR spectra of FITC_PEG3_N_3

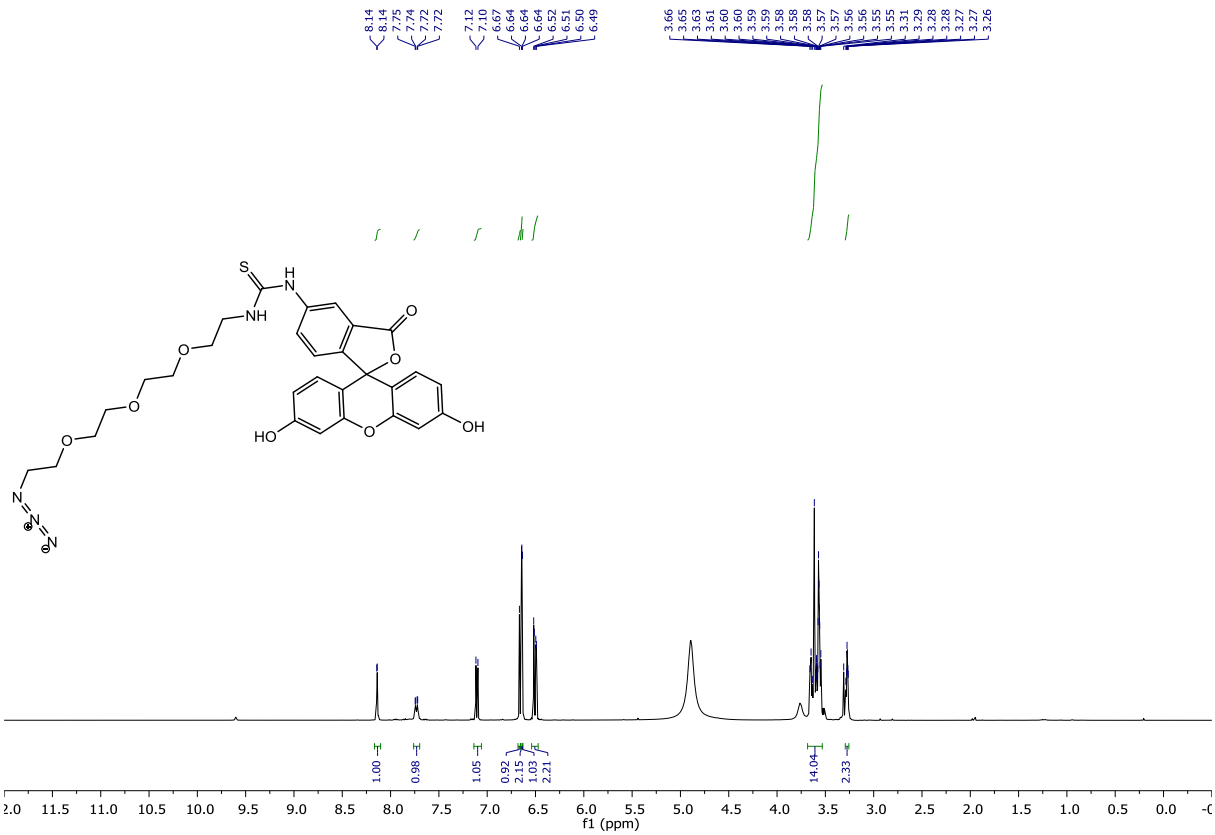

Figure 6.143 ^{1}H NMR spectrum of FITC_PEG3_N_3 in MeOD

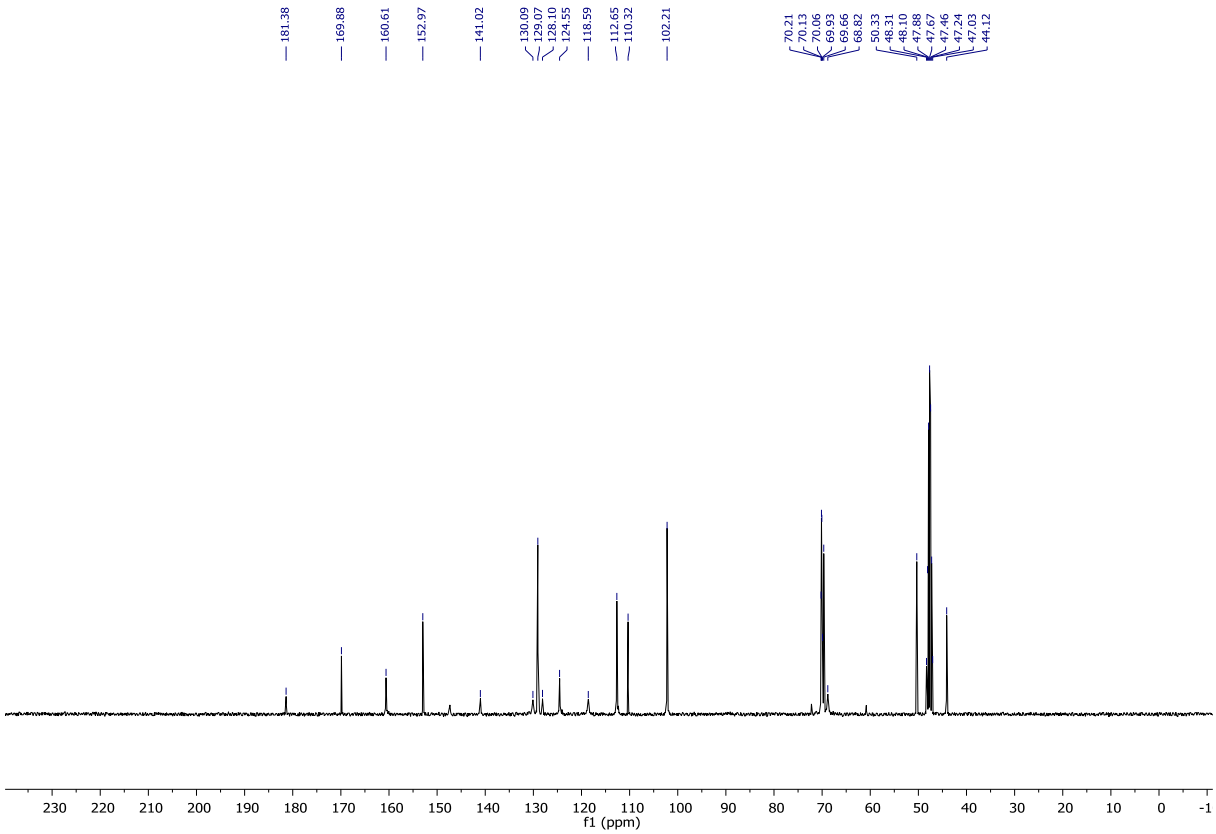

Figure 6.144 ^{13}C NMR spectrum of FITC_PEG3_N_3 in MeOD

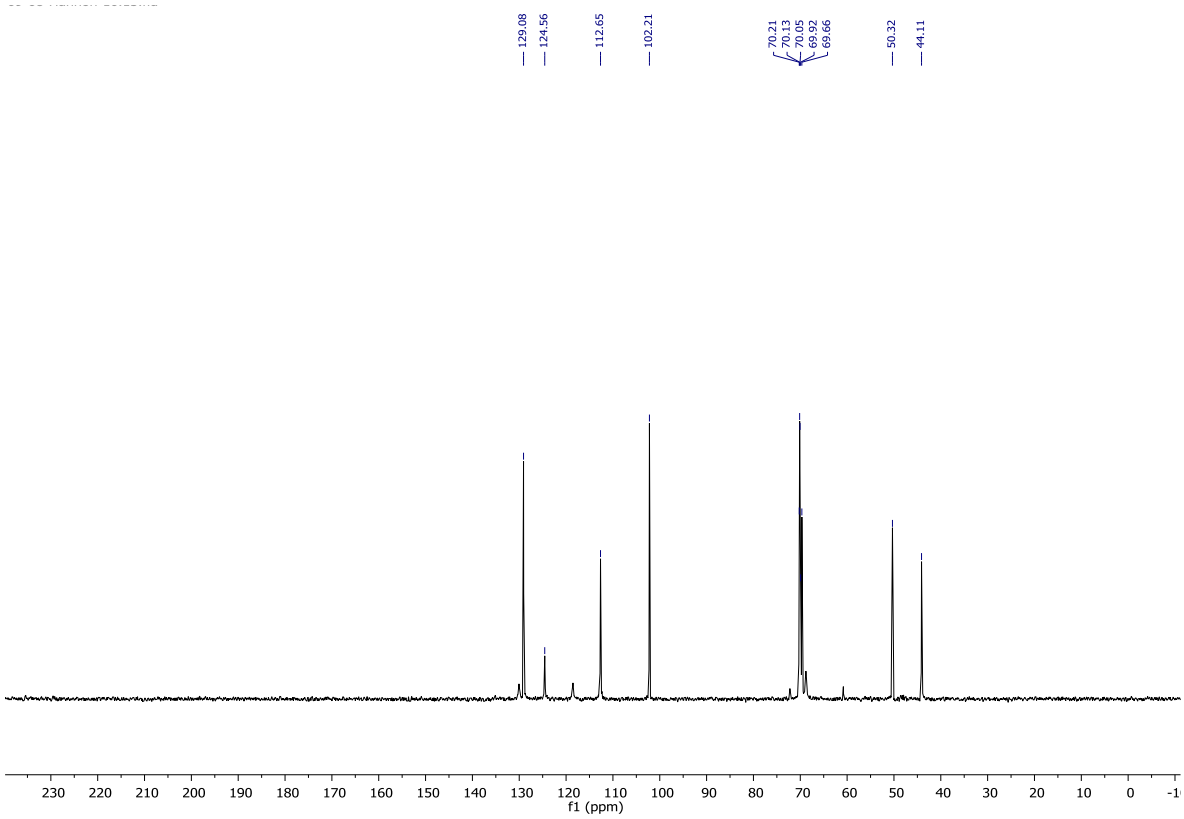

Figure 6.145 ^{13}C NMR spectrum of FITC_PEG3_N_3 in MeOD

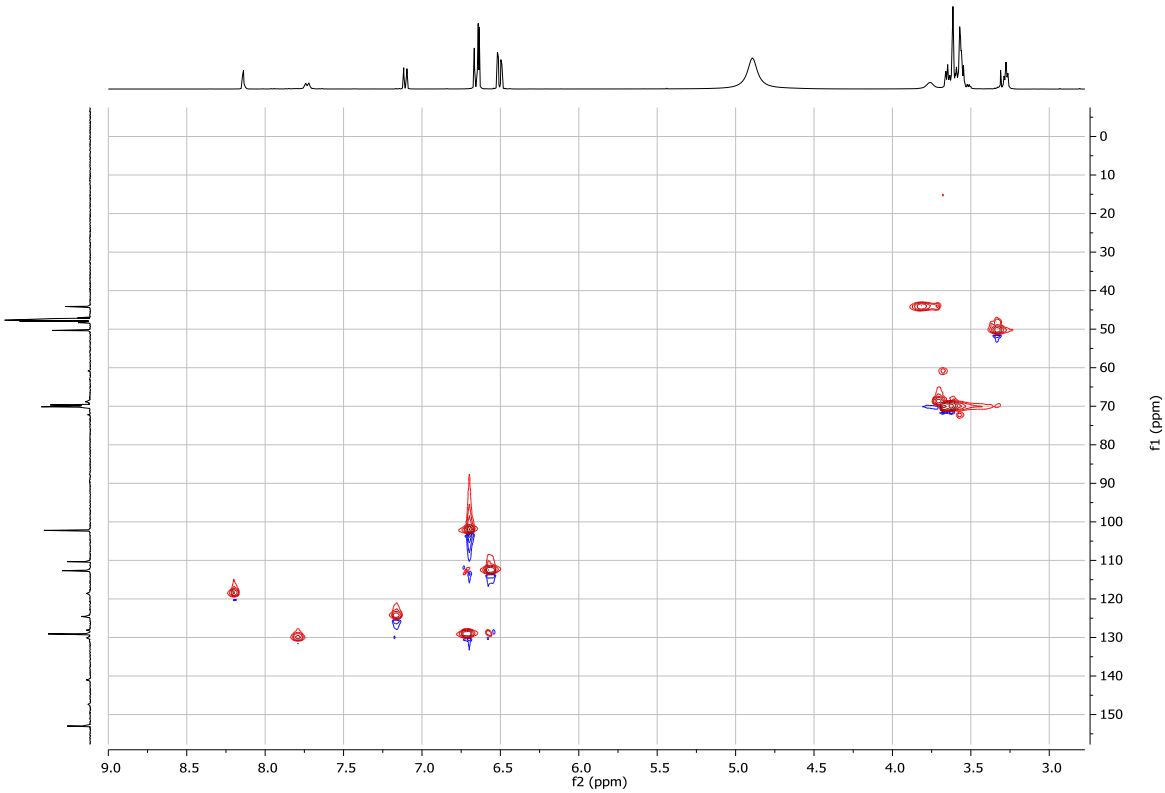

Figure 6.146 HSQC NMR spectrum of FITC_PEG3_N_3 in MeOD

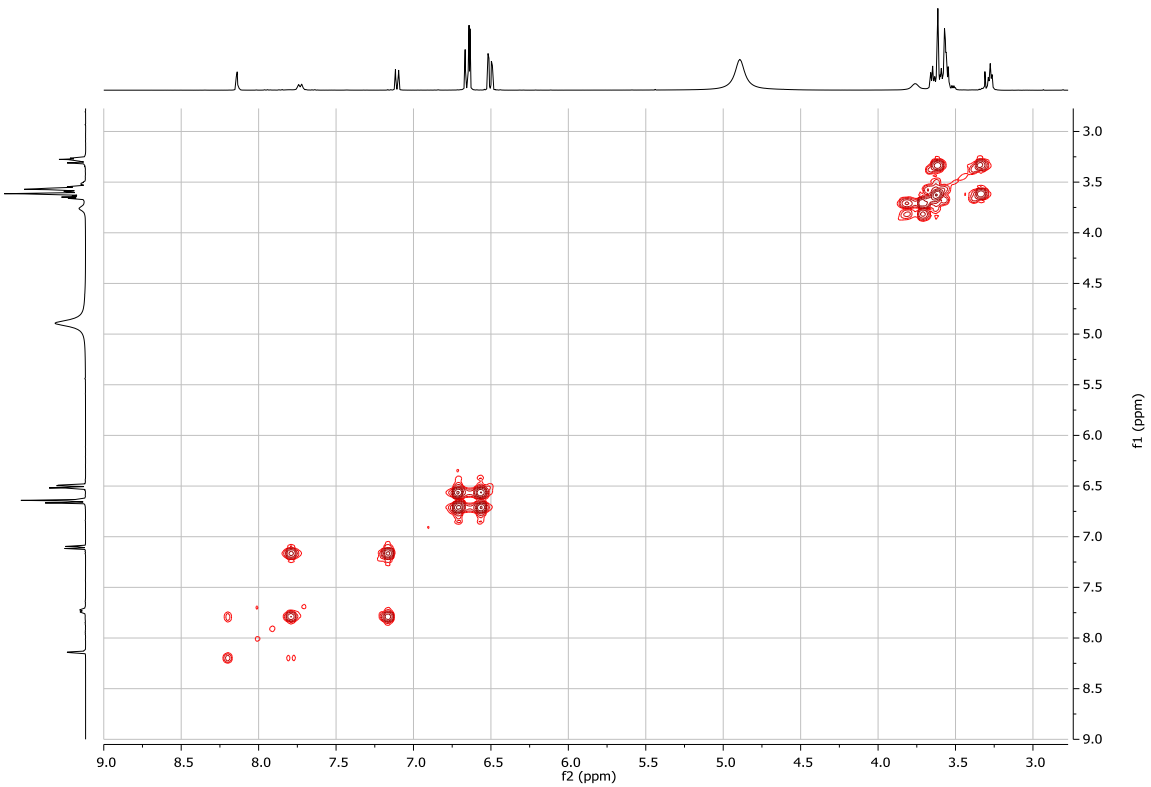

Figure 6.147 COSY NMR spectrum of FITC_PEG3_N_3 in MeOD

6.40 NMR spectrum of L^{TB5}

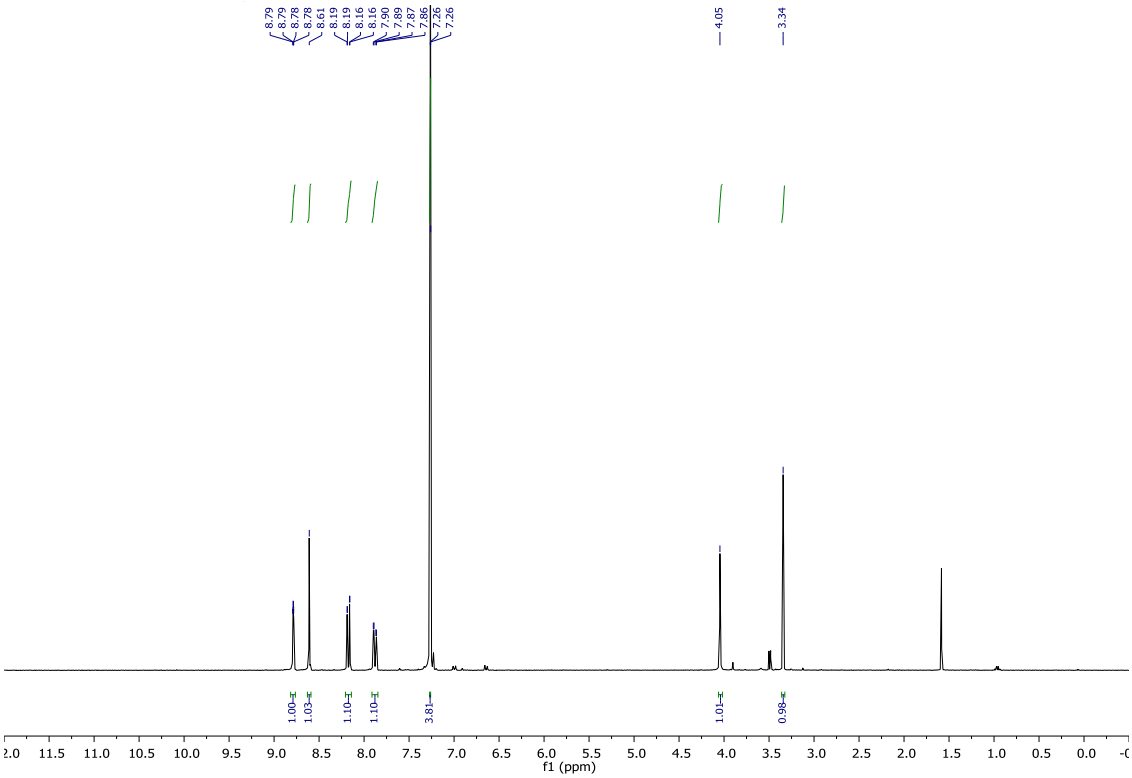

Figure 6.148 ^{1}H NMR spectrum of L^{TB5} in $CDCl_3$